PhD-FSTC-2018-04
The Faculty of Sciences, Technology and Communication

DISSERTATION

Defence held on 17/01/2018 in Luxembourg

to obtain the degree of

DOCTEUR DE L'UNIVERSITÉ DU LUXEMBOURG

EN BIOLOGIE

by

Anne Marie Elisabeth DIRKSE

Born on 25th August 1986 in Luxembourg (Luxembourg)

ADAPTIVE CAPACITIES OF CANCER CELLS IN GLIOBLASTOMA

Dissertation defence committee

Dr. Simone P. Niclou, dissertation supervisor and Vice-Chairman
Professor, University of Bergen (Norway)
Luxembourg Institute of Health (Luxembourg)

Dr. Serge Haan, Chairman
Professor, Université du Luxembourg (Luxembourg)

Dr. Bernard Rogister
Professor, Université de Liège (Belgium)
GIGA-Neurosciences, Liège

Dr. Petra Hamerlik
Danish Cancer Society Research Center, Copenhague (Denmark)

Dr. Elisabeth Letellier
Université du Luxembourg (Luxembourg)

The study in this thesis was performed at the Luxembourg Institute of Health (LIH) and funded by an individual AFR grant provided by the Luxembourg National Research Fond (FNR) and supported by the Fondation du Pélican de Mie et Pierre Hippert-Faber, under the aegis of the Fondation de Luxembourg. The project was realized in collaboration with the University of Applied Sciences in Dresden, the Technical University of Dresden and the Luxembourg Centre for Systems Biomedicine of the University of Luxembourg.

Affidavit

I hereby confirm that the PhD thesis entitled “Adaptive capacities of Cancer Cells in Glioblastoma” has been written independently and without any other sources than cited.

Luxembourg, 10.12.2017

Anne Dirkse

To Liette and Hanno

Acknowledgment

The last four years had been a very special and challenging time in my life which I could not manage without the help of many people. This support had many forms as motivating, guiding, and as well correcting me when I was wrong.

To start I would love to express my highest gratitude to the foundations, the Fonds National de la Recherche (FNR) of Luxembourg (AFR grant to AD) and the Fondation du Pélican de Mie et Pierre Hippert-Faber, under the aegis of the Fondation de Luxembourg. Without their financial support the PhD project could not have been realized in first place.

I want to thank all the collaborators which had been involved in this thesis project. Our collaborators in Dresden, Andreas Deutsch and Anja Voss-Böhme who gave me a very warm welcome during my stays in their institute. I am especially grateful that Thomas Buder took a lot of time and patients to explain me the Markov model and for a great collaboration. Single cell sequencing was performed with Alexander Skupin and Suresh Poovathingal had also been very fruitful and added an extra note to my project. Subsequent bioinformatical analysis was done by Arnaud and Petr from the Proteome and Genome Research Unit at LIH who were always happy to give me advice on computing or statistical questions. And of course, Elise and Nathalie our lab neighbors, were always ready for sharing equipment and experience. I am thankful as well for the statistical assistance of Sonia Leite and Nicolas Sauvageot from the Centre of Competence for Methodology and Statistics at LIH.

I also give big thanks to the National Flow Cytometry Platform, with Coralie Guérin and Léa Guyonnet for letting me use the FACSAria whenever I needed and for the realization of the ImageStream experiments. Especially René Brons, who became in meantime a cheerful friend. You thought me so much about flow machines; handling, maintenance and even repairing (and keeping the patience when I had been the culprit). I am very glad we stayed in contact after your retirement as I finally found someone who plays board games as seriously and eager as I do.

I give special thanks to Anais and Virginie B. who performed the mice transplantations and were so patient to teach me how to do this. As well for Steffi, Chantal (rest in peace) and Romain who did take care so nicely about the mice and were always ready for a vivid conversation during lunch.

All past and present members of the A-office; Katja, Virginie N., Anne and Ann-Christin, thank you so much for your discussions, suggestions and being a friend. Siu-Thin, for being such a great uncomplicated secretary and friend.
In also want to mention Jill the-best-technician-ever, Amandine, Vanessa, Katrin, Monika and Celine, always ready to help to make research on where to find things in the lab and always giving a hand. Sabrina, I thank you for your help on TCGA database and explaining it in a way I understood. Hélène it was always nice to speak with a PhD companion. Fred, Eric, Carole, Olivier, Alessandro, Matthieu G. and the entire Norlux group for great and inspiring discussions. You have all been great and helpful in the last years. As well Mathieu S. and Dzjemma for the great preliminary work with which they contributed to this thesis.

Anna, already the first week I worked with you, I realized that I am a lucky person to have you as a supervisor. You always gave me the freedom (unless you needed some autophagy western blots), to do whatever I wanted and let me do my planning. Your corrections and advices have sustainably influenced me. Anna without you, this adventure would not have been that cool and straight forward.

Simone, I thank you for giving me this big opportunity to work in your lab. You enormously encouraged and inspired me in my actions the last years. You were the boss with ready solutions, a clear plan and an open door.

I would also like to thank Serge Haan as member of my thesis committee and as the head of the doctoral school. In my time as student representative with Sean, you were always open for new ideas and projects. I also thank Sean for good team work.

I thank my study colleagues from university, Kata, Jan, Thomas, Johanna and Hanna it has been an honor to meet and study with you. Maastricht times continue, especially due to Anna, Sophie, and Elke. My friends here in Luxembourg, Patricia, Bob, Lynn, Seiler, Anne, Maxime, Marisa, Steffi, Ahmed, Jeannot, Laurent, Yves K., Martine, Yves R., Aline, Patrice, Franco, Claire. Thanks for distracting me when I needed it.

Of course my family, my lifelong support and backbone. Jang my walking lexicon, you were improving my general knowledge since I can remember. My parents, your endurance throughout my school career was impressive, not to forget that you almost lost hope that I would past successfully my high school. This is all your work.
At the very end, Mike, I thank you.

Table of contents

List of abbreviations

A

AACR - American Association for Cancer Research
aCGH - Array-Comparative Genomic Hybridization
AML - Acute Myeloid Leukemia
APL - Acute Promyelocytic Leukemia
ASCL1 - Achaete-Scute Family bHLH Transcription Factor 1
ATRA - All-Trans Retinoic Acid
ATRX - Alpha Thalassemia/mental Retardation Syndrome X-linked

B

BBB - Blood Brain Barrier
BCAN - Brevican
bFGF - Basic Fibroblast Growth Factor
BRAF - B-Raf Proto-Oncogene, Serine/Threonine Kinase
BSA - Bovine Serum Albumin

C

Ca2+ - Ionized Calcium
CaCl2 - Calcium Chloride
CDK - Cyclin Dependent Kinase
CDKN - Cyclin Dependent Kinase Inhibitor
cDNA - Complementary Deoxyribonucleic Acid
CDV - Cardiovascular Diseases
CHI31 - Chitinase 3 Like 1
CNER - National Ethics Committee for Research
CNS - Central Nervous System
CNV - Copy Number Variation
CO_2 - Carbon Dioxide
CSC - Cancer Stem Cell
CV - Coefficient of Variation

D

dH_2O - Distilled Water
DAPI - 4′,6-Diamidin-2-phenylindol
DC - Dendritic Cells

PDGFRA - Platelet Derived Growth Factor Receptor Alpha
DGE - Digital Gene Expression
DLL3 - Delta Like Canonical Notch Ligand 3
DMEM - Dulbecco's Modified Eagle Medium
DMSO - Dimethyl Sulfoxide
DNA - Deoxyribonucleic Acid
dNTP - Nucleoside Triphosphate
DSF - Disulfiam
DT - Doubling Time

E

ECM - Extracellular Matrix Components
EDTA - Ethylenediaminetetraacetic Acid
eGFP - enhanced Green Fluorescent Protein
EGF - Epidermal Growth Factor
EGFR - Epidermal Growth Factor Receptor
ELC - Electron Transporter Chain
EU - European Union
EV - Extracellular Vesicles

F

FACS - Fluorescence Activated Cell Sorting
FBS - Fetal Bovine Serum
FDA - Food and Drug Administration
FGFR - Fibroblast Growth Factor Receptor
FOV - Field of View
FSC - Forward Scatter
FUT4 - Fucosyltransferase 4

G

GABRA1 - Gamma-Aminobutyric Acid Type A Receptor Alpha1 Subunit
GBM - Glioblastoma
GFAP - Glial Fibrillary Acidic Protein

H

H&E - Hematoxylin and Eosin

HA - Hyaluran
HBSS - Hank’s Balanced Salt Solution
HIF - Hypoxia Inducible Factor

I

IDH - Isocitrate Dehydrogenase

J

JAK - Janus Kinase

K

KRAS - KRAS Proto-Oncogene, GTPase

L

LDA - Limiting Dilution Assay
LeX - Lewis X
LIF - Leukemia Inhibitory Factor

M

MAT - Matrix Size
MAP2 - Microtubule-Associated Protein 2
MDM - MDM Proto-Oncogene
MET - MET Proto-Oncogene, Receptor Tyrosine Kinase
Mg2+ - Ionized Magnesium
MRI - Magnetic Resonance Images
mRNA - Messenger Ribonucleic Acid

N

N_2 - Nitrogen
n_B - Number of Biological repeats
NEFL - Neurofilament Light
NES - Nestin
NF1 - Neurofibromin 1
NKX2-2 - NK2 Homeobox 2
Nod/Scid - Non-Obese Diabetic/ Severe Combined Immunodeficiency
NOS - Not Otherwise Specified

NSC - Neural Stem Cell

n_T - Number of Technical Repeats

O

O_2 - Oxygen

Olig2 - Oligodendrocyte Transcription Factor 2

OPN - Osteopontin

P

PBS - Phosphate Buffered Saline

PCR - Polymerase Chain Reaction

PCNA - proliferating Cell Nuclear Antigen

PDMS - Polydimethylsiloxane

PDX - Patient Derived Xenograft

PI - Propidium Iodide

PI3K - Phosphatidylinositol-4,5-Bisphosphate 3-Kinase Catalytic Subunit Alpha

PFA - Paraformaldehyde

PMT - Photomultiplier Tube

pO_2 - Oxygen Pressure

PROM1 - Prominin 1

PTEN - Phosphatase and Tensin Homolog

Q

QOM-Algorithm - Quasi-Optimization of the Root Matrix-Algorithm

R

RB1 - RB Transcriptional Corepressor 1

RNA - Ribonucleic Acid

RNA-seq - RNA-Sequencing

RTK - Receptor Tyrosine Kinase

S

scDNA-seq - Single Cell DNA Sequencing

scRNA-seq - Single Cell RNA Sequencing

SEM - Standard Error of the Mean

SLC12A5 - Solute Carrier Family 12 Member 5

SSC - Side Scatter
SSEA-1 - Stage-Specific Embryonic Antigen 1
STAT - Signal Transducer and Activator of Transcription
SPF - Specific-Pathogen-Free
SYT1 - Synaptotagmin 1

T

TBS - Tris-Buffered Saline
TCF4 - Transcription Factor 4
TCGA - The Cancer Genome Atlas
TIC - Tumor Initiating Cell
TMZ - Temozolomide
TOP2A - DNA Topoisomerase II Alpha
TP53 - Tumor Protein P53
tRNA - Transfer Ribonucleic Acid
tSNE - t-Distributed Stochastic Neighbor Embedding
TUBB3 - Tubulin Beta 3 Class III

U

U - Unit
UMI - Unique Molecular Identifier
USA - United States of America

V

VEGF - Vascular Endothelial Growth Factor
VHL - van Hippel-Lindau
VIM - Vimentin

W

WE - Window Extension
WES - Whole Exome Sequencing
WHO - World Health Organization

List of figures and tables

Summary

Glioblastoma (GBM) is a highly malignant brain tumor where no curative treatment is available. According to the cancer stem cell (CSC) hypothesis GBMs rely on a small subpopulation of cancer cells with stem-like properties responsible for tumor progression and recurrence. Recent experimental data from GBM and other cancers however suggest that CSCs cannot be defined by a specific marker expression and may in fact not be a stable entity but a population of cells adapting to a changing microenvironment. Here we examined inter- and intra-tumoral heterogeneity of GBM cells and their adaptation capacity based on stem cell-associated marker expression profiles. Tumor cell subpopulations were classified based on their expression of four chosen cell membrane markers (CD133, CD15, A2B5 and CD44) using multicolor flow cytometry. 16 subpopulations were separated and analyzed for their self-renewal capacity and their ability to reform the original heterogeneous cell population in different environmental conditions (normoxia, hypoxia, differentiation and *in vivo*). Mathematical modeling was applied to calculate state transitions between phenotypes and predict the adaptive response of tumor cells. Similar to GBM biopsies, we observed markers to be heterogeneously expressed in glioma stem-like cells and primary cultures. All analyzed tumor cell subpopulations were able to proliferate indefinitely and carried stem-cell properties including self-renewal potential. Moreover, all subpopulations were able to adapt their marker expression profiles to give rise to the original subpopulations. Interestingly, mathematical modeling revealed a different propensity in reforming the original heterogeneity between subpopulations over time, which was independent of their proliferation index. Each environment presented its specific equilibrium with defined proportions of the subpopulations. This equilibrium was reversible upon environmental change for each tested condition. Single cell RNA-seq analysis revealed no transcriptomic differences between subpopulations. Our results suggest that glioma stem-like cells do not represent a stable entity and that intra-tumoral heterogeneity in GBM at least partially results from a high cellular adaptation capacity. This implies that glioma treatment approaches should take into account the strong propensity of cancer cells for phenotypic state transitions.

Introduction

1. Brain tumors

Since 2010 cancer is the first cause of death in Luxembourg (Townsend et al., 2016, Santé, 2014). For many cancers such as breast, prostate or colorectal cancers, early diagnosis and improved therapy decreased mortality rates significantly in the Western world. Brain cancer, however, remains an exception. In Luxembourg, the mortality due to brain and other nervous system cancers is close to its incidence (5.9 deaths vs 7.5 new cases per 100'000 people), whereas only 1/3 of brain and other nervous system cancers in the United States of America (USA) is malignant (Ferlay J, 2012, Quinn T. Ostrom, 2016). Since 2012 Luxembourg has set up a national cancer register whose data evaluation may indicate similar mortality rates observed in the USA. Amongst all ages and sexes in Luxembourg and the European Union (EU), cancers of the brain and nervous system are the 16th most prominent cancers (**Fig. 1**) (Ferlay et al., 2013). The 2016 World Health Organization (WHO) classification of tumors of the central nervous system (CNS) distinguishes 17 groups of tumor types with each consisting of numerous subtypes representing distinct diseases (Louis et al., 2016). The most common non-malignant CNS tumor subtype is meningioma and the most common malignant tumor subtype is Glioblastoma (GBM). With an incidence rate of 5,47 per 100 000 children CNS tumors represent also the most common neoplasm under the age of 14 years (Quinn T. Ostrom, 2016).

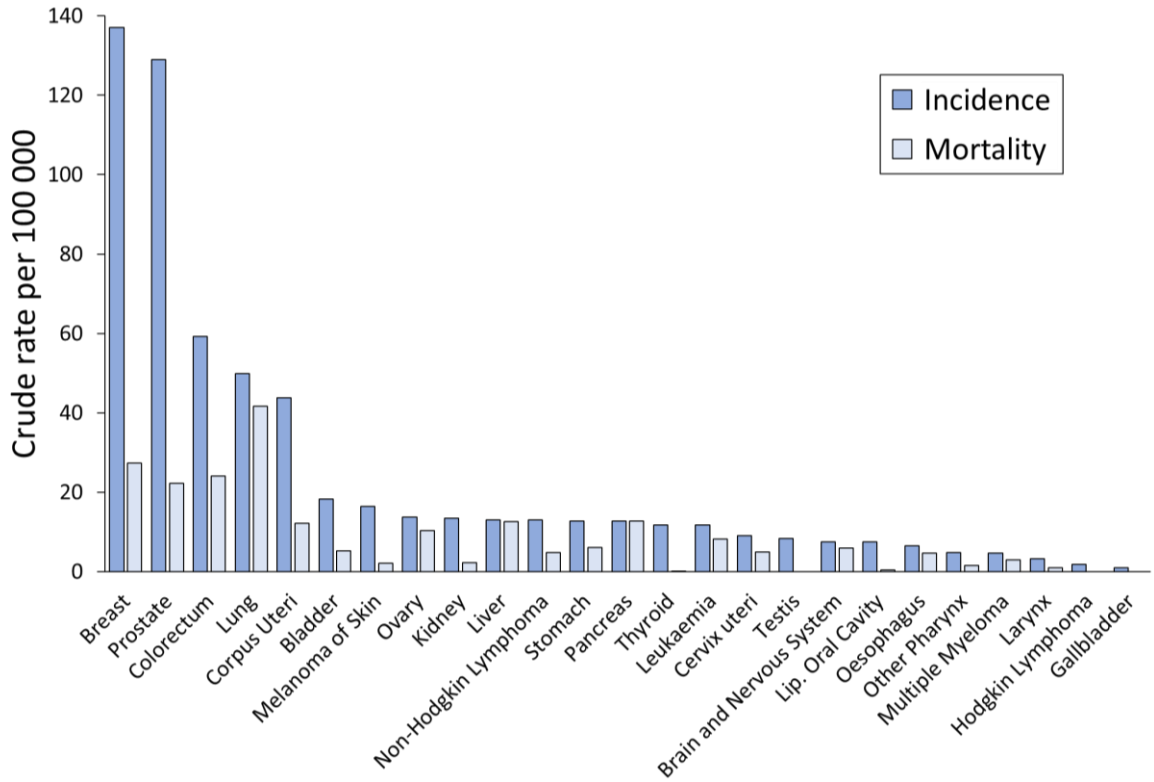

Figure 1: Incidence and mortality rate of different tumor types in 2012 in Luxembourg. Data was derived from the Globocan webtool (Ferlay J, 2012). Bar plot displays a ranking of the incidence ('dark blue') and mortality ('light blue') of the 25th most common cancers in Luxembourg. Number of

deaths and of new cancer cases are represented as a crude rate per population of 100'000 people. While breast and prostate cancers show highest incidence, less than 25% of these cases result in death. In contrary, brain and CNS cancers are less common (16th place), but survival is very low.

1.1. Diffuse gliomas

Brain and nervous system cancers are distinguished based on their cell of origin. For instance, meningiomas arise from the meninges whereas schwannomas originate from Schwann cells. This thesis focuses on diffuse gliomas that are derived from the glial tissue present in the brain. In the USA, diffuse gliomas represent the most common CNS cancer type and account for 80% of all malignant brain tumors (Quinn T. Ostrom, 2016).

Traditionally diffuse gliomas were defined based on their histopathological features (Louis et al., 2007). Since 2016 the WHO classification of CNS tumors includes in addition molecular profiling (Louis et al., 2016). Amongst diffuse gliomas belong grade II and III diffuse astrocytic tumors, grade II and III oligodendrogliomas and grade IV GBMs where tumor grading scheme was taken over from the previous WHO classification (Louis et al., 2007, Louis et al., 2016). These diffuse gliomas are distinguished based on the presence or absence of a mutation in the isocitrate dehydrogenase gene (IDH) (**Fig. 2**). Most common IDH mutations are the R132 for IDH1 and on the R172 for IDH2 (reviewed extensively by (Megova et al., 2014)). IDH mutated diffuse gliomas are further subdivided in diffuse gliomas characterized by the TP53 mutation and loss of ATRX (astrocytic lineage) and 1p/19q codeleted gliomas (oligodendroglial lineage) (Louis et al., 2016). Although presently not clear, IDH mutant GBM most likely represent an aggressive version of diffuse astrocytoma grade III, as oligodendroglioma grade III normally do not develop into grade IV tumors (Yan et al., 2009). IDH wild-type gliomas are mostly primary GBM (99,1%), and only rare cases of IDH wild-type lower grade gliomas are described (0.9%). The latter is only a provisional WHO category as it is less defined. Although glioma classification has improved by the integration of molecular characteristics, some uncertainties, such as IDH wild-type lower grade glioma and IDH mutant GBM subtypes, need to be resolved in future.

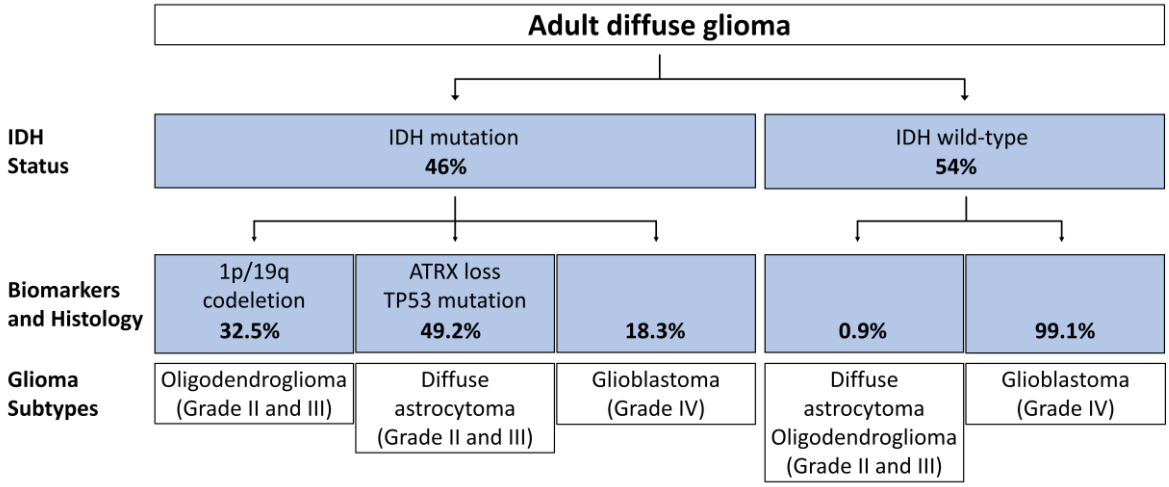

Figure 2: Classification of diffuse gliomas based on genetic characteristics *(Louis et al., 2016, Paul et al., 2017, Louis et al., 2007)*. Diffuse gliomas are classified based on IDH mutation status into IDH wild-type resulting in grade IV GBM or lower grade glioma (diffuse astrocytoma grade II and III or oligodendroglioma grade II and III) and IDH mutated. Presence of 1p/19q codeletion marks oligodendroglioma grade II and III whereas ATRX loss combined with TP53 mutation characterizes diffuse astrocytoma (grade II and III). IDH mutated GBM most probably develops from diffuse astrocytoma grade III. Percentages were described from (Paul et al., 2017) based on the glioma TCGA dataset. Tumor samples were categorized based on the 2016 WHO classification (Louis et al., 2016) and tumor grades were applied according to 2007 WHO classification (Louis et al., 2007).

1.2. Glioblastoma

GBM is the most aggressive grade IV brain tumor with a median survival of 14 months and a 2-year survival rate of only 26% (Stupp et al., 2005). Primary GBM accounts for 90% of all GBM incidences. They develop de novo and are present in more elderly patients, whereas secondary GBM arises from lower grade astrocytoma (Ohgaki and Kleihues, 2013). GBM is regarded as a sporadic cancer, however, it can be associated with Turcat syndrome B and Cowden disease (Collins, 2004). To date, no risk factors for GBM are known.

1.2.1. Histopathological features of GBM

Morphologically primary and secondary GBM are undistinguishable (Furnari et al., 2007). Both present a necrotic core accompanied with abnormal newly formed blood vessel (angiogenesis) (**Fig. 3.a**). Tumor borders are not clearly delineated due to its highly infiltrative behavior towards healthy brain tissue. An invasive front is particularly visible through the corpus callosum. Therefore, both hemispheres are commonly affected with cancer cells. Another macroscopic feature of GBM comprise squeezed ventricles, which results from an increased tumor volume. Furthermore, the blood-brain-barrier and blood vessels in the tumor core are disrupted and leaking (Louis et al., 2007, Kleihues et al., 1993). GBM was shown to develop with no preference in each part of the brain (frontal, parietal, temporal, occipital and the cerebellum) (Denicolai et al., 2016) and GBM development may be multifocal (Kleihues et al., 1993).

Histologically, GBM tumor cells are highly mitotic compared to non-tumor cells and demonstrate atypical nuclei. Other common features show hypercellularity and cellular pleomorphism (**Fig. 3.b**). As GBM cells are highly proliferative, cells in the tumor core experience nutritional shortage, which the tumor attempts to overcome by the formation of new vessels. However, these vessels are often immature, enlarged, tortuous and hyperpermeable resulting in abnormal blood flow (**Fig. 3.c**). Nutritional shortage results eventually in cell death, which can be observed by the necrotic core surrounded by “pseudopallisading” cells (**Fig. 3.d**) (Kleihues et al., 1993, Furnari et al., 2007, Miller and Perry, 2007). GBMs demonstrate these histopathological features at different degrees which may vary between patients.

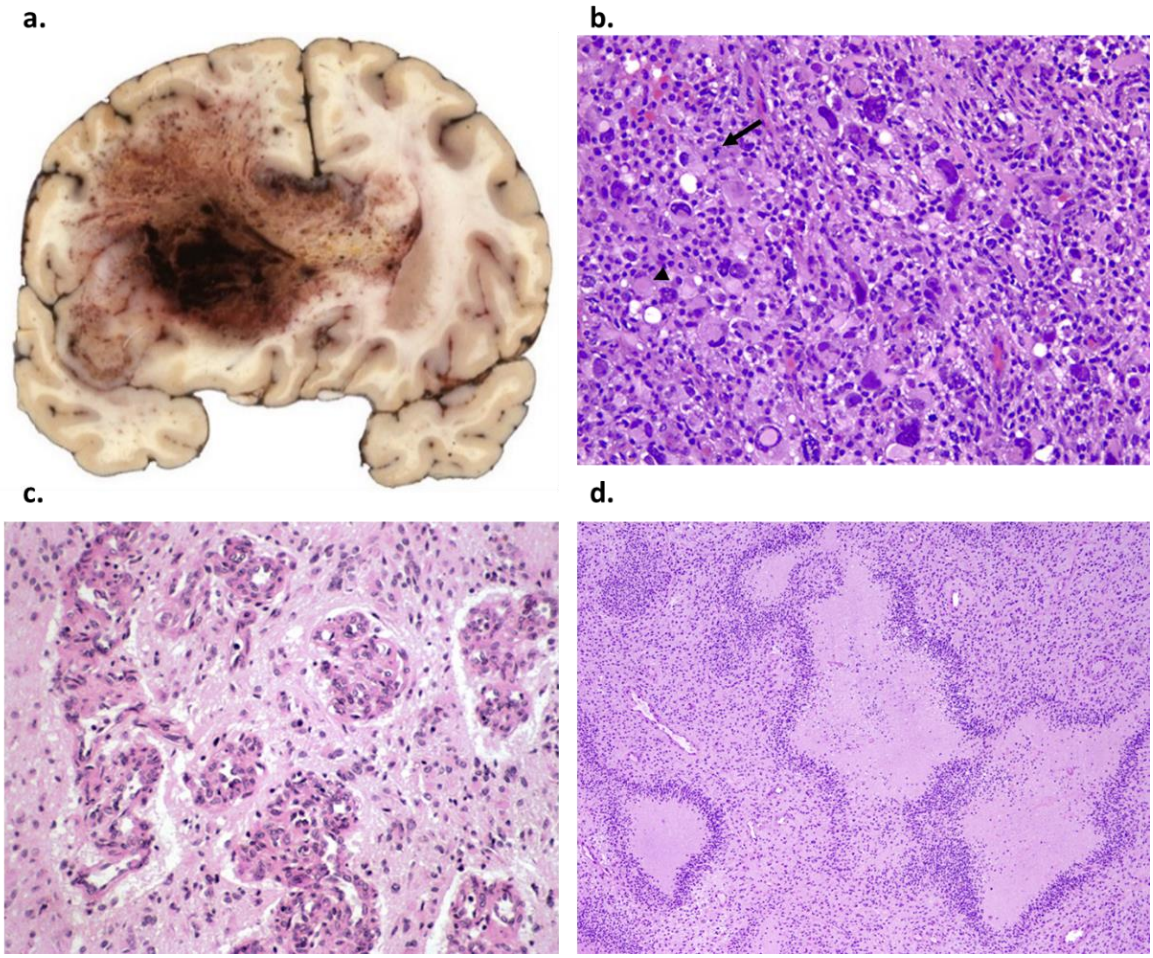

Figure 3: Macro and microscopic features of GBM. a. Coronal brain section displays GBM tumor. Tumor has a necrotic core with hemorrhages and is highly infiltrative into adjacent tissue. Figure was used from (PubCan, 2014). **b.** Microscopic hematoxylin and eosin (H&E) staining shows cellular anaplasia (arrow) and giant cancer cells (arrow head). **c.** Increased proliferation of blood vessel endothelial cells is typical for GBM. **d.** Necrotic cores are surrounded by 'pseudopallisading' cells.Figure 5.b,5.c and 5.d was used from (Agamanolis, 2017).

1.2.2. Glioblastoma treatment

Current treatment of GBM consists of maximal surgical resection, radio and chemotherapy with temozolomide (TMZ). This treatment was shown to prolong survival from 12.1 to 14.6 months (Stupp et al., 2005). Despite these advances, most GBMs reoccur in a more aggressive phenotype (Weil, 2006). Therefore, most treatment approaches are palliative and intend to increase quality of life by relieving pain and other symptoms.

Maximal tumor resection is supported by specifically visualizing GBM tumor cells with 5-Aminolevulinic-based fluorescence during surgical intervention. However, even very aggressive surgical removal does not target all infiltrative tumor cells. Therefore, additional post-operative irradiation doses of 5000 to 6000 cGy attempt to eliminate residual tumor

cells. Methylated promoter regions of the *MGMT* gene were shown as positive prognostic factor for adjuvant TMZ therapy (Esteller et al., 2000, Hegi et al., 2005).

Drug treatment for GBM encounters a special requirement compared to cancers in other body parts. Drugs need to pass the BBB and to be instantly effective as patient survival is very short. In the last decade, only few drugs appeared promising before entering clinical trials. Anti-angiogenic treatment, which targets new blood vessel formation and stimulates its normalization, was intensively tested in clinical trials, but none of the tested antiangiogenic agents such as bevacizumab and cediranib, showed improved overall survival (Gerstner and Batchelor, 2012). Although clinical phase III trials did not show a survival benefit, bevacizumab was shown to prolong disease free survival and was therefore approved for recurrent GBM by the Food and Drug Administration (FDA) in the United States (US) (Chinot et al., 2014, Fine, 2014). Effective treatment for GBM patients is still not in sight.

1.2.3. Molecular characterization of GBM

GBM has been extensively characterized in the last years at the genetic and transcriptomic level. Through projects such as the Cancer Genome Atlas (TCGA), the genetic profile of GBMs has been unraveled. 291 GBM patient samples were sequenced and analyzed for their genetic aberrations. The majority of dysregulated genes comprised *TP53*, *PTEN*, *NF1*, *EGFR*, *RB1*, *PIK3RI* and *PIK3CA*. Most gene amplifications were detected in *EGFR*, *PDGFRA* and *MET* proto-oncogene (RTK signaling) (Cancer Genome Atlas Research, 2008, Brennan et al., 2013). Similarly, in a study of 55 GBM biopsies, signaling pathways involving the proteins involved in RB signaling (p16(INK4A), p15(INK4B), CDK4/6 and pRb), TP53 signaling (p14(ARF), MDM2/4 and p53) and RTK signaling (EGFR, VEGFR, PDGFRA and PTEN) were dysregulated in 87%, 87% and 71% of the cases, respectively (Yin et al., 2009). Comparable results were obtained from other groups (Ohgaki and Kleihues, 2013, Parsons et al., 2008, Beroukhim et al., 2007). Collectively these data identified 5 signaling pathways mostly affected by genetic aberrations in GBM: RTK (66%), PI3K (60%), MAPK (13%), TP53 (86%) and RB1 (79%) signaling (Brennan et al., 2013) (**Fig. 4.a**).

At the transcriptional level, gene expression data were extensively analyzed for subgroup classification according to patient survival. In 2006, Phillips and colleagues subdivided high grade gliomas into proneural, proliferative and mesenchymal GBMs based on the signature of 35 genes in a cohort of 76 tumor samples (Phillips et al., 2006). Subgroups varied in patient survival, where proneural and mesenchymal demonstrated worst prognosis.

However, tumor samples in this study were not all GBM, but contained several grade III astrocytoma.

Besides genetic aberrations, the TCGA project in 2008 measured also DNA methylation pattern and transcriptomic data of GBM and lower grade glioma samples. The database contains clinical and molecular information from 1122 patients (Brennan et al., 2013, Ceccarelli et al., 2016). These publicly available data of glioma samples were further analyzed and classified into four subgroups: mesenchymal, neural, proneural and classical (Verhaak et al., 2010) (**Fig. 4.b**.) Analysis was performed by consensus average linkage hierarchical clustering of 173 GBM patient samples (Monti et al., 2003), where gene signature for each subcategory was based on the expression of 210 genes. To date, the GBM classification of Verhaak based on gene expression data is most widely used in the scientific community although the clinical relevance was only clear in proneural GBM. This subgroup contained a higher percentage of secondary GBM than the other GBM subgroups. Since IDH mutated GBM show longer survival, overall survival benefit is also observed in the proneural subgroup (Ceccarelli et al., 2016). Subgroups correlate to genetic aberrations of *PDGFRA* amplification/*IDH* and *PIK3R1* mutation (proneural), *NF1* mutation/loss (mesenchymal) and *EGFR* amplification (classical and neural), however the genetic aberrations are not exclusive for specific subgroups (Verhaak et al., 2010, Brennan et al., 2013, Cancer Genome Atlas Research, 2008). These genetic aberrations lead to the activation of core signaling pathways; in proneural cancer cells HIF1α, PI3K and PDGFRA signaling is often upregulated, whereas TNF combined with NFκB pathways and Notch with SHH pathways are frequently active in mesenchymal and classical subgroups (Verhaak et al., 2010, Agnihotri et al., 2013). However, recent work of the Verhaak group based on tumor-intrinsic signature demonstrated that the neural subgroup originated from the gene signature found in healthy brain tissue (Wang et al., 2017). Therefore, the transcriptomic classification in GBM should be adjusted to solely 3 subgroups, similar to the proposal of Phillips et al. in 2006. Moreover, a major drawback of subgroup classification comes along with cancer cell variety within one tumor samples. Transcriptomic analysis at single cell level and of multiple biopsies of one tumor revealed that multiple subgroups coexist within one patient sample, showing that classification of one patient tumor based on bulk transcriptomic data does not reflect entire intratumoral complexity (Patel et al., 2014, Sottoriva et al., 2013).

a.

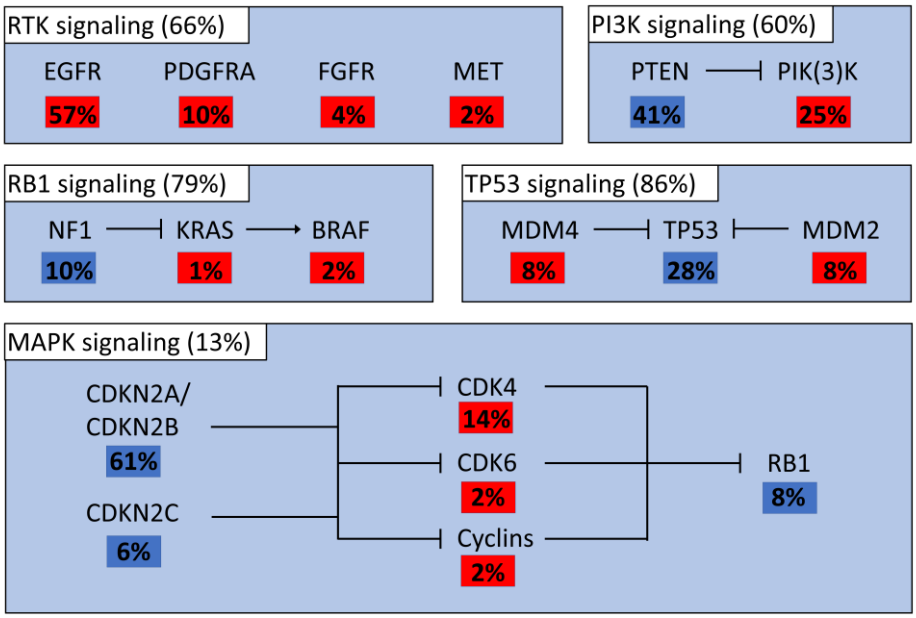

b.

GBM subgroups	Proneural	Mesenchymal	Neural	Classical
Genetic Marker	Amplification: PDGFRA (11%) Mutation: IDH (30%) TP53 (54%) PIK3R1 (19%) Loss/Mutation: CDKN2A (n.a.) PTEN (16%)	Loss/Mutation: NF1 (37%) TP53 (32%) PTEN (32%)	Amplification: EGFR (26%)	Amplification/ Mutation: EGFR (32%) Loss: CDKN2A (n.a.) Loss/Mutation: PTEN (23%)
Transcriptional Marker	Olig2 PDGFRA NKX2-2 BCAN DLL3 ASCL1 TCF4	CHI31 CD44 VEGF MET	NEFL GABRA1 SYT1 SLC12A5	PCNA TOP2A NES EGFR
Signaling Pathway	HIF1α, PI3K and PDGFRA pathway activation	TNF family and NFκB pathway activation	Gene signature similar to normal brain	Notch and SHH pathway activation

Figure 4: a) Most common genetic aberrations in GBM (adapted from (Brennan et al., 2013, Verhaak et al., 2010). Whole-exome sequencing analysis was performed on a cohort of 291 patient samples. Copy number variations and mutations were analyzed and revealed five major dysregulated pathways in GBM. The overall frequency of genetic aberrations in RTK, PI3K, MAPK, TP53 and RB1 pathways are indicated. In red and blue are depicted activating and inactivating genetic aberrations, respectively **b) GBM subclasses based on transcriptional heterogeneity.** 4 subgroups of primary and secondary GBM were identified based on gene expression data obtained from TCGA project.: proneural, mesenchymal, neural and classical. Certain genetic aberrations correlated with subclasses, but were not exclusive. Each subclass has its own specific gene signature and more frequently characterized by certain transcriptional markers and signaling pathway activation (Verhaak et al., 2010).

1.3. Models for tumor heterogeneity

GBM has been described as a heterogeneous tumor mostly due to its high variability in histopathologic features and genetic and transcriptomic profiles between patients (intertumoral) and within one patient (intratumoral). In the last decade, two major models for tumoral heterogeneity have been pointed out: the clonal evolution and the cancer stem cell model.

1.3.1. Clonal evolution model and genetical heterogeneity

The most popular and well characterized model explaining the generation of intratumoral heterogeneity is the stochastic and sequential acquirement of genetic aberrations or epigenetic changes in time. Genetic alterations might result from external factors such as radiation, bacteria, viruses or chemical agents, that affect normal cells in the human body, or genetic instability (Burrell et al., 2013). The best studied example of the generation of a neoplasm in a sequential multistep process is the adenoma-carcinoma model of human colorectal carcinogenesis. Fearon and Vogelstein showed that adenoma develops from genetic instability from a normal epithelial cell. The accumulation of further mutations results in the generation of an adenocarcinoma with final metastasis (Fearon and Vogelstein, 1990).

In 1976, Peter Nowell presented the linear clonal succession model of cancer evolution (Nowell, 1976) (**Fig. 5**). Aberrations arise stochastically in one single cell turning into a tumorigenic cell clone. Hence, tumors originate in this model from a single cell. This parental clone creates upon subsequent de novo mutations genetically divergent "daughter" cell clones. Clonal variability is created following a hierarchical structure by the accumulation of genetical aberrations leading to an irreversible evolution. Each clone has its specific genetic aberrations that, in analogy to a trait of an organism, are subject to the Darwinian evolution. The genetic aberrations within a cell clone can be advantageous, neutral or disadvantageous. Subsequent positive or negative selection depends on the microenvironment they encompass. Thus, if the aberration represents no environmental disadvantage, the cell will survive. Tumor progression results due to selection of most aggressive traits/advantageous mutation (Cairns, 1975). Cells with disadvantageous mutations are unable to survive and eventually vanish from the tumor cell pool. Most interesting are neutral aberrations. Upon environmental change (e.g. upon treatment pressure or metastasis), certain changes can become advantageous and a neutral clone in the initial environment, now becomes the most prominent (Greaves and Maley, 2012, Rubben and Araujo, 2017, Clevers, 2011, Gupta and Somer, 2017).

Although initially described for genetic aberrations, the clonal evolution model can be used to explain epigenetic heterogeneity as well. Like genetic aberrations, changes to the epigenome are heritable and can be transmitted from parental to daughter cells (Easwaran et al., 2014). However, epigenetic changes are reversible.

Following the clonal evolution model, different genetic and epigenetic backgrounds are generated in cancer cells of one tumor creating intratumoral heterogeneity which leads to distinct functional and phenotypic patterns among cancer cells (Meyer et al., 2015).

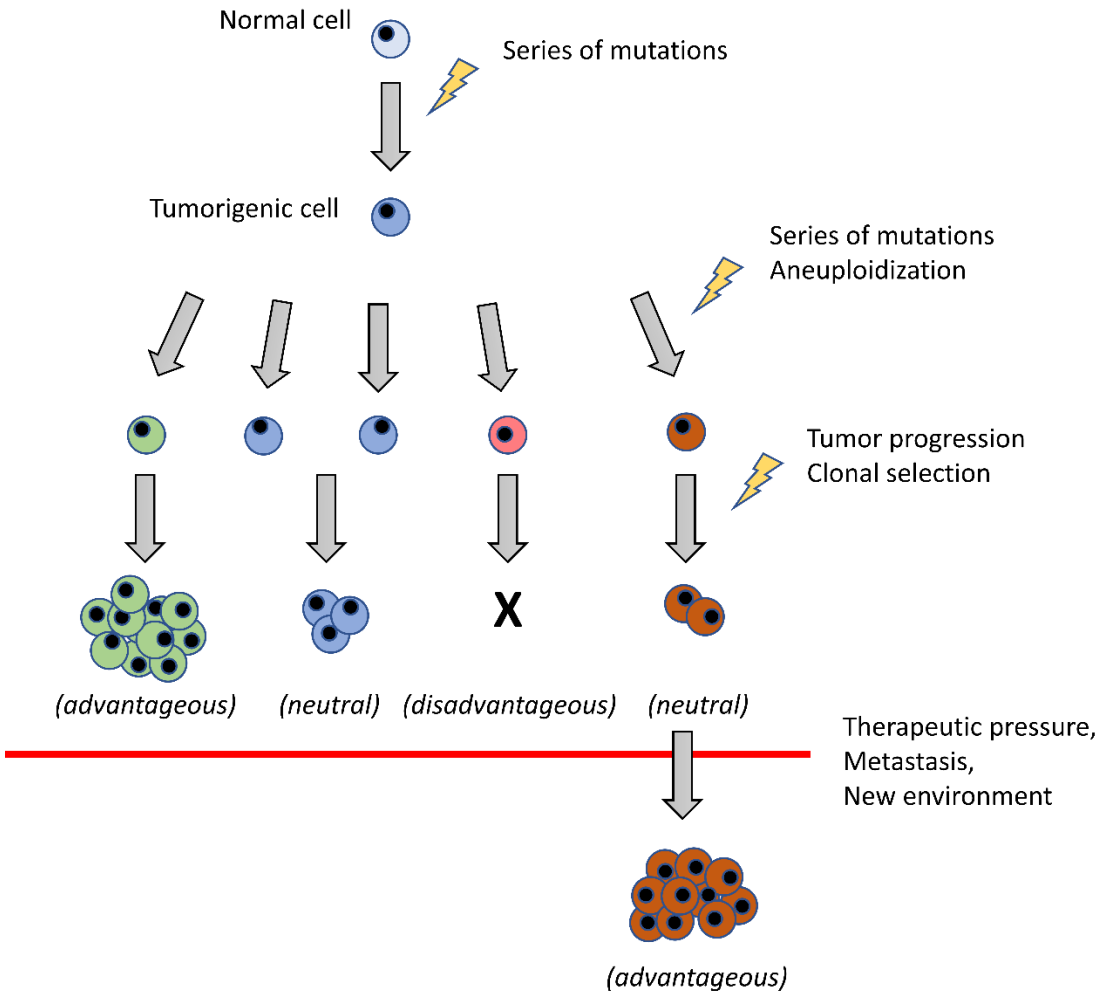

Figure 5: Model of clonal evolution in a tumor. A series of mutations in a normal cell turn it into a tumorigenic cell. After continuous accumulation of genetic aberrations and aneuploidization, multiple tumor clones with distinct genetic backgrounds develop (distinct colors represent genetically different cell clones). DNA transformations might be disadvantageous, neutral of advantageous in a given microenvironment. This leads to the selection of the fittest 'trait' and the most aggressive clones contribute to tumor growth. Neutral mutations lead to coexistence of genetic clones in a tumor although not contributing to its growth. On the other side, disadvantageous characteristics will lead to cell death. Upon therapeutic pressure or environmental change as in metastasize, neural mutations might become advantageous and become most prominent clone in a tumor mass whereas tumor clones being the fittest in the initial environment become subject of a negative selection.

1.3.2. Genetic intratumoral heterogeneity in GBM

Already in the early 80's, researchers detected by karyotyping the presence of divergent clones within one GBM tumor (Shapiro et al., 1981). Tumors were karyotyped and cultured at a clonal level for functional analysis. Clones derived from a single tumor demonstrated variability in growth and chemosensitivity, however, a link to specific karyotypes was not done. More recently, our lab has shown that GBM patient samples distinguished two genetically divergent clones, aneuploid and pseudodiploid by combined measurement of DNA content and copy number variations (Stieber et al., 2013). Aneuploidization appeared as a late event in GBM evolution, where aneuploid clones were found to coexist with pseudodiploid clones in polygenomic tumors.

Evolutionary dynamics were studied by Sottoriva and colleagues who isolated tumor fragments from different parts of GBM patient tumors (Sottoriva et al., 2013). High throughput measurement of DNA copy number variations and RNA-sequencing (RNA-seq) revealed the presence of multiple genetic clones within one patient. Similar results were later confirmed by other multisector studies in GBM patient tumors (Kim et al., 2015, Kumar et al., 2014, Lee et al., 2017). Kim et al. analyzed copy number variations and gene mutations of paired primary and recurrent GBM patient samples for longitudinal studies on genetic aberrations. Two main observations on recurrent GBM were seen: distally recurrent GBM displayed strong genetic differences compared to the initial tumor mutations, with major variations detected in driver genes. Locally recurrent GBM shared most of genetic aberrations with the initial tumor suggesting that clonal selection was more prominent at distant recurrences. Although these experiments clearly demonstrated the existence of distinct genetically divergent clones in GBM, the total number of clones might be underestimated due to bulk tumor sequencing.

The novel technique of single cell DNA sequencing methods enabled high throughput analysis of copy number variations in single cells of patient biopsies (Wang et al., 2014). Reports from breast cancer show that copy number variations can be detected using single cell DNA sequencing (scDNA-seq) and identified up to three genetically different profiles within one breast tumor (Navin et al., 2011). To date, copy number variations in GBM were only inferred from single cell RNA-seq data (scRNA-seq) (Patel et al., 2014), scDNA-seq technology has not yet been applied to gliomas. Interestingly, not all GBM tumors displayed strong genetic heterogeneity. scRNA-seq of 5 GBM patient samples revealed both monogenomic and polygenomic tumors. Similarly, oligodendrogliomas were as well shown by RNA-seq analysis as genetically homogeneous and heterogeneous tumors (Tirosh et al., 2016b). This is in accordance to previous reports from Sottoriva et al. describing GBM as multiclonal tumors, however, most genetic aberrations were retained per tumor and only

minor changes were observed. Indeed, Patel et al. and Tirosh et al. inferred the number of CNVs from gene expression patterns obtained by scRNA-seq, which may underestimate the number of smaller CNVs. With improved single cell analysis techniques, this inconsistency might be solved.

Meyer and colleagues approached analysis of genetic variability by dissociating and clonally expanding GBM tumor cells for subsequent combined genomic and functional analysis (Meyer et al., 2015). Clones derived from one tumor exhibited distinct functional profiles concerning growth, differentiation capacities, tumorigenic ability and drug response to TMZ. Unfortunately, no correlation between genomic and functional profiles could be established. Furthermore, genetic variability might be underestimated due to clonal selection upon primary culture step.

1.3.3. Cancer stem cell model

A largely debated model for intratumoral heterogeneity is the cancer stem cell (CSC) model. As many biomedical hypotheses, the concept of a CSC dates back to Rudolf Virchow in the 19th century. The German pathologist examined, amongst many biological tissues, also human tumors. By histology, he was the first to describe morphological heterogeneity within tumors and tumor resemblance to embryonic tissues (Virchow, 1855). In 1863, he stated in his embryonal rest theory that tumors develop from embryo-like cells that remained in the tissue after organ development (Virchow, 1863). Ten years later, in 1874, Cohnheim and Durante extended this theory referring to the rest cell theory (Durante, 1874). Excess of embryonic rudiments remaining in tissues of fully differentiated organs could develop into tumors in adults. Rippert proposed in 1911 that the environment of these rudimental cells is the critical factor determining the phenotype of the tumor (Rippert, 1904). Thus, already at that time, scientists developed hypotheses about cancer development based on simple histological observations that are still partially accepted today. Although, technically speaking, these observations describe tumor initiating capacities, they are seen as corner stone for CSC research since stemness capacities were linked to cancer cells. With emerging technical tools like the development of the fluorescent-activated cell sorting (FACS) in 1972 by Herzenberg at Standford, improved cell culture systems and the development of xenotransplantation assays, CSC research gained popularity (Bonner, 1972).

1.3.3.1. Definition of cancer stem cells

The term CSC is used very loosely in scientific publications creating a lot of confusion and is often confound with the term tumor initiating cell (TIC). TICs should be considered as cells responsible for initiating a tumor, therefore referring to the origin of tumor. CSC on the other hand refer to subpopulation of tumor cells responsible for maintenance of tumor growth and regrow of tumors after resection and treatment. The CSC hypothesis does not make a distinction on the origins of a CSC; thus, a CSC does not necessarily derive from a normal stem cell (Jordan, 2009). Of note, for many cancers it is not clear whether the TICs originate from a healthy stem, progenitor or fully differentiated cell. The confusion in terminology arises from two issues: (1) it is often assumed that CSCs have to arise from normal stem cells; (2) researchers often apply the TIC terminology to refer to putative CSC populations initiating tumors in experimental models.

It took over 50 years to find a consensus on the definition of a CSCs as the identification of these cancer subpopulations is problematic. No universal marker exists, and putative CSCs

need to be determined using functional assays. These tests were slowly developed with improved culture systems and analysis methods. In 2006 during the AACR (American Association for Cancer Research) workshop on CSCs in Lansdowne, Virginia, the scientific community proposed the CSC definition: “CSCs are a population of cells in the tumor that have self-renewal capacity and can give rise to all the heterogeneous cell population that comprise the tumor.” (Clarke et al., 2006). Accordingly, a CSC cannot be identified by marker expression alone, but needs to fulfil several functional properties.

Following the CSC hypothesis, a subpopulation of cells at the apex of a hierarchical organization creates intra-tumoral heterogeneity via a one-way differentiation process (**Fig. 6**). The CSC produces in analogy to normal stem cells in the body, progenitor cells that in their turn generate fully differentiated cancer cells. CSCs are able to divide symmetrically giving rise to either two CSCs or two progenitor cells. Asymmetric division results in one CSC and one progenitor cell. CSC are able to proliferate indefinitely, self-renew and form heterogeneous tumors upon transplantation assays. Properties of progenitor cells on the other hand are not that well defined. Two views are discussed in the scientific field, either they are fast, or they are slowly proliferating with a limited number of cell divisions. Moreover, it is still unclear whether cells defined as progenitors should be able to self-renew and produce tumors *in vivo* with gradually decreasing capacities upon increased differentiation status. Finally, at the bottom of the hierarchical structure are the fully differentiated cancer cells. They do not have the potential to self-renew, to generate a tumor *in vivo* and do not show stemness properties in functional analysis. Thus, the differentiated cancer cell has no multipotent abilities (Meacham and Morrison, 2013, Shackleton et al., 2009). Most studies performed tests on putative CSCs and non-CSCs, here non-CSCs may represent progenitors and/or fully differentiated cells.

Several CSCs of distinct genetic backgrounds might coexist within one tumor (Visvader and Lindeman, 2012, Piccirillo et al., 2015, Stieber et al., 2013). Genetic aberrations might influence CSC marker expression. Similarly, the epigenome determines cell fate specifications during differentiation process wherein transcriptional profiles vary accordingly (Wainwright and Scaffidi, 2017). Applied on the CSC model, epigenetic, transcriptional and phenotypical heterogeneity is created by the presence of cancer cells in the tumor bulk at different stages of the one-way differentiation process.

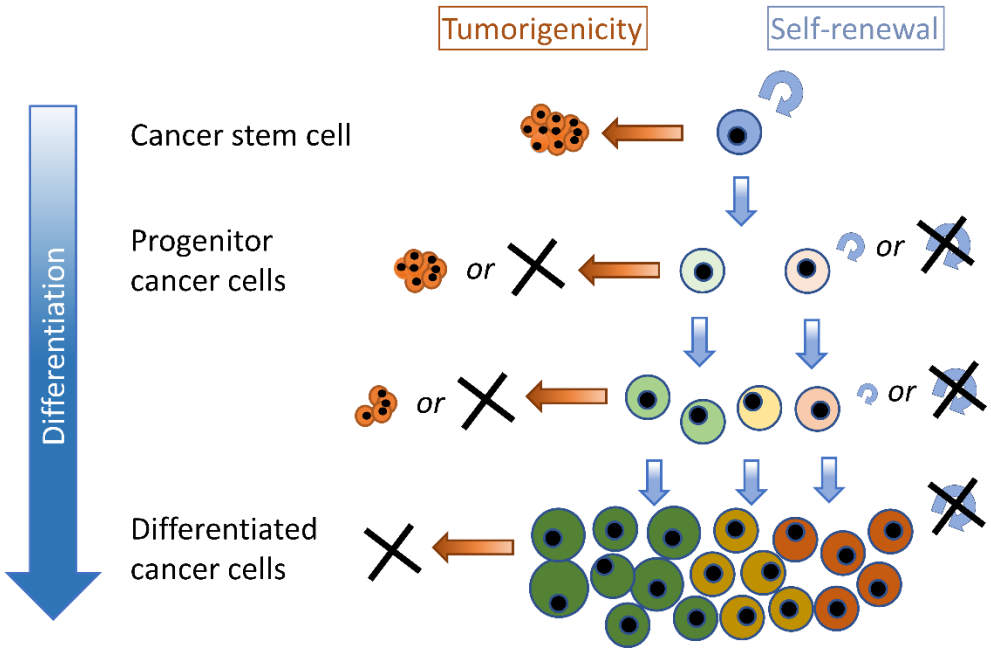

Figure 6: The cancer stem cell model. A single CSC at the apex of a hierarchical organization is able to self-renew, proliferate indefinitely and give rise to heterogeneous tumors upon transplantation into experimental models/immunodeficient animals. A CSC generates more differentiated progenitor cells which finite proliferating capacities and extensively contribute to tumor mass. Fully differentiated cancer cells are at the bottom of the one-way differentiation process and are not able to generate de novo tumors in transplantation assays. There are two variations of the CSC model; the first assumes that progenitor cells have self-renewal and tumorigenic capacities. The second model clearly states that progenitors are not able to self-renew and cannot form tumors *in vivo.*

1.3.3.2. Functional properties of CSCs

Although many properties of CSCs are derived from normal stem cells, it is a major misunderstanding that CSCs demonstrate the same characteristics as normal stem cells in the body. E.g. the frequency of a normal stem cell in the healthy tissue is constant and very low, whereas the number of CSCs within a tumor is thought to vary from patient to patient and several distinct CSCs might be present within one tumor (Jordan, 2009). It has been suggested that the number of CSCs within a tumor increases with malignancy (Jordan, 2009). Moreover, stem cells in the healthy tissue are comprised in well-defined niches with well-regulated external stimuli, whereas the tumor niche is a more dynamic entity that may change with tumor progression (Jordan, 2009).

1.3.3.2.1. Sphere forming ability

In 1992, Reynolds and Weiss developed culture conditions to maintain and propagate neural stem cells (NSCs) *in vitro* as neurospheres (Reynolds and Weiss, 1992). Growth medium deprived from serum and supplemented with defined growth factors, particularly basic fibroblast growth factor (bFGF) and epidermal growth factor (EGF), were shown to be sufficient to derive and maintain NSCs *in vitro* (Conti et al., 2005). EGF and bFGF are

necessary for stem cell self-renewal, proliferation and maintenance (Haley and Kim, 2014, Hebert et al., 2009). Similarly, Ignatova and colleagues applied these growth conditions to anaplastic astrocytoma and recurrent GBM patient-derived samples. As a result, GBM cells formed spherical cellular aggregates similar to neurospheres (Ignatova et al., 2002). These conditions are often considered to enrich for CSCs. The ability to form sphere structures is seen as a general prerequisite for CSCs due to the similarity to the NSC culture (Reynolds and Vescovi, 2009). Sometimes leukemia inhibitory factor (LIF) is added to the culture medium, although it is not necessary to maintain GBM CSC cultures (Yuan et al., 2004) (Beier et al., 2007). LIF is predominantly used in mouse embryonic stem cell cultures to promote self-renewal capacities via the JAK-STAT pathway (Ernst and Jenkins, 2004). Plating GBM patient-derived cultures in serum-free medium on laminin or other extracellular matrix coatings was shown to maintain the CSC state in long-term adherent culture (Pollard et al., 2009). The addition of serum in the medium turns CSCs into a differentiated-like state with decreased tumorigenic potential (Reynolds and Vescovi, 2009, Gunther et al., 2008).

1.3.3.2.2. Unlimited self-renewal and proliferative ability

Self-renewal ability is the capacity of a cell to remain in an undifferentiated state through symmetric or asymmetric cell division whereby at least one daughter cell is equally multipotent than the parental cell. By symmetric division a CSC gives rise to a CSC and a progenitor cells, whereas a CSC gives rise to two identical daughter cells upon symmetric division either producing two new CSCs or differentiated progenitor cells (He et al., 2009). By time-lapse microscopy GBM CSCs were analyzed for their symmetric and asymmetric division frequency. Non-CSCs were identified by the presence of differentiation markers MAP2 or GFAP which are expressed by neurons and astrocytes, respectively (Lathia et al., 2011b). Interestingly, the rate to which a putative CSC performs symmetric or asymmetric division can be affected by culture conditions. In EGF and bFGF enriched medium, more than 80% of CSCs exhibited symmetric division producing two stem-like daughter cells. 12.6 % of CSCs generated by symmetric division two differentiated daughter cells. Only 3.6% of CSCs underwent asymmetric division. The frequency of asymmetric division was enhanced (20%) upon growth factor depletion whereas symmetric division to two CSCs was reduced to approximately 70% (Lathia et al., 2011b). This shows that the decision to undergo symmetric or asymmetric cell division is influenced by the microenvironment.

Since the ability to form a sphere *in vitro* is regarded as self-renewal potential, sphere forming assays have been introduced as measurement for self-renewal ability. However, a lot of variation exist in the execution of this test with impact on symmetric and asymetric division rates as described above; culture medium composition, volume of culture medium, cell density, surface area of the culture dish and duration of cell culture (Chaichana et al.,

2006). Two main assays have been pointed out in the last years; self-renewal test at single cell level over several passages or limiting dilution assay (LDA) which is suitable for rare CSCs.

First, self-renewal test at clonal density over several passages is mainly used for a cancer population that is enriched for CSCs. Here single cells are cultured until sphere formation occurs. Testing sphere forming capacity at the single cell level in independent cultures prevents false positives through cell aggregation. At the first passage, the percentage of formed spheres represents their clonogenic ability. Surviving cells from the 1st passage are collected and seeded as single cells for a second passage to test sphere forming capacities and the number of spheres is counted after formation. To test the CSC model where progenitor cells have limited self-renewal capacities, serial passages need to be performed to dilute eventual progenitor cells. By the consecutive passages, the number of formed spheres reduces in case of progenitors. In contrary, CSCs are expected to keep their sphere forming ability over time and demonstrate self-renewal ability throughout passages by demonstrating a stable number of formed sphere during testing. Differentiated cells do not form spheres at all.

Often sphere size is used as a read out for differentiation status of a cell. However, caution must be taken in data interpretation. Here CSCs are thought to form bigger spheres than progenitor cells due to their unlimited self-renewal and proliferative capacities. On the other hand, a second variation of the CSC model might suggest that CSC are quiescent and only form progenitors when needed. The later are fast proliferative and generate the tumor bulk. In this case, spheres from CSCs and their differented progenitors have similar sizes.

For the LDA test, the cancer cell population is seeded at different dilutions (e.g. 100, 500 and 1000 cells per culture) to increase the chance a CSC is present. Consequently, LDA is best suited to determine the frequency of rare CSCs in a cancer cell population. The number of formed spheres is counted for each seeding dilution separately and the final frequency of self-renewing cells within a cancer cell population can be statistically estimated. Several online tools using different estimation strategies (e.g. generalized linear models or maximum likelihood) have been made accessible (Hu and Smyth, 2009).

CSCs exhibit indefinite proliferative ability where both symmetric and asymmetric cell divisions are accounted to cell proliferation (Bu et al., 2013, Bose et al., 2014). The measurement of indefinite cell proliferation is rather challenging due to its unlimited timeframe. Therefore, experimental design needs to define a minimal number of cell passages required for unlimited proliferation. The number of passages may strongly depend on the cancer type used. Therefore, cell proliferation between a CSC population and a non-CSC cell population is generally compared for several passages. Following the CSC

hypothesis, non-CSCs are regarded not to have proliferative capacities in case of fully differentiated cancer cells or to lose their proliferative ability after several cell passages until complete cell cycle arrest in case of progenitor cells.

1.3.3.2.3. Tumorigenic ability

The main prerequisite of putative CSCs is the ability to generate a tumor with the same heterogeneous pattern as the original tumor upon transplantation into mice. In 1937, Furth and Kahn were able to show by transplanting cancer cell lines into mice that a single cell is able to induce cancer. The frequency of inducing cancer by this approach was however, highly variable (Furth, 1937). This implied that only few cancer cells were able to form tumors. Pierce and Speers suggested later that tumors were hierarchically structured and only the cancer cells atop of the organization could induce tumors (Pierce, 1988). Tumorigenic assays are best performed by orthotopic transplantations i.e. that tumor cells are implanted at the same location in mice as it developed in the human body. For instance, patient GBM tumors are implanted intracranially into the brain of immunodeficient animals. This is done to approximate the microenvironment of the original cancer; although human cancer cells are generally transplanted into immunodeficient mice which are impaired in their immune system. Of note, the tumor resulting from implanted human patient-derived cancer tissue or primary cells is considered as a patient-derived xenograft (PDX). Therefore, immunocompromised animals are used to ensure the most permissive environment for tumor development.

In transplantation assays, a tumorigenic and non-tumorigenic cancer populations have been demonstrated for several tumors: breast cancer (Al-Hajj et al., 2003), colorectal cancer (O'Brien et al., 2007), GBM (Singh et al., 2004b), ovarian cancer (Stewart et al., 2011). Following the CSC model, the non-tumorigenic cancer population represents fully differentiated and/or progenitor cancer cells depending on the model variations. The tumorigenic cells are putative CSCs when they show multipotent abilities. E.g., in GBM it was shown that $CD133^-$ fraction of the cancer was not tumorigenic, but the $CD133^+$ cell fraction was (Singh et al., 2003). Even more, $CD133^+$ cancer cells were able to produce $CD133^-$ cancer cells. Thus, in vivo transplantation assays are a powerful tool to analyze CSC capacities, however several considerations must be taken into account.

Importantly, it was shown that the use of several distinct strains of immunocompromised mice with different degrees of immunogenicity affects the frequency of tumorigenic CSCs. Quintana et al. showed that melanoma cells engrafted into NOD/SCID interleukin-2 receptor gamma chain null mice increased the frequency of tumorigenic cells and tumors grew faster compared to cancer cells transplanted into NOD/SCID mice (Quintana et al., 2008). Thereby, the real frequency of tumorigenic cells might be underestimated depending on the

mouse strain used for transplantation, which might result from the xenogeneic immune response. Human cells injected to mice are recognized as foreign and therefore removed by cells from the immune system. Another mechanism that results in the underestimation of tumorigenic cells are the lack of human specific adhesion molecules or growth factors necessary for tumor development. To overcome that engrafted cancer cells do not survive transplantation, it has been shown that an admixture of cancer cells with carrier cells or extracellular matrix should be used for assays. Cancer cells with different tumorigenic capacities were all able to form tumors in mice to similar rates when co-engrafted with irradiated cancer cells (Gupta et al., 2011).

The number of tumorigenic cells is not necessarily rare. In acute myeloid leukemia (AML) 10% of engrafted cells were generating tumors (Kelly et al., 2007). In contrast, the minimal number necessary for successful tumor generation in GBM can be as low as 10-100 cells of a CSC-enriched cell population (Singh et al., 2004b). In melanoma, one single cancer cell was sufficient for tumor growth in NOD/SCID Il2rg-/- mice (Quintana et al., 2008).

It has been shown that high self-renewal ability *in vitro* does not necessarily predict tumor formation upon transplantation assays (Barrett et al., 2012). In orthotopic transplantation assays, the tumorigenicity of high grade glioma cells with limited self-renewal ability was compared to high grade glioma cells with high self-renewal capacity. Interestingly, cells with low self-renewal ability marked faster and higher penetrance of generated tumors.

1.3.3.3. Identification of CSCs

In analogy to NSC research, identification of CSCs by the expression of stemness markers has been widely attempted. These CSC markers represent proteins or other molecular components (e.g. sugars, lipids) expressed by a cancer cell and are often used to enrich for putative CSC subpopulations in GBM patient-derived cultures. Most of these markers are not unique to GBM CSCs, but were reported to identify putative CSCs in other cancers as well. Examples for intracellular CSC markers in GBM are Sox2 (Stoltz et al., 2015), Vimentin (Reifenberger et al., 1989), Nestin (Singh et al., 2004b), Olig2 (Ligon et al., 2004), ALDH1 (Charafe-Jauffret et al., 2009, Ginestier et al., 2007) and Oct-4 (Krogh Petersen et al., 2016). Traditionally, specific cell surface markers are used for CSC enrichment/identification as it allows subsequent functional testing on the FACS-isolated subpopulations. In GBM and other cancers a plethora of cell membrane markers were described; e.g. CD133 (Singh et al., 2003), CD44 (Anido et al., 2010), A2B5 (Tchoghandjian et al., 2010), CD15 (Son et al., 2009), NG2 (Al-Mayhani et al., 2011), CD9 (Podergajs et al., 2016), CD151 (Tilghman et al., 2016), integrin-α 6 (CD49f) (Lathia et al., 2010), CD24 (Vassilopoulos et al., 2008), CD29 (Vermeulen et al., 2008) and CD90 (Yang et al., 2008). In this thesis, we will focus on the four cell surface markers CD133, CD44, A2B5 and CD15.

1.3.3.3.1. CD133

CD133 is a type I glycoprotein composed of five transmembrane domains with two intracellular and two extracellular loops and one cytoplasmic domain (Corbeil et al., 2010, Miraglia et al., 1997, Yin et al., 1997). The human CD133 gene *Prominin 1* (*PROM1)* has six distinct tissue specific promoters suggesting cell type specific CD133 regulation (Sompallae 2013. Article 209). The coding region of the gene contains 28 exons, whereof 7 are optionally expressed (Bauer et al., 2008, Yu et al., 2002). *PROM1* has 12 known splice variants (reviewed (Fargeas et al., 2007)). To date the CD133 has no known ligands. The extracellular domain of CD133 contains 8 possible glycosylation sites (Yin et al., 1997). CD133 (*PROM1*) is the most prominent putative CSC marker. In non-tumoral cells, CD133 is expressed in brain endothelial cells (Golebiewska et al., 2013) and in hematopoietic, neural stem and progenitor cells (Corbeil et al., 2010, Bauer et al., 2011, Uchida et al., 2000, Corbeil et al., 1998, Tamaki et al., 2002). Positive marker expression is used to isolate neural stem cells from human fetal brain (Uchida et al., 2000). CD133 is present in membrane protrusions, filopodia and lamellipodia of mouse neuroepithelial stem cells (Weigmann et al., 1997). CD133 expression may be linked with poor patient survival. However, the prognostic value of CD133 expression in GBM is highly debated in literature due to imperfect sample sizes and analysis methods (Pallini et al., 2008, Zhang et al., 2016, Wu et al., 2015). Presence of $CD133^+$ cancer subpopulations have been demonstrated in many different cancer types: GBM (Singh et al., 2003, Bao et al., 2006a, Galli et al., 2004), colon (Ricci-Vitiani et al., 2007, O'Brien et al., 2007) (Todaro et al., 2007), liver (Ma et al., 2007), prostate (Richardson et al., 2004), melanoma (Monzani et al., 2007), ovarian cancer (Curley et al., 2009) and hepatocellular carcinoma (Song et al., 2008).

Experiments performed in $CD133^+$ GBM patient-derived cultures showed that the C-terminal tyrosine residue of CD133 interacts with the PI3K regulatory subunit p85 thereby activating the PI3K/AKT signaling pathway (Wei et al., 2013, Liu et al., 2017). Supporting evidence comes from CD133 overexpression experiments in gastric cancer cells, here CD133+ cells had higher activated PI3K/AKT/ribosomal protein S6 than cancer cells with silenced CD133 (Zhu et al., 2014). Concordantly, CD133 knockdown in $CD133^+$ GBM sphere cultures resulted in reduced activity of PI3K and AKT proteins and was essential for self-renewal and tumorigenic ability (Wei et al., 2013).

$CD133^+$ GBM cells showed higher proliferation, self-renewal and invasion *in vitro* than $CD133^-$ GBM cells grown on equal culture conditions (Wang et al., 2016, Singh et al., 2004b). In these experiments, only CD133 cells were able to generate tumors *in vivo*. shRNA depletion of CD133 resulted in decreased cell growth and clonogenicity combined with reduced tumorigenic potential in CD-1 nude mice (Brescia et al., 2013b). However,

these data are conflicting with other reports, demonstrating CSC properties as well in CS133- GBM subpopulations (see **section 1.3.4**). The percentage of $CD133^+$ cells vary from rare to highly expressed between GBM patient derived-cultures. Moreover, the portion of $CD133^+$ cells in CSCs cultures changes with culture conditions; CD133 surface epitope expression decreases in serum containing medium supplemented with retinoic acid (Campos et al., 2011b). Western blot analysis of total CD133 protein (intra and extracellular), however, did not show significant variations between differentiation and normal culture conditions. Commonly used antibodies for CD133 antibody target the AC133 or AC141 glycosylated cell membrane epitopes (Miraglia et al., 1997, Green et al., 2000). It is hypothesized that the AC133 epitope on the second loop of CD133 is masked upon differentiation and thereby not accessible for antibody binding (Kemper et al., 2010). Thus, the lack of AC133 positive cells does not always reflect the absence of CD133 protein.

In primary GBM cultures Bao and colleagues demonstrated that the percentage of $CD133^+$ cells were higher in irradiated cells than in the initial condition without treatment. They concluded that $CD133^+$ cells were more resistant to radiation than $CD133^-$ cells due to higher DNA damage repair efficiency (Bao et al., 2006a). Moreover, CD133 expression is increased in hypoxia (Campos et al., 2011b, Griguer et al., 2008). Upon stress conditions, the genetic depletion of mitochondrial DNA and the inhibition of electron transporter chain (ETC) by compounds suggests that CD133 might be upregulated (Griguer et al., 2008).

1.3.3.3.2. CD44

CD44 is a transmembrane glycoprotein receptor expressed in numerous cell types (Jaggupilli and Elkord, 2012) ranging from blood cells and hematopoietic stem cells to epithelial cells (Basakran, 2015) to keratinocytes, hair follicles, dendritic cells (Yasaka et al., 1995). It is therefore not surprising that CD44 positive cells with CSC properties were discovered in many cancer types, e.g. in GBM (Anido et al., 2010), bladder (Chan et al., 2009), breast (Al-Hajj et al., 2003), colorectal (Dalerba et al., 2007), lung (Leung et al., 2010), ovarian (Zhang et al., 2008), pancreatic (Li et al., 2007) and prostate cancer (Collins et al., 2005). CD44 expression is linked to the mesenchymal subgroup and poor survival in GBM (Guadagno et al., 2016, Phillips et al., 2006).

The *CD44* gene has 19 exons, whereof the first 16 exons are designated to the extracellular domain and its specific splice variants. Exon 17 encodes for the hydrophobic transmembrane domain followed by exon 18 and 19 for the intracellular domain common to all isoforms. To date, 12 splice variants are known (Screaton et al., 1992, Morath et al., 2016). The most described isoforms are CD44s (standard), CD33 variant 3 (CD44v3) and CD44 variant 6 (CD44v6). The later is preferentially expressed in GBM (Jijiwa et al., 2011). All isoforms contain hyaluran (HA), laminin and collagen binding site (Peach et al., 1993).

Only CD44s cannot bind osteopontin (OPN) (Ishii et al., 1993, Weber et al., 1996, Katagiri et al., 1999). Upon OPN ligand binding, CD44v6 induces AKT signaling resulting in an increased sphere forming capacity of mouse tumor cells (Jijiwa et al., 2011).

Generally, CD44 is implicated in cell-cell interactions and adhesion to extracellular matrix (Zoller, 2011). In GBM, CD44 expression is related to tumor invasiveness *in vivo* (Su et al., 2003). CD44 is related to several processes in the nervous system as myelination, astrocyte migration and $Ca2^{+}$ clearance (Dzwonek and Wilczynski, 2015).

OPN binding leads to γ-secretase dependent proteolytic cleavage of CD44 with the intracellular domain translocating to the nucleus where it is involved with the expression of stemness genes via CBP/p300 increased HIF-2α (Morath et al., 2016). Addition of TGF-β induced CD44 epitope expression in GBM cells via Id1 and Id3 activation (Anido et al., 2010). Inhibition of TGF-β receptor leads to decreased tumor initiation and volume in orthotopic transplantation assays.

1.3.3.3.3. A2B5

A2B5 is an epitope of the c-series of gangliosides on the surface of cells (Saito et al., 2001). Gangliosides are glycosphingolipids composed of hydrophobic ceramide and a hydrophilic group containing oligosaccharides, silialic acids and a sugar chain. C-series gangliosides are formed by an enzyme cenoded by the gene *ST8SIA1*. However, a specific pathway with complete list and functioning of modulating enzymes is largely unknown (Svennerholm, 1963, Yu et al., 2008). In the cell membrane, the acidic glycosphingolipids interact with other lipids, cholesterol and sphingomyelin and can form lipid rafts, micro domains and caveolae (Simons and Ikonen, 1997). Gangliosides are typically found in the brain and are mainly implemented in cell-cell signaling, recognition and adhesion. A2B5 recognizes neural stem and progenitor cells (Eisenbarth et al., 1979, Abney et al., 1983). However very little is known of its function in cancer, except for its putative role as a CSC marker. Several studies were performed on GD3 a b-series ganglioside which is a precursor to the c-series gangliosides. Here, normal melanocytes have low levels of GD3, but experience a dramatic increase of this gangliosides in metastatic melanoma (Carubia et al., 1984, Ravindranath et al., 1991), suggesting a role in promotion of tumor metastasis. Addition of GD3 molecules to the medium of GBM and anaplastic astrocytic cell lines induced VEGF release (Koochekpour et al., 1996) and overexpression in GBM patient derived cultures is associated with tumorigenicity (Yeh et al., 2016). Tchoghandjian et al. reported A2B5 as a heterogeneously expressed marker in GBM and a putative marker for CSCs (Tchoghandjian et al., 2010, Auvergne et al., 2013, Han et al., 2015). Within the CD133 negative population, A2B5 positive cells were able to generate tumors in immunocompromised mice (Ogden et al., 2008). The $CD133^{-}$ $A2B5^{+}$ GBM subpopulation

was shown to have strong migratory capacities *in vitro* and *in vivo* (Sun et al., 2015). Self-renewal and migratory abilities of A2B5 positive CSCs have been negatively associated to PAR1 and miR-218-5p, respectively (Auvergne et al., 2016, Wu et al., 2016).

1.3.3.3.4. CD15

CD15 also known as stage-specific embryonic antigen 1 (SSEA-1) or Lewis X (LeX), is expressed during all embryonic stages of neuronal development and in the adult brain on neural stem and progenitor cells (Capela and Temple, 2002, Capela and Temple, 2006). It is also expressed in kidney, primordial germ cells and mouse embryonic stem cells (Rauvala, 1976, Fox et al., 1981, Marani et al., 1986). CD15 is a glycosphingolipid belonging to the neolacto-series and is formed from paragloboside by fucosyltransferase 4 (FUT4) (Yanagisawa, 2011, Yu et al., 2008). The sialylated glycan is commonly linked to glycoproteins and glycolipids on tumor cell surfaces and regarded as an adhesion molecule (Varki, 1997). CD15 was also shown to be heterogeneously expressed within GBM (Son et al., 2009) and other brain tumors as medulloblastoma (Ward et al., 2009, Andolfo et al., 2012, Read et al., 2009) and gliomas (Mao et al., 2009). Expression of CD15 is described as well in breast cancer, Hodgkin disease, B-cell chronic lymphocytic leukemias, and AML (Brooks and Leathem, 1995, Hall and D'Ardenne, 1987, Ball et al., 1991). In medulloblastoma, CD15 positive CSCs demonstrate specific sensitivity to PI3K inhibitors but are resistant to common brain chemotherapeutic agents as TMZ and cisplatin.
Furthermore, CD15 is associated with cell-cell interaction and the compaction and adhesion of mouse embryos at the morula stage (Gomperts et al., 1994, Fenderson et al., 1984, Eggens et al., 1989).

1.3.4. Critical assessment of CSC marker expression

Many functional studies validated CSC-marker negative cells as less proliferative, with less self-renewal and tumorigenic abilities (Singh et al., 2004a, Singh et al., 2004b, Ogden et al., 2008, Tchoghandjian et al., 2010, Son et al., 2009, Anido et al., 2010, Lathia et al., 2010). These results suggest that a CSC is not quiescent, but more proliferative than progenitor cells. Furthermore, these reports indicate that marker negative progenitor cells have limited self-renewal and tumorigenic abilities. Thus, stemness abilities may not be exclusive for CSCs, but are found at limited degree in more differentiated progenitor cells. This raises the question whether CSC markers as well may be expressed to a limited extend on progenitor cells.
Moreover, CSCs markers cannot be generalized and markers validated in one cancer may not work for another cancer specimen (Al-Hajj et al., 2003). As example, it has been

demonstrated that $CD133^+$ cancer cells have self-renewal properties and are able to generate tumors *in vivo* whereas $CD133^-$ cancer subpopulations cannot (Bao et al., 2006a, Singh et al., 2004b). Meanwhile several research groups found similar characteristics in $CD133^-$ GBM cells (Beier et al., 2007, Ogden et al., 2008, Wang et al., 2008). Chen and colleagues showed experimental evidence for CD133 positive and negative GBM cells able to form tumors in transplantation assays (Chen et al., 2010). Here all marker positive cells demonstrated stemness abilities. However, within the $CD133^-$ population two subpopulations were distinguished, whereof Nestin and FABP7 positive cancer cells carried stemness abilities and Nestin and FABP7 negative cancer cells did not demonstrate stemness properties. Wang and colleagues demonstrated that tumors generated from $CD133^-$ GBM cells reacquire CD133 expression. Hence, CD133 is not an ultimate marker for CSC. This holds true for other markers as well and it was therefore proposed that a combination of several CSC enrichment markers is necessary to illustrate the hierarchical organization in a GBM tumor (Beier et al., 2007, Piccirillo et al., 2009, Penuelas et al., 2009, Wang et al., 2008). Moreover, CD133 is increased upon hypoxia in CSC cultures. Enrichment of CD133 in hypoxia is reversible in subsequent normoxic condition (Griguer et al., 2008). This raises the question whether CD133 enrichment or loss happens through selection of the best fitting cell clone or through marker changes in expression through adaptation. Unfortunately, most reports do not include apoptotic tests to show/exclude a selection process. Comparable controversial results were also found for other CSC markers. In GBM, CD15 negative cells were shown to produce $CD15^+$ cells *in vitro* (Kenney-Herbert et al., 2015). In breast cancer, $CD44^-$ were shown as well to be proliferative, self-renewing and tumorigenic upon transplantation (Lehmann et al., 2012, Mosoyan et al., 2013). Thus, hierarchical organization of a tumor could not yet be clearly determined based on the CSC markers, which questions whether there is a marker combination able to define CSCs able to reproduce phenotypic heterogeneity.

In GBM it was shown that CD133 positive cells from patient-derived cultures were able to produce upon symmetric and asymmetric cell division CSCs and differentiated cancer cells (Lathia et al., 2011b). Differentiated cells showed expression of either astrocytes (GFAP) or neurons (MAP2). Alike NSCs, the CD133 positive cells population showed multilineage differentiation and was able to self-renew. Moreover, it was shown that the CD133 positive cell is proliferating over a long-time period and produces tumors upon transplantation assays. CD133 negative cells did not retain these properties suggesting a higher differentiation status in these cells than in CD133 positive cells (Singh et al., 2003, Singh et al., 2004b). Thus, during the differentiation process, along the hierarchical organization,

cells accumulate or lose lineage specific properties as the expression of extra and intracellular markers (Campos et al., 2010).

1.3.5. From CSC towards adaptivity

The CSC model has increasingly been criticized in recent years due to conflicting results in CSC marker validity. Moreover, experiments from breast cancer and melanoma report non-hierarchical state transitions (Gupta et al., 2011, Quintana et al., 2010, Chaffer et al., 2013). Here, cells of distinct phenotypic states were each able to recreate phenotypic heterogeneity until each population reached a common equilibrium with fixed proportions of phenotypic states. Using mathematical modeling, Gupta et al. showed that in breast cancer cell lines state transitions between stem-like ($CD44^+$ $CD24^-$ $EpCAM^{low}$), basal ($CD44^+$ $CD24^-$ $EpCAM^-$) and luminal ($CD44^{low}$ $CD24^+$ $EpCAM^+$) cells were stochastic and phenotypical states interconverted, although at different rates. These experiments suggested high plasticity of cancer cells with no apparent differentiation status. As the CSC model implicates fixed phenotypic states and all of the cells represented CSC properties, results can be interpreted in two ways. Either the used CSC markers were not CSC specific or the CSC hypothesis does not hold true as it cannot explain the generated phenotypic variability. To this end, an adaptive model was proposed which is able to explain inconsistencies in the CSC hypothesis. According to the adaptive model, the CSCs are not a distinct subpopulation of tumor cells but rather a changing entity (Easwaran et al., 2014, Cabrera et al., 2015). Hence, a heterogeneous tumor population consists of cancer cells occupying different states e.g. a stem cell state or more differentiated states.

Similar to the CSC model, the adaptive model represents variations in the abilities of different cell types (e.g. CSC, progenitor, differentiated cells or simply cancer cells with no gradient in differentiation status). Within the adaptive models, we distinguish two extreme models: the dedifferentiation model with the limited number of state interconversions (**Fig. 7.a**) and the plastic model where each cancer cell may acquire each phenotypic state present in a tumor (**Fig. 7.b**).

The dedifferentiation model emphasizes the dedifferentiating ability of each cancer cell regardless of their grade of differentiation (**Fig. 7.a**). This process is also referred to as bidirectional interconversion and is thought to be dependent on the environment a cancer cell is encompassed. This model still distinguishes between CSCs, progenitor cells and fully differentiated cells organized in a hierarchical structure, however the differentiation process is reversible. In that sense a progenitor cell can turn into a CSC or a fully differentiated cell. A fully differentiated cell is able to turn into a progenitor cell, but cannot change into a CSC directly. As CSCs, progenitor cells are able to self-renew and form tumors with the same

variability present in the initial tumor. Only differentiated cells may not have self-renewal and tumorigenic abilities.

On the other hand, the adaptive model does not distinguish between differentiation status of cancer cells as they are all able to directly change into another cell state (**Fig. 7.b**). Here all the cells have unlimited self-renewal and tumorigenic abilities. No organizational structure as hierarchy can be identified in this model since the cancer cells have equal plastic behavior.

As the dedifferentiation and plastic models represents the two most extreme interpretations of the adaptive model, the degree of hierarchical organization ranges from high to shallow to non-existent. The degree of hierarchy may depend on the cancer type and on genetic profiles (Meacham and Morrison, 2013). The rate to which a certain state is 'favored' depends on the environmental cues (extrinsic features) and stochastic cell-autonomous mechanisms (intrinsic features) (Marusyk and Polyak, 2010). Extrinsic features are factors originating from the tumor microenvironment. Intrinsic features might only depend on genetic and epigenetic background. Although, extrinsic features have a major influence on tumorigenicity and phenotypic states, the impact of intrinsic features cannot be disregarded.

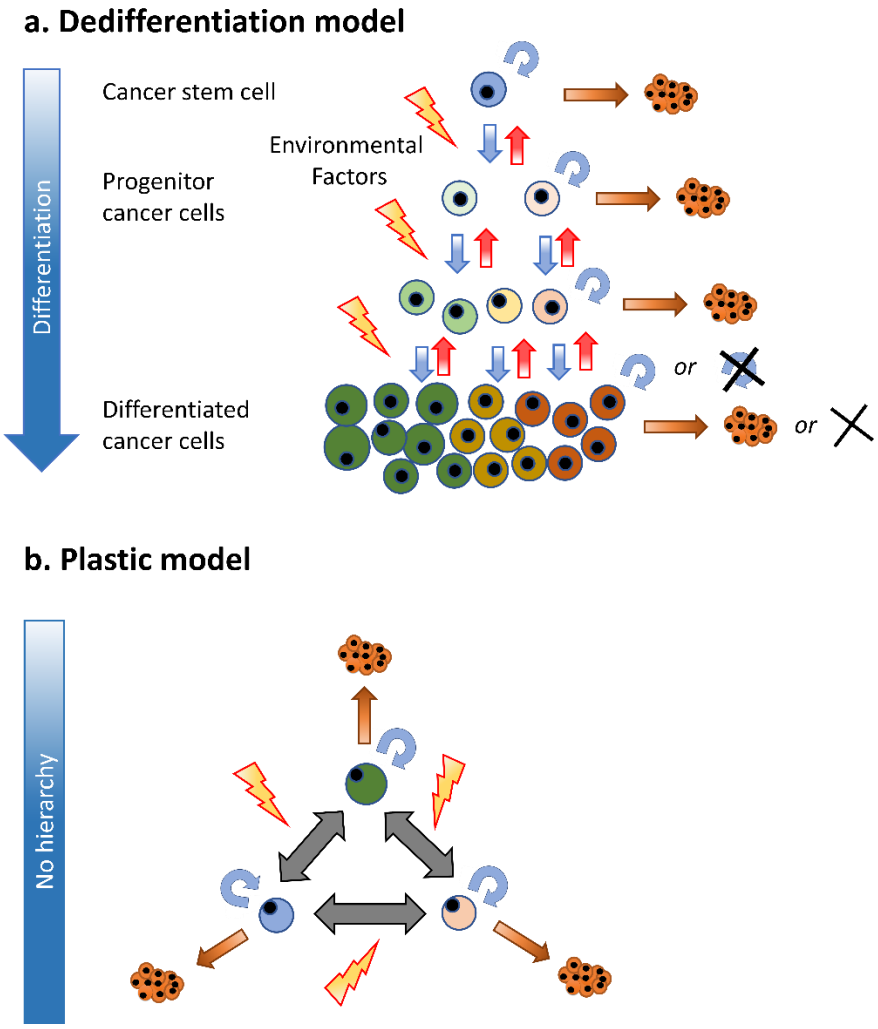

Figure 7: The adaptive models. a. In the dedifferentiation model, the differentiation process is reversible, meaning differentiated cancer cells can acquire stem-like properties. Cancer cells are distinguished based on their differentiation status thereby arranged in a hierarchical organization **b.** In the plastic model, cell plasticity is very high, and cells are able to convert to all phenotypic states. Here, no hierarchical organization is present. State transitions are thought to be mainly influenced by environmental factors. The two adaptive models vary in the degree of plasticity which might depend on cancer type and intrinsic features.

1.3.6. Transcriptomic stem cell associated intratumoral heterogeneity in GBM

Besides the analysis of genetic intratumoral heterogeneity, Sottoriva et al. examined the GBM tumor sections from different tumor regions at the transcriptional level as well. Therefore, transcriptional profiles of tumor sections were divided into the four GBM subgroups defined by Verhaak et al.(Verhaak et al., 2010). In 6 out of 10 patients, several transcriptional distinct subgroups within one tumor were detected, suggesting the coexistence of phenotypically divergent clones. This was one of the first studies revealing the transcriptomic intratumoral heterogeneity in GBM patients (Sottoriva et al., 2013). Transcriptomic data at the single cell level supported the presence of several transcriptomic subgroups within one tumor (Patel et al., 2014). Although reports could not infer genetic aberrations at the point mutation level, the results may indicate that transcriptional heterogeneity does not necessarily arise through chromosomal aberrations and thereby may not solely originate from clonal evolution. Subsequently, transcriptomic profiles of serum-free GBM sphere cultures and serum-dependent adherent GBM monolayers were used for either stemness and differentiated gene signatures. All tested GBM patient samples demonstrated a stemness gradient which was inversely related to cell proliferation suggesting that the stem-like cells were slower cycling. Since hierarchy from stem-like to differentiated cells was not divided into discrete subentities, no clear CSC or progenitor states were identified (Patel et al., 2014).

scRNA-seq in IDHm oligodendrogliomas revealed a hierarchical organization with a stem-like and two differentiated phenotypes. Gene transcription profiles showed that the highest variation was based on gene signature correlated to an astrocyte-like and an oligodendrocyte-like state (Tirosh et al., 2016b). Further discrepancies in transcriptomic profiles were based on the expression of stemness markers suggesting that stem-like phenotype was able to differentiate into two different lineages proving multipotency. Moreover, each genetically different clone (differences in copy number variation) contained stem-like and differentiated cell phenotypes which shows that the phenotypic states were not entirely correlated to genetic aberrations. In contrast to high grade GBMs, stem-like cells in low grade IDHmut gliomas displayed high cell cycling expression pattern. In contradiction to the authors interpretations, the representated stem-like phenotype did not define a distinct entity in oligodendroglioma, but rather a gradient from most stem-like to differentiated phenotype similar to GBM.

A third RNA-seq study at the single cell level on IDH-mutant gliomas, revealed transcriptomic similarities between oligodendrocytomas and astrocytomas (Venteicher et al., 2017). In both oligodendrogliomas and astrocytomas a stemness transcription profile similar to NSCs was identified that was associated with high proliferation. Differences in the

expression profile between glioma subtypes were mostly attributed to genetic aberrations and tumor microenvironmental composition where astrocytomas displayed a gene signature enriched for macrophages/microglia. Of note, transition from stem-like to differentiated phenotype in both astrocytomas and oligodendrogliomas appeared rather gradually as no descrete subpopulations could be identifyied based on transcritional profiles. A major drawback of transcriptomic analysis is the fact that they only give a snapshot in time and do not allow to subsequently perform functional studies which renders scRNA-seq data inconclusive on model types present in GBM (e.g. CSC or adaptive model). Therefore, different transcriptomic profiles can only inform on the presence of possible subpopulations or states at a specific moment in time.

1.4. Tumor microenvironments

The importance of the microenvironment on tumor progression and maintenance is increasingly recognized as a hallmark of cancer (Hanahan and Weinberg, 2000, Hanahan and Weinberg, 2011). As proposed for the adaptive model, the cell state may vary depending on extrinsic cues originating from the microenvironment. It is proposed that tumor microenvironment assures self-renewal and multipotency in CSCs and prevent differentiation by direct cell contact and secreted factors (Calabrese et al., 2007). Many studies have shown that exposure to different environmental cues such as low oxygen, extracellular metabolites or ECM components, changes the gene expression of the cells and may induce a switch in cellular state (Egeblad et al., 2010). E.g. it was shown that tumorigenic capacities of cancer cells are increased by the addition of ECM or irradiated cancer cells in transplantation assays (Kelly et al., 2007, Quintana et al., 2008, Gupta et al., 2011). The unresolved question is whether all tumor cells are able to function as a CSC under certain microenvironments and adapt to the best fitting phenotype or whether certain microenvironments select for survival of specific cell subpopulations.

In the brain, the tumor microenvironment involves interaction with different cell types as endothelial cells, pericytes, glial cells, astrocytes, NSCs, neurons, macrophages and microglia; and extracellular matrix components (ECM) such as fibrous proteins, proteoglycans and hyaluronic acid (HA) (Egeblad et al., 2010). Furthermore, bone marrow derived cells can be recruited to the tumor site (Burrell et al., 2014). Glioblastoma displays several tumor microenvironments such as the invasive, perivascular, hypoxic and/or acidic niches (Lathia et al., 2011a, Hjelmeland et al., 2011a, Hjelmeland et al., 2011b). These niches may coexist within one single tumor. In this thesis, we concentrate on the perivascular and hypoxic niches in GBM and do not consider immune cell-tumor interactions.

1.4.1. Perivascular niche

The perivascular niche delineates the areas around blood vessels where CSCs were described to be enriched (Calabrese et al., 2007). In several brain cancer samples, i.e. GBM and medulloblastoma, nestin^{+} CD43^{-} tumor cells are located in proximity of blood vessels suggesting that the microenvironment in the perivascular area is favorable for the CSC state. Similarly, NSCs are reported to reside in this perivascular niche. NSCs (nestin^{+}) coculture with endothelial cells was shown to maintain their stem cell state by Notch and Hes-1 activation (Shen et al., 2004). Using the same activation process, CSC may also keep their stemness abilities in the perivascular niche.

Next to endothelial cells, cancer cells residing in the perivascular niche secrete vascular endothelial growth factor (VEGF), fibroblast growth factors (FGF) and platelet derived growth factor (PDGF) to their environment (Hambardzumyan and Bergers, 2015, Bao et al., 2006b). VEGF represents to date the most studied cell signaling molecule contributing to the perivascular niche of CSC. In PDXs, VEGF-A concentration is elevated in the perivascular niche and was shown to be secreted particularly by CSCs ($CD133^+$) (Bao et al., 2006b, Skog et al., 2008). These growth factors induce angiogenesis (Olsson et al., 2006) and thereby maintains the perivascular niche that is important for the stem cell state. This was confirmed *in vitro* where conditioned medium from CSC secreting EVs containing VEGF-A induced migration and tube formation of human brain endothelial cells using a tubulogenesis and sprouting assay (Treps et al., 2017). Most importantly, VEGF is also induced by HIF in hypoxia. Targeted treatment of the perivascular niche with VEGF antagonists (e.g. Bevacizumab) decreased self-renewing abilities of these cells (Calabrese et al., 2007).

Nitric oxide (NO) is another molecule secreted by endothelial cells in the tumor bulk that could be related to the maintenance of the stemness state of a cell. NO was shown to activate Notch pathway in CSCs ($Nestin^+$). Activated Notch signaling induces increased sphere forming capacities *in vitro* and tumorigenic potential *in vivo* (Charles et al., 2010). Increased self-renewal in cancer cells was also achieved by the expression of the Notch ligands DLL4 and JAGGED1 by either cancer cells for autocrine activation or endothelial cells (Zhu et al., 2011). Other factors produced by endothelial cells that promote the CSC niche are angiopoietin (Ang1) or sonic hedgehog (Shh). They stimulate tumor growth and self-renewal ability (Liu et al., 2010, Clement et al., 2007).

1.4.2. Hypoxic niche

GBM is a rapidly growing tumor with leaky and disorganized blood vessels (**Fig. 8**). Hence, nutrient supply to the tumor core is very poor and eventually becoming a necrotic area. Oxygen (O_2) can diffuse approximately 100µm into the tissue (Heddleston et al., 2011). The average physiological oxygen concentration in the brain is around 7% (53mmHg), but ranges from 0.4% (3mmHg) in the midbrain to 8% (60mmHg) in the Pia mater (Evans et al., 2004). O_2 pressure (pO_2) is measured in millimeter of mercury (mmHg). In tumor tissue oxygen levels can decrease to less than 1% (Mohyeldin et al., 2010), where necrotic zones are formed in anoxic tumor regions. The definition of hypoxia is not fixed as O_2 levels vary throughout tumor tissue (Milotti et al., 2017, Bertout et al., 2008). Tumor areas are regarded as mildly hypoxic with 0.5-2.5% O_2 (4-20mmHg) and severe hypoxic at 0.1-0.5% (≤4mmHg). Most GBM tumors present a hypoxic gradient with an average O_2 pressure of

2.4mmHg (0.25% O_2) (Evans et al., 2008, Evans et al., 2004). Similar results were found by Colligridge et al in other gliomas (Collingridge et al., 1999). The presence of hypoxic areas in GBM are correlated with poor survival (Walsh et al., 2014).

The hypoxic response in a cell is largely mediated by two transcription factors known as hypoxia-inducible factors (HIF1 and HIF 2). In normoxia, the HIF-1α subunit is degraded via van Hippel-Lindau (VHL)-mediated proteasome degradation, whereas it is stabilized and dimerizes with HIF-1β to a functional transcription factor in hypoxia. In GBM, HIF-1α is mainly localized in pseudopalisading cells around necrotic areas and in invasive cells at the edge of the tumor (Zagzag et al., 2000). *In vitro* cultures showed that HIF-1α is activated in acute hypoxia, but only temporarily in chronic hypoxia (Holmquist-Mengelbier et al., 2006). In hypoxic environment cancer cells upregulate autophagy in a HIF-1α-dependent process for cell survival and growth (Mazure and Pouyssegur, 2010, Abdul Rahim et al., 2017, Hu et al., 2012).

HIF-1α is thus shown to regulate the general GBM cell response to hypoxia, whereas HIF-2α gene regulation is mostly linked to stemness maintenance and promotion of self-renewal abilities (Heddleston et al., 2009, Seidel et al., 2010, Li et al., 2009). Interestingly, in medulloblastoma HIF-2α expression is continued in chronic hypoxia and even persists after reoxygenation (Holmquist-Mengelbier et al., 2006, Holmquist et al., 2005) suggesting an oxygen independent role in stemness maintenance. In knock-down experiments of either HIF-1α or HIF-2α, Seidel and colleagues demonstrated in GBM sphere cultures that HIF-2α is mediating the hypoxia-dependent response leading to the CSC phenotype. In this case CSC phenotype was defined by the expression of side population genes (ASPHD2, MAML3, NFE2L2, ABL2 and NFATc2) (Seidel et al., 2010). McCord and colleagues showed that HIF-2α is active at 7% O_2 concentration but not HIF-1α (McCord et al., 2009). He observed higher clonogenicity of GBM sphere cultures at 7% O_2 compared to normoxia. These results indicate that sphere formation capacities are regulated in HIF-2α-dependent manner.

Generally, it is observed that CSC markers as CD133, SOX2, OCT4, Nestin and KLF4 are increased upon hypoxia and differentiation markers (GFAP and β3 Tubulin) are decreased indicating that low oxygen levels supports the induction and maintenance of stemness (Soeda et al., 2009, Bar et al., 2010, Heddleston et al., 2009, McCord et al., 2009).

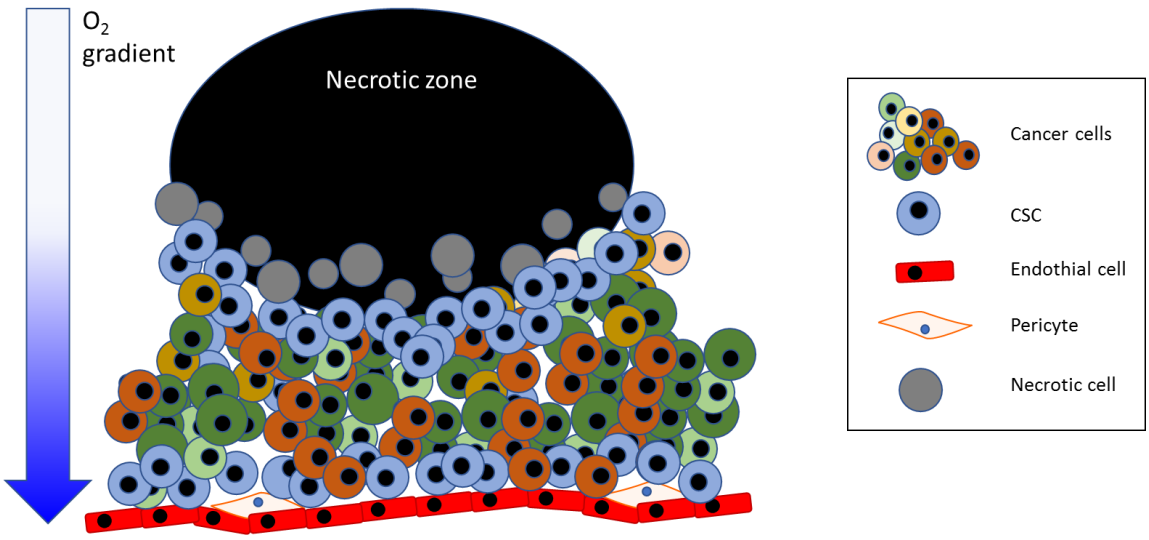

Figure 8: The perivascular and hypoxic CSC niche. The perivascular niche is found near the blood vessels delineated by endothelial cells and pericytes. The hypoxic niche is located near the necrotic zone, which is anoxic. Oxygen levels gradually increase with the proximity to blood vessels.

1.5. Therapeutic targeting of CSC-like states

The ultimate goal of cancer treatment is the complete eradication of cancer cells in a tumor. Different treatment approaches must be taken into consideration depending on the organization of a tumor. In case of a strict hierarchical structure, where CSCs are responsible for tumor growth, conventional therapy targeting bulk tumor mass is believed to be ineffective (**Fig. 9**). It is suggested that CSCs have increased radio- and chemoresistant capacities and thereby are not sensitive and tumor eventually relapses (Bao et al., 2006a). Hence, cancer treatment must take into account CSCs and target them specifically to overcome tumor recurrence. If CSCs are eliminated from a tumor bulk, cancer cannot progress since progenitor and fully differentiated cells have no tumorigenic potential. Several approaches are considered to eliminate CSCs in patients.

First therapeutic strategy involves cancer vaccines. They are designed for specific elimination of CSC surface marker positive cells. In the phase 1 trial in recurrent GBM, the ICT-121 dendritic cells (DCs) isolated from white blood cells of cancer patients are cultured and prepared with CD133 peptides for vaccination. This immunotherapy envisages to induce the formation of cytotoxic T cells specific for CD133 positive cells including CD133 expressing CSC in cancer patients (ClinicalTrials.gov identifier: NCT02049489). Therapy appears to be generally well tolerated in the ongoing clinical trial. Another DC-vaccine involves 6 peptides whose expression is associated with GBM CSCs: MAGE-1, HER-2, AIM-2, TRP-2, gp100 and IL-13Rα2 (Wen et al., 2015, Phuphanich et al., 2013). Phase 2 trial results show the HLA-A2 MGMT arm with increased progression free survival due to a higher immunologic activity compared to HLA-A1 patients. A phase 3 trial is envisaged.

A second approach to specifically target CSCs uses compounds to inhibit signaling pathways involved in the regulation and maintenance of stemness. These include TGF-β, Hedgehog, WNT, Notch or Ephrin pathways. The compounds can be subdivided into antibodies or small molecules with a maximal size of 900 daltons, which enables the latter to freely diffuse through cell membranes. Antibodies target cell surface structures, whereas small molecules interact with intracellular targets (for a complete list of compounds and clinical trial identifiers see (Marcucci et al., 2016)). Disulfiam (DSF) a small molecule for chronic alcoholism therapy is used in a phase II trial in newly diagnosed GBM (ClinicalTrials.gov identifier: NCT01777919). DSF was shown to inhibit $ALDH^+$ CSCs and MGMT activity (Liu et al., 2012, Paranjpe et al., 2014). Furthermore, it easily crosses BBB making it all together a promising drug.

Another alternative is to develop cancer vaccines that the target tumor microenvironment to eliminate CSC favorable tumor niches. The FDA approved bevacizumab is currently tested in combination with heat shock protein peptide complex-96 in recurrent GBM

(ClinicalTrials.gov identifier: NCT01814813) (Silver et al., 2016). Changing the tumor microenvironment by treatment pressure, may lead to negative selection of the CSC clone. Another treatment strategy for CSC eradication is the differentiation therapy, where a CSCs is forced to differentiate and lose their chemoresistant and tumorigenic potential. The best studied inducer of differentiation is all-trans-retinoic acid (ATRA) or also called tretinoin. In a phase II clinical trial in acute promyelocytic leukemia (APL) over 80% of the patients could be cured (ClinicalTrials.gov identifier: NCT02273102). However, in other AML patients, tretinoin was ineffective. In GBM, ATRA treatment was shown to inhibit tumor growth in PDXs and was shown to have antimigratory and antiagiogenic outcome (Campos et al., 2010). Another possible differentiation inducer is BMP4. It directs NSCs towards an astroglial fate. BMP4 treatment on CSCs in GBM induces *in vitro* and *in vivo* the expression of astrocytic markers and renders GBM cells sensitive to TMZ (Bonaguidi et al., 2005, Lee et al., 2008, Piccirillo et al., 2006). BMP4 treatment combined with bevacizumab reduces tumor size and invasive capacities in GBM PDXs (Rahman et al., 2013). One major drawback is the difficult BBB passing of BMP4 (Mangraviti et al., 2016).

In contrast, CSC-specific therapy in a tumor where the differentiation process is reversible due to environmental cues results in tumor regrowth. Here, a single differentiated cancer cell may acquire stem-like abilities and regenerate tumor mass (Vermeulen et al., 2012). Cancers with no hierarchical structure with adaptive phenotypes need to be additionally treated by targeting the adaptive processes. Therefore, it is indispensable to know how a certain tumor is organized to increase efficacy of cancer therapy.

Scope and aims of the thesis

2. Scope and aims of the thesis

To this date no curative treatment for GBM is available. One major reason for therapy failure is tumor heterogeneity. In this thesis, we focus on understanding inter- and intra-tumoral phenotypic heterogeneity. It has been proposed that CSCs create phenotypic diversity in GBM in an irreversible differentiation-like process. This small subpopulation of cancer cells with stem-like characteristics is made responsible for tumor progression and recurrence. However, currently none of the proposed CSC markers was able to identify a pure CSC population in GBM, neither alone or in combination with other markers. Numerous other experimental data indicate however that CSCs cannot be defined by specific marker expression and may in fact not be a distinct entity. Following the latter hypothesis, phenotypic heterogeneity is formed by adaptive abilities of cells where dynamic reversible state transitions may depend on microenvironmental clues (e.g. oxygen level, nutrient shortage, growth factors/inhibitors and inflammatory signals).

The identification of a true distinct CSC subpopulation in GBM would guide the treatment towards a cell specific targeted therapy. By specifically eliminating the cells at the apex of a one-way hierarchical organization, tumor progression could be arrested as tumor growth and chemoresistance would be hindered. On the other hand, if tumor heterogeneity is created by transitory cell states, CSC-targeted therapies would become unsuccessful since all cancer cells in a tumor would be able to generate new cancer cells.

Due to the recent evidence supporting an adaptive model for phenotype transitions in other solid tumors as melanoma and breast cancer (Gupta et al., 2011, Quintana et al., 2010, Chaffer et al., 2013), we hypothesized that GBM might modulate their phenotype as well by transitory cell states. The overall aim of this thesis was to elucidate whether changes in phenotype expression upon environmental change occur via one-way hierarchical organization or adaptive abilities.

To this end, we first assess phenotypical heterogeneity in a plethora of GBM patient-derived xenografts and GBM cell cultures. Furthermore, we simultaneously analyze four putative CSC-markers by multicolor flow cytometry. This analysis leads to a comprehensive study on the adaptive capacities of CSC-associated subpopulations in several environmental settings. Using mathematical modeling we elucidate the process in which phenotypical heterogeneity is created over time. Finally, transcriptomic differences between individual cells of CSC-associated subpopulations are assessed by single cell sequencing.

The major specific objectives of this thesis were:

- To characterize phenotypic inter- and intra-tumoral heterogeneity in GBM using cell membrane-associated CSC markers

- To assess stem cell properties of phenotypically defined CSC subpopulations in GBM

- To appraise hierarchical organization versus reversible adaptive phenotype as origin of CSC-associated heterogeneity

- To assess the effect of environmental factors on CSC-associated heterogeneity

- To analyze CSC-associated transcriptomic heterogeneity at single cell level

Materials and methods

3. Materials and methods

3.1. Bioinformatical analysis of the TCGA GBM database

Gene expression across GBM patients was investigated using The Cancer Genome Atlas (TCGA) cohort (160 GBM samples, provisional dataset on 25.10.2016) (Cancer Genome Atlas Research et al., 2013). TCGA data with appropriate heatmaps were analyzed and generated using Gitools software (Perez-Llamas, 2011 #525). The gene expression value corresponded to the median-centered RNA-seq data. DNA methylation data originated from a merged dataset of 25,978 probes shared by the HM27 and HM450 platforms analysis (#syn2486658). Genomic copy number alterations were obtained from PanCan12 Genom (for detailed analysis see https://www.synapse.org/). Group comparison was performed in Gitools using Mann-Whitney-Wilcoxon and Benjamini-Hochberg procedure was applied for multiple test correction. GBM samples were classified following the four GBM expression subgroups previously described by Verhaak (Verhaak et al., 2010): neural (n=28), mesenchymal (n=51), proneural (n=39) and classical (n=40) group. The analysis was performed with the help of Dr. Sabrina Fritah (Norlux Laboratory, LIH).

3.2. GBM research models

3.2.1. Clinical GBM samples and spheroids derivation

GBM samples were collected from the Centre Hospitalier in Luxembourg (Neurosurgical Department, Luxembourg) from patients that signed an informed consent. A prior approval from the National Ethics Committee for Research (CNER) in Luxembourg was given for tumor collection. Some tumors (P3, P8 and P13) used in this study have been obtained from the Haukeland University Hospital (Bergen, Norway). All collected biopsies were diagnosed as grade IV GBM IDH wilde-type. After removal, the tumor tissue was immediately kept on ice and proceeded as fast as possible. The tissue was cut with scalpels in order to obtain very small tumor pieces. Subsequently, the minced tumor sample was grown in medium consisting of DMEM 4.5g/L glucose w/o L-glutamine (Lonza) completed with 10% Fetal Bovine Serum (FBS) (ThermoFisher Scientific), 10 000U/ml Penicillin and Streptomycin (Pen-Strep) (Sigma-Aldrich), 200mM UltraGlutamine I (Lonza) and 10mM Non-Essential Amino Acid Solution (Lonza) in precoated agar-flasks. To coat flasks, BD Difco™ Agar (BD Biosciences) was heated to dissolve in sterile water to the final concentration of 0.85%. The agar solution was mixed 1:2.5 with above described medium to coat flasks subsequently. The cells were kept at 37°C and the medium was changed every 5 days. After 1-2 weeks in culture, first generation spheroids were collected by

decantation and stored in liquid nitrogen in DMEM 20% FBS with 10% dimethyl sulfoxide (DMSO) (Sigma-Aldrich) until orthotopic transplantation. This work was performed by the technical specialists of the laboratories in Luxembourg and Bergen.

3.2.2. Orthotopic patient-derived xenografts

To obtain orthotopic patient-derived xenografts (PDXs), spheroids obtained from GBM patient samples were implanted in the brain of eGFP expressing Nod/Scid mice (Bougnaud et al., 2016, Golebiewska et al., 2013, Niclou et al., 2008). The mice were anesthetized with an intra-peritoneal injection of 100mg/kg Ketamine and 10mg/kg Xylazine. The local anesthesia Marcain with 0.25% adrenaline was injected subcutaneously at incision site. The head of the mouse was subsequently fixed in a stereotactic frame (Narishige SR-5R) and the Hamilton syringe prepared with the organotypic GBM spheroids was introduced at the coordinate X=2mm, Y=1mm and Z=0mm (when the bregma is representing position 0,0,0 on a X-Y-Z axis). 4-5 spheroids were slowly injected (coordinate 2,1,2) and the needle was retracted after 2 minutes of incubation. The hole in the skull was closed using bone wax and the skin was sewed together by separated knots (Ethilon 3-0). The animals were placed in a warming chamber until wake up and were later kept in specific-pathogen-free (SPF) condition. Once a week the animals were weighted and they were as well controlled every day for neurological symptoms, such as uncontrolled movements, locomotor problems, lordosis, behavioral abnormalities in nesting and hyperactivity. At the appearance of at least one these symptoms the mice were sacrificed. The surgical protocol and handling of the mice was performed by Anais Oudin and Virginie Baus (Norlux Laboratory, LIH) in agreement to the European Directive on animal experimentation (2010/63/EU) and the local ethical committees.

3.2.3. GBM cell cultures

3.2.3.1. 3D GBM stem-like cultures

The GBM stem-like cells NCH644, NCH421k, NCH660h, NCH601 and NCH465 derived from primary IDH wild-type GBM samples, were kindly provided by Dr Christel Herold-Mende (Department of Neurosurgery, University of Heidelberg) (Campos et al., 2010). Non-adherent sphere cultures NCH421k, NCH660h, NCH601, and NCH465 were kept in DMEM-F12 medium (Lonza) containing 1xBIT100 (Provitro), 2mM L-Glutamine, 30U/ml Pen-Step, 1U/ml Heparin (Sigma-Aldrich), 20ng/ml bFGF (Miltenyi) and 20ng/ml EGF (Provitro). When spheres reached a size of approximately 150 - 200µm, they were mechanically dissociated and then passaged 1:3 twice a week. NCH644 cells also grown as non-adherent spheres, were cultured in Neurobasal® base medium (Life Technologies) supplemented with 1xB-27 (Life Technologies), 2mM L-Glutamine, 30U/ml Pen-Step, 1U/ml

Heparin, 20ng/ml bFGF and 20ng/ml EGF. At a size of 200µm the spheres were mechanically dissociated. NCH644 were passaged 1:3-4 twice a week. The remaining GBM sphere cultures TB101 and TB107 which were kindly provided by Dr. Håkan Hedman, (Umeå University, Sweden) were cultured in DMEM-F12 medium with 1xB27 and 1xN2 supplements (Provitro), 2mM L-Glutamine, 30U/ml Pen-Step, 1U/ml Heparin, 20ng/ml bFGF and 20ng/ml EGF. These cell cultures were mechanically dissociated to be split at a ratio of 1:3-4 twice a week. All centrifugation steps of cells were performed for 3 minutes at 1200rpm.

3.2.3.2. Conventional GBM cell cultures

The adherent GBM cell lines U87 and U251 were cultured in DMEM medium (Lonza) supplemented with 10% FBS, 30U/ml Pen-Step and 2mM L-Glutamine. When cells reached sub-confluency of approximately 80%, they were splited 1:8 twice a week. Passaging of cells was performed by washing with Versene (Phosphate Buffered Saline (PBS) (Lonza) complemented with 10mM EDTA (ThermoFisher Scientific)) followed by trypsinization (1xTrypsin (Lonza)). All centrifugation steps of cells were performed for 3 minutes at 1200rpm.

3.2.3.3. Normoxic and hypoxic culture systems

Classical normoxic cultures were kept at 37°C under 5% CO_2 and atmospheric oxygen in Thermo Scientific® Steri-cycle CO_2 incubator (ThermoFisher Scientific). Hypoxic conditions of 0.5% O_2, were maintained in the hypoxic incubator chamber (Galaxy 48R incubator, New Brunswick) at 37°C under 5% CO_2. O_2 levels were regulated by injecting N_2. Every 4 days, new medium was added to 3D GBM stem-like cultures kept at 0.5% O_2 and big spheres were dissociated by pipetting. Medium of conventional adherent cell lines was exchanged every 4 days. Phenotypic reversibility to hypoxic environment was measured by culturing NCH644 and NCH421k GBM stem-like cultures for 7 days in hypoxia and passing them to normoxic conditions.

3.2.4. Orthotopic cell line-derived xenografts

NCH660h, NCH601 and NCH465 sphere cultures were mechanically dissociated to single cells and concentrated to 300’000 cells/µl in DMEM-F12 with no supplements. For GBM stem-like cultures NCH644 and NCH421k 50’000 cells/µl in Neurobasal and DMEM-F12, respectively, were used for transplantation. 1µl per GBM stem-like culture were implanted orthotopically into NOD/SCID mice as described above (**Heading 3.2.2.**) (2-3 mice per condition). Phenotype reversibility of tumor cells of NCH644 and NCH421k cell culture-derived xenografts (2 mice of each GBM stem-like culture) to normoxic culture system was

performed by dissociating tumors to single cells (**Heading 3.3.1**.). Tumor cells were kept under normal normoxic *in vitro* culture conditions with their respective culture media.

3.2.4.1. *In vivo* limiting dilution assay

Single NCH644 cells were stained with 1µg/ml LIVE/DEAD® Fixable Near-IR Dead Cell Stain solution for 15 minutes in the dark at room temperature, followed by one HBSS washing step. Sterile FACS-sorted viable single cells were collected and serial dilutions of 100, 300, 500, 1000 and 5000 cells/2µl were injected. 3 nude mice per condition were used.

3.2.4.2. Tumor formation and survival assay

To analyze the tumor formation capacities of NCH644 CSC-associated subpopulations 2, 6, 11 and 15 (**Heading 3.3.3**.), 5000 FACS-sorted viable single cells of each subpopulation were engrafted separately into nude mice directly after sort (n=6-7). Viable sorted NCH644 cells were used as control. Animals were monitored daily and were evaluated for a survival study based on the following criteria: (1) loss of more than 10% of body weight, (2) exhibition of strong neurological signs (difficulty ambulating or abnormal movement), (3) increased lordosis or (4) swollen belly. The criteria were scored as follows: 0 = none, 1 = early, 2 = established, 3 = severe signs and animals were sacrificed when 3 criteria with grade 2 or 1 criterion with grade 3 were reached. Survival curves and corresponding statistics (Gehan-Breslaw-Wilcoxon Test) were generated by GraphPad Prism 5.

3.2.4.3. Tumor volume measurement

Tumor volume was measured by Magnetic Resonance Imaging (MRI) on a 3T preclinical scanner MR Solutions ('Preclinical Scan' acquisition software), equipped with a mouse head volume coil. The Fast Spin Echo T2-weighted 2D sequence protocol was used with the following parameters: echo time of 68ms, repetition time of 3000 ms and echo train of 8. The MRI imaged an area of 25x25 mm with a matrix size of 256x240. 15 slices of 1 mm thickness with no gaps between slices in the sequence were captured. The animals were placed prone in the cradle and were sedated with gas anesthesia (2% isoflurane mixed in medical air). The body temperature was maintained at 37°C and breathing frequency was monitored throughout the scan session. The total scanning time for T2 weighted scan took 6 minutes and 12 seconds. Obtained MR images of one brain were opened as a stack on ImageJ. Tumor was delineated using the polygon selection tool and the delineated area was measured by analysis tool. The size of the tumor was defined as: $pixel\ area = \frac{FOVx * FOVy}{MATx * MATy}$, where Field of View (FOV) and Matrix size (MAT) was defined beforehand in the MRI acquisition software. When tumor areas of each stack image were calculated,

tumor areas were multiplied by slice thickness (1mm) and volumes were added to obtain total tumor volume. Statistical differences were calculated using Student t-test.

3.3. Flow cytometry analysis

3.3.1. Cell dissociation of GBM xenografts and sphere cultures

To obtain a single cell solution from GBM xenografts generated in the mouse brain, MACS Neural Tissue Dissociation Kit (P) (Miltenyi) was used following manufacturer's protocol. The brain was first removed, minced with scalpels and collected into a tube with HBSS w/o Ca2+/Mg2+ for washing. Tissue was resuspended in 37°C prewarmed EM1 solution (50µl Enzyme P, 1900µl Buffer X and 2,5µl 2-mercaptoethanol) and the mixture was incubated for 15 minutes at 37°C by reverting the tube regularly. In the following step EM2 (20µl Buffer Y and 10µl Enzyme A) was added and the tissue was mechanically dissociated using glass pipettes. The solution was incubated 10 minutes at 37°C by inverting the tube every 5 minutes. Mechanical dissociation was repeated and cells were washed with HBSS. Cells were passed through a 50µm sterile filter and the tumor cell number was counted using a hemocytometer. 10^6 tumor cells were aliquoted per sample.
Sphere cultures were mechanically dissociated to obtain single cells. Single cell suspension was filtered (50µm pore size) and counted to aliquot 10^6 cells per test. All cells were kept in flow buffer (2% FBS, 10mM Hepes (Sigma-Aldrich), HBSS) until further processing.

3.3.2. Cell membrane staining

Single cell suspensions were subsequently stained with 1µg/ml LIVE/DEAD® Fixable Near-IR Dead Cell Stain for dead cell discrimination. Generally, antibody staining for cell surface markers was realized in flow buffer at 4°C for 30 minutes to 2 hours followed by one washing step (see **Table 1** for list of antibodies and concentrations). For tumor cells derived from orthotopic transplantations into non-eGFP mice, human specific CD90 antibody was additionally added to the panel to distinguish human tumor cells from mouse stroma. Cells were subsequently washed once with flow buffer and diluted to 10^6 cells per 100µl for acquisition on flow cytometer (for flow cytometer settings and the antibody panel see **Annex 1**). BD™ Compensation Beads Negative Control (FBS) and BD™ Compensation Beads Anti-Mouse Ig,κ were used to determine the amount of spillover to enable fluorescence compensation. Cell surface marker testing in GBM PDXs and multicolor panel was setup with the help of Dr. Anna Golebiewska (Norlux Laboratory, LIH).

3.3.3. Identification of CSC-associated subpopulations

CSC-associated subpopulations of GBM stem-like cultures were distinguished by multicolor flow cytometry. Therefore, single cells were simultaneously stained with the four CSC-associated cell surface markers, CD133/1, CD44, CD15, A2B5 and LIVE/DEAD® Fixable Near-IR Dead Cell Stain (1µg/ml). The staining was performed on ice for 30 minutes followed by one washing step (see **Table 1** for list of antibodies and concentrations). Cells were subsequently diluted to 10^6 cells per 100µl for acquisition on flow cytometer (for flow cytometer settings and the antibody panel see **Annex 1.a-b**). Using DIVA software, the cells were divided into 16 subpopulations based on the intensity of fluorescence measured for each cell surface marker.

3.3.4. Intracellular marker phenotyping

The cells were stained with 1µg/ml LIVE/DEAD® Fixable Near-IR Dead Cell Stain for 15 minutes in the dark. In case of tumors derived from xenografts, human specific CD90 antibody staining was performed simultaneously with LIVE/DEAD® Fixable Near-IR Dead Cell staining for 30 minutes on ice in the dark. Once washed with HBSS, the cells were fixed with the BD Cytofix fixation buffer (BD Bioscience) for 30 minutes at room temperature. Cells were subsequently washed twice in 1x Perm/Wash buffer (BD Bioscience) and permeabilized for 10 minutes at room temperature. Antibodies and the appropriate isotype controls were added to the cells for staining during 1 hour on ice in the dark (**Table 1**). Cells were washed twice with 1x Perm/Wash buffer and were resuspended in the flow buffer. Cells were kept on ice until measurement on flow cytometer (for flow cytometer settings and antibody panel see **Annex 1.a and c**). BD™ Compensation Beads Negative Control (FBS) and BD™ Compensation Beads Anti-Mouse Ig,κ were used to determine the amount for spillover and enable compensation. The experiment was conducted in 3 biological replicates with 3 technical replicates each.

3.3.5. Flow cytometer recording

3.3.5.1. FACS Aria™ SORP cytometer

The FACS Aria™ SORP cytometer (BD Biosciences) was fitted with a red, a UV, a violet, a blue and a yellow/green laser (for flow cytometer lasers and filters see **Annex 1.a**). The flow cytometer was stabilized for at least 1 hour before laser alignment and data acquisition. The Coefficient of Variation of the instrument (%CV) was routinely examined before each experiment. A 100µm (routinely) or 85µm (for differentiation experiments and sorting of NCH421k and NCH644 subpopulation 2 and 6 for single cell sequencing) nozzle and window extension (WE) 3 were used for data acquisition and sorting. PMT voltages were

adjusted each time with Cytometer Setup & Tracking Beads (BD Biosciences) to keep fluorescent signals comparable between experiments. Cells were collected at a maximum rate of 2500 events/s. For data analysis, approximately 30'000 viable single cells (or viable, single tumor cells in case of PDXs samples) were recorded per tube. For CSC-associated subpopulation distinction, at least 50'000 viable single cells or tumor cells were collected. Data acquisition and analysis were performed using DIVA software (BD Bioscience). Histograms were prepared with the FlowJo software.

3.3.5.2. ImageStream imaging cytometer

Imaging flow cytometry was performed with ImageStream imaging cytometer (Amnis) fitted with a near-UV, a blue, a yellow-green, a red and an infrared laser (for flow cytometer lasers and filters see **Annex 1.b**). Pictures were recorded at 60x magnification at low speed high sensitivity mode. 50'000 viable single cells were collected at a maximal speed of 1200 cells/s. Acquisition and analysis was carried out using IDEAS® image analysis software. Acquisition was performed at the Paris Cardiovascular Research Center (Inserm U970, Flow Cytometry Core Facility) in France by Dr. Coralie Guerin.

3.3.5.3. FACS Canto II cytometer

FACS Canto II cytometer (BD Biosciences) was equipped with a red and a blue laser (for flow cytometer lasers and filters see **Annex 1.c**). Performance of the cytometer was controlled each time with the Cytometer Setup & Tracking Beads. For data acquisition, a window extension (WE) of 7 was used. Cells were collected at a speed of maximal 2500 events/s and approximately 30'000 viable single (tumor) cells were recorded per tube. Data acquisition and analysis were performed using DIVA software (BD Bioscience). Histograms were prepared with the FlowJo software and cell cycle histograms were analyzed using the ModFit software.

3.3.6. Sterile FACS-sorting

Cell membrane staining for sterile sorting was performed as previously described (**Heading 3.3.2.**). All reagents were sterile and handling was performed under laminar flow. Furthermore, flow buffer was supplemented with 10µg/ml DNAse I and 30U/ml Pen-Step. Before cell acquisition, FACS Aria™ SORP cytometer was rinsed for 30 minutes with sterile H_2O to remove decontaminants. Sorting was performed at 4°C.

Table 1: List of antibodies and reagents used for flow cytometry and immunohistochemistry

Epitope	Conjugate	Clone	Supplier	Dilution
A2B5	APC/PE	105-HB29	Miltenyi	FC:10µl/test
A2B5	AF488	MAB312RX	Chemicon	ICC:1:20
AnnexinV	APC		Immunotools	FC:10µl/test
TUBB3	Alexa Fluor 647	TUJ1	BD Bioscience	FC:5µl/test
CD15/SSEA-1	Alexa Fluor 647	MC-480	Biolegend	FC:5µl/test ICC:1:50
CD15/SSEA-1	PE	MEM-158	Immunotools	FC:10µl/test
CD15/SSEA-1	PERCP-Cy5.5	W6D3	Biolegend	FC:5µl/test
CD24	PE	SN3	Immunotools	FC:10µl/test
CD29	APC	MEM-101A	Immunotools	FC:10µl/test
CD44	FITC	MEM-85	Immunotools	FC: 10µl/test
CD44	PE-Cy7	IM7	eBioscience	FC:1.2µl/test ICC:1:50
CD56	PE-Cy7	N-CAM	BD Bioscience	FC:5µl/test
CD90	PE-Cy7/APC	5E 10	BD Bioscience	FC:5µl/test
CD95	APC	Fas/APO1	BD Bioscience	FC:20µl/test
CD133-1	PE /APC	293C3/AC133	Miltenyi	FC:10µl/test ICC:1:50
CD195	PE	2D7/CCR5	BD Bioscience	FC:20µl/test
EGFR	PE	EGFR.1	BD Bioscience	FC:20µl/test
GFAP	AF647	1B4	BD Bioscience	FC:5µl/test
Isotype control IgG1	FITC	PPV-06	Immunotools	FC:5µl/test
Isotype control IgG1κ	PerCP-Cy5.5	MOPC-21	BD Bioscience	FC:5µl/test
Isotype control IgG2a	Alexa Fluor 647	eBR2a	eBioscience	FC:5µl/test
Isotype control IgG2b	Alexa Fluor 647	eB1491/10H5	eBioscience	FC:5µl/test
NES	PercPcy5.5	25/NESTIN	BD Bioscience	FC:5µl/test
NG2	PE	LHM-2	R&D	FC:10µl/test
VIM	FITC	V9	Thermo Fischer	FC:5µl/test

FC = Flow cytometry (test 10^6 cells/100µl); ICC = Immunocytochemistry

3.4. GBM *in vitro* functional assays

3.4.1. Cell growth assay

To test cell growth, 50'000 single cells of every GBM cell line were plated for each measuring point. For sphere cultures, medium was added every 3-4 days and spheres were mechanically dissociated if necessary. Cells were cultured at normoxia or hypoxia (0.5% O_2). Medium of adherent cell lines was replaced every 3-4 days. After 3, 7, 10 and 14 days, cells were collected (adherent cells were trypsinized). A 1:1 dilution of the cell suspension with 0.4% Trypan blue (Invitrogen) was used to distinguish dead cells. Total viable cell number was recorded with the Countess® cell counter (Invitrogen). The experiment was performed in 3 biological replicates with 3 technical replicates each. Statistical differences were calculated using Student t-test.

Similarly, proliferative capacities of CSC-associated NCH644 subpopulations were examined in normoxia and hypoxia, except proliferative capacities were measured over an extended time period (14 days vs 60/70 days depending on O_2 levels). 300 cells of each subpopulation were sorted per well of a 48-well plate and cultured for 20, 30 and 70 days at normoxia and for 30 and 60 days at 0.5% O_2 hypoxia. At each time point cells were derived from each subpopulation and total viable cell number was measured as described above. To compare proliferation rates of NCH644 subpopulations doubling time was calculated as follows: $doubling\ time = \frac{t_2 - t_1}{log_2 \frac{cell\ number_2}{cell\ number_1}}$, where t_1 and t_2 represented time points. The experiment was repeated 3-6 and 6-12 biological repeats in normoxia and 0.5% O_2 hypoxia, respectively. The significance of the differences from doubling times between subpopulations were tested with the help of Ms. Sonia Leite, Dr. Nicolas Sauvageot (Competence Center for Methodology and Statistics at LIH) and Dr. Petr Nazarov (Proteome and Genome Research Unit, LIH) used mixed linear models with subpopulation as fixed-effects and considered plate's effect as random.

3.4.2. Cell viability assay

To test viability of GBM cell cultures at different O_2 levels, the number of viable, apoptotic and necrotic cells was measured. Therefore, cells were cultured at normoxia or hypoxia 0.5% O_2 for 16 hours, 2 and 7 days. 10^6 cells per sample were resuspended in 100µl of binding buffer (HBSS w/o Ca2+/Mg2+ (Sigma-Aldrich), 2% FBS and 0.01M Hepes pH 7,4, 0.14M NaCl (Sigma-Aldrich) and 2.5mM CaCl2 (Sigma-Aldrich)). Staining with AnnexinV (**Table 1**) was performed in the dark for 30 minutes at room temperature. The cells were subsequently washed with binding buffer and kept on ice until analysis on the flow cytometer. 50µg/ml propidium iodide (PI) (Invitrogen) was added 5 minutes before data

acquisition to minimize its toxicity for cells (for flow cytometer settings and the antibody panel see **Annex 1.c**). The experiment was performed in 3 biological replicates with 3 technical replicates each. Statistical differences were calculated using Student t-test with Bonferroni multiple-significance-test correction for four comparisons.

3.4.3. Proliferative activity assay

To measure the percentage of proliferative cells, cell cycle analysis was performed by DNA quantification. Cells were cultured in normoxia or hypoxia 0.5% O_2 for 16 hours, 2 and 7 days. 10^6 single cells were aliquoted per sample, centrifuged and resuspended in HBSS containing 1µg/ml LIVE/DEAD® Fixable Near-IR Dead Cell Stain (Invitrogen). After 15 minutes of incubation in the dark at room temperature, the cells were washed once with HBSS. Cells were subsequently fixed in ice cold 80% ethanol and kept at -20°C over night. The next day, ethanol was removed and the cells were stained in the dark for 30 minutes at room temperature with PI staining buffer (0,1% Triton, 0.2µg/ul RNAse and 1µg/ml PI (Invitrogen) in HBSS). The volume was adjusted to 100µl and the samples were measured on flow cytometer (for flow cytometer settings and the antibody panel see **Annex 1.c**). The experiment was performed in 3 biological and 3 technical replicates each. Statistical differences were calculated using Student t-test with Bonferroni multiple-significance-test correction for three comparisons.

In contrast to the DNA staining of fixed cells, cell cycle analysis of NCH644 CSC-associated subpopulations was performed using viable cells. Therefore, single cells were resuspended in their growth culture media (10^6 cells/100µl) provided with 10mM Hepes and 5µg/ml Hoechst 33342 (Sigma-Aldrich) and incubated for 2 hours at 37°C on a shaker in the incubator (Stieber et al., 2014). Cells were immediately put on ice to avoid efflux of Hoechst and resuspended in ice cold flow buffer. The entire subsequent cell membrane staining procedure was performed on ice. The experiment was performed in 3 biological replicates and statistical differences were calculated using Student t-test with Bonferroni multiple-significance-test correction for two comparisons.

3.4.4. Sphere forming assays

To test the clonogenic abilities of 3D GBM stem-like cultures and conventional GBM cell lines, the cell suspensions were prestained with 1µg/ml LIVE/DEAD® Fixable Near-IR Dead Cell Stain (Invitrogen) solution. After 15 minutes incubation in the dark at room temperature followed with one HBSS washing, single viable cells were FACS-sorted into 96-well plates (1 cell per well, 1 plate per cell line) containing 200µl culture medium (for flow cytometry sorting settings see **Heading 3.3.6**.). Plates were kept at normoxia or hypoxia (0.5% O_2). Every 4-5 days, fresh medium was added. After 4 weeks, the number of formed spheres

per plate were counted. Images of the spheres were recorded on Leica® DMI6000 B inverted microscope with a Leica® DFC320R2 camera with its concordant Leica Application Suite® software. Sphere size was measured using the "Ruler Tool" on Adobe Photoshop. The experiment was conducted in 4 biological repeats for sphere number calculation. Sphere sizes were measured of 20 spheres from one biological experiment. Statistical differences were calculated using Student t-test.

To test self-renewal ability of CSC-associated subpopulations, the above described protocol was applied and continued. The formed spheres of each subpopulation were collected (passage 1) and single viable cells were resorted (one 96-well plate/subpopulation, 1 cell/well). Replating was repeated three times (passages 2-4). Total sphere number and average sphere size (n=20 per subpopulation if available) were recorded at each passage before cell collection. Each subpopulation at each passage was phenotyped as described above (**Heading 3.4.2.**). FACS-sorted NCH644 viable single cells were used as a control. The experiment was repeated independently 4-6 and 2-4 times in normoxia and hypoxia, respectively. Significant differences of sphere number across populations and passages were tested with the Kruskal-Wallis test. Significant differences of sphere size between populations and passages were tested with mixed linear models with either subpopulation or passage as fixed-effects and considering plate's effect as random. The statistical analyses for sphere number and sphere size were performed with the help of Ms. Sonia Leite and Dr. Nicolas Sauvageot (Competence Center for Methodology and Statistics at LIH). Statistical differences of phenotypic states were calculated using Student t-test with Bonferroni multiple-significance-test correction for sixteen comparisons.

3.4.5. Invasion assay

Invasive abilities were measured by Boyden chamber assay. Chambers of 8µm pore size fitting into a well of a 24-well plate (Thincert cell culture inserts, Greiner) were coated with 0.05mg/ml collagen type I (Sigma-Aldrich), 0.5mg/ml protein of ECM gel (Sigma-Aldrich) in 1:1 PBS-DMEM-F12 mixture for 2 hours at 37°C. Non-polymerized coating was removed before plating 50'000 cells per upper inlay of the Boyden chamber. Medium supplemented with 10% FBS was added in the lower well of the 24-well plate. Incubation time varied between 2 to 3 days depending on GBM cultures used. Cells in Boyden chambers were fixed in 4% PFA for 15 minutes and washed briefly 3 times in PBS. Cells were stained with 0.05% Crystal Violet Solution (Sigma-Aldrich) for 15 minutes and then washed in dH_2O. Non-invading cells in the upper part of the chamber were removed using a cotton swab and the chamber was air-dried. 5 random pictures of the porous membrane per chamber were taken per inlay on a Leica® DMI6000 B inverted microscope equipped with a Leica® DFC320R2 camera and the Leica Application Suite® software. The cell number per area

was assessed using ImageJ. The percentage of invading cells was calculated as follows: $percentage\ of\ invading\ cells = \frac{mean\ of\ invaded\ cells\ per\ area * 100}{total\ number\ of\ cells}$, where the total number of cells was obtained by multiplying the number of plated cells with the growth rate for the time period the experiment was performed. The experiment was conducted in 3 biological replicates with the help of Dr. Anne Schuster (Norlux Laboratory, LIH). Statistical differences were calculated using Student t-test.

3.4.6. Immunocytochemistry

Protocol to obtain frozen sphere sections, NCH644 cells were cultured 7 days until they formed big spheres (approximately 300µm of diameter). These were washed carefully twice with PBS and collected by gravity with Tissue-Tek® O.C.T.™ Compound (Sakura Finetek). Spheres were flash frozen in -80°C precooled iospentane for 5 minutes. Frozen sphere blocks were cut to 10µm sections on the LEICA CM 1850 UV cryostat (Leica Biosystems) and mounted on glass coverslips. Slides were dried and subsequently fixed in 4% PFA for 10 minutes. Sections were blocked for 30 minutes in TBS (Tris-buffered saline) supplied with 2% FBS and incubated with conjugated primary antibodies (**Table 1**) and 1µg/ml DAPI (4′,6-Diamidin-2-phenylindol) (Invitrogen). Slides were washed consecutively 3 times 5 minutes in TBS. After a final short rinse in dH_2O, they were water-mounted using Fluoromount™ Aqueous Mounting Medium (Sigma-Aldrich). One day later, the sections were sealed with nail polish. For image acquisition Leica® DMI6000 B inverted microscope with a Leica® DFC350FXR2 camera was supported by the Leica Application Suite® software.

3.4.7. Temozolomide treatment

Temozolomide (TMZ) (Sigma-Aldrich) was added at subleathal doses of 200µmol for NCH644 and 50µmol for NCH421k GBM stem-like cells for short-time (12 hours and 2 days) and long term (7 days) treatment. In a second culture condition DMSO was added in an equal volume than TMZ. These cells were used as a control to TMZ treatment because TMZ was dissolved in DMSO. Every 4 days, new TMZ/DMSO containing culture medium was added and big spheres were dissociated by pipetting. Cells were subsequently collected and stained for flow cytometric analysis. The experiment was performed in 3 biological replicates with 3 technical replicates each. Statistical differences were calculated using Student t-test with Bonferroni multiple-significance-test correction for sixteen comparisons.

3.4.8. Differentiation assay

For differentiation assays, flasks were precoated with 1:20 ECM gel (Sigma-Aldrich) in Neurobasal for NCH644 or DMEM-F12 for NCH421k cultures. Flasks were incubated for 1,5h at 37°C and excess liquid was subsequently removed. NCH644 and NCH421k were added in their corresponding growth medium. Cells were allowed to attach for 24h then medium was replaced with DMEM-F12/Neurobasal medium supplemented with 10% FBS and 10µg/ml all-trans retinoic acid (ATRA) (Sigma-Aldrich). The medium was changed every second day and flasks were kept in dark. The experiment was conducted in normoxia and 0.5% hypoxia. After 14 days of adherent culture, single cells were detached using Accutase Solution (Sigma-Aldrich). The cells were divided in two parts: on part was used for flow cytometric analysis. The other part was kept as non-adherent 3D cultures in normoxia and the cells were again phenotyped after 14 days. Non-treated 3D sphere cultures were used as control to evaluate changes upon non-adherent 3D to adherent 2D culture system in normoxia and hypoxia, 2D differentiation in normoxia and hypoxia and the reversibility of differentiated and non-differentiated 2D cultures upon non-adherent 3D reculture in normoxia. Images of cell cultures were taken on EVOS®fl (AMG-Advanced Microscopy Group) digital inverted microscope. The experiment was performed in 3 biological replicates with 3 technical replicates each for NCH644 cultures. 1 biological replicate with 3 technical replicates were realized for NCH421k cultures. Statistical differences for internal marker expression were calculated using Student t-test. Additional Bonferroni multiple-significance-test correction for sixteen comparisons was applied for the statistical analysis of phenotypical states.

3.4.9. Plasticity/multipotency test

To examine multipotent capacities of NCH644 subpopulations, 300 cells of each subpopulation were sorted to a 48-well plate and cultured for 20, 30 and 70 days in the culture medium at normoxia or 60 days at 0.5% O_2 hypoxia. At each time point cells were derived from each subpopulation and were phenotyped as described above. The experiment was repeated for each NCH644 subpopulation independently in 9-12 and 6-12 biological repeats in normoxia and hypoxia, respectively. The proportion of each subpopulation was calculated as percentage of the viable single cells. Alluvial plots have been generated under R (Team, 2013) using the package *alluvial* available at https://github.com/mbojan/alluvial (R, 2016) with the help of Arnaud Muller (Proteome and Genome Research Unit, LIH). Statistical differences of phenotypic states were calculated using Student t-test with Bonferroni multiple-significance-test correction for sixteen comparisons.

3.5. Mathematical modeling

3.5.1. Principles of discrete Markov chain modeling

In order to quantify the transitions between the 16 phenotypes Markov chain modeling was applied. This part was performed in collaboration with Thomas Buder, Dr. Andreas Deutsch and Dr. Anja Voss-Böhme (Zentrum für Informationsdienste und Hochleistungsrechnen (ZIH), Technische Universität Dresden, Dresden, Germany and Fakultät Informatik / Mathematik, Hochschule für Technik und Wirtschaft Dresden, Dresden, Germany Technische Universität Dresden) who implemented the model in the freely available R package *CellTrans* (Buder et al., 2017) (http://github.com/tbuder/CellTrans).

The model is based on the assumptions that cell state alterations occur due to stochastic cell state transitions only depending on the current state of the cell and possibly the experimental environment (e.g. hypoxia) and that proliferation rates of the involved phenotypes are approximately equal. This approach leads to the estimations of a Markov chain with a transition matrix containing the probabilities of state transitions (**Annex 2.a** for matrix construction). This matrix allowed to discriminate frequent and non-frequent state transitions and identify hierarchical or non-hierarchical transition behavior. If the underlying network is irreducible, each state can transit directly or via intermediate steps into any other state. This behavior implies that the stochastic state transitions are non-hierarchical and therefore reversible in biological sense. In contrast, if the transition network has a tree structure, this corresponds to a perfect hierarchy. In general, intermediate network structures are possible as well, which imply some degree of hierarchy between transient states at the top of the hierarchy and recurrent states at the bottom of the hierarchy (**Annex 2.b** for Krackhardt calculation). Moreover, transition matrixes can be used to investigate whether the cell state transitions between positive and low/negative expression of one marker in normoxia and hypoxia were dependent on the level of expression of the other markers (**Annex 2.c** for marker dependency calculation). Most importantly, on the basis of the estimated transition matrix, it is possible to predict the composition of the population in equilibrium by calculating the Markov chain stationary state. In addition, the time from a specific initial composition until an approximate equilibrium is reached can be estimated.

3.5.2. Markov model validation

To test predictional capacities of the transition probabilities obtained by Markov modeling, two cell population compositions were designed to reach initial equilibrium after 39 days in normoxic culture system. Mix A contained 53, 38, 57, 19, 53, 0, 0, 0, 0, 0, 0, 0, 0, 21, 34, 25 cells from subpopulations 1 to 16, respectively (error < 1%). Mix B contained 75, 74, 36, 115, 0, 0, 0, 0, 0, 0, 0, 0, 0, 0, 0, 0 cells from subpopulations 1 to 16, respectively (error <

2.5%). Additionally, CSC-associated subpopulations 2, 4, 5, 9 and 11 were predicted to reach final heterogenic distribution after 63, 72, 84, 90 and 108 days of normoxic culture, respectively. Mixture of cell subpopulations and CSC-associated subpopulations were accordingly FACS-sorted to a well of a 48-wells plate (300 cells per well). A third approach tested short time predictions. Phenotypic state of subpopulations 2 and 3 were predicted to adapt in an 'irregular' manner upon initial culture of 100% pure subpopulation 4. 2000 viable single cells of subpopulation 4 were FACS-sorted into a well of 6-wells plate and cultured for 11 and 18 days.

Staining and FACS-sort was performed as described in **Heading 3.6.1.** and **3.4.6.**. After predicted days of culture, cells were collected for flow cytometric analysis. The experiments were performed in 3 technical replicates.

3.6. Single cell RNA-seq using Drop-seq

For single cell sequencing, tumor cells from GBM patient-derived xenografts P3, P8 and P13 were isolated (**Heading 3.4.1**) and pre-selected for viable single hCD90-positive tumor cells (staining and FACS-sort was performed as described in **Heading 3.4.2**, **3.4.5** and **Annex 2**). Moreover, viable single cells of NCH421k (600'000 cells), NCH644 (400'000 cells), and subpopulation P2 (200'000 cells) and P6 (400'000 cells) of NCH644 were sorted on FACS as previously described (staining and FACS-sort was performed as described in **Heading 3.4.5.** and **3.6.1.**). After sorting cells were centrifuged for 10 minutes at 1200rpm and resuspended in cold HBSS with 0.5% Bovine Serum Albumin (BSA) (Sigma-Aldrich). The cells were stored on ice until the start of the Drop-seq experiment. Prior to cell loading on the Drop-seq chips, cell viability was verified and the concentration was adjusted to ~150 cells/ml. This was an optimal concentration based on Poissonian statistics to achieve single cell encapsulation within each droplet of ~1nm droplet size. All samples analyzed in this work had a cell viability above 95%.

Subsequent procedure and analysis was performed by Dr. Suresh Kumar Poovathingal from the Luxembourg Centre for Systems Biomedicine at the University of Luxembourg (Alexander Skupin Group), Dr. Petr V. Nazarov and Arnaud Muller from the Proteome and Genome Research Unit at the Luxembourg Institute of Health.

Results

Results

Chapter 4.1

Characterization of CSC marker expression in GBM

4. Results

4.1. Characterization of CSC-associated marker expression in GBM

GBM is a highly heterogeneous tumor at the histological, genetic, epigenetic, metabolic and transcriptional level. In this work, we focus on phenotypic heterogeneity which is following the CSC hypothesis created by a subpopulation of cells with stem-like abilities. In search for eligible CSC markers, we tested the expression of a panel of CSC-associated cell surface epitopes in GBM. Putative CSC identifiers should exclusively be expressed by this subpopulation, whereas progenitor and differentiated cancer cells are marker negative. Consequently, a tumor population following the CSC model consists of CSCs, progenitor and differentiated cancer cells with distinct phenotypes. Therefore, heterogeneous expression profiles are expected in GBM using putative CSC markers. We assessed the CSC-associated marker expression in several GBM models *in vitro*, *in vivo* and clinical samples. By combining data from the TCGA GBM patient database with cell surface marker expression in patient-derived xenografts and GBM stem-like cultures we aimed to identify the most suitable cell surface epitopes to study the generation of phenotypic heterogeneity in GBM.

4.1.1. GBM patient samples display heterogeneous stem cell associated transcriptional expression patterns

In order to identify cell surface epitopes that generate a heterogenous expression profile, the gene expression of 11 cell surface markers (CD90, CD15, CD195, CD29, CD44, CD95, CD133, CD56, CD24, A2B5 and NG2) was analyzed in GBM patient samples. They represent cell membrane epitopes which had previously been described as putative CSC markers (He et al., 2012, Son et al., 2009, Al-Hajj et al., 2003, Singh et al., 2003, Tchoghandjian et al., 2010, Svendsen et al., 2011, Collins et al., 2005, Singh et al., 2004b, Kleber et al., 2008, Long et al., 2012, Vassilopoulos et al., 2008, Shimojima et al., 2003). RNA sequencing data of 166 GBM patient samples was obtained from the publicly available Cancer Genome Atlas (TCGA) database (Cancer Genome Atlas Research, 2008). RNA expression of the cell surface markers was compared to known cancer drivers in GBM (**Fig. 9.a**). *CDKN2A, EGFR, PTEN*, *TP53*, *PDGFRA*, *BRAF* and *CDKN2C* belong to the genes most often dysregulated in GBM (Cancer Genome Atlas Research, 2008). All analyzed genes were differentially expressed in GBM patient samples, revealing strong inter-tumoral heterogeneity. The RNA expression levels of the CSC marker genes did not significantly correlate to the high confidence driver genes (**Fig. 9.b and 9.c**). This indicates that the

heterogeneous expression of putative CSC cell surface markers is not associated with the main driver mutations.

Interestingly, we observed a trend of putative CSC marker-specific expression patterns following the Verhaak classification (Verhaak et al., 2010). Indeed, correlation of gene expression between four proposed transcriptional subgroups (neural, mesenchymal, proneural and classical) showed amongst others that *CCR5*, *ITGB1*, *CD44, FAS* show higher expression in the mesenchymal subtype compared to the proneural subtype (**Fig. 9.d**), whereas *NCAM1* and *CD24* revealed a significantly higher expression in proneural subtype compared to the mesenchymal and classical subgroups (**Fig. 9.e**). These data confirm the results by Brown and colleagues (Brown et al., 2015) who previously described a correlation between CSC markers and GBM subtypes.

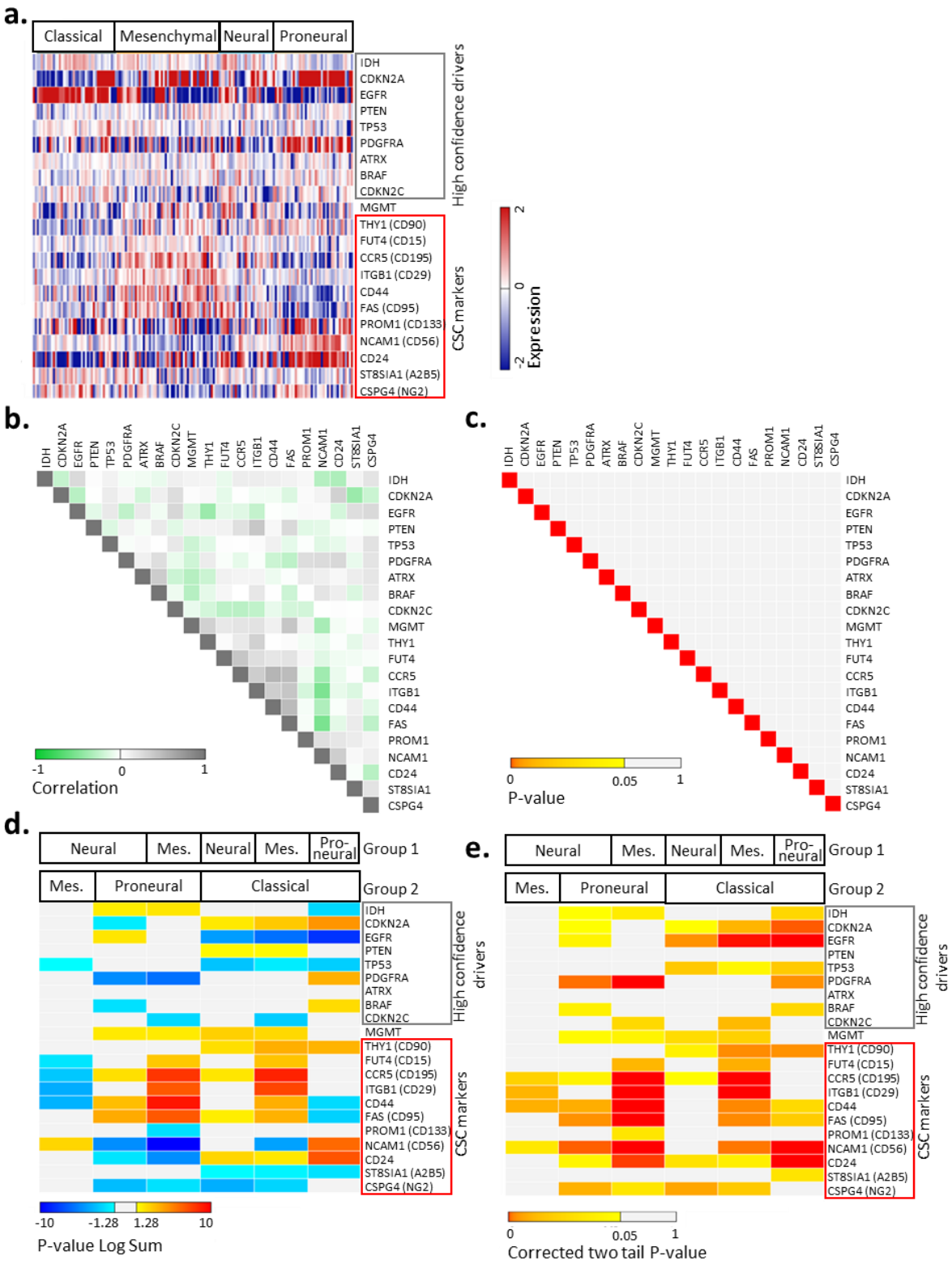

Figure 9: CSC-associated heterogeneity in GBM patient samples and correlation of CSC marker expression to GBM subtypes. a. RNA sequencing data from 160 GBM patients of the TCGA cohort were classified following the GBM subtypes proposed by Verhaak (Verhaak et al., 2010). Heatmap displaying heterogeneous expression pattern of high confidence drivers ('grey' box) and putative CSC markers ('red' box) in GBM ('red', high gene expression levels; 'blue', low/absent gene expression levels). **b.** Heatmap showing Pearson's correlation ('grey', positive correlation; 'green', negative correlation) and **c.** statistical significance ('red', low standard error; 'white', high

standard error) of co-expression between genes of CSC-associated markers and main drivers in GBM patients. No significant interdependence was detected. **d.** Heatmap displaying correlation of gene expression data between GBM subgroups (p-value log sum; right-tail significance yields a positive p-value log sum, left-tail significance yields a negative). One square represents the correlation value calculated using gene expression data of all patients classified to one subgroup compared to another subgroup. In order to perform all possible comparisons between GBM subgroups, two 'groups' were designed. 'Group 1' containing neural, mesenchymal and proneural subgroups was compared to 'group 2' with mesenchymal, proneural and classical subgroups ('yellow-red', higher expression in group 1; 'blue', higher expression in group 2). Many significant correlations in CSC-associated gene expression and GBM subtypes were detected. **e.** Heatmap displays the statistical significance of correlation data shown in **d** (Corrected two-tail p-value for each comparison; 'yellow-red', significant correlation; 'white' not significant correlation). Significant differences in gene expression of putative CSC-markers were found mostly between the mesenchymal subgroup compared to the proneural and the classical subgroup. Figure 18. was realized with the help of Dr. Sabrina Fritah (Norlux Laboratory, LIH).

To exclude that variations in gene expression data from CSC-associated genes result from mutations and/or chromosomal aberrations, the genes of the putative CSC markers were analyzed for genetic aberrations. TCGA data show that high confidence drivers (*CDKN2A*, *EGFR*, *PTEN* and *TP53*) display numerous mutations and/or loss or gain in gene sequences (**Fig. 10.a**). In contrast only 4 out of 11 CSC-associated marker genes (*FAS*, *ST8SIA1*, *NCAM1* and *CSPG4)* depicted isolated mutations and/or aberrations in their DNA sequence, suggesting that heterogeneous gene expression arising from these markers is not a result of genetic aberrations.

Next, we analyzed whether heterogeneous marker expression is originating from epigenetic gene regulation. A well-known gene that is often hyper-methylated in GBM is *MGMT* (Mellai et al., 2012), where promoter methylation is associated with better response to chemo therapy in patients. DNA methylation analysis revealed that *FUT4* is highly methylated at the promoter region in 18% of GBM patients (**Fig. 10.b**). Other CSC-associated and high confidence driver genes did not show promoter methylation, except for one patient in *CD44*. The fact that not all patient samples demonstrated *FUT4* promoter methylation may at least partially explain a heterogeneous expression in RNA between patient tumors. Indeed, *FUT4* mRNA expression and promoter methylation anti-correlated, confirming regulation of FUT4 gene expression by DNA methylation of its promoter (**Fig. 10.c**). This is in line with reports from Li and colleagues (Li et al., 2012). Comparing methylations of *FUT4* with *MGMT* revealed no significant correlation (p-value = 0.086) (**Fig. 10.d**).

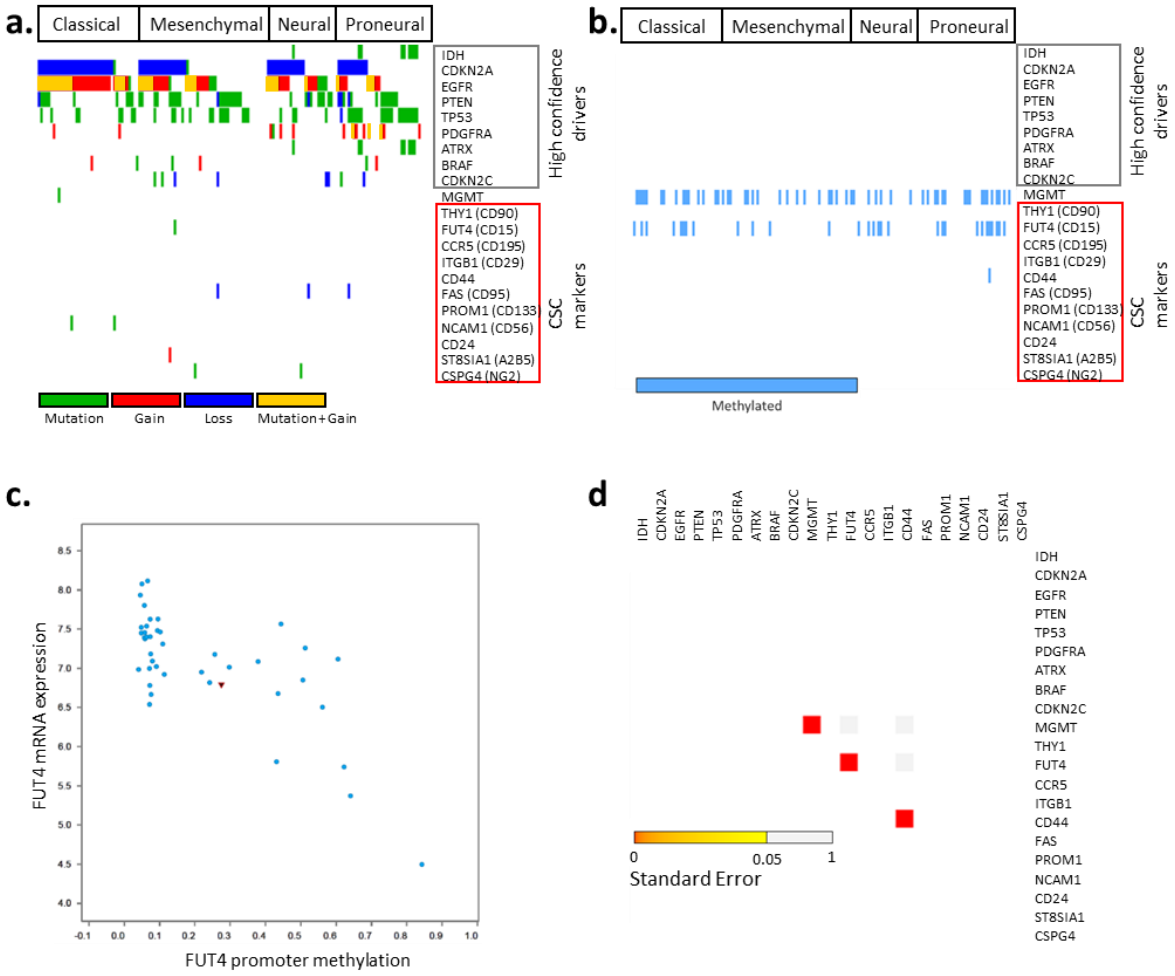

Figure 10: Genetic aberrations and promoter methylations in GBM patient samples. a. Heatmap displays GBM cases containing mutations, gain and loss of genes and mutations combined with gain of copy number in genes of interest. CSC marker genes rarely display mutations and copy number aberrations within the different GBM expression subgroups. **b.** Heatmap shows promoter methylation status of selected genes in patient samples. Only *MGMT* and *FUT4* displayed high methylation pattern in a subgroup of patients. **c.** No significant correlation (standard error; p-value 0.086) in methylation pattern was found between the two genes. **d.** Correlation between *FUT4* mRNA expression and *FUT4* promoter methylation revealed anti-correlation (Pearson -0.633; Spearman -0.592) (purple triangle depicts frameshift mutation; blue dots non-mutated *FUT4* gene sequence). Figure 4.2.2 was realized with the help of Dr. Sabrina Fritah (Norlux Laboratory, LIH).

In summary, the analysis of TCGA patient data revealed that CSC-associated marker expression is heterogeneous at the transcriptional level. In most cases, inter-patient differences in marker expression do not originate from genetic aberrations or epigenetic promoter regulation. An exception is *FUT4*, where promoter methylation anticorrelated with gene transcription.

4.1.2. GBM patient-derived xenografts recapitulate inter-patient and intra-tumoral phenotypic heterogeneity

We showed high variation in CSC-associated genes expression in GBM patient samples, however, data is based on bulk tumor analysis containing tumor and non-tumor cells. Therefore, the results may be biased by the presence of stromal cells as all markers were described to be expressed by tumor cells and different stromal cell types (Inoue et al., 2016, Zozulya et al., 2007, Ransohoff and Engelhardt, 2012, Barraud et al., 2007). For example, CD133 has been shown to be present both on tumor and endothelial cells in patient biopsies and GBM patient-derived xenografts (PDXs) (Golebiewska et al., 2013). Furthermore, a recent publication of Verhaak and colleagues showed that the specification into four GBM subclasses based on transcriptional profiling was strongly influenced by stromal cells. The mesenchymal subclass was associated with microglia and macrophage gene signatures whereas the neural subclass was shown to originate from non-neoplastic cells (Wang et al., 2017). PDXs are also a very powerful model to mimic GBM occurring in patients. As a previous publication from our lab has shown by ploidy measurement, PDXs recapitulate genetically divergent clones from primary tumors (Stieber et al., 2014). Therefore, we took advantage of GBM PDXs to assess phenotypic expression of CSC-associated markers between and within PDX tumors. Here organotypic spheroids derived from patient biopsies were implanted intracranially into immunodeficient mice. GBM tumors that develop upon xenografting consist of human cancer cells, which can be discriminated from mouse stroma using flow cytometry (**Fig. 11.a**). The gating strategy was based on the following parameters: Single cells from dissociated mouse xenografts were distinguished from debris based on their size and granularity using forward (FSC) and side scatter (SSC) (1). Cell doublets and aggregates were eliminated from the analysis comparing the height (FSC-H) vs area (FSC-A) of the voltage pulse in FSC created by a photomultiplier tube when a cell passes a laser beam (2). FSC-H measures the intensity of the signal whereas FSC-H multiplied by pulse width (FSC-W) equals to FSC-A. Cell doublets were identified due to disproportions in pulse height vs area; cell doublets have double the area value of single cells, whereas the height is approximately equal in cell doublets vs single cells. To assure analysis of viable cells, dead cells were excluded based on a dead cell marker (3). The discrimination between stromal and tumor cells was possible using the eGFP-expressing NOD/SCID mice with GFP positive mouse cells and GFP negative human tumor cells (Niclou et al., 2008). Thus, the selection of single, viable tumor cells was only possible using the above-mentioned gating strategy.

Eleven GBM PDXs (T101, T185, T233, T239, T251, P8, T16, T238, P3 and P13) with different genetic backgrounds were analyzed for the epitope expression of CSC-associated

markers previously assessed in GBM patients (**Fig. 11.b**). EGFR was used as control for heterogeneity, since it is known to be differentially expressed among GBM tumors. Similarly, the expression profiles of CD90, CD56, CD29, NG2, CD95, CD24 and CD195 were highly variable between different PDXs (**Fig. 11.b**). Expression signals of EGFR, NG2, CD56 and CD95 ranged each from low (mean fluorescent intensity (MFI) of marker is equal to negative control) to high positive (MFI is 100x higher than negative control) (for flow histograms see **Annex 5**). Some markers (CD90 and CD29) were uniformly highly expressed in most tumors whereas others (CD24 and CD195) were less detected. The expression profile for the 8 markers tested was relatively uniform within PDXs. Only T238 showed internal variability in CD195 expression. Similar to the gene expression profiles of CSC-associated genes in patient biopsies from TCGA data, does the epitopes expression of these genes demonstrate high variability between different GBM PDXs.

a.

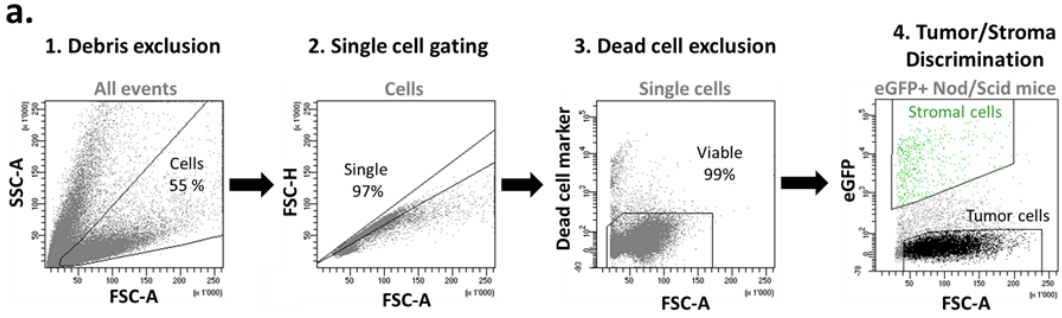

b.

	EGFR	CD90	CD56	CD29	NG2	CD95	CD24	CD195
T101	++	++	+	++	+	+	low	+
T185	++	++	low	++	low	+	-	-
T233	+	++	low	+	+	+	-	n.a.
T239	low	++	+	++	+	++	low	low
T251	+	+	+	++	low	+	-	-
P8	++	++	+	+	low	low	-	-
T16	++	++	+	++	+	+	-	-
T238	++	++	low	++	+	++	-	65%
P3	+	++	+	+	+	+	-	-
P13	+	++	+	++	+	low	+	low

Figure 11: Analysis strategy for tumor/stroma discrimination and marker expression profiles of EGFR, CD90, CD56, CD29, NG2, CD95, CD24 and CD195 in GBM patient-derived xenografts. **a.** Flow cytometric scatter plots depict gating strategy for the analysis of tumor cells in PDXs. GBM cells were distinguished from debris using forward (FSC) and side (SSC) scatters (1), followed by cell doublet and aggregate elimination (FSC-A/FSC-H) (2). Dead cells were recognized as positive for dead cell marker (3). Single viable cells were discriminated into eGFP positive stromal and eGFP negative tumor cells (4). **b.** Flow cytometric analysis of 8 cell surface markers in 11 GBM PDXs. Negative, low, positive and high positive cells were categorized based on their mean fluorescence intensity (MFI) ('-', MFI = negative control; 'low', MFI < 10x negative control; '+', 10x < MFI < 100x negative control; '++', MFI > 100x negative control). PDXs show high variability between patient samples.

Interestingly, the other 4 markers (CD133, CD44, CD15 and A2B5) of the panel showed remarkable intra-tumoral heterogeneity for most PDXs (**Fig. 12**). For CD133, we were able to discriminate between negative and positive cells ('black gating' - black line on histogram), whereas for CD44, A2B5 and CD15 expression additionally between low and high expression levels ('red gating' – red line on histogram). No link between the different histopathological phenotypes of GBM PDXs and their CSC marker epitope expression was observed as marker expression profile was not uniform to solely one histopathological phenotype. The next experiments focused on the four markers CD133, CD44, A2B5 and CD15 as they presented the highest intra-tumoral heterogeneity in PDXs, a premise necessary for a putative CSC marker. Marker expression between PDXs of the four markers was highly variable as well. For instance, CD15 expression varied from 0.3% in T16 to 75% in T239. Similar results were obtained from Brescia et al. who described a highly variable CD133 expression in both GBM patient biopsies and their respective sphere cultures (Brescia et al., 2013b).

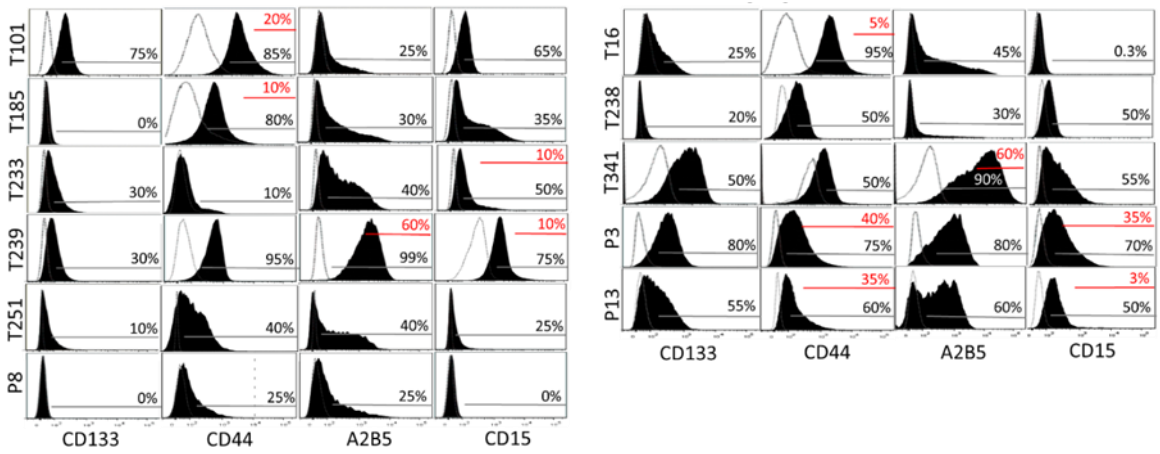

Figure 12: Expression profiles of CD133, CD44, A2B5 and CD15 markers in GBM PDXs. Flow cytometric analysis in 11 PDXs for CD133, CD44, A2B5 and CD15 epitopes ('black', negative vs. positive; 'red', low vs. high). All PDXs show high variability between PDXs and within the PDXs tumors for the expression of the 4 markers. Figure 12 was realized with the help of Dr. Anna Golebiewska (Norlux Laboratory, LIH).

4.1.3. GBM stem-like cultures display inter- and intra-tumoral phenotypic heterogeneity in CSC-associated subpopulations

To further analyze variability in CSC marker expression we used GBM stem-like cultures. These cells were grown as 3D spheres in serum free medium. On genetic and transcriptomic level 3D cultures are described as a better model for GBM than adherent cultures (Ishiguro et al., 2017, De Witt Hamer et al., 2008, Lee et al., 2006). Unlike adherent GBM cultures in serum-containing medium, GBM stem-like culture spheres were able to generate complex tumors upon xenografting with similar histopathology than GBM patients (Bougnaud et al., 2016). Moreover, this allowed us to work with a genetically more homogeneous population and avoid a possible bias of divergent genetic clones (Stieber et al., 2014).

The expression of the CSC-associated markers (CD133, CD44, CD15 and A2B5) were tested in 7 GBM stem-like cultures (NCH421k, NCH465, NCH601, NCH644, NCH660h, TB101 and TB107). Similar to PDXs, the GBM stem-like cultures displayed strong inter- and intra-tumoral heterogeneity (**Fig. 13.a**). We have been distinguishing between negative and positive cells ('black' gating - black line on flow histograms) and cells with high and low marker expression levels ('red' gating - red line on flow histograms). To define intra-tumoral heterogeneity for further experiments, discrimination of cells was performed on low vs. high expression levels ('red' gating), except for cell populations where discrimination could only be performed on negative and positive cells ('black' gating). Because GBM stem-like cultures recapitulate inter- and intra-tumoral heterogeneity, they appear to be a good model to study CSC-associated marker expression.

The analysis was performed on the four markers (CD133, CD44, A2B5 and CD15) simultaneously by multicolor flow cytometry enabling combined measurement of the four markers on one single cell (**Fig. 13.b**). This allowed us to discriminate between 16 distinct subpopulations (**Fig. 13.c**). According to the discrimination pattern subpopulation 1 was $CD133^+$ $CD44^-$ $A2B5^+$ $CD15^-$. Subpopulation 6 was positive/high for all markers ($CD133^+$ $CD44^+$ $A2B5^+$ $CD15^+$) whereas expression for the four epitopes ($CD133^-$ $CD44^-$ $A2B5^-$ $CD15^-$) was not detected/low in subpopulation 11.

Simultaneous multicolor phenotyping was performed for the 7 GBM stem-like cultures. Only some of the 16 possible subpopulations could be detected in NCH421k, NCH601 and TB101 cultures (**Fig. 13.d**). NCH421k was predominantly composed of subpopulation 2 ($CD133^+$ $CD44^-$ $A2B5^+$ $CD15^+$), TB101 of subpopulation 16 ($CD133^-$ $CD44^+$ $A2B5^-$ $CD15^+$) and NCH601 mainly of subpopulation 11 ($CD133^-$ $CD44^-$ $A2B5^-$ $CD15^-$), being negative for all markers. In contrast to these stem-like cultures, NCH644, NCH465, NCH601 and TB107 contained all 16 phenotypes. From the 7 analyzed GBM stem-like cultures, NCH644

appeared most heterogeneous with the most equal distribution of subpopulations. Subsequent experiments were based on NCH644 stem-like cultures as they allowed us to isolate a reasonable cell number of each subpopulations for further investigation.

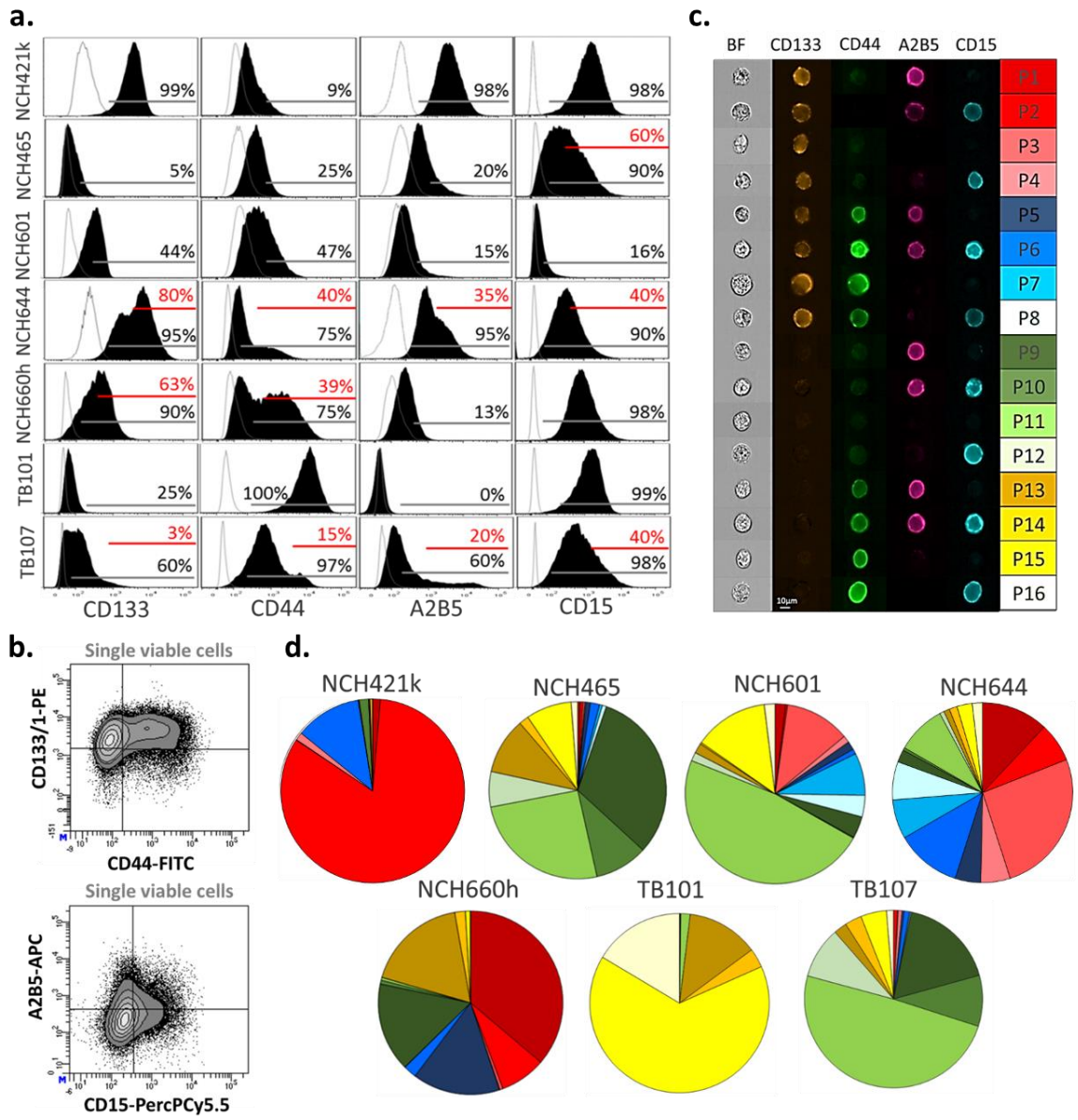

Figure 13: Inter- and intra-tumoral heterogeneity in GBM stem-like cultures. **a.** Flow cytometric analysis in 7 GBM cultures for CD133, CD44, A2B5 and CD15 epitopes ('black line': negative vs. positive; 'red line': low vs. high). Marker expression showed high variability between and within each GBM stem-like culture (n_B=1-3, n_T=1-3). **b.** Flow cytometric density plots of simultaneous multicolor staining of single viable NCH644 stem-like cells. NCH644 demonstrated a highly heterogeneous expression of the four markers. **c.** Discrimination of 16 subpopulations based on the expression pattern of four markers in NCH644 cells. Bar indicates 10µm. Microscopic images acquired by ImageStream show 16 different subpopulations based on different intensities of simultaneous CD133, CD44, A2B5 and CD15 epitope staining. The color code for different subpopulations is applied on figures throughout this thesis. **d.** Quantification of multicolor flow cytometry analysis of 4 markers performed in 7 GBM stem-like cultures. Pie charts show the distribution of 16 subpopulations discriminated based on the marker expression profiles. Division in 16 subpopulations demonstrates inter- and intra-tumoral heterogeneity in all cultures (mean percentage; n=3).

4.1.4. All CSC-associated subpopulations proliferate in spheres

CSC sphere cultures are described to contain non-cycling cells at the inner core and highly proliferative cells at the outer layer of the 3D sphere (Smith et al., 2012). As several research groups reported higher proliferation in CD133 positive cells (Jaksch et al., 2008, Barrantes-Freer et al., 2015), therefore we expected to find CD133 positive staining at the border of the spheres.

Since flow cytometric analysis was based on single cell measurement, the location of the four markers was investigated within individual 3D spheres by immunocytochemistry (**Fig. 14.a**). As antibodies might not be able to penetrate to the core of a sphere, CSC spheres were flash frozen and cut into sections for staining to assure optimal antibody coverage. Expression of the four markers showed a strong phenotypic heterogeneity within each sphere with no specific localization pattern within sphere compartments. In contrary, the proliferation marker Ki67 was mainly expressed at the edges of the spheres confirming Smith et al. reporting a highly proliferative outer layer of 3D spheres (Smith et al., 2012). Interestingly, Ki67 showed no association with the four markers analyzed.

We further investigated whether one of the CSC-associated subpopulations was more prone to be proliferative. Therefore, cell cycle was measured in the 16 NCH644 subpopulations. The standard protocol for cell cycle measurement uses ethanol fixation which renders cell membranes porous and can change the structure of cell membrane epitopes, which may affect CSC-associated marker stainings. Therefore, DNA staining was performed in viable cells to assure proper identification of the 16 subpopulations Hoechst fluorescent dye. However, this did not allow an accurate discrimination between S, M and G2 phases of the cell cycle (**Fig. 14.b**). Hence, this analysis was limited to distinguish between proliferative (S/G2/M phases) and non-proliferative (G0/G1 phases) cells, revealing that all 16 subpopulations contained cycling cells (**Fig. 14.c**). NCH644 sphere cultures grown in serum depleted medium were used as control and are referred in this thesis as original NCH644 population. Compared to this population significantly fewer proliferating cells were detected in subpopulation 9 ($CD133^-$ $CD44^-$ $A2B5^+$ $CD15^-$), 10 ($CD133^-$ $CD44^-$ $A2B5^+$ $CD15^+$), 11 ($CD133^-$ $CD44^-$ $A2B5^-$ $CD15^-$), 12 ($CD133^-$ $CD44^-$ $A2B5^-$ $CD15^+$), 13 ($CD133^-$ $CD44^+$ $A2B5^+$ $CD15^-$) and 15 ($CD133^-$ $CD44^+$ $A2B5^-$ $CD15^-$). Interestingly these subpopulations were all negative for CD133, suggesting that the $CD133^+$ expression is associated with a higher proliferative potential. This data agrees with previous cell cycle analysis showing increased CD133 epitope expression in proliferative colon epithelial cancer cells (Jaksch et al., 2008) and GBM cell cultures (Brown et al., 2017). Brown and colleagues analyzed simultaneous expression of CD133 and CD44 and

confirms lower proliferation in CD133$^-$ CD44$^-$ cells compared to CD133$^+$ CD44$^-$ and CD133$^+$ CD44$^+$cells. In general, all subpopulations were shown to contain cycling cells.

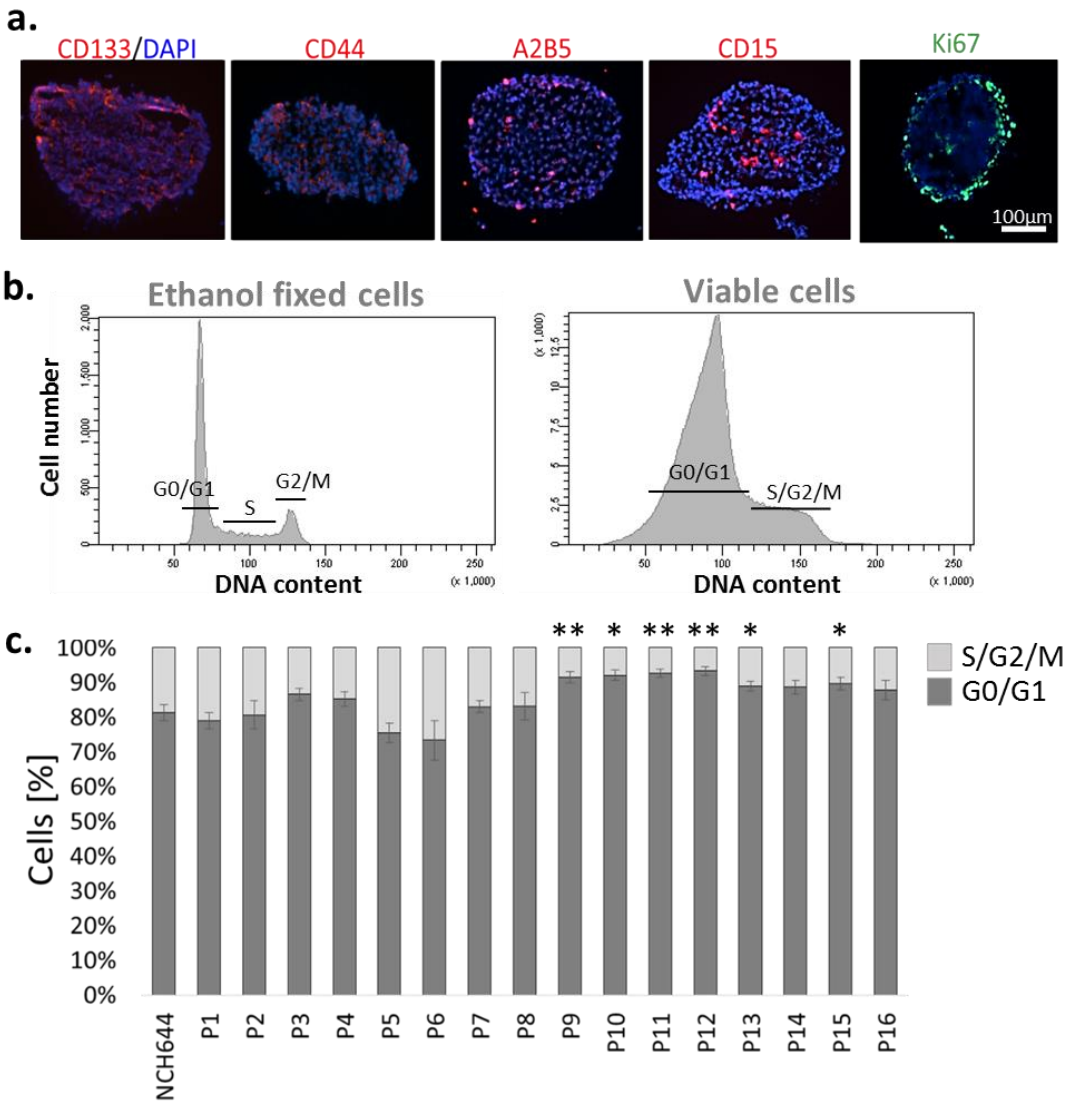

Figure 14: Spatial distribution of marker expression and cell cycle analysis in GSCs. **a.** Microscopic images show IHC for CD133, CD44, A2B5, CD15 and Ki67 in frozen sections of NCH644 spheres. Bar indicates 100µm. Except for Ki67, all markers were expressed throughout the spheres at no distinct localization. Figure was realized with the help of Dr. Anna Golebiewska (Norlux Laboratory, LIH). **b.** Histogram depicts DNA staining of either ethanol fixed cells (DNA staining performed with PI) or non-fixed cells (DNA staining performed with Hoechst). Clear discrimination of the different cell cycle phases G0/G1, S and G2/M is feasible in fixed cells whereas only between G0/G1 and S/G2/M phases can be distinguished in viable cells. **c.** Barplots represent cell cycle analysis of NCH644 subpopulations. Cells in S/G2/M cell cycle phases were distinguished from G0/G1 phases based on Hoechst flow cytometric profile combined with multicolor phenotyping in viable cells. Cell cycle analysis showed that every subpopulation contained proliferative cells (n_B=6). t-test was used to calculate significance between subpopulations and viable NCH644 control population (mean percentage ± SEM; * = p-value < 0.05, ** = p-value < 0.01, *** = p-value < 0.001)

4.1.5. CSC-associated subpopulations display minor phenotypical changes upon treatment pressure

Previous reports describe CSCs to be responsible for chemotherapy resistance whereas non-CSCs were eliminated by adjuvant therapy (Bao et al., 2006a, Reya et al., 2001, Liu et al., 2006, Eramo et al., 2006). We tested CSC-associated marker expression upon treatment with Temozolomide (TMZ), a chemotherapy compound used in GBM patients. We expected that non-CSC subpopulations would be depleted and subpopulations representing true CSCs were enriched. We treated NCH644 cells which are resistant to TMZ (IC50 of ±227mM) and TMZ-sensitive NCH421k cells (IC50 of ±272µM) with sublethal doses. In both cultures, we observed a change towards $CD44^+$, $CD15^-$ and $A2B5^-$ subpopulations upon long-term (7 days) TMZ treatment whereas an enrichment of $CD133^-$ subpopulations was registered only in TMZ-sensitive GBM cells. At the subpopulation level in NCH644 cultures, we were only able to detect a significant reduction in percentage of subpopulation 4 ($CD133^+$ $CD44^-$ $A2B5^-$ $CD15^+$), 9 ($CD133^-$ $CD44^-$ $A2B5^+$ $CD15^-$) and 12 ($CD133^-$ $CD44^-$ $A2B5^-$ $CD15^+$) and a gain in subpopulation 5 ($CD133^+$ $CD44^+$ $A2B5^+$ $CD15^-$) (**Fig. 15.a;** see **Annex 6.a** for all statistical comparisons of phenotypical states and single marker expression between time points). In TMZ-sensible cultures GBM stem-like cultures (NCH421k), short and long-term treatment resulted in enrichment of all $CD133^-$ subpopulations (P9-P16) and a major decrease in subpopulation 2 ($CD133^+$ $CD44^-$ $A2B5^+$ $CD15^+$) (**Fig. 15.b;** see **Annex 6.b** for all statistical comparisons of phenotypical states and single marker expression between time points). Beier et al. showed similarly to our results a decrease in $CD133^+$ subpopulations upon treatment of sublethal TMZ doses (Beier et al., 2008). More interestingly, they showed that TMZ was shown to inhibit proliferation in $CD133^+$ CSC lines. Therefore, the observed phenotypic shift from $CD133^+$ to $CD133^-$ subpopulations might be linked to the higher proliferation rates in $CD133^+$ subpopulations (**Fig. 14.c**). On the other hand, Liu et al treated $CD133^-$ and $CD133^+$ subpopulations independently with a series of TMZ concentrations for two days and demonstrated higher number of viable cells in $CD133^+$ GBM cells. The controversial results may be explained by the use of lethal drug doses that may be more effective on proliferating cells.

Moreover, phenotype changes appear more dramatic upon 7 days TMZ treatment in TMZ-sensitive NCH421k cells than in TMZ-resistant NCH644 cells suggesting that the cell function of TMZ-resistant cells is longer intact than in TMZ-sensitive cells. Of note, the changes in percentage of subpopulations upon short and long-term treatment were not always gradual in time in both cultures. This suggests that intermediate states were enriched and subsequently depleted over time and vice versa. Moreover, changes in resistant NCH644 were observed upon short term treatment suggesting fast adaptive

capacities. Since sublethal does were applied no excessive cell death was observed in cultures. This shows that clonal selection does not eliminate $CD133^+$ cells upon therapeutic pressure and the decrease of $CD133^+$ is regulated in a cell death-independent process.

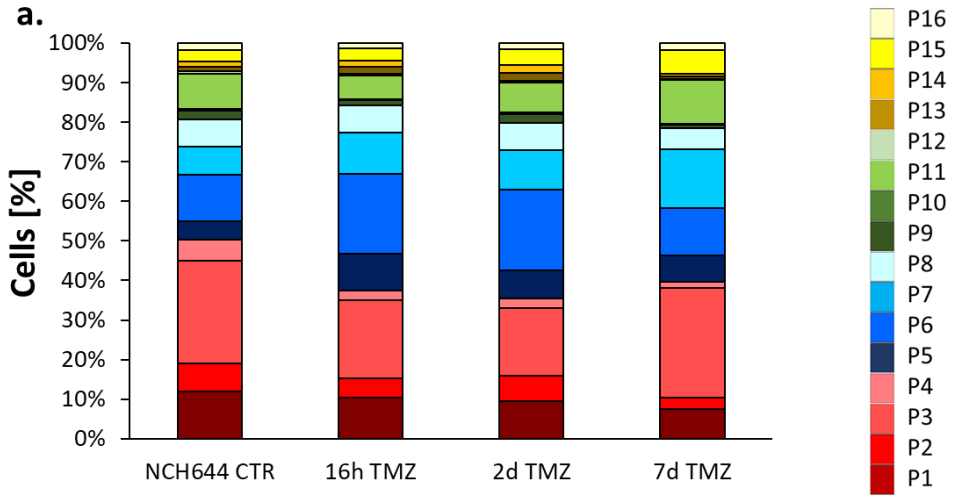

Conditions/Phenotypic states	P1	P2	P3	P4	P5	P6	P7	P8	P9	P10	P11	P12	P13	P14	P15	P16
CTR vs. 16h_TMZ				*	**				*			*				
CTR vs. 2d_TMZ				*												
CTR vs. 7d_TMZ				***					**			**				

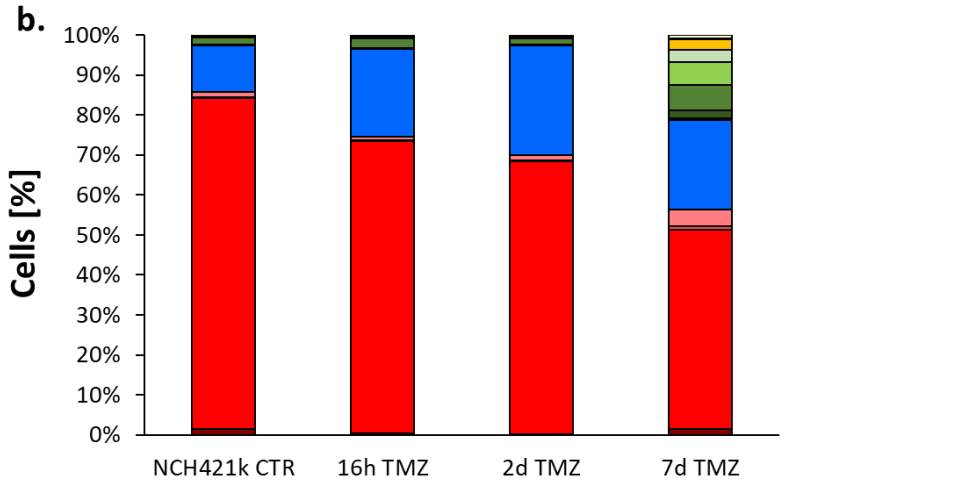

Conditions/Phenotypic states	P1	P2	P3	P4	P5	P6	P7	P8	P9	P10	P11	P12	P13	P14	P15	P16
CTR vs. 16h_TMZ																
CTR vs. 2d_TMZ		*				*										
CTR vs. 7d_TMZ		***						**	**	***	*	*				***

Figure 15: Response of CSC-associated marker expression to TMZ treatment. Bar plots show the distribution of the 16 subpopulations in **a.** NCH644 upon short (16h and 2d) and long-term treatment (7d) with 200µmol TMZ (mean percentage, n_B=4, n_T=3) and in **b.** NCH421k upon long and short-term treatment with 50µmol TMZ (mean percentage, n_B=3-4, n_T=3). Error bars are not depicted for visualization purposes. Statistical significances of phenotypic states between non-treated and TMZ-treated conditions are depicted in table below the graph (t-test with Bonferroni multiple-significance-test correction).

To summarize, 4 out of 11 CSC-associated markers showed high variability in their expression profiles between and within all analyzed PDXs and GBM stem-like cultures. The latter were subsequently used as experimental models since they represent sphere cultures that are often associated with cancer stem cells and are optimal to perform functional assays *in vitro* to investigate how CSC-associated marker heterogeneity is created.
Differential marker expression was demonstrated in single cells, but also in 3D sphere cultures. No direct association with spatial localization and proliferative marker (Ki67) were observed. Chemotherapy pressure suggests that changes in marker expression of stem-like cultures does not result from selection but rather from adaptive capacities.

Results

Chapter 4.2

Analysis of stem cell properties and phenotype transitions of GBM CSC-associated subpopulations

4.2. Analysis of stem cell properties and phenotype transitions of GBM CSC-associated subpopulations

In the last part, CSC-associated inter- and intra-tumoral heterogeneity was assessed at the transcriptomic level in GBM patient samples and at the level of epitope expression using flow cytometric analysis of patient-derived xenografts and GBM stem-like cultures. To date, there are two hypothesis that might explain the observed phenotypic heterogeneity. First, the CSC hypothesis postulates that a small subpopulation of cells with stem-like abilities creates differentiated progeny in a one-way hierarchical process. The second model suggests that phenotypic heterogeneity may arise by adaptive phenotypes where differentiation is a reversible process and each cancer cell is able to generate heterogeneity. To determine which subpopulations carry stemness properties and whether the intra-tumoral heterogeneity is created via a hierarchical one-way differentiation or an adaptation process, we used GBM stem-like cultures and analyzed their FACS-isolated CSC-associated subpopulations for stemness characteristics and adaptive abilities. Phenotypical changes of CSC-associated subpopulations were further analyzed by mathematical modeling to elucidate state transitions.

4.2.1. All GBM CSC-associated subpopulations carry stem cell properties.

In order to identify putative CSCs, the 16 NCH644 subpopulations defined by their CSC-associated marker expression profile (CD133, CD44, A2B5 and CD15) were analyzed for stemness characteristics. NCH644 GBM stem-like cultures were phenotyped by multicolor flow cytometry and divided into the 16 CSC-associated subpopulations (**Fig. 16**). For sterile sorting, we applied a more stringent gating strategy (‘blue’ gates) (**Fig. 16.a**) as for phenotyping (**Fig. 13.b**). This prevented contamination with neighboring phenotypic subpopulations that may have interfered with the results. The 16 subpopulations were subsequently tested for self-renewal ability and indefinite proliferation, two main characteristics of stemness (**Fig. 16.b**).

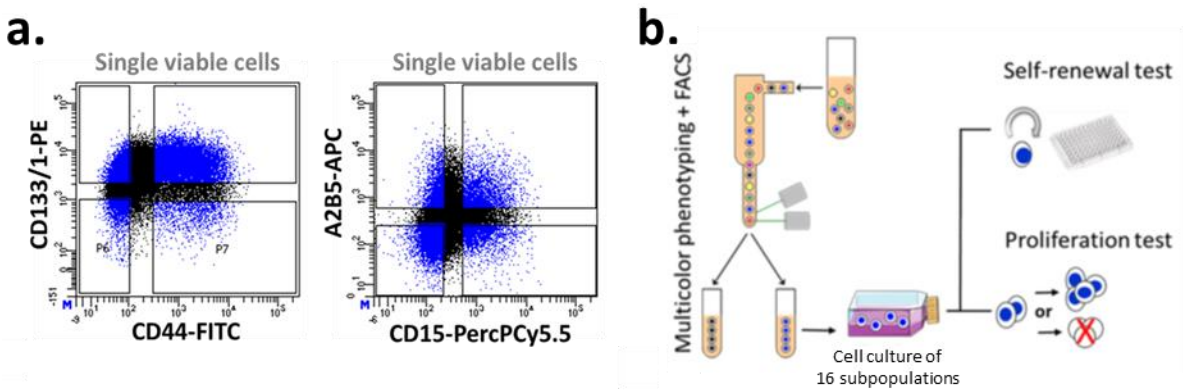

Figure 16: **Analysis of stemness characteristics. a.** NCH644 cultures were divided into 16 subpopulations by a stringent gating strategy ('blue') based on CD133, CD44, A2B5 and CD15 epitope expression for FACS-sorting experiments. **b.** After sterile FACS-sorting, the 16 subpopulations were individually tested for their self-renewal and proliferative capacities.

4.2.1.1. All CSC-associated subpopulations display self-renewal abilities

Self-renewal ability is classically evaluated by sphere forming capacities. The CSC hypothesis states that spheres are formed by CSCs producing progenitors and fully differentiated cells or are producing progenitors that give rise to fully differentiated cells. As CSCs and progenitor cells cannot be distinguished upon their clonogenic ability in the first passage, the cells need to be plated consecutively several times. Since progenitor cells only have a limited capacity to form fully differentiated cancer cells and do not carry self-renewal potential, they will be eliminated upon several passages. This experimental setup will eventually deliver self-renewing subpopulations (Pastrana et al., 2011). Hence, we have applied a self-renewal test that assessed clonogenic potential of single tumor cells upon 4 consecutive passages. Furthermore, self-renewal test in our analysis was feasible at clonal level since sphere forming ability of NCH644 stem-like cells was high.

Our results show that all 16 subpopulations were able to produce progeny, and none was diluted upon passaging (**Fig. 17.a**). FACS-sorted cells of the original NCH644 stem-like cells were used as control. Significant differences were observed only for subpopulation 11 ($CD133^-$ $CD44^-$ $A2B5^-$ $CD15^-$), where an increase in clonogenic ability was observed upon the second and the third passage compared to passage 1. However, the self-renewal potential did not significantly differ between subpopulations at consecutive passages. Next, we measured the sphere size as differences in sphere diameter may suggest the presence of progenitor cells forming smaller spheres than putative CSCs. The sphere size of each subpopulation did not differ significantly (**Fig. 17.b**). Thus, the same self-renewal ability can be attributed to all 16 subpopulations.

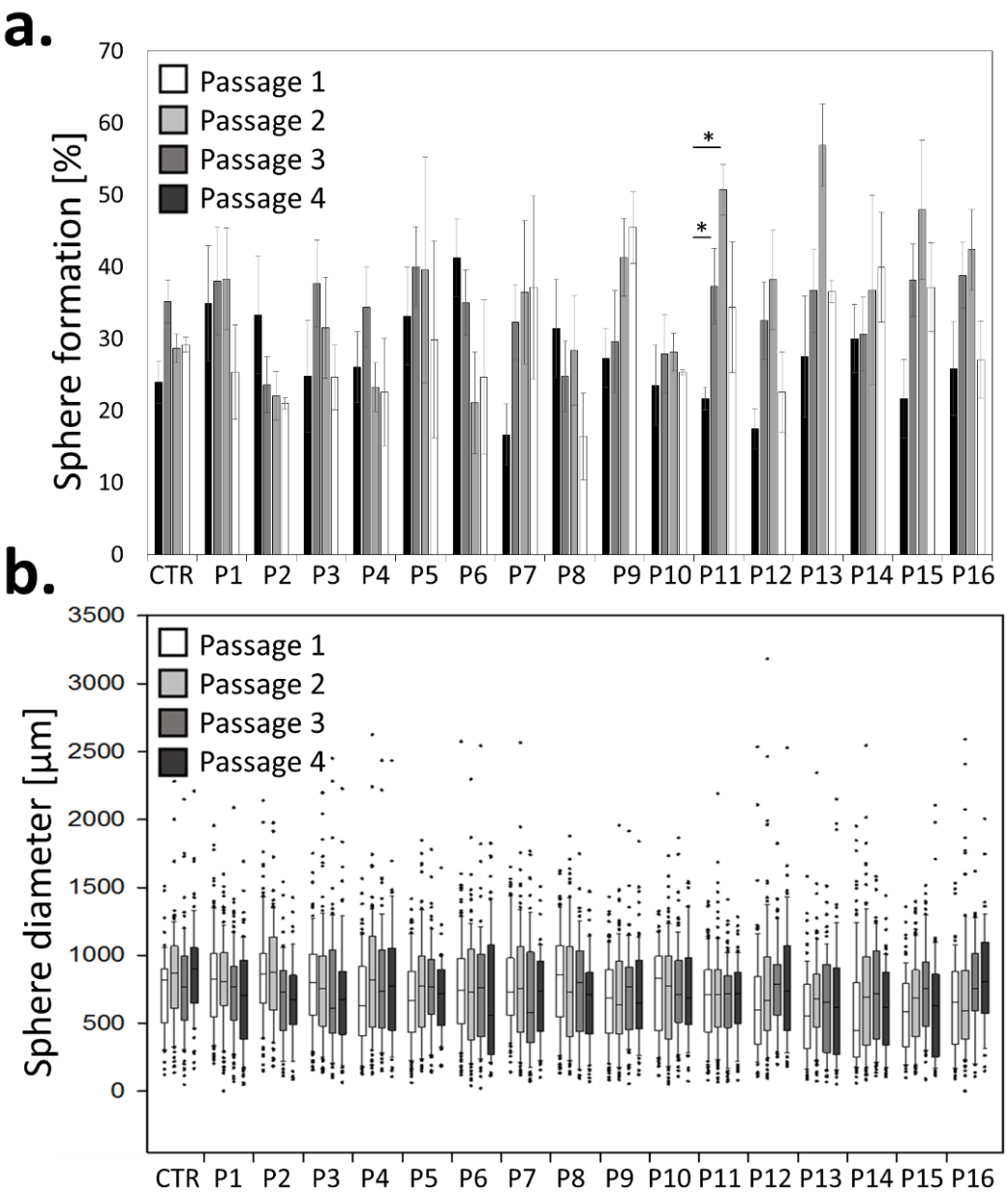

Figure 17: Sphere number and size of GBM subpopulations upon self-renewal test. a. FACS-sorted cells of each NCH644 CSC-associated subpopulation and original NCH644 cells (CTR) were individually cultured. Sphere number was counted (first passage) and cells were collected to be replated for second and subsequent third and fourth passages. All subpopulations were able to form new spheres upon 4 consecutive passages, proving self-renewal properties of all subpopulations (mean percentage ± SEM; n_B=3-6; Kruskal-Wallis test * = p-value < 0.05). **b.** The sphere diameter did not change between GBM subpopulations (mean ± SEM; n_B=3-6, n_T=20; mixed model F-test). The statistical analysis was realized by Sonia Leite and Dr. Nicolas Sauvageot (Centre of Competence for Methodology and Statistics, LIH).

4.2.1.2. All CSC-associated subpopulations display proliferative abilities

Indefinite proliferation is a second stemness characteristic attributed to CSCs. To examine this ability, CSC-associated subpopulations were separated by FACS (300 cells per replicate) and recultured. After 20 and 30 days the cell number was determined. All 16 subpopulations had a similar cell count at 20 and 30 days indicating similar proliferation capacities. From these data doubling-times were calculated by dividing culture time by the logarithmic number of grown cells. Doubling-times were not statistically distinct when compared to another and to original NCH644 control cells (**Fig. 18**). Thus, all CSC-associated subpopulations showed proliferative capacities which is in line with the previous experiment displaying cells in S/G2/M phases in each subpopulation (**Fig. 14.c**). Discrepancies observed between several $CD133^+$ and $CD133^-$ subpopulations may result from bulk culture compared to individual culture of CSC-associated subpopulations.

As all subpopulations showed similar stem cell properties (self-renewal and indefinite proliferation), it appears that distinct functional subpopulations may not be identified by CSC-marker expression.

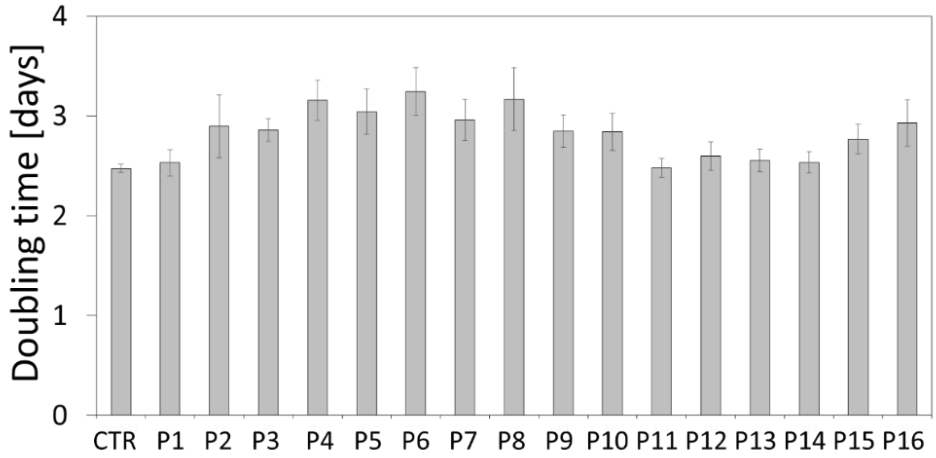

Figure 18: Proliferation rate of GBM subpopulations. Cell number of each NCH644 subpopulation was measured 20 and 30 days after sort. Chart represents calculated doubling times in days. All subpopulations proliferated with comparable growth rates compared to original NCH644 control (FACS-sorted viable single cells) where no statistical significance was observed (mean ± SEM) (n_B=3-4, n_T=2-3). The mixed model F-test was used as statistical test. Statistical analysis was realized by Sonia Leite and Dr. Nicolas Sauvageot (Centre of Competence for Methodology and Statistics, LIH) and Dr. Petr Nazarov (Proteome and Genome Research Unit, LIH).

4.2.2. CSC-associated subpopulations create phenotypical heterogeneity

In analogy to normal stem cells, CSCs are proposed to be multipotent by producing differentiated progeny with distinct phenotypes. In that scenario, multipotent CSCs should give rise to all phenotypes whereby progenitors only should generate partial heterogeneity as they would display impaired multipotency. At last, fully differentiated non-CSCs would appear unipotent and represent their own phenotype of the parental cell line. To test whether the subpopulations have the ability to reform the initial heterogeneity, NCH644 FACS-sorted subpopulations cultured for different time periods (20, 30 and 70 days) were assessed for their phenotypic profile by multicolor phenotyping (**Fig. 19.a**). Interestingly, analysis revealed that none of the subpopulations retained its initial phenotype suggesting that all subpopulations were multipotent and that none was representing a truly 'differentiated' phenotype according to the one-way CSC hierarchical organization. Furthermore, all subpopulations generated a heterogeneous distribution consisting of all initial 16 phenotypic states which attributes to all subpopulations similar multipotent capacities (**Fig. 19.b**).

We used alluvial plots for data representation to emphasize the phenotypic changes over time (**Fig. 19.c)**. Alluvial plots order subpopulations from top to down by highest to lowest percentage. The predominant phenotypes in subpopulations 1 to 4 ($CD133^+$ $CD44^-$) remained $CD133^+$ and $CD44^-$ phenotypic states. Similarly, subpopulations 6 to 8 ($CD133^+CD44^+$) showed at later time points a higher percentage of $CD133^+$ and $CD44^+$ phenotypic states compared to other subpopulations. Except for subpopulation 16, all other subpopulations created a heterogeneous distribution that was significantly different from the original NCH644 population (**Annex 7.a**). However, at 70 days subpopulations 2, 4 and 12 showed phenotype distribution similar to the original NCH644 cultures.

The results strongly indicate that CSC marker-based heterogeneity is not the result of a one-way CSC hierarchical organization. This is supported by the lack of differentiated GBM subpopulations seen with the self-renewal and proliferation test.

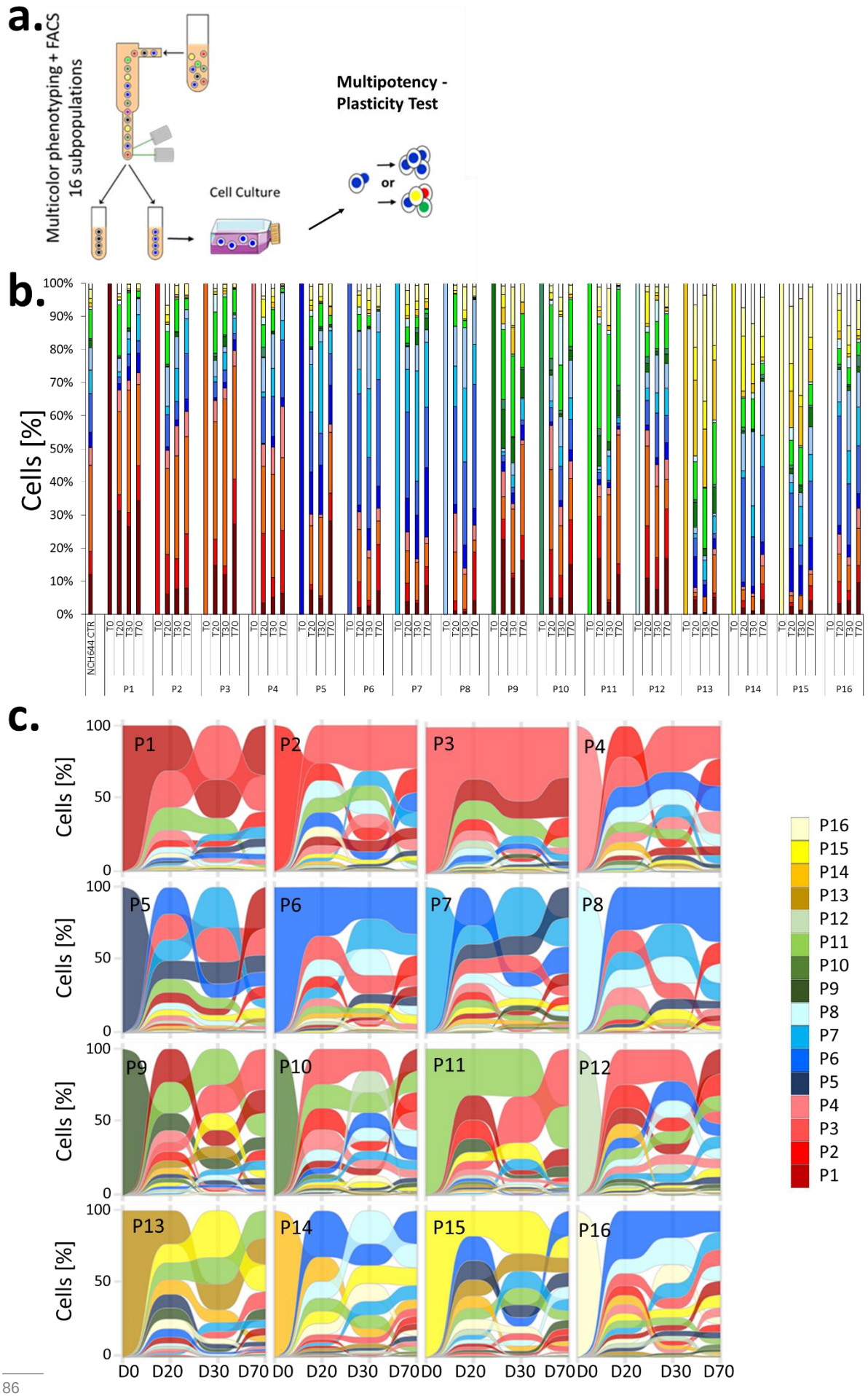
a.
Multicolor phenotyping + FACS
16 subpopulations
Cell Culture
Multipotency -
Plasticity Test
or
b.
Cells [%]
100%
90%
80%
70%
60%
50%
40%
30%
20%
10%
0%
NCH644 CTR
T0
T20
T30
T70
P1
P2
P3
P4
P5
P6
P7
P8
P9
P10
P11
P12
P13
P14
P15
P16
c.
Cells [%]
100
50
0
P1
P2
P3
P4
P5
P6
P7
P8
P9
P10
P11
P12
P13
P14
P15
P16
D0
D20
D30
D70

Figure 19: Dynamic plasticity in GBM subpopulations. a. To analyze which subpopulations were multipotent and thereby able to recapitulate phenotypic heterogeneity, we analyzed each FACS-sorted subpopulation after 20, 30 and 70 days in culture. Subpopulations retaining their phenotypic state are unipotent whereas subpopulations generating all other phenotypes are multipotent. **b.** All subpopulations were able to reform a heterogeneous expression profile, although the distribution of the four markers differed between subpopulations (mean percentages; n_B=3-4, n_T=1-3). Error bars are not depicted for visualization purposes. See **Annex 7.a** for statistical differences. **c.** Alluvial plots represent the dynamic state transitions in time, where the most abundant subpopulation (highest percentage) is at the top and the least abundant or absent phenotype at the bottom. Error bars are not depicted for visualization purposes. The Alluvial plots were realized with the help of Arnaud Muller (Proteome and Genome Research Unit, LIH).

4.2.2.1. Phenotypic heterogeneity is reformed by single cells

The number of plated cells plays an important role as autocrine and paracrine signals from neighboring cells may influence the potency of generating the distinct phenotypic states. Hence, generated heterogeneity might differ upon the number of initially plated cells. As the previous experiment was performed in a bulk sort using 300 cells per population, we tested whether single cells of each subpopulation demonstrate the above observed multipotent ability. To this aim, single FACS-isolated cells from each of the 16 subpopulations were phenotyped at each passage of self-renewal test (**Fig. 20)**. Similar to multipotency test, we expected that progenitor and differentiated cells showed reduced capacity of recreating original phenotypic heterogeneity. However, after each of the 4 assessed passages, single cells were able to produce phenotypic diversity of all 16 subpopulations. This proved that single cells were as well able to recapitulate CSC-associated heterogeneity. Similar to the previous multipotency test on bulk cells predominant phenotypic states in subpopulations 1 to 4 ($CD133^+$ $CD44^-$) were $CD133^+$ and $CD44^-$. $CD133^+$ and $CD44^+$ phenotypes were exceeding in subpopulations 5 to 8 ($CD133^+CD44^+$). Statistical analysis revealed that phenotypic states differed between subpopulations and phenotype distribution of the initial NCH644 cultures (**Annex 5.a**). However, hardly any statistical differences were detected between passages within each subpopulation (data not shown). This finding suggests that generation of heterogeneity is retarded upon single cell plating compared to bulk cell growth, but that single cells from each of the 16 subpopulations are able to reconstitute the original CSC marker profile.

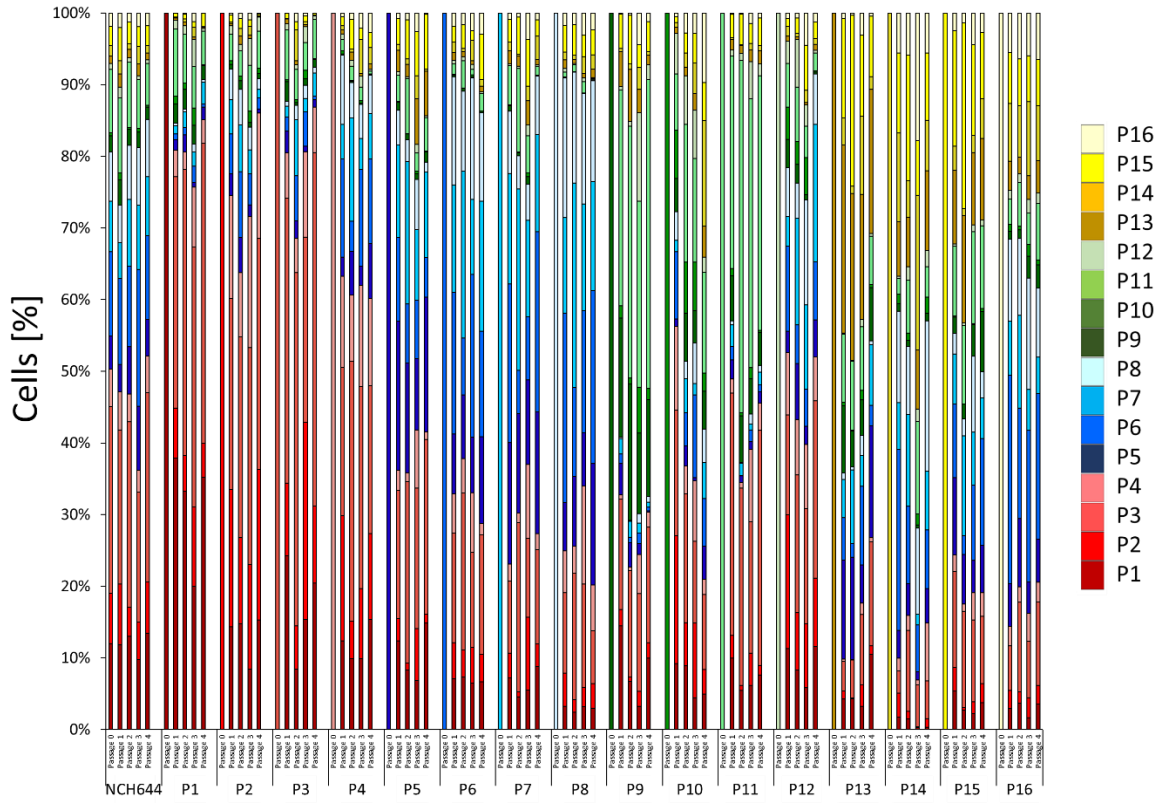

Figure 20: Phenotypic heterogeneity of single GBM cells. Barplots show the distribution of 16 subpopulations upon self-renewal test in 4 consecutive passages. For re-phenotyping, all single spheres of a subpopulation were pooled at each passage (mean percentage; n_T=3-6). Error bars are not depicted for visualization purposes.

4.2.2.2. CSC-associated phenotypic heterogeneity is recreated in other GBM stem-like cultures

A second GBM stem-like culture (NCH421k) was tested for its plastic behavior to assure that the observed adaptive capacities were not a cell line specific effect. As this culture demonstrated a relatively homogenous distribution of the four CSC-associated markers, the adaptive capacities in CD133, CD44, A2B5 and CD15 marker expression were tested separately. Both positive (‘red’ gating) and negative (‘blue’ gating) populations for the four markers were able to reform the initial expression pattern upon 25 days of culture (**Fig. 21**). This suggests that marker associated plasticity is a general phenomenon of GBM stem-like cultures.

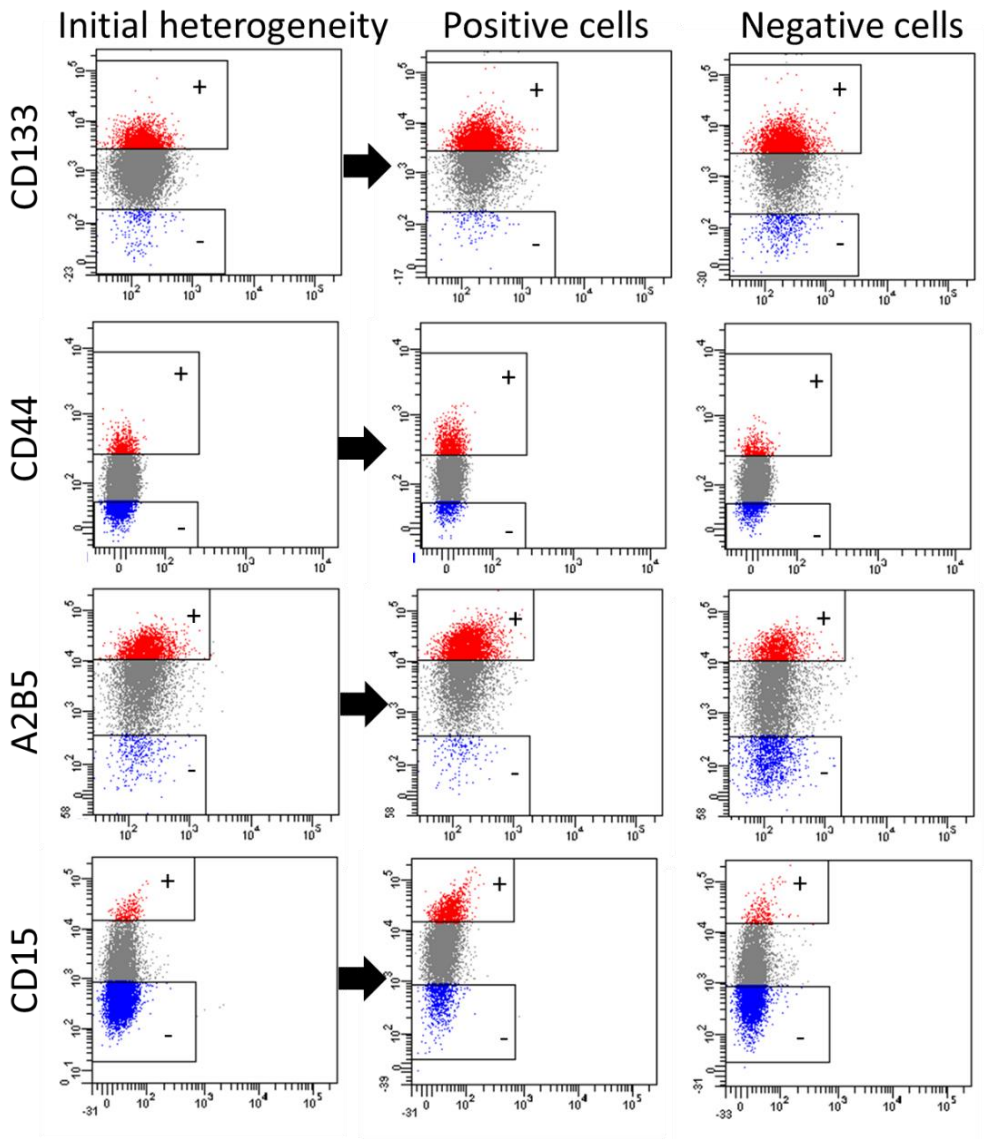

Figure 21: Adaptive capacities of NCH421k stem-like cultures. 500 CD133, CD44, A2B5 or CD15 positive and negative cells were FACS-sorted. After 25 days in culture cells were phenotyped for marker expression. All populations were able to recreate initial heterogeneity.

4.2.3. Markov chain modeling predicts stochastic CSC-associated state transitions in time.

As phenotype state transitions appeared very dynamic over time, we asked whether the phenotypic changes are the result of stochastic processes. We took advantage of mathematical modeling to predict state transitions in time between the different phenotypes. We specifically used Markov modeling as it allowed quantification of state transitions from the observed changes in phenotype distribution measured for multipotency test (**Fig. 19.b**). Andrey Andreyevich Markov, a Russian mathematician of the University of St. Petersburg, first introduced the Markov chains on stochastic processes in 1913 (Jurafsky, 2008). He

used his newly developed model to estimate the probability that the next letter in the text sequence of Pushkin's novel 'Eugine Onegin' would be a vowel or a consonant. Previsional, today's main application of the advanced hidden Markov model lies in language processing programs. The Markov chain calculates the probability of a sequence of events. In our case, the model calculated the probability of one subpopulation forming another phenotypic state in time. As time represents the sequence and the event represents the phenotype state transitions, the model was defined more specifically as the discrete-time Markov chains model. The model was based on several assumptions. First, cell state transitions are only dependent on the current phenotype of the cell. Second, state transitions are stochastic. Third, the sum of transition probabilities equals to 1. To calculate phenotype transitions additional prerequisites were required. Proliferation rates of the subpopulations need to be equal and phenotype transitions occur once in a time-step (e.g. one transition per day). As no significant differences in proliferation rates were observed between CSC-associated subpopulations (**Fig. 18**), different growth kinetics did not interfere with Markov modeling.

The application of the mathematical model on the evolving CSC-associated phenotype diversity observed during multipotency test (**Fig. 19.b**) led to an estimated transition network (**Fig. 22.a**). Phenotype transition probabilities are represented by arrows, where the thickness of the arrow is related to the increased chance of transition. The calculated transition matrix shows the probabilities of a subpopulation at a present state to form a given subpopulation in the next future state (**Fig. 22.b**). E.g., the probability that subpopulation 1 forms subpopulation 2 equals 0.4% and to form subpopulation 3 was higher (2.37%). This shows that certain state transitions are more likely to occur, suggesting that subpopulations differ in their ability to change their phenotype. The probability to form itself, thus self-renewing, was highest for each subpopulation.

The transition matrix revealed that only 65 of 240 possible direct state transitions did not occur. To investigate whether the improbable transitions (zeros in the transition matrix) result from progenitor-like cells, the transition network was analyzed for hierarchical structures. First the network appeared irreducible, meaning that each state can transit directly or via intermediate states into any other state. Moreover, no obvious bottlenecks were detected. A graph hierarchy was calculated as a hierarchy measurement in an organization structure. This model was proposed by Krackhardt and colleagues to analyze the degree of hierarchy in social systems (Krackhardt, 1994). The Krackhardt hierarchy is defined by the reciprocity of the state transitions that are asymmetric. To have a pure hierarchy, no direct and indirect reciprocal relations should be detected. In that case Krackhardt hierarchy equals to 1. In contrary, when all transitions are reciprocated (e.g. in a cycle, where each state can be reached via direct or indirect transitions), no hierarchy

exists and the Krackhardt value equals 0. Here, in the transition network of the CSC-associated phenotype transitions the calculated Krackhardt hierarchy equaled 0. These observations imply that the stochastic state transitions were non-hierarchical and therefore reversible.

a.

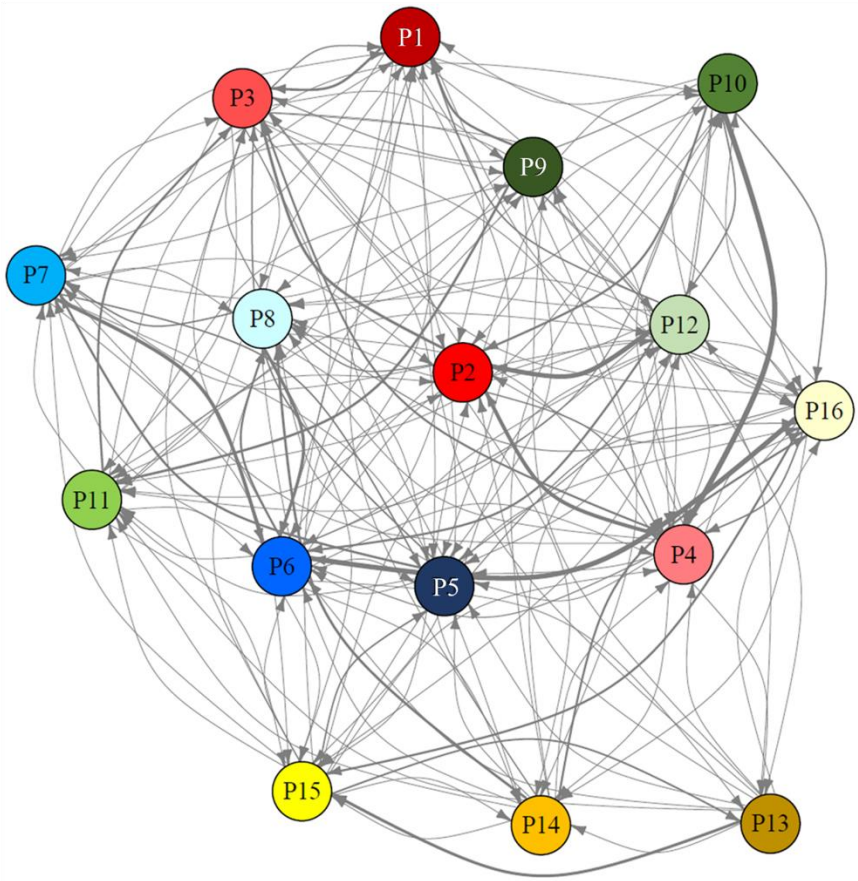

b.

Future state transitions

Present state	P1	P2	P3	P4	P5	P6	P7	P8	P9	P10	P11	P12	P13	P14	P15	P16
P1	95,18	0,4	2,37	0,3	0,49	0,03	0,08	0,14	0	0	0,74	0	0	0	0	0,25
P2	0,24	92,23	2,5	1,4	0	0,17	0,49	1,28	0	0,04	0,21	0	0	0,01	0,15	1,27
P3	1,34	0,41	95,71	0,87	0,14	0,13	0,13	0,3	0,11	0	0,8	0	0,02	0	0	0,05
P4	0	4,14	1,93	88,42	0,27	0,82	0,58	0,68	0	0,92	0	1,37	0,21	0,53	0	0,13
P5	0,63	0	1,62	0	91,86	0,91	2,28	0	0	0	0,58	0,21	0	0	0,33	1,58
P6	0,23	0,55	0,66	0,9	0,43	93,93	0,48	2,08	0,08	0	0,05	0,03	0,1	0,44	0,03	0
P7	0,1	0,1	0,49	0	1,45	3,95	92,69	0,11	0,38	0,26	0	0	0	0,21	0,24	0
P8	0	0	1,25	0,13	0,47	2,75	1,54	92,18	0	0	0,13	0	0	0	0,16	1,4
P9	2,32	0,57	0	1,01	0,33	0	0,09	0,7	91,4	0,15	2,36	0	1,02	0,01	0	0,05
P10	0	2,06	0,73	7,13	1,26	1,99	0	1,23	0	80,81	0,61	1,91	0	0	0,45	1,81
P11	0,48	0,67	2,04	0	0	0,08	0,14	0	0,74	0	94,8	0,2	0	0	0,84	0
P12	1,19	4,56	0,16	0,17	0,03	2,85	0	0,21	0,1	1,41	0,1	89,02	0,07	0	0,12	0,02
P13	0,24	0,28	0	0,14	0,57	0,69	0	0	0,72	0	0,6	0	92,83	0,95	2,92	0,05
P14	0,22	1,25	0	0,03	0,14	0,53	0	2,53	0	0,42	0,08	0,43	0	91,9	0,26	2,2
P15	0	0	0,48	0,07	1,67	0,06	0,19	0,58	0,24	0	0,23	0,16	1,89	0,44	92,86	1,12
P16	0,24	0,15	0,6	2	0,02	6,01	0	1,05	0,14	0,11	0	0,21	0	0,28	2,27	86,91

Figure 22: State transition probabilities calculated by Markov modeling. a. The network depicts the probability of state transitions to occur. The thickness of the arrows increases with the probability of state transitions. **b.** The transition matrix displays in percentage the probability of phenotypic changes. Subpopulations demonstrate variations in the probability of changing their phenotype.

Figure 31 was realized with the help of Thomas Buder (Zentrum für Informationsdienste und Hochleistungsrechnen (ZIH), Technical University of Dresden).

Using the calculated transition matrix, we were able to predict the final equilibrium, where the distribution of subpopulations and transition changes reach a stationary state of the Markov chain, one major property of Markovian chains. For this Markov chain, mathematical calculations yielded one unique stationary state regardless of the initial phenotypic state. Interestingly, the theoretically calculated equilibrium was similar to the initial phenotype distribution in the original NCH644 stem-like cultures (**Fig. 23**). Hence, for statistical comparisons we used in the following experiments the phenotype distribution present in original NCH644 stem-like cultures as stationary state control (CTR). This was necessary as statistical analysis can only be performed between two groups and predicted equilibrium of Markov modeling delivered only one single phenotype distribution. Of note, the original composition was not used to calculate the transition matrix. The strong similarity between predicted equilibrium and original NCH644 population phenotype distribution strongly supports the validity of the estimated transition matrix. These data also imply that each phenotype composition will reach the same predicted equilibrium at a given time point and supports the hypothesis that all subpopulations observed at 70 days (**Fig. 19.b**) may eventually result in one common heterogeneous phenotype if cultured long enough.

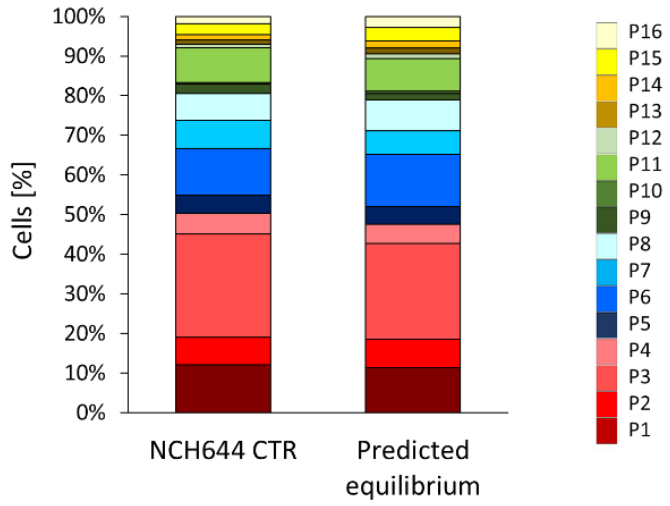

Figure 23: Final distribution predicted by Markov model. Phenotypic distribution found in original NCH644 stem-like cultures (NCH644 CTR) and predicted equilibrium of Markov chains obtained from multipotency data were very similar. Data for predicted equilibrium was obtained with the help of Thomas Buder (Zentrum für Informationsdienste und Hochleistungsrechnen (ZIH), Technical University of Dresden).

4.2.4. Markov model validation

To further validate the mathematical model, we took advantage of its potential to estimate the time an initial cell population needed to reach a second distribution. Markov chains allowed to design the phenotype composition of two cell populations (mix A and mix B) that reach equilibrium after 39 days of culture (**Fig. 24**). This was feasible using the estimated transition matrix to predict the time to reach final equilibrium. The two subpopulation composites were purified by multicolor FACS-sorting and cultured (day 0). At day 39 the cell cultures were re-phenotyped and demonstrated a highly similar phenotypic profile to the initial equilibrium of the NCH644 stem-like cultures. Only a slight difference between phenotypic state 9 from mix A and the control NCH644 was detected. These data underscore the prediction ability of the Markov modeling when applied to dynamic state transitions of GBM stem-like cells.

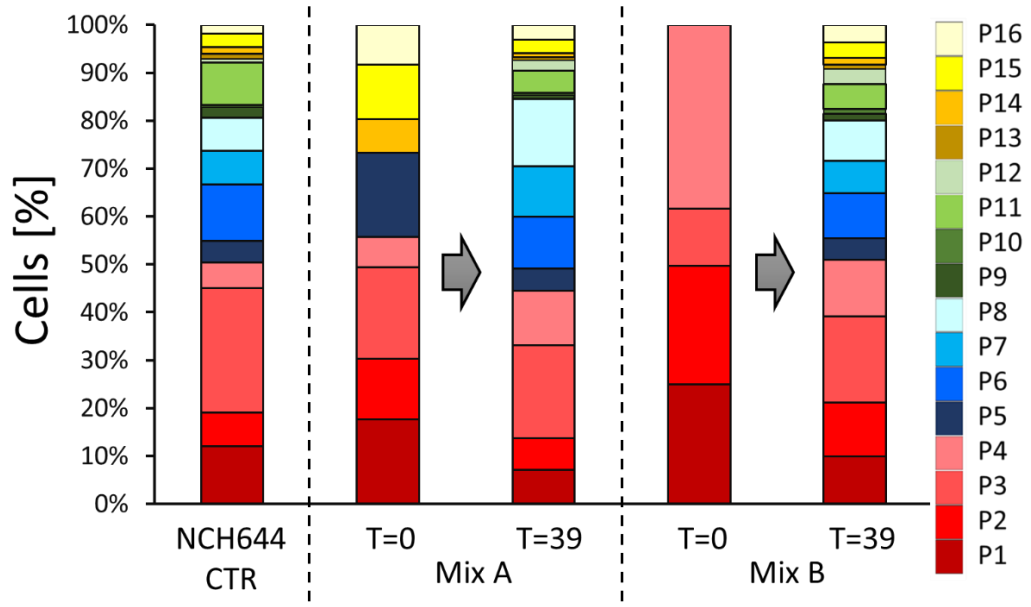

Conditions/ Phenotypic states	P1	P2	P3	P4	P5	P6	P7	P8	P9	P10	P11	P12	P13	P14	P15	P16
CTR vs Mix A									*							
CTR vs Mix B																

Figure 24: Test of predictive ability of the Markov model. Two mixes of FACS-sorted subpopulations were tested for their ability to recreate predicted distribution. Mathematical model predicted a stationary state after 39 days of culture (mean percentage; n_T=3). Error bars are not depicted for visualization purposes. Statistical significances of phenotypic states between original and measured data after 39 days are depicted in table below the graph (t-test with Bonferroni multiple-significance-test correction). Predictive data was obtained with the help of Thomas Buder (Zentrum für Informationsdienste und Hochleistungsrechnen (ZIH), Technical University of Dresden).

4.2.5. Evolution of phenotype distribution

The evolution of phenotypic transitions starting from single subpopulations revealed several interesting observations. For instance, Markov modeling predicted during the generation of phenotypic heterogeneity starting with 100% subpopulation 4 a strong increase for both subpopulations 2 (black arrow) and 3 (grey arrow). This was accompanied with a decrease of subpopulation 2 after only a few days of culture (**Fig. 25**). Although, time measurements were taken only at 20, 30 and 70 days the model is able to predict short-term phenotypic changes. To test whether these predicted observations occur as well in reality, subpopulation 4 was cultured and phenotyped after 11 and 18 days. Indeed, the strong increase in both subpopulations and subsequent decrease of subpopulation 2 was detected (**Fig. 25**). This event represents only an example as these observations are frequent and were also described by Sellerio et al. as an overshoot phenomenon (Sellerio et al., 2015). A strong enrichment of marker negative cells accompanied with a decrease was observed for both CD271$^-$ and CXCR6$^-$ melanoma cells. These results further strengthen the validity of the Markov model and its utility to study early phenotype changes.

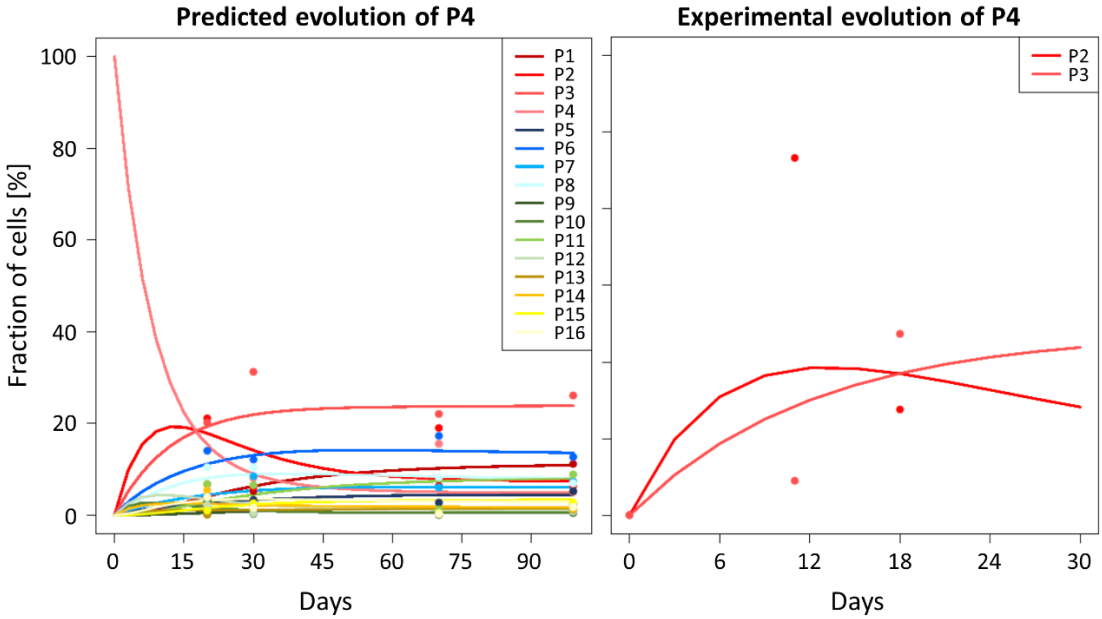

Figure 25: Evolution of phenotype distribution in subpopulation 4 (CD133$^+$ CD44$^-$ A2B5$^-$ CD15$^+$). Left panel shows evolution of subpopulation P4 over time as predicted by Markov model. Right panel shows FACS-sorted subpopulation 4 that was cultured for 11 and 18 days. The percentages of subpopulations 2 and 3 were measured by flow cytometry (mean percentage, n_T=3). The measured data (dots on graph) correspond to the predicted data (Markov model curve). Figure was realized with the help of Thomas Buder (Zentrum für Informationsdienste und Hochleistungsrechnen (ZIH), Technical University of Dresden).

4.2.6. CSC-associated subpopulations reach phenotypic equilibrium at different timepoints

Transition matrix showed that certain state transitions were more likely to occur than others, however, CSC-associated subpopulations were all predicted to create the same phenotype diversity suggesting that subpopulations differ in time needed to reach final equilibrium. Thus, time to reach steady state was calculated for each subpopulation using Markov chains. All subpopulations were predicted to reach equilibrium between 63 to 120 days, but at different time points (**Fig. 26**). Subpopulation 2 ($CD133^{+}CD44^{-}A2B5^{+}CD15^{+}$), 4 ($CD133^{+}CD44^{-}A2B5^{-}CD15^{+}$) and 12 ($CD133^{-}CD44^{-}A2B5^{-}CD15^{+}$) were predicted to reach equilibrium already at day 63, 72 and 66 days, respectively. This lead to the assumption that subpopulation 2, 4 and 12 might be more adaptive compared to other phenotypes under these conditions.

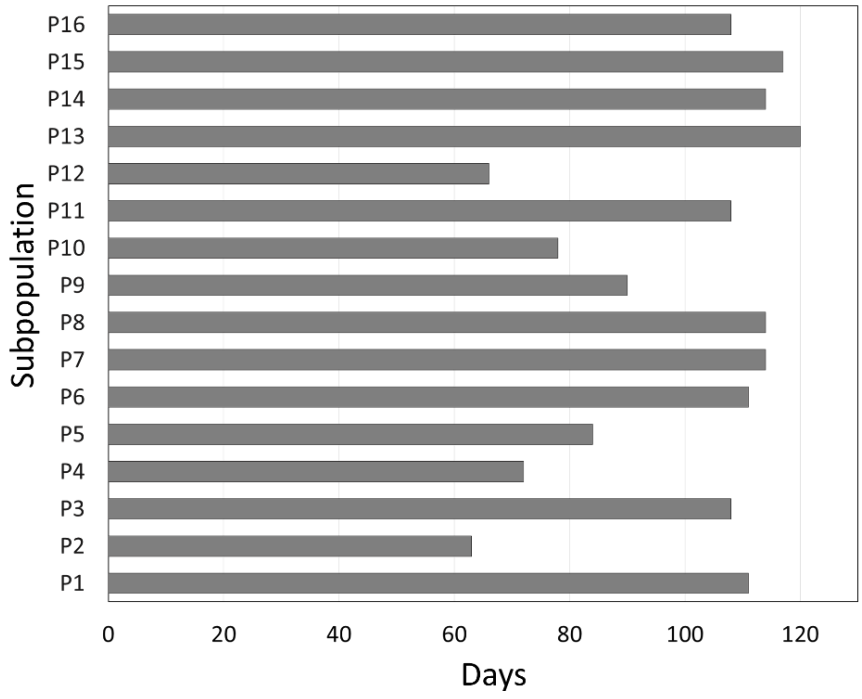

Figure 26: Predicted time to reach equilibrium from single subpopulations. Markov model was used to estimate the number of days the transition matrix reaches steady state when starting with 100% pure subpopulation. Subpopulation 2, 4 and 12 appeared the most adaptive. Data for this figure was obtained with the help of Thomas Buder (Zentrum für Informationsdienste und Hochleistungsrechnen (ZIH), Technical University of Dresden).

To test whether the time to reach equilibrium from single subpopulations as predicted by the Markov model were correct, subpopulations 2, 4, 5, 9 and 11 were cultured for 63, 72, 84, 90 and 108 days, respectively. Subsequently, all cell cultures were measured and their phenotypic distribution was compared to the distribution of NCH644 CTR. Indeed

subpopulation 9 reached equilibrium at the predicted time point and did not differ statistically from NCH644 CTR. Although subpopulations 2, 4, 5 and 11 showed some differences compared to NCH644 CTR, the reached phenotypic distribution was relatively close to the equilibrium (**Fig. 27**). The fact that subpopulations needed different times to reach equilibrium cannot be explained by differences in proliferation (see **Fig. 18**), suggesting that phenotype changes are not cell cycle dependent. Deviations from Markov model predictions might arise from cell culturing or the use of only one biological replication. Also, the model itself may demonstrate some weakness in predicting these complex biological phenotypical state transitions. Generally, taking into account the results demonstrating the generation of phenotypical heterogeneity (**Fig. 19.b**) and especially the model validation experiments (**Fig. 24, 25** and partially **Fig. 27**), strongly suggest that the partial inconsistencies observed in Fig. 27 results from technical issues rather than model weaknesses.

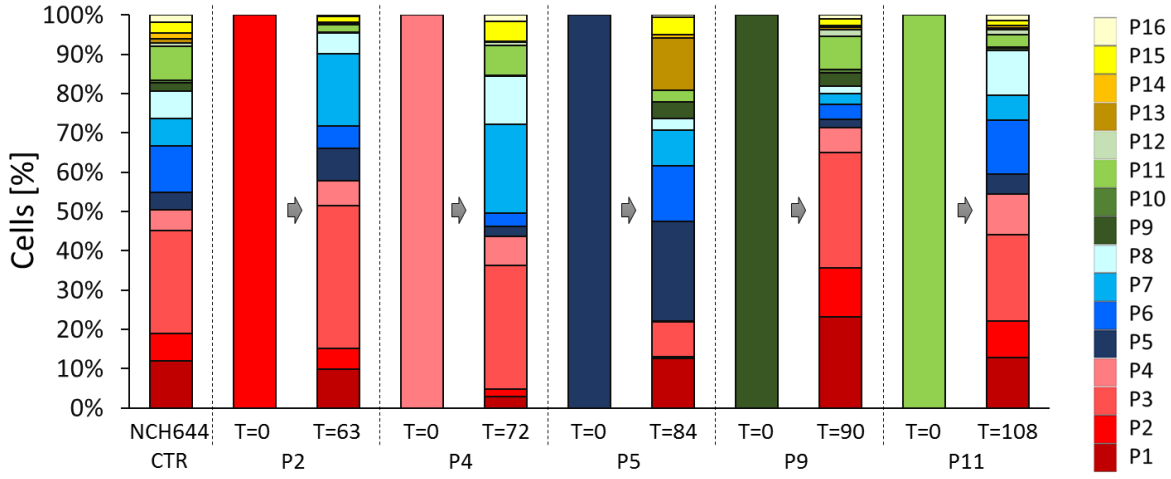

Conditions/Phenotypic states	P1	P2	P3	P4	P5	P6	P7	P8	P9	P10	P11	P12	P13	P14	P15	P16
CTR vs P2									***	**	**		***	***		
CTR vs P4	***	**				***			***	**			**	***		
CTR vs P5		***		**						**		***				
CTR vs P9																
CTR vs P11									**		*		*			

Figure 27: Time to reach initial distribution of single subpopulations. Predictions of figure 35 were tested for subpopulation 2, 4, 5, 9, and 11. Redistribution of subpopulations were partially similar to the distribution at equilibrium (mean percentage; n_T=3). Error bars are not depicted for visualization purposes. Statistical significances of phenotypic states between original and measured data after 39 days are depicted in table below the graph (t-test with Bonferroni multiple-significance-test correction).

4.2.7. CSC-associated marker expression is independent

Markov modeling was further used to test independency of the expression of the four markers CD133, CD44, A2B5 and CD15 during state transitions. The final equilibrium of each individual marker (CD133, CD44, A2B5 and CD15) was calculated under the assumption of dependence and independence (see **Annex 2.c** for details).
Calculations of the composition of the two obtained equilibria revealed no differences (**Fig. 28**), suggesting that CD133, CD44, A2B5 and CD15 expression is independent in GBM cells. Thus, the transitions between positive and low/negative expression of one marker are independent of the level of expression of the other markers

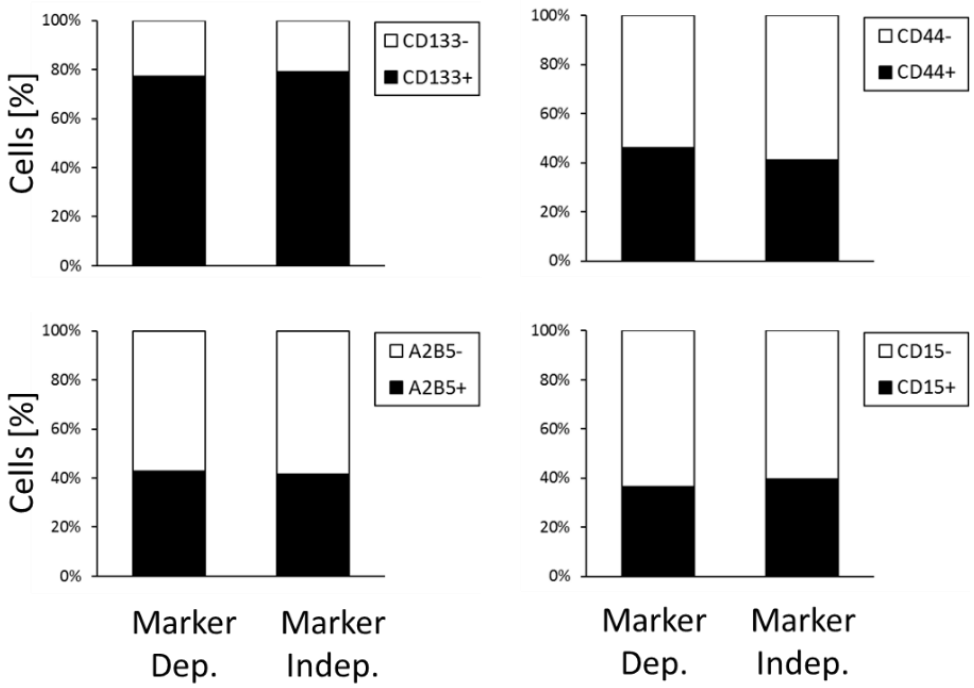

Figure 28: CSC-associated markers are independent from each other. Single marker equilibria were calculated either by the assumption of independency by adding probabilities of single marker transition matrixes or deviated from the predicted proportions by Markov modeling of 4 markers simultaneously. As equilibria did not differ, markers appeared to be independent. Data for figure was realized by Thomas Buder (Zentrum für Informationsdienste und Hochleistungsrechnen (ZIH), Technical University of Dresden).

In summary, our data shows that all analyzed tumor cell subpopulations were able to proliferate and carried stem-cell properties including self-renewal potential. Moreover, all subpopulations were multipotent and able to give rise to the original heterogeneous cultures. Using mathematical modeling we were able to predict state transitions over time for individual subpopulations. Moreover, the Markov model revealed a different propensity for reforming the original heterogeneity between subpopulations over time, which was independent of their proliferation index. Finally, phenotype state transitions were

independent of marker expression. Markov modeling represented an appropriate model to calculate state transitions and predictions were proven to correspond to measured data.

Results

Chapter 4.3

Identification of survival mechanisms of GBM cultures to hypoxia

4.3. Identification of survival mechanisms of GBM cultures to hypoxia

GBM tumors are heterogeneous tumors comprising several environmental niches, i.e. hypoxic, perivascular and invasive niches. One well characterized and major hallmark of GBMs is the hypoxic zone surrounding necrotic areas. Cancer cells residing in this sparse environment activate survival mechanisms such as decreased proliferation (Hubbi and Semenza, 2015, Carmeliet et al., 1998), enhanced invasiveness (Joseph et al., 2015), upregulation of anti-apoptotic pathways (Kumar and Choi, 2015, Graeber et al., 1996), autophagy (**Annex 11**, (Abdul Rahim et al., 2017)) or upregulation of anaerobic glycolysis (Lin and Yun, 2010)(**Annex 10**, (Sanzey et al., 2015)). It has been suggested that the CSC population within a tumor bulk is more prone to survive and adapt to hypoxia than non-CSCs (Lathia et al., 2011a). In order to elucidate the survival mechanisms of putative CSCs and non-CSCs in hypoxia, we first characterized several bulk GBM cell cultures under severe oxygen deprivation. The response to hypoxia was assessed in patient-derived stem-like cultures and classical serum dependent GBM cells. Cell growth, death and apoptosis, proliferation, clonogenic ability and invasive behavior was analyzed in normoxia, short and long-term hypoxia.

4.3.1. GBM cultures display reduced cell counts in hypoxia

To assess the behavior of GBM cells in hypoxia, cell growth of several GBM cell cultures was evaluated for up to 7 days under low oxygen condition which were defined at 0.5% O_2. We interrogated the adherent serum grown U87 and U251 GBM cell cultures and the non-adherent serum-free NCH644, NCH421k, NCH660, NCH601 and NCH465 stem-like cultures.

All GBM cells regardless of the culture condition significantly decreased in cell number upon hypoxia compared to normoxia, albeit to a different extent (**Fig. 29**). NCH465 displayed the least significant reduction in cell number counts in hypoxia compared to the normoxic condition. The most extreme behavior was observed for NCH421k cells which resulted in a net cell loss of 72% compared to the initial number of plated cells (from 50´000 to 14´000 cells in hypoxia) indicating that most cells do not survive in hypoxia. However, all other cell lines demonstrated an increased cell number after 14 days of culture in normoxia and hypoxia showing that cells are able to proliferate in both conditions. Proliferation rates in hypoxia and normoxia may be similar or vary. In case cells equally divide in both conditions the decreased cell number in hypoxia compared to normoxia may result from an increased cell death as suggested for NCH421k cell line. On the other hand, a decreased proliferation rate in hypoxia might leads also to a lower cell number count.

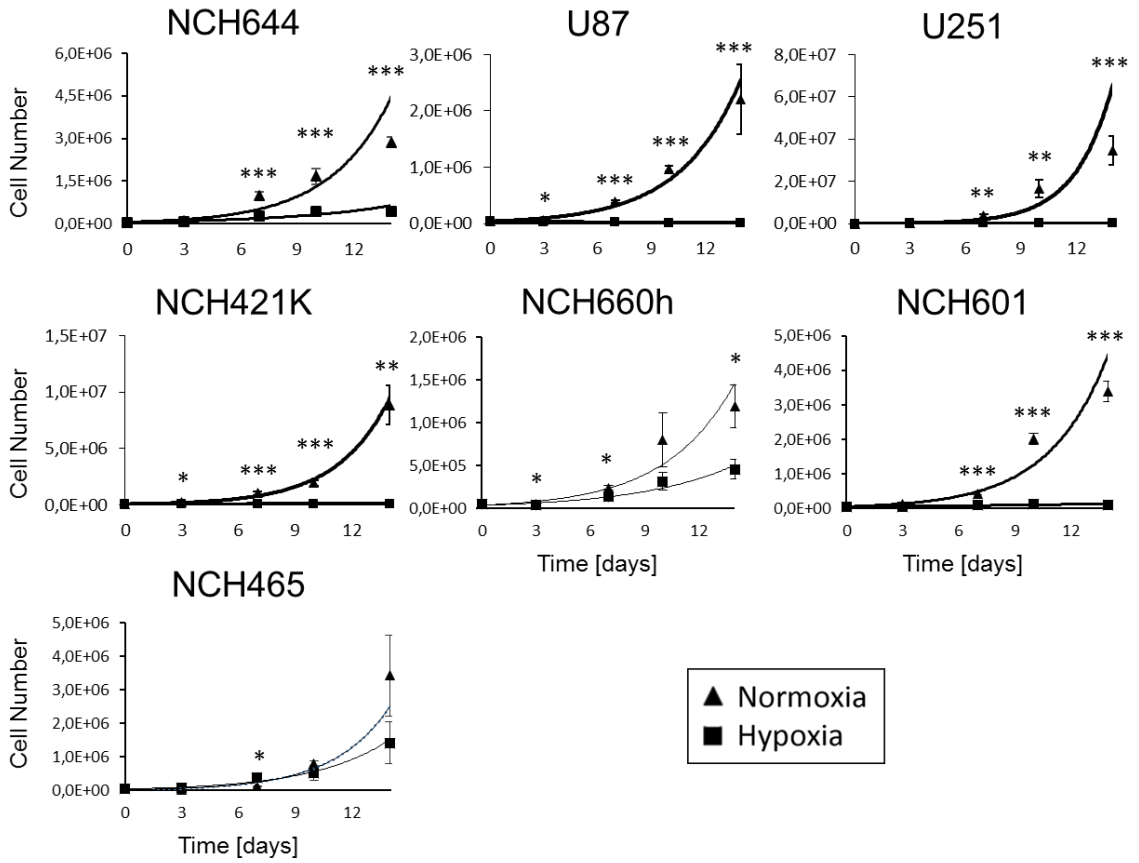

Figure 29: Cell number counts of GBM cell cultures are lower in hypoxia than in normoxia. Graphs represent changes in growth between standard normoxic and hypoxic condition. Cell number was counted 3, 7, 10 and 14 days after plating. Data is represented as a mean cell number with standard error of the mean (n_B=3-4, n_T=2-3). Statistical differences between cell number in hypoxia and normoxia were calculated using t-test ($p<0.05$ = *, $p<0.01$ = ** and $p<0.001$ = ***).

4.3.2. GBM stem-like cells display increased apoptosis and cell death in hypoxia

Reduced cell growth may result from multiple cellular processes, such as increased cell death, slower cell cycle or reduced clonogenicity. To assess cell death upon exposure to hypoxia, we performed an apoptosis/necrosis test using AnnexinV/PI staining after 16 hours and 7 days of culture. By flow cytometry, we were able to exclude debris from cells by forward (FSC-A) and side scatter (SSC-A). Single cells were discriminated from doublets by area and height forward scatter (FSC-A; FSC-H). In combination with PI staining we were able to distinguish between viable ($AnnexinV^{-}PI^{-}$), early apoptotic ($AnnexinV^{+}PI^{-}$), late apoptotic ($AnnexinV^{+}PI^{+}$) and necrotic cells ($AnnexinV^{-}PI^{+}$) (**Fig. 30.a**). The majority of the stem-like GBM cultures (NCH660h, NCH601 and NCH465) marked a high number of late apoptotic and necrotic cells already in short-term hypoxia (16h) (**Fig. 30.b**). Consequently, the number of viable cells significantly decreased in these cultures (73.51 to 32.14% in NCH660h, 83.22 to 29.2% in NCH601 and 73.56 to 25.85% in NCH465).

The reduction of viable cells was even more dramatic upon long-term hypoxia (7d) in NCH421k (81.1 to 16.2%). Amongst GBM stem-like cultures, NCH644 was most resistant to low oxygen levels and displayed a moderate increase of late apoptotic cells (4.44 to 12.11%) only in long-term hypoxia. The percentage of necrotic cells, however, did not significantly increase. These results suggest that a reduced cell growth of NCH421k, NCH660h, NCH601 and NCH465 stem-like cultures in hypoxia compared to normoxia may result at least partially from increased apoptosis and cell death. Surprisingly, cell viability was not significantly impaired in adherent cell cultures in hypoxia although a slight tendency towards increased number of necrotic cells for U251 was observed. Neither was a significant increase in apoptotic or necrotic cells detected suggesting that a decreased proliferation rate or clonogenicity might cause a reduced cell growth in hypoxia.

Even more, these observations showed that distinct culture systems (e.g. adherent and sphere forming cultures) do react differently to low oxygen conditions. Most stem-like cultures showed increased apoptosis and/or cell death in hypoxia compared to normoxia with only a small percentage of surviving cells whereas in adherent cultures only a few cells enter apoptosis or die. These results contrast with the general assumption that serum independent stem-like cultures are more opt to survive in deprived environments than adherent cell cultures.

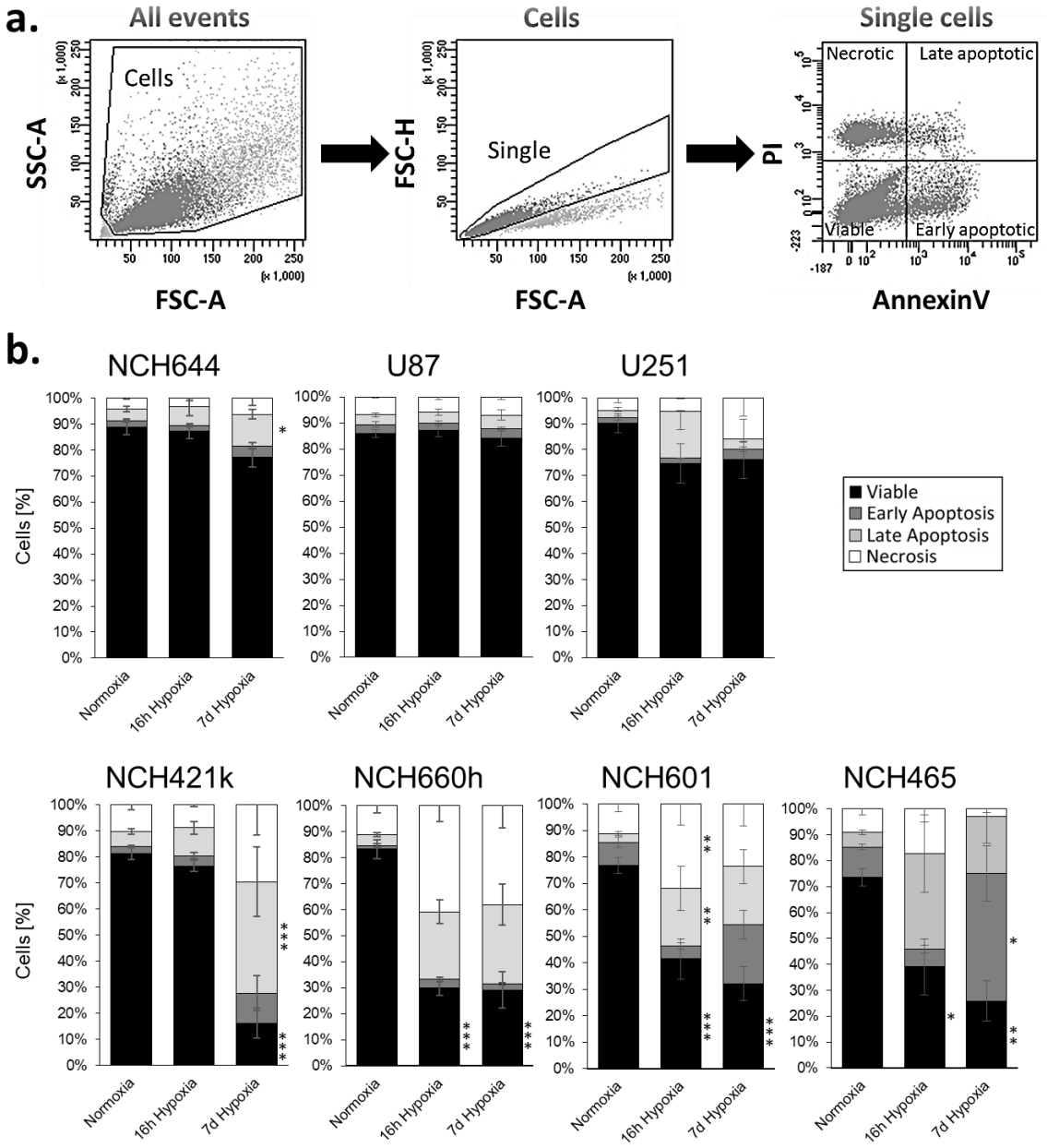

Figure 30: Apoptosis test of GBM cultures upon short and long-term hypoxia. a. Flow cytometric scatter plots depict gating strategy for the analysis of apoptotic cells in GBM cultures. GBM cells were distinguished from debris using forward (FSC) and side (SSC) scatters, followed by cell doublet and aggregate elimination (FSC-A/FSC-H). Single cells were divided into four categories: viable (AnnexinV$^-$ PI$^-$), early apoptotic (AnnexinV$^+$ PI$^-$), late apoptotic (AnnexinV$^+$ PI$^+$) and necrotic (AnnexinV$^-$ PI$^+$). **b.** Apoptosis and necrosis in GBM cell cultures was analyzed in normoxic, 16h and 7d hypoxic conditions. Bar plots represent percentage of cells (mean ± SEM, n_B=2-3, n_T=2-3). t-test was performed to test statistical significant differences between categories and conditions (Bonferroni multiple-significance-test correction; p<0.05 = *, p<0.01 = ** and p<0.001 = ***).

4.3.3. All GBM cell cultures were able to proliferate in severe hypoxia

Increased cell death accounted partially for the reduced growth rates in all GBM cell cultures in hypoxia. We hypothesized that surviving cancer cells might survive severe hypoxia by switching to a non-proliferative G1/G0 state. To determine the cell cycle activity, DNA content was measured in GBM cell cultures in normoxia, short and long-term hypoxia. By flow cytometric analysis, debris were excluded as described for apoptosis test. Cell doublets and aggregates were eliminated using area and width of the forward scatter or, alternatively, of the PI staining. Using a dead cell marker, we could discriminate between viable and dead cells to assure cell cycle analysis on pure single viable cells (**Fig. 31.a**). Although at distinct levels, all GBM cell cultures were able to proliferate in long-term hypoxic conditions (**Fig. 31.b**). Interestingly, the number of G2/M/S cells in NCH644 (±40%), U251 (±50%), NCH660h (±40%) and NCH465 (±60%) remained constant from normoxic up to severe hypoxic conditions. Since a reduced proliferation rate was not a cause for reduced cell number count in hypoxia (**Fig. 29**) we suggested that apoptosis and cell death (**Fig. 30.b**) have been the major reason. In contrast, U87, NCH421k and NCH601 GBM cultures experienced a significant reduction in proliferating cells upon severe hypoxia (G2/M/S cells from 30.9 to 8.58% in U87, from 39.13 to 21.85% in NCH421k and 33.74 to 18.33% in NCH601) (**Fig. 31.b**). Simultaneously, these cultures displayed an increased number of non-cycling cells. We have previously shown that U87 cells have a similar percentage of viable cells in normoxia than in hypoxia indicating that the low cell number count observed in hypoxia is a result from a decreased proliferation rate. In NCH421k and NCH601 an increased cell death/apoptosis and decreased proliferation was observed suggesting that a combined effect of these two processes was responsible for a reduced growth in hypoxia. Of note, no distinct proliferative behavior between cell culture systems (e.g. adherent or sphere forming) was observed.

In summary, we show that GBM cell cultures significantly decrease cell number upon severe hypoxia. The decreased cell number is a consequence of increased cell death and decreased proliferation rate. The extent of reduced cell number depends on the proportion of proliferating and apoptotic/necrotic cells. It is either solely based on a reduced proliferation rate (U87) or solely an increased cell death (NCH644, U251, NCH660h and NCH465). A combined influence of reduced proliferation and increased cell death (NCH421k and NCH601) was also observed.

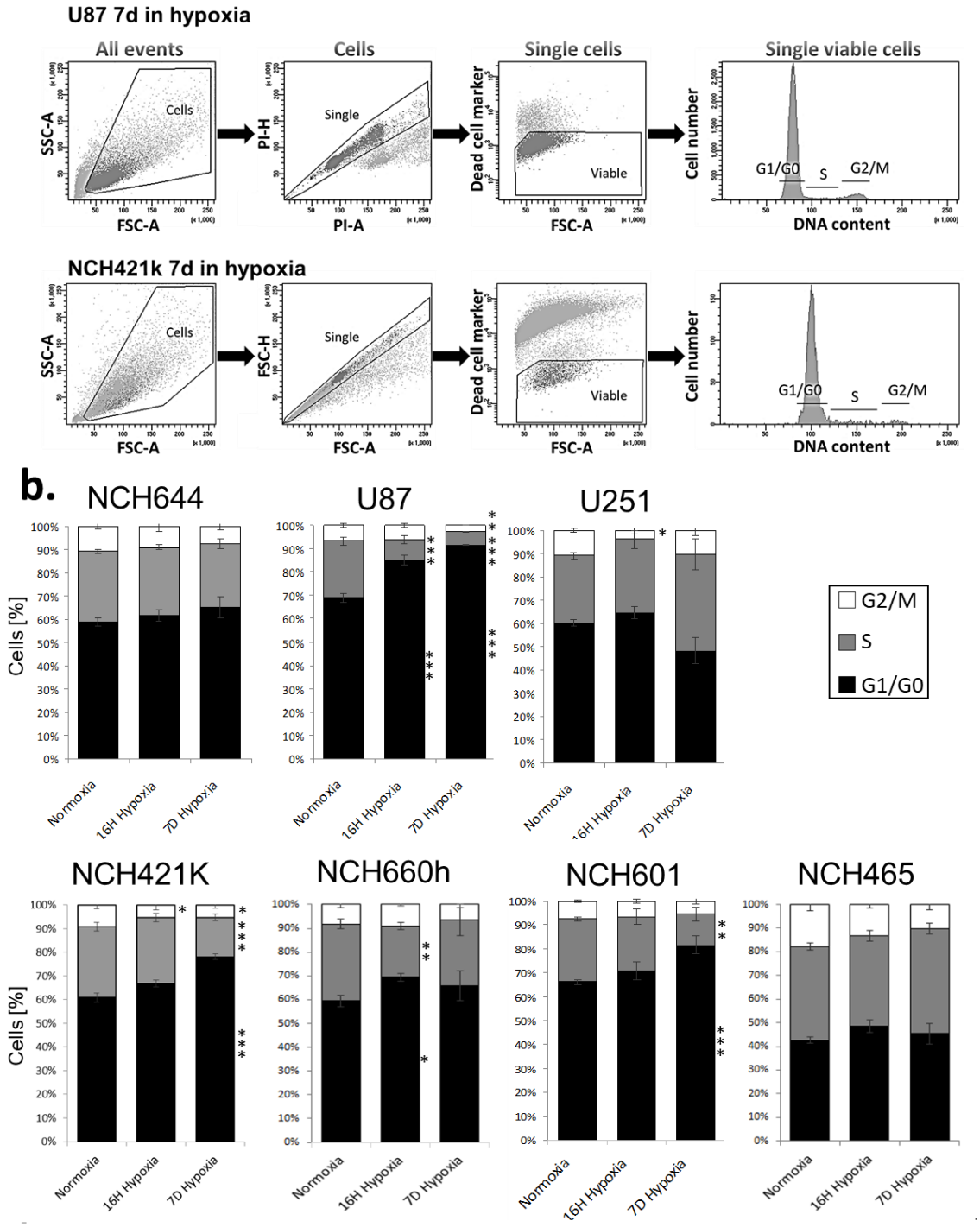

Figure 31: Cell cycle analysis during short and long-term hypoxia. a. Flow cytometric scatter plots depict gating strategy for the cell cycle analysis of GBM cultures. Cells were distinguished from debris using forward (FSC) and side (SSC) scatters, followed by cell doublet and aggregate elimination (FSC-A/FSC-H or PI-A/PI-H). Dead cells were recognized as positive for dead cell marker. Final histogram depicts DNA staining where cells in different cell cycle phases can be discriminated: G1/G0, S and G2/M states. **b.** GBM cell cultures were analyzed for their cell cycle activity in normoxia, 16h and 7d hypoxia (0.5% O_2). The cells were categorized into 3 groups according to the cell cycle phase: G1/G0, S and G2/M. Data is shown as percentage of viable cells (mean ± SEM; n_B=2-3, n_T=2-3). t-test was performed to test statistical significant differences between hypoxic to normoxic conditions (Bonferroni multiple-significance-test correction; $p<0.05$ = *, $p<0.01$ = ** and $p<0.001$ = ***).

4.3.4. All GBM cell cultures display clonogenic potential in hypoxia

A reduced growth rate may originate from an impaired ability to form progeny after exposure to hypoxia. We performed a colony formation assay, also referred to as the clonogenic assay, to assess the percentage of cells with the potential to form a clone. The experiment is performed at the single viable cell level in separate cultures to assure the measurement of the colony forming efficiency of one single cell. All GBM cultures regardless their culture type (e.g. serum dependent or independent) were able to form colonies in normoxia as well as in hypoxia. Surprisingly, only NCH644 (from 25% to 8%) and NCH421k (from 27% to 22%) showed a significant reduction in clonogenicity in hypoxia compared to normoxic condition (**Fig. 32.a**). For GBM stem-like cultures, the measurement of sphere diameters revealed that NCH644, NCH421k and NCH660h cultures recreated significantly smaller spheres in hypoxia (**Fig. 32.b**). Spheres of NCH601 and NCH465 were already relatively small at the initial normoxic state. Since we did not observe a decreased proliferation rate for NCH644 and NCH660h we suggest that sphere size is not always directly correlated to proliferative capacities in contrast to Mori et al (Mori et al., 2006). Here, sphere size of neural stem/progenitor cells was shown to gradually increase in a dependent manner with proliferation rate.

Thus, additionally to reduced proliferation and increased cell death, a decreased clonogenic ability and a smaller sphere size contribute to the reduced cell number of NCH644, NCH421k and NCH660h in hypoxic condition. Furthermore, serum independent cultures, considered to be enriched for CSCs, do not demonstrate an increase in clonogenic potential compared to adherent cultures.

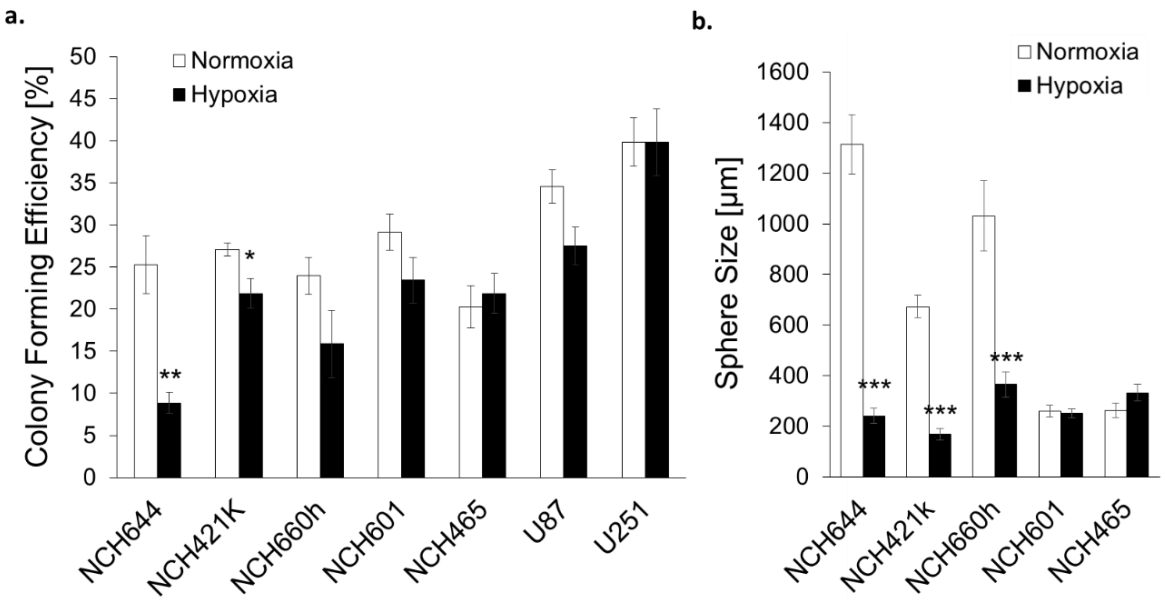

Figure 32: Clonogenic potential of GBM cells upon normoxia and hypoxia. a. Single viable FACS-sorted cells of each GBM culture were individually cultured in either normoxia or hypoxia.

Colony forming efficiency was calculated from the number of formed clones (mean percentage ± SEM; n_B=4). All GBM cultures demonstrated clonogenic potential in normoxia and hypoxia. Significant differences between colony forming efficiency between normoxia and hypoxia were calculated using t-test where p<0.05 = *, p<0.01 = **, p<0.001 = *** marked significant. **b.** Sphere size is represented as mean percentage ± SEM (n_B=1, n_T=20). Significance between sphere size in normoxia and hypoxia was tested with t-test (p<0.05 = *, p<0.01 = ** and p<0.001 = ***).

4.3.5. Hypoxic environment promotes a switch in invasive potential

Hypoxic GBM tumors are shown to have increased invasive/migratory behavior. It is hypothesized that tumor formation at distal locations in the brain is realized by so called tumor initiating cells (TICs) which are often described with stem-like characteristics (Zhou et al., 2009). *In vitro* assays with GBM cancer cells demonstrated an increased invasiveness at low oxygen levels as well (Joseph et al., 2015). Antiangiogenic treatment *in vivo* reduces oxygen delivery to the tumor and was shown to increase invasiveness in PDXs (Keunen et al., 2011). Furthermore, we hypothesized that concordant to the 'go or grow' hypothesis migrating cells might not be able to proliferate or produce progenitors at the same time. Therefore, an increased migratory ability might reduce cell growth in hypoxia. We therefore tested the invasive capacities of the GBM stem-like cultures at low oxygen concentrations using the Boyden chamber assay. To obtain a net percentage of invasive cells, the counted number of invasive and non-invasive cells was corrected for their cell growth to control for differences in cell death and proliferation between normoxia and hypoxia. In standard normoxic conditions GBM cultures demonstrated a distinct invasive potential (**Fig. 33**). NCH644 and NCH421k had a very low invasive ability in contrast to NCH660h, NCH601 and NCH465. These data correlate with their histopathological phenotype upon orthotopic transplantation into immunodeficient mice *in vivo* (Bougnaud et al., 2016). NCH644 generated tumors display a poorly invasive angiogenic phenotype, NCH421k an intermediate and NCH660h, NCH601 and NCH465 a highly invasive phenotype. Surprisingly, the change to hypoxia inverted this behavior *in vitro*. NCH644 showed a significant increase (from 5% to 33%) of invasive cells whereas NCH601 and NCH465 encounter a significant decrease in invasive potential. No significant difference in invasive cell number between normoxic and hypoxic condition was observed in NCH421k and NCH660h. These results show that not all GBM cells become invasive upon low oxygen levels. Of note, NCH465 cultures show a significant reduction in invasive cell number, however, growth rate is only minimally affected by low oxygen levels.

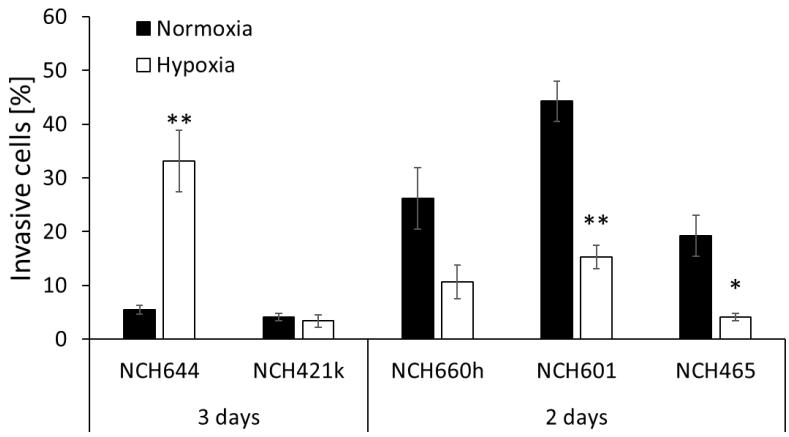

Figure 33: Invasion ability upon normoxia and hypoxia. Invasiveness of GBM cell cultures were measured using Boyden chamber assays. Cells were cultured for 2 or 3 days in normoxia and hypoxia. Invasive cell number is presented as mean percentage of total cells (mean ± SEM, n_B=3). Significance between normoxic and hypoxic conditions was tested with t-test ($p<0.05$ = *, $p<0.01$ = ** and $p<0.001$ = ***).

To summarize, we showed that all GBM cell cultures displayed a reduced cell number upon severe hypoxia. This observation is a combined consequence of increased cell death, decreased proliferative index, reduced clonogenicity and/or formation of smaller spheres. Nevertheless, all cell cultures were able to survive and continued to grow in hypoxic conditions, albeit to a variable extent. Although, GBM cultured underwent a negative selection pressure, remaining cells activated survival mechanism (e.g. reduce proliferation, clonogenicity) in hypoxia. The remaining cells might have increased adaptive capacities and may have higher stemness capacities since this property was described to favor survival in hypoxia (Lathia et al., 2011a).

There was no clear distinction in proliferation or colony forming efficiency between adherent and sphere forming GBM cultures, however lower levels of cell death in hypoxia were detected in adherent cultures than in sphere cultures. Furthermore, depending on GBM culture invasive capacities were either in or decreased from normoxic to hypoxic conditions. Although it is not clear why GBM cultures behave to different degrees, a putative explanation might result from distinct genetic and/or epigenetic backgrounds.

Results

Chapter 4.4

Analysis of stem cell properties and phenotype transitions of GBM CSC-associated subpopulations in hypoxia

4.4. Analysis of stem cell properties and phenotype transitions of GBM CSC-associated subpopulations in hypoxia

Certainly, the most popular theory in evolutionary biology is Darwin's survival of the fittest. When applied to cancer development, the cancer cell with the most advantageous properties survives different environmental pressures. Classically, research on clonal evolution of cancer focusses on genomic alterations as selective traits. Neutral mutations in a defined environment (e.g. perivascular niche) may be advantageous following an environmental change e.g. when the tumor core becomes hypoxic due to massive cell proliferation and reduced nutrient supply. However, some reports suggest that clonal competition in certain environments does not solely rely on DNA mutations (Vermeulen et al., 2013), but also on epigenetic factors and phenotypic heterogeneity (Greaves and Maley, 2012).

Cancer adaptability reflects the property of a cell to change its behavior to best fit the environment it encompasses. The change from aerobic oxidative phosphorylation to anaerobic glycolytic metabolism upon oxygen deprivation represents one of the best described adaptational abilities in cancer (Eales et al., 2016).

In this part, we analyzed to what extend the phenotypic heterogeneity is dependent on the hypoxic environment and how the hypoxic niche governs the CSC state. We took advantage of our CSC-associated subpopulations to assess phenotypical heterogeneity. We further evaluated whether stochastic adaptation can take place in hypoxia or if phenotypical changes result from selection of the most fitted phenotype(s). Therefore, subpopulations were characterized for their stemness abilities in hypoxia, e.g. self-renewal, indefinite proliferation and multipotency.

4.4.1. Hypoxia leads to a change in phenotypic heterogeneity

First, we assessed the impact of the environmental change from normoxia (21% O_2) to hypoxia (0.5% O_2) on CSC-associated marker expression. CSC marker expression was analyzed in GBM stem-like cultures after short and long-term hypoxia. A mild but distinct change in marker expression compared to normoxia was already observed after 16 hours and 2 days culture in low oxygen environment. This shift in phenotype became more prominent upon long term hypoxia (7 to 60 days). In general, hypoxic NCH644 stem-like cells expressed higher levels of CD133 (from 80.58% to 95.41%), CD44 (from 37.32% to 62.76%) and A2B5 (from 40.59% to 53.18%) whereas CD15 expression was decreased (from 35.51% to 14.46%) (**Fig. 34.a;** see **Annex 3.c** for all statistical comparisons of phenotypical states and single marker expression between time points). In particular,

subpopulations 5 ($CD133^+$ $CD44^+$ $A2B5^+$ $CD15^-$) and 7 ($CD133^+$ $CD44^+$ $A2B5^-$ $CD15^-$) were enriched, whereas numerous subpopulations including 2 ($CD133^+$ $CD44^-$ $A2B5^+$ $CD15^+$), 10 ($CD133^-$ $CD44^-$ $A2B5^+$ $CD15^+$) and 12 ($CD133^-$ $CD44^-$ $A2B5^-$ $CD15^+$) were predominantly reduced. The changes were also detected in more homogeneous NCH421k GBM stem-like cultures where, contrary to NCH644 stem-like cultures, CD44 (from 12.43% to 3.86%) expression was significantly reduced upon long-term hypoxia. Subpopulations 1 ($CD133^+$ $CD44^-$ $A2B5^+$ $CD15^-$) and 4 ($CD133^+$ $CD44^-$ $A2B5^-$ $CD15^+$) showed a tendency for enrichment upon hypoxia. A significant decrease was observed for subpopulation 2 ($CD133^+$ $CD44^-$ $A2B5^+$ $CD15^+$), 6 ($CD133^+$ $CD44^+$ $A2B5^+$ $CD15^+$) and 11 ($CD133^-$ $CD44^-$ $A2B5^-$ $CD15^-$) (**Fig. 34.b;** see **Annex 3.d** for all statistical comparisons of phenotypical states and single marker expression between time points). Even thought, phenotypic changes occurred over the entire measured time period (60 days for NCH644 and 7 days for NCH421k), the first alterations were already observed at early stages (12 hours and 2 days). Then rapid changes in phenotypic heterogeneity suggest an adaptation rather than clonal selection as the underlying process. The results are in accordance to McCord et al. who demonstrated that CD133 epitope expression in $CD133^+$ GBM populations remains high and increases CD133 in $CD133^-$ populations in 7% O_2 hypoxia (McCord et al., 2009). Similarly to TMZ treatment, changes were not always gradual in time, suggesting indirect state transitions via other phenotypic states in time before reaching a new hypoxic equilibrium. Nevertheless, we cannot exclude selection for a specific CSC-associated subpopulation by cell death observed in the previous chapter.

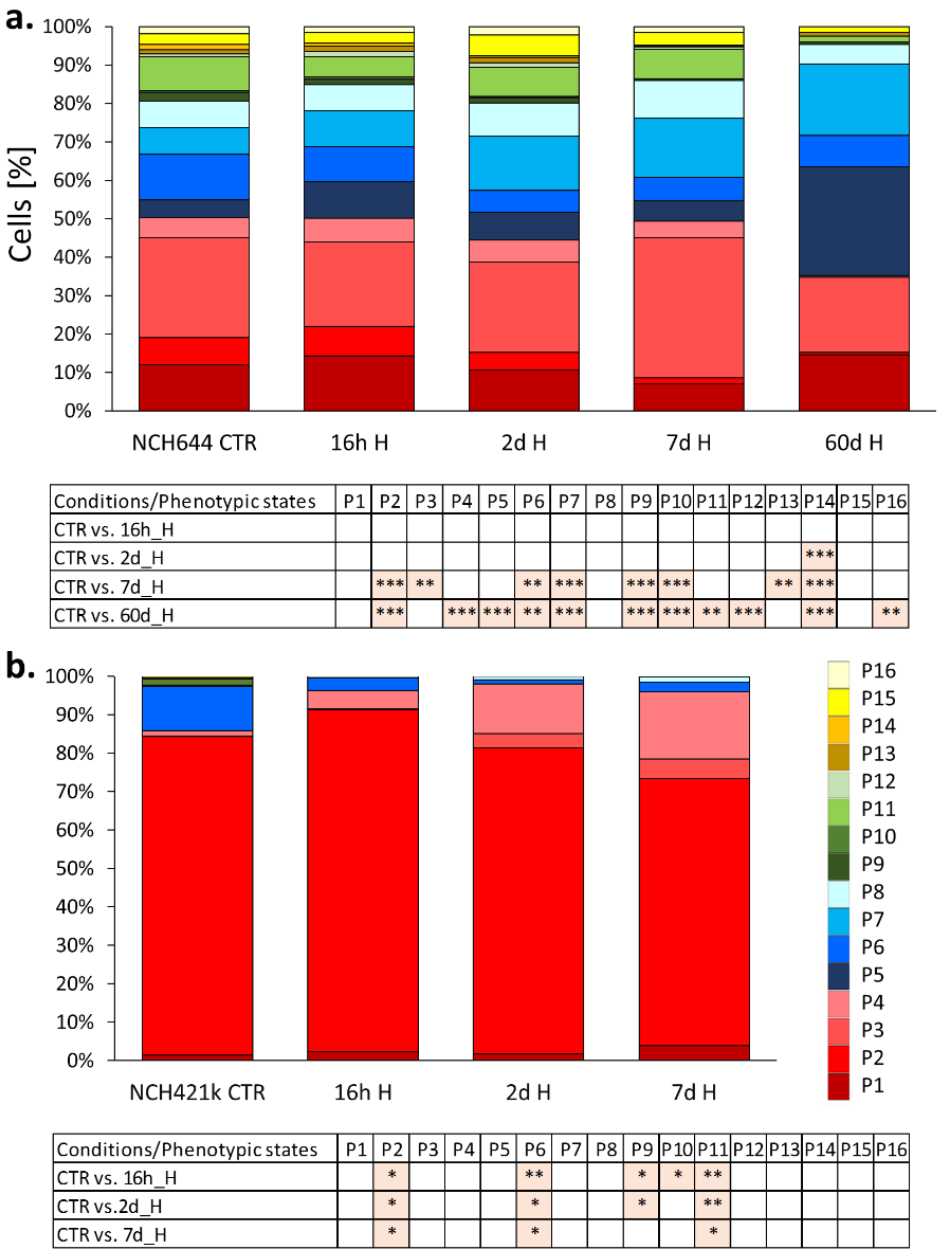

Conditions/Phenotypic states	P1	P2	P3	P4	P5	P6	P7	P8	P9	P10	P11	P12	P13	P14	P15	P16
CTR vs. 16h_H																
CTR vs. 2d_H														***		
CTR vs. 7d_H		***	**			**	***		***	***			**	***		
CTR vs. 60d_H		***		***	***	**	***		***	***	**	***		***		**

Conditions/Phenotypic states	P1	P2	P3	P4	P5	P6	P7	P8	P9	P10	P11	P12	P13	P14	P15	P16
CTR vs. 16h_H		*				**			*	*	**					
CTR vs.2d_H		*				*			*		**					
CTR vs. 7d_H		*				*					*					

Figure 34: Phenotypic adaptation upon exposure to hypoxic environment. a. NCH644 GBM stem-like cultures were cultured at 0.5% O_2 for short (16 hours, 2 days) and long term (7-60 days). CSC-associated marker expression (CD133, CD44, A2B5 and CD15) was measured by simultaneous multicolor flow cytometry (mean percentage; n_B=3, n_T=2-3). After long term hypoxia, CD133 and CD44 epitope expression was increased whereas CD15 and A2B5 were decreased. Error bars are not depicted for visualization purposes. Statistical analysis of phenotypic changes between states in normoxic vs hypoxic conditions is depicted in table below the graph (t-test with Bonferroni multiple-significance-test correction; $p<0.05$ = *, $p<0.01$ = ** and $p<0.001$ = ***). **b.** NCH421k GBM stem-like cultures demonstrated lower number of $CD44^+$ cells (mean percentage; n_B=8). Error bars are not depicted for visualization purposes. Statistical differences of phenotypic states between normoxic and hypoxic conditions are depicted in table below the graph (t-test with Bonferroni multiple-significance-test correction; $p<0.05$ = *, $p<0.01$ = ** and $p<0.001$ = ***).

4.4.2. Hypoxia induces differences in stemness abilities of CSC-associated subpopulations

As the switch from normoxic to hypoxic condition led to a change in phenotypic heterogeneity, we further assessed whether this was modulated by differences in stemness abilities between CSC-associated subpopulations. The observed enrichment of subpopulations 5 and 7 in hypoxia could arise from increased or decreased clonogenicity or proliferative index of these subpopulations. To test self-renewal and proliferative characteristics in hypoxia, we followed the same experimental strategy used in normoxia.

4.4.2.1. Impaired clonogenic ability of CSC-associated subpopulations in hypoxia

We first tested self-renewal capacities of CSC-associated subpopulations. Single viable cells from each subpopulation were individually FACS-sorted and cultured for four weeks in hypoxia. The number and size of spheres derived from each FACS-sorted subpopulation were measured. All derived spheres were further collected to replate again single viable cells for a second passage. This was followed by third and fourth passaging. Between each passage, the cells were cultured for 4 weeks. FACS-sorted viable single cells from bulk NCH644 stem-like cultures served as a control.

Generally, the average sphere size was smaller in hypoxia (±400µm) compared to normoxia (±750µm) (**Fig 35.a**) regardless of the CSC-associated subpopulation which is in accordance to results found in the previous chapter 4.3 (**Fig. 32.b**). No differences in sphere size were detected between the passage number and the same subpopulation. Only subpopulation 13 ($CD133^-$ $CD44^+$ $A2B5^+$ $CD15^-$) demonstrated significant difference in sphere size between the consecutive passages (189.64µm vs 256.79µm and 347.05µm, respectively), suggesting its adaption to hypoxia over long time.

However, numerous differences in sphere number were detected between the subpopulations with the same passage number (**Fig. 35.b-c**). The clonogenic ability was impaired for few subpopulations during first passage in hypoxia. The percentage of formed spheres of subpopulations 10 ($CD133^-$ $CD44^-$ $A2B5^+$ $CD15^+$) (3.39%), 12 ($CD133^-$ $CD44^-$ $A2B5^-$ $CD15^+$) (3.91%) and 14 ($CD133^-$ $CD44^+$ $A2B5^+$ $CD15^+$) (16.41%) was significantly lower compared to other subpopulations during the first passage (21.61-39.58%). Subsequently, their self-renewing ability increased at passage 2 and was maintained at passages 3 and 4, where no more statistical differences were observed between clonogenic potential of subpopulations.

Although the initial clonogenic potential of subpopulation 11 at passage 1 was similar to other remaining subpopulations, a significant increase in sphere forming ability during the first three passages was observed (from 29.69% to 43.75% and 45.01%).

At the second passage, subpopulations 3 ($CD133^+$ $CD44^-$ $A2B5^-$ $CD15^-$) (47.87%), 11 ($CD133^-$ $CD44^-$ $A2B5^-$ $CD15^-$) (43.75%) and 15 ($CD133^-$ $CD44^+$ $A2B5^-$ $CD15^-$) (43.49%), all low in A2B5 and CD15 expression displayed a significantly higher sphere number compared to other subpopulations. Differences between subpopulations in clonogenic potential were lost at later passages (3 and 4) which might be explained by an adaptation of all subpopulations to hypoxic condition (**Fig. 35.b-c**).

The decreased clonogenicity of subpopulations 10, 12 and 14 upon the first passage is in accordance with the observed reduction of these subpopulations upon environmental change to hypoxia. Reduced clonogenicity may suggest an increased cell death of these phenotypes in hypoxia at the initial time point. On the other hand, the increase in self-renewal ability of subpopulation 3 at the second passage may account for its enrichment. Other significant results could not be associated with the redistribution of the phenotypic heterogeneity upon change to hypoxia.

Importantly, none of the subpopulations was eliminated or ‘diluted’ in hypoxia. Variations in self-renewal abilities might rather result from an initial partial selective cell death of specific subpopulations and adaptive capacities of surviving clones. However, the statistical differences were generally lost at passage 3 and 4, suggesting that all the CSC-associated subpopulations were able to self-renew and adapt to hypoxia.

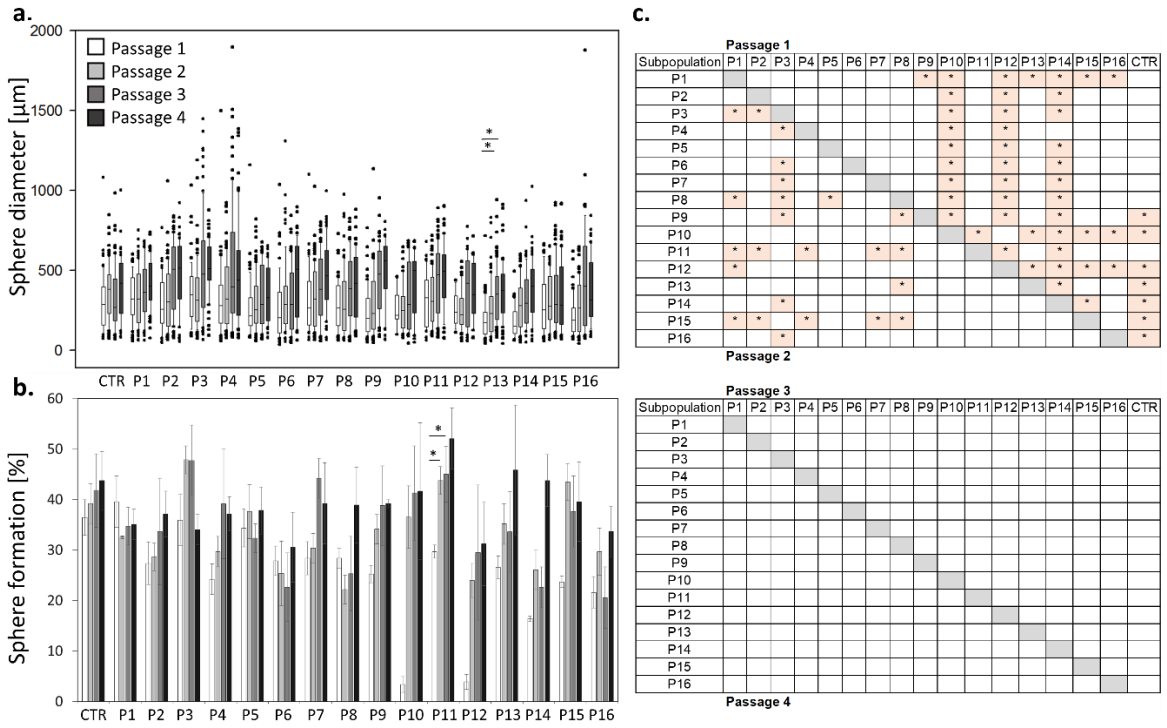

Figure 35: Sphere number and size of GBM subpopulations in hypoxia upon self-renewal test. a. Sphere number and size was measured during 4 passages of viable single cells of each FACS sorted subpopulation. The formed spheres did not differ in diameter between GBM subpopulations. Only subpopulation 13 showed an increase on second and third passage compared to the first passage (mean ± SEM; n_B=2-4, n_T=6-20; mixed model F-test). **b.** All subpopulations were able to form new spheres upon 4 consecutive passages, proving self-renewal properties of all subpopulations (mean percentage ± SEM; n_B=2-4). **c.** Kruskal-Wallis test was used to calculate statistical differences in sphere formation between subpopulations within one passage. Interestingly, most significant changes in clonogenicity were observed for subpopulations 10, 12 and 14 at passage 1 and for subpopulations 3, 11 and 15 at passage 2, (Kruskal-Wallis test * = p-value < 0.05). No statistical differences were present at passage 3 and 4. Statistical analysis for figure 18 was realized with the help of Sonia Leite and Dr. Nicolas Sauvageot (Centre of Competence for Methodology and Statistics, LIH).

4.4.2.2. Differential proliferative potential of CSC-associated subpopulations in hypoxia

We further investigated whether the enrichment in subpopulation 5 and 7 observed after an environmental switch from normoxia to hypoxia might result from an increased proliferative ability. The doubling time (dt) was calculated from the cell number measured at 30 and 60 days after FACS sorting in hypoxia of each cultured subpopulation.

All subpopulations were able to proliferate, although at a lower rate than in normoxia (CTR NCH644: 6.8 days ± 0.2 SEM vs 2.85 days ± 0.16 SEM) (**Fig. 36**). Since all subpopulations proliferated at a similar rate, the enrichment and depletion of CSC-associated phenotypes in long-term hypoxia only partially resulted from discrepancies in stemness abilities (i.e. clonogenicity of subpopulation 10, 12 and 14). Although we found small differences in

stemness abilities (i.e. self-renewal), all subpopulations were able to self-renew and proliferate indefinitely. Therefore, it is likely that the redistribution of CSC-associated heterogeneity upon environmental change to hypoxia arises from phenotypic adaptation.

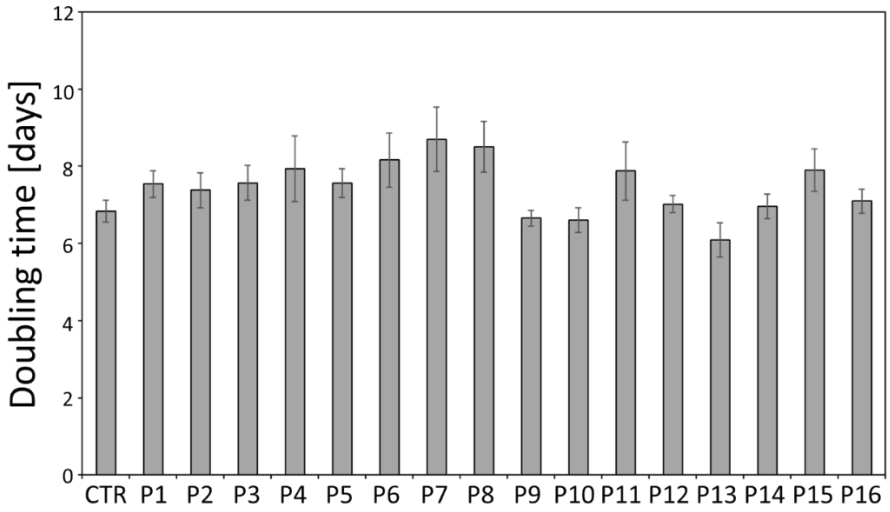

Figure 36: Doubling time of GBM subpopulations in hypoxia. a. Cell number of each NCH644 subpopulation was measured at 30 and 60 days after FACS-sort. No difference in dt was observed including that all subpopulations were able to proliferate at similar rate (mean ± SEM; n_B= 3-4, n_T=2-3). No statistical difference was detected between subpopulations and CTR NCH644 cells. The mixed model F-test was used as statistical test. Statistical analysis for this figure was realized with the help of Sonia Leite, Dr. Nicolas Sauvageot (Centre of Competence for Methodology and Statistics, LIH) and Dr. Petr Nazarov (Proteome and Genome Research Unit, LIH).

4.4.3. Phenotypic heterogeneity is created via adaptive state transitions of CSC-associated subpopulations

Since all subpopulations possessed stemness abilities and none of the subpopulations were lost in hypoxia, we hypothesized that changes in phenotypic equilibrium upon exposure to hypoxia cannot arise from clonal selection of the best fitted phenotypes. The above-mentioned results suggest strong adaptive capacities of surviving cells to a changed environment.

4.4.3.1. All CSC-associated subpopulations recapitulate phenotypic heterogeneity in hypoxia

To test whether all CSC-associated subpopulations were able to generate phenotypic heterogeneity in hypoxia, we analyzed the expression patterns of CD133, CD44, A2B5 and CD15 in FACS-sorted NCH644 subpopulations cultured for 60 days in 0.5% O_2. Similar to normoxic condition, all subpopulations were able to recreate CSC-associated heterogeneity

and none retained its initial phenotype (**Fig. 37**. None of the subpopulations appeared as a fully differentiated unipotent progeny in hypoxia.

All subpopulations created a phenotypic distribution statistically different from normoxic equilibrium but very similar to control cells at day 60 in hypoxia (**Annex 4.b**), indicating that the phenotypic distribution of all subpopulations is more similar to a hypoxia specific equilibrium than to a normoxic equilibrium. The predominant phenotypes in subpopulations 1 to 3 ($CD133^+$ $CD44^-$) and 9 to 11 ($CD133^-$ $CD44^-$) remained $CD133^+$ and $CD44^-$ subpopulations, whereas subpopulations 4 ($CD133^+$ $CD44^-$), 12 ($CD133^-$ $CD44^-$), 5 to 8 ($CD133^+$ $CD44^+$) and 13 to 16 ($CD133^-$ $CD44^+$) were mainly CD133 and CD44 positive.

Even though statistical differences were still observed between a proportion of phenotypic states in distinct subpopulations the similarities between phenotype proportions suggest that all CSC-associated subpopulations adapt to a similar phenotypic distribution in hypoxia and may eventually reach a same phenotypic equilibrium as observed for normoxic condition.

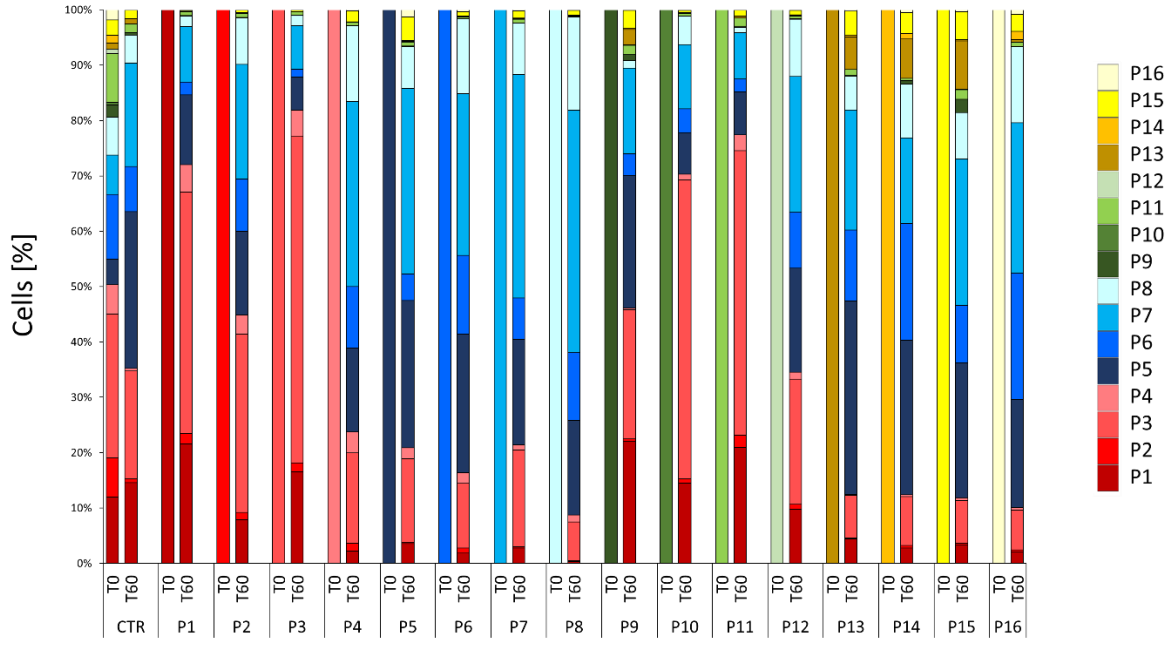

Figure 37: Plasticity test of GBM subpopulations in hypoxia. To analyze whether subpopulations were able to recapitulate phenotypic heterogeneity, CSC-associated marker expression patterns were analyzed in each FACS-sorted subpopulation after 60 days in hypoxia culture (0.5 O_2). As control, FACS-sorted NCH644 cultures were used. All subpopulations were able to reform a heterogeneous expression profile, although the distribution of four markers differed between subpopulations (mean percentages; n_B=3-4, n_T=2-3). Statistical significances of phenotypic states between CSC-associated subpopulations at day 60 and NCH644 control at 0 (T0) and 60 days in hypoxia (T60) are depicted in the Annex 4.b (t-test with Bonferroni multiple-significance-test correction). Error bars are not depicted for visualization purposes.

4.4.3.2. Single cells from CSC-associated subpopulations recapitulate phenotypic heterogeneity in hypoxia

We next tested whether a single cell demonstrates the same plasticity as a bulk of 300 cells used in the previous experiment (**Fig. 37**). Therefore, cells from each CSC-associated subpopulation were FACS-sorted and cultured as single cells to eliminate cell to cell communication. After 4 weeks of hypoxic cultures, formed spheres were collected and phenotyped for four consecutive passages. All single cells could produce phenotypic diversity during the four passages (**Fig. 38)**. CSC-associated phenotypic heterogeneity followed similar preferences for CD133+ CD44- and CD133+ CD44+ populations as found in the previous bulk-sorting experiment, except for subpopulations 13-16. These discrepancies might originate from different time periods in culture (60 vs. 28 days). The result showed that single cells had the full capacity to recapitulate CSC-associated heterogeneity.

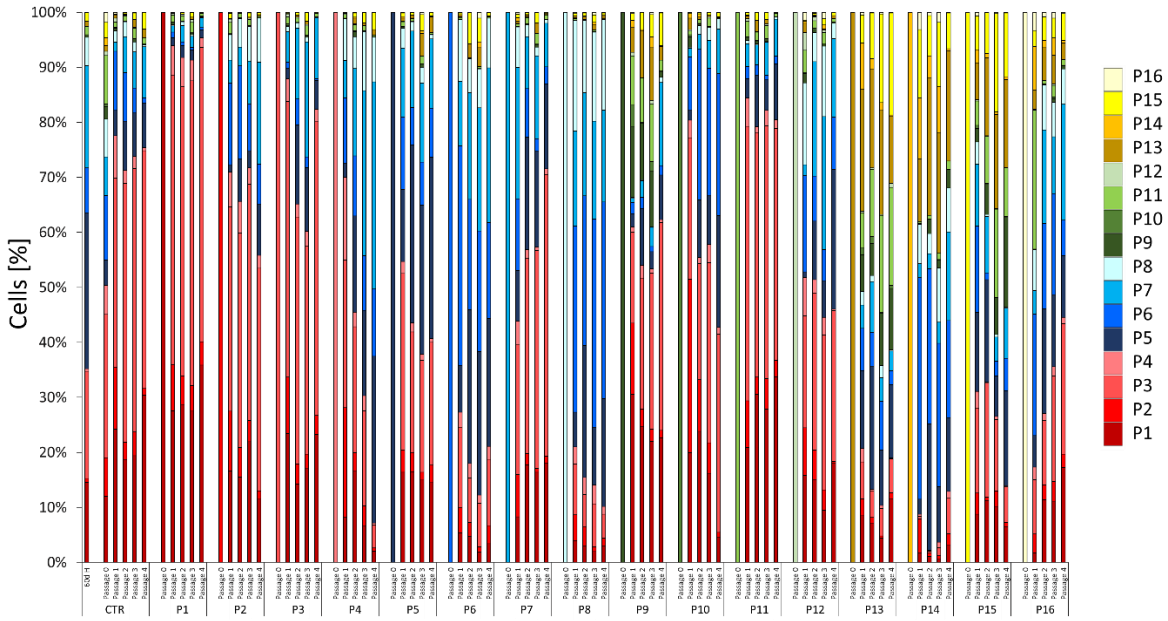

Figure 38: Phenotypic heterogeneity of single GBM cells in hypoxia. Barplots show the distribution of 16 subpopulations upon self-renewal test in 4 consecutive passages. For re-phenotyping, all single spheres of each subpopulation were pooled at each passage (mean percentage; n_B=2-4). Statistical significances of phenotypic states between normoxic NCH644 control (CTR), NCH644 control 60 days in hypoxia and subpopulations at different passage numbers in hypoxia are depicted in Annex 5.b (t-test with Bonferroni multiple-significance-test correction). Error bars are not depicted for visualization purposes.

4.4.4. Adaptive state transitions of CSC-associated subpopulations are stochastic in time

As we proofed that Markov chains successfully address CSC-associated state transitions in normoxia, we applied the mathematical model on the observed phenotypic changes in hypoxia (**Fig. 37**). To shed light on the process of phenotypic redistribution observed upon environmental change to hypoxia. Furthermore, mathematical modeling should allow to predict phenotypic state transitions in time to evaluate adaptive capacities of CSC-associated subpopulations.

4.4.4.1. Markov modeling predicts state transition probabilities for all CSC-associated subpopulations

We applied the Markov model to predict state transitions between the different phenotypes in time. Although the doubling times of subpopulations 7 and 13 were slightly different, we omitted this discrepancy as proliferative indexes did not correlate with phenotype redistribution upon hypoxia. Thus, proliferation rates were assumed to be equal between subpopulations and phenotype transitions to occur at equal discrete time steps. The predicted state transition network in hypoxia appeared less dense in possible phenotype changes (depicted by arrows) than in normoxia (**Fig. 39.a)**. This was confirmed by the transition matrix, where only 103 out of 240 possible direct transitions were predicted to be possible (**Fig. 39.b)**. Similar to normoxia, the self-renewal ability (probability to form itself) was highest for each subpopulation. Interestingly, subpopulation 10 ($CD133^-$ $CD44^-$ $A2B5^+$ $CD15^+$) could not be formed by any other subpopulation but was able to reform other phenotypes. Thus subpopulation 10 represented a transient state. Of note, an absorptive state is a state which is formed by other phenotypes but itself cannot form other phenotypes. States that are neither transient nor absorptive simply represent a recurrent state. The depletion of subpopulation 10 upon environmental change to hypoxia may result from its low clonogenic potential in hypoxia at passage 1 (**Fig. 35.b**) combined with its transient state predicted by Markov model (self-renewal 83.68%). Furthermore, subpopulations with low/absent CD133 expression were predicted to be formed by fewer phenotypes (<6) than $CD133^+$ subpopulations. Hence, the enrichment of subpopulations 3, 5 and 7 in hypoxia could be explained by a possible generation from numerous phenotypic states (>9). As subpopulation 10 represented a transient state, we further investigated the organizational hierarchy in the hypoxic network. Indeed, the degree of hierarchy calculated by Krackhardt test was equal to 0.125. Although subpopulation 10 could represent a potential CSC-like

state in hypoxia, as it cannot be formed by other phenotypic states, its self-renewal capacity did not differ from other subpopulations.

The results suggest that phenotypic heterogeneity in hypoxia results from adaptive stochastic state transitions rather than a hierarchical organization and that subpopulation 10 is not a favorable state in hypoxia. All subpopulations appear to survive by adapting to the best fitted phenotypic equilibrium in hypoxia.

a.

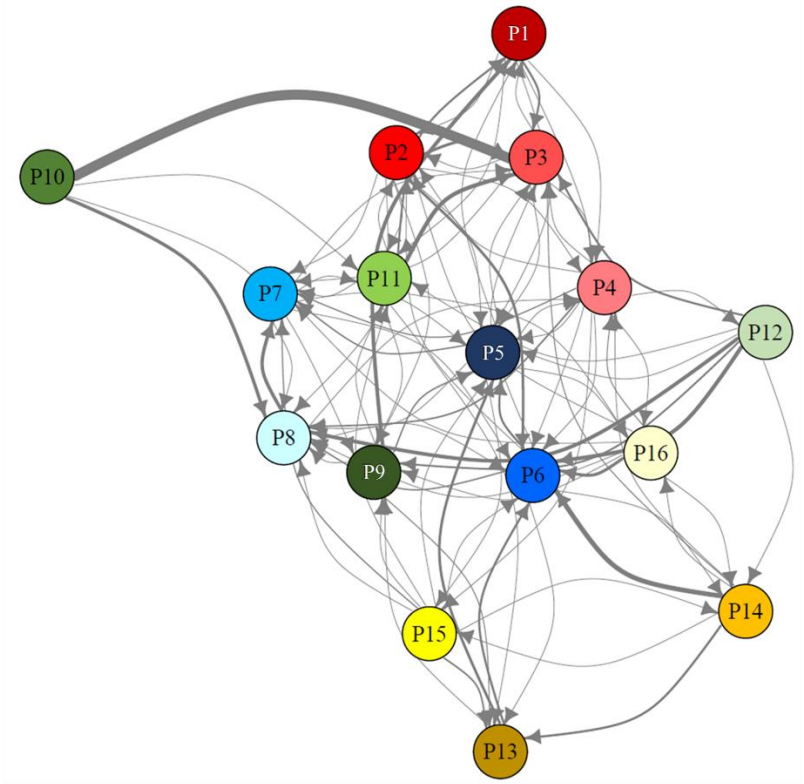

b.

Future state transitions

Present state

	P1	P2	P3	P4	P5	P6	P7	P8	P9	P10	P11	P12	P13	P14	P15	P16
P1	96,52	0,21	1,99	0,41	0,74	0,09	0	0	0	0	0,03	0	0	0,02	0	0
P2	0	91,7	2,97	0,62	0,26	2,93	0,55	0,51	0,11	0	0,35	0	0	0	0	0
P3	0,94	0,06	98,58	0,27	0,02	0	0,11	0	0	0	0,01	0,01	0	0	0	0
P4	0	0,91	0,66	94,16	0,15	0,48	1,32	1,78	0	0	0	0,08	0	0	0,37	0,08
P5	0,14	0	0,24	0,12	97,09	0	1,57	0,1	0	0	0	0	0	0	0,51	0,22
P6	0	0,45	0	0	2,1	95,75	0	1,62	0	0	0	0	0,04	0,04	0	0
P7	0	0	0,57	0	0,9	0,49	97,45	0,54	0	0	0,05	0	0	0	0	0
P8	0	0	0	0,26	0	0,99	3,54	95,2	0	0	0	0	0	0	0	0
P9	3,96	0	0	0	1,5	0	0	0,43	92,6	0	0,33	0	1,19	0	0	0
P10	0	0	11,95	0	0	0	0	3,89	0,26	83,68	0,22	0	0	0	0	0
P11	2,07	0,04	4,32	0	0	0	0,55	0	0,42	0	92,16	0,02	0,12	0	0	0,28
P12	0	0	2,18	0	0,01	4,49	0	4,23	2,07	0	0,81	85,61	0	0,6	0	0
P13	0	0	0	0	2,68	2,28	0	0	0,16	0	0	0	94,88	0	0	0
P14	0	0	1,24	0,08	0	5,24	0	0	0	0	0	0	2,37	90,85	0,21	0
P15	0	0	0	0	0,02	0,37	1,42	0,58	0,26	0	0,61	0	1,8	0,12	94,82	0
P16	0	0,61	0	1,08	0	3,13	0,55	0,14	0,83	0	0	0	0	0,86	0	92,8

Figure 39: State transition probabilities in hypoxia calculated by Markov modeling. a. The network depicts the probabilities of state transitions. The thickness of the arrows represents the probability of state transitions. **b.** The transition matrix displays percentages of the exact probabilities in phenotype changes for 1 day. Subpopulations demonstrate variations in the probabilities of changing their phenotype with subpopulation 10 representing a transient state. Figure 39 was realized with the help of Thomas Buder (Zentrum für Informationsdienste und Hochleistungsrechnen (ZIH), Technical University of Dresden).

4.4.4.2. Differential abilities in recapitulating final phenotypic distribution of CSC-associated subpopulations in time

To determine whether all subpopulations were able to reach the same phenotypic heterogeneity in hypoxia, we analyzed the hypoxic transition matrix and calculated its stationary state to obtain the final equilibrium. Even though the hypoxic transition probability matrix was reducible (meaning that not every state can be produced directly or indirectly by another state), we found a unique steady state. A matrix was reducible when at least one state (phenotypic state 10) could not be directly or indirectly formed. It is possible, that reducible transition matrices never reach a steady state or have several ones when the outcome is dependent on the initial state. Interestingly, the final predicted equilibrium in hypoxia did not exactly correspond to the equilibrium of the original NCH644 cells grown for 60 days in hypoxia (**Fig. 40.a**). This may suggest that longer times were needed for final equilibrium. However, we used in the following experiments the phenotype distribution of NCH644 stem-like cultures grown for 60 days in hypoxia as CTR for comparisons as we did not have data for longer hypoxia cultures and phenotype distribution obtained by Markov model was not suitable for statistical analysis (i.e. only one data value). To determine how long CSC-associated subpopulations need to reach final phenotypic distribution in hypoxia, time to equilibrium was calculated for each subpopulation. None of the subpopulations was able to recapitulate final phenotypic hypoxic equilibrium after only 60 days (**Fig. 40.b**). 13 out of 16 subpopulations were predicted to require over 250 days to reach the phenotypic equilibrium. This increased time to reach steady state compared to normoxia may result from the strong decrease in proliferation of GBM stem-like subpopulations in low oxygen concentrations. Subpopulations 2, 9 and 12 which needed less than 250 days to recapitulate final hypoxic phenotypic distribution, appeared most adaptive. Subpopulation 2 was predicted to reach equilibrium after 80.5 days, confirming its close resemblance to the control at day 60.

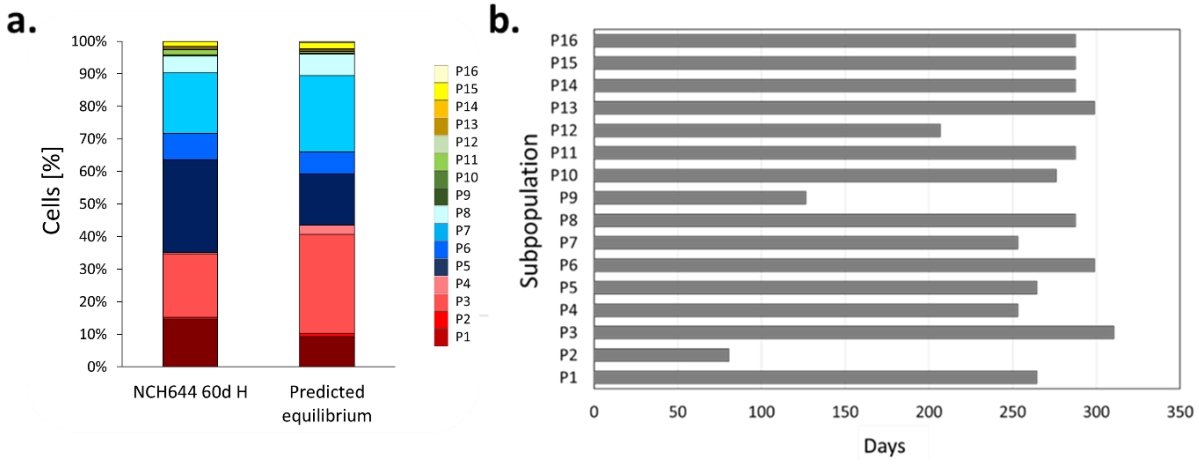

Figure 40: Markov model predictions on final phenotypic distribution in hypoxia in time. a. Stationary state was calculated for the hypoxic transition matrix. Phenotypic distribution of NCH644 after 60 days of hypoxia and predicted equilibrium are not the same. **b.** Markov model was used to estimate the number of days the transition matrix reaches steady state when starting with 100% pure subpopulation. Subpopulation 2, 9 and 12 appeared the most adaptive. Figure 40 was realized with the help of Thomas Buder (Zentrum für Informationsdienste und Hochleistungsrechnen (ZIH), Technical University of Dresden).

4.4.4.3. Independence of marker expression of CD133, A2B5 and CD15 in hypoxia

We next tested if the expression of the four markers CD133, CD44, A2B5 and CD15 was independent. Therefore, the same mathematical methodology was used as in normoxia (**Annex. 2.c**) applying the data from Fig. 46. Comparing the equilibria of each marker obtained under the assumption of dependence and independence revealed similar distributions of absent/low and high expression of CD133, A2B5 and CD15. Only CD44 showed a slight discrepancy between the calculated marker distributions (73.2 vs. 55.79% $CD44^+$ cells) (**Fig. 41**). This suggest that CD133, A2B5 and CD15 are inter-independent whereas CD44 expression may depend to some extent on the presence of the other markers.

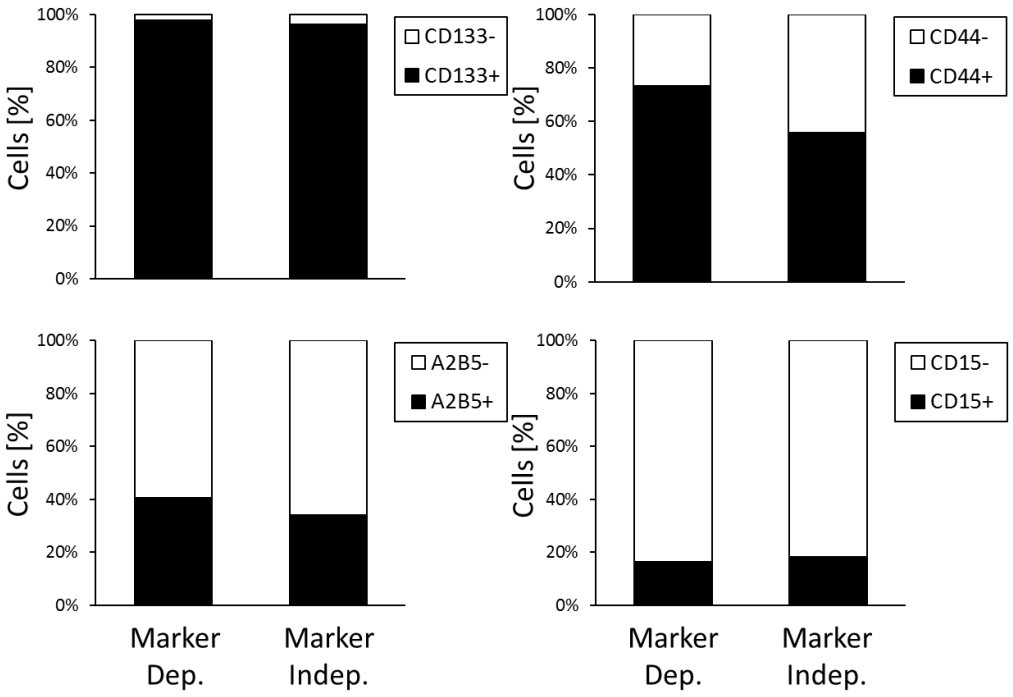

Figure 41: Calculation for marker independency. Equilibria for each marker were calculated either by the assumption of independency or independency using the data from fig. 46. As equilibria did not differ for CD133, A2B5 and CD15, markers appear to be independent. However, CD44 might depend on the combination of CD133, A2B5 and CD15 expression profiles. Data for this figure was realized with the help of Thomas Buder (Zentrum für Informationsdienste und Hochleistungsrechnen (ZIH), Technical University of Dresden).

4.4.5. CSC-associated phenotypic adaptation to hypoxia is reversible

Highly adaptive capacities were observed for all subpopulations in hypoxia (**Fig. 37**) and normoxia (**Fig. 19.b**). Furthermore, the observed phenotypical change from normoxia to hypoxia could be largely explained by adaption and only partially by selection. Therefore, we wondered whether the phenotypical change in hypoxia could be reversed upon reculture in normoxia. To this aim, NCH644 stem-like cells were cultured in low oxygen environment (0.5% O_2) for 7 days and subsequently transferred to high O_2 (21%) condition for another 7 and 14 days.

The expression of the 4 markers generally reversed upon reculture in normoxia. The number of $CD133^+$ cells decreased (from 79.27% to 74.6%), $A2B5^+$ cells (from 70.6% to 61.08%) and $CD15^+$ cells (from 68.97% to 41.5%) decreased whereas $CD44^+$ cells were increased after 14 days of normoxia culture (from 36.62% to 45.34%). Despite similar levels of $CD44^+$ and $A2B5^+$ cells, percentage of $CD133^+$ and $CD15^+$ cells in 14 days reculture in normoxia did not reach original levels yet (**Fig. 42;** see **Annex 3.e** for all statistical comparisons of phenotypical states and single marker expression between time points). Furthermore, the percentage of enriched subpopulations in hypoxia decreased (e.g. subpopulation 7 (from 15.46% to 9.84%)). On the other hand, subpopulations 2 (from 1.49% to 7.01%) and 12 (from 0.58% to 1.17%), which were reduced upon low oxygen levels, were reformed again. This data suggests that the phenotypic adaptation observed upon environmental change from normoxia to hypoxia is reversible. Although distinct, the phenotypic distribution upon 7 and 14 days re-normoxia resembled the normoxic equilibrium. Markov modeling predicted that the phenotypic profile seen at 7 days hypoxia needed 37 days to revert to the normoxic equilibrium. Thus, the differences in phenotypic distribution after 7 and 14 days re-normoxia are expected to disappear on time.

Reversibility of CD133 marker expression was also shown for adherent U251MG cells in at 1% O_2 hypoxia. Also here cells needed longer to regain initial state. Negative at the start of the experiment, where they increased to almost 50% positivity at day3 and going to nearly 0 after 6 days (Griguer et al., 2008)

We next used Markov modeling to predict the phenotypical distribution after 7 and 14 days of renormoxia. The comparison between predicted and measured phenotype distributions revealed that measured data were more similar to normoxic equilibrium than the predicted. In this context the mathematical predictions might be imprecise as the model does not take into account environmental changes. This means that cells may need to adapt fast to new environments suggesting 39 days predicted to reach normoxic equilibrium may be not required.

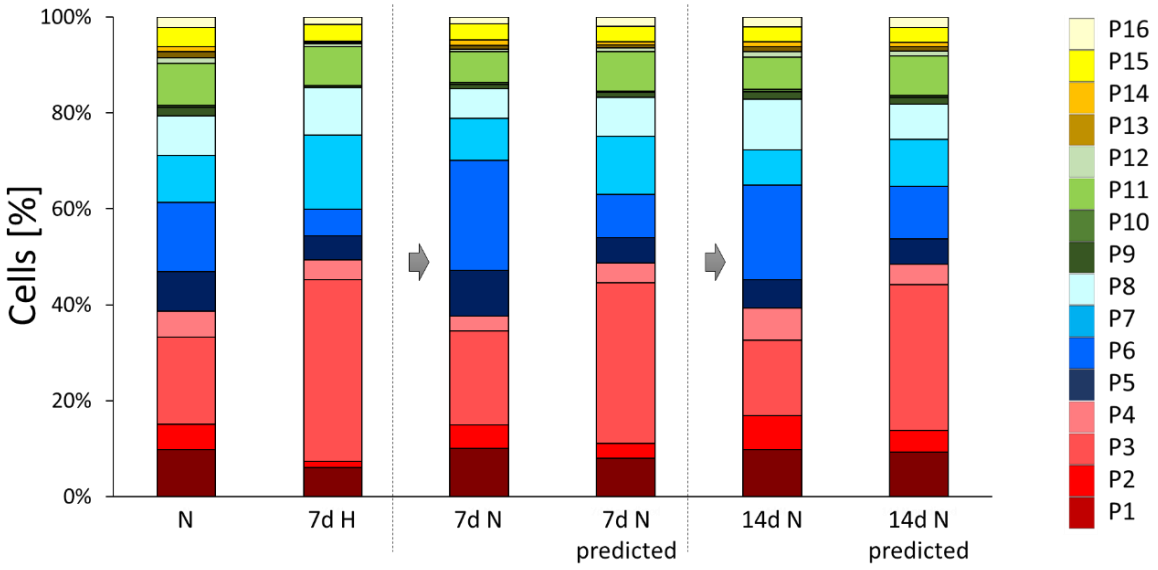

Conditions/Phenotypic states	P1	P2	P3	P4	P5	P6	P7	P8	P9	P10	P11	P12	P13	P14	P15	P16
CTR vs 7d h		***	**			**	***		***	***			**	***		
CTR vs 7d re-normoxia									**							
CTR vs 14d re-normoxia			**			*										

Figure 42: Reversibility of phenotypic adaptation to hypoxia. NCH644 stem-like cultures were kept for 7 days in hypoxia (0.5% O_2) and transferred back to high oxygen. CSC-associated heterogeneity was measured 7 and 14 days after environmental change (mean percentage; n_B=3, n_T=3). Statistical significances of phenotypic states between normoxic NCH644 control and experimental conditions are depicted in in table below graph (t-test with Bonferroni multiple-significance-test correction). Error bars are not depicted for visualization purposes.

Taken together these results suggest that the phenotypic shift observed during hypoxia results through strong adaptation and is a reversible process. Although we cannot exclude a partial selection against the least fitted phenotypic states, all CSC-associated states survived in hypoxia and recapitulate phenotypic heterogeneity. Similar to normoxia, Markov modeling identified subpopulation 2 to be most adaptive.

Results

Chapter 4.5

Analysis of differentiation capacities of the CSC-associated phenotypes

4.5. Analysis of differentiation capacities of the CSC-associated phenotypes

CSCs are thought to give rise to fast proliferative progenitor cells that generate the tumor mass and produce finally differentiated cells based at the bottom of a one-way hierarchical organization. Similar to NSCs which give rise to neurons and glial cell, CSCs in GBM are proposed to generate differentiated cancer cell with neuronal-like and glial-like characteristics. According to the one-way differentiation process terminally differentiated cells should not reacquire stemness abilities and therefore would not contribute to tumor growth. To eradicate CSCs and their progenitors, differentiation therapy has been proposed as a treatment strategy for GBM patients (Park et al., 2017). However, this approach cannot be effective should the differentiation process be reversible. In previous chapters, we demonstrated profound cellular adaptability, rather than a stem cell hierarchy at the origin of CSC-associated phenotypic heterogeneity. In this part, we assessed lineage commitment of GBM stem-like cell and analyzed whether a differentiated state can be reversed to a stem-like state. Differentiation and dedifferentiation into glial- and neuronal-like lineages was assessed using intracellular markers and CSC-associated cell surface epitopes. To evaluate whether the differentiation abilities are dependent on environmental factors, experiments were performed under normoxic and hypoxic conditions.

4.5.1. GBM cells display impaired differentiation process

4.5.1.1. Differentiation induces morphological changes in GBM stem-like cultures

Since GBM stem-like cultures can differentiate into neuronal-like and glial-like cells, dramatic morphological changes are expected such as the formation of neurite outgrowth as observed in normal neuronal cells. Single cells were attached to an extracellular matrix (ECM) layer in order to obtain a 2D culture system. Differentiation of GBM stem-like cultures was induced with All-Trans Retinoic acid (ATRA) and FBS added to the culture medium for 14 days. The influence of oxygen levels on the differentiation process was assessed using normoxic (21% O_2) and hypoxic (0.5% O_2) culture systems.

When grown as 2D cultures in CSC medium, single cells attached to the ECM layer and kept a round-shaped morphology. The cells subsequently formed adherent spheres. In contrast, cells in 2D differentiation conditions formed short protrusions which became continuously more prominent and reminiscent of neurite outgrowths (**Fig. 43**). This behavior was observed for NCH644 (**Fig. 43.a**) and to lesser extend in NCH421k (**Fig. 43.b**) GBM stem-like cultures. Morphologically, there was no difference observed between normoxic and hypoxic conditions, suggesting no influence of oxygen concentration on cell shape.

In order to investigate whether the observed morphological 'differentiation' was irreversible, cells were recultured for 2 weeks in 3D CSC medium condition (**Fig. 43**). Regardless of oxygen levels, differentiated GBM stem-like cultures (NCH644 and NCH421k) were all able to reform spheres in standard 3D culture system in CSC medium. This result shows that morphological changes are reversible and are dependent on differentiation cues (e.g. ATRA, EGF, bFGF).

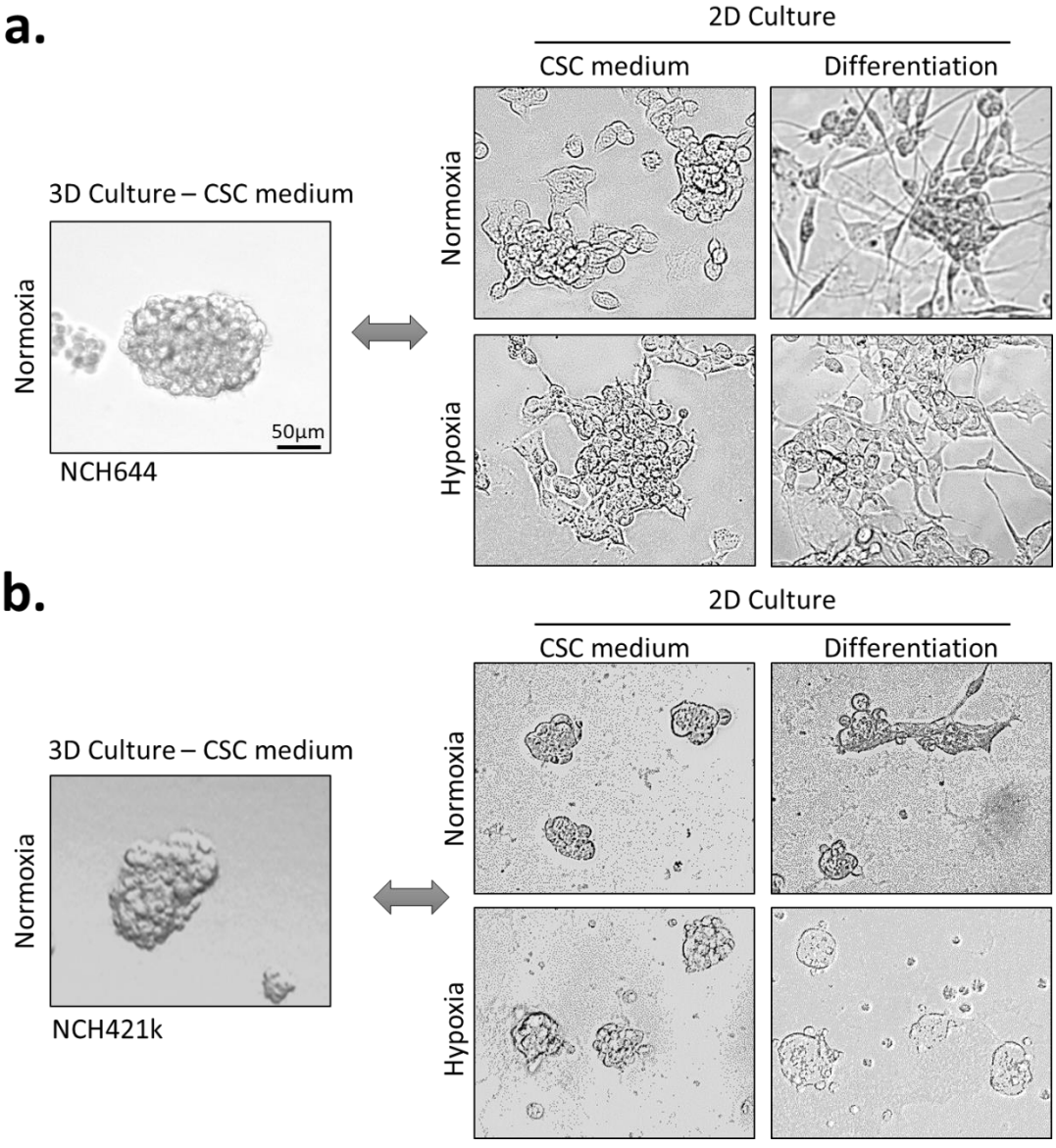

Figure 43: Morphological changes of GBM stem-like cells upon differentiation. Differentiation test was performed in medium depleted from EGF and bFGF and supplemented with ATRA and FBS. In standard condition, GBM stem-like cultures grew in 3D spheres. Since differentiation required exposure to ECM layer, 2D adherent cells in CSC medium were used as second control. Experiment was performed in normoxic (21% O_2) and hypoxic (0.5% O_2) condition. Morphologically, differentiated GBM cells displayed neurite-like extensions. Pictures (10x magnification) were taken upon 7 days of culture for NCH644 (**a.**) and NCH421k (**b.**) GBM stem-like cultures.

4.5.1.2. Differentiation is aberrant in GBM stem-like cultures

To assess the differentiation process at the molecular level, we measured several stemness and differentiation markers by flow cytometry. In normal neural stem cells, the stemness markers vimentin and nestin are downregulated upon differentiation. β-III tubulin is exclusively found in neurons, whereas glial fibrillary acidic protein (GFAP) expression is a marker for astrocytes. As retinoic acid is favoring the differentiation of GBM stem-like cells towards the neuronal lineage, we expected β-III tubulin to be strongly upregulated and GFAP showing only a slight increase in expression. Moreover, we expected the upregulation of differentiation markers to be impaired under hypoxia, as this environment was reported to enrich for the CSC phenotype (Lathia et al., 2011a).

In normoxic NCH644 differentiated cultures, stemness marker expression (vimentin and nestin) was not lost, but the neuronal marker β-III tubulin was increased (from 38.5% to 78.3% β-III tubulin$^+$ cells) (**Fig. 44.a**). Similarly, GFAP levels were higher in differentiated cultures compared to non-ATRA treated cells (from 1.5% to 30% GFAP$^+$ cells). Upregulation of differentiation markers by ATRA treatment was confirmed by Campos et al. (Campos et al., 2010). Of note, the change from 3D to 2D culture system did not affect marker expression. Results show coexpression of stemness and differentiation markers in cancer cells upon ATRA treatment indicating that differentiated NCH644 GBM stem-like cells increase lineage specific marker expression, but keep their stemness-associated phenotype at the same time. Comparable results were observed for NCH421k GBM stem-like cultures (**Fig. 44.b**). Stemness markers did not change expression levels upon differentiation cues, but GFAP was upregulated (from 11,6% to 50,2% GFAP$^+$ cells). Noteworthy, β-III tubulin expression is already high in the normoxic NCH421k 3D sphere cultures, underlining an aberrant differentiation process. Observations suggest that the differentiation process in GBM cells is either not fully completed after 14 days of treatment or the differentiation process is aberrant with no clear differentiation states.

The change to hypoxia did not show a distinct stemness marker expression in NCH644 culture from normoxia (**Fig. 44.a**). Unexpectedly, hypoxia provoked an increase in β-III tubulin (from 38.5% to 72.9% β-III tubulin$^+$ cells) and GFAP expression (from 1.5% to 16.7% GFAP$^+$ cells), despite the lack of morphological change. This upregulation of differentiation markers was even increased by the addition of differentiation cues to levels similar (± 30% GFAP$^+$ cells) or higher (18.3% in normoxia vs. 92.6% β-III tubulin$^+$ cells in hypoxia) to normoxic differentiation culture. Similarly, NCH421k cultures demonstrated higher levels of GFAP+ cells in differentiation condition in hypoxia than in normoxia (50.2% in normoxia vs. 84% in hypoxia), although hypoxia alone did not lead to an increased expression of the differentiation marker (**Fig. 44.b**). These results show that hypoxia does not impair the

expression of differentiation markers suggesting that hypoxia alone does not promote a stem cell state.

In a next step, the reversibility of the upregulation of differentiation markers was analyzed by reculturing cells in normoxic 3D sphere culture system (⟷) for 14 days. Vimentin and Nestin expression for both NCH644 and NCH421k cultures was not affected (**Fig. 44**). In NCH644 cultures, β-III tubulin expression was fully reversed to initial 3D expression levels from all tested conditions. Furthermore, marker expression of GFAP was downregulated to the original level found in the 3D sphere cultures from NCH644 and NCH421k cells. These results suggest that the differentiation program is reversible.

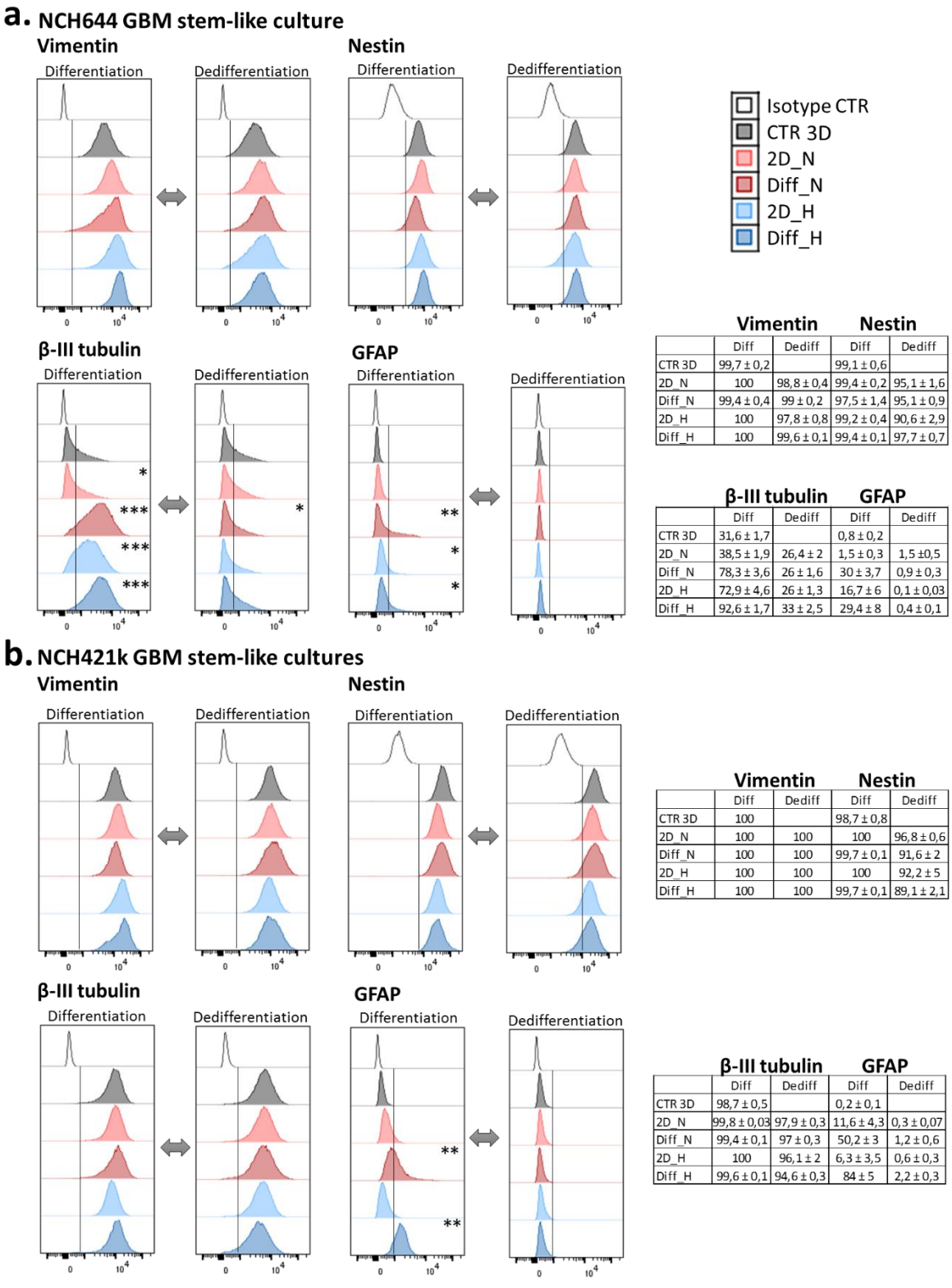

	Vimentin		Nestin	
	Diff	Dediff	Diff	Dediff
CTR 3D	99,7 ± 0,2		99,1 ± 0,6	
2D_N	100	98,8 ± 0,4	99,4 ± 0,2	95,1 ± 1,6
Diff_N	99,4 ± 0,4	99 ± 0,2	97,5 ± 1,4	95,1 ± 0,9
2D_H	100	97,8 ± 0,8	99,2 ± 0,4	90,6 ± 2,9
Diff_H	100	99,6 ± 0,1	99,4 ± 0,1	97,7 ± 0,7

	β-III tubulin		GFAP	
	Diff	Dediff	Diff	Dediff
CTR 3D	31,6 ± 1,7		0,8 ± 0,2	
2D_N	38,5 ± 1,9	26,4 ± 2	1,5 ± 0,3	1,5 ±0,5
Diff_N	78,3 ± 3,6	26 ± 1,6	30 ± 3,7	0,9 ± 0,3
2D_H	72,9 ± 4,6	26 ± 1,3	16,7 ± 6	0,1 ± 0,03
Diff_H	92,6 ± 1,7	33 ± 2,5	29,4 ± 8	0,4 ± 0,1

	Vimentin		Nestin	
	Diff	Dediff	Diff	Dediff
CTR 3D	100		98,7 ± 0,8	
2D_N	100	100	100	96,8 ± 0,6
Diff_N	100	100	99,7 ± 0,1	91,6 ± 2
2D_H	100	100	100	92,2 ± 5
Diff_H	100	100	99,7 ± 0,1	89,1 ± 2,1

	β-III tubulin		GFAP	
	Diff	Dediff	Diff	Dediff
CTR 3D	98,7 ± 0,5		0,2 ± 0,1	
2D_N	99,8 ± 0,03	97,9 ± 0,3	11,6 ± 4,3	0,3 ± 0,07
Diff_N	99,4 ± 0,1	97 ± 0,3	50,2 ± 3	1,2 ± 0,6
2D_H	100	96,1 ± 2	6,3 ± 3,5	0,6 ± 0,3
Diff_H	99,6 ± 0,1	94,6 ± 0,3	84 ± 5	2,2 ± 0,3

Figure 44: Differentiation and dedifferentiation of GBM stem-like cultures. Flow cytometric histograms show the expression of two stemness (Vimentin and Nestin), one neuronal (β-III tubulin) and one astrocytic (GFAP) marker upon 2 weeks of differentiation in culture medium depleted from growth factors and enriched with ATRA and FBS in (**a.**) NCH644 (mean ± SEM; n_B=3, n_T=3) and (**b.**) NCH421k GBM stem-like cells (mean ± SEM; n_B=1, n_T=3). Negative control for antibody staining is shown for each marker (Isotype CTR). Black lines discriminate between negative and positive cells. Dotted line indicates mode expression in control cells. Differentiated cultures were then dedifferentiated using standard normoxic 3D sphere condition for two weeks and reanalyzed. Marker

phenotypes were expressed at similar levels as original expression profiles of 3D sphere GBM stem-like cultures. Statistical analysis between 3D normoxic condition and 2D conditions was performed using t-test (mean percentage ± SEM; t-test: * = p-value < 0.05, ** = p-value < 0.01, *** = p-value < 0.001).

4.5.2. CSC-associated marker expression changed in differentiation condition

4.5.2.1. CD133 expression was decreased and CD44 expression was enriched upon differentiation treatment in normoxia

As the differentiation environment did not induce a major change on intracellular stemness and markers were not affected by differentiation cues, we tested if the CSC-associated phenotype was influenced by this environmental change. Therefore, we measured the distribution of the 16 subpopulations based on CD133, CD44, A2B5 and CD15 expression upon forced differentiation and subsequent dedifferentiation. Identical experimental setup was used as described above (**Chapter 4.5.1**).

The change from 3D to the 2D culture system led to minor changes in marker distribution in normoxic cells. Phenotype changes were small, but statistically significant. NCH644 stem-like cultures displayed an enrichment in subpopulations 3 ($CD133^+$ $CD44^-$ $A2B5^-$ $CD15^-$) and 7 ($CD133^+$ $CD44^+$ $A2B5^-$ $CD15^-$). Many subpopulations, like subpopulation 2 ($CD133^+$ $CD44^-$ $A2B5^+$ $CD15^+$), 6 ($CD133^+$ $CD44^+$ $A2B5^+$ $CD15^+$) and 10 ($CD133^-$ $CD44^-$ $A2B5^+$ $CD15^+$) were decreased (**Fig. 45.a.I,** see **Annex 3.f** for all statistical comparisons of phenotypical states and single marker expression between time points). In NCH421k, numerous subpopulations, such as subpopulation 4 ($CD133^+$ $CD44^-$ $A2B5^-$ $CD15^+$), 12 ($CD133^-$ $CD44^-$ $A2B5^-$ $CD15^+$) and 16 ($CD133^-$ $CD44^+$ $A2B5^-$ $CD15^+$) were increased whereas subpopulation 2 ($CD133^+$ $CD44^-$ $A2B5^+$ $CD15^+$) was reduced (**Fig. 45.b.I** see **Annex 3.g** for all statistical comparisons of phenotypical states and single marker expression between time points**)**. These results show that cell surface marker expression is more sensible to changes in culture system (i.e. sphere vs. adherent) than internal stemness and differentiation marker expression.

ATRA driven differentiation in normoxia lead to a significant phenotypic shift towards $CD133^-$ (from 80.58% to 4.40%), $A2B5^-$ (from 10.59% to 8.11%) and $CD15^-$ (from 35.51% to 21.84%) subpopulations. Only CD44 marker expression was significantly enriched (from 37.32% to 69.29%). Consequently, most enriched subpopulations were 11 ($CD133^-$ $CD44^-$ $A2B5^-$ $CD15^-$), 15 ($CD133^-$ $CD44^+$ $A2B5^-$ $CD15^-$) and 16 ($CD133^-$ $CD44^+$ $A2B5^-$ $CD15^+$) (**Fig. 45.a.II**). Although to a less extent, NCH421k stem-like cultures experienced a similar change in marker expression. A decrease in CD133 (from 97.54% to 67.27%), CD15 (from 98.3% to 93.25%) and A2B5 (from 98.18% to 78.5%) was observed. CD44 was enriched (from 12.2% to 53.69%). Subpopulations 6 ($CD133^+$ $CD44^+$ $A2B5^+$ $CD15^+$) and 14 ($CD133^-$

CD44^{+} A2B5^{+} CD15^{+}) were increased upon differentiation (**Fig. 45.b.II**). Reduced CD133 expression is in accordance to Campos et al. (Campos et al., 2010).

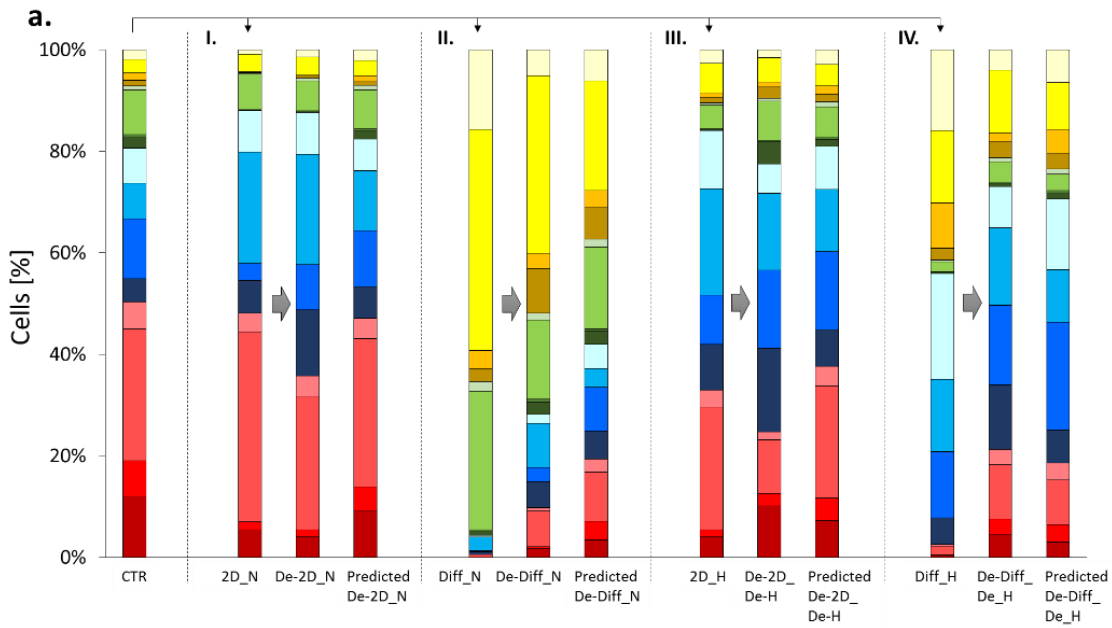

Conditions/Phenotypic states	P1	P2	P3	P4	P5	P6	P7	P8	P9	P10	P11	P12	P13	P14	P15	P16
CTR vs 2D_N		**	*			***	***		***	***		**	***	***		
CTR vs De-2D _N	***	***					***		***	***			**	***		
CTR vs Diff_N	***	***	***	***	***	***		***	*		*				***	***
CTR vs De-Diff_N	***	***	***	***		***		***			*	*	*		***	**
CTR vs 2D_H	***	***					***	*	***	***						
CTR vs De-2D _De-H		**	***	**	**											
CTR vs Diff_H	***	***	***	***					***	*	***	**			*	**
CTR vs De-Diff_De-H	***	*	**						***	*	*				*	

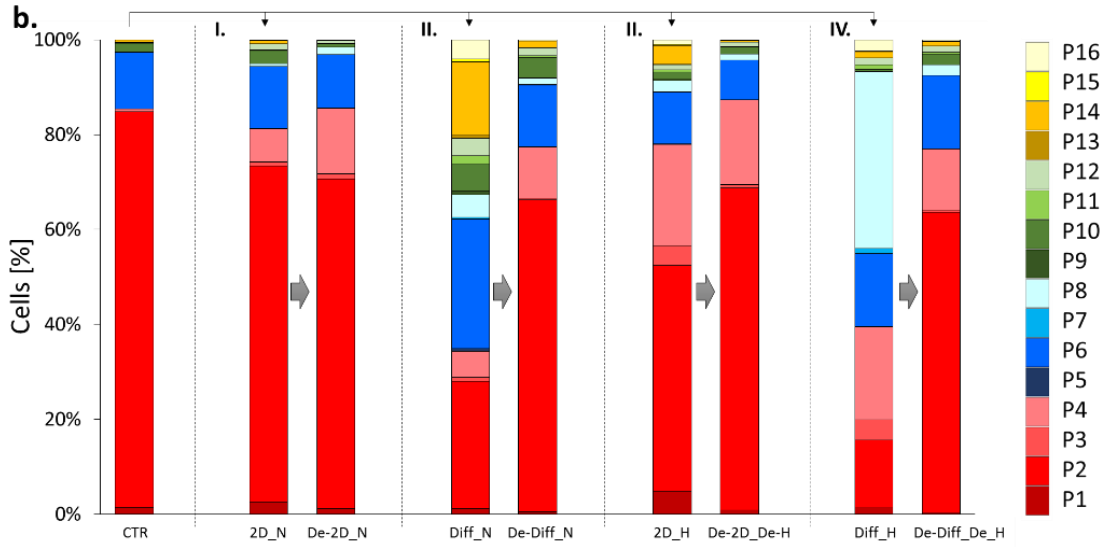

Conditions/Phenotypic states	P1	P2	P3	P4	P5	P6	P7	P8	P9	P10	P11	P12	P13	P14	P15	P16
CTR vs 2D_N			**	***	**		***	***				***				***
CTR vs De-2D _N			***	***	*		***	***								*
CTR vs Diff_N		***	***	***	***		***	***	***		***	***	***	***	***	***
CTR vs De-Diff_N				***			**	***				***			**	***
CTR vs 2D_H	*	*	***	***	**		***	***								
CTR vs De-2D _De-H			***	***			**	***				*				
CTR vs Diff_H		***	***	***	***		***	***			***	***			**	***
CTR vs De-Diff_De-H			**	***			***	***				***				***

Figure 45: Reversibility of CSC-associated marker expression upon differentiation in normoxia and hypoxia in NCH644 and NCH421k GBM cultures. Barplots show the distribution of 16 CSC-associated subpopulations based on CD133, CD44, A2B5 and CD15 expression. NCH644 (**a**) and NCH421k (**b**) stem-like cells were cultured for 14 days in 2D normoxia non-ATRA treatment (2D_N) (I), in 2D normoxia ATRA treatment (Diff_N) (II), in 2D hypoxia non-ATRA treatment (2C_H)(III) or in 2D hypoxia ATRA treatment (Diff_H) (IV) conditions. CTR represent GBM stem like cells in 3D standard cultures (NCH644: mean percentage; n_B=3-4, n_T=2-3) (NCH421k: mean percentage; n_B=1, n_T=3). Subsequently, cells of all conditions were dedifferentiated in 3D sphere culture system in normoxia for 14 days (depicted by grey flash and condition names were prefixed with 'De-'). For NCH644 stem-like cultures Markov model predictions were performed to obtain phenotypic distribution after 14 days of culture and time to equilibrium was calculated. Error bars are not depicted for visualization purposes. Statistical significances of phenotypic states between normoxic NCH644 3D control and other conditions are depicted in in table below graph (t-test with Bonferroni multiple-significance-test correction).

4.5.2.2. CD44 expression was enriched upon differentiation treatment in hypoxia

Since we showed previously that hypoxia leads to an increase in CD133 expression, we further evaluated the combined effect of hypoxic condition with ATRA treatment to see whether the loss of CD133 observed in normoxic differentiation condition was impaired.

We first tested whether the change from 3D to 2D culture systems impacted CSC-associated marker expression. Similar to 3D NCH644 stem-like cultures in hypoxia, cells in 2D culture at low oxygen levels significantly reduced CD15 (from 35.5% to 29.94%) and expression and increased CD133 (from 80.58% to 84.02%) and CD44 (from 37.32% to 61.51%) expression (**Fig. 45.a.III**). However, contrary to 3D hypoxia, the number of $A2B5^+$ (from 40.59% to 26.59%) cells was reduced in 2D hypoxia. In NCH421k stem-like cultures A2B5 (from 98.18% to 69.3%) and CD15 (from 98.3% to 89.84%) expression changed significantly from 3D culture in normoxia to 2D culture in hypoxia (**Fig. 45.b.III)**. As for NCH644 stem-like cultures, NCH421k stem-like culture CSC-profile could only partially be explained by hypoxic environment change alone. This suggests that the switch from 3D to 2D system culture led to additional accumulative change in phenotypic equilibrium.

Upon 2D culture in hypoxia combined to ATRA treatment, both GBM stem-like cultures showed similar reduction of subpopulations (NCH644: subpopulations 2, 6, 10; NCH421k: subpopulation 2). Interestingly, this reduction was consistent between normoxia and hypoxia ATRA treatment cells. Generally, combined ATRA treatment with hypoxic culture conditions, lead to a depletion in $CD133^+$ $CD44^-$ subpopulations (from 41.5% to 2.53%) and increase of $CD133^-$ and $CD44^+$ subpopulations (from 8.56% to 41.41%) (**Fig. 45.a.IV)**. CD133 and CD44 marker changes were observed in NCH421k stem-like cultures as well (**Fig. 45.b.IV)**. Even though changes in marker distribution appear less affected in hypoxia than in normoxia upon differentiation, we found in both cases a decrease in CD133 and A2B5 expression and an increase in CD44 levels for the two tested GBM stem-like cultures. Of note, CD133 loss observed in normoxic differentiation is compensated in hypoxia, in

agreement with previous data showing that CD133 expression is upregulated in low oxygen environment (**Fig. 34**).

4.5.3. Differentiation induced cell surface marker change is reversible

In the next step, cells of the four 2D culture conditions (e.g. normoxia, hypoxia, ATRA treated and non-ATRA treated conditions) were transferred to non-coated flasks containing normal CSC medium to generate 3D spheres in normoxia. With that we aimed to reverse CSC-associated phenotype changes. Within 14 days all cultures had partially returned towards their original profile in both NCH644 and NCH421k cultures (**Fig. 45.a and b**), however, the initial phenotypic distribution was not reached yet. Indeed, Markov modeling predicted that NCH644 non-differentiated cells in normoxia and hypoxia in 2D cultures only needed 30 and 42 days, respectively, to reach equilibrium of the initial 3D condition. Reversibility from differentiated conditions was predicted to take longer, with 75 and 84 days in normoxia and hypoxia, respectively to reach final equilibrium confirming that phenotypical change upon ATRA treatment was more dramatic than in non-ATRA treated conditions. Furthermore, differentiated and non-differentiated 2D cultures in hypoxia, needed longer time to reach initial phenotypic heterogeneity than in normoxia which might be explained by a slower proliferation status in hypoxia compared to normoxia.
Although phenotypic change was shown to be partial reversible, mathematical predictions appeared closer to the final equilibrium than the measured phenotypic distribution. Similar to reversibility of sphere cultures in hypoxia (**Fig. 42**), the small discrepancies might be explained by the complex environmental change from 2D to 3D culture systems combined with ATRA treatment and different oxygen levels. Where the adaptation process might need longer time. Even though we could only show partial reversibility upon differentiation, Markov model predictions support that CSC-associated heterogeneity will eventually reach final equilibrium as we found in normoxia and hypoxia.

To conclude, GBM stem-like cultures underwent a morphological differentiation process, intracellular marker expression revealed an aberrant differentiation process as stemness proteins and lineage specific markers were simultaneously expressed. CSC-associated phenotype expression was strongly altered upon differentiation, which was mainly reflected by CD133 and A2B5 decrease and enrichment of CD44. Phenotypical changes in hypoxia were less dramatic than in differentiation condition. Combined effects of different environments were observed (e.g. extracellular matrix (2D) culture combined with differentiation factors and/or oxygen levels). Importantly, the differentiation phenotype was reversible for all ATRA treated conditions. These results strongly suggest that GBM cells

do not underlie a one way-differentiation hierarchy but represent a highly plastic GBM phenotype.

Results

Chapter 4.6

Analysis of tumorigenicity of the CSC-associated phenotypes *in vivo*

4.6. Analysis of the CSC-associated phenotypes *in vivo*

Our previous *in vitro* results have shown that GBM stem-like cultures generate CSC-associated phenotypic heterogeneity by adaption of existing cells to the most fitted phenotype rather than by hierarchical differentiation. This was true for normoxic (**Chapter 4.2**), hypoxic (**Chapter 4.4**) and differentiation-inducing (**Chapter 4.5**) environments. Each environment led to a specific phenotypic profile of subpopulations. As cell culture systems are not able to fully recapitulate the cancer microenvironment, orthotopic xenografts are best used to simulate complete tumoral environments including hypoxic, perivascular and invasive niches allowing for differentiated and non-differentiated cell states, in reciprocal contact with stromal cells. Following the CSC hypothesis, one major characteristic of CSCs, besides self-renewal and indefinite proliferation, is the capacity to generate a tumor and the recapitulation of its original heterogeneity *in vivo*. Thus, we next analyzed the tumor formation potential and the CSC-associated expression patterns of GBM stem-like cultures *in vivo*. We further asked whether individual CSC-associated subpopulations are tumorigenic and can give rise to phenotypic heterogeneity *in vivo*. Finally, we addressed whether the redistribution of CSC-associated markers *in vivo* is reversible.

4.6.1. CSC-associated marker expression was strongly altered in all GBM stem-like cultures derived xenografts

In the last chapters, we analyzed CSC-associated marker expression *in vitro*. Here we performed multicolor phenotyping of tumors derived from several GBM stem-like cultures, which had been orthotopically transplanted into the brain of mice. In this experimental setup, the use of eGFP-expressing Nod/Scid mice was not feasible as the GFP signal would interact with the CSC-associated marker panel for multicolor flow cytometry. Instead, we made advantage of the high CD90 expression observed in GBM PDXs (**Fig. 11.b**). CD90 antibody is specific for human cells and thereby enables discrimination between tumor (CD90 positive) and stromal cells (CD90 negative) (**Annex 2**). Implanted NCH644, NCH421k, NCH660h and NCH601 stem-like cultures were able to give rise to tumors in the brain of Nod/Scid mice. Furthermore, they strongly adapted their CSC-associated phenotype to the brain environment (**Fig. 46**). In general, $CD133^{-}CD44^{-}$ phenotype (subpopulations 9-12) were strongly enriched, whereas $CD133^{+}CD44^{+}$ (subpopulations 5-8) and $CD133^{-}CD44^{+}$ (subpopulations 13-16) cells were reduced. Interestingly, no correlation in the grade of heterogeneity between cell types was observed between *in vitro* and *in vivo* phenotype. For instance, NCH421k stem-like cultures expressed CSC-associated markers rather homogeneously in normoxia but strongly increased

heterogeneity upon xenotransplantation. In contrast, NCH601 stem-like cultures displayed reduced heterogeneity following orthotopic transplantation into mice, with a strong enrichment of subpopulations 9 ($CD133^-$ $CD44^-$ $A2B5^+$ $CD44^-$) and 10 ($CD133^-$ $CD44^-$ $A2B5^+$ $CD44^+$). The expression of cell surface markers *in vivo* reflected none of the previously analyzed environments *in vitro*, suggesting a key role of additional environmental factors present in the brain that affect the phenotype equilibrium *in vivo*.

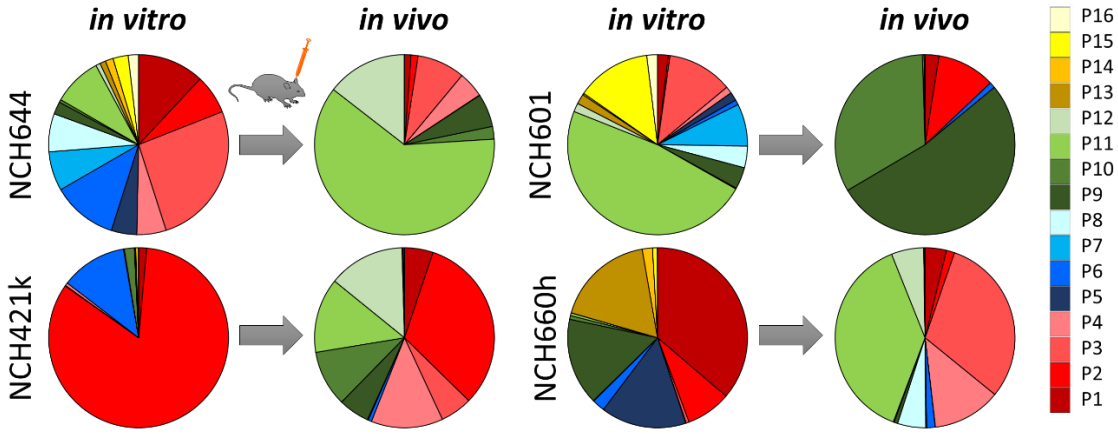

Figure 46: CSC-associated heterogeneity in GBM stem-like derived xenografts. Pie charts show the distribution of the 16 subpopulations based on CD133, CD44, A2B5 and CD15 marker expression in tumors from 4 different GBM stem-like cultures derived xenografts. Nod/Scid mice were sacrificed when symptoms became visible: around day 30 for NCH644, day 60 for NCH421k, day 130 for NCH601 and day 230 for NCH660h xenograft (average percentage; n_B=2-3).

4.6.2. CSC-associated subpopulations were able to generate a phenotypic heterogeneous tumor *in vivo*

CSCs are reported to reproduce a tumor *in vivo* with as little as 100 transplanted cells demonstrating a high tumorigenicity (Clarke et al., 2006). However, the number of cells needed for reconstitution of tumors upon xenografting differs between cell cultures (Quintana et al., 2008). To assess the minimal number of cells needed for tumor development in a life time of a nude mouse is tested by an *in vivo* limited dilution assay, where a range of cell dilutions between 50 and 50´000 cells per mouse are engrafted to a mouse. We tested a series of dilutions (100, 300, 500, 1000 and 5000 single cells) of NCH644 stem-like cultures. Viable single cells were FACS-sorted and instantly implanted to nude mice. We found that at least 5000 NCH644 FACS-sorted cells were needed to generate a tumor *in vivo* in a reasonable time frame (i.e. 6 weeks) (**Fig. 47.b**). Using 5000 cells per brain, tumor evolution could be followed by magnetic resonance imaging (MRI) as early as 3 weeks after implantation. Until the endpoint of the mice at 6 weeks, the tumor grew constantly (**Fig. 47.a**). The use of only 5000 cells (**Fig. 47.a**) retarded tumor

development by approximately 2 weeks compared to the standard protocol for xenografting with 50 000 cells per brain (**Fig. 47**). This time delay likely represents the time needed to increase the tumor population by 10-fold.

We next determined whether CSC-associated subpopulations carry equal tumorigenic potential and whether they can reconstitute heterogeneity. The tumorigenic potential of different phenotypic states was tested by implanting 5000 cells of each individual subpopulation directly after FACS-sorting. We expected that all subpopulations were able to generate tumors as all demonstrated strong adaptive capacities in previous experiments (e.g. normoxic, hypoxic and differentiation environment). We focused on four out of the sixteen phenotypic states: subpopulations 2, 6, 11 and 15. Subpopulations 6 ($CD133^+$ $CD44^+$ $A2B5^+$ $CD44^+$) and 15 ($CD133^-$ $CD44^+$ $A2B5^-$ $CD44^-$) were chosen as they were strongly depleted in NCH644 derived xenograft tumors *in vivo* (**Fig. 47**). Subpopulation 11 ($CD133^-$ $CD44^-$ $A2B5^-$ $CD44^-$) was strongly enriched *in vivo* and subpopulation 2 ($CD133^+$ $CD44^-$ $A2B5^+$ $CD44^+$) represented the most 'adaptive' state in normoxia and hypoxia which was partially depleted *in vivo*.

All four subpopulations were able to form tumors upon xenotransplantation of 5000 cells per brain (**Fig. 47.c**) and all mice per condition developed a tumor indicating a very high tumorigenic potential. Only for subpopulation 15 4 of 6 mice did show tumor development. This shows as well that all four subpopulations survive *in vivo* and none was eliminated by a selection process. Differences in tumor size evolution between subpopulations were observed by MRI imaging (**Fig. 47.d**). Only mice bearing subpopulation 2 developed tumors as fast as the parental NCH644 cultures, whereas subpopulations 6, 11 and 15 grew significantly slower. These results were reflected in the survival of the mice, however, eventually all mice succumbed to their tumor (**Fig. 47.e**). Mice bearing tumors from subpopulations 6 (77.86 days ± 10.4 SEM), 11 (58.29 days ± 2.7 SEM) and 15 (67.75 days ± 9 SEM) survived longer without symptoms than mice bearing the NCH644 control population (47.14 days ± 1.7 SEM) and subpopulation 2 (44.29 days ± 2.6 SEM). As subpopulation 2 demonstrated the fastest tumor growth, this data suggested again that this subpopulation is the most adaptive. Multicolor flow cytometric phenotyping of end-stage tumors revealed that all four subpopulations were able to give rise to phenotypic heterogenic tumors *in vivo*. The resulting CSC-associated heterogeneity resembled strongly the phenotype obtained in original NCH644 stem-like derived tumors *in vivo* (**Fig. 47.f**). Statistical analysis revealed almost no differences in phenotypic distribution between *in vivo* tumors (**Fig. 47.g**. see **Annex 3.h** for all statistical comparisons of phenotypical states and single marker expression between engrafted tumors). Similarly to experiments performed in normoxia and hypoxia *in vitro*, these results suggest that CSC-associated

subpopulations adapt *in vivo* to the same final phenotypic equilibrium as the distribution observed in control NCH644 xenografts. Differences in time of tumor development may be due to different probabilities of state transitions.

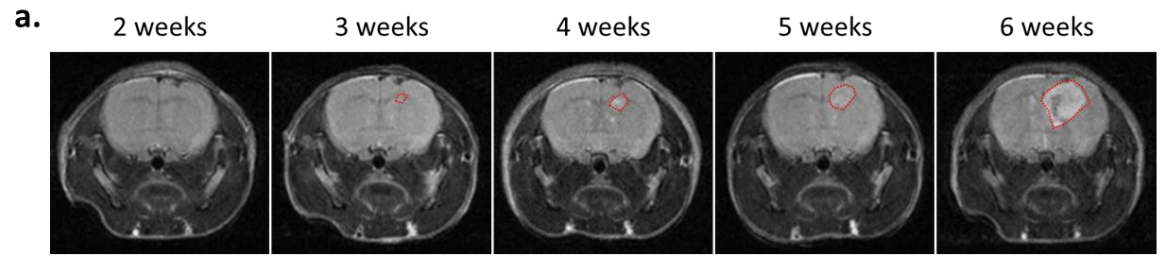

b.

Cell Number	Tumors Formed
100	0/3
300	0/3
500	0/3
1000	0/3
5000	3/3

c.

Cell Subpopulation	Tumors Formed
CTR	7/7
P2	7/7
P6	7/7
P11	7/7
P15	4/6

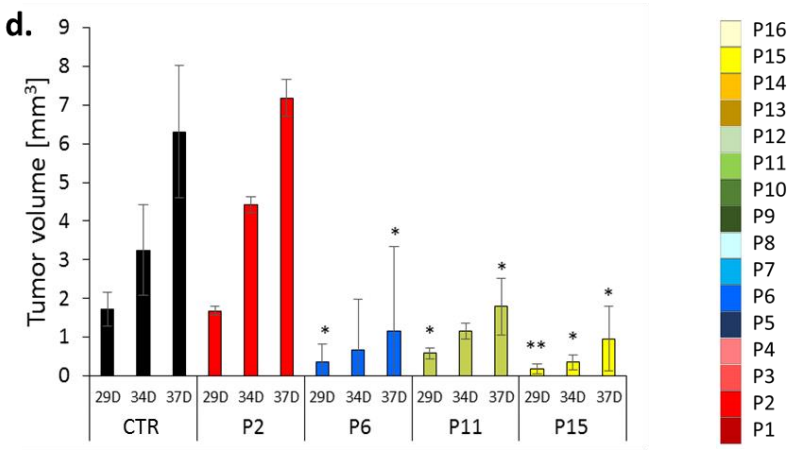

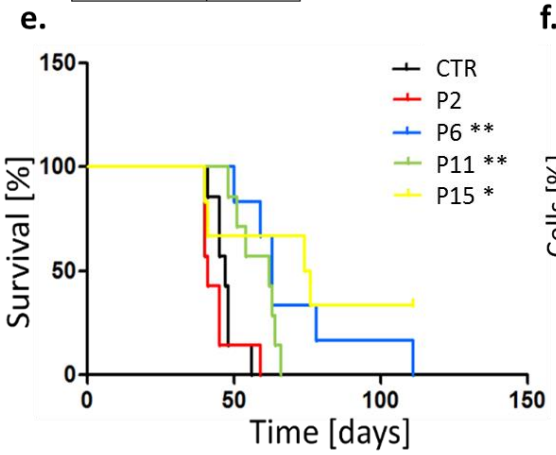

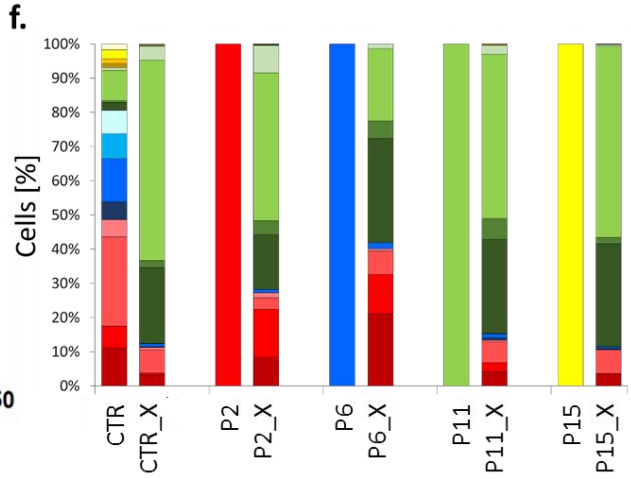

g.

Conditions/Phenotypic states	P1	P2	P3	P4	P5	P6	P7	P8	P9	P10	P11	P12	P13	P14	P15	P16
CTR_X vs P2 _X																
CTR_X vs P6_X											*					
CTR_X vs P11_X																
CTR_X vs P15_X																

Figure 47: Tumorigenic potential of CSC-associated subpopulations. a. T2 weighted MRI scans show the evolution of a tumor originating from 5000 FACS-sorted NCH644 stem-like cells (tumor area circled in red). **b.** Limiting dilution assay *in vivo* was performed for 100, 300, 500, 1000 and 5000 NCH644 stem-like cells implanted per nude mouse. A minimal number of 5000 cells was needed to develop a tumor in 42 days (n_B=3). **c.** All implanted NCH644 subpopulations (2, 6, 11 and NCH644 control) generated a tumor *in vivo*. In subpopulation 15 only 4 out of 6 mice developed a tumor whereas the other subpopulations demonstrated 100% tumorigenicity (n_B=6-7). **d.** Nude mice

were scanned by MRI at day 29, 34 and 37 and tumor volumes were measured. Differences in tumor size between control NCH644 and subpopulations was calculated using t-test (average mean ± SEM; n_B=4-7; * = p-value < 0.05, ** = p-value < 0.01, *** = p-value < 0.001). Tumor volumes of mice bearing NCH644 control population and subpopulation 2 were significantly larger at the 3 measured time points compared to subpopulations 6, 11 and 15. **e.** Kaplan-Meier plot shows survival of mice bearing tumors from the different subpopulations. Subpopulations 6, 11 and 15 demonstrated significant longer survival compared to NCH644 control and P2 mice (Gehan-Breslow-Wilcoxon Test: * = p-value < 0.05, ** = p-value < 0.01, *** = p-value < 0.001). **f.** Multicolor flow analysis of developed tumors at the time of sacrifice. Barplots revealed that each subpopulation was able to generate multiple phenotypes with a similar distribution as found in the NCH644 control tumors (mean percentage; n_B=3-4). Error bars are not depicted for visualization purposes. **g.** Table summarized statistical analysis between phenotypic distribution in xenografts between NCH644 control and other implanted subpopulations (t-test with Bonferroni multiple-significance-test correction; * = p-value < 0.05).

4.6.3. Internal and cell surface CSC-associated marker adaptation *in vivo* is reversible

Similar to normoxic, hypoxic and differentiation conditions CSC-associated marker expression was highly adaptive and generated an environment-specific phenotype in the complex environment of the brain. As adaptive capacities were shown to be reversible in *in vitro* conditions (e.g. hypoxia and differentiation), we next tested whether this was also the case *in vivo*. Therefore, 50´000 single cells of NCH644 and NCH421k stem-like cultures were implanted into nude mice and sacrificed upon appearance of symptoms (at around 4 and 8 weeks, respectively). Internal and cell surface CSC-marker expression in dissociated mouse brain was analyzed by flow cytometry, where stromal and tumor cells were discriminated by human CD90 expression (**Annex 4**). Subsequently, dissociated cells from NCH644 and NCH421k-derived xenografts were recultured for 4 and 8 weeks, respectively, in standard 3D normoxic condition *in vitro* and rephenotyped.

The cytoplasmic stemness markers vimentin and nestin were strongly decreased in NCH644-derived xenografts compared to *in vitro* cultures (**Fig. 48.a**). However, contrary to differentiation conditions the neuronal differentiation markers were not upregulated; β-III-tubulin expression was lost, whereas GFAP expression was barely detectable from the start. This was in contrast to the differentiation *in vitro* which drastically increased the expression of the differentiation marker β-III-tubulin and to lesser extend GFAP. Reculture of tumor cells *in vitro* for four weeks reversed their marker expression to the original *in vitro* state of NCH644 stem-like cultures. Similarly to NCH644-derived xenografts, NCH421k-derived xenografts did demonstrate a decrease in the expression of vimentin and nestin stemness markers from *in vitro* to *in vivo*/ environmental changes (**Fig. 48.c**). Similar to NCH644-derived xenografts, differentiation marker expression of β-III-tubulin was reduced in NCH421k generated tumors. Reculture *in vitro* reversed marker expression changes.

Based on intracellular marker expression, tumor cells *in vivo* did not resemble neither a stem-like nor a differentiated phenotype.

Interestingly, a CSC-associated phenotype distribution was recreated after 4 and 8 weeks of NCH644 and NCH421k-derived xenograft tumor reculture *in vitro* resembling the initial normoxic equilibrium (**Fig. 48.b** and **48.d**). The original phenotypic equilibrium in normoxia was not yet reached. This is in line with the Markov model that predicted 67 days for phenotype reversal in NCH644 cells. These data strongly suggest that similar to hypoxic and differentiation conditions, the *in vivo* phenotype profile eventually may reach normoxic equilibrium upon reculture in standard *in vitro* conditions. Phenotypic reversibility found in internal and cell-surface markers are a strong indicator that GBM cells are able to adapt to the environment and that phenotypic changes are not a result of a selection process.

NCH644 GBM stem-like culture

a.

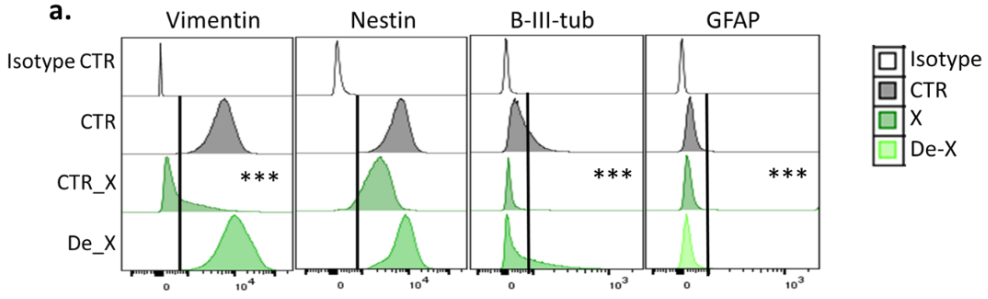

	Vimentin	Nestin	B-III-tub	GFAP
CTR	100	100	31,6 ± 1,7	0,8 ± 0,2
CTR_X	35,5 ± 1,1	94,1 ± 0,1	1,9 ± 0,5	5,6 ± 0,7
De_X	97 ± 0,4	97,1 ± 0,5	32,7 ± 1,3	0,5 ± 0,1

b.

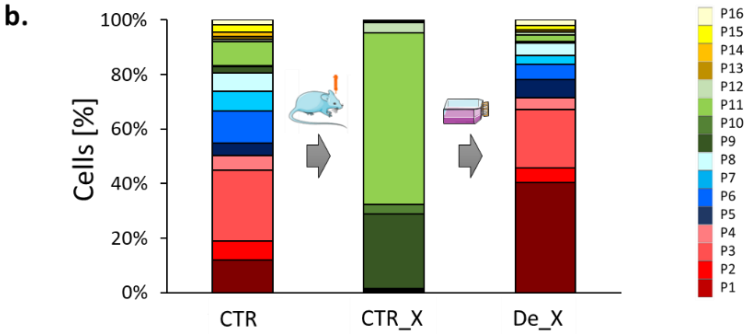

Conditions/Phenotypic states	P1	P2	P3	P4	P5	P6	P7	P8	P9	P10	P11	P12	P13	P14	P15	P16
CTR vs CTR_X	**	**	**	*	**	***	*	**	**		***		**	*		
CTR vs De-X	***					**			***	**	**			**		

NCH421k GBM stem-like cultures

c.

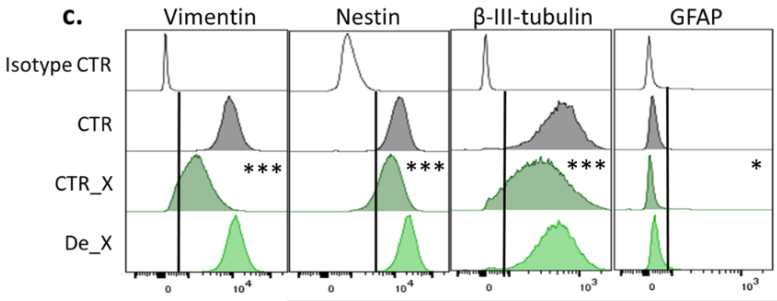

	Vimentin	Nestin	B-III-tub	GFAP
CTR	100	100	100	0,2 ± 0,1
CTR_X	96,5 ± 0,3	77,1 ± 1,2	76,2 ± 3,6	7,1 ± 2,8
De_X	100	100	100	1,9 ± 0,4

d.

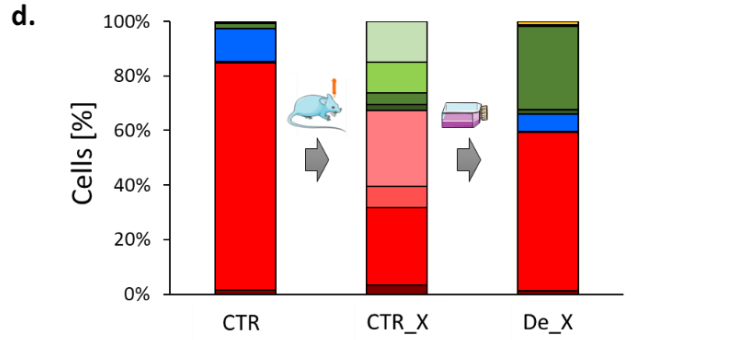

Conditions/Phenotypic states	P1	P2	P3	P4	P5	P6	P7	P8	P9	P10	P11	P12	P13	P14	P15	P16
CTR vs X		**	***	***					***		***	***				
CTR vs De-X		**								***						

Figure 48: Reversibility of phenotypic heterogeneity *in vivo*. To test reversibility of intracellular and cell surface markers *in vivo*, NCH644 and NCH421k stem-like cells (CTR) were implanted into nude mice (CTR_X). Upon disease symptoms mice were sacrificed and tumor cells were isolated and recultured for 4 weeks (NCH644) or 8 weeks (NCH421k) in standard normoxic condition *in vitro* (De_X) **a.** (NCH644) and **c.** (NCH421k) Flow cytometric histograms show the expression of two stemness (Vimentin, Nestin), one neuronal (B-III-tub) and one astrocytic (GFAP) marker in CTR, CTR_X and De_X conditions (mean ± SEM; n_B=2, n_T=1-3 for NCH644 and n_B=1, n_T=3 for NCH421k). **b.** (NCH644) and **d.** (NCH421k) Barplots depict phenotypic heterogeneity of CTR, CTR_X and re-*in vitro* conditions (mean ± SEM; n_B=2, n_T=1-3 for NCH644 and n_B=1, n_T=3 for NCH421k). Error bars are not depicted for visualization purposes. Table summarizes statistical analysis between phenotypic distribution between CTR and CTR_X and De_X (t-test with Bonferroni multiple-significance-test correction; * = p-value < 0.05, ** = p-value < 0.01, *** = p-value < 0.001).

To summarize, all tested GBM stem-like cultures and NCH644 CSC-associated subpopulations were able to generate phenotypically heterogeneous tumors *in vivo*. The ability of CSC-associated subpopulations to reacquire other phenotypic states *in vivo* suggests strong adaptive capacities of GBM cells. In analogy to normoxic and hypoxic states, results confirm that subpopulations varied in their potential to adapt to the environment (e.g. subpopulation 2) as measured by the time to reach steady state equilibrium. Nevertheless, since the change in phenotypic heterogeneity upon xenotransplantation is reversible, similar to other conditions (e.g. hypoxia, differentiation) which argues against a selection process *in vivo*. Furthermore, tumor cells in vivo lose their stemness markers vimentin and nestin which is not accompanied by gain of differentiation markers β-III-tubulin or GFAP.

Results

Chapter 4.7

Characterization of CSC-associated phenotypes at single cell transcriptional level

4.7. Characterization of CSC-associated phenotypes at single cell transcriptional level

We assessed phenotypical heterogeneity in several GBM models (including GBM patient TCGA data, patient-derived xenografts and stem-like cultures), and revealed that CSC-associated heterogeneity was created by stochastic state transitions where certain subpopulations (i.e. subpopulation 2) demonstrated faster adaptation than others. We took advantage of the novel single cell RNA sequencing technology combined with flow cytometry and microfluidics (Drop-seq) (Macosko et al., 2015) which allowed assessment of gene expression at the single cell level. Three GBM patient-derived xenografts and two GBM stem-like cultures were analyzed for transcriptomic inter- and intra-tumoral heterogeneity at the CSC level. CSC-associated subpopulations 2 and 6 of NCH644 stem-like cultures were analyzed to correlate intratumoral heterogeneity at the phenotypic and transcriptomic level. This work was performed in collaboration with Dr. Suresh Poovathingal and Dr. Alexander Skupin from Luxembourg Centre for Systems Biomedicine (LCSB) at the University of Luxembourg (Luxembourg). Further data analysis was performed by Dr. Petr Nazarov and Arnaud Muller from the Proteome and Genome Research Unit at the LIH (Luxembourg).

4.7.1. Single cell transcriptomics clusters GBM cells by tumor of origin

Drop-seq protocol was performed on FACS-isolated single, viable tumor cells of three patient-derived xenografts (P3, P8 and P13) (as described in **Annex 2**) and two GBM stem-like cultures (NCH644 and NCH421k) to detect transcriptional variety at single cells level. By Drop-seq analysis approximately 6000 transcripts corresponding to 2430 gene on average was detected per cell. The expression profile analysis revealed GBM sample-specific clusters upon non-linear dimensionality reduction (t-distributed stochastic neighbor embedding tSNE) followed by density clustering (**Fig. 49**). By tSNE algorithm high dimensional data are reduced to 2D or 3D data points. Visualization on a scatterplot locates similar data points nearby whereas distinct points are mapped distantly.

As expected single cells grouped by tumor of origin (Demeure et al., 2016). At this level, only limited number of subclusters within different tumor samples were observed within the NCH644 and P3 samples. Due to variable number of cells depicted, visualization displays a higher heterogeneity within patient-derived samples. However, cell-to-cell variation in each GBM sample showed a similar coefficient of variation meaning that intratumoral gene expression diversity is similar in all analyzed tumor samples. Furthermore, the closer the coefficient of variation is to 1, the higher is cell-to-cell transcriptional diversity suggesting a

high variability within each GBM sample. Variation in the number of cells between tumor samples (P3 lowest to NCH644 highest) resulted from technical variations and stringent pre-processing analysis steps which included filtering of cells with at least 1500 expressed genes or genes expressed in at least 20 cells.

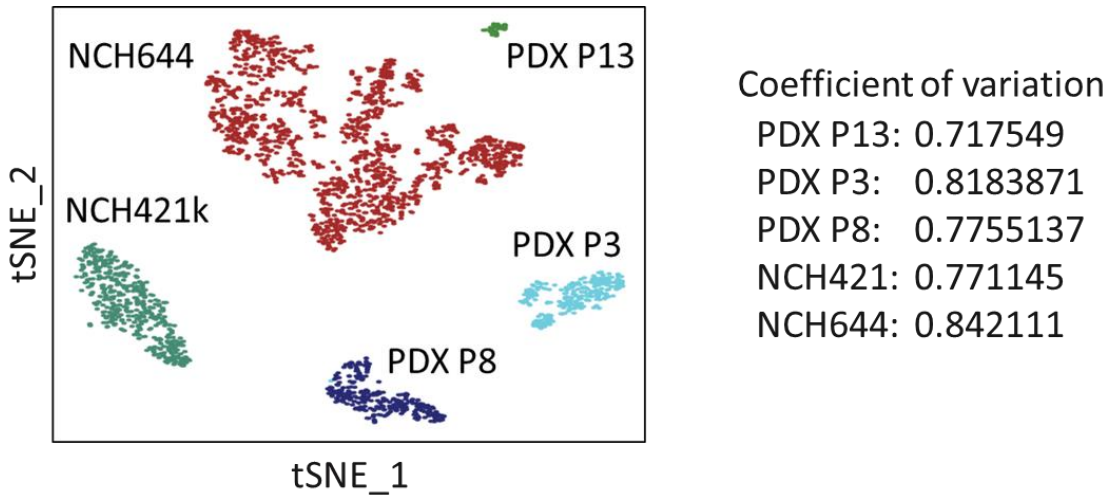

Figure 49: Single cell sequencing on P13, P3 and P8 GBM PDXs and NCH644 and NCH421 GBM cell cultures. tSNE plot showing the overall gene expression relationship between single cells of FACS-sorted tumor cells of 3 GBM patient-derived xenografts (P3, P8 and P13) and 2 stem-like cultures (NCH644 and NCH421k) with more than 1500 genes detected by Drop-seq. Different tumor origins are color coded. Single cells cluster by tumor of origin.

4.7.1.1. GBM tumor cells with distinct phenotypic states carry similar transcriptome

We next analyzed cell-to-cell variation at the single gene level in GBM cells of different tumor origins. Therefore, the expression of CSC-associated extracellular marker genes (*PROM1*, *CD44*, *ST8SIA1*, *FUT4*, *THY1* and *ITGB1*), intracellular stemness genes (*NES*, *VIM*) and differentiation genes (*GFAP*, *TUBB3* and *MAP2*) were displayed on tSNE plots to visualize the expression levels. EGFR was used as a control, since it is known to be differentially expressed between P8 (high expression), P3 (low expression) and P13/NCH644/NCH421k (negative) (Demeure et al., 2016).

Generally, gene expression of analyzed markers was highly heterogeneous within different GBM tumor cell clusters, however, no subclusters could be identified based on the expression of a single gene (**Fig. 50**). This was in accordance with the FACS-assessed cell membrane epitopes, which showed expression gradients, rather than distinct cellular subpopulations.

RNA expression of several genes was not detected, although prior flow cytometric analysis measured high protein abundance (**Fig. 50.a**). In NCH644 cells, CD15 epitope is highly expressed in 40% of the cells, however *FUT4* (CD15) transcripts were not detected. Similar

β-III-tubulin protein is uniformly expressed in NCH421k cells, but not one cell with *TUBB3* transcripts was identified. Furthermore, transcripts of *THY1* (CD90) and *ITGB1* (CD29) genes that were uniformly positive at the protein level in all GBM PDXs, were heterogeneously transcribed at the single cell level. Generally, transcripts coding for cell membrane epitopes were detected at very low levels indicating that the marker profile by flow cytometry cannot be correlated with gene expression data of the markers. The Drop-seq method is known to capture mainly abundant transcripts which might explain a low detection of cell surface marker transcripts. These observations indicate that gene expression of cell surface markers as detected at the single cell level does not always directly correlate with expression of cell membrane epitopes which is in accordance to previous reports showing differences in AC133 epitope presentation and *PROM1* gene expression (Barrantes-Freer et al., 2015, Campos et al., 2011b). Furthermore, transcripts coding for cell membrane, intracellular stemness and differentiation markers were uniformly distributed across each tumor sample without forming specific clusters. Therefore, we were not able to discriminate phenotypic states based on markers' RNA expression levels.

For better visualization purposes of the expression levels of *PROM1* (CD133), *ST8SIA1* (A2B5), *CD44* and *VIM*, we concentrated tSNE plots only on NCH644 (**Fig. 50.b**) and NCH421k stem-like cultures (**Fig. 50.c**). Expression of all four genes varied between not detected (cells depicted in yellow) and highly expressed (cells depicted in red). Again, single cells expressing these genes were distributed across the entire cell population on the tSNE plot with no specific subclustering. These results emphasize once more the transcriptional heterogeneity within each tumor.

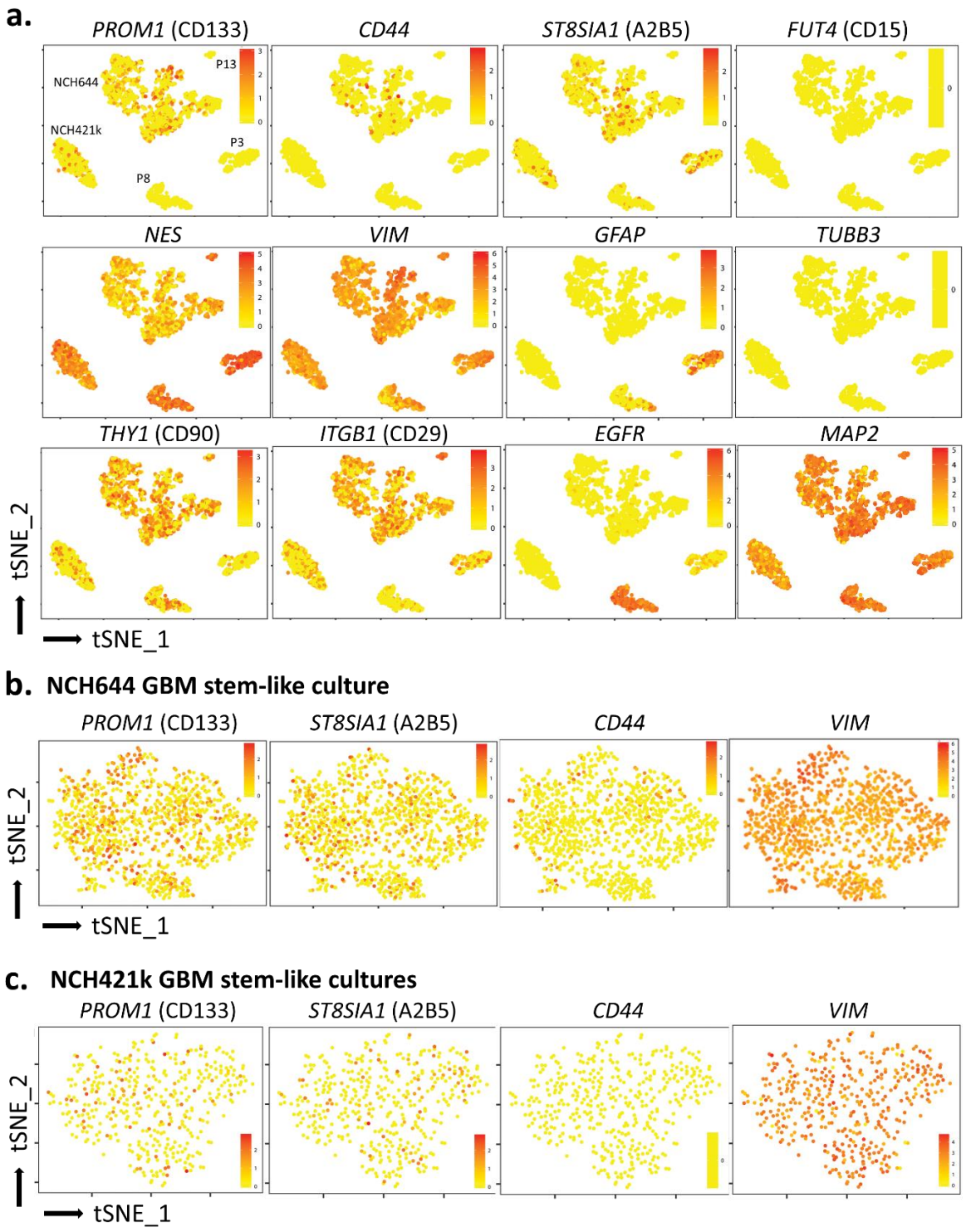

Figure 50: Inter- and intra-tumoral transcriptional heterogeneity. a. tSNE plots showing the expression of CSC-associated marker genes (*PROM1*, *CD44*, *ST8SIA1*, *FUT4*, *THY1* and *ITGB1*), stemness genes (*NES*, *VIM*), differentiation genes (*GFAP*, *TUBB3* and *MAP2*) and *EGFR* in different GBM tumor samples (PDXs: P13, P3 and P8; stem-like cultures: NCH644 and NCH421k). The expression gradient is color coded ('yellow' – not detected or low expression, 'red'- highly expressed). **b.** tSNE plots showing the expression of CSC-associated marker genes (*PROM1*, *CD44* and *ST8SIA1*) and the stemness genes *VIM* in NCH644 stem-like cultures. The expression gradient is color coded ('yellow' – not detected/low expression, 'red'- highly expressed). **c.** tSNE plots showing the expression of CSC-associated marker genes (*PROM1*, *CD44* and *ST8SIA1*) and stemness

genes *VIM* in NCH644 stem-like cultures. The expression gradient is color coded ('yellow' – not detected/low expression, 'red'- highly expressed).

4.7.1.2. *PROM1, ST8SIA1, CD44* and *VIM* transcripts were present in cells of each cell cycle phase

To verify if variations in gene expression was linked to different cell cycle states, single cells of NCH644 stem-like cultures were clustered by G1/S and G2/M specific gene sets (**Fig. 51**). Cells with transcripts of genes expressed during G1 to S phase transition were plotted horizontally, whereas cells with gene expression correlated to G2/M cell cycle transition signature were distributed vertically. Cell cluster located at the bottom left of the plot were in G0/G1 phase. The presence of two main cell clusters showed that NCH644 stem-like cultures contained cycling cells and the Drop-seq method did not select for cells in a specific cell cycle phase. Moreover, expression of four marker genes (*PROM1*, *ST8SIA1*, *CD44* and *VIM*) were found throughout the analyzed cells without forming a specific cluster which indicates that the transcriptional variability previously observed (**Fig. 50**) is not linked to cell proliferation state.

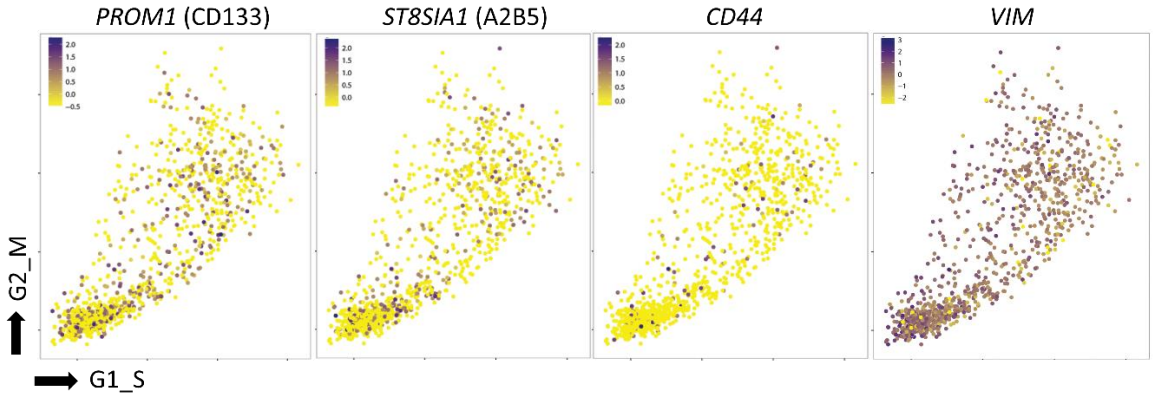

Figure 51: Gene expression in cell cycle phases. Cell cycle state of individual NCH644 cells is estimated on the basis of relative expression of G1/S and G2/M gene sets. Plots displayed the expression of PROM1, ST8SIA1, CD44 and VIM genes in NCH644 single cells distributed by their cell cycle gene expression. The expression gradient of marker genes is color coded.

4.7.2. Single cell sequencing of CSC-associated subpopulations revealed minimal transcriptomic differences

Since we were not able to discriminate CSC-associated phenotypic subpopulations based on marker gene expression profiles at the single cell transcriptomic level, FACS-sorting combined with Drop-seq was applied to subpopulation 2 and 6 of NCH644 stem-like cultures. These subpopulations were chosen for single cell sequencing as subpopulation 2

represented the most adaptive phenotypic state in normoxia, hypoxia and *in vivo*, whereby subpopulation 6 was positive for the four-assessed stem cell-associated markers and showed a lower level of adaptability.

scRNA-seq revealed only 6 differentially expressed genes between the two phenotypic subpopulations (FDR<0.01, |logFC|>0.5) (**Fig 52.a**). Compared to subpopulation 2, subpopulation 6 had significantly upregulated *Macrophage migration inhibitory factor* (*MIF*), a known ligand of the CD74/CD44-receptor complex (Shi et al., 2006), *S100 calcium binding protein A6* (*S100A6*), *Nestin* (*NES*), *Galectin 1* (*LGALS1*) and *Histone cluster 1 H1 family member e* (*HIST1H1E*). Gene transcripts of *Parathymosin* (*PTMS*) were more abundant in subpopulation 2 than in subpopulation 6. These results need however caution, even though analysis detected significantly differentially expressed genes, their |logFC| values remained low, indicating that subpopulations 2 and 6 were only minimally different at the transcriptional level.

Based on the four CSC-associated markers, subpopulations 2 ($CD133^+$ $CD44^-$ $A2B5^+$ $CD15^+$) and 6 ($CD133^+$ $CD44^+$ $A2B5^+$ $CD15^+$) are only phenotypically distinct by their CD44 epitope expression. Although, differences in CD44 gene expression were visible on tSNE, the two subpopulations were not statistically distinct at the transcriptional level based on CD44 as CD44 transcripts were detected for both $CD44^-$ and $CD44^+$ subpopulations (**Fig. 52.b**). Other CSC-associated genes as *PROM1* (CD133), *ST8SIA1* (A2B5), *THY1* (CD90) and stemness marker gene *VIM* appeared to have the same degree of heterogeneity in both analyzed subpopulations. These data indicate that transcriptomic differences between the two analyzed CSC-associated subpopulations are very small. The observed functional differences in terms of plasticity (e.g. subpopulation 2 is most fast adaptive) are likely to be regulated at the post-transcriptional level.

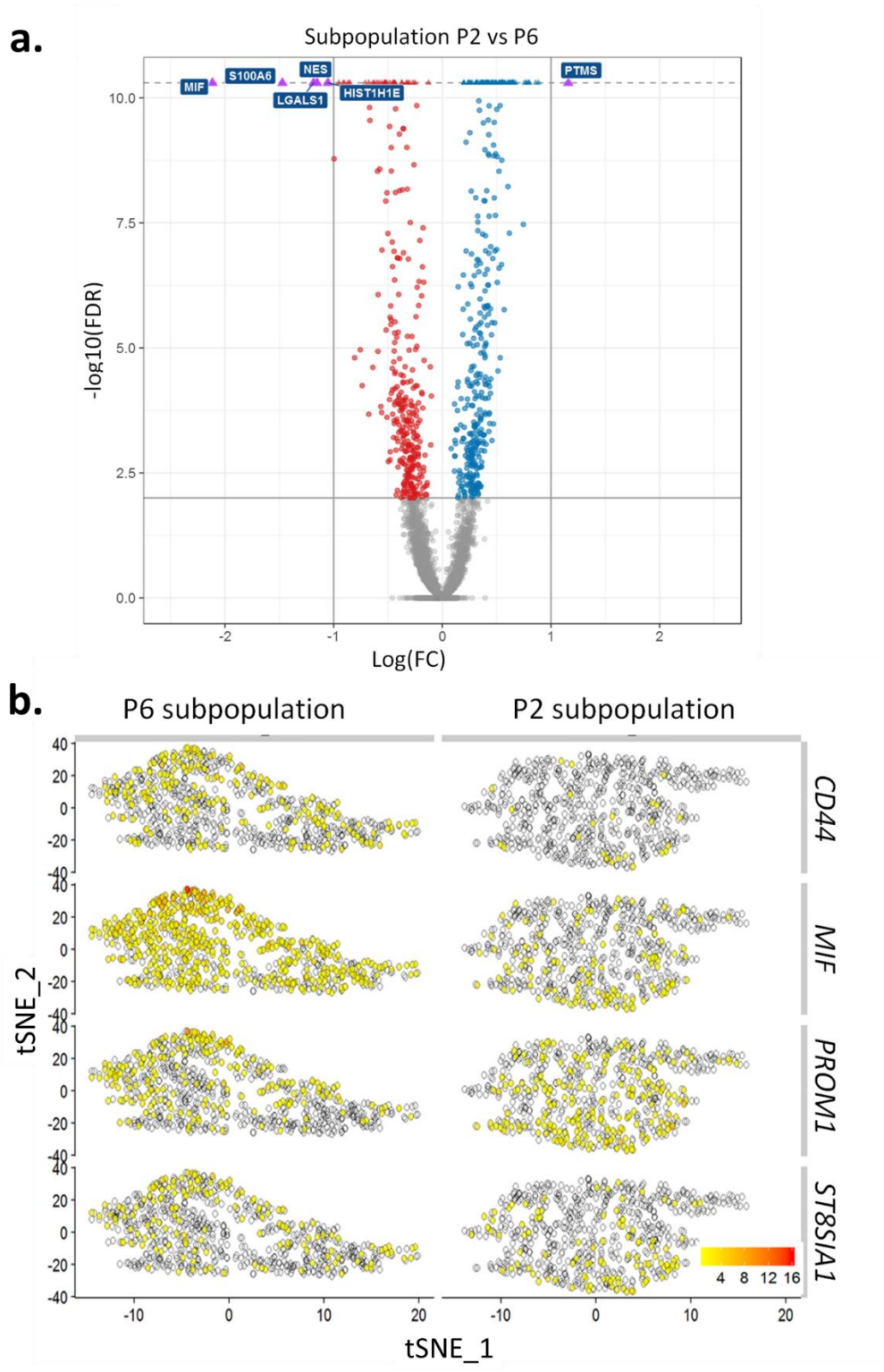

Figure 52: Differentially expressed genes between CSC-associated subpopulation 2 and 6. a. Volcano plot displays transcriptionally differentially expressed genes between single cells of subpopulation 6 versus subpopulation 2. Threshold for differential expression was set at FDR<0.01 and |logFC|>0.5. Only 6 differentially expressed genes (*MIF*, *S100A6*, *NES*, *LGALS1*, *HIST1H1E* and *PTMS*) were detected between the two CSC-associated subpopulations **b.** tSNE plots showing the transcriptional expression of 4 genes in FACS sorted subpopulations 2 and 6. The expression gradient is color coded. For visualization purposes cells with no reads were displayed as transparent. *MIF* and *CD44* were expressed at higher levels in FACS-sorted P6 subpopulation. *PROM1* and *ST8SIA1* transcripts were detected in similar proportion of cells in the two subpopulations.

In summary, as phenotypic states defined by CSC marker expression did not differ at the transcriptomic level the regulation of adaptive properties must occur at other molecular levels e.g. translational, post-translational or metabolic. Moreover, lack of distinct subpopulations at the transcriptomic level further supports the lack of a hierarchical organization in GBM.

Discussion

5. Discussion

The importance of understanding tumor organization is fundamental for successful therapeutic treatment. In case of a hierarchical one-way differentiation structure, treatment strategies should target CSCs at the apex of the hierarchy. On the other hand, if the CSC state is flexible and can be adopted by all cancer cells, treatment should be targeted against the bulk, since all cancer cells may be tumorigenic. Therefore, we aimed to elucidate in this thesis whether phenotypic variability in GBM is organized following a hierarchic CSC model or following an adaptive model. To this end, we examined CSC-associated expression profiles in several GBM models (e.g. patient biopsies, PDXs and GBM stem-like cultures) for eligible CSC markers. We found strong inter- and intra-tumoral variability in the interrogated models based on the expression profile of four selected cell surface markers: CD133, CD15, A2B5 and CD44. Subsequent characterization of tumor cell subpopulations distinguished by the expression of these markers was performed in GBM stem-like cultures as the sphere culture model is thought to be composed stem, progenitor and differentiated cancer cells. All examined subpopulations demonstrated CSC properties (e.g. self-renewal, proliferation, multipotency and tumorigenicity), indicating that phenotypic variability does not originate from one unique subpopulation of CSCs, but from all cancer cell subpopulations. An adaptive model of GBM tumor organization is also supported by mathematical modeling that revealed state transitions between different phenotypes. Markov modeling predicts that the original heterogeneous phenotype can be created from each CSC-associated subpopulation through direct and indirect state transitions, although with different timing. The variability in time may result in differences in adaptation behavior which could also affect tumorigenic assays in vivo. However, no apparent hierarchical structure could be observed suggesting a high plasticity in each CSC-associated subpopulation. Interestingly, cancer cells recreate an optimal phenotypic equilibrium which seems to be required for growth in each specific environmental condition (normoxia, hypoxia, differentiation and *in vivo*). These changes observed in each microenvironment were fully reversible. We also found that differences differences in CSC-associated subpopulations do not rely on distinct transcriptional profiles, suggesting that phenotypic changes are mediated by subtler molecular processes.

5.1. Towards a new model of GBM progression taking into account the plasticity of cancer cells

It has been a debate over the last years whether phenotypic heterogeneity in GBM is created by CSCs or a cell state adapting to the environment. Over the last chapters, we have accumulated by extensive functional testing and mathematical modeling evidence that phenotypic heterogeneity of GBM subpopulations is created by intrinsic cell plasticity influenced by the tumor microenvironment. We show to which extent a cancer cell population is able to change its phenotype and how this adaptive capability is governed by different environments.

5.1.1. Phenotypic adaptivity is intrinsic to cancer cells

5.1.1.1. Each cancer cell can recreate full phenotypic heterogeneity

A crucial property of CSCs is the ability to recreate full phenotypic variability in a cancer population. Our experiments show that all CSC-associated subpopulations, regardless of their initial marker expression profile, are able to recreate positive and negative cell fractions. Most interestingly, full heterogeneity of 16 phenotypic states is regained by each single subpopulation demonstrating that all subpopulations are multipotent, and no hierarchical structure is observed. Several reports using less CSC-associated markers show similar results where marker positive cells form marker negative cells and vice versa to recreate initial phenotypical heterogeneity (Wang et al., 2008, Brown et al., 2017, Chen et al., 2010, Brescia et al., 2013a, Kenney-Herbert et al., 2015). One of the first reports showing phenotype interconversion in GBM was published by Wang et al. who show that $CD133^-$ GBM cells are able to form $CD133^+$ cancer cells upon transplantation into the rat brain (Wang et al., 2008). *In vitro* studies of GBM sphere cultures show that either CD133 positive or negative cells alone or combined with CD44 marker positive or negative expression are all able to regain phenotypical heterogeneity (Brown et al., 2017, Brescia et al., 2013b). Kenney-Herbert et al. demonstrate multipotency in CD15 positive and negative sorted GBM sphere cultures (Kenney-Herbert et al., 2015). On the other hand, Chen et al report a hierarchical structure by clonally expanding $CD133^-$ and $CD133^+$ cancer cells *in vitro*. The $CD133^+$ population demonstrated CSC properties, whereas two distinct subpopulations with different behavior were detected in the $CD133^-$ population: one aggressive with multipotent ability and one more differentiated phenotype which was not able to reform $CD133^+$ cells (Chen et al., 2010). It should be noted that upon clonal expansion two genetically different subpopulations may have developed from the $CD133^-$ population which might explain the distinct functional phenotypes. Other initial studies that

described CSCs in GBM did not test for multipotency *in vitro* (Singh et al., 2004b, Singh et al., 2003).

5.1.1.2. Phenotype changes are stochastic and bidirectional

We applied mathematical modeling to predict phenotypic changes over time. A common mathematical model in economics that predicts the evolution of present states is the Markov model. In our study, phenotype transitions can be calculated from phenotypic proportions reformed by individual subpopulations measured at different time points. The model fits well to our study as it was shown to predict state transitions with similar or even higher precision using less detailed information than other described mathematical models (Buder et al., 2017). Furthermore, the Markov model was successfully applied previously for the estimation of state transitions in breast cancer subpopulations (Gupta et al., 2011, Quintana et al., 2010, Chaffer et al., 2013, Zapperi and La Porta, 2012). The choice of the Markov model is further supported by equal proliferative and self-renewal properties observed in our CSC-associated subpopulations which are a prerequisite for this model.

Our data suggest that phenotypic heterogeneity is created via stochastic state transitions according to the Markov model. Each phenotypic state may be reached directly or indirectly via another state in a transient stochastic manner. As no hierarchy was perceived, the one-way differentiation model could not be validated. Moreover, not a single analyzed phenotypic state was unipotent and irreversible (e.g. transient or absorptive state). Markov chains imply that each state transition is stochastic, independent from precedent states except from the current one. Non-hierarchical state transitions have been reported previously i.e. in breast and melanoma cancer (Gupta et al., 2011, Quintana et al., 2010, Chaffer et al., 2013, Zapperi and La Porta, 2012), where different cellular states are able to recreate phenotypic heterogeneity until reaching a stable equilibrium consisting of an admixture of phenotypic states represented at fixed proportions. Comparably, Markov chains on our data reach a steady state similar to the phenotype distribution observed in initial stem-like cultures. This equilibrium is identical for all individually cultured CSC-associated subpopulations indicating that each subpopulation is able to recreate original phenotypic heterogeneity by stochastic state transitions.

5.1.1.3. Subpopulations show different adaptive capacities that do not result from distinct transcriptional profiles

Although all CSC-associated subpopulations are plastic and change their phenotype by state transitions in a non-hierarchical manner, not each state transition is predicted to occur (65 of 240 not possible) and state transition probabilities vary across subpopulations and the phenotype to be produced. In addition, time to reach the final phenotypic distribution differs between CSC-associated subpopulations with subpopulation 2 being the fastest. Hence, we show for the first time that despite a lack of a hierarchical organization, certain phenotypes are more plastic and can potentially adapt faster to the surrounding environment. This is supported by our transplantation studies in mice where subpopulation 2 is the most fitting phenotype and demonstrates the fastest tumor growth.

However, it is not clear why some phenotypic states appear more plastic than others. Little is known about the functional consequences of the marker expression and how a cell population communicates to gain a heterogenic expression profile. Single cell RNA-sequencing applied to several PDXs and GBM stem-like cultures revealed that each GBM sample retained a similar transcriptomic profile although they carry phenotypically distinct subpopulations. Within GBM samples, no distinct subclusters were identified which is in contrast to studies in breast cancer (Gupta et al., 2011, Chaffer et al., 2013). Stem, basal and luminal breast cancer subpopulations could be differentiated at the transcriptional level suggesting that these phenotypic states are functionally and/or genetically more distinct in breast cancer than in GBM.

Similarly, two GBM CSC-associated subpopulations (subpopulation 2 vs. 6) with differential properties (i.e. subpopulation 2 being the most adaptive phenotype) show only a minimal number of differentially expressed genes, suggesting that distinct phenotypes arise most probably from translational and post-translational modifications. This is also in agreement with the poor correlation of gene expression and epitope presentation of many of the marker proteins. Subpopulation 6 shows higher *MIF* gene expression than subpopulation 2 which can be associated to CD44 protein expression that is higher in subpopulation 6 compared to subpopulation 2. Indeed, *MIF* is associated with the activation of the CD74/CD44 receptor complex in immune cells (Shi et al., 2006). In glioma, *MIF* expression is related to immune escape and malignancy (Mittelbronn et al., 2011) and is proposed as a therapeutic target due to its tumor promoting effect (Kindt et al., 2016).

5.1.2. The cancer cell microenvironment shapes the tumor phenotype

5.1.2.1. Environment-specific phenotypic distribution

Similar to normoxia, the Markov model calculates a hypoxia-specific transition matrix and predicts a final hypoxia-specific phenotypic equilibrium. GBM stem-like cultures also changed their phenotypic distribution upon ATRA driven differentiation *in vitro* and transplantation *in vivo*. As normoxic and hypoxic environment have their own specific phenotypic equilibrium, we suggest that long-term growth of cells in differentiation environment *in vitro* and in the mouse brain *in vivo* eventually results in an optimal phenotypic distribution. The environment specific phenotypes suggest that state transitions are tightly regulated by the microenvironment within the boundaries of the intrinsic cancer cell phenotypic capacity.

In hypoxia, CD133 and CD44 expression was upregulated whereas differentiation cues lead to a downregulation of CD133. When ATRA-driven differentiation was combined with low oxygen levels, CD133 reduction upon differentiation was diminished, suggesting that the different environmental cues have a combined effect on the final phenotypic equilibrium. The phenotypic heterogeneity observed *in vivo* cannot be considered a simple combination of hypoxic and differentiation factors. E.g. CD44 epitope expression was downregulated in contrary to all tested environments. The strong decrease of cell surface markers and the phenotypic variability upon transplantation assays is likely to be affected by the brain microenvironment. Immune cells (Bhat et al., 2013) and an acidic environment (Lathia et al., 2010) were shown to influence CSC-associated marker expression and may further contribute to the phenotypical heterogeneity observed *in vivo*.

Although all subpopulations showed CSC properties in hypoxia, mathematical modeling revealed a minor hierarchical organization due to subpopulation 10 which could not be recreated by other subpopulations. However, this is in contrast with the functional analysis showing rather decreased CSC abilities (decreased clonogenicity) compared to other CSC-associated subpopulations. These results suggest that subpopulation 10 is rather quickly changing its phenotype. The disappearance of subpopulation 10 in hypoxia might be linked to an unfavorable cell function in hypoxia.

5.1.2.2. Environment specific phenotypes are reversible

Most importantly we show that phenotypic adaptation upon environmental change was reversible in all tested conditions and the initial heterogeneity was recreated. Reversibility

of increased CD133 expression was already previously shown in other reports using adherent GBM cell lines and several low oxygen concentrations to mimic hypoxia, which suggested that CD133 is involved in a basic survival function under in hypoxia (Griguer et al., 2008, McCord et al., 2009). Our data show that phenotype distribution in more complex environments, e.g. hypoxia combined with differentiation condition or *in vivo* environment with different stromal cells, is reversible suggesting strong adaptive capacities of CSC-associated subpopulations. Interestingly, the time needed to reverse the phenotypic distribution back to the initial equilibrium was markedly longer than for the primary phenotypic change. This delay suggests that despite their high adaptive capacities cancer cells may not thrive under constant environmental changes. Future experiments may explore whether increased cell death is observed when the culture environment is repeatedly changed.

5.1.3. Treatment strategies should target all cancer cells and not only those with stemness properties

5.1.3.1. CSC-targeted therapies

Many current treatment strategies that are tested in clinical trials target specifically CSCs, using cancer vaccines targeting cell surface marker positive cells or compounds interfering with stemness regulatory mechanisms. The high cancer cell plasticity described here suggests that CSC-targeted therapies will be ineffective since full marker phenotypic heterogeneity may be regained once the treatment is discontinued. Although, it is not clear yet, how effective CSC targeted therapy in GBM is (Silver et al., 2016), we speculate that the outcome will largely depend on cell plasticity. To increase the success of cell surface targeting therapies, the ability of a cancer cell to change its phenotype needs to be inhibited. To this goal I propose to specifically target proteins that regulate CSC-associated marker expression. For instance, Perrot demonstrated that CD44 is internalized in an LRP-1 dependent manner (Perrot et al., 2012). Inhibition of this protein leads to a permanent epitope exposure of CD44, thereby presenting a suitable target for CD44-specific therapy. However, it remains questionable to target CSC-associated cell surface markers in GBM patients since their functional relevance is not yet fully understood.

5.1.3.2. Bulk treatment

The CSC hypothesis presumes a better survival of cancer cells with stemness properties upon chemo and radiotherapy. In accordance with previous reports we find that sublethal doses of TMZ on GBM stem-like cells results in a reduction of $CD133^+$ cells (Beier et al.,

2008, Lemke et al., 2014). To validate whether TMZ specifically represses the $CD133^+$ phenotype, functional assays (e.g. self-renewal, indefinite proliferation and multipotency) need to be performed. Moreover, sphere cultures are more resistant to TMZ than adherent cultures probably due to a low penetrance of the compound to the sphere cores (data not shown). Many reports, addressing CSC chemoresistance determine drug sensitivity in sphere cultures for putative CSCs compared to adherent cultures for differentiated cancer cells. Data are interpreted as CSCs in sphere cultures to be more resistant to treatment than differentiated cells although discrepancies in drug sensitivity relies on the comparison of two different culture systems (Ghods et al., 2007, Hsieh et al., 2011).

Reduced chemosensitivity could be explained by a transient lower proliferation rate of some subpopulations, as TMZ requires cell cycle initiation to be effective. Based on microenvironmental stimuli, the proliferation rate may however adapt over time. It needs to be investigated whether phenotype transitions are cell cycle dependent. Markov modeling of our data does not couple phenotype transitions with cell division rates. Phenotype interconversions occur within one day which is faster than the cell doubling time (2.6 days in normoxia). On the other hand, it was shown that the number of asymmetric cell divisions increased with changing culture conditions (i.e. reduction of growth factors) which could lead to a faster adaptation of the phenotypic equilibrium (Lathia et al., 2011b).

5.2. Critical appraisal of methodologies to identify cancer cells with stemness properties

To identify a cancer cell population with functional stemness characteristics and able to recreate phenotypical intratumoral heterogeneity, we applied several functional tests including self-renewal, proliferation, multipotency and differentiation abilities *in vitro*, and tumorigenic capacities in immunocompromised mice *in vivo*. Our tests reveal that each CSC-associated subpopulation carries functional CSC properties indicating that stemness is not a hallmark of a restricted CSC subpopulation. The importance of applying appropriate assays and carefully interpretation of the results is discussed below.

5.2.1. Utility of functional tests to identify cancer cells with CSC properties

Good tests and models are crucial to determine CSC properties. Often reports are negligent by testing short term clonogenicity and not indefinite self-renewal capacities (Suva et al., 2009). Many reports solely show sphere forming capacity and tumorigenic ability *in vivo*, although on its own this does not prove multipotent ability which is necessary to demonstrate phenotypic variability (Singh et al., 2003). To compare properties of different subpopulations all subpopulations in question requires to be experimentally tested, which is often neglected due to the vast amount of work (e.g. many studies test CD133 positive but not negative populations). A clear distinction between CSC and non-CSC can only be made if CSC properties of all subpopulations are compared in order to identify CSC (full CSC properties), progenitor (no or finite CSC properties) and fully differentiated cancer cells (no CSC properties). Taken together, often data is not reliable when tests are incomplete and can be interpreted differently.

A major problem in functional testing is the use of different GBM models (e.g. patient biopsies, sphere forming GBM cells). Functional analysis of primary patient material is hampered by the presence of dying cells, debris and stromal cells. Here, cancer cells cannot be accurately separated from stromal cells due to the lack of good markers. Often marker positive and negative tumor cells are separated by columns with magnetic beads loaded with CSC-specific antibodies. Using this technique, the cell suspension purified in the column is enriched with marker positive subpopulations whereas the cell suspension that did not bind the column contains dead cells, debris, marker positive and negative cells. In this scenario, it can be expected that the flow-through cell suspension is less healthy, less viable and hence less tumorigenic than the bound marker positive cells. Using FACS, marker positive and negative cell populations can be individually purified from debris and

dead cells, however, the “contamination” with stromal cells remains. The problematic becomes evident upon functional testing, when marker negative populations are not proliferating or/and not tumorigenic due to cell debris. Singh et al. analyzed CD133 positive and negative cell fractions from patient biopsies for their stemness properties and found the $CD133^-$ cell population to have no sphere forming capacities and no *in vivo* tumorigeneicity (Singh et al., 2004b, Singh et al., 2003). The observed discrepancy in stemness properties between $CD133^-$ and $CD133^+$ cells may result from stromal cells.

5.2.2. Pitfalls of *in vivo* tumorigenic tests

One main criteria of a CSC is the ability to generate a tumor *in vivo*. In our experiments, all subpopulations demonstrate tumorigenic abilities, although some subpopulations are able to develop a tumor *in vivo* faster than others. This could be interpreted as such that subpopulation 2 represents a CSC whereas the other 3 engrafted subpopulations are progenitors due to slower tumor development. However, our previous results on self-renewal, proliferation and multipotency demonstrate similar stemness abilities between the subpopulations, which points to differences in adaptive capacities *in vivo*. Thus, different phenotypes independent of marker expression are able to generate tumors *in vivo.* This is in contrast to the initial CSCs reports in GBM. which suggested that only marker positive cells were able to reform GBM tumors *in vivo* (Singh et al., 2004b, Son et al., 2009, Tchoghandjian et al., 2010), However later studies showed that either no difference was observed between marker positive and negative fractions (Wang et al., 2008o, Ogden et al., 2008, Kenney-Herbert et al., 2015), or both fractions were tumorigenic, but with different potency (Chen et al., 2010, Auvergne et al., 2013, Auffinger et al., 2014, Brescia et al., 2013a).

Differences in tumorigenicity between these studies can often be clarified by the different GBM model used. Other factors that may influence tumorigenicity of implanted cells is the use of the mouse strain and the number of cells that be explained by different adaptation kinetics (see below). This was impressively shown by Quintana et al. who demonstrated that the less mice are immunogenic the higher the frequency of tumorigenic cells in melanoma (Quintana et al., 2008). Also the coimplantation of extracellular matrix or irradiated stromal cells with together with cancer cells increases tumor forming capacity *in vivo* (Gupta et al., 2011). Kenny-Herbert coinjected CD15 positive and negative GBM cells with extracellular matrix, which may have boosted tumor development of less tumorigenic subpopulations. Wang et al. and Ogden et al. were both implanting into nude rats suggesting that rat brains might be a more permissive environment for tumor formation compared to mouse brains.

Our data also suggest that different adaptation kinetics in cancer subpopulations might result in different experimental outcomes, highlighting the importance of experimental endpoints. At a given endpoint subpopulations may not have reached their final tumor volume. Indeed, we detect major differences in tumor size at early stages of tumor development and differences in survival. Most tumorigenic assays do not show survival studies or may not wait long enough for tumor development, thereby partially missing that all subpopulations may eventually be lethal. Auvergne et al. sacrificed mice injected with either A2B5 positive and negative cells six weeks after operation (Auvergne et al., 2013). At this timepoint A2B5 negative cells had not developed tumors, however, using a higher cell number led to 100% tumor formation as well in the A2B5 negative cell fraction ($5x10^3$ vs $2.5x10^4$ cells per injection). This indicates that A2B5 negative cells are capable of forming a tumor, but with a delay (Auffinger et al., 2014). In our study, some subpopulations needed twice as long (i.e. 120 days) to generate a lethal tumor compared to the fastest subpopulation (60 days). Thus depending on the interpretation of results opposite conclusions can be reported from *in vivo* xenografting assays, which may explain at least some of the controversy in the CSC field.

5.2.3. Identification of cancer cells with CSC properties using cell surface markers

The use of cell surface markers to identify cancer cells with stemness properties is highly debated. On the one hand, marker positive cells are often shown to display stemness properties, on the other hand no unique marker for cancer cells with stemness properties has been identified in GBM.

5.2.3.1. Cell surface markers recapitulate inter- and intra-tumoral heterogeneity in GBM

Next to progenitors and fully-differentiated cancer cells, the CSC hypothesis posits that CSCs represent only a subpopulation of a tumor population. Therefore, a CSC-specific cell surface marker is expected to display a heterogeneous expression profile. In this thesis, we found that most cell surface markers demonstrate a relatively homogeneous expression profile within PDX tumors. Only a subset of the tested cell membrane markers (CD133, CD44, A2B5 and CD15) fulfilled the CSC criteria and demonstrated strong inter-patient and intra-tumoral heterogeneity at the epitope expression level in PDXs and *in vitro* cultures in agreement with previous reports (Brescia et al., 2013b, Auffinger et al., 2014). In several

PDXs the percentage of marker positive cells exceeded half of the total cancer cell population. It may be that in the first reports identifying a small CD133 positive cancer subpopulation as CSCs might simply be explained by inter- and intra-tumoral heterogeneity. Intratumoral expression of these cell surface markers was highly variable within cells of the same PDX and ranged from undetectable/low to highly positive. Similarly, our single cell transcriptional profile analysis on PDXs and stem-like cultures did not identify distinct cell subpopulations but rather clear gradients in different GBM samples. This is in accordance with the scRNA-seq observations in GBM patient samples which did not reveal distinct transcriptional profiles belonging to clear subpopulations, but a gradient in gene expression profiles (Patel et al., 2014). The existence of a gradient and the absence of at least two distinct subpopulations suggest that putative CSC do not represent a discrete entity.

5.2.3.2. Marker expression cannot be correlated to cell function

Unfortunately, association between functional properties and CSC-associated subpopulations is rather elusive and more investigation is needed to understand the cellular function of these markers. Under this aspect it becomes obvious that CD133 expression though markedly decreased upon differentiation, cannot be used as a unique marker to assess the degree of differentiation (Campos et al., 2010). Following the CSC hypothesis, varying expression patterns across patient samples can be explained by the grade of differentiation of the tumor. Accordingly, a marker positive tumor would be mainly composed of CSCs, whereas marker negative tumors are thought to contain largely differentiated cancer cells. This hypothesis suggests that tumors containing CSCs are more aggressive and rapidly growing compared to tumors containing less CSCs. However, this cannot be confirmed by our data; NCH644 cells (80% $CD133^+$) show shorter mouse survival than NCH421k cells (99% $CD133^+$) upon engraftment into nude mice.

It is however not clear where the strong inter-patient heterogeneity and its distinct phenotypic distribution in different GBM are resulting from. Our analysis did not reveal a particular link between expression of CSC-associated markers and any analyzed GBM drivers nor genetic aberrations. Other intrinsic features as heterogeneous epigenetic profiles or uncommon/non-peered genetic mutations or microenvironment may cause inter-tumoral variability.

5.3. Proliferative potential of cells with CSC properties: quiescent or higher proliferative?

It is generally proposed that CSC resistance to therapy results from a quiescent state and tumor mass is created by fast proliferating progenitor cells. Although some data is available in colon cancer (Kreso et al., 2013) or melanoma (Roesch et al., 2010) where unfrequently cycling cells with tumorigenic capacities are described, however, only rare studies in GBM have addressed the proliferative state of putative CSCs (Deleyrolle et al., 2011).

5.3.1. Functional tests

It is reported that cancer cells with dye-retaining properties have tumor initiating capacities. Upon cell division, fluorescent dyes are equally distributed to the two daughter cells, thereby fast proliferating cells lose the staining faster than slowly proliferating cells. It has been shown that both slow cycling cells and bulk cancer cells in *in vitro* GBM stem-like cultures have tumorigenic capacities in immunocompromised mice but to different extent. Interestingly, slow cycling cells have higher tumor forming capacities than overall cancer cell population (Deleyrolle et al., 2011).

We showed that self-renewal and proliferative ability for all CSC-associated subpopulations is equal and that all subpopulations are able to form spheres of similar size. This indicates that subpopulations have a similar degree of stemness/differentiation. This is also supported by data showing two forms of division (e.g. symmetric and asymmetric) in CD133 positive cells with a preferential to symmetric cell division (83% vs. 3,6% of cell divisions)(Lathia et al., 2011b). Since the majority of cell divisions in GBM cell cultures are thought to be symmetric, CSC-associated subpopulations with self-renewal ability should show as well indefinite proliferative ability. Our data show that cancer cells with CSC properties are highly proliferative.

5.3.2. Single cell transcriptome analysis

Recent studies analyzing GBM at the transcriptomic level provide conflicting data on the association between stemness and cell cycle (Venteicher et al., 2017, Patel et al., 2014, Tirosh et al., 2016b). Patel et al. shows that GBM cells with a transcriptional profile similar to GBM sphere cultures are slow cycling whereas GBM cells with a transcriptional profile similar to adherent GBM cultures are cycling at a fast rate. In this study stemness and differentiated transcription signatures are correlated solely with the transcription profiles of sphere forming and adherent GBM cultures, respectively. In contrast Venteicher and colleagues report that in lower grade glioma, cells with stem cell properties are faster

proliferating than cells with a more differentiated profile. Here the stemness profile of cancer cells was defined differently from the Patel study as it was deduced from PCA analysis revealing a differentiation gradient from cancer cells with expression of stemness genes to astrocytic and oligodendroglial gene expression. Thus, these studies conclude that in lower grade glioma CSCs are fast-proliferating whereas CSCs from high grade GBM appear to be more quiescent. This data highlights the inconsistency in results with regard to proliferative potential of CSCs in glioma. It remains to be seen whether these results are dependent on glioma grade or on the different reference stemness gene set applied.

5.3.3. Cell cycle

I found that when proliferative activity was measured in bulk GBM cancer cells a change in cell cycle activity was observed between $CD133^+$ and $CD133^-$ cells. All CSC-associated subpopulations contained proliferative cells but in 6 out of 8 CD133 low subpopulations cell cycle activity was reduced. In previous reports CD133 expression was shown to fluctuate across the cell cycle where cells in S, G2 and M phase displayed higher CD133 epitope expression (Barrantes-Freer et al., 2015, Griguer et al., 2008, Jaksch et al., 2008, Jordan, 2009, Soeda et al., 2009). Differences in proliferative capacities in individual CSC-associated subpopulations and bulk cultures are the culture conditions. Upon cell cycle analysis, cells were grown in bulk together with all other subpopulations. By cell-to-cell signaling, CD133 positive cells might be favored to enter cell cycle or CD133 might be upregulated upon cell division. It is as well suggested that the CD133 epitope is more apparent during cell cycle due to conformational change of the cell shape (Campos et al., 2011b). To resolve this, flowcytometry combined with microscopy (ImageStream) could be performed to analyze on a large cell number cell cycle state combined with cell size/shape and expression of cell surface markers. Nevertheless, individually cultured CD133 negative cells adapt to the environment and are proliferative. In fact, our cell cycle analysis excludes that only CD133 positive cells in a cell population are able to proliferate. None of the other tested CSC-associated markers (CD44, A2B5 and CD15) was associated with increased or reduced cell growth or self-renewal capacities.

5.4. Is phenotypic adaptation upon environmental change accompanied by selection?

According to CSC hypothesis specific CSC subpopulations are positively selected upon environmental pressure (for instance hypoxia, treatment, …) to regrow a heterogenic tumor. Our data shows that the cell number is reduced in hypoxia in several GBM cultures as a result of decreased proliferation and/or increased cell death. However, these data could not be linked to specific CSC-associated subpopulations. Moreover, all examined CSC-associated subpopulations proliferate at similar rates and were able to self-renew. This shows that different phenotypes are not selected due to differences in the replicative potential.

Moreover, phenotype changes upon hypoxia cannot be explained exclusively by partial selection of subpopulations, as each subpopulation was multipotent. Nevertheless, the clonogenic test suggested that single cells of subpopulations 10, 12 and 14 were more prone for clonal selection than in bulk. To investigate this, dilution of several cell densities could be performed for clonogenic testing. Although partial selection cannot be excluded, the data strongly favors that phenotypic changes occur by adaptation process and not by selection of subpopulations.

5.5. Differentiation therapy ineffective due to aberrant differentiation capacities

Many reports suggest the clinical application of differentiation therapy to inhibit tumor growth using ATRA or BMP4 treatment (Campos et al., 2010, Bonaguidi et al., 2005, Lee et al., 2008, Piccirillo et al., 2006, Rahman et al., 2013). Here we found that NCH644 stem-like cultures upregulate the intracellular differentiation markers GFAP and β-III-tubulin upon ATRA-driven differentiation. At the same time, cancer cells also kept their stemness marker expression (e.g. vimentin and nestin). These results demonstrate that the differentiation is incomplete compared to normal neural stem cells where stemness markers are lost upon differentiation. Similar data were shown by (Wolanczyk et al., 2010, Lottaz et al., 2010), although many other studies claim differentiation of CSCs. However, many studies investigating differentiation capacity did not assess stemness markers (Campos et al., 2010, Forte et al., 2013). A general concept in 3D GBM stem-like cultures is that not all cells in the sphere have CSC properties. However our results show that all subpopulations in the sphere demonstrate CSC properties. Moreover, no particular expression pattern is observed within the sphere indicating that the markers are not bound to sphere organization

with quiescent core and proliferative outer layer. Taken together, sphere cultures are not composed of cancer cells with distinct differentiation potential.

In some instances, marker comparison was done in 3D spheres versus 2D cultures, without controlling for antibody penetrance to the sphere core through multiple cell layers compared to 2D culture (Campos et al., 2010, Forte et al., 2013). Impaired differentiation in GBM is often linked to defective retinoic acid signaling, which is associated to resistance towards differentiation therapy (Campos et al., 2015, Campos et al., 2011a). Of note, all CSC-associated subpopulations retained their stemness marker expression upon ATRA-driven differentiation in our experiments. Furthermore, the marker expression upon differentiation was reversible, indicating that all subpopulations are able to adapt their internal marker expression. We propose that GBM cancer cells are able to reverse their phenotypes upon differentiation because they retain stemness properties. Similar to the microenvironment-induced changes, phenotype reversibility from differentiation conditions, further indicates that GBM are not organized in a one-way hierarchical process. Similarly to CSC-marker targeted therapy, differentiation therapy is likely to be ineffective to target cancer cells with stemness properties since tumor cells retain their ability to dedifferentiate once therapy is discontinued.

Outlook

6. Outlook

- **Phenotypic heterogeneity in GBM is created by adaptive capacities of cancer cells governed by the microenvironment.**

  The results of our comprehensive study on CSC-associated subpopulations demonstrate that GBM CSCs do not represent a stable entity and that phenotypical intra-tumoral heterogeneity in GBM results from a high intrinsic adaptation capacity that is modulated by the environment. The adaptive capacities and thereby cellular plasticity have major advantages to survive environmental changes such as hypoxia or nutrient shortcoming during tumor development and upon treatment. Therefore, the underlying molecular mechanisms enabling phenotype transitions need to be elucidated as well as the cellular function of CSC-associated markers. Treatment approaches should tackle adaptational mechanisms and the tumor microenvironment.

- **Mathematical modeling as a prospective tool to understand tumor development**

  To gain a deeper understanding of the interplay of the different levels of heterogeneity (e.g. genetic, epigenetic, functional) more performant mathematical models need to be developed to unravel cellular plasticity responsible for therapy failure. Currently available mathematical models are not able to predict the evolution of subpopulations taking into account all parameters involved in tumor development. To obtain a comprehensive model of tumor development parameters as migratory properties, spatial inhibition, nutritional shortage, age of cells, cell selection, death and quiescence. should be incorporated (Enderling et al., 2009). Eventually, treatment effects on cancer populations, and genetic and epigenetic backgrounds (Abernathy and Burke, 2016, Bozic et al., 2016) need to be unified into a convoluted model in order to scope phenotypic heterogeneity. Especially, the dynamic behavior of the cellular phenotype is difficult to grasp: indeed, state transitions are difficult to demonstrate experimentally since most measures are not continuous and only show a snap-shot of an ongoing dynamic process. Therefore, mathematical models will be very helpful.

Annex

a. FACS Aria SORP cytometer

Laser	UV Laser 355nm (60mW)		Violet Laser 405nm (50mW)							Blue Laser 488nm (100mW)			Yellow-Green Laser 561nm (50mW)				Red Laser 640nm (30mW)		
Channel	UV-1	UV-2	Vio-1	Vio-2	Vio-3	Vio-4	Vio-5	Vio-6	Vio-7	SSC	B1	B2	YG-1	YG-2	YG-3	YG-4	Red-1	Red-2	Red-3
BP Filter	450/50	660/40	427/10	460/36	525/50	610/20	661/11	730/45	775/50	488/10	530/30	710/50	586/15	610/20	670/14	775/50	670/14	690	775/50
LP Filter		600		445	505	570	645	685	755		520	635		600	630	710		730/45	755
Fluorochrome											FITC	PerCP-Cy5.5	PE				APC		
Tube 1											CD44	CD15	CD133/1				A2B5		Live/Dead Marker
Tube 2											CD44	CD15	CD133/1			CD90	A2B5		Live/Dead Marker
Tube 3	Hoechst	Hoescht									CD44	CD15	CD133/1				A2B5		Live/Dead Marker
Tube 4											VIM	NES				CD90	TUBB3		Live/Dead Marker
Tube 5																CD90	GFAP		Live/Dead Marker

b. ImageStream imaging cytometer

Laser	Blue Laser 488nm		Yellow-Green Laser 561nm					UV Laser 375nm			Red Laser 642nm	Darkfield 785nm
Channel	Brightfield	2	3	4	5	6	7	8	Brightfield	10	11	12
BP Filter	420-480	480-560	560-595	595-642	642-745	745-800	430-505	505-570	570-595	595-642	642-745	745-800
Fluorochrome		FITC	PE					BV510			APC	
Tube 1	Brightfield	CD44	CD133/1					CD15	Brightfield		A2B5	Live/Dead Marker

c. FACS Canto II cytometer

Laser	Blue Laser 488nm (20mW)					Red Laser 633nm (17mW)	
Channel	SSC	FITC	PE	PerCP-Cy5.5	PE-Cy7	APC	APC/Cy7
BP Filter	488/10	530/30	585/42		780/60	660/20	780/60
LP Filter		502	556	655-670	735		735
Fluorochrome		Alexa-488				APC	
Tube 1						GFAP	Live/Dead Marker
Tube 2		VIM		NES		TUBB3	Live/Dead Marker
Tube 3				PI			Live/Dead Marker
Tube 4				PI		Annexin V	

Annex 1: Multicolor flow cytometer panels with laser and filter set up. a. CSC-associated multicolor staining for GBM cell cultures (Tube 1), patient-derived and cell culture-derived xenografts with additional hCD90 (Tube 2) was analysed on FACS Aria SORP cytometer. For cell cycle measurement combined with CSC-associated multicolor staining for GBM cell cultures additional Hoescht staining was used (Tube 3). Intracellular stemness and differentiation marker staining was performed in GBM cell culture-derived xenografts (Tube 4 and 5) **b.** CSC-associated multicolor staining for GBM cell cultures was acquired on ImageStream imaging cytometer (Tube 1) **c.** Intracellular stemness and differentiation marker staining in GBM cell cultures were performed on FACS Canto II (Tube 1 and 2). Staining for cell cycle measurement (Tube 3) and apoptosis test (Tube 4) was used for functional analysis of several GBM cell cultures.

Annex 2: Mathematical modeling using discrete Markov Chains

a. Matrix construction

The construction of the data matrices was performed as follows. $w_{i,j}^{(t)}$ denoted the experimentally observed mean proportion of phenotype $j, j = 1, \dots, 16,$ in the experiment starting with pure subpopulations of phenotype $i, i = 1, \dots, 16,$ at time t. Subsequently, a phenotype proportion matrix at time t was constructed as follows:

$$\mathrm{W}^{(\mathrm{t})} = \begin{pmatrix} \mathrm{w}_{1,1}^{(\mathrm{t})} & \cdots & \mathrm{w}_{1,16}^{(\mathrm{t})} \\ \vdots & \ddots & \vdots \\ \mathrm{w}_{16,1}^{(\mathrm{t})} & \cdots & \mathrm{w}_{16,16}^{(\mathrm{t})} \end{pmatrix}$$

Note that the phenotype proportion matrix describing the initial proportions was the $16x16$ identity matrix, i.e.

$$W^{(0)} = \begin{pmatrix} 1 & 0 & \cdots & \cdots & 0 \\ 0 & 1 & 0 & \cdots & 0 \\ \vdots & \ddots & \ddots & \ddots & \vdots \\ \vdots & \ddots & \ddots & \ddots & 0 \\ 0 & 0 & \cdots & 0 & 1 \end{pmatrix}.$$

The transitions between the phenotypes were estimated as probabilities per time-step length of an underlying Markov chain which was defined here as one day. This lead to three phenotype matrices from the obtained data in normoxia: $W^{(20)}$ after 20 days, $W^{(30)}$ after 30 days and $W^{(70)}$ after 70 days. In hypoxia, one matrix, namely $W^{(60)}$ for the measurements after 60 days was constructed. Markov chain theory allowed to connect the initial phenotype proportion matrix with the corresponding matrix after n time-steps with the equation $W^{(0)}P^n = W^{(n)}$. This equation, derived from observations at time n, was solved for the underlying transition matrix P, i.e.

$$\hat{P}_{(n)} = \left(\left(W^{(0)}\right)^{-1} W^{(n)}\right)^{\frac{1}{n}}.$$

Hence, three transition matrices $\hat{P}_{(20)}$, $\hat{P}_{(30)}$ and $\hat{P}_{(70)}$ in normoxia were regularized using the QOM-algorithm (Quasi-optimization of the root matrix) in case the root of the matrix was not stochastic, i.e. Negative values or row sums not equal to one. The average over the three matrices resulted in a final estimate for the transition matrix P, i.e. $\hat{P} = \frac{\hat{P}_{(20)} + \hat{P}_{(30)} + \hat{P}_{(70)}}{3}$. In hypoxia, the transition matrix $P = \hat{P}_{(60)}$ was used.

b. Krackhardt hierarchy

In order to estimate the degree of hierarchy of the estimated transition matrixes from data obtained under different environmental conditions, graph hierarchy introduced by Krackhardt was calculated (Krackhardt, 1994). The degree of deviation from pure hierarchy,

i.e. tree structure, is assessed by counting the number of pairs that have reciprocated ties relative to the number of pairs where there is any tie, i.e. the proportion *p* of all tied pairs having reciprocated ties. Krackhardt hierarchy is then defined as 1-*p*. A perfect hierarchy is characterized by no reciprocated ties and exhibits a Krackhardt hierarchy of one. Calculations were performed in R using "*hierarchy*" function with "*Krackhardt*" measure. The analysis was realized with the help of Thomas Buder (Zentrum für Informationsdienste und Hochleistungsrechnen (ZIH), Technische Universität Dresden, Dresden, Germany and Fakultät Informatik / Mathematik, Hochschule für Technik und Wirtschaft Dresden, Dresden, Germany Technische Universität Dresden).

c. Marker dependency calculation

We investigated whether the cell state transitions between positive and low/negative expression of one marker in normoxia and hypoxia were dependent on the level of expression of the other markers. For each marker, we distinguished two phenotypic states with respect to positive and low/negative expression of this marker.

In detail, the multipotency data was modeled in two separate ways (**Fig. 54**). To calculate final equilibrium for marker dependence, the data was processed as shown previously by using the Markov model to obtain a 16x16 state transition probability matrix of the 16 CSC-associated subpopulations. Subsequently, state transition probabilities were summed for subpopulation and phenotypic states being positive or negative/low for a specific marker expression. For instance, to obtain 2x2 transition matrix for CD133 phenotype changes, transition probabilities of subpopulations 1 to 8 to form phenotypic states 1 to 8 were added in order to get the transition probability of a $CD133^+$ cell to keep the $CD133^+$ state. To calculate the transition probability of $CD133^+$ cells to switch to a $CD133^-$ state, probabilities of subpopulations 1 to 8 to form phenotypic states 9 to 16 were summed up. This quantification was performed for each state transition possibilities for the 4 markers used. Finally, Markov model was used to predict the final equilibrium for each individual marker transition matrix.

The second path to model the multipotency data was used to predict final equilibria in case marker expression was independent. First, we aimed to calculate 2x2 matrix for each individual marker. Using the original data, the percentages of formed phenotypic states of each subpopulation were added together for each individual marker as described above for state transitions. Subsequently, 2x2 state transition probability matrixes for each marker were obtained by Markov modeling. Under the assumption of independence, state transition probabilities for all 16 subpopulations were calculated by multiplying state transition probabilities of the 4 markers. For example, to calculate the transition probability of subpopulation 4 ($CD133^+$ $CD44^-$ $A2B5^-$ $CD15^+$) to change into phenotypic state of

subpopulation 10 ($CD133^-$ $CD44^-$ $A2B5^+$ $CD15^+$) we multiplied state transitions of CD133 2x2 matrix from $CD133^+$ to $CD133^-$, state transition of CD44 2x2 matrix from $CD44^-$ to $CD44^-$, state transition of A2B5 2x2 matrix from $A2B5^-$ to $A2B5^+$ and state transition of CD15 2x2 matrix from $CD15^+$- to $CD15^+$. Thereby we obtained a 16x16 independent state transition probability matrix for all CSC-associated subpopulations. Final equilibrium was predicted using Markov model. The percentages of equilibria for each individual marker was obtained by summing subpopulations for their specific marker expression. Thus, to obtain the final equilibrium of CD133 marker, percentages of $CD133^+$ or $CD133^-$ subpopulations were combined. Finally, we compared the marker equilibria obtained from dependence and independence calculations. If the two equilibria were similar, then the markers were independent from each other. In contrast, differences in calculated equilibria suggested that the markers were dependent on the expression of the other markers.

The analysis was realized with the help of Thomas Buder (Zentrum für Informationsdienste und Hochleistungsrechnen (ZIH), Technische Universität Dresden, Dresden, Germany and Fakultät Informatik / Mathematik, Hochschule für Technik und Wirtschaft Dresden, Dresden, Germany Technische Universität Dresden).

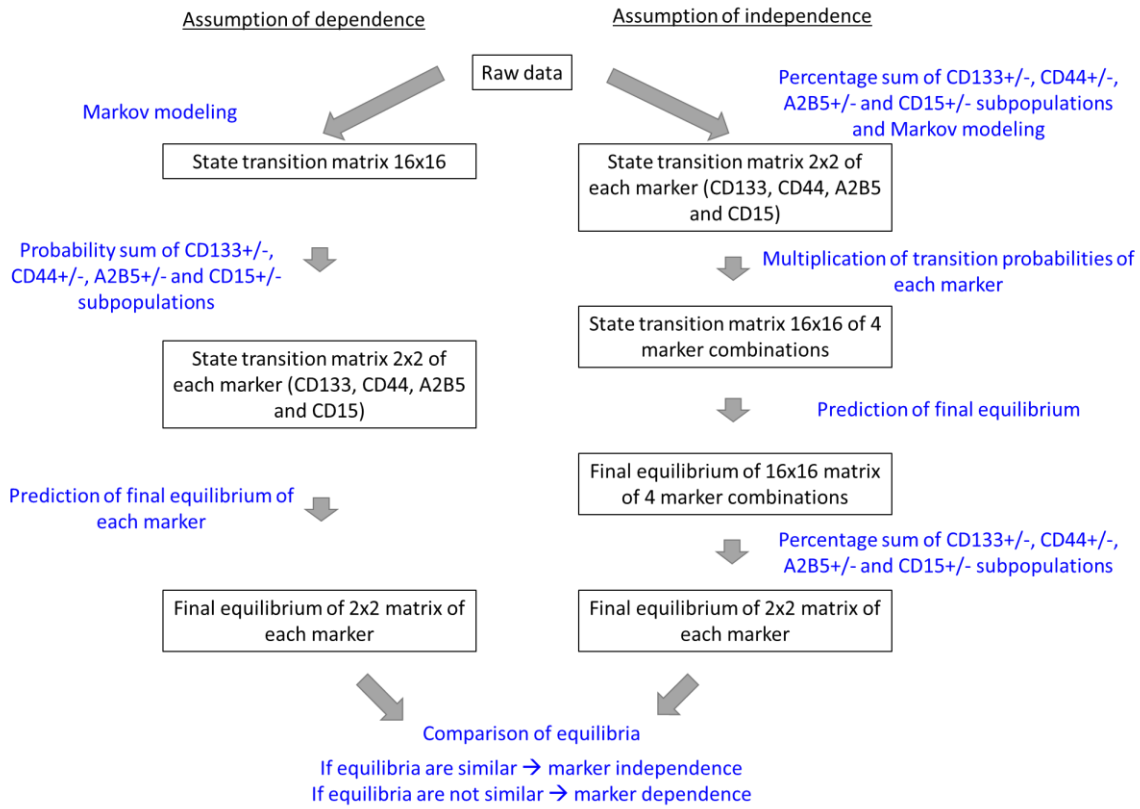

Figure 53: Calculation scheme for marker dependency. Flowchart displays mathematical methodology for marker dependence analysis. Boxes represent obtained data and in blue the mathematical calculations.

Annex 3: Single cell RNA-seq using Drop-seq

a. Mircrofluidics Fabrication

Subsequent procedure and analysis was performed by Dr. Suresh Kumar Poovathingal from the Luxembourg Centre for Systems Biomedicine at University of Luxembourg (Alexander Skupin Group). Microfluidics devices were fabricated using a previously published design (Macosko et al., 2015). Softlithography was performed using SU-8 2050 photoresist (MicroChem) on 4" silicon substrate to obtain a feature aspect depth of 100mm. After overnight silanization (using Chlorotrimethylsilane, Sigma), the wafer masks were used for microfluidics fabrication. Drop-seq chips were fabricated using a silicon based polymerization chemistry, with the previously published protocol (Mazutis et al., 2013). Briefly, Polydimethylsiloxane (PDMS) base and crosslinker (Dow Corning), was mixed at the 10:1 ratio, mixed and degassed before pouring the mix onto the Drop-seq master template. PDMS was cured on the master template, at 80^0C for 2h. After the incubation and cooling, the PDMS slabs were cut and the inlet/outlet ports were punched with 1.25mm biopsy punchers (World Precision Instruments). The PDMS monolith was plasma-bonded to a clean microscopic glass slide using Harrick plasma cleaner. Immediately after pairing the plasma-treated surfaces of the PDMS monolith and the glass slide, the flow channels of the Drop-seq chip was treated for hydrophobicity treatment using 1H,1H,2H,2H-Perfluorodecyltrichlorosilane (in 2% v/v in FC-40 oil; Alfa Aeser/Sigma). After 5 minutes of treatment, excessive silane was blown out through the inlet/outlet ports. The chip was further incubated at 80°C for 15 minutes.

b. Single cell droplet suspension

The experiments performed align with the original Drop-seq protocol (Macosko et al., 2015). Minor changes relevant to this work are described below. Pre-fabricated Drop-seq chip was used for the emulsion generation. Specially synthesized barcoded beads (Chemgenes corp.) were co-encapsulated with the cells inside the droplet containing optimized lysis reagent (for reagents see (Macosko et al., 2015)). The cellular mRNA was captured on beads via the barcoded oligo (dT) handles synthesized on the surface. To ensure low proportion of two or more beads co-encapsulating within a single droplet, the optimal bead concentration of 200 beads/ml was applied. The beads were prepared in the Drop-seq Lysis buffer medium.

2ml of the cell and the bead suspensions were loaded into 3ml syringes (BD Bioscience). Due to the stark density difference of the beads, a micro-stirrer was used (VP scientific). The QX 200 carrier oil (Bio-rad) was used as a continuous phase in the droplet generation. The oil was loaded into a 20ml syringe (BD Bioscience). For the droplet generation, 3.6ml/h

and 13ml/h were used for the dispersed and continuous phases, respectively, using KD scientific Legato syringe pumps. This generated droplets of the diameter ~115µm (~ 1nl volume). After the stabilization of the droplet formation, the droplet suspension was collected into a 50ml Falcon tube. The collection of the emulsion was carried out until 1µl of the single cell suspension was dispensed. The droplet consistency and stability was evaluated in a bright-field inverted microscope using an INCYTO C-Chip Disposable Hemacytometer (ThermoFisher Scientific). The bead occupancy within the droplets was carefully monitored avoid the multiple bead occupancy.

The subsequent steps of the droplet breakage, bead harvesting, reverse transcription and the exonuclease treatment was carried out in accordance with the earlier work (Macosko et al., 2015). The RT buffer contained: 1x Maxima RT buffer, 4% Ficoll PM-400 (Sigma-Aldrich), 1µM dNTPs (ThermoFisher Scientific), 1U/ml RNase Inhibitor (Lucigen), 2.5µM Template Switch Oligo (Macosko et al., 2015), and 10U/ml Maxima H-RT (ThermoFisher Scientific). Post Exo-I treatment, the bead counts were estimated using INCYTO C-Chip Disposable Hemacytometer, and 10,000 beads were aliquoted in 0.2ml Eppendorf PCR tubes. PCR mix was dispensed in a volume of 50µl using 1x Hifi HotStart Readymix (Kapa Biosystems) and 0.8mM Template-Switch-PCR primer. The thermocycling program for the PCR amplification was adapted from the previous work, except for the final PCR cycles:

1 cycle:	95°C – 3 minutes
4 cycles:	98°C – 20 seconds
	65°C – 45 seconds
	72°C – 3 minutes
10 cycles:	98°C – 20 seconds
	67°C – 20 seconds
	72°C – 3 minutes
1 cycle:	72°C – 5 minutes

Post PCR amplification, the libraries were purified with 0.6x Agencourt AMPure XP beads (Beckman Coulter), in accordance with the manufacturer's protocol. Finally, the purified libraries were eluted in 20µl RNase/DNase-free molecular grade water. Prior to the sequencing library preparation, the quality and the concentration of the libraries were assessed using BioAnalyzer High Sensitivity Chip (Agilent Technologies).

c. NGS preparation for Drop-seq libraries

The 3' end enriched cDNA libraries were prepared by the tagmentation reaction of 600 pg cDNA library using the standard Nextera XT tagementation kit (Illumina). The reactions were performed according to the manufacturer's instruction, except for the 400 nM primer sets of: Primer 1

(AATGATACGGCGACCACCGAGATCTACACGCCTGTCCGCGGAAGCAGTGGTA TCAACGCAGAG T*A*C) and Primer 2 (N703: CAAGCAGAAGACGGCATACGAGA TTTCTGCCTGTCTCGTGGGCTCGG for the NCH644 subpopulation 6 and N709: CAAGCAGAAGACGGCATACGAGATAGCGTAGCGTCTCGTGGGCTCGG for NCH644 subpopulation 2, NCH644 and NCH421k). The PCR amplification cycling program used was:

1 cycle:	95°C – 30 seconds
14 cycles:	95°C – 10 seconds
	55°C – 30 seconds
	72°C – 30 seconds
1 cycle:	72°C – 5 minutes

The libraries were purified twice to reduce the primers and short DNA fragments, with 0.6x Agencourt AMPure XP beads (Beckman Coulter) followed by 1x Agencourt AMPure XP beads, in accordance with the manufacturer's protocol. Finally, the purified libraries were eluted in 15µl molecular grade water. The quality and quantity of tagmented cDNA library was evaluated using BioAnalyzer High Sensitivity DNA Chip. The average size of the tagemented libraries prior to sequencing was between 400-700 bases pairs.

Purified Drop-seq cDNA libraries were sequenced using Illumina NextSeq 500. Sequencing protocol recommended by the manufacturer was followed, except for 6pM of custom primer (GCCTGTCCGCGGAAGCAGTGGTATCAACGCAGAGTAC) applied for priming of read 1. Paired end sequencing was performed with the read 1 of 20 bases (covering the random cell barcode 1-12 bases and the rest 13-20 bases of random unique molecular identifier (UMI)) and read 2: 50 bases of the genes.

d. Bioinformatics processing and data analysis

The FASTQ files were assembled from the raw BCL files using Illumina's bcl2fastq converter and ran through the FASTQC codes (Babraham bioinformatics; https://www.bioinformatics.babraham.ac.uk/projects/fastqc/) to check for the consistency in the library qualities. The monitored quality assessment parameters were: a.) quality per base sequence (especially for the read 2 of the gene); b.) per base N content; c.) per base sequence content and d.) overrepresented sequences. The libraries, which showed significant deviation were re-sequenced. The FASTQ files were then merged and converted to binaries using PICARD's fastqtosam algorithm.

We have applied the Drop-seq bioinformatics pipeline (Macosko et al., 2015). The sequencing reads were converted to digital gene expression matrix (DGE). To normalize for the transcript loading between the beads, the averaged normalized expression levels ($\log_2$(TPM+1)) were calculated. To distinguish between the beads exposed to the cell and

empty beads, a cumulative function of the total number of transcripts per barcode was plotted. Then, a thresholding was applied empirically on the resulting “knee plot” to estimate the beads exposed to the cell content. To filter the poor-quality reads and cells reporting low transcript content, the following threshold filters were used: only cells that expressed at least 1500 genes and, only genes which were expressed in at least 20 cells were considered for further analysis. The average number of UMI-collapsed transcripts per cell was 5970 corresponding to the 2430 genes detected per cell on average.

To remove batch effect, we used independent component analysis ICA (R fastICA package) decomposing the original expression matrix into a product of statistically independent signals and weight matrices:

$$X_{nm} = S_{nk} \times M_{km} ,$$

where X_{nm} is the log-transformed count matrix for n genes and m cells, S_{nk} is a matrix of k independent components and M_{km} is the weight matrix for each component over m cells. Stability of the ICA decomposing was tested by 100 runs of ICA. The log-transformed count matrix was decomposed using 8 independent components. The optimal number of the components was selected by minimizing the correlation between rows of weight matrix. We observed that the weight of component #7 was strongly linked to experimental batch. In accordance with (Biton et al., 2014), this component was suppressed by setting its weight ($M_{7,i}$, where i = 1..m) to 0, and the normalized data were recovered by matrix multiplication of the components by their weights.

Estimation of the highly variable genes and principal component reduction and tSNE dimensionality reduction was implemented using SEURAT R package (http://satijalab.org/seurat/) or the R package *Rtsne* with an initial PCA, a *perplexity* of 40 and a *learning rate* of 200 (5000 iterations) (https://github.com/jkrijthe/Rtsne). For reproducibility with the original algorithm, the *theta* value has been set to zero.

Correlation coefficient has been calculated between each cell after filtering using the Pearson method; the mean value is represented for each group/subpopulation/fraction. Differential expression analysis was performed using DESeq2 package of R (Love et al., 2014). Here the raw integer counts were used for consistency with the algorithm requirements. Centering of the gene expression value, was performed by obtaining the relative expression levels, by subtracting the average expression value ($\log_2$(TPM+1)) of each gene from all the cells of the gene expression matrix. For cell cycle analysis we have applied two prominent gene expression programs of the G1/S (100 genes) and G2/M phases (133 genes) (Whitfield et al., 2002), shown to overlap in the two programs (Tirosh et al., 2016a, Macosko et al., 2015).

Due to the sparsity of the single cell RNAseq data, the expression data for each cell cycle phase was refined by evaluating the correlation data between each of the genes in the scRNAseq data with the average gene expression values of all the genes involved in the respective cell cycle program (G1/S & G2/M), and including all the genes with high correlation value ($R^2 > 0.3$; $P_{val} < 0.05$). Hierarchical clustering of the data demonstrates that some cells are cycling with high relative expression of most of the genes included in either of the cell cycle program or both of the programs, while other cells shows basal expression for most of these genes (data not shown). The biaxial plot of G1/S and G2/M programs is the average score of all the genes involved in the respective cell cycle programs. It further represents the expression value of different genes of interest by mapping the expression value onto the respective cells.

Annex 4: Flow cytometric gating strategy for the analysis of tumor cells in PDXs. GBM cells were distinguished from debris using forward (FSC) and side (SSC) scatters (1), followed by cell doublet and aggregate elimination (FSC-A/FSC-H) (2). Dead cells were recognized as positive for dead cell marker (3). Single viable cells were discriminated by human CD90 positive cancer and human CD90 negative stromal cells (4).

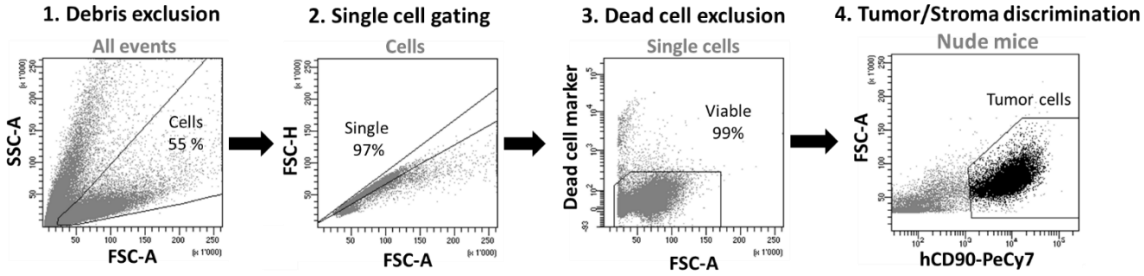

Annex 5: Flow cytometric analysis of 8 cell surface markers in 11 GBM PDXs. Negative, low, positive and high positive cells were categorized based on their mean fluorescence intensity (MFI) ('-', MFI = negative control; 'low', MFI < 10x negative control; '+', 10x < MFI < 100x negative control; '++', MFI > 100x negative control). All 8 tested markers demonstrated high variability between PDXs (e.g. green square) whereas their expression was uniform within a PDX. Only T238 showed a variable expression profile in CD195 (delineated by blue square).

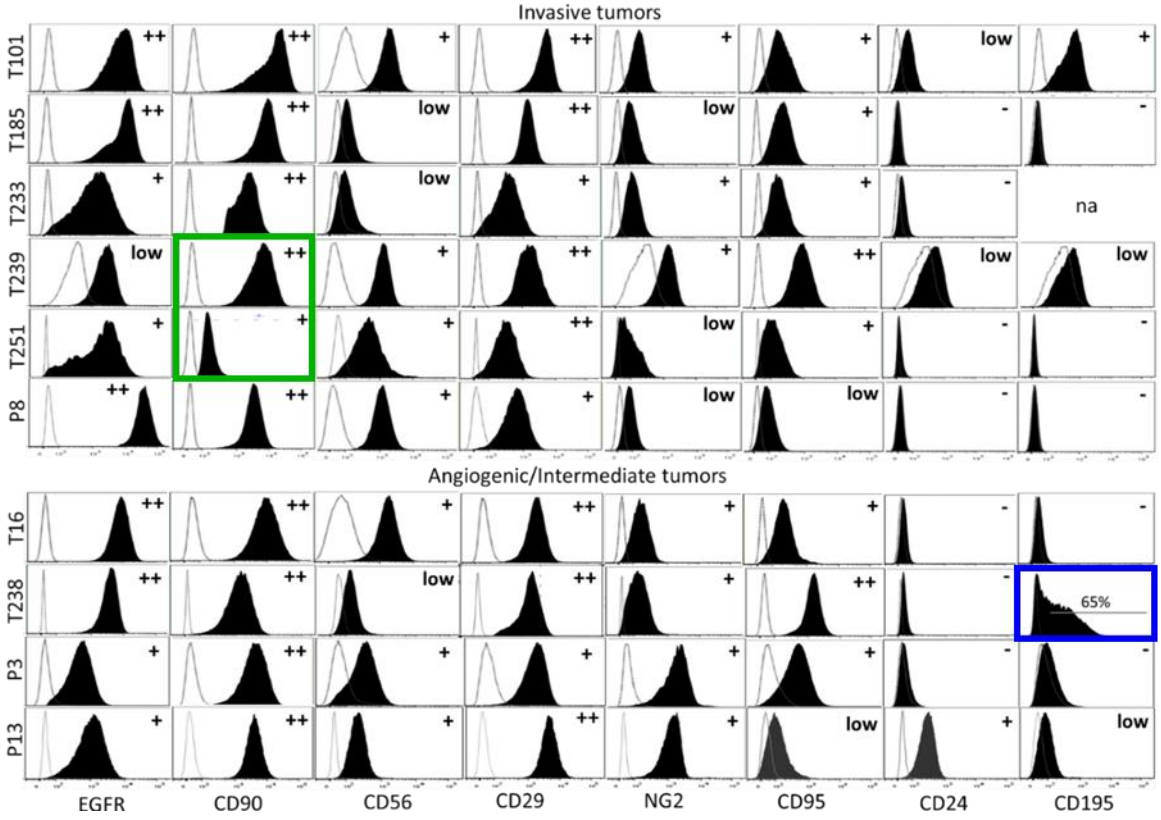

Annex 6: Statistical analysis of CSC-associated phenotypic heterogeneity. Statistical analysis was performed with the Student t-test with a Bonferroni multiple-significance-test correction for 16 phenotypic states. Differences between proportion of phenotypic states (PSs) in different conditions, treatments and FACS-sorted subpopulations and vs. control cells (CTR = control cells cultures in normoxia; CTR_H = control cells cultured 60 days in hypoxia) are presented if p-value *<0.05; **<0.01; ***<0.001.

a. Phenotypic analysis of NCH644 cultures upon TMZ treatment. TMZ treatment was performed for 16h, 2 and 7 days (NCH644 TMZ data from figure 24.a).
b. Phenotypic analysis of NCH421k cultures upon TMZ treatment. TMZ treatment was performed for 16h, 2 and 7 days (NCH421k TMZ data from figure 24.b).
c. Phenotypic analysis of NCH644 cultures upon hypoxic cultures. Hypoxia (H) was applied for 16h, 2, 7 and 60 days (NCH644 Hypoxia data from figure 43.a).
d. Phenotypic analysis of NCH421k cultures upon hypoxic cultures. Hypoxia (H) was applied for 16h, 2 and 7 days (NCH421k Hypoxia data from figure 43.b).
e. Phenotypic analysis between NCH644 cultures recultured in normoxia for 7 (7d renorm) and 14 days (14d renorm) after 7 days (7d h) in hypoxic cultures. Additionally, phenotypic proportions of all conditions were compared to NCH644 in normoxia (CTR) (NCH644 Reversibility from H to N data from figure 51).
f. Phenotypic analysis of NCH644 cultures upon differentiation (Diff)and de-differentiation (De-Diff) in normoxic (N) and hypoxic (H) conditions. 2D cultures in stem cell medium were used as additional control (2D) (NCH644 Differentiation data from figure 54.a).
g. Phenotypic analysis of NCH421k cultures upon differentiation (Diff)and de-differentiation (De-Diff) in normoxic (N) and hypoxic (H) conditions. 2D cultures in stem cell medium were used as additional control (2D) (NCH421k Differentiation data from figure 54.b).
h. Phenotypic analysis of NCH644 cultures upon xenografting (X). Phenotypic equilibrium of FACS-sorted subpopulations (P2, P6, P11, P15) was compared to control cultures in normoxia in vitro (CTR) and bulk NCH644 xenografted in vivo (CTR_X) (NCH644 Subpopulation Xenografting data from figure 56.f).
i. Phenotypic analysis of NCH644 cultures upon xenografting (X). Phenotypic equilibrium of xenografted NCH644 tumor cells recultured in vitro was compared to control cultures in normoxia in vitro (CTR) and bulk NCH644 xenografted in vivo (CTR_X) (NCH644 Xenografting data from figure 57.b).
j. Phenotypic analysis of NCH421k cultures upon xenografting (X). Phenotypic equilibrium of xenografted NCH421k tumor cells recultured in vitro was compared to control cultures in normoxia in vitro (CTR) and bulk NCH644 xenografted in vivo (CTR_X) (NCH421k Xenografting data from figure 57.d).

a. NCH644 TMZ	Conditions/Phenotypic states	P1	P2	P3	P4	P5	P6	P7	P8	P9	P10	P11	P12	P13	P14	P15	P16		CD133+/-	CD44+/-	A2B5+/-	CD15+/-
	CTR vs. 16h_TMZ				*	**				*			*						*	***		
	CTR vs. 2d_TMZ				*															***		
	CTR vs. 7d_TMZ				***					**			**							**		*
	16h_TMZ vs. 2d_TMZ																					
	16h_TMZ vs. 7d_TMZ													**							*	*
	2d_TMZ vs. 7d_TMZ													**								*
b. NCH421k TMZ	Conditions/Phenotypic states	P1	P2	P3	P4	P5	P6	P7	P8	P9	P10	P11	P12	P13	P14	P15	P16		CD133+/-	CD44+/-	A2B5+/-	CD15+/-
	CTR vs. 16h_TMZ																			*		
	CTR vs. 2d_TMZ		*				*													**		
	CTR vs. 7d_TMZ		***						**	**	***	*	*				***		***	*	***	**
	16h_TMZ vs. 2d_TMZ																					
	16h_TMZ vs. 7d_TMZ		***						***	**	***	*	*		*		***		***		***	***
	2d_TMZ vs. 7d_TMZ	*	***						**	*	***						***		***		**	**
c. NCH644 Hypoxia	Conditions/Phenotypic states	P1	P2	P3	P4	P5	P6	P7	P8	P9	P10	P11	P12	P13	P14	P15	P16		CD133+/-	CD44+/-	A2B5+/-	CD15+/-
	CTR vs. 16h_H																					
	CTR vs. 2d_H														***							
	CTR vs. 7d_H		***	**			**	***		***	***			**	***				*		***	***
	CTR vs. 60d_H		***		***	***	**	***		***	***	**	***		***		**		***	**	*	***
	16h_H vs.2d_H																					
	16h_H vs. 7d_H	**		***				*		*				*							***	**
	16h_H vs. 60d_H					***							*		*		**		**	**		**
	2d_H vs. 7d_H			**																		
	2d_H vs. 60d_H					*											**		**	*	*	*
	7d_H vs. 60d_H			*		***					*	*			**		***		**	**	***	
d. NCH421k Hypoxia	Conditions/Phenotypic states	P1	P2	P3	P4	P5	P6	P7	P8	P9	P10	P11	P12	P13	P14	P15	P16		CD133+/-	CD44+/-	A2B5+/-	CD15+/-
	CTR vs. 16h_H		*				**			*	*	**							*	*		
	CTR vs.2d_H		*				*			*		**								**		
	CTR vs. 7d_H		*				*					*								*		
	16h_H vs.2d_H																					
	16h_H vs. 7d_H																					
	2d_H vs. 7d_H																					

e. NCH644 Reversibility from H to N	Conditions/Phenotypic states	P1	P2	P3	P4	P5	P6	P7	P8	P9	P10	P11	P12	P13	P14	P15	P16		CD133+/-	CD44+/-	A2B5+/-	CD15+/-
	CTR vs 7d h		***	**			**	***		***	***			**	***				*		***	***
	CTR vs 7d renorm									**									**			*
	CTR vs 14d renorm			**			*												**			
	7d h vs 7d renorm							*											**	*		
	7d h vs 14d renorm		***	***			**	***		*	***		***	*	***				***	*		
	7d renorm vs 14d renorm												*						***	*		
f. NCH644 Differentiation	Conditions/Phenotypic states	P1	P2	P3	P4	P5	P6	P7	P8	P9	P10	P11	P12	P13	P14	P15	P16		CD133+/-	CD44+/-	A2B5+/-	CD15+/-
Normoxia	CTR vs 2D_N		**	*			***	***		***	***		**	***	***				**		***	***
	CTR vs De-2D _N	***	***					***		***	***			**	***				**	**		**
	2D_N vs De-2D_N																					
	CTR vs Diff_N	***	***	***	***	***	***		***	*		*				***	***		***	***	***	**
	CTR vs De-Diff_N	***	***	***	***		***		***			*	*	*		***	**		***	***	**	***
	Diff_N vs De-Diff_N	***	***	***	***	**	**		**								***		***		**	
Hypoxia	CTR vs 2D_H	***	***					***	*	***	***									***	*	
	CTR vs De-2D _De-H		**	***	**	**														**		*
	2D_H vs De-2D_De-H								*												**	
	CTR vs Diff_H	***	***	***	***					***	*	***	**			*	**		***	***		*
	CTR vs De-Diff_De-H	***	*	**						***	*	*				*			*	***		
	Diff_H vs De-Diff_De-H	**	*	*	**												**		**	***		*
g. NCH421k Differentiation	Conditions/Phenotypic states	P1	P2	P3	P4	P5	P6	P7	P8	P9	P10	P11	P12	P13	P14	P15	P16		CD133+/-	CD44+/-	A2B5+/-	CD15+/-
Normoxia	CTR vs 2D_N			**	***	**		***	***				***				***				***	*
	CTR vs De-2D _N			***	***	*		***	***								*				***	
	2D_N vs De-2D_N									*			*						**			*
	CTR vs Diff_N		***	***	***	***		***	***	***		***	***	***	***	***	***		***	***	***	***
	CTR vs De-Diff_N				***			**	***				***			**	***		**		***	
	Diff_N vs De-Diff_N		***	*		**	**	*	**	***		**		**	**	*	**		***	***	**	***

h. NCH421k Differentiation	Conditions/Phenotypic states	P1	P2	P3	P4	P5	P6	P7	P8	P9	P10	P11	P12	P13	P14	P15	P16		CD133+/-	CD44+/-	A2B5+/-	CD15+/-
Hypoxia	CTR vs 2D_H	*	*	***	***	**		***	***												***	***
	CTR vs De-2D _De-H			***	***			**	***				*								***	
	2D_H vs De-2D_De-H	***		*								**			*				**		*	***
	CTR vs Diff_H		***	***	***	***		***	***			***	***			**	***			***	***	**
	CTR vs De-Diff_De-H			**	***			***	***				***				***				***	
	Diff_H vs De-Diff_De-H		***	*	*	**	*	*	*	***	*	*	*	**	***	*	**		***	***	**	***
i. NCH644 Subpopulation Xenografting	Conditions/Phenotypic states	P1	P2	P3	P4	P5	P6	P7	P8	P9	P10	P11	P12	P13	P14	P15	P16		CD133+/-	CD44+/-	A2B5+/-	CD15+/-
	CTR vs CTR_X	**	**	**	*	**	***	*	**	**		***		**	*				***	***	*	***
	CTR vs P2 _X			***		**	***	*	**					**	*				**	***		
	CTR vs P6_X			**	*	**	**	*	**	*				**	**				**	***	**	*
	CTR vs P11_X	**		**	*	*	***	*	**	***		**			**				***	***		**
	CTR vs P15_X	**	*	**	*	*	***	*	*	***		***		*	*				***	***		***
	CTR_X vs P2 _X																					
	CTR_X vs P6_X											*									**	
	CTR_X vs P11_X																					
	CTR_X vs P15_X																					
	P2_X vs P6_X																					
	P2 _Xvs P11_X																					
	P2 _Xvs P15_X																					
	P6_X vs P11_X																					
	P6 _Xvs P15_X																					
	P11_X vs P15_X																					
j. NCH644 Xenografting	Conditions/Phenotypic states	P1	P2	P3	P4	P5	P6	P7	P8	P9	P10	P11	P12	P13	P14	P15	P16		CD133+/-	CD44+/-	A2B5+/-	CD15+/-
	CTR vs CTR_X	**	**	**	*	**	***	*	**	**		***		**	*				***	***	*	***
	CTR vs re-in vitro	***					**			***	**	**			**				***	**	***	***
	CTR_X vs re-in vitro	***	***	**	**	***	**	***	***	*		***				**	*		***	***	***	**
k. NCH421k Xenografting	Conditions/Phenotypic states	P1	P2	P3	P4	P5	P6	P7	P8	P9	P10	P11	P12	P13	P14	P15	P16		CD133+/-	CD44+/-	A2B5+/-	CD15+/-
	CTR vs X		**	***	***					***		***	***						***		***	***
	CTR vs De-X		**								***								***			
	X vs De-X			***	***		*		**		*	***	***		*					***	***	***

Annex 7: Statistical analysis of phenotypic state transitions of FACS-sorted subpopulation upon time. Statistical analysis was performed with the Student t-test with a Bonferroni multiple-significance-test correction for 16 phenotypic states. Statistical differences between proportion of phenotypic states (PSs) in different FACS-sorted subpopulations vs. control cells (CTR = control cells cultures in normoxia; CTR_H = control cells cultured 60 days in hypoxia) at the same time point are presented if pvalue *<0.05; **<0.01; ***<0.001. Statistical results in **a.** displays multipotency test in normoxia whereas **b.** shows multipotency test in hypoxia.

a. Multipotency in normoxia

20d	Conditions/Phenotypic states	P1	P2	P3	P4	P5	P6	P7	P8	P9	P10	P11	P12	P13	P14	P15	P16
	CTR vs P1						***	**		***				***			
	CTR vs P2					***		*		***							
	CTR vs P3					***		**						***			
	CTR vs P4	*				***		**		***				***			
	CTR vs P5		***							***							
	CTR vs P6	***								***				***			
	CTR vs P7	**								***							
	CTR vs P8	***								***	***		***	***			
	CTR vs P9			**			***	**	***								
	CTR vs P10	*				**	*	*									
	CTR vs P11			***		*	***	**	***								
	CTR vs P12					**											
	CTR vs P13		***	***	*			**	*					*			
	CTR vs P14	***		***	**	**				***							
	CTR vs P15	***	***	***	*												
	CTR vs P16	**		*						*							
30d	Conditions/Phenotypic states	P1	P2	P3	P4	P5	P6	P7	P8	P9	P10	P11	P12	P13	P14	P15	P16
	CTR vs P1						*			**	***			**			*
	CTR vs P2					*											
	CTR vs P3		**			**			**								**
	CTR vs P4									*							
	CTR vs P5	**	***		***			**					**	**			**
	CTR vs P6	***	***	*						*							
	CTR vs P7	*	***	**	***			**				*					
	CTR vs P8	***	***		**			*		***	***	**	***	*			
	CTR vs P9		***				***										
	CTR vs P10																
	CTR vs P11	***	***			**	***		**		**	*			***		
	CTR vs P12					*											
	CTR vs P13	***	***	***	***		***		***				*	*		***	
	CTR vs P14	***	***	***	***					***							
	CTR vs P15	***	***	***	***												
	CTR vs P16	*		***													
70d	Conditions/Phenotypic states	P1	P2	P3	P4	P5	P6	P7	P8	P9	P10	P11	P12	P13	P14	P15	P16
	CTR vs P1						*			***	***	***	***		***		*
	CTR vs P2									***	***		***				**
	CTR vs P3						***		***	**	***		***		***		**
	CTR vs P4									***	***	***		***		*	**
	CTR vs P5								***	**	***	*	***		***		***
	CTR vs P6			***						***	***	***	***		***		
	CTR vs P7			***								***					**
	CTR vs P8	*		***						***	***	***	***	**	***		
	CTR vs P9				**		***		***				***		***		**
	CTR vs P10														***		
	CTR vs P11				*	***	***		***					**	***	*	**
	CTR vs P12			**											***		
	CTR vs P13		***				***		***								
	CTR vs P14			***													
	CTR vs P15	*		***	**												
	CTR vs P16																

b. Multipotency in hypoxia

Conditions/Phenotypic states	P1	P2	P3	P4	P5	P6	P7	P8	P9	P10	P11	P12	P13	P14	P15	P16
CTR vs CTR_H		***		***	*		**		**	***	**	***		***		**
CTR vs P1		***				***		*	***	***	***	***	***	***	**	***
CTR vs P2		***					**		***	***	***	***	***	***	*	**
CTR vs P3		***	***			***		**	***	***	***	***	***	***	*	**
CTR vs P4	***	***					**		***	***	***	***	***	***		**
CTR vs P5		***				**	***		***	***	***	***	***	***		
CTR vs P6	***	***					**		***	***	***	***	***	***	*	
CTR vs P7	**	***		**			***		***	***	***	***	***	***		**
CTR vs P8	***	***					***		***	***	***	***	***	***		**
CTR vs P9		***		***	***	***		***		***	***	***		**		**
CTR vs P10		**	***	**		**			***	**	**	***	**	***		*
CTR vs P11		*				***		***	***	***	***	***		***		**
CTR vs P12		***		**			*		***	**	***	***	*	***		*
CTR vs P13		***	**	***	***		*		***	***	***	***		**		*
CTR vs P14	***	***	*	***	*		*			***	***	***				
CTR vs P15	*	***	**	***	**		*			***	**	***		***		**
CTR vs P16	***	***	***	***	*		*		***	***	***	***				
CTR_H vs P1																
CTR_H vs P2																
CTR_H vs P3			**		*		**									
CTR_H vs P4	*															
CTR_H vs P5							*									
CTR_H vs P6	**															
CTR_H vs P7	*						*									
CTR_H vs P8	**						*									
CTR_H vs P9																
CTR_H vs P10			**													
CTR_H vs P11					*											
CTR_H vs P12																
CTR_H vs P13																
CTR_H vs P14																
CTR_H vs P15																
CTR_H vs P16	*															

Annex 8: Statistical analysis of phenotypic state transitions of FACS-sorted subpopulation upon 4 consecutive passages in self-renewal analysis. Statistical analysis was performed with the Student t-test with a Bonferroni multiple-significance-test correction for 16 phenotypic states. No statistical differences were detected between the same subpopulations at different passages. Statistical differences between proportion of phenotypic states (PSs) in different subpopulations and control cells (CTR = control cells cultures in normoxia; CTR_H = control cells cultured 60 days in hypoxia) at the same passage is presented if pvalue < 0.05;*<0.05; **<0.01; ***<0.001. NCH644 exp corresponds to FACS-sorted bulk NCH644 cells w/o discrimination of 16 subpopulations. Statistical results in **a.** displays self-renewal test in normoxia whereas **b.** shows self-renewal test in hypoxia.

a. Self-renewal in normoxia

Passage 1	Conditions/Phenotypic states	P1	P2	P3	P4	P5	P6	P7	P8	P9	P10	P11	P12	P13	P14	P15	P16
	CTR vs NCH644 exp																
	CTR vs P1	*					***		**						**		
	CTR vs P2		*		**					**					**		
	CTR vs P3	*					***		**						**		
	CTR vs P4				*					***		*					
	CTR vs P5					*											
	CTR vs P6									***		*					
	CTR vs P7			**		*					*		*				
	CTR vs P8	**								***		**					
	CTR vs P9				**		***		**	**				*	*		
	CTR vs P10		*		*	*											
	CTR vs P11						**		**						**		
	CTR vs P12																
	CTR vs P13		*	***	**				**	**			*	**			
	CTR vs P14	***		***								*					*
	CTR vs P15																
	CTR vs P16	**		***											***		
Passage 2	Conditions/Phenotypic states	P1	P2	P3	P4	P5	P6	P7	P8	P9	P10	P11	P12	P13	P14	P15	P16
	CTR vs NCH644 exp																
	CTR vs P1	**					***		**								
	CTR vs P2																
	CTR vs P3									***							
	CTR vs P4						**			***		*					
	CTR vs P5		**		*	**					*						
	CTR vs P6									***					*		
	CTR vs P7	**	**							***	*				**		
	CTR vs P8	**						**	*	***	*	*					
	CTR vs P9		**		*		***		**			***		*			
	CTR vs P10									**							
	CTR vs P11		*		*	*	***		**			***			**		
	CTR vs P12																
	CTR vs P13		**	**	*		**		**		*			*			
	CTR vs P14	***	*							*						**	
	CTR vs P15	**	**		*		**				*					**	
Passage 3	Conditions/Phenotypic states	P1	P2	P3	P4	P5	P6	P7	P8	P9	P10	P11	P12	P13	P14	P15	P16
	CTR vs NCH644 exp						*										
	CTR vs P1					**	**		*								
	CTR vs P2									*							
	CTR vs P3					*				*							
	CTR vs P4									***		*					
	CTR vs P5																
	CTR vs P6									***		*					
	CTR vs P7																
	CTR vs P8	*								***	*	*					
	CTR vs P9	**					***		*		*	*					
	CTR vs P10	*				**							*				
	CTR vs P11						**										
	CTR vs P12																
	CTR vs P13	**															
	CTR vs P14	***	**	*	*					**							
	CTR vs P15	**															
	CTR vs P16	**		*													
Passage 4	Conditions/Phenotypic states	P1	P2	P3	P4	P5	P6	P7	P8	P9	P10	P11	P12	P13	P14	P15	P16
	CTR vs NCH644 exp																
	CTR vs P1						***		**					*	**		
	CTR vs P2		*		**	**	***		*	*				**	**		
	CTR vs P3			*		*	***		*					**	**		
	CTR vs P4									***		**					
	CTR vs P5		*						*		*						
	CTR vs P6									**							
	CTR vs P7									***	*	*	*				
	CTR vs P8	**		**						***	*	**	*				
	CTR vs P9					**	***		*								
	CTR vs P10			*													
	CTR vs P11		*				***		*								
	CTR vs P12									***							
	CTR vs P13		*		*	*	**		**								
	CTR vs P14	***	*	**												**	
	CTR vs P15	*		*										*			
	CTR vs P16	**															

b. Self-renewal in hypoxia

Passage 1	Conditions/Phenotypic states	P1	P2	P3	P4	P5	P6	P7	P8	P9	P10	P11	P12	P13	P14	P15	P16
	CTR vs NCH644 exp									**		*		*			
	CTR vs CTR_H		***		***	*		**		**	***	**	***		***		**
	CTR vs P1	*		**			***		**	**		*		**	**		
	CTR vs P2					*				***				**	**		
	CTR vs P3						***		*	***		*		**	**		
	CTR vs P4									***	*	*		**	**		
	CTR vs P5					**				***		*	*		*		
	CTR vs P6									***	*	**	**	*			
	CTR vs P7									***	*	**	**				
	CTR vs P8	*		**						***	*	**	*	**	*		
	CTR vs P9	**			*		***		**	**							
	CTR vs P10								*			*					
	CTR vs P11			*			**		**	**					**		
	CTR vs P12					*											
	CTR vs P13			**		*								***			
	CTR vs P14	**		***	*		*			***	*	**	**		*		
	CTR vs P15																
	CTR vs P16	**								***			*				
	CTR_H vs NCH644 exp		*					**			*						
	CTR_H vs P1			*				**					**				
	CTR_H vs P2		*		***			*			*		*				
	CTR_H vs P3																
	CTR_H vs P4												***				
	CTR_H vs P5																
	CTR_H vs P6		*														
	CTR_H vs P7				*												
	CTR_H vs P8		*														
	CTR_H vs P9							**		**							
	CTR_H vs P10							*									
	CTR_H vs P11				*			*			*		*				
	CTR_H vs P12							**									
	CTR_H vs P13							*						***			*
	CTR_H vs P14						*	*							*		
	CTR_H vs P15																
	CTR_H vs P16							*									
Passage 2	Conditions/Phenotypic states	P1	P2	P3	P4	P5	P6	P7	P8	P9	P10	P11	P12	P13	P14	P15	P16
	CTR vs NCH644 exp									***	*	*	*	*	**		
	CTR vs P1			**			***		*	***	*	*		**	**		
	CTR vs P2									***	*	*	**	**	**		
	CTR vs P3								*	***	*	*			**		
	CTR vs P4											*	*		*		
	CTR vs P5					*			*	***	*	**	*		**		
	CTR vs P6	*		**		*				***	*	**	**		**		
	CTR vs P7									***	*	*	**		**		
	CTR vs P8	**		***		*				***	*	**	**		**		
	CTR vs P9						**		**				**		*		
	CTR vs P10									**		*	*				
	CTR vs P11				*		**		**	**	*	*	*		**		
	CTR vs P12									**					*		
	CTR vs P13		*	***	*				*					**			
	CTR vs P14	***	**	***	*						*	*	**				
	CTR vs P15		**		*		***		**		*		**				
	CTR vs P16			*		**				***		**	**				
	CTR_H vs NCH644 exp												*				
	CTR_H vs P1		**	*				*									
	CTR_H vs P2							*									
	CTR_H vs P3																
	CTR_H vs P4		***		*												
	CTR_H vs P5																
	CTR_H vs P6																
	CTR_H vs P7																
	CTR_H vs P8																
	CTR_H vs P9							*									
	CTR_H vs P10							*									
	CTR_H vs P11							*									
	CTR_H vs P12																
	CTR_H vs P13													*			
	CTR_H vs P14							*									
	CTR_H vs P15																
	CTR_H vs P16																

Passage 3	Conditions/Phenotypic states	P1	P2	P3	P4	P5	P6	P7	P8	P9	P10	P11	P12	P13	P14	P15	P16
	CTR vs NCH644 exp									**	*	*	*		**		
	CTR vs P1	**		***			***		**	***		*			**		
	CTR vs P2			*						***	*	*		*	**		
	CTR vs P3						**		*	***	*	*			**		
	CTR vs P4					**				***	*	*	*		**		
	CTR vs P5		*			***				**	*	*	**				
	CTR vs P6	**	*	*		***				***	*	**	**				
	CTR vs P7		**		*		**			**	*	*	**		**		
	CTR vs P8	**	*	*		*				***	*	**	**				
	CTR vs P9						**		*								
	CTR vs P10									**					*		
	CTR vs P11			*			***		**	**	*				**		
	CTR vs P12									**							
	CTR vs P13		**	**	*									*			
	CTR vs P14	***	**	***							*	*	**				
	CTR vs P15				*		**		**	*			*				
	CTR vs P16																
	CTR_H vs NCH644 exp												*				
	CTR_H vs P1			**				**					*				
	CTR_H vs P2										**		**				
	CTR_H vs P3																
	CTR_H vs P4																
	CTR_H vs P5																
	CTR_H vs P6																
	CTR_H vs P7																
	CTR_H vs P8																
	CTR_H vs P9																
	CTR_H vs P10																
	CTR_H vs P11																
	CTR_H vs P12																
	CTR_H vs P13																
	CTR_H vs P14							*									
	CTR_H vs P15							*		**							
	CTR_H vs P16																
Passage 4	Conditions/Phenotypic states	P1	P2	P3	P4	P5	P6	P7	P8	P9	P10	P11	P12	P13	P14	P15	P16
	CTR vs NCH644 exp						**		*	**			*		*		
	CTR vs P1	*		*			***		*	**		*		*	*		
	CTR vs P2									***		*	*		*		
	CTR vs P3	*		**			***		*	***		*	*	*	*		
	CTR vs P4	**	*	**		***		***		***		*	*		*		
	CTR vs P5								*	***		*	*		*		
	CTR vs P6	*				**		*		***		*	*	*	*		
	CTR vs P7						*		*	***		*	*		*		
	CTR vs P8	*		**		***	*		**	***		*	*				
	CTR vs P9						**										
	CTR vs P10									**							
	CTR vs P11	**		*		*	**		*	***		*	*	*	*		
	CTR vs P12		*		*					**		*	*		*		
	CTR vs P13		*	**	*		**		*						*		
	CTR vs P14	*		**									*				
	CTR vs P15		*	**	*				*				*	***			
	CTR vs P16											*	*				
	CTR_H vs NCH644 exp																
	CTR_H vs P1				*			*									
	CTR_H vs P2																
	CTR_H vs P3			*													
	CTR_H vs P4																
	CTR_H vs P5																
	CTR_H vs P6																
	CTR_H vs P7																
	CTR_H vs P8						*										
	CTR_H vs P9																
	CTR_H vs P10																
	CTR_H vs P11																
	CTR_H vs P12																
	CTR_H vs P13																
	CTR_H vs P14																
	CTR_H vs P15													**			
	CTR_H vs P16																

Annex 9: Submitted publication from thesis project

Stem cell-associated heterogeneity in Glioblastoma is a result of intrinsic tumor plasticity shaped by the microenvironment

AUTHORS

Anne Dirkse[1,2*], Anna Golebiewska[1*], Thomas Buder[3,4], Petr V. Nazarov[5], Arnaud Muller[5], Suresh Poovathingal[6], Nicolaas H.C. Brons[7], Sonia Leite[8], Nicolas Sauvageot[8], Dzjemma Sarkisjan[1], Mathieu Seyfrid[1], Sabrina Fritah[1], Daniel Stieber[1], Alessandro Michelucci[1,6], Christel Herold-Mende[9], Rolf Bjerkvig[1,10,11], Francisco Azuaje[5], Alexander Skupin[6], Andreas Deutsch[3], Anja Voss-Böhme[3, 4] and Simone P. Niclou[1,11].

*These authors contributed equally

AFFILIATIONS

[1]NorLux Neuro-Oncology Laboratory, Luxembourg Institute of Health, L-1526 Luxembourg, Luxembourg; [2]Faculty of Science, Technology and Communication, University of Luxembourg, L-4365 Esch-sur-Alzette, Luxembourg; [3]Zentrum für Informationsdienste und Hochleistungsrechnen, Technische Universität Dresden, D-01069 Dresden, Germany; [4]Fakultät Informatik / Mathematik, Hochschule für Technik und Wirtschaft Dresden, D-01069 Dresden, Germany; [5]Proteome and Genome Research Unit, Department of Oncology, Luxembourg Institute of Health, L-1526 Luxembourg, Luxembourg; [6]Luxembourg Centre for Systems Biomedicine, University of Luxembourg, L-4367 Belvaux, Luxembourg; [7]National Cytometry Platform, Department of Infection and Immunity, Luxembourg Institute of Health, L-1526 Luxembourg, Luxembourg; [8]Centre of Competence for Methodology and Statistics, Luxembourg Institute of Health, L-1445 Strassen, Luxembourg, [9]Division of Neurosurgical Research, Department of Neurosurgery, University of Heidelberg, 69120 Heidelberg, Germany; [10]NorLux Neuro-Oncology, Department of Biomedicine, University of Bergen, N-5019 Bergen, Norway, [11]KG Jebsen Brain Tumour Research Center, Department of Biomedicine, University of Bergen, N-5019 Bergen, Norway;

CORRESPONDING AUTHOR/ LEAD CONTACT

Simone P. Niclou, PhD

Luxembourg Institute of Health

Department of Oncology

NorLux Neuro-Oncology Laboratory

84, Val Fleuri, L- 1526 Luxembourg

tel. + 352-26970-273

fax.+ 352-26970-390

simone.niclou@lih.lu

SUMMARY

Cancer stem cells (CSCs) have been proposed to underlie the hierarchical organization of Glioblastoma (GBM) causing resistance to treatment, however the identity of CSCs in solid tumors remains largely elusive. Here we show that GBM cells expressing stem cell markers do not represent a clonal entity defined by distinct functional properties and transcriptomic profiles but rather a changing identity that any cell can adapt. Phenotypic heterogeneity arises from reversible cellular state transitions organised in a non-hierarchical manner where the final phenotypic equilibrium depends on microenvironmental conditions. While all subpopulations survive and adjust their phenotype, their adaptation speed may differ resulting in variable tumor growth rates *in vivo*. Thus stem cell-associated phenotypic heterogeneity is a result of a stochastic reversible cellular plasticity which impacts the outcome of functional assays. This intrinsic plasticity should be taken into account for future treatment strategies targeting cancer stem-like states.

KEYWORDS: Glioblastoma, Cancer stem cells, Intra-tumoral heterogeneity, Phenotypic plasticity, Markov modeling

INTRODUCTION

Glioblastoma (GBM) shows an extensive cellular heterogeneity which represents a major obstacle for effective therapies. Similar to many other cancers, tumor progression has been proposed to be maintained by cancer stem cells (CSC), postulated to be responsible for tumor recurrence and resistance to therapy. According to the CSC hypothesis 1. tumors follow a hierarchical cellular organization via a unidirectional differentiation process, 2. only a limited number of cells within the tumor have tumorigenic potential, and 3. CSCs are intrinsically different from their differentiated derivatives. Thus CSCs are thought to display stem cell properties and to be highly tumorigenic in experimental models *in vivo* (Vescovi et al., 2006*)*., This hypothesis has however been challenged, with growing evidence suggesting that CSCs do not constitute a defined cellular entity, but rather a cellular state adapting to microenvironmental cues, a concept which has major implications for treatment strategies (Meacham and Morrison, 2013).

Identification of CSCs is largely based on the expression of cell membrane antigens, which are amenable to targeted treatments (Scott et al., 2012). Although many studies in GBM rely on cell membrane markers for CSC isolation, such as CD133, CD15/SSEA, CD44, or A2B5 (Singh et al., 2004, Ogden et al., 2008, Tchoghandjian et al., 2010, Son et al., 2009, Anido et al., 2010), no single marker is able to solely define CSCs (Chen et al., 2010). There is controversy whether marker-expressing cells fulfill the functional criteria of bona fide CSCs (Beier et al., 2007, Piccirillo et al., 2009, Penuelas et al., 2009, Wang et al., 2008) and whether CSCs represent a quiescent or a proliferative subpopulation. These conflicting data could be explained by: 1. inter-patient heterogeneity preventing the identification of a universal CSC marker, 2. the presence of multiple CSC clones within each tumor, 3. a CSC signature based on multiple markers, or 4. strong phenotypic plasticity between cellular states. Recent data support the plasticity model over a strict hierarchical organization (Easwaran et al., 2014, Cabrera et al., 2015), pointing to a role of the microenvironment in shaping the phenotype. Indeed, GBM cells expressing stem cell markers are often attributed to specific tumor niches, such as perivascular and hypoxic areas (Lathia et al., 2011). However, it remains unclear whether the microenvironment selects for survival of specific CSCs or whether tumor cells adapt within new microenvironments.

Recent marker-independent analysis by single cell transcriptomics revealed stem cell-signatures to be associated with the most proliferative cells in IDH1-mutated gliomas (Tirosh et al., 2016) and stemness increasing with tumor grade (Venteicher et al., 2017). Such an organization was less clear in GBMs, which displayed a continuum of stemness profiles that were anti-correlated with the cell cycle (Patel et al., 2014) and a tendency towards an astrocytic program (Venteicher et al., 2017). Importantly, such data describe

heterogeneity at a given snapshot in time without considering the dynamic properties of tumor cells. Similarly, recent genetic barcoding suggesting an invariant proliferative hierarchy in GBM (Lan et al., 2017) did not address the evolution of phenotypic states over time.

Here we asked whether cancer cells with stem cell properties are a defined entity at the apex of a hierarchical organization or whether they represent one of many phenotypic states that cells can reversibly adapt in response to environmental cues. We find that phenotypic heterogeneity arises from intrinsic cancer cell plasticity via bidirectional non-hierarchical state transitions, tending towards a phenotypic equilibrium within a given environment. Therefore therapies targeting primarily a transitory stem cell state may ultimately be unsuccessful.

RESULTS

Strong inter-tumor heterogeneity but limited intra-tumor heterogeneity of putative CSC markers.

To determine CSC-associated marker expression in GBM we analyzed the gene expression of putative CSC markers in the GBM patient cohort of TCGA. Analysis of these patients indicated highly variable expression levels across tumors **(Fig. 1A)**. CSC marker genes were rarely associated with genetic or epigenetic alterations (**Fig. S1A-C**) and no significant correlations were detected between marker genes and main GBM drivers (**Fig. 1B**). As expected (Brown et al., 2015), several markers were enriched in previously defined transcriptional subgroups (**Table S1**).

Transcriptional profiles of bulk analysis in GBM patients represent mean values of tumor and stroma (Wang et al., 2017) and we have previously shown that cell membrane epitopes are present in both compartments (Golebiewska et al., 2013). Moreover, it is known that gene expression does not always correspond to the epitope presentation of CSC markers (Campos and Herold-Mende, 2011). Therefore, we used GBM patient-derived xenografts (PDXs) in eGFP-expressing mice (Niclou et al., 2008) to phenotype the tumor compartment in an unbiased manner (**Fig. S2A-B**) by multicolor flow cytometry. Similar to gene expression analysis, we observed highly variable epitope presentation of 12 CSC markers between tumors from different patients (**Fig. 1C**, **Fig. S3A-B)**. CD90 and CD29 were strongly positive in most GBM, whereas CD24 and CD195 were largely absent. In most cases, marker expression was homogeneous within one GBM while only 4/12 markers (CD133, CD44, CD15 and A2B5) showed relevant intra-tumoral heterogeneity (**Fig. 1C**), which would be expected from a bona fide CSC marker.

Genetically distinct clones adapt marker expression *in vivo*.

We have previously shown that genetic intra-tumor heterogeneity in GBM is also seen at the ploidy level, with pseudodiploid and aneuploid clones present in the same tumor (Stieber et al., 2014). Here, we find that genetically divergent clones can differ in the pattern of CSC-associated marker expression as shown for CD133 and A2B5 (**Fig. 1D**). We then FACS-purified pseudodiploid and aneuploid cells and separately implanted them in the mouse brain. Both clones changed marker expression *in vivo*, i.e., pseudodiploid tumors retained a heterogeneous A2B5 profile and increased CD133 (from 12.5 to 80%), while aneuploid tumors significantly increased A2B5 epitope presentation (from 4 to 65%) (**Fig. 1D**). This shows that CSC associated marker expression *in vivo* is adaptable following clonal selection, most probably reflecting an adaptation to the new microenvironment.

Heterogeneity in GBM stem-like cultures.

In order to correlate marker presentation with CSC functional properties, we turned to GBM stem-like cultures grown as 3D spheres. This allowed us to work with a genetically more homogeneous population (Stieber et al., 2014). Similar to patient biopsies and PDXs, stem-like cultures displayed remarkable inter-patient heterogeneity of CSC markers (**Fig. S3B**). CD133, CD44, CD15 and A2B5 showed again the strongest heterogeneity within the same culture. Focusing on these four markers, we performed multicolor flow cytometry, which led to the discrimination of 16 subpopulations (labeled P1-P16; **Fig 1E-F**, **Fig. S2C-D**). Some cultures contained a limited number of predominant subpopulations, while 4/7 cultures contained a substantial amount of all 16 subpopulations. The strong heterogeneity was present at the single sphere level without a particular localization pattern, nor a link with proliferative cells more prominent at sphere edges (**Fig. 1G**). All subpopulations were able to proliferate, although some $CD133^{-}CD44^{-}$ cells (P9-P12) contained less cells in S/G2/M (**Fig. S4A**). This may reflect the fluctuation of CD133 across the cell cycle (Barrantes-Freer et al., 2015). Thus, GBM stem-like cultures recapitulate the intra-tumoral phenotypic heterogeneity of CSC marker expression observed in patient biopsies and PDXs.

All GBM subpopulations carry similar stem cell properties.

To investigate the functional stem cell properties of the cells we performed self-renewal, proliferation and multipotency tests on all 16 subpopulations (**Fig. 2A**). We focused on the most heterogeneous culture (NCH644) allowing to obtain a sufficient number of cells of each subpopulation. We found that all FACS-sorted subpopulations were able to self-renew over multiple passages with no significant differences between each other (**Fig. 2B**). In analogy to normal stem cells, no dilution of differentiated counterparts and progenitors was

observed as indicated by similar sphere size. All subpopulations proliferated indefinitely at a similar rate (**Fig. 2C**). This indicated that phenotypically heterogeneous GBM cells have similar stem cell properties, suggesting a lack of hierarchical organization in specific differentiation states.

GBM subpopulations undergo stochastic state transitions in a non-hierarchical pattern.

We next performed multipotency tests by multicolor phenotyping for each of the FACS-purified subpopulation over time to reveal which subpopulations were responsible for creating the phenotypic heterogeneity. Surprisingly, none of the subpopulations maintained its original phenotype **(Fig. 2D**, **Fig. S5A**), indicating that none represented a unipotent 'differentiated' phenotype as expected in a one-way hierarchical model. This was also true for single cells phenotyped following the self-renewal test (**Fig. S5B)**. Most phenotypic states were already reestablished after 20 days (D20), although the adaptation was dynamic over time and varied between subpopulations as shown by the alluvial plots (**Fig. 2D**)**.** However, at day 70 (D70), all 16 subpopulations were reconstituted in each sample suggesting a tendency towards the original phenotypic equilibrium. This was confirmed in other GBM cultures (NCH421k) (**Fig. S4B**).

To quantify the state transitions in time between the different phenotypes and predict the time of equilibrium, we applied CellTrans, a mathematical model based on the Markov chain (Thomas Buder et al., 2017). The model estimated the occurrence of 175 of 240 possible direct state transitions (**Fig. 2E, Fig. S5C**). The estimated transition matrix appeared irreducible with no bottlenecks, i.e., each phenotype could transit to other states either directly or through intermediate steps. No hierarchies or sub-hierarchies were detected between the phenotypes (Krackhardt hierarchy score= 0). Moreover, transitions between positive and negative states of one marker were independent of the other markers (**Table S5A**). Of note, the theoretical equilibrium was very similar to the original composition (**Fig. 2F**).

We next tested the validity of the model by comparing the predicted values with experimental data. We designed two combinations of subpopulations (mix A and B, time=0) predicted to reach the equilibrium in 39 days. Indeed, the FACS-sorted admixtures reverted to the original equilibrium at the predicted time point (**Fig. 2G**). Interestingly, although the model predicted that all subpopulations would reach the same equilibrium, subpopulations varied in the time needed to reach equilibrium (**Fig. 2H**), with P2 and P12 showing the fastest transitions. In conclusion, all subpopulations retain full capacity to generate other

phenotypic states in a highly predictable manner. Despite differences in pace, heterogeneity is recapitulated in time from each phenotypic state in a non-hierarchical manner.

Hypoxia leads to phenotypic adaptation

We then asked to what extent the phenotypic heterogeneity is dependent on the microenvironment. We first focused on hypoxia, reportedly influencing GBM stem-like properties (Heddleston et al., 2009) and potentially selecting for CSCs (Soeda et al., 2009, Pistollato et al., 2009). Exposure to hypoxia led to a clear shift in phenotype. Hypoxic NCH644 cells were more positive for CD133, CD44 and A2B5, whereas CD15 was decreased (**Fig. 3A**). In particular, P5 and P7 were enriched, whereas several subpopulations (e.g. P2, P10) were reduced. Changes were not always gradual in time, suggesting indirect state transitions before reaching a new hypoxia-specific equilibrium. A similar adaptation to hypoxia was detected in NCH421k (**Fig. S4C**).

To test whether the changes were a result of selection or phenotypic adaptation we next FACS-sorted 16 subpopulations and performed functional assays under hypoxia (**Fig. 2A**). Again, all subpopulations self-renewed (**Fig. 3B**) and proliferated (**Fig. 3C**). Certain subpopulations differed in self-renewal potential during initial passages (**Table S6**). P10, P12 and P14 showed low clonogenic potential at the first passage, which was in accordance with their reduction in long term hypoxia (**Fig. 3A**), pointing to a possible partial selection at early time points. These differences were however lost in later passages, indicating efficient adaptation. Although single cells gave rise to smaller spheres compared to normoxia, hypoxic spheres did not differ in size between each other (**Fig. 3B**). The decreased self-renewal did not correlate with the proliferation index as only two subpopulations statistically differed from each other (**Fig. 3C**). All subpopulations proliferated indefinitely, though at a decreased rate. The lack of correlation between phenotypes enriched in hypoxia and their proliferation index suggests a strong role of phenotypic adaptation to a changing environment.

GBM state transitions in hypoxia

To model phenotypic adaptation to hypoxia we analyzed FACS-sorted subpopulations after 60 days in hypoxia. All subpopulations created a phenotypic distribution resembling the original hypoxic cultures, rather than the normoxic equilibrium (**Fig. 3D**). Statistical differences were still observed, suggesting that the equilibrium had not been reached yet. Nevertheless, all subpopulations recreated a CSC-associated heterogeneity in hypoxia. This was also true for single cell clones reformed following the self-renewal test (**Fig. S5D**).

Markov chain modeling revealed that, although direct state transitions were more restricted compared to normoxia (103/240; **Fig 3E**, **Fig. S5E**), all subpopulations could transit to other states except to P10. This was in accordance with the very low proportion of P10 observed in hypoxia (**Fig. 3A**) and its low self-renewal potential at initial passage (**Fig. 3B**). Notably, P10 survived hypoxia and could transform to other states, preferentially to P3. Subpopulations enriched in hypoxia (e.g. P5, P7) could be formed from numerous phenotypic states (≥9). The transition matrix appeared reducible with one transient state (P10, i.e. no phenotype can transit into P10 and P10 is depleted from the hypoxic equilibrium), but no absorbing state (i.e. exit from this state is not possible). Most populations needed >250 days to reach hypoxic equilibrium (**Fig. 3F**), compared to 92 days for the bulk culture. Of note, the subpopulations enriched in hypoxia (e.g. P5, P7) did not carry an advantage to reach equilibrium faster, rather, the subpopulations not enriched in hypoxia (P2, P9 and P12) were most adaptive. Interestingly, they also belonged to the fastest adapting subpopulations in normoxia (**Fig. 2H**). Altogether these results suggest that the phenotypic shift in low oxygen conditions occurs through adaptation of existing cells. Only a very limited hierarchy (Krackhardt hierarchy score=0.125) was observed. Although we cannot exclude a partial selection for certain phenotypic states, all subpopulations survived hypoxia and readapted to reach a hypoxia-specific equilibrium.

GBM differentiation program is incomplete and reversible

We further tested the differentiation ability of GBM cultures. Upon differentiation cells underwent morphological changes both in normoxia (**Fig. 4A**) and hypoxia (**Fig. S6A**). Although expression of neuronal (β-III-tubulin) and astrocytic (GFAP) markers increased, CSC-associated intracellular markers (e.g. Nestin, Vimentin) remained expressed, suggesting an incomplete differentiation process (**Fig. 4B; Fig S6B**). In normoxia, differentiation resulted in a strong shift towards CD133- and CD44+ subpopulations (P13-P16), although CD133-CD44- cells (P11) were also enriched (**Fig. 4C)**. Although similar changes were observed in hypoxia, the phenotypic shift under these condition was clearly the result of two environmental pressures, i.e. a decrease of CD133+ cells upon differentiation was compensated by increased CD133 in hypoxia (**Fig. 4C**). Similar data were obtained for NCH421k, which lost the predominance of the P2 subpopulation both in normoxia and hypoxia (**Fig. S6D**).

We next assessed the phenotypic heterogeneity upon returning to normoxic 3D sphere conditions. Regardless of the differentiation status and oxygen level, GBM cells regrew morphologically as 3D spheres and regained the expression of intracellular stem cell markers (**Fig. S6C**). This was accompanied by a partial regain of the initial membrane

marker heterogeneity at day 14 (**Fig. 4C, Fig S6D**). Markov modeling predicted a longer time to revert to normoxic equilibrium from differentiated states in NCH644 cells (75 and 84 days from Diff_N and Diff_H conditions, respectively). Reversibility of the phenotypic shift was also possible from adherent undifferentiated cultures and 3D hypoxic conditions (not shown). In summary, GBM cells undergo an incomplete and reversible differentiation program, which is independent of oxygen level.

Reversible adaptation of the CSC-associated phenotype *in vivo*

We next asked whether the reversible phenotypic adaptation occurs in the mouse brain. All implanted GBM cultures adapted their phenotype to the brain environment (**Fig. 4D; Fig. S6E-F**) with a strong tendency towards enrichment of CD133-CD44- cells (P9-P12) and depletion of CD133+CD44+ (P5-P8) and CD133-CD44+ (P13-P16) cells. These changes were different from the equilibria observed in hypoxic and differentiation conditions *in vitro*, suggesting the impact of additional factors in the complex *in vivo* microenvironment. This was also true for the intracellular stem cell and differentiation markers (**Fig. 4E, Fig. S6G**). Again, the phenotypic change *in vivo* was reversible and xenografted tumor cells regained the heterogeneous profile when returned to *in vitro* conditions (**Fig. 4D, Fig. S6E**). Xenografted cells were recultured for a time period equivalent to the tumor development time (28 days for NCH644, 56 days for NCH421k), at which point the phenotypic equilibrium of the original cultures was not yet reached, in accordance with mathematical modeling (estimated at 67 days for NCH644).

To rule out a negative selection against certain subpopulations, we implanted individual subpopulations directly after FACS sorting, focusing on four phenotypic states: P6 and P15 strongly depleted *in vivo*; P11 strongly enriched *in vivo* (**Fig. 4D**); and P2 the most 'adaptive' state in normoxia and hypoxia (**Fig. 2H**, **Fig. 3F**), partially depleted *in vivo*. While all subpopulations formed tumors, we observed a difference in mouse survival (**Fig. 4F**). Only mice bearing P2 developed tumors as fast as the parental cells, whereas P6, P11 and P15 grew significantly slower. Interestingly, all subpopulations changed phenotype *in vivo* resembling the original *in vivo* equilibrium (**Fig. 4G**). This shows that the subpopulations were able to undergo state transitions *in vivo*, further confirming the strong adaptive capacities of GBM cells. In analogy to the hypoxic condition, subpopulations varied in time to reach the environment-specific equilibrium, which may explain the differences in mouse survival.

The phenotypic states display a similar transcriptome

To correlate intra-tumoral heterogeneity at the phenotypic and transcriptomic level we applied single cell sequencing using the Drop-seq method (Macosko et al., 2015) on three PDX (P3, P8, P13) and two GBM cultures (NCH644, NCH421k). As expected, cells grouped by tumor of origin related to their different genetic background (**Fig. 5A**). Although a certain degree of intra-tumoral heterogeneity was observed within each tumor, we did not detect distinct sub-clusters and each tumor showed similar transcriptional cell-to-cell variability (cell-to-cell correlation coefficients: 0.72-0.86). If detected, transcripts coding for cell membrane markers were uniformly distributed across the tumor (**Fig. 5B**, **Fig. S7A**) and their expression was not linked to the cell cycle (**Fig. 5C**). This was also true for intracellular stemness (*NES, VIM*) and differentiation markers (*GFAP*) (**Fig. S7A**).

As transcripts coding for cell membrane markers were generally detected at low levels (**Fig. S7B***)*, we were not able to discriminate phenotypic states based on mRNA expression. Therefore, we performed Drop-seq on two NCH644 subpopulations: P2 (representing the most adaptive phenotypic state in normoxia, hypoxia and *in vivo*) and P6 (representing cells positive for all stem cell-associated markers, but being less adaptive). Interestingly, the two phenotypic states displayed similar transcriptomic profiles to each other and to the heterogeneous parental culture (**Fig 5 D, Fig. S7C-D**). The lack of distinct cell subpopulations at the transcriptomic level further questions a hierarchical organization of GBMs.

DISCUSSION

Functional heterogeneity of cancer cells is determined not only by the genetic makeup but also by non-genetic programs such as stemness features and interactions with the microenvironment. Although it is widely appreciated that cancer cells with stem cell properties exist within solid tumors, increasing controversy surrounds the significance of the initial CSC theory. We show that phenotypic heterogeneity in GBM is not a result of a one-way hierarchical structure, but a dynamic process of reversible state transitions. All GBM subpopulations were able to display stem cell properties and were tumorigenic, supporting the notion that cancer cells are highly plastic in response to microenvironmental cues. These data argue against the targeting of a small subpopulation of cancer stem cells and highlight the importance of considering these dynamic processes during treatment design.

Our study confirms previous reports showing strong inter-patient heterogeneity and the difficulty to identify bona fide CSC markers. Only a subset of markers fulfilled the CSC

criteria of heterogeneous expression within tumors. We show that the expression of CSC markers *in vivo* is not intrinsic to specific genetic clones, but is an adaptation process in response to environmental cues. In GBM stem-like cultures the CSC-associated phenotype was flexible, all subpopulations carried stemness properties and reconstituted heterogeneity. We further show that phenotypic heterogeneity is created via stochastic state transitions between phenotypic states, which do not follow a hierarchical organisation. Not a single phenotypic state was unipotent and irreversible. GBM cells also reverted from a 'differented state', questioning the effectiveness of differentiation factors as a therapeutic strategy (Lee et al., 2008, Natsume et al., 2013). Although differences between solid tumors can be expected, our data is in agreement with reports from other cancers such as breast and melanoma (Gupta et al., 2011, Quintana et al., 2010, Chaffer et al., 2013). While we cannot exclude a partial selection upon environmental pressure, we did not observe the complete eradication of subpopulations under any conditions. All populations adapted towards the most optimal environment-specific equilibrium, suggesting that state transitions are tightly regulated to find the best fitted balance. This is in contrast to previous reports suggesting targeted selection of stem-like cells and the loss of differentiation capacities in hypoxia (Soeda et al., 2009, Pistollato et al., 2009). Although further studies are needed to identify the factors leading to phenotypic adaptation *in vivo*, stromal cells and the metabolic landscape of the brain are likely to play a role. Concordantly, macrophage/microglia (Bhat et al., 2013) and an acidic environment (Lathia et al., 2010) were implicated in the phenotypic shift.

Although all cell populations carried stem cell properties and were tumorigenic, we observed differences in their adaptive capacity to reach to the most fitting equilibrium composition. This could explain some of the controversies reported in the CSC literature. Initial reports on GBM suggested that only CSC-marker positive cells were multipotent and able to form tumors (Singh et al., 2004, Son et al., 2009, Tchoghandjian et al., 2010), while later studies reported either no difference in tumorigenic potential (Wang et al., 2008, Ogden et al., 2008, Kenney-Herbert et al., 2015), or both fractions being tumorigenic, but with different potency (Chen et al., 2010, Auvergne et al., 2013, Auffinger et al., 2014, Brescia et al., 2013). Here we show that while all cells were plastic, certain adapted faster to new environments, leading to differences in *in vitro* self-renewal and *in vivo* transplantation assays. Even cells with a similar self-renewal potential *in vitro*, could differ in tumor development time. In agreement with previous reports (Quintana et al., 2008, Barrett et al., 2012) we conclude that the outcome of an assay strongly depends on experimental conditions and end-point.

Why some states appear more plastic than others is currently not clear. In addition to the genomic status, epigenetic flexibility regulating transcriptional networks may play a role in adaptive capacities (Easwaran et al., 2014, Wainwright and Scaffidi, 2017). Here we find that phenotypically distinct subpopulations retain a largely similar transcriptome, suggesting more subtle differences between GBM subpopulations compared to e.g. breast cancer (Gupta et al., 2011, Chaffer et al., 2013). This is in line with recent single cell RNA-seq data in GBM, revealing a continuous stem cell signature rather than clear subpopulations of stem-like versus non-stem-like cells (Patel et al., 2014).

In addition to clonal selection, the importance of cell plasticity in therapy resistance is emerging (Sharma et al., 2010). Mathematical simulations of state transitions following combinatorial treatment predicted the survival of the most plastic clones (Mathis et al., 2017, Leder et al., 2010). In breast cancer, it has been shown that the tumorigenic potential was lost by inhibiting the transition from CD44-low towards CD44-high cells (Chaffer et al., 2013). Caution is warranted towards therapies targeting epitope expressing cells including vaccine immunotherapies (Ji et al., 2014). Further elucidating state transition programs and mechanisms driving cellular plasticity will be essential to overcome current therapeutic limitations.

AUTHORS CONTRIBUTIONS

Conceptualization: A.G., R.B. and S.P.N; Methodology: A.D., A.G., N.H.C.B, S.P., Investigation: A.D., A.G., S.P., D.S, M.S., D.S., A.M., Formal analysis: T.B., P.V.N. A.M., S. P., S.L., N.S., S.F., Resources: C.H-M., Supervision: A.G., F.A., A.S., A. D., A.V-B., S.P. N. Writing – Original Draft: A.G., S.P.N., Writing-Review & Editing: all authors

DECLARATION OF INTEREST

The authors declare no competing interests.

ACKNOWLEDGMENTS

We thank A. Oudin and V. Baus for technical assistance. We are grateful to the Department of Neurosurgery of the Centre Hospitalier Luxembourg and the Clinical and Epidemiological Investigation Center of the LIH for help in tumor collection. We thank H. Hedman (Department of Radiation Sciences, Umeå University, Sweden) for providing glioma cultures and C. Guérin for assistance in the ImageStream experiments (Amnis, Inserm

U970, Flow Cytometry Core Facility, France). We are grateful to S. Senn (Competence Centre for Methodology and Statistics, LIH) and T. Bastogne (cINRIA-BIGS & Centre de Recherche en Automatique de Nancy, France) for advice in statistics and mathematical modeling. We acknowledge financial support by the Luxembourg Institute of Health, the Fonds National de la Recherche of Luxembourg (AFR grant to AD), the Fondation du Pélican de Mie et Pierre Hippert-Faber (Fondation de Luxembourg), Sächsisches Staatsministerium für Wissenschaft und Kunst (SMWK) project INTERDIS-2, Deutsche Krebshilfe and DFG-SFB-TRR79 project M8.

REFERENCES

ANIDO, J., SAEZ-BORDERIAS, A., GONZALEZ-JUNCA, A., RODON, L., FOLCH, G., CARMONA, M. A., PRIETO-SANCHEZ, R. M., BARBA, I., MARTINEZ-SAEZ, E., PRUDKIN, L., CUARTAS, I., RAVENTOS, C., MARTINEZ-RICARTE, F., POCA, M. A., GARCIA-DORADO, D., LAHN, M. M., YINGLING, J. M., RODON, J., SAHUQUILLO, J., BASELGA, J. & SEOANE, J. 2010. TGF-beta Receptor Inhibitors Target the CD44(high)/Id1(high) Glioma-Initiating Cell Population in Human Glioblastoma. *Cancer Cell,* 18**,** 655-68.

AUFFINGER, B., TOBIAS, A. L., HAN, Y., LEE, G., GUO, D., DEY, M., LESNIAK, M. S. & AHMED, A. U. 2014. Conversion of differentiated cancer cells into cancer stem-like cells in a glioblastoma model after primary chemotherapy. *Cell Death Differ,* 21**,** 1119-31.

AUVERGNE, R. M., SIM, F. J., WANG, S., CHANDLER-MILITELLO, D., BURCH, J., AL FANEK, Y., DAVIS, D., BENRAISS, A., WALTER, K., ACHANTA, P., JOHNSON, M., QUINONES-HINOJOSA, A., NATESAN, S., FORD, H. L. & GOLDMAN, S. A. 2013. Transcriptional differences between normal and glioma-derived glial progenitor cells identify a core set of dysregulated genes. *Cell Rep,* 3**,** 2127-41.

BARRANTES-FREER, A., RENOVANZ, M., EICH, M., BRAUKMANN, A., SPRANG, B., SPIRIN, P., PARDO, L. A., GIESE, A. & KIM, E. L. 2015. CD133 Expression Is Not Synonymous to Immunoreactivity for AC133 and Fluctuates throughout the Cell Cycle in Glioma Stem-Like Cells. *PLoS One,* 10**,** e0130519.

BARRETT, L. E., GRANOT, Z., COKER, C., IAVARONE, A., HAMBARDZUMYAN, D., HOLLAND, E. C., NAM, H. S. & BENEZRA, R. 2012. Self-renewal does not predict tumor growth potential in mouse models of high-grade glioma. *Cancer Cell,* 21**,** 11-24.

BEIER, D., HAU, P., PROESCHOLDT, M., LOHMEIER, A., WISCHHUSEN, J., OEFNER, P. J., AIGNER, L., BRAWANSKI, A., BOGDAHN, U. & BEIER, C. P. 2007. CD133(+)

and CD133(-) glioblastoma-derived cancer stem cells show differential growth characteristics and molecular profiles. *Cancer Res,* 67**,** 4010-5.

BHAT, K. P. L., BALASUBRAMANIYAN, V., VAILLANT, B., EZHILARASAN, R., HUMMELINK, K., HOLLINGSWORTH, F., WANI, K., HEATHCOCK, L., JAMES, J. D., GOODMAN, L. D., CONROY, S., LONG, L., LELIC, N., WANG, S., GUMIN, J., RAJ, D., KODAMA, Y., RAGHUNATHAN, A., OLAR, A., JOSHI, K., PELLOSKI, C. E., HEIMBERGER, A., KIM, S. H., CAHILL, D. P., RAO, G., DEN DUNNEN, W. F. A., BODDEKE, H., PHILLIPS, H. S., NAKANO, I., LANG, F. F., COLMAN, H., SULMAN, E. P. & ALDAPE, K. 2013. Mesenchymal differentiation mediated by NF-kappaB promotes radiation resistance in glioblastoma. *Cancer Cell,* 24**,** 331-46.

BITON, A., BERNARD-PIERROT, I., LOU, Y., KRUCKER, C., CHAPEAUBLANC, E., RUBIO-PEREZ, C., LOPEZ-BIGAS, N., KAMOUN, A., NEUZILLET, Y., GESTRAUD, P., GRIECO, L., REBOUISSOU, S., DE REYNIES, A., BENHAMOU, S., LEBRET, T., SOUTHGATE, J., BARILLOT, E., ALLORY, Y., ZINOVYEV, A. & RADVANYI, F. 2014. Independent component analysis uncovers the landscape of the bladder tumor transcriptome and reveals insights into luminal and basal subtypes. *Cell Rep,* 9**,** 1235-45.

BOUGNAUD, S., GOLEBIEWSKA, A., OUDIN, A., KEUNEN, O., HARTER, P. N., MADER, L., AZUAJE, F., FRITAH, S., STIEBER, D., KAOMA, T., VALLAR, L., BRONS, N. H., DAUBON, T., MILETIC, H., SUNDSTROM, T., HEROLD-MENDE, C., MITTELBRONN, M., BJERKVIG, R. & NICLOU, S. P. 2016. Molecular crosstalk between tumour and brain parenchyma instructs histopathological features in glioblastoma. *Oncotarget,* 7**,** 31955-71.

BRESCIA, P., ORTENSI, B., FORNASARI, L., LEVI, D., BROGGI, G. & PELICCI, G. 2013. CD133 Is Essential for Glioblastoma Stem Cell Maintenance. *STEM CELLS,* 31**,** 857-869.

BROWN, D. V., DANIEL, P. M., D'ABACO, G. M., GOGOS, A., NG, W., MOROKOFF, A. P. & MANTAMADIOTIS, T. 2015. Coexpression analysis of CD133 and CD44 identifies proneural and mesenchymal subtypes of glioblastoma multiforme. *Oncotarget,* 6**,** 6267-80.

CABRERA, M. C., HOLLINGSWORTH, R. E. & HURT, E. M. 2015. Cancer stem cell plasticity and tumor hierarchy. *World J Stem Cells,* 7**,** 27-36.

CAMPOS, B. & HEROLD-MENDE, C. C. 2011. Insight into the complex regulation of CD133 in glioma. *Int J Cancer,* 128**,** 501-10.

CANCER GENOME ATLAS RESEARCH, N., WEINSTEIN, J. N., COLLISSON, E. A., MILLS, G. B., SHAW, K. R., OZENBERGER, B. A., ELLROTT, K., SHMULEVICH,

I., SANDER, C. & STUART, J. M. 2013. The Cancer Genome Atlas Pan-Cancer analysis project. *Nat Genet,* 45**,** 1113-20.

CHAFFER, C. L., MARJANOVIC, N. D., LEE, T., BELL, G., KLEER, C. G., REINHARDT, F., D'ALESSIO, A. C., YOUNG, R. A. & WEINBERG, R. A. 2013. Poised chromatin at the ZEB1 promoter enables breast cancer cell plasticity and enhances tumorigenicity. *Cell,* 154**,** 61-74.

CHEN, R., NISHIMURA, M. C., BUMBACA, S. M., KHARBANDA, S., FORREST, W. F., KASMAN, I. M., GREVE, J. M., SORIANO, R. H., GILMOUR, L. L., RIVERS, C. S., MODRUSAN, Z., NACU, S., GUERRERO, S., EDGAR, K. A., WALLIN, J. J., LAMSZUS, K., WESTPHAL, M., HEIM, S., JAMES, C. D., VANDENBERG, S. R., COSTELLO, J. F., MOOREFIELD, S., COWDREY, C. J., PRADOS, M. & PHILLIPS, H. S. 2010. A hierarchy of self-renewing tumor-initiating cell types in glioblastoma. *Cancer Cell,* 17**,** 362-75.

EASWARAN, H., TSAI, H. C. & BAYLIN, S. B. 2014. Cancer epigenetics: tumor heterogeneity, plasticity of stem-like states, and drug resistance. *Mol Cell,* 54**,** 716-27.

GOLEBIEWSKA, A., BOUGNAUD, S., STIEBER, D., BRONS, N. H., VALLAR, L., HERTEL, F., KLINK, B., SCHROCK, E., BJERKVIG, R. & NICLOU, S. P. 2013. Side population in human glioblastoma is non-tumorigenic and characterizes brain endothelial cells. *Brain,* 136**,** 1462-75.

GUPTA, P. B., FILLMORE, C. M., JIANG, G., SHAPIRA, S. D., TAO, K., KUPERWASSER, C. & LANDER, E. S. 2011. Stochastic state transitions give rise to phenotypic equilibrium in populations of cancer cells. *Cell,* 146**,** 633-44.

HEDDLESTON, J. M., LI, Z., MCLENDON, R. E., HJELMELAND, A. B. & RICH, J. N. 2009. The hypoxic microenvironment maintains glioblastoma stem cells and promotes reprogramming towards a cancer stem cell phenotype. *Cell Cycle,* 8**,** 3274-84.

JI, J., JUDKOWSKI, V. A., LIU, G., WANG, H., BUNYING, A., LI, Z., XU, M., BENDER, J., PINILLA, C. & YU, J. S. 2014. Identification of novel human leukocyte antigen-A*0201-restricted, cytotoxic T lymphocyte epitopes on CD133 for cancer stem cell immunotherapy. *Stem Cells Transl Med,* 3**,** 356-64.

KENNEY-HERBERT, E., AL-MAYHANI, T., PICCIRILLO, S. G., FOWLER, J., SPITERI, I., JONES, P. & WATTS, C. 2015. CD15 Expression Does Not Identify a Phenotypically or Genetically Distinct Glioblastoma Population. *Stem Cells Transl Med,* 4**,** 822-31.

KRACKHARDT, D. 1994. Graph theoretical dimensions of informal organizations. *Computational organization theory,* 89**,** 123-140.

LAN, X., JORG, D. J., CAVALLI, F. M. G., RICHARDS, L. M., NGUYEN, L. V., VANNER, R. J., GUILHAMON, P., LEE, L., KUSHIDA, M. M., PELLACANI, D., PARK, N. I., COUTINHO, F. J., WHETSTONE, H., SELVADURAI, H. J., CHE, C., LUU, B., CARLES, A., MOKSA, M., RASTEGAR, N., HEAD, R., DOLMA, S., PRINOS, P., CUSIMANO, M. D., DAS, S., BERNSTEIN, M., ARROWSMITH, C. H., MUNGALL, A. J., MOORE, R. A., MA, Y., GALLO, M., LUPIEN, M., PUGH, T. J., TAYLOR, M. D., HIRST, M., EAVES, C. J., SIMONS, B. D. & DIRKS, P. B. 2017. Fate mapping of human glioblastoma reveals an invariant stem cell hierarchy. *Nature,* 549**,** 227-232.

LATHIA, J. D., GALLAGHER, J., HEDDLESTON, J. M., WANG, J., EYLER, C. E., MACSWORDS, J., WU, Q., VASANJI, A., MCLENDON, R. E., HJELMELAND, A. B. & RICH, J. N. 2010. Integrin alpha 6 regulates glioblastoma stem cells. *Cell Stem Cell,* 6**,** 421-32.

LATHIA, J. D., HEDDLESTON, J. M., VENERE, M. & RICH, J. N. 2011. Deadly teamwork: neural cancer stem cells and the tumor microenvironment. *Cell Stem Cell,* 8**,** 482-5.

LEDER, K., HOLLAND, E. C. & MICHOR, F. 2010. The therapeutic implications of plasticity of the cancer stem cell phenotype. *PLoS One,* 5**,** e14366.

LEE, J., SON, M. J., WOOLARD, K., DONIN, N. M., LI, A., CHENG, C. H., KOTLIAROVA, S., KOTLIAROV, Y., WALLING, J., AHN, S., KIM, M., TOTONCHY, M., CUSACK, T., ENE, C., MA, H., SU, Q., ZENKLUSEN, J. C., ZHANG, W., MARIC, D. & FINE, H. A. 2008. Epigenetic-mediated dysfunction of the bone morphogenetic protein pathway inhibits differentiation of glioblastoma-initiating cells. *Cancer Cell,* 13**,** 69-80.

LOVE, M. I., HUBER, W. & ANDERS, S. 2014. Moderated estimation of fold change and dispersion for RNA-seq data with DESeq2. *Genome Biol,* 15**,** 550.

MACOSKO, E. Z., BASU, A., SATIJA, R., NEMESH, J., SHEKHAR, K., GOLDMAN, M., TIROSH, I., BIALAS, A. R., KAMITAKI, N., MARTERSTECK, E. M., TROMBETTA, J. J., WEITZ, D. A., SANES, J. R., SHALEK, A. K., REGEV, A. & MCCARROLL, S. A. 2015. Highly Parallel Genome-wide Expression Profiling of Individual Cells Using Nanoliter Droplets. *Cell,* 161**,** 1202-14.

MATHIS, R. A., SOKOL, E. S. & GUPTA, P. B. 2017. Cancer cells exhibit clonal diversity in phenotypic plasticity. *Open Biol,* 7.

MAZUTIS, L., GILBERT, J., UNG, W. L., WEITZ, D. A., GRIFFITHS, A. D. & HEYMAN, J. A. 2013. Single-cell analysis and sorting using droplet-based microfluidics. *Nat Protoc,* 8**,** 870-91.

MEACHAM, C. E. & MORRISON, S. J. 2013. Tumour heterogeneity and cancer cell plasticity. *Nature,* 501**,** 328-37.

NATSUME, A., ITO, M., KATSUSHIMA, K., OHKA, F., HATANAKA, A., SHINJO, K., SATO, S., TAKAHASHI, S., ISHIKAWA, Y., TAKEUCHI, I., SHIMOGAWA, H., UESUGI, M., OKANO, H., KIM, S. U., WAKABAYASHI, T., ISSA, J. P., SEKIDO, Y. & KONDO, Y. 2013. Chromatin regulator PRC2 is a key regulator of epigenetic plasticity in glioblastoma. *Cancer Res,* 73**,** 4559-70.

NICLOU, S. P., DANZEISEN, C., EIKESDAL, H. P., WIIG, H., BRONS, N. H., POLI, A. M., SVENDSEN, A., TORSVIK, A., ENGER, P. O., TERZIS, J. A. & BJERKVIG, R. 2008. A novel eGFP-expressing immunodeficient mouse model to study tumor-host interactions. *Faseb J,* 22**,** 3120-8.

OGDEN, A. T., WAZIRI, A. E., LOCHHEAD, R. A., FUSCO, D., LOPEZ, K., ELLIS, J. A., KANG, J., ASSANAH, M., MCKHANN, G. M., SISTI, M. B., MCCORMICK, P. C., CANOLL, P. & BRUCE, J. N. 2008. Identification of A2B5+CD133- tumor-initiating cells in adult human gliomas. *Neurosurgery,* 62**,** 505-14; discussion 514-5.

PATEL, A. P., TIROSH, I., TROMBETTA, J. J., SHALEK, A. K., GILLESPIE, S. M., WAKIMOTO, H., CAHILL, D. P., NAHED, B. V., CURRY, W. T., MARTUZA, R. L., LOUIS, D. N., ROZENBLATT-ROSEN, O., SUVA, M. L., REGEV, A. & BERNSTEIN, B. E. 2014. Single-cell RNA-seq highlights intratumoral heterogeneity in primary glioblastoma. *Science,* 344**,** 1396-401.

PENUELAS, S., ANIDO, J., PRIETO-SANCHEZ, R. M., FOLCH, G., BARBA, I., CUARTAS, I., GARCIA-DORADO, D., POCA, M. A., SAHUQUILLO, J., BASELGA, J. & SEOANE, J. 2009. TGF-beta increases glioma-initiating cell self-renewal through the induction of LIF in human glioblastoma. *Cancer Cell,* 15**,** 315-27.

PEREZ-LLAMAS, C. & LOPEZ-BIGAS, N. 2011. Gitools: analysis and visualisation of genomic data using interactive heat-maps. *PLoS One,* 6**,** e19541.

PICCIRILLO, S. G., COMBI, R., CAJOLA, L., PATRIZI, A., REDAELLI, S., BENTIVEGNA, A., BARONCHELLI, S., MAIRA, G., POLLO, B., MANGIOLA, A., DIMECO, F., DALPRA, L. & VESCOVI, A. L. 2009. Distinct pools of cancer stem-like cells coexist within human glioblastomas and display different tumorigenicity and independent genomic evolution. *Oncogene,* 28**,** 1807-11.

PISTOLLATO, F., CHEN, H. L., ROOD, B. R., ZHANG, H. Z., D'AVELLA, D., DENARO, L., GARDIMAN, M., TE KRONNIE, G., SCHWARTZ, P. H., FAVARO, E., INDRACCOLO, S., BASSO, G. & PANCHISION, D. M. 2009. Hypoxia and HIF1alpha repress the differentiative effects of BMPs in high-grade glioma. *Stem Cells,* 27**,** 7-17.

QUINTANA, E., SHACKLETON, M., FOSTER, H. R., FULLEN, D. R., SABEL, M. S., JOHNSON, T. M. & MORRISON, S. J. 2010. Phenotypic heterogeneity among tumorigenic melanoma cells from patients that is reversible and not hierarchically organized. *Cancer Cell,* 18**,** 510-23.

QUINTANA, E., SHACKLETON, M., SABEL, M. S., FULLEN, D. R., JOHNSON, T. M. & MORRISON, S. J. 2008. Efficient tumour formation by single human melanoma cells. *Nature,* 456**,** 593-8.

R, B. M. E. 2016. alluvial: R Package for Creating Alluvial Diagrams.

SCOTT, A. M., WOLCHOK, J. D. & OLD, L. J. 2012. Antibody therapy of cancer. *Nat Rev Cancer,* 12**,** 278-87.

SHARMA, S. V., LEE, D. Y., LI, B., QUINLAN, M. P., TAKAHASHI, F., MAHESWARAN, S., MCDERMOTT, U., AZIZIAN, N., ZOU, L., FISCHBACH, M. A., WONG, K. K., BRANDSTETTER, K., WITTNER, B., RAMASWAMY, S., CLASSON, M. & SETTLEMAN, J. 2010. A chromatin-mediated reversible drug-tolerant state in cancer cell subpopulations. *Cell,* 141**,** 69-80.

SHI, X., LENG, L., WANG, T., WANG, W., DU, X., LI, J., MCDONALD, C., CHEN, Z., MURPHY, J. W., LOLIS, E., NOBLE, P., KNUDSON, W. & BUCALA, R. 2006. CD44 is the signaling component of the macrophage migration inhibitory factor-CD74 receptor complex. *Immunity,* 25**,** 595-606.

SINGH, S. K., HAWKINS, C., CLARKE, I. D., SQUIRE, J. A., BAYANI, J., HIDE, T., HENKELMAN, R. M., CUSIMANO, M. D. & DIRKS, P. B. 2004. Identification of human brain tumour initiating cells. *Nature,* 432**,** 396-401.

SOEDA, A., PARK, M., LEE, D., MINTZ, A., ANDROUTSELLIS-THEOTOKIS, A., MCKAY, R. D., ENGH, J., IWAMA, T., KUNISADA, T., KASSAM, A. B., POLLACK, I. F. & PARK, D. M. 2009. Hypoxia promotes expansion of the CD133-positive glioma stem cells through activation of HIF-1alpha. *Oncogene,* 28**,** 3949-59.

SON, M. J., WOOLARD, K., NAM, D. H., LEE, J. & FINE, H. A. 2009. SSEA-1 is an enrichment marker for tumor-initiating cells in human glioblastoma. *Cell Stem Cell,* 4**,** 440-52.

STIEBER, D., GOLEBIEWSKA, A., EVERS, L., LENKIEWICZ, E., BRONS, N. H., NICOT, N., OUDIN, A., BOUGNAUD, S., HERTEL, F., BJERKVIG, R., VALLAR, L., BARRETT, M. T. & NICLOU, S. P. 2014. Glioblastomas are composed of genetically divergent clones with distinct tumourigenic potential and variable stem cell-associated phenotypes. *Acta Neuropathol,* 127**,** 203-19.

TCHOGHANDJIAN, A., BAEZA, N., COLIN, C., CAYRE, M., METELLUS, P., BECLIN, C., OUAFIK, L. & FIGARELLA-BRANGER, D. 2010. A2B5 cells from human glioblastoma have cancer stem cell properties. *Brain Pathol,* 20**,** 211-21.

THOMAS BUDER, ANDREAS DEUTSCH, MICHAEL SEIFERT & VOSS-BOHME, A. 2017. CellTrans: An R package to quantify stochastic cell state transitions. *Software,* in press.

TIROSH, I., VENTEICHER, A. S., HEBERT, C., ESCALANTE, L. E., PATEL, A. P., YIZHAK, K., FISHER, J. M., RODMAN, C., MOUNT, C., FILBIN, M. G., NEFTEL, C., DESAI, N., NYMAN, J., IZAR, B., LUO, C. C., FRANCIS, J. M., PATEL, A. A., ONOZATO, M. L., RIGGI, N., LIVAK, K. J., GENNERT, D., SATIJA, R., NAHED, B. V., CURRY, W. T., MARTUZA, R. L., MYLVAGANAM, R., IAFRATE, A. J., FROSCH, M. P., GOLUB, T. R., RIVERA, M. N., GETZ, G., ROZENBLATT-ROSEN, O., CAHILL, D. P., MONJE, M., BERNSTEIN, B. E., LOUIS, D. N., REGEV, A. & SUVA, M. L. 2016. Single-cell RNA-seq supports a developmental hierarchy in human oligodendroglioma. *Nature,* 539**,** 309-313.

VENTEICHER, A. S., TIROSH, I., HEBERT, C., YIZHAK, K., NEFTEL, C., FILBIN, M. G., HOVESTADT, V., ESCALANTE, L. E., SHAW, M. L., RODMAN, C., GILLESPIE, S. M., DIONNE, D., LUO, C. C., RAVICHANDRAN, H., MYLVAGANAM, R., MOUNT, C., ONOZATO, M. L., NAHED, B. V., WAKIMOTO, H., CURRY, W. T., IAFRATE, A. J., RIVERA, M. N., FROSCH, M. P., GOLUB, T. R., BRASTIANOS, P. K., GETZ, G., PATEL, A. P., MONJE, M., CAHILL, D. P., ROZENBLATT-ROSEN, O., LOUIS, D. N., BERNSTEIN, B. E., REGEV, A. & SUVA, M. L. 2017. Decoupling genetics, lineages, and microenvironment in IDH-mutant gliomas by single-cell RNA-seq. *Science,* 355.

VESCOVI, A. L., GALLI, R. & REYNOLDS, B. A. 2006. Brain tumour stem cells. *Nat Rev Cancer,* 6**,** 425-36.

WAINWRIGHT, E. N. & SCAFFIDI, P. 2017. Epigenetics and Cancer Stem Cells: Unleashing, Hijacking, and Restricting Cellular Plasticity. *Trends Cancer,* 3**,** 372-386.

WANG, J., SAKARIASSEN, P. O., TSINKALOVSKY, O., IMMERVOLL, H., BOE, S. O., SVENDSEN, A., PRESTEGARDEN, L., ROSLAND, G., THORSEN, F., STUHR, L., MOLVEN, A., BJERKVIG, R. & ENGER, P. O. 2008. CD133 negative glioma cells form tumors in nude rats and give rise to CD133 positive cells. *Int J Cancer,* 122**,** 761-8.

WANG, Q., HU, B., HU, X., KIM, H., SQUATRITO, M., SCARPACE, L., DECARVALHO, A. C., LYU, S., LI, P., LI, Y., BARTHEL, F., CHO, H. J., LIN, Y. H., SATANI, N.,

MARTINEZ-LEDESMA, E., ZHENG, S., CHANG, E., SAUVE, C. G., OLAR, A., LAN, Z. D., FINOCCHIARO, G., PHILLIPS, J. J., BERGER, M. S., GABRUSIEWICZ, K. R., WANG, G., ESKILSSON, E., HU, J., MIKKELSEN, T., DEPINHO, R. A., MULLER, F., HEIMBERGER, A. B., SULMAN, E. P., NAM, D. H. & VERHAAK, R. G. W. 2017. Tumor Evolution of Glioma-Intrinsic Gene Expression Subtypes Associates with Immunological Changes in the Microenvironment. *Cancer Cell,* 32**,** 42-56 e6.

WHITFIELD, M. L., SHERLOCK, G., SALDANHA, A. J., MURRAY, J. I., BALL, C. A., ALEXANDER, K. E., MATESE, J. C., PEROU, C. M., HURT, M. M., BROWN, P. O. & BOTSTEIN, D. 2002. Identification of genes periodically expressed in the human cell cycle and their expression in tumors. *Mol Biol Cell,* 13**,** 1977-2000.

STAR METHODS

TCGA gene expression analysis

The gene expression pattern across GBM patients was investigated using The Cancer Genome Atlas (TCGA) cohort (160 GBM samples, provisional dataset on 25.10.2016) (Cancer Genome Atlas Research et al., 2013). A heatmap was generated using Gitools software (Perez-Llamas and Lopez-Bigas, 2011). Expression value corresponds to median-centered RNA-seq data, DNA methylation data were from a merged dataset on 25,978 probes shared by the HM27 and HM450 platforms analysis (#syn2486658)), and genomic copy number alterations were from PanCan12 Genom (details of the analysis https://www.synapse.org/). Group comparison was performed in Gitools using Mann-Whitney-Wilcoxon, and Benjamini Hochberg multiple test correction was applied (at P = 0.05, Mann-Whitney-Wilcoxon null hypothesis: correlation = 0). GBM expression subgroups were categorized as: Neural (n=28), Mesenchymal (n=51), Proneural (n=39), Classical (n=40), NA (n=2)

Clinical glioblastoma samples and patient-derived xenografts

Glioblastoma samples were collected at Centre Hospitalier in Luxembourg (Neurosurgical Department) or Haukeland University Hospital (Bergen, Norway) from patients having given informed consent, and with approval from the local ethics committees (National Ethics Committee for Research (CNER), Luxembourg; local ethics committee Haukeland University Hospital, Bergen). All biopsies were from grade IV glioblastomas. Organotypic GBM spheroids from patient samples were implanted in the brain of eGFP expressing Nod/Scid mice as previously described (Golebiewska et al., 2013, Niclou et al., 2008). Animals were sacrificed at the appearance of neurological symptoms and/or weight loss. The handling of the animals and the surgical procedures were performed in accordance with the European Directive on animal experimentation (2010/63/EU) and the local ethical committees approved the protocol.

Glioblastoma cell cultures

The glioblastoma stem-like cells NCH421k, NCH660h, NCH465, NCH601 and NCH644, were provided by Dr Christel Herold-Mende (Department of Neurosurgery, University of Heidelberg) and cultured as described before (Bougnaud et al., 2016). NCH421k, NCH660h, NCH465, and NCH601 were cultured as non-adherent spheres in DMEM-F12 medium (Lonza) containing 1xBIT100 (Provitro), 2mM L-Glutamine, 30U/ml Pen-Step, 1U/ml Heparin (Sigma), 20ng/ml bFGF (Miltenyi, 130-093-841) and 20ng/ml EGF (Provitro, 1325950500). NCH644 grew in Neurobasal® base medium (Life Technologies)

supplemented with 1xB27 (Life Technologies) 2mM L-Glutamine, 30U/ml Pen-Step, 1U/ml Heparin (Sigma), 20ng/ml bFGF (Miltenyi, 130-093-841) and 20ng/ml EGF (Provitro, 1325950500). The glioblastoma stem-like cells TB101 and TB107, kindly provided by Dr. Håkan Hedman, (Umeå University, Sweden) were cultured in DMEM-F12 medium (Lonza) containing 1xB27 and 1xN2 supplements (Provitro), 2mM L-Glutamine, 30U/ml Pen-Step, 1U/ml Heparin (Sigma), 20ng/ml bFGF (Miltenyi, 130-093-841) and 20ng/ml EGF (Provitro, 1325950500). Classical normoxic cultures were performed at 37°C under 5% CO_2 atmospheric oxygen.

Hypoxia and differentiation conditions

During hypoxia cells were maintained at 0.5% O_2 in a hypoxic incubator (Galaxy 48R incubator, New Brunswick) for the indicated time points (16h, 48h, 7 and 60 days). Experiments were repeated independently three times (n_B=3) with three technical replicates per subpopulation (n_T=3). For differentiation, cells were grown as adherent cultures in 10x diluted Matrigel in original medium depleted from bFGF and EGF and supplemented with 10% FBS and 10ng/ml All-Trans Retinoic acid (ATRA, Sigma) for 14 days. Cells were readapted to normoxic 3D sphere cultures for an additional 14 days in original culture media. Experiments were repeated independently three times (n_B=3) with three technical replicates per subpopulation (n_T=3).

Immunostaining

After washing, NCH644 spheres were embedded in Tissue-Tek® O.C.T.™ Compound (Sakura Finetek) and flashfrozen at -80°C. Immunocytochemistry was performed on 10µm sections, subsequently fixed in 4% PFA for 10 minutes. Adherent cultures were fixed in 4% PFA for 10 minutes directly in the plates. Fixed samples were blocked for 30 min in TBS supplied with 0.1% Triton-X100 and 2% FBS and incubated with primary antibodies (see **Table S7** for antibodies used) and 1µg/ml DAPI (Invitrogen). Secondary antibody staining was performed when needed. For image acquisition a Leica® DMI6000 B inverted microscope with a Leica® 350 FX camera was used with its concordant Leica Application Suite® software.

Flow cytometry settings

Data acquisition was performed on a FACS Aria™ SORP cytometer (BD Biosciences) fitted with a 640nm (30mW) red laser, a 355nm (60mW) UV laser, a 405nm (50mW) violet laser, a 488nm (100mW) blue laser and a 561nm (50mW) yellow/green laser. The Hoechst dye was excited by the UV laser and fluorescence was collected in two channels: 'UV-1' 450/50

band-pass (BP) filter and 'UV-2' 660/40 long-pass (LP) filter. An LP635nm dichroic mirror was used to split the emission wavelengths. The instrument was calibrated each time with Cytometer Setup&Tracking Beads (BD Bioscience) and stabilized for at least 1h before laser alignment and data acquisition. The Coefficient of Variation of the instrument (%CV) was routinely examined before each experiment. Routinely, a 100µm nozzle and window extension (WE) 3 were used for data acquisition and sorting. Imaging flow cytometry was performed with an ImageStream imaging cytometer (Amnis) fitted with a 375 UV laser, a 488 blue laser, a 561 yellow-green laser, a 642 red laser and a 785nm infrared laser. Acquisition was performed with the INSPIRE® software and analysis was performed using IDEAS® image analysis software. Pictures were taken at 60x magnification at low speed high sensitivity mode.

Multicolor cell membrane phenotyping

Cell cultures were dissociated using Accutase® (Sigma-Aldrich) to obtain a single cell suspension. Xenografts were dissociated with MACS Neural Tissue Dissociation Kit (P) (Miltenyi) following the manufacturers' instructions. Single cells were resuspended in HBSS, 2% FBS, 10mM HEPES buffer (100 µl/test). Cells were incubated with the IR-LIVE/DEAD® Fixable Dead Cell Stains (Invitrogen; 1µg/ml) and appropriate preconjugated antibodies for 30 min at 4°C in the dark (**Table S7**). For cell cycle analysis in viable cells, cells were prestained with Hoechst 33342 (5µg/ml, Bisbenzimide, Ho342; Sigma) at 37°C as described before (Stieber et al., 2014). Data acquisition was performed on a FACS Aria™ SORP cytometer (BD Biosciences) and ImageStream imaging cytometer (Amnis). Data acquisition and analysis were done for FACSAria with DIVA software (BD Bioscience); and INSPIRE and IDEAS® for ImageStream. Histograms were prepared with the FlowJo software.

Intracellular marker phenotyping

Cell cultures were dissociated using Accutase® (Sigma-Aldrich) to obtain a single cell suspension. Xenografts were dissociated with MACS Neural Tissue Dissociation Kit (P) (Miltenyi) following the manufacturers' instructions. Single cells were resuspended in HBSS, 2% FBS, 10mM HEPES buffer (100 µl/test). Cells were incubated with the IR-LIVE/DEAD® Fixable Dead Cell Stains (Invitrogen; 1µg/ml) and appropriate preconjugated antibodies for 30 min at 4°C in the dark (**Table S7**). Cells were fixed with the BD Cytofix™ solution for 20 min and permeabilised in the BD Perm/Wash™ for 10min at RT. Cells were incubated with appropriate preconjugated antibodies for 30 min at 4°C in the dark (**Table S7**). Data acquisition was performed on a FACS Aria™ SORP cytometer (BD Biosciences).

Selfrenewal test

Single cells from 16 subpopulations were FACS-sorted to a 96 well plate (1 cell/well; one 96 well plate per subpopulation) and cultured for 4 weeks in normoxia or 0.5% O_2 hypoxia. Spheres derived from each subpopulation were collected (passage 1) and single viable cells were resorted and plated as single cells (one 96 well plate/subpopulation, 1 cell/well). Replating was done 3 times to reach 4 passages in total. Only spheres >40µm were considered as a positive result for sphere forming capacity. Total sphere number and average sphere size (n=20 per subpopulation if available) were recorded at each passage before cell harvesting. Each subpopulation at each passage was phenotyped as described above. FACS-sorted viable single cells from the bulk cells were used as control. The experiment was repeated independently four times. Significant differences in sphere number across populations and passages were evaluated with the Kruskal-Wallis test. Significant differences in sphere size were tested with mixed linear models with either subpopulation or passage as fixed-effects and considering batch effect as random.

Proliferation and mulitpotency test

300 cells of each NCH644 subpopulation were FACS-sorted to a 48 well plate and cultured for 20, 30 and 70 days in normoxia or 0.5% O_2 hypoxia. At each time point, cells derived from each subpopulation were phenotyped as described above. Total cell number was recorded with the Countess® cell counter (Invitrogen) after 20 and 30 days of culture to determine the proliferation rate. Doubling time was calculated as follows: $doubling\ time = \frac{t_2 - t_1}{log_2 \frac{cell\ number_2}{cell\ number_1}}$, where t_1 and t_2 represented time points. FACS-sorted single viable cells from bulk were used as control. The experiment was repeated independently four times (n_B=4) with three technical replicates per subpopulation (n_T=3). Significant differences of doubling times were tested with mixed linear models with subpopulation as fixed-effects and considering plate effects as random. The proportion of each subpopulation was calculated as the percentage of viable single cells. The column chart graphs show mean percentage of technical and biological replicates. Error bars were omitted for visualization purposes. Alluvial plots have been generated under R using the package *alluvial* available at https://github.com/mbojan/alluvial (R, 2016). Significant differences between phenotypic states were calculated with the Student's t-test with Bonferroni's multiple comparison test/correction.

Mathematical Modeling

Markov model principles

In order to quantify the transitions between the 16 phenotypes we applied Markov chain modeling implemented in the freely available R package *CellTrans* (http://github.com/tbuder/CellTrans) (Buder et al., 2017). The model is based on the assumptions that cell state alterations occur due to stochastic cell state transitions only depending on the current state of the cell and possibly the experimental environment (e.g. hypoxia) and that proliferation rates of the involved phenotypes are approximately equal. This led to the estimation of a Markov chain with a transition matrix containing the probabilities of state transitions allowing to discriminate frequent and non-frequent state transitions and identify hierarchical or non-hierarchical transition behavior. If the underlying network is irreducible, each state can transit directly or via intermediate steps into any other state. This behavior implies that stochastic state transitions are non-hierarchical and therefore reversible in a biological sense. In contrast, if the transition network has a tree structure, it corresponds to a perfect hierarchy. Intermediate network structures are possible as well, which imply some degree of hierarchy between transient states at the top of the hierarchy and recurrent states at the bottom of the hierarchy. Moreover, on the basis of the estimated transition matrix, it is possible to predict the composition of the population in equilibrium by calculating the Markov chain stationary state. In addition, the time from a specific initial composition until an approximate equilibrium is reached can be estimated.

Construction of data matrices. Let $w_{i,j}^{(t)}$ denote the experimentally observed mean proportion of phenotype $j, j = 1, \dots, 16$, in the experiment starting with pure subpopulations of phenotype $i, i = 1, \dots, 16$, at time t. Then, one can construct a phenotype proportion matrix at time t as follows.

$$W^{(t)} = \begin{pmatrix} w_{1,1}^{(t)} & \cdots & w_{1,16}^{(t)} \\ \vdots & \ddots & \vdots \\ w_{16,1}^{(t)} & \cdots & w_{16,16}^{(t)} \end{pmatrix}$$

Note that the phenotype proportion matrix describing the initial proportions is the $16x16$ identity matrix, i.e.

$$W^{(0)} = \begin{pmatrix} 1 & 0 & \cdots & \cdots & 0 \\ 0 & 1 & 0 & \cdots & 0 \\ \vdots & \ddots & \ddots & \ddots & \vdots \\ \vdots & \ddots & \ddots & \ddots & 0 \\ 0 & 0 & \cdots & 0 & 1 \end{pmatrix}.$$

The transitions between the phenotypes were estimated as probabilities of state transition per time-step of the underlying Markov chain. Importantly, the implications of the model with respect to hierarchical structure, equilibrium composition and relaxation time are highly

independent of the choice of the time-step length. Here, we choose a time-step length of one day. We obtained three phenotype matrices from the experimental data in normoxia: $W^{(20)}$ after 20 days, $W^{(30)}$ after 30 days and $W^{(70)}$ after 70 days. In hypoxia we constructed only one matrix, namely $W^{(60)}$ for the measurement after 60 days.

Estimation of the transition probabilities. Markov chain theory allows to connect the initial phenotype proportion matrix with the phenotype matrix after n time-steps with the equation $W^{(0)}P^n = W^{(n)}$. This equation can be solved for the underlying transition matrix P, i.e.

$$\hat{P}_{(n)} = \left(\left(W^{(0)}\right)^{-1} W^{(n)}\right)^{\frac{1}{n}}.$$

Hence, we obtained the three transition matrices $\hat{P}_{(20)}$, $\hat{P}_{(30)}$ and $\hat{P}_{(70)}$ in normoxia which needed to be regularized in order to obtain stochastic matrices, see (Buder et al., 2017) for details. These matrices were averaged to obtain a final estimate for the transition matrix P, i.e. $\hat{P} = \frac{\hat{P}_{(7)} + \hat{P}_{(10)} + \hat{P}_{(23)}}{3}$. In hypoxia, $P = \hat{P}_{(60)}$ was used since there was only one time point of measurement.

Krackhardt Hierarchy. In order to estimate the degree of hierarchy of the estimated transition matrixes from data obtained under different environmental conditions, graph hierarchy introduced by Krackhardt was calculated (Krackhardt, 1994). The degree of deviation from pure hierarchy, i.e. tree structure, is assessed by counting the number of pairs that have reciprocated ties relative to the number of pairs where there isn't? any tie, i.e. the proportion *p* of all tied pairs having reciprocated ties. Krackhardt hierarchy is then defined as 1-*p*. A perfect hierarchy is characterized by no reciprocated ties and exhibits a Krackhardt hierarchy of one. Calculations were performed in R using "*hierarchy*" function with "*Krackhardt*" measure.

Marker dependency calculation. We investigated whether the cell state transitions between positive and low/negative expression of one marker in normoxia and hypoxia were dependent on the level of expression of the other markers. For each marker, we distinguished two phenotypic states with respect to positive and low/negative expression of this marker. In detail, we added the percentage of all CSC-associated subpopulations with positive or low/negative expression of that marker in the measured plasticity data for each time-point of measurement. This resulted in 2x2 cell state proportion matrixes per time point. This coarse-grained data could be utilized to derive corresponding 2x2 cell state transition matrixes and corresponding steady states by applying CellTrans (Buder et al., 2017).

The steady states of these 2x2 cell state transition matrices could then be compared to the fractions of the corresponding phenotype when considering all 4 markers in the analysis.

Therefore, percentage of subpopulations with the same expression of a single marker were added to obtain the steady state proportion for each individual marker. Nearly equal equilibrium proportions indicate independent transitions whereas large differences indicate a dependency. Calculations were performed for normoxic and hypoxic datasets.

Cell line-derived xenografts and *in vivo* tumor formation test

GBM patient-derived cultures were implanted intracranially to NOD/Scid mice (50,000 per mouse for NCH644 and NCH421k, 300'000 cells for NCH660h and NCH601, n=3) into the right frontal cortex using a stereotactic device. Animals were sacrificed at the appearance of neurological symptoms and weight loss. To test tumorigenicity *in vivo*, 5000 cells of P2, P6, P11 and P15 subpopulations and original NCH644 cells were engrafted into nude mice directly after sort (n=7 per group). Animals were monitored daily and the following criteria were evaluated: (1) loss of more than 10% of body weight, (2) exhibition of strong neurological signs (difficulty ambulating or abnormal movement), (3) increased lordosis or (4) swollen belly. The criteria were scored as follows: 0 = none, 1 = early, 2 = established, 3 = severe signs and animals were sacrificed when 3 criteria with grade 2 or 1 criterion with grade 3 were reached. Tumor developed in xenografted mice were FACS phenotyped as described above. The handling of the animals and the surgical procedures were performed in accordance with the European Directive on animal experimentation (2010/63/EU) and the local ethical committees approved the protocol.

Single cell RNAseq using Drop-seq

Cell preparation

To obtain a pure population of single viable cells all GBM cultures were FACS-sorted (NCH644, NCH421k bulk cultures and NCH644 subpopulations P2 and P6). For GBM PDXs we have pre-selected hCD90-positive tumor cells. FACS-sorted populations were collected in HBSS, 0.5% BSA and stored on ice until the start of the Drop-seq experiment. Prior to cell loading on the Drop-seq chips, the viability of cells was verified and concentration was adjusted to ~150 cells/μl as optimal concentration to achieve single cell encapsulation within each droplet of ~1 nl . All samples analysed had a cell viability > 95%.

Mircrofluidics Fabrication

Microfluidics devices were fabricated using a previously published design (Macosko et al., 2015). Softlithography was performed using SU-8 2050 photoresist (MicroChem) on 4" silicon substrate to obtain a feature aspect depth of 100μm. After overnight silanization (using Chlorotrimethylsilane, Sigma), the wafer masks were used for microfluidics fabrication. Drop-seq chips were fabricated using silicon based polymerization chemistry,

with the previously published protocol (Mazutis et al., 2013). Briefly, Polydimethylsiloxane (PDMS) base and crosslinker (Dow Corning), were mixed at a 10:1 ratio, mixed and degassed before pouring onto the Drop-seq master template. PDMS was cured on the master template, at 80°C for 2h. After incubation and cooling, PDMS slabs were cut and the inlet/outlet ports were punched with 1.25 mm biopsy punchers (World Precision Instruments). The PDMS monolith was plasma-bonded to a clean microscopic glass slide using a Harrick plasma cleaner. Immediately after pairing the plasma-treated surfaces of the PDMS monolith and the glass slide, flow channels of the Drop-seq chip were subjected to a hydrophobicity treatment using 1H,1H,2H,2H-Perfluorodecyltrichlorosilane (in 2% v/v in FC-40 oil; Alfa Aeser/Sigma). After 5 min of treatment, excessive silane was blown through the inlet/outlet ports. Chips were further incubated at 80°C for 15 minutes.

Single cell droplet suspension

Experiments followed the original Drop-seq protocol (Macosko et al., 2015) with minor changes described below. Synthesized barcoded beads (Chemgenes corp., USA) were co-encapsulated with cells inside the droplets containing lysis reagents using an optimal bead concentration of 200 beads/μl in Drop-seq Lysis buffer medium. Cellular mRNA was captured on the beads via barcoded oligo (dT) handles synthesised on the surface.

For cell encapsulation, 2 ml of cell and bead suspensions were loaded into 3 ml syringes (BD), respectively. To keep beads in homogenous suspension a micro-stirrer was used (VP scientific). The QX 200 carrier oil (Bio-rad) used as continuous phase in the droplet generation was loaded into a 20 ml syringe (BD). For droplet generation, 3.6 ml/hr and 13 ml/hr were used in KD scientific Legato syringe pumps for the dispersed and continuous phase flows, respectively. After stabilization of droplet formation, the droplet suspension was collected into a 50 ml Falcon tube. Collection of the emulsion was carried out until 1μl of the single cell suspension was dispensed. Droplet consistency and stability were evaluated by bright-field microscopy using INCYTO C-Chip Disposable Hemacytometer (Fisher Scientific). Bead occupancy within droplets was carefully monitored to avoid multiple bead occupancy.

The subsequent steps of droplet breakage, bead harvesting, reverse transcription and exonuclease treatment were carried out in accordance to (Macosko et al., 2015). RT buffer contained 1x Maxima RT buffer, 4% Ficoll PM-400 (Sigma), 1 μM dNTPs (ThermoScientific), 1 U/ml Rnase Inhibitor (Lucigen), 2.5 μM Template Switch Oligo, and 10 U/ml Maxima H-RT (ThermoScientific). Post Exo-I treatment, the bead counts were estimated using INCYTO C-Chip Disposable Hemacytometer, and 10,000 beads were aliquoted in 0.2 ml Eppendorf PCR tubes. PCR mix was dispensed in a volume of 50μl using 1x Hifi HotStart Readymix (Kapa Biosystems) and 0.8 mM Template-Switch-PCR

primer. The thermocycling program for the PCR amplification was modified for the final PCR cycles by 95°C (3 min), four cycles of 98°C (20s), 65°C (45s), 72°C (3 min), 10 cycles of 98°C (20s), 67°C (20s), 72°C (3 min) and followed by a final extension step of 72°C for 5 min. Post PCR amplification, libraries were purified with 0.6x Agencourt AMPure XP beads (Beckman Coulter), in accordance with the manufacturer's protocol. Finally, the purified libraries were eluted in 20 µl RNAase/DNAase-free molecular grade water. Quality and concentration of the sequencing libraries were assessed using BioAnalyzer High Sensitivity Chip (Agilent Technologies).

NGS preparation for Drop-seq libraries

The 3' end enriched cDNA libraries were prepared by tagmentation reaction of 600 pg cDNA library using the standard Nextera XT tagmentation kit (Illumina). Reactions were performed according to the manufacturer's instructions, except for the 400nM primer sets replaced by Primer 1 (AATGATACGGCGACCACCGAGATCTACACGCCTGTCCGCGG AAGCAGTGGTA TCAACGCAGAG T*A*C) and Primer 2 (N703: CAAGCAGAAGACGGCATACGAGA TTTCTGCCTGTCTCGTGGGCTCGG for the NCH644 subpopulation 6 and N709: CAAGCAGAAGACGGCATACGAGATAGCGTAGCGTCTCGTGGGCTCGG for NCH644 subpopulation 2, NCH644 and NCH421k). The PCR amplification cycling program used was: 95°C 30s; fourteen cycles of: 95°C (10s), 55°C (30s), 72^0C (30s) followed by a final extension step of 72°C (5 min). Libraries were purified twice to reduce primers and short DNA fragments with 0.6x and 1x Agencourt AMPure XP beads (Beckman Coulter), respectively, in accordance with the manufacturer's protocol. Finally, purified libraries were eluted in 15 µl molecular grade water. Quality and quantity of the tagmented cDNA library was evaluated using BioAnalyzer High Sensitivity DNA Chip. The average size of the tagmented libraries prior to sequencing was between 400-700 bps.

Purified Drop-seq cDNA libraries were sequenced using Illumina NextSeq 500 with the recommended sequencing protocol except for 6pM of custom primer (GCCTGTCCGCGGAAGCAGTGGTATCAACGCAGAGTAC) applied for priming of read 1. Paired end sequencing was performed with the read 1 of 20 bases (covering the random cell barcode 1-12 bases and the rest 13-20 bases of random unique molecular identifier (UMI) and for read 2 the 50 bases of the genes.

Bioinformatics processing and data analysis

The FASTQ files were assembled from the raw BCL files using Illumina's bcl2fastq converter and ran through the FASTQC codes [Babraham bioinformatics; https://www.bioinformatics.babraham.ac.uk/projects/fastqc/] to check for consistency in library qualities. The monitored quality assessment parameters were a) quality per base

sequence (especially for the read 2 of the gene), b) per base N content, c) per base sequence content and d) overrepresented sequences. Libraries that showed significant deviation were re-sequenced. The FASTQ files were then merged and converted to binaries using PICARD's fastqtosam algorithm.

The sequencing reads were converted to a digital gene expression matrix (DGE) using the Drop-seq bioinformatics pipeline (Macosko et al., 2015). To normalize for the transcript loading between the beads, the averaged normalized expression levels ($\log_2$(TPM+1)) were calculated. Beads without cellular mRNAs were identified by using a cumulative function of the total number of transcripts per barcode and empirical thresholding on the resulting "knee plot". To filter poor quality reads and cells with low transcript content, only cells with at least 1500 expressed genes and genes at least expressed in 20 cells were considered for further analysis. The average number of UMI-collapsed transcripts per cell was 5970 corresponding to the 2430 genes detected per cell on average.

To remove batch effect, we used independent component analysis ICA (R fastICA package) decomposing the original expression matrix into a product of statistically independent signals and weight matrices: $X_{nm} = S_{nk} \times M_{km}$, where X_{nm} is the log-transformed count matrix for n genes and m cells, S_{nk} is a matrix of k independent components and M_{km} is the weight matrix for each component over m cells. Stability of the ICA decomposing was tested by 100 runs of ICA. The log-transformed count matrix was decomposed using 8 independent components. The optimal number of components was selected by minimizing the correlation between rows of weight matrix. We observed that the weight of component #7 was strongly linked to the experimental batch. In accordance with (Biton et al., 2014), this component was suppressed by setting its weight ($M_{7,i}$, where i = 1..m) to 0, and the normalized data were recovered by matrix multiplication of the components by their weights. Estimation of the highly variable genes and principal component reduction and tSNE dimensionality reduction was implemented using SEURAT R package (http://satijalab.org/seurat/) or the R package *Rtsne* with an initial PCA, a *perplexity* of 40 and a *learning rate* of 200 (5000 iterations) (https://github.com/jkrijthe/Rtsne). For reproducibility with the original algorithm, the *theta* value was set to zero.

The correlation coefficient was calculated between each cell after filtering using the Pearson method; the mean value is represented for each group/subpopulation/fraction. Differential expression analysis was performed using DESeq2 package of R (Love et al., 2014). Here the raw integer counts were used for consistency with the algorithm requirements. Centering of the gene expression value was performed by obtaining the relative expression levels, by subtracting the average expression value ($\log_2$(TPM+1)) of each gene from all the cells of the gene expression matrix. For cell cycle analysis we have

applied two prominent gene expression programs of the G1/S (100 genes) and G2/M phases (133 genes) (Whitfield et al., 2002), shown to overlap in the two programs (Macosko et al., 2015).

Due to the sparsity of the single cell RNAseq data, the expression data for each cell cycle phase was refined by evaluating the correlation data between each of the genes in the scRNAseq data with the average gene expression values of all the genes involved in the respective cell cycle program (G1/S & G2/M), and including all the genes with high correlation value ($R^2 > 0.3$; $P_{val} < 0.05$). Hierarchical clustering of the data demonstrated that some cells are cycling with high relative expression of most of the genes included in either of the cell cycle program or both of the programs, while other cells show basal expression for most of these genes (data not shown). The biaxial plot of G1/S and G2/M programs illustrated in the Figure 5C is the average score of all the genes involved in the respective cell cycle programs. Figure 5C, further represents the expression value of different genes of interest by mapping the expression value onto the respective cells.

Figure 1. CSC-associated heterogeneity in GBM. A. Inter-patient heterogeneity at the gene expression level for a panel of CSC-associated markers and selected GBM drivers. See further analysis in **Fig. S1** and **Table S1**; **B.** Pearson gene expression correlation between CSC-associated markers and main GBM drivers. No significant correlation was observed. **C.** Flow cytometric analysis of tumor cells for CD133, CD44, A285 and CD15 in 3 GBM PDXs (P3, P8, P13). Percentage of positive cells ('black' gate) is indicated vs. negative control and vs. high expressing cells ('red' gate). See **Fig. S2** for gating strategy and **Fig. S3** for more examples. **D**. Marker expression profiles in the genetically heterogeneous T16 PDX (all tumor ('black'), pseudodiploid ('blue') and aneuploid ('red') clones). Separately implanted pseudodiploid (blue) and aneuploid clones (red) adapted the CSC-associated profiles in the xenograft (right). **E.** Multicolor phenotyping**.** Representative ImageStream images are shown for NCH644 subpopulations. Right pannel presents color code for 16 subpopulations applied in consecutive figures. **F.** Distribution of the subpopulations in 7 stem-like cultures (mean percentage, error bars were ommitted for visualization purposes) as determined by flow cytometry. For color code see E. **G.** Distribution of CSC-associated markers and Ki67 proliferating cells in 3D NCH644 spheres (bar = 100µm).

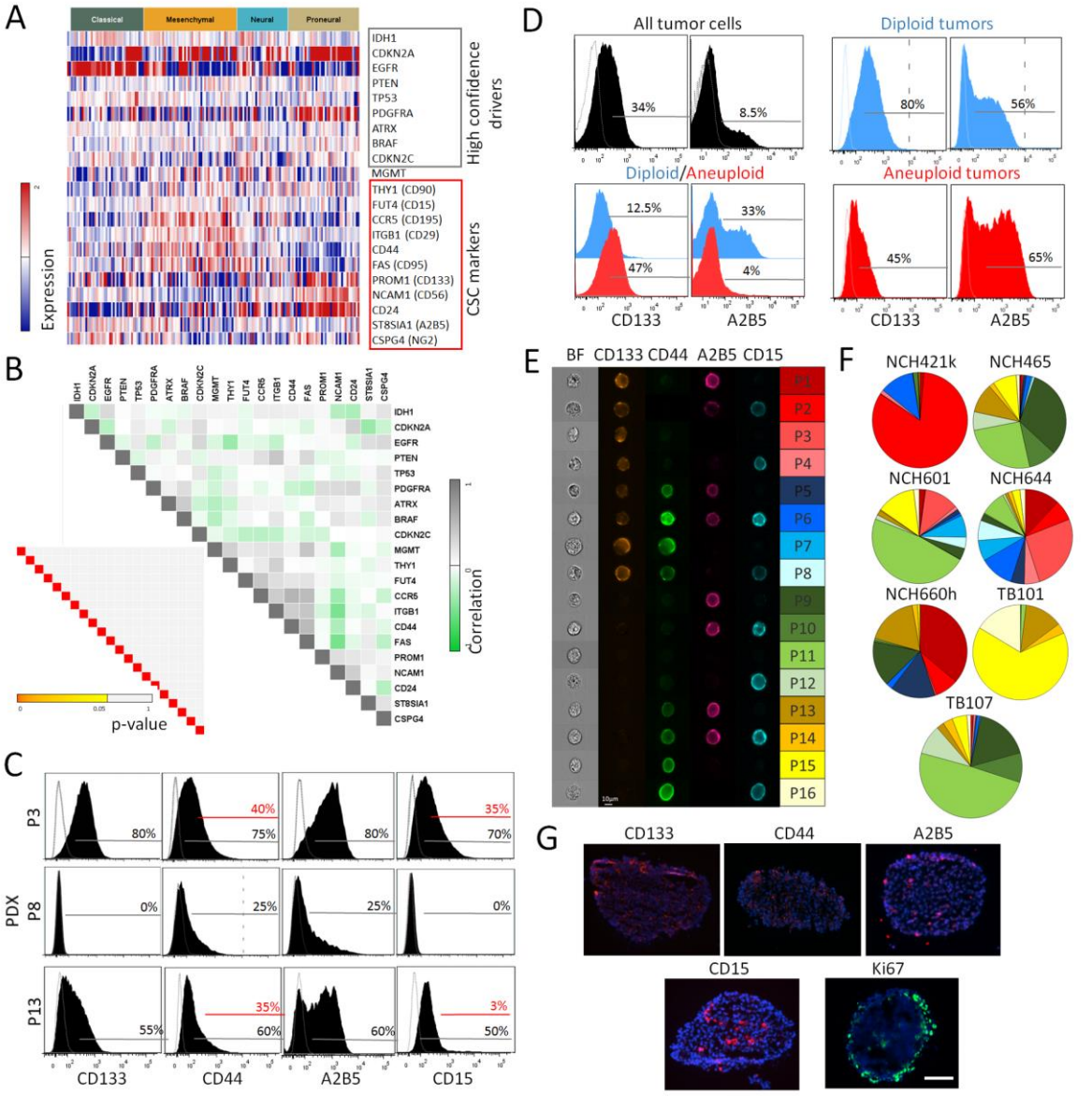
A
Classical
Mesenchymal
Neural
Proneural
IDH1
CDKN2A
EGFR
PTEN
TP53
PDGFRA
ATRX
BRAF
CDKN2C
High confidence drivers
MGMT
THY1 (CD90)
FUT4 (CD15)
CCR5 (CD195)
ITGB1 (CD29)
CD44
FAS (CD95)
PROM1 (CD133)
NCAM1 (CD56)
CD24
ST8SIA1 (A2B5)
CSPG4 (NG2)
CSC markers
Expression
B
Correlation
p-value
C
P3
PDX P8
P13
80%
40%
75%
80%
35%
70%
0%
25%
25%
0%
55%
35%
60%
60%
3%
50%
CD133
CD44
A2B5
CD15
D
All tumor cells
34%
8.5%
Diploid tumors
80%
56%
Diploid/Aneuploid
12.5%
47%
33%
4%
Aneuploid tumors
45%
65%
CD133
A2B5
E
BF CD133 CD44 A2B5 CD15
P1
P2
P3
P4
P5
P6
P7
P8
P9
P10
P11
P12
P13
P14
P15
P16
F
NCH421k
NCH465
NCH601
NCH644
NCH660h
TB101
TB107
G
CD133
CD44
A2B5
CD15
Ki67

Figure 2. GBM subpopulations undergo state transitions in a non-hierarchical manner. A. Experimental setup of FACS sorting and functional analysis performed on 16 subpopulations. See **Fig. 2E** for gating strategy. Data is shown for the 16 subpopulations of NCH644 cells. **B.** Self-renewal test, including sphere formation and sphere diameter (mean +/- SEM). Bulk cells were used as control (CTR). No statistical difference was observed, except for P11 passages 1 vs. 2 and 1 vs. 3 ($p^* \leq 0.05$). **C**. Proliferation test (mean doubling time +/- SEM). No statistical differences were observed. **D.** Multipotency test. Marker expression over time: FACS-sorting day 0 (D0) and re-phenotyping after 20 (D20), 30 (D30) and 70 (D70) days in culture. The order of subpopulations in alluvial plots is based on highest to lowest percentage at each time point. See **Fig. S5** for column chart and **Table S3A** for statistics. For color code see **Fig.1E E.** Markov modeling of state transitions between 16 subpopulations. Arrows represent predicted direct state transitions between subpopulations, thickness of lines corresponds to transition probabilities. See **Fig. S5C** for transition matrix. **F.** Proportions of subpopulations predicted in equilibrium state is similar to initial culture. **G.** Validation of Markov modeling. FACS-sorted admixtures (time 0) were re-phenotyped at the predicted equilibrium time (39 days) showing the accuracy of the mathematical model. See **Table S2A** for statistics. **H.** Predicted time to reach equilibrium for each subpopulation.

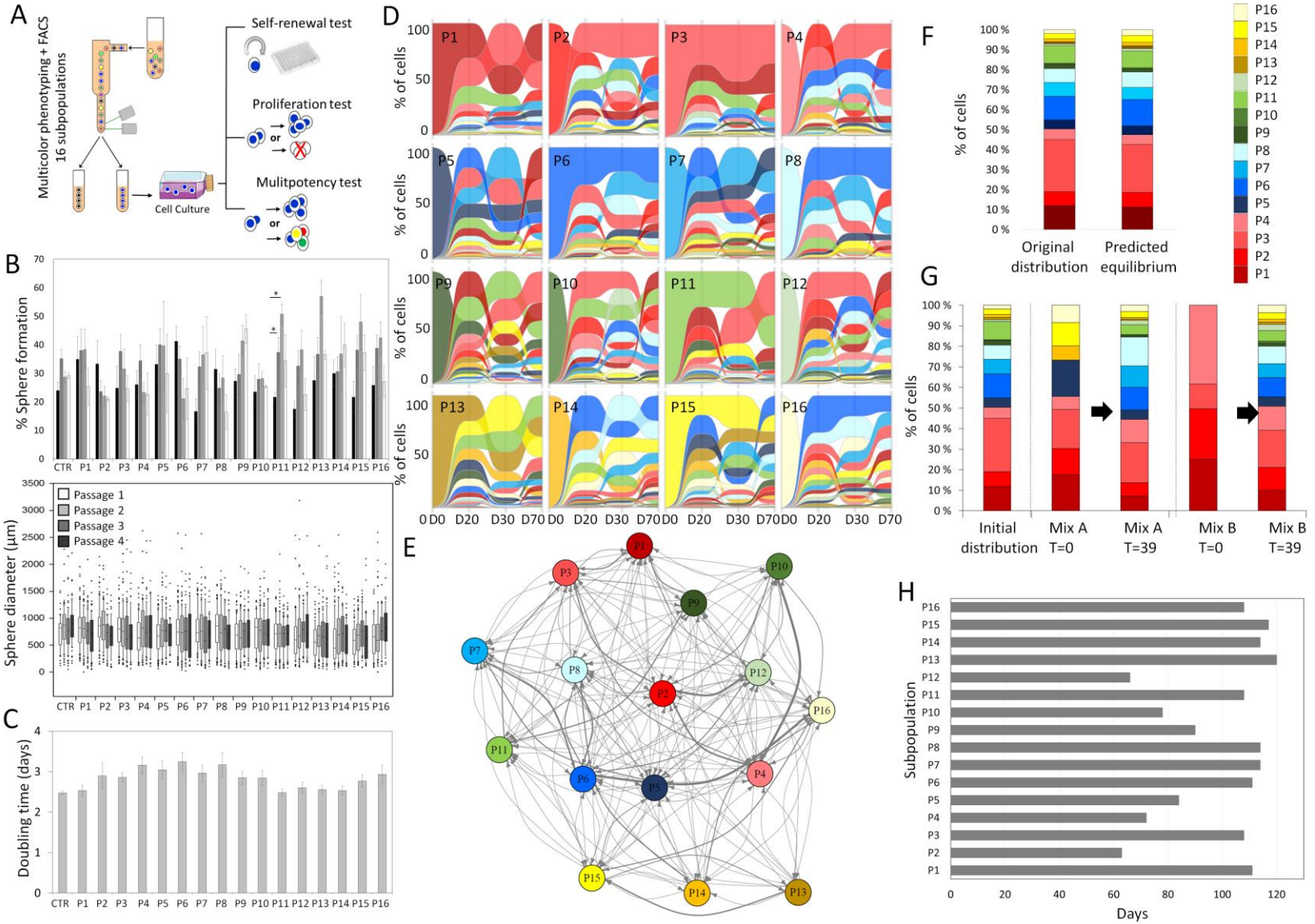
A
Multicolor phenotyping + FACS
16 subpopulations
Cell Culture
Self-renewal test
Proliferation test
Mulitpotency test
or
or
B
% Sphere formation
CTR P1 P2 P3 P4 P5 P6 P7 P8 P9 P10 P11 P12 P13 P14 P15 P16
Sphere diameter (µm)
Passage 1
Passage 2
Passage 3
Passage 4
C
Doubling time (days)
D
% of cells
P1 P2 P3 P4 P5 P6 P7 P8 P9 P10 P11 P12 P13 P14 P15 P16
D0 D20 D30 D70
E
F
% of cells
Original distribution
Predicted equilibrium
G
% of cells
Initial distribution
Mix A T=0
Mix A T=39
Mix B T=0
Mix B T=39
H
Subpopulation
Days

7

Figure 3. Adaptation of GBM subpopulations to hypoxia. A. Distribution of subpopulations in hypoxia (H). Normoxia (N) is shown as control (CTR) and hypoxia (H) at 16h, 48h, 7 and 60 days. Data is shown for NCH644, additional cultures are shown in **Fig. S4C**. See **Table S2B** for statistics. For color code see **Fig.1E.** Self-renewal test of 16 subpopulations in hypoxia (mean +/- SEM). Bulk cells were used as control (CTR). Statistical differences within the same subpopulations are shown (*p_{value}≤0.05). See **Table S6** for statistical differences at different passages**. C**. Proliferation test in hypoxia (mean doubling time +/- SEM). Bulk cells were used as control (CTR). Statistical difference was only found between P7 and P13. **D.** Distribution of 16 subpopulations after 60 days in hypoxia. For each FACS-sorted subpopulation day 0 (left) and 60 (right) are presented. See **Table S3B** for statistics. **E.** Markov modeling of state transitions in hypoxia. Arrows represent direct state transitions between subpopulations, thickness of lines corresponds to transition probabilities. See **Fig. S5E** for transition matrix. **F.** Predicted time needed to reach equilibrium for each subpopulation in hypoxia.

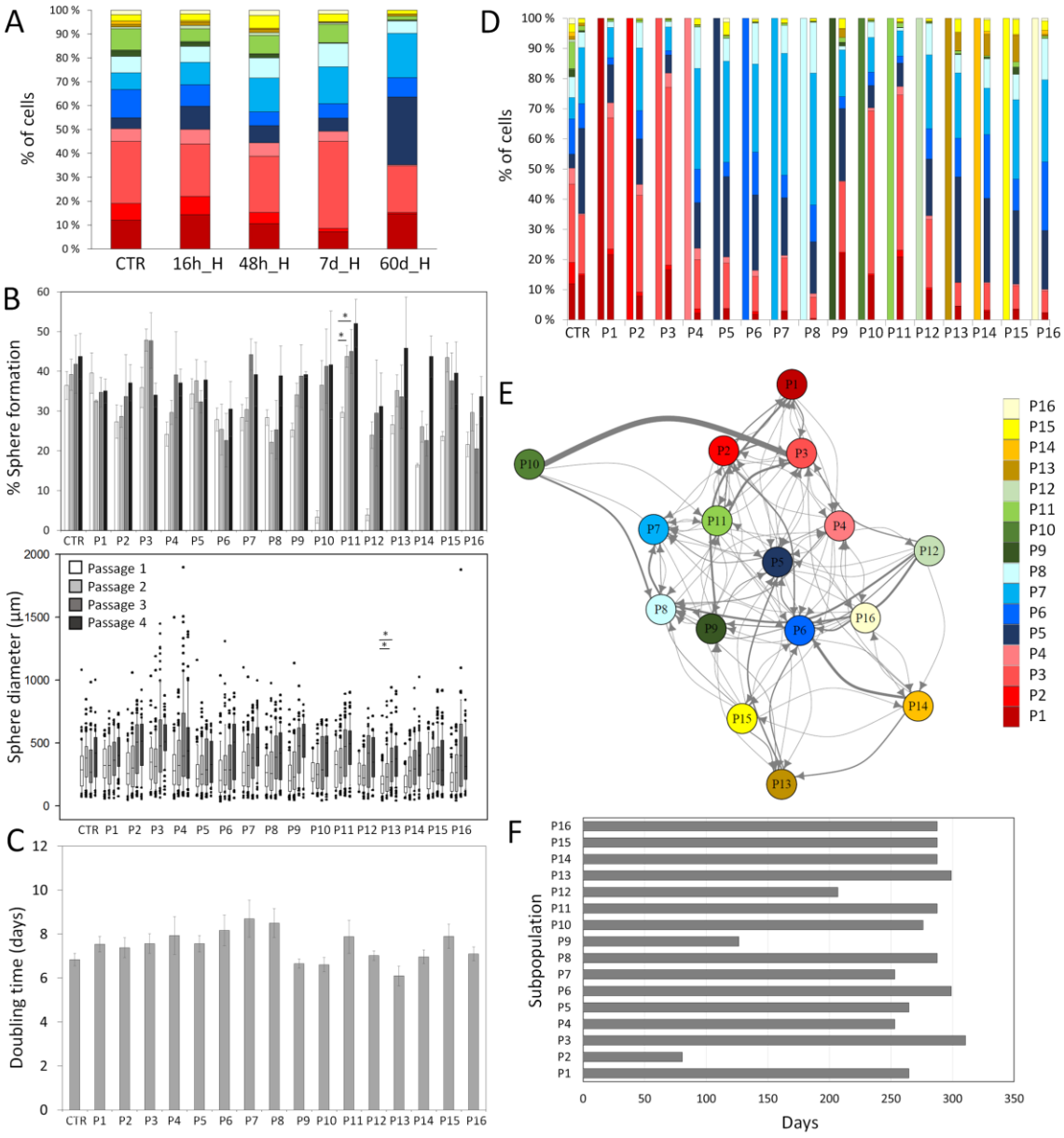
A
% of cells
CTR
16h_H
48h_H
7d_H
60d_H
D
% of cells
CTR P1 P2 P3 P4 P5 P6 P7 P8 P9 P10 P11 P12 P13 P14 P15 P16
B
% Sphere formation
Sphere diameter (µm)
Passage 1
Passage 2
Passage 3
Passage 4
E
P1 P2 P3 P4 P5 P6 P7 P8 P9 P10 P11 P12 P13 P14 P15 P16
C
Doubling time (days)
F
Subpopulation
Days

Figure 4. Reversible adaptation after *in vitro* differentiation and *in vivo* growth.

A. Examples of NCH644 grown as adherent cultures in stem cell (Undiff_N) or differentiation (Diff_N) conditions in normoxia. **B.** Flow cytometric analysis of intracellular markers in control 3D sphere cultures (CTR), differentiation (Diff) conditions. N= normoxia, H= hypoxia. Black lines discriminate between negative and positive cells. Dotted line indicate mode expression in control cells. **C.** Distribution of subpopulations under different environmental conditions compared to 3D spheres in normoxia (CTR). For each condition phenotyping was performed after 14 days of environmental change (left) and 14 days after subsequently reverting to original 3D sphere culture (right). See **Table S2D** for statistics. **D.** Distribution of subpopulations in xenografted NCH644 tumors *in vivo* (X) and after regrowth *in vitro* (De-X). NCH644 cultured in normoxia are shown as control (CTR). See **Table S2F** for statistics. **E.** Flow cytometric analysis of intracellular markers. Black lines discriminate between negative and positive cells. Dotted line indicate mode expression in control cells. **F.** Kaplan-Meier survival curves of xenotransplanted mice. Subpopulations P2, P6, P11 and P15 were implanted directly after FACS. FACS-sorted bulk cells were used as control (CTR) (*$p_{value} \leq 0.05$; **$p_{value} \leq 0.01$). **G.** Distribution of subpopulations in xenografted tumors. For each subpopulation, day of implant and day of mouse sacrifice are presented. See **Table S2H** for statistics.

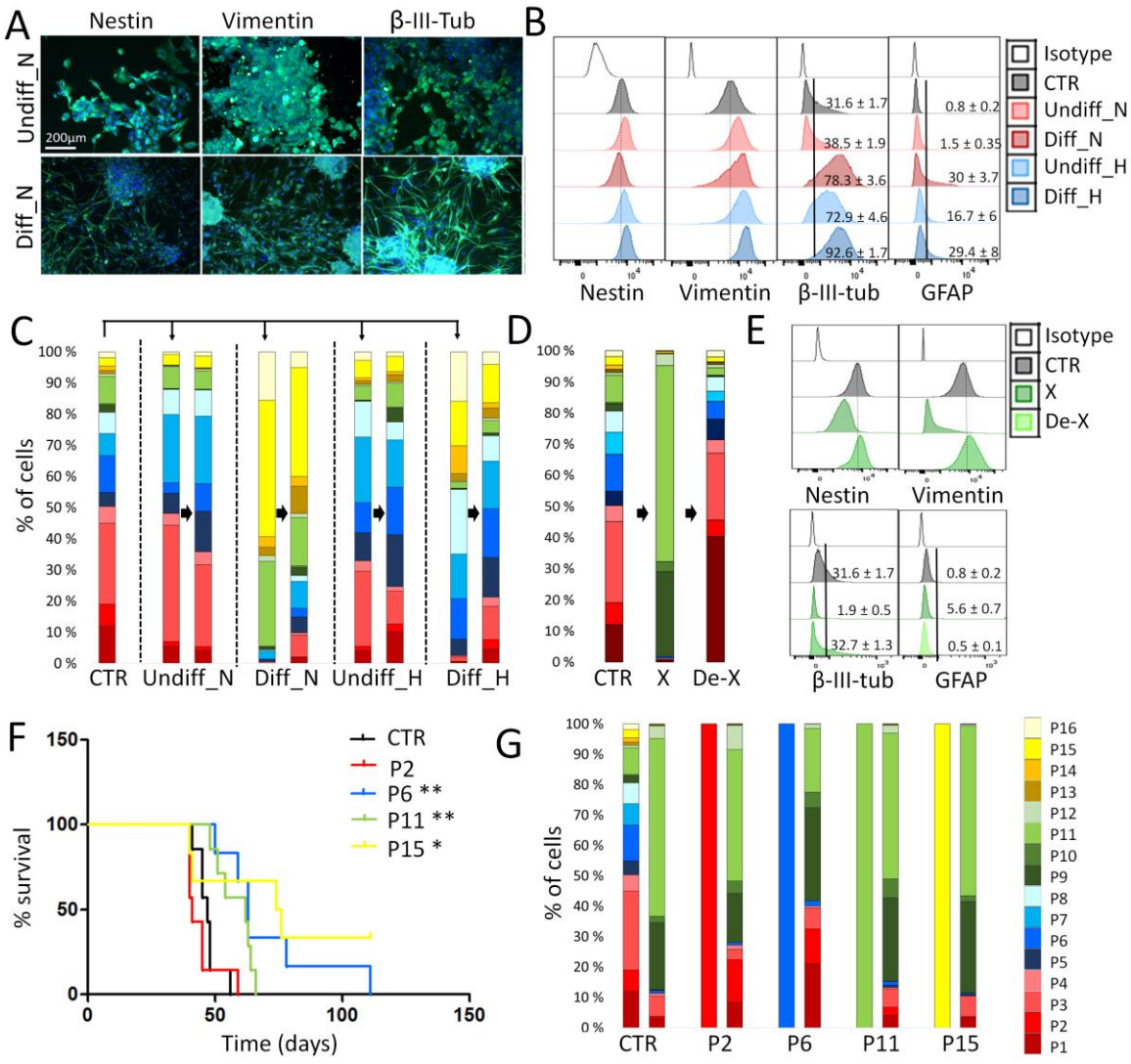
A
Nestin
Vimentin
β-III-Tub
Undiff_N
Diff_N
200µm
B
Isotype
CTR
Undiff_N
Diff_N
Undiff_H
Diff_H
31.6 ± 1.7
0.8 ± 0.2
38.5 ± 1.9
1.5 ± 0.35
78.3 ± 3.6
30 ± 3.7
72.9 ± 4.6
16.7 ± 6
92.6 ± 1.7
29.4 ± 8
Nestin
Vimentin
β-III-tub
GFAP
C
% of cells
CTR
Undiff_N
Diff_N
Undiff_H
Diff_H
D
CTR
X
De-X
E
Isotype
CTR
X
De-X
Nestin
Vimentin
31.6 ± 1.7
0.8 ± 0.2
1.9 ± 0.5
5.6 ± 0.7
32.7 ± 1.3
0.5 ± 0.1
β-III-tub
GFAP
F
% survival
Time (days)
CTR
P2
P6 **
P11 **
P15 *
G
% of cells
CTR
P2
P6
P11
P15
P16
P15
P14
P13
P12
P11
P10
P9
P8
P7
P6
P5
P4
P3
P2
P1

Figure 5. Distinct phenotypic states carry similar transcriptome. A. Overall gene expression relationship between single cells of 3 GBM PDXs and 2 stem-like cultures. Patient-derived cells are color coded. **B.** Expression of marker genes in NCH644. The expression gradient is color coded. **C.** Estimation of cell cycle state of individual NCH644 cells on the basis of relative expression of G1/S and G2/M gene sets. The expression gradient of marker genes is color coded. **D.** Gene expression relationship between FACS-sorted subpopulations P2 and P6 and the original heterogeneous NCH644 (CTR). Each sample is color coded.

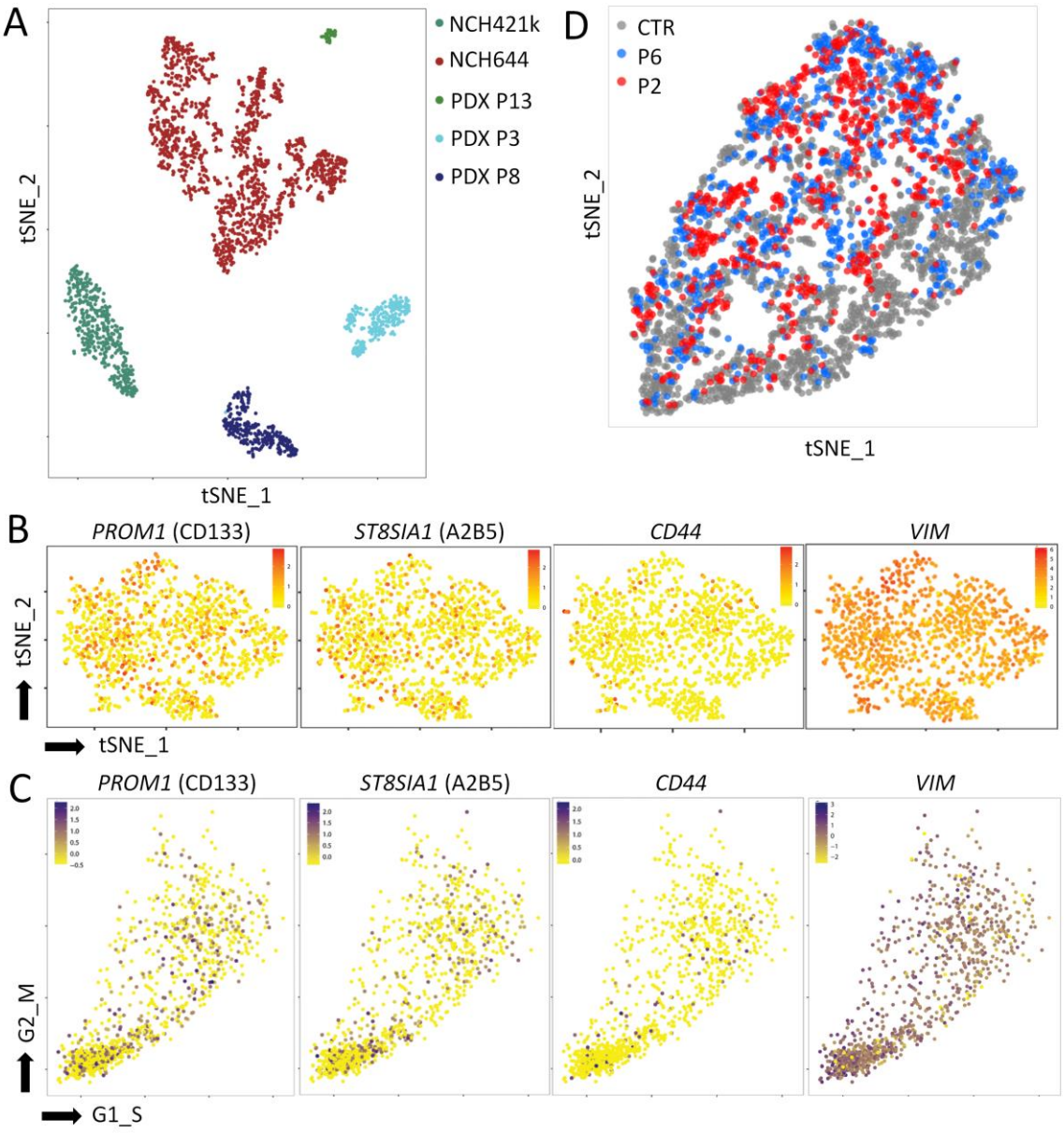
A
NCH421k
NCH644
PDX P13
PDX P3
PDX P8
tSNE_2
tSNE_1
D
CTR
P6
P2
tSNE_2
tSNE_1
B
PROM1 (CD133)
ST8SIA1 (A2B5)
CD44
VIM
tSNE_2
tSNE_1
C
PROM1 (CD133)
ST8SIA1 (A2B5)
CD44
VIM
G2_M
G1_S

Figure S1. Genetic aberrations and mutations in GBM patient samples. Analysis of genetic alterations in main cancer and selected stem cell markers in GBM. **A.** Heatmap showing an integrated value dimension for genomic alterations (mutation and/or copy number alteration) in the different GBM expression subgroups (Proneural, Neural, Mesenchymal and Classical) **B.** Heatmap showing promoter methylation of some genes in clinical samples. **C.** Heatmap of Pearson correlation significance calculated from promoter methylation data. Only the *FUT4* promoter displayed altered DNA methylation, which was not correlated to the *MGMT* promoter methylation (p=0.086).

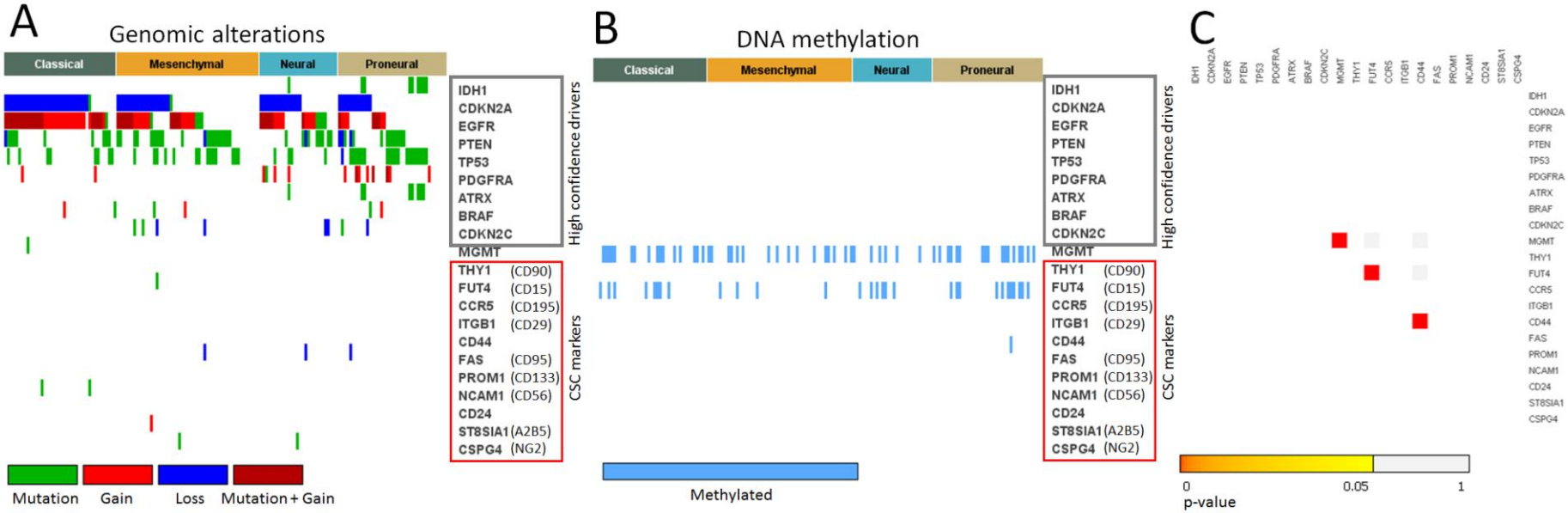
A
Genomic alterations
Classical
Mesenchymal
Neural
Proneural
IDH1
CDKN2A
EGFR
PTEN
TP53
PDGFRA
ATRX
BRAF
CDKN2C
MGMT
THY1 (CD90)
FUT4 (CD15)
CCR5 (CD195)
ITGB1 (CD29)
CD44
FAS (CD95)
PROM1 (CD133)
NCAM1 (CD56)
CD24
ST8SIA1 (A2B5)
CSPG4 (NG2)
High confidence drivers
CSC markers
Mutation
Gain
Loss
Mutation + Gain
B
DNA methylation
Classical
Mesenchymal
Neural
Proneural
Methylated
C
p-value
0
0.05
1

Figure S2. Gating strategy for multicolor phenotypic analysis and sorting. A. The step-by-step gating strategy for FACS analysis is shown for the intracranial NCH644 xenograft. The same strategy was used for all subsequent experiments using single viable cells. (**1)** Cells were distinguished from debris on the flow cytometric profile based on the Forward Scatter (FSC) and Side Scatter (SSC). (**2)** Cell doublets and aggregates were gated out based on their properties displayed on the FSC area (FSC-A) versus height (FSC-H) dot plot. (**3)** Dead cells were recognized by their strong positivity for the dead cell discrimination marker. **B.** In xenografts, human tumor cells were selected as the eGFP negative population (eGFP+ Nod/SCID mice) or hCD90 positive cells (nude mice and non-eGFP Nod/SCID mice). **C.** Multicolor phenotyping was performed by simultaneous staining for four CSC-associated markers: CD133, CD44, CD15, and A2B5. **D.** 16 subpopulations were distinguished based on the presence/absence of the expression of the four cell membrane markers. **E.** For multicolor sorting more stringent gates were applied to ensure no overlap between the 16 subpopulations. FACS-sorting gates were applied near the brightest and dimmest ends of the spectrum.

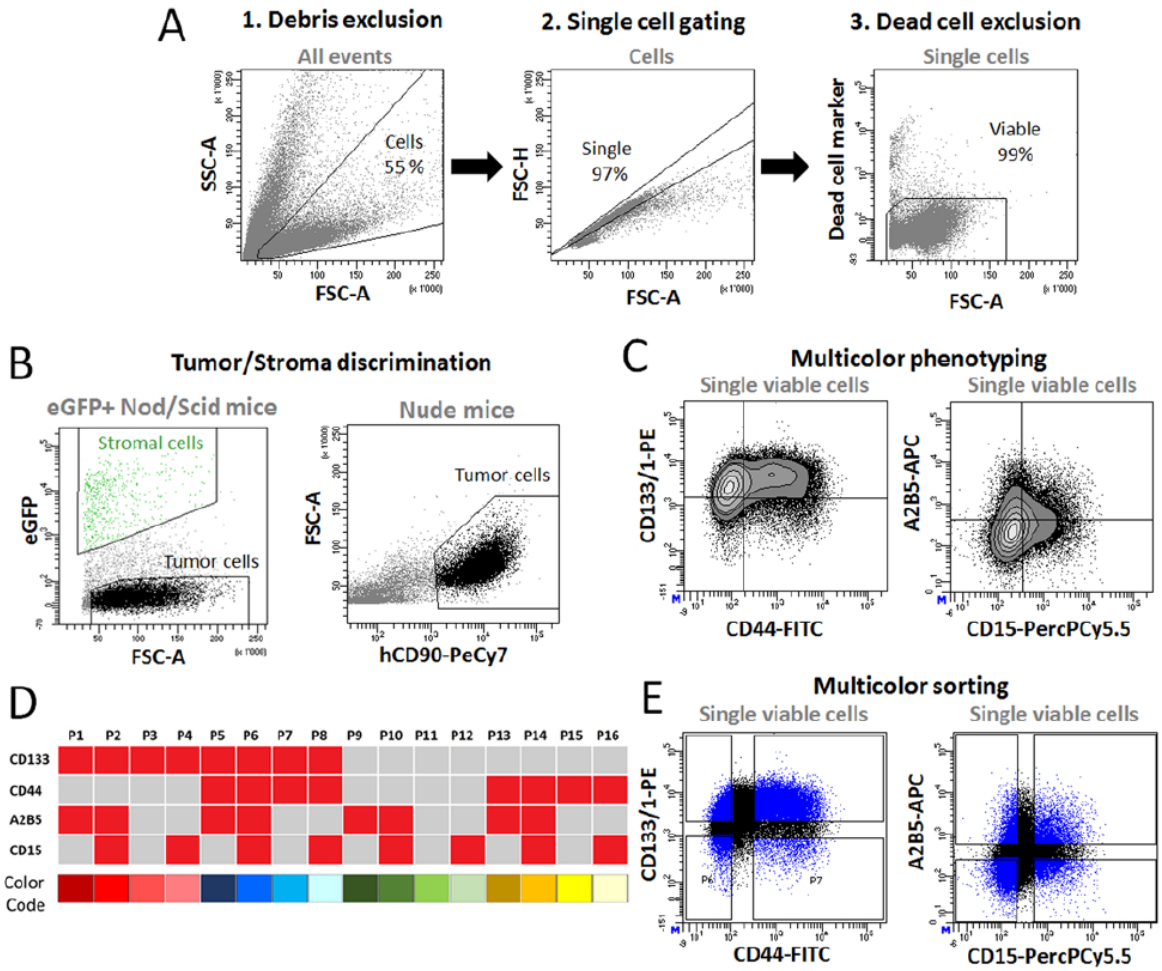
A
1. Debris exclusion
All events
SSC-A
FSC-A
Cells
55 %
2. Single cell gating
Cells
FSC-H
FSC-A
Single
97%
3. Dead cell exclusion
Single cells
Dead cell marker
FSC-A
Viable
99%
B
Tumor/Stroma discrimination
eGFP+ Nod/Scid mice
eGFP
FSC-A
Stromal cells
Tumor cells
Nude mice
FSC-A
hCD90-PeCy7
Tumor cells
C
Multicolor phenotyping
Single viable cells
CD133/1-PE
CD44-FITC
Single viable cells
A2B5-APC
CD15-PercPCy5.5
D
P1 P2 P3 P4 P5 P6 P7 P8 P9 P10 P11 P12 P13 P14 P15 P16
CD133
CD44
A2B5
CD15
Color Code
E
Multicolor sorting
Single viable cells
CD133/1-PE
CD44-FITC
P6
P7
Single viable cells
A2B5-APC
CD15-PercPCy5.5

Figure S3. CSC-associated marker expression profiles in GBM PDXs and stem-like cultures. A. Flow cytometric analysis of tumor cells showing inter-patient heterogeneity for a panel of CSC-associated epitopes in GBM PDXs. Expression was considered negative (-) when positive staining was equal to negative control, low when mean fluorescence intensity (MFI) of positive staining was less than 10x negative control (low), positive with 10-100x difference in MFI (+) and high when MFI was >100x higher compared to negative control (++). **B.** Flow cytometric analysis of tumor cells showing inter-patient heterogeneity for the CD133, CD44, CD15 and A2B5 epitopes in GBM PDXs (left panels) and stem-like cultures (right panels). Percentage of positive cells is indicated for all markers vs. negative control ('black' gating, positive vs. negative cells). For intratumoral heterogeneity discriminating negative, low and high expressing cells additional gating was applied ('red' gating). For defining 16 distinct subpopulations heterogeneity based on low vs. high expression levels ('red' gating) had priority over negative vs. positive discrimination ('black' gating) if applicable. See **Fig. S2** for gating strategy.

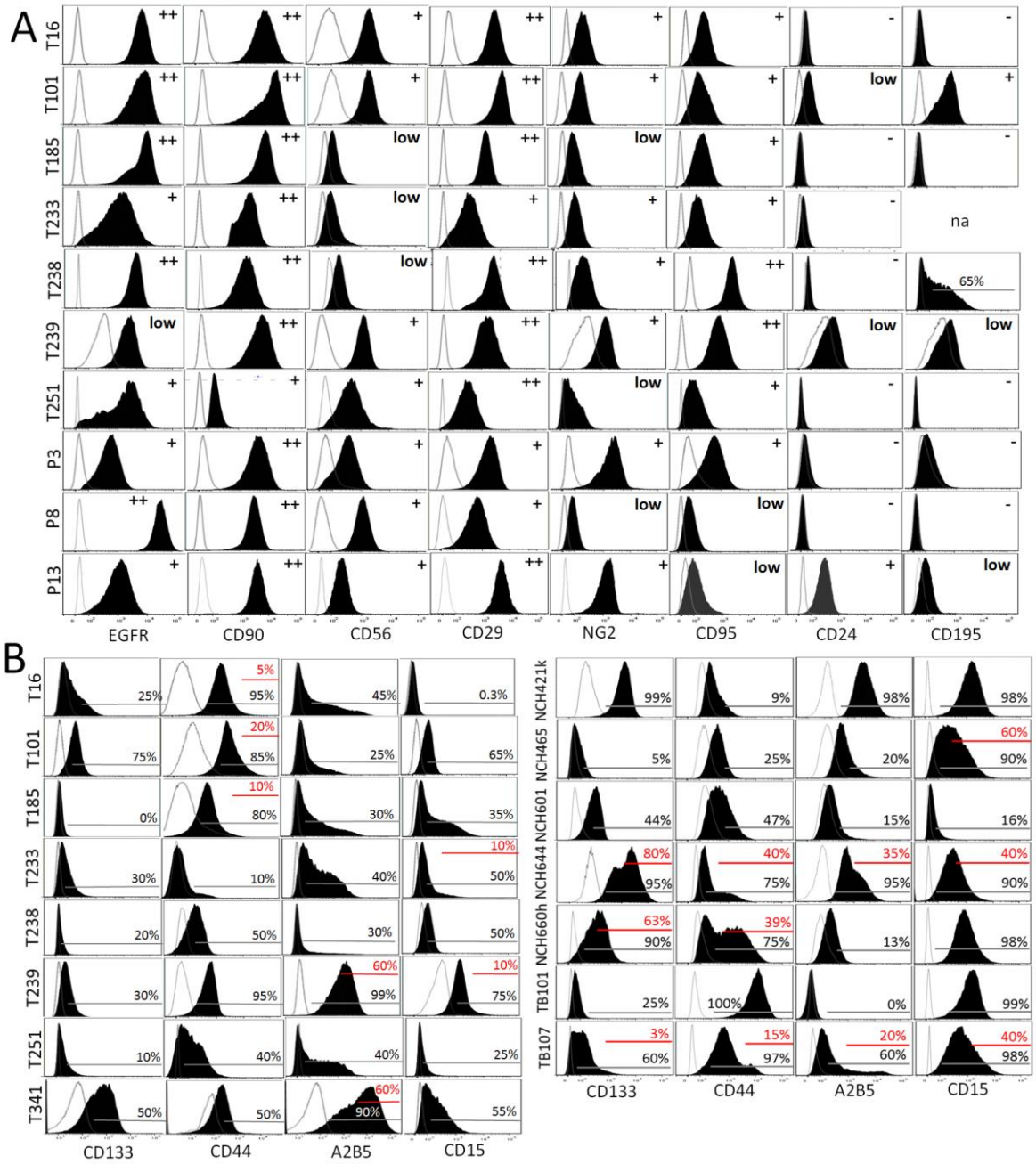
A
T16
T101
T185
T233
T238
T239
T251
P3
P8
P13
EGFR
CD90
CD56
CD29
NG2
CD95
CD24
CD195
B
T16
T101
T185
T233
T238
T239
T251
T341
CD133
CD44
A2B5
CD15
NCH421k
NCH465
NCH601
NCH644
NCH660h
TB101
TB107
CD133
CD44
A2B5
CD15

Figure S4. Characterization of intratumoral CSC-associated heterogeneity. A. Cell cycle analysis of 16 subpopulations of NCH644 cells. Cells in S/G2/M cell cycle phase were distinguished from the G1 phase based on the Hoechst flow cytometric profile combined with multicolor phenotyping in viable cells (n=3, mean +/- SEM, ttest, *p_{value}≤0.05; **p_{value}≤0.01; ***p_{value}≤0.001). **B.** Multipotency of NCH421k cells. NCH421k cells were stained with one epitope at a time (CD133, CD44, A2B5 and CD15). 500 positive and negative cells were FACS-sorted, cultured (n=4) and re-phenotyped after 25 days for the presence of the same markers. All populations were able to recreate initial heterogeneity. **C.** Distribution of NCH644 subpopulations upon hypoxia. NCH421k cells were cultured in normoxia (N) and hypoxia (H) for 16h, 48h, and 7 days. Distribution of subpopulations is presented as a mean percentage of each subpopulation in viable single cells (n_B=3; n_T=3). See **Table S2C** for statistics.

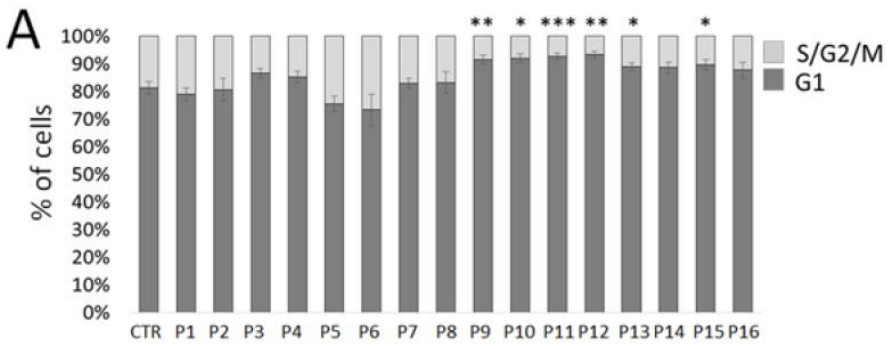
A
100%
90%
80%
70%
60%
50%
40%
30%
20%
10%
0%
% of cells
S/G2/M
G1
** * *** ** * *
CTR P1 P2 P3 P4 P5 P6 P7 P8 P9 P10 P11 P12 P13 P14 P15 P16

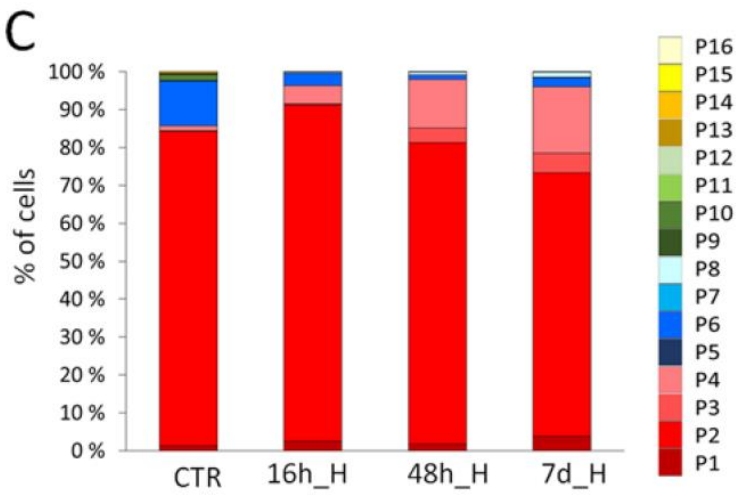
C
100 %
90 %
80 %
70 %
60 %
50 %
40 %
30 %
20 %
10 %
0 %
% of cells
CTR
16h_H
48h_H
7d_H
P16
P15
P14
P13
P12
P11
P10
P9
P8
P7
P6
P5
P4
P3
P2
P1

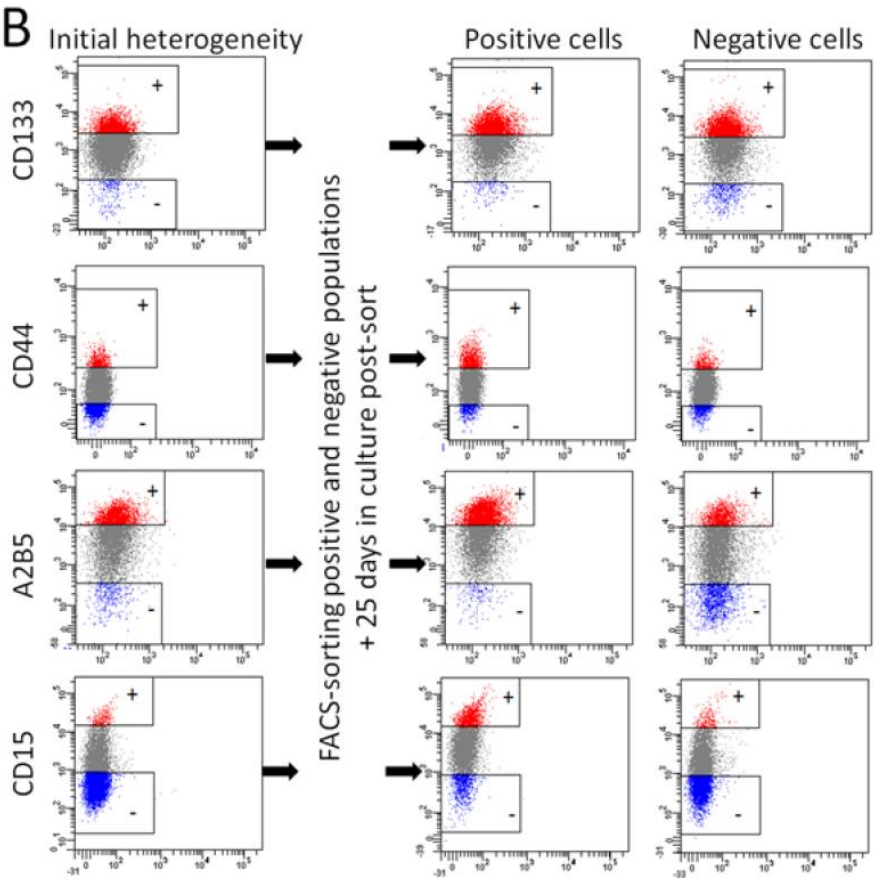
B
Initial heterogeneity
Positive cells
Negative cells
CD133
CD44
A2B5
CD15
FACS-sorting positive and negative populations
+ 25 days in culture post-sort

Figure S5. GBM state transitions in normoxia and hypoxia. A. Distribution of 16 FACS-sorted NCH644 subpopulations over time. Re-phenotyping was performed 20 (D20), 30 (D30) and 70 (D70) days after FACS (D0) for each subpopulation (n_B=4; n_T=3). The distribution of subpopulations is presented as a mean percentage of each subpopulation in viable single cells. Distribution of 16 subpopulations is presented for control NCH644 cultures (CTR). See **Table S3A** for statistics. **B.** Distribution of 16 subpopulations after single cell sorting (self-renewal test). Re-phenotyping was performed at each self-renewal passage for each subpopulation (all single spheres gathered together in one pool, n=4). Distribution of subpopulations is presented as a mean percentage of each subpopulation in viable single cells. NCH644 viable single cells were sorted as a control (CTR_EXP). See **Table S4A** for statistics. **C.** Markov modeling of state transitions in normoxia. Probabilities of state transitions within one time-step (1 day) are presented for each subpopulation. Y axis displays subpopulations in the present state. X axis displays the probabilities of each subpopulation to change to respective phenotypes. **D**. Graphs represent distribution of 16 subpopulations after single cell sorting (self-renewal test) cultivated in hypoxia. Re-phenotyping was performed at each self-renewal passage for each subpopulation (n=4). Distribution of subpopulations is presented as a mean percentage of each subpopulation in viable single cells. NCH644 viable single cells were sorted as a control (CTR_EXP). See **Table S4B** for statistics. Distribution of 16 subpopulations of control NCH644 cultures after 60 days in hypoxia is presented as an environmental control (CTR_H). **E.** Markov modeling of state transitions in hypoxia. Probabilities of state transitions within one time-step (1 day) are presented for each subpopulation. Y axis displays subpopulations in the present state. X axis displays probabilities of each subpopulation to change to respective phenotypes.

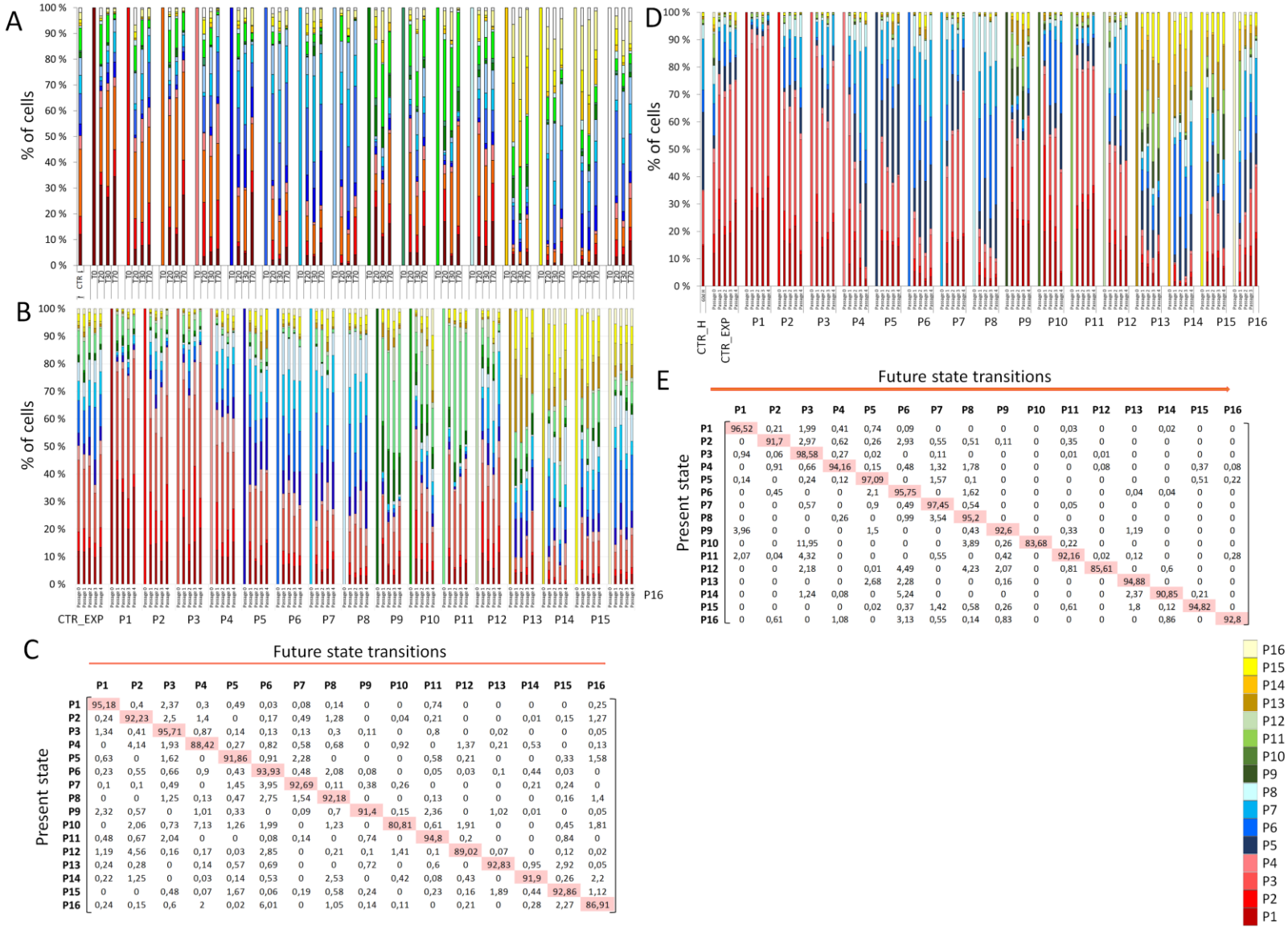

C

Future state transitions

Present state

	P1	P2	P3	P4	P5	P6	P7	P8	P9	P10	P11	P12	P13	P14	P15	P16
P1	95,18	0,4	2,37	0,3	0,49	0,03	0,08	0,14	0	0	0,74	0	0	0	0	0,25
P2	0,24	92,23	2,5	1,4	0	0,17	0,49	1,28	0	0,04	0,21	0	0	0,01	0,15	1,27
P3	1,34	0,41	95,71	0,87	0,14	0,13	0,13	0,3	0,11	0	0,8	0	0,02	0	0	0,05
P4	0	4,14	1,93	88,42	0,27	0,82	0,58	0,68	0	0,92	0	1,37	0,21	0,53	0	0,13
P5	0,63	0	1,62	0	91,86	0,91	2,28	0	0	0	0,58	0,21	0	0	0,33	1,58
P6	0,23	0,55	0,66	0,9	0,43	93,93	0,48	2,08	0,08	0	0,05	0,03	0,1	0,44	0,03	0
P7	0,1	0,1	0,49	0	1,45	3,95	92,69	0,11	0,38	0,26	0	0	0	0,21	0,24	0
P8	0	0	1,25	0,13	0,47	2,75	1,54	92,18	0	0	0,13	0	0	0	0,16	1,4
P9	2,32	0,57	0	1,01	0,33	0	0,09	0,7	91,4	0,15	2,36	0	1,02	0,01	0	0,05
P10	0	2,06	0,73	7,13	1,26	1,99	0	1,23	0	80,81	0,61	1,91	0	0	0,45	1,81
P11	0,48	0,67	2,04	0	0	0,08	0,14	0	0,74	0	94,8	0,2	0	0	0,84	0
P12	1,19	4,56	0,16	0,17	0,03	2,85	0	0,21	0,1	1,41	0,1	89,02	0,07	0	0,12	0,02
P13	0,24	0,28	0	0,14	0,57	0,69	0	0	0,72	0	0,6	0	92,83	0,95	2,92	0,05
P14	0,22	1,25	0	0,03	0,14	0,53	0	2,53	0	0,42	0,08	0,43	0	91,9	0,26	2,2
P15	0	0	0,48	0,07	1,67	0,06	0,19	0,58	0,24	0	0,23	0,16	1,89	0,44	92,86	1,12
P16	0,24	0,15	0,6	2	0,02	6,01	0	1,05	0,14	0,11	0	0,21	0	0,28	2,27	86,91

E

Future state transitions

Present state

	P1	P2	P3	P4	P5	P6	P7	P8	P9	P10	P11	P12	P13	P14	P15	P16
P1	96,52	0,21	1,99	0,41	0,74	0,09	0	0	0	0	0,03	0	0	0,02	0	0
P2	0	91,7	2,97	0,62	0,26	2,93	0,55	0,51	0,11	0	0,35	0	0	0	0	0
P3	0,94	0,06	98,58	0,27	0,02	0	0,11	0	0	0	0,01	0,01	0	0	0	0
P4	0	0,91	0,66	94,16	0,15	0,48	1,32	1,78	0	0	0	0,08	0	0	0,37	0,08
P5	0,14	0	0,24	0,12	97,09	0	1,57	0,1	0	0	0	0	0	0	0,51	0,22
P6	0	0,45	0	0	2,1	95,75	0	1,62	0	0	0	0	0,04	0,04	0	0
P7	0	0	0,57	0	0,9	0,49	97,45	0,54	0	0	0,05	0	0	0	0	0
P8	0	0	0	0,26	0	0,99	3,54	95,2	0	0	0	0	0	0	0	0
P9	3,96	0	0	0	1,5	0	0	0,43	92,6	0	0,33	0	1,19	0	0	0
P10	0	0	11,95	0	0	0	0	3,89	0,26	83,68	0,22	0	0	0	0	0
P11	2,07	0,04	4,32	0	0	0	0,55	0	0,42	0	92,16	0,02	0,12	0	0	0,28
P12	0	0	2,18	0	0,01	4,49	0	4,23	2,07	0	0,81	85,61	0	0,6	0	0
P13	0	0	0	0	2,68	2,28	0	0	0,16	0	0	0	94,88	0	0	0
P14	0	0	1,24	0,08	0	5,24	0	0	0	0	0	0	2,37	90,85	0,21	0
P15	0	0	0	0	0,02	0,37	1,42	0,58	0,26	0	0,61	0	1,8	0,12	94,82	0
P16	0	0,61	0	1,08	0	3,13	0,55	0,14	0,83	0	0	0	0	0,86	0	92,8

Figure S6. Reversible adaptation upon differentiation and in vivo microenvironment. **A.** Examples of ICC after 14d of adherent NCH644 cultures in stem cell (Undiff_H) or differentiation (Diff_H) conditions in hypoxia. **B.** Flow cytometric analysis of internal stem cell (Nestin, Vimentin) and differentiation markers (β-III-tubulin, GFAP) in control 3D NCH421k cultures (CTR), and differentiation (Diff) conditions after 14 days. N= normoxia, H= hypoxia (n=3). Negative control for antibody staining is shown for each type of cells (Isotype). Black lines discriminate between negative and positive cells. Dotted line indicate mode expression in control cells. **C.** Flow cytometric analysis of internal stem cell (Nestin, Vimentin) and differentiation markers (β-III-tubulin, GFAP) in control 3D NCH644 and NCH421k cultures (CTR), and 14 day 3D cultures that were previously subjected to differentiation (De-Diff) conditions. N= normoxia, H= hypoxia (n_B=3; n_T=3). Negative control for antibody staining is shown for each marker (Isotype). Black lines discriminate between negative and positive cells. Dotted line indicate mode expression in control cells. **D.** Distribution of NCH421k subpopulations upon differentiation (Diff) conditions, N= normoxia, H= hypoxia (n=3). For each condition equilibrium is presented after 14 days of environmental change (left) and 14 days after consecutive change to original 3D stem cell conditions (right). NCH421k cultured as 3D spheres in normoxia are shown as control (CTR). See **Table S2E** for statistics. **E.** Graphs represent distribution of 16 subpopulations in xenografted NCH601 and NCH660h tumor cells (X). Normoxic cultures are shown as a control (CTR). (n=3). **F.** Distribution of 16 subpopulations in xenografted NCH421k tumor cells (X) and 56 days after regrowth in vitro as 3D cultures (De-X) (n_B=2; n_T=3). NCH421k cultured in normoxia are shown as a control (CTR). See **Table S2G** for statistics. **G.** Flow cytometric analysis of internal stem cell (Nestin, Vimentin) and differentiation markers (β-III-tubulin, GFAP) in control NCH421k cultures (CTR), tumor cells in tumor mass developed upon xenografting (X) and xenografted cells recultured in vitro for 56 days (De-X). Negative control for antibody staining is shown for each marker (Isotype). Black lines discriminate between negative and positive cells. Dotted line indicate mode expression in control cells (n_B=2; n_T=3).

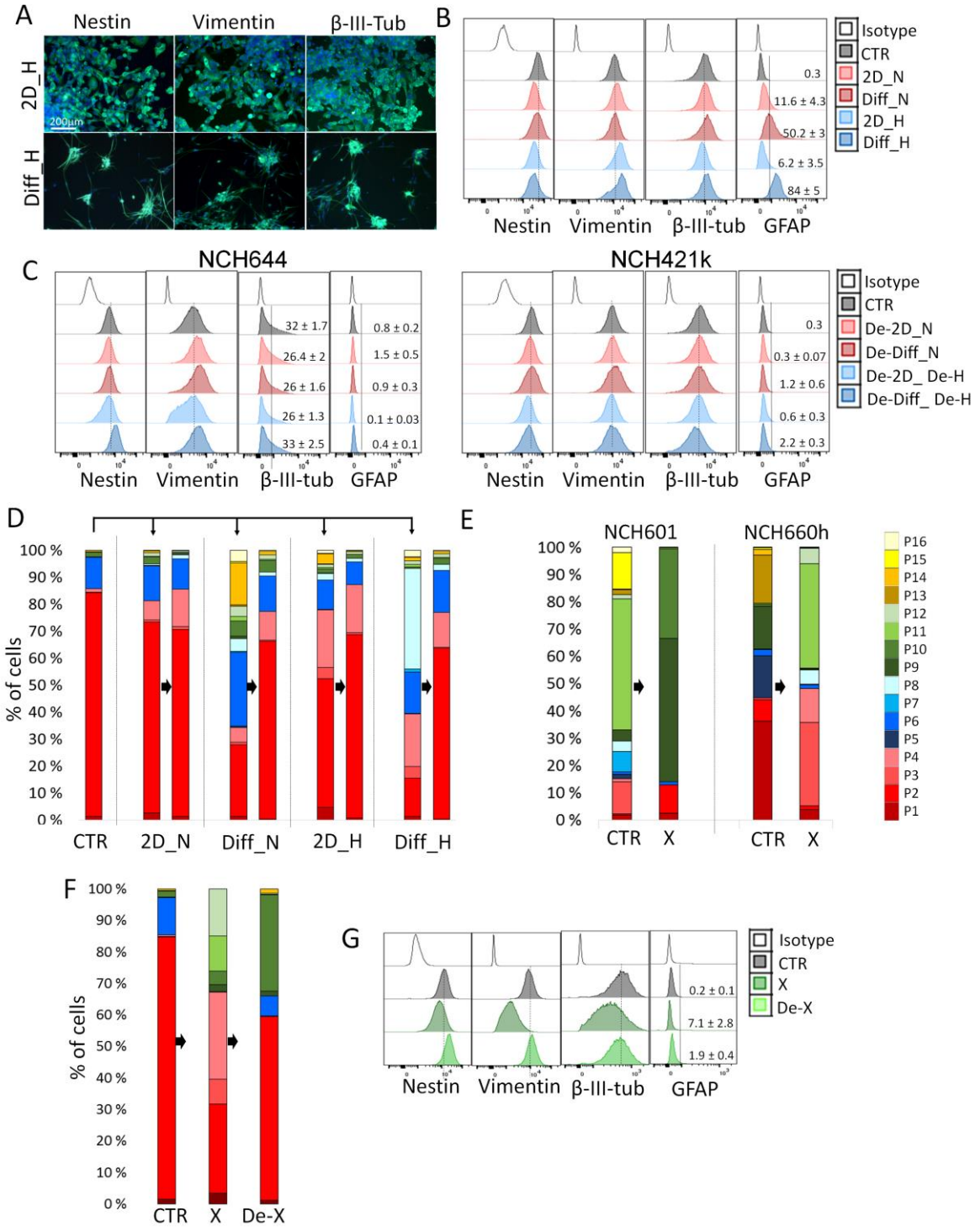
A
Nestin
Vimentin
β-III-Tub
2D_H
Diff_H
200µm
B
Isotype
CTR
2D_N
Diff_N
2D_H
Diff_H
0.3
11.6 ± 4.3
50.2 ± 3
6.2 ± 3.5
84 ± 5
Nestin
Vimentin
β-III-tub
GFAP
C
NCH644
NCH421k
32 ± 1.7
26.4 ± 2
26 ± 1.6
26 ± 1.3
33 ± 2.5
0.8 ± 0.2
1.5 ± 0.5
0.9 ± 0.3
0.1 ± 0.03
0.4 ± 0.1
0.3
0.3 ± 0.07
1.2 ± 0.6
0.6 ± 0.3
2.2 ± 0.3
Isotype
CTR
De-2D_N
De-Diff_N
De-2D_ De-H
De-Diff_ De-H
D
% of cells
CTR
2D_N
Diff_N
2D_H
Diff_H
E
NCH601
NCH660h
CTR
X
P16
P15
P14
P13
P12
P11
P10
P9
P8
P7
P6
P5
P4
P3
P2
P1
F
% of cells
CTR
X
De-X
G
0.2 ± 0.1
7.1 ± 2.8
1.9 ± 0.4
Isotype
CTR
X
De-X

Figure S7. Single cell Drop-seq analysis. A-B. tSNE plots showing the expression of marker genes in FACS-sorted tumor cells of 3 GBM PDXs (P3, P8, P13) and 2 patient derived stem-like cultures (NCH644, NCH421k). The expression gradient is color coded. See top-left graph for tSNE plot showing the overall gene expression relationship between single cells of different patient-derived cells. Plots in (A) show the expression of stem cell-associate markers highlighting inter-patient and intratumoral heterogeneity. Plots in (B) show the expression of cell membrane markers (CD90, CD29) with high levels in most tumors and relatively uniform expression profile as detected by flow cytometry. *EGFR* is presented as a control expected to be highly expressed by P8 cells. **C.** Differential gene expression analysis between single cells of subpopulation P2 versus P6. Threshold for differential expression was set at FDR<0.01 and |logFC|>0.5. Only 6 genes were found to be differentially expressed between the 2 subpopulations (FDR<0.01, |logFC|>1). **D.** tSNE plots showing the expression of marker genes in FACS-sorted subpopulations P2 and P6. The expression gradient is color coded. For visualization purposes cells with no reads were displayed as transparent. *MIF* and *CD44* were expressed at higher levels in FACS-sorted P6 subpopulation. *PROM1* and *ST8SIA1* were detected in a similar proportion of cells. P6 showed upregulation of *Macrophage migration inhibitory factor (MIF),* a known ligand of the CD74/CD44-receptor complex (Shi et al., 2006). CD44 mRNA, the phenotypic discriminator between two subpopulations, was also detected at higher, though not significant, level in the CD44+ P6 subpopulation.

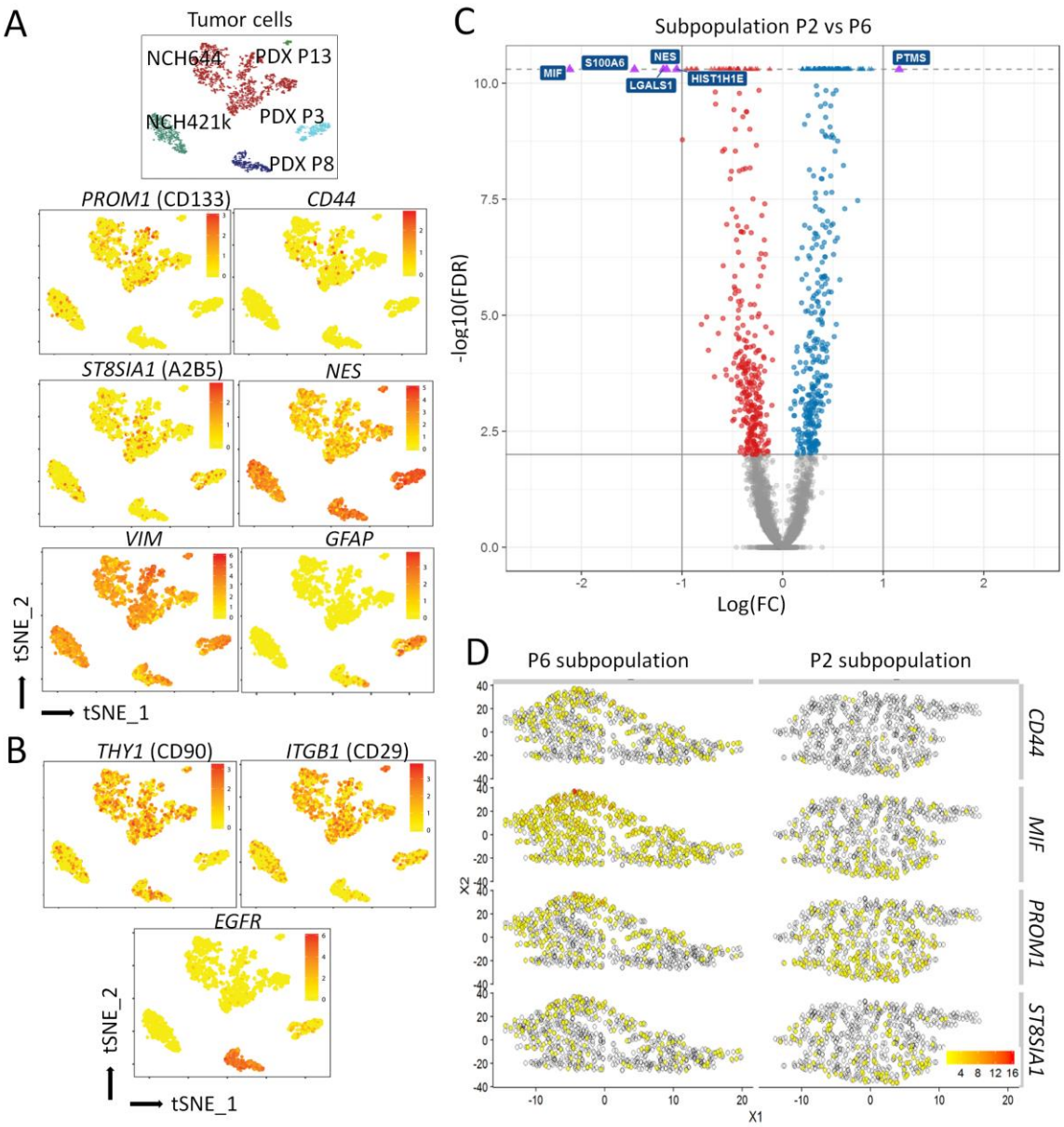
A
Tumor cells
NCH644
PDX P13
NCH421k
PDX P3
PDX P8
PROM1 (CD133)
CD44
ST8SIA1 (A2B5)
NES
VIM
GFAP
tSNE_2
tSNE_1
B
THY1 (CD90)
ITGB1 (CD29)
EGFR
tSNE_2
tSNE_1
C
Subpopulation P2 vs P6
MIF
S100A6
NES
LGALS1
HIST1H1E
PTMS
-log10(FDR)
Log(FC)
D
P6 subpopulation
P2 subpopulation
CD44
MIF
PROM1
ST8SIA1
X2
X1
4 8 12 16

SUPPLEMENTAL TABLE LEGENDS (submitted as a separate excel file)

Table S1. Group comparison for CSC-associated gene expression in GBM patient subgroups. Related to Fig. 1A.

Group comparison was performed in Gitools using mannWhitneyWilcoxon and Benjamini Hochberg multiple test correction was applied. The GBM expression subgroup were considered as: Neural Group (n=28, Mesenchymal (n=51),Proneural (n=39),Classical (n=40).

A. Group comparison for CSC-associated gene expression in the different GBM subgroups (column headers). P value log summary is depicted in left panel as follows: yellow-to-red is represented if values in Group 1 are significantly shifted

B. Statistical analysis of group comparisons.

Several markers were correlated with previously defined transcriptional subgroups e.g. CCR5 (CD195), ITGB1 (CD29), CD44 and FAS (CD95) are more expressed in the mesenchymal subtype, whereas PROM1 (CD133), NCAM (CD56) and CD24 are enriched in the proneural subtype.

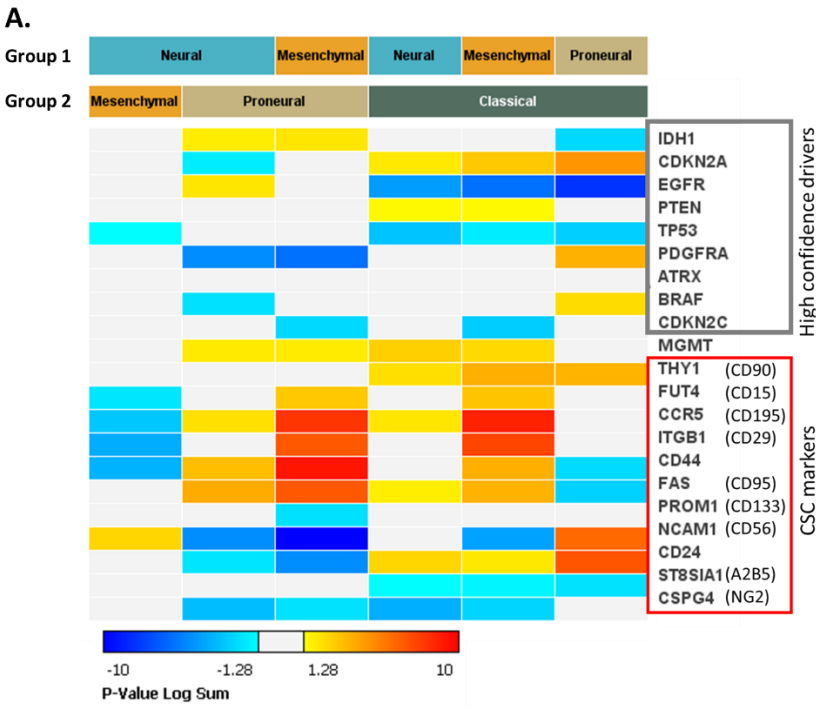
A.
Group 1
Neural
Mesenchymal
Neural
Mesenchymal
Proneural
Group 2
Mesenchymal
Proneural
Classical
IDH1
CDKN2A
EGFR
PTEN
TP53
PDGFRA
ATRX
BRAF
CDKN2C
High confidence drivers
MGMT
THY1 (CD90)
FUT4 (CD15)
CCR5 (CD195)
ITGB1 (CD29)
CD44
FAS (CD95)
PROM1 (CD133)
NCAM1 (CD56)
CD24
ST8SIA1 (A2B5)
CSPG4 (NG2)
CSC markers
-10
-1.28
1.28
10
P-Value Log Sum

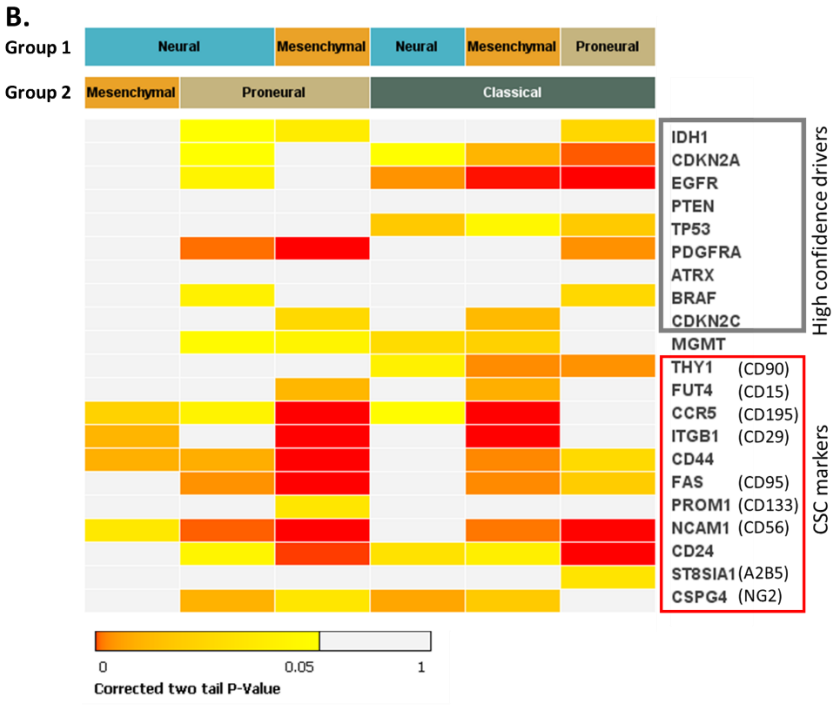
B.
Group 1
Neural
Mesenchymal
Neural
Mesenchymal
Proneural
Group 2
Mesenchymal
Proneural
Classical
IDH1
CDKN2A
EGFR
PTEN
TP53
PDGFRA
ATRX
BRAF
CDKN2C
High confidence drivers
MGMT
THY1 (CD90)
FUT4 (CD15)
CCR5 (CD195)
ITGB1 (CD29)
CD44
FAS (CD95)
PROM1 (CD133)
NCAM1 (CD56)
CD24
ST8SIA1 (A2B5)
CSPG4 (NG2)
CSC markers
0
0.05
1
Corrected two tail P-Value

Table S2. Statistical analysis of phenotypic states distribution upon treatment and adaptation to changing environment. Statistical analysis was performed with the Student t-test with a Bonferroni multiple-significance-test correction for 16 phenotypic states. Statistical differences between proportion of phenotypic states are presented for each subpopulation if pvalue < 0.05. Each line represents statistical comparison between proportions of each phenotypic state present in defined environmental conditions. *<0.05; **<0.01; ***<0.001

A. Markov model validation in pre-designed NCH644 equilibria. Related to Fig. 2G.
MixA and MixB subpopulation combinations were cultured for 39 days after FACS.
B. Phenotypic analysis of NCH644 cultures upon hypoxic cultures. Related to Fig. 3A
Hypoxia (H) was applied for 16h, 48h, 7 and 60 days.
C. Phenotypic analysis of NCH421k cultures upon hypoxic cultures. Related to Fig. S4C
Hypoxia (H) was applied for 16h, 2 and 7 days.
D. Phenotypic analysis of NCH644 cultures upon differentiation (Diff) and de-differentiation (De-Diff) in normoxic (N) and hypoxic (H) conditions. Related to Fig. 4C
E. Phenotypic analysis of NCH421k cultures upon differentiation (Diff) and de-differentiation (De-Diff) in normoxic (N) and hypoxic (H) conditions. Related to Fig. S6D
F. Phenotypic analysis of NCH644 cultures (CTR) upon xenografting (X) and reculture of xenografted cells in 3D normoxic conditions (De-X). Related to Fig. 4D
G. Phenotypic analysis of NCH421k cultures (CTR) upon xenografting (X) and reculture of xenografted cells in 3D normoxic conditions (De-X). Related to Fig. S6F
H. Phenotypic analysis of NCH644 subpopulations upon xenografting (X). Phenotypic equilibrium of FACS-sorted subpopulations (P2, P6, P11, P15) was compared to control cultures in normoxia in vitro (CTR) and bulk NCH644 xenografted in vivo (X). Related to Fig. 4G

a. NCH644 TMZ	Conditions/Phenotypic states	P1	P2	P3	P4	P5	P6	P7	P8	P9	P10	P11	P12	P13	P14	P15	P16		CD133+/-	CD44+/-	A2B5+/-	CD15+/-
	CTR vs. 16h_TMZ				*	**				*			*						*	***		
	CTR vs. 2d_TMZ				*															***		
	CTR vs. 7d_TMZ				***					**			**							**		*
	16h_TMZ vs. 2d_TMZ																					
	16h_TMZ vs. 7d_TMZ													**							*	*
	2d_TMZ vs. 7d_TMZ													**								*
b. NCH421k TMZ	Conditions/Phenotypic states	P1	P2	P3	P4	P5	P6	P7	P8	P9	P10	P11	P12	P13	P14	P15	P16		CD133+/-	CD44+/-	A2B5+/-	CD15+/-
	CTR vs. 16h_TMZ																			*		
	CTR vs. 2d_TMZ		*				*													**		
	CTR vs. 7d_TMZ		***						**	**	***	*	*				***		***	*	***	**
	16h_TMZ vs. 2d_TMZ																					
	16h_TMZ vs. 7d_TMZ		***						***	**	***	*	*		*		***		***		***	***
	2d_TMZ vs. 7d_TMZ	*	***						**	*	***						***		***		**	**
c. NCH644 Hypoxia	Conditions/Phenotypic states	P1	P2	P3	P4	P5	P6	P7	P8	P9	P10	P11	P12	P13	P14	P15	P16		CD133+/-	CD44+/-	A2B5+/-	CD15+/-
	CTR vs. 16h_H																					
	CTR vs. 2d_H														***							
	CTR vs. 7d_H		***	**			**	***		***	***			**	***				*		***	***
	CTR vs. 60d_H		***		***	***	**	***		***	***	**	***		***		**		***	**	*	***
	16h_H vs.2d_H																					
	16h_H vs. 7d_H	**		***				*		*				*							***	**
	16h_H vs. 60d_H					***							*		*		**		**	**		**
	2d_H vs. 7d_H			**																		
	2d_H vs. 60d_H					*											**		**	*	*	*
	7d_H vs. 60d_H			*		***					*	*			**		***		**	**	***	
d. NCH421k Hypoxia	Conditions/Phenotypic states	P1	P2	P3	P4	P5	P6	P7	P8	P9	P10	P11	P12	P13	P14	P15	P16		CD133+/-	CD44+/-	A2B5+/-	CD15+/-
	CTR vs. 16h_H		*				**			*	*	**							*	*		
	CTR vs.2d_H		*				*			*		**								**		
	CTR vs. 7d_H		*				*					*								*		
	16h_H vs.2d_H																					
	16h_H vs. 7d_H																					
	2d_H vs. 7d_H																					

e. NCH644 Reversibility from H to N	Conditions/Phenotypic states	P1	P2	P3	P4	P5	P6	P7	P8	P9	P10	P11	P12	P13	P14	P15	P16		CD133+/-	CD44+/-	A2B5+/-	CD15+/-
	CTR vs 7d h		***	**			**	***		***	***			**	***				*		***	***
	CTR vs 7d renorm									**									**			*
	CTR vs 14d renorm			**			*												**			
	7d h vs 7d renorm							*											**	*		
	7d h vs 14d renorm		***	***			**	***		*	***		***	*	***				***	*		
	7d renorm vs 14d renorm												*						***	*		
f. NCH644 Differentiation	Conditions/Phenotypic states	P1	P2	P3	P4	P5	P6	P7	P8	P9	P10	P11	P12	P13	P14	P15	P16		CD133+/-	CD44+/-	A2B5+/-	CD15+/-
Normoxia	CTR vs 2D_N		**	*			***	***		***	***		**	***	***				**		***	***
	CTR vs De-2D _N	***	***					***		***	***			**	***				**	**		**
	2D_N vs De-2D_N																					
	CTR vs Diff_N	***	***	***	***	***	***		***	*		*				***	***		***	***	***	**
	CTR vs De-Diff_N	***	***	***	***		***		***			*	*	*		***	**		***	***	**	***
	Diff_N vs De-Diff_N	***	***	***	***	**	**		**								***		***		**	
Hypoxia	CTR vs 2D_H	***	***					***	*	***	***									***	*	
	CTR vs De-2D _De-H		**	***	**	**														**		*
	2D_H vs De-2D_De-H								*												**	
	CTR vs Diff_H	***	***	***	***					***	*	***	**			*	**		***	***		*
	CTR vs De-Diff_De-H	***	*	**						***	*	*				*			*	***		
	Diff_H vs De-Diff_De-H	**	*	*	**												**		**	***		*
g. NCH421k Differentiation	Conditions/Phenotypic states	P1	P2	P3	P4	P5	P6	P7	P8	P9	P10	P11	P12	P13	P14	P15	P16		CD133+/-	CD44+/-	A2B5+/-	CD15+/-
Normoxia	CTR vs 2D_N			**	***	**		***	***				***				***				***	*
	CTR vs De-2D _N			***	***	*		***	***								*				***	
	2D_N vs De-2D_N									*			*						**			*
	CTR vs Diff_N		***	***	***	***		***	***	***		***	***	***	***	***	***		***	***	***	***
	CTR vs De-Diff_N				***			**	***				***			**	***		**		***	
	Diff_N vs De-Diff_N		***	*		**	**	*	**	***		**		**	**	*	**		***	***	**	***

h. NCH421k Differentiation	Conditions/Phenotypic states	P1	P2	P3	P4	P5	P6	P7	P8	P9	P10	P11	P12	P13	P14	P15	P16		CD133+/-	CD44+/-	A2B5+/-	CD15+/-
Hypoxia	CTR vs 2D_H	*	*	***	***	**		***	***												***	***
	CTR vs De-2D _De-H			***	***			**	***				*								***	
	2D_H vs De-2D_De-H	***		*								**			*				**		*	***
	CTR vs Diff_H		***	***	***	***		***	***			***	***			**	***			***	***	**
	CTR vs De-Diff_De-H			**	***			***	***				***				***				***	
	Diff_H vs De-Diff_De-H		***	*	*	**	*	*	*	***	*	*	*	**	***	*	**		***	***	**	***
i. NCH644 Subpopulation Xenografting	Conditions/Phenotypic states	P1	P2	P3	P4	P5	P6	P7	P8	P9	P10	P11	P12	P13	P14	P15	P16		CD133+/-	CD44+/-	A2B5+/-	CD15+/-
	CTR vs CTR_X	**	**	**	*	**	***	*	**	**		***		**	*				***	***	*	***
	CTR vs P2 _X			***		**	***	*	**					**	*				**	***		
	CTR vs P6_X			**	*	**	**	*	**	*				**	**				**	***	**	*
	CTR vs P11_X	**		**	*	*	***	*	**	***		**			**				***	***		**
	CTR vs P15_X	**	*	**	*	*	***	*	*	***		***		*	*				***	***		***
	CTR_X vs P2 _X																					
	CTR_X vs P6_X											*									**	
	CTR_X vs P11_X																					
	CTR_X vs P15_X																					
	P2_X vs P6_X																					
	P2 _Xvs P11_X																					
	P2 _Xvs P15_X																					
	P6_X vs P11_X																					
	P6 _Xvs P15_X																					
	P11_X vs P15_X																					
j. NCH644 Xenografting	Conditions/Phenotypic states	P1	P2	P3	P4	P5	P6	P7	P8	P9	P10	P11	P12	P13	P14	P15	P16		CD133+/-	CD44+/-	A2B5+/-	CD15+/-
	CTR vs CTR_X	**	**	**	*	**	***	*	**	**		***		**	*				***	***	*	***
	CTR vs re-in vitro	***					**			***	**	**			**				***	**	***	***
	CTR_X vs re-in vitro	***	***	**	**	***	**	***	***	*		***				**	*		***	***	***	**
k. NCH421k Xenografting	Conditions/Phenotypic states	P1	P2	P3	P4	P5	P6	P7	P8	P9	P10	P11	P12	P13	P14	P15	P16		CD133+/-	CD44+/-	A2B5+/-	CD15+/-
	CTR vs X		**	***	***					***		***	***						***		***	***
	CTR vs De-X		**								***								***			
	X vs De-X			***	***		*		**		*	***	***		*					***	***	***

Table S3. Statistical analysis of phenotypic state transitions of FACS-sorted subpopulation upon time in normoxia (A.) and in hypoxia (B.). Related to Fig. 2D and Fig. 3D respectively. Statistical analysis was performed with the Student t-test with a Bonferroni multiple-significance-test correction for 16 phenotypic states . Each line represents statistical comparison between proportions of each phenotypic state present in FACS-sorted subpopulations at a defined self-renewal passage. No statistical differences were detected between the same subpopulations at different passages. Statistical differences between proportion of phenotypic states (PSs) in different subpopulations and control cells (CTR = control cells cultures in normoxia; CTR_H = control cells cultured 60 days in hypoxia) at the same passage is presented if pvalue < 0.05 NCH644 exp corresponds to FACS-sorted bulk NCH644 cells w/o discrimination of 16 subpopulations

*<0.05; **<0.01; ***<0.001

a. Multipotency in normoxia

20d	Conditions/Phenotypic states	P1	P2	P3	P4	P5	P6	P7	P8	P9	P10	P11	P12	P13	P14	P15	P16
	CTR vs P1						***	**		***				***			
	CTR vs P2					***		*		***							
	CTR vs P3					***		**						***			
	CTR vs P4	*				***		**		***				***			
	CTR vs P5		***							***							
	CTR vs P6	***								***				***			
	CTR vs P7	**								***							
	CTR vs P8	***								***	***		***	***			
	CTR vs P9			**			***	**	***								
	CTR vs P10	*				**	*	*									
	CTR vs P11			***		*	***	**	***								
	CTR vs P12					**											
	CTR vs P13		***	***	*			**	*					*			
	CTR vs P14	***		***	**	**				***							
	CTR vs P15	***	***	***	*												
	CTR vs P16	**		*						*							
30d	Conditions/Phenotypic states	P1	P2	P3	P4	P5	P6	P7	P8	P9	P10	P11	P12	P13	P14	P15	P16
	CTR vs P1						*			**	***			**			*
	CTR vs P2					*											
	CTR vs P3		**			**			**								**
	CTR vs P4									*							
	CTR vs P5	**	***		***			**					**	**			**
	CTR vs P6	***	***	*						*							
	CTR vs P7	*	***	**	***			**				*					
	CTR vs P8	***	***		**			*		***	***	**	***	*			
	CTR vs P9		***				***										
	CTR vs P10																
	CTR vs P11	***	***			**	***		**		**	*			***		
	CTR vs P12					*											
	CTR vs P13	***	***	***	***		***		***				*	*		***	
	CTR vs P14	***	***	***	***					***							
	CTR vs P15	***	***	***	***												
	CTR vs P16	*		***													
70d	Conditions/Phenotypic states	P1	P2	P3	P4	P5	P6	P7	P8	P9	P10	P11	P12	P13	P14	P15	P16
	CTR vs P1						*			***	***	***	***		***		*
	CTR vs P2									***	***		***				**
	CTR vs P3						***		***	**	***		***		***		**
	CTR vs P4									***	***	***		***		*	**
	CTR vs P5								***	**	***	*	***		***		***
	CTR vs P6			***						***	***	***	***		***		
	CTR vs P7			***								***					**
	CTR vs P8	*		***						***	***	***	***	**	***		
	CTR vs P9				**		***		***				***		***		**
	CTR vs P10														***		
	CTR vs P11				*	***	***		***					**	***	*	**
	CTR vs P12			**											***		
	CTR vs P13		***				***		***								
	CTR vs P14			***													
	CTR vs P15	*		***	**												
	CTR vs P16																

b. Multipotency in hypoxia

Conditions/Phenotypic state	P1	P2	P3	P4	P5	P6	P7	P8	P9	P10	P11	P12	P13	P14	P15	P16
CTR vs CTR_H		***		***	*		**		**	***	**	***		***		**
CTR vs P1		***				***		*	***	***	***	***	***	***	**	***
CTR vs P2		***					**		***	***	***	***	***	***	*	**
CTR vs P3		***	***			***		**	***	***	***	***	***	***	*	**
CTR vs P4	***	***					**		***	***	***	***	***	***		**
CTR vs P5		***				**	***		***	***	***	***	***	***		
CTR vs P6	***	***					**		***	***	***	***	***	***	*	
CTR vs P7	**	***		**			***		***	***	***	***	***	***		**
CTR vs P8	***	***					***		***	***	***	***	***	***		**
CTR vs P9		***		***	***	***		***		***	***	***		**		**
CTR vs P10		**	***	**		**			***	**	**	***	**	***		*
CTR vs P11		*				***		***	***	***	***	***		***		**
CTR vs P12		***		**			*		***	**	***	***	*	***		*
CTR vs P13		***	**	***	***		*		***	***	***	***		**		*
CTR vs P14	***	***	*	***	*		*			***	***	***				
CTR vs P15	*	***	**	***	**		*			***	**	***		***		**
CTR vs P16	***	***	***	***	*		*		***	***	***	***				
CTR_H vs P1																
CTR_H vs P2																
CTR_H vs P3			**		*		**									
CTR_H vs P4	*															
CTR_H vs P5							*									
CTR_H vs P6	**															
CTR_H vs P7	*						*									
CTR_H vs P8	**						*									
CTR_H vs P9																
CTR_H vs P10			**													
CTR_H vs P11					*											
CTR_H vs P12																
CTR_H vs P13																
CTR_H vs P14																
CTR_H vs P15																
CTR_H vs P16	*															

Table S4. Statistical analysis of phenotypical state transitions upon 4 consecutive self-renewal passages in normoxia (A.) and in hypoxia (B.). Related to Fig. S5B and Fig. S5D respectively.

a. Self-renewal in normoxia

Passage 1	Conditions/Phenotypic states	P1	P2	P3	P4	P5	P6	P7	P8	P9	P10	P11	P12	P13	P14	P15	P16
	CTR vs NCH644 exp																
	CTR vs P1	*					***		**						**		
	CTR vs P2		*		**					**					**		
	CTR vs P3	*					***		**						**		
	CTR vs P4				*					***		*					
	CTR vs P5					*											
	CTR vs P6									***		*					
	CTR vs P7			**		*					*		*				
	CTR vs P8	**								***		**					
	CTR vs P9				**		***		**	**				*	*		
	CTR vs P10		*		*	*											
	CTR vs P11						**		**						**		
	CTR vs P12																
	CTR vs P13		*	***	**				**	**			*	**			
	CTR vs P14	***		***								*					*
	CTR vs P15																
	CTR vs P16	**		***											***		
Passage 2	Conditions/Phenotypic states	P1	P2	P3	P4	P5	P6	P7	P8	P9	P10	P11	P12	P13	P14	P15	P16
	CTR vs NCH644 exp																
	CTR vs P1	**					***		**								
	CTR vs P2																
	CTR vs P3									***							
	CTR vs P4						**			***		*					
	CTR vs P5		**		*	**					*						
	CTR vs P6									***					*		
	CTR vs P7	**	**							***	*				**		
	CTR vs P8	**						**	*	***	*	*					
	CTR vs P9		**		*		***		**			***		*			
	CTR vs P10									**							
	CTR vs P11		*		*	*	***		**			***			**		
	CTR vs P12																
	CTR vs P13		**	**	*		**		**		*			*			
	CTR vs P14	***	*							*						**	
	CTR vs P15	**	**		*		**				*					**	
Passage 3	Conditions/Phenotypic states	P1	P2	P3	P4	P5	P6	P7	P8	P9	P10	P11	P12	P13	P14	P15	P16
	CTR vs NCH644 exp						*										
	CTR vs P1					**	**		*								
	CTR vs P2									*							
	CTR vs P3					*				*							
	CTR vs P4									***		*					
	CTR vs P5																
	CTR vs P6									***		*					
	CTR vs P7																
	CTR vs P8	*								***	*	*					
	CTR vs P9	**					***		*		*	*					
	CTR vs P10	*				**							*				
	CTR vs P11						**										
	CTR vs P12																
	CTR vs P13	**															
	CTR vs P14	***	**	*	*					**							
	CTR vs P15	**															
	CTR vs P16	**		*													
Passage 4	Conditions/Phenotypic states	P1	P2	P3	P4	P5	P6	P7	P8	P9	P10	P11	P12	P13	P14	P15	P16
	CTR vs NCH644 exp																
	CTR vs P1						***		**					*	**		
	CTR vs P2		*		**	**	***		*	*				**	**		
	CTR vs P3			*		*	***		*					**	**		
	CTR vs P4									***		**					
	CTR vs P5		*						*		*						
	CTR vs P6									**							
	CTR vs P7									***	*	*	*				
	CTR vs P8	**		**						***	*	**	*				
	CTR vs P9					**	***		*								
	CTR vs P10			*													
	CTR vs P11		*				***		*								
	CTR vs P12									***							
	CTR vs P13		*		*	*	**		**								
	CTR vs P14	***	*	**												**	
	CTR vs P15	*		*										*			
	CTR vs P16	**															

b. Self-renewal in hypoxia

Passage 1	Conditions/Phenotypic states	P1	P2	P3	P4	P5	P6	P7	P8	P9	P10	P11	P12	P13	P14	P15	P16
	CTR vs NCH644 exp									**		*		*			
	CTR vs CTR_H		***		***	*		**		**	***	**	***		***		**
	CTR vs P1	*		**			***		**	**		*		**	**		
	CTR vs P2					*				***				**	**		
	CTR vs P3						***		*	***		*		**	**		
	CTR vs P4									***	*	*		**	**		
	CTR vs P5					**				***		*	*		*		
	CTR vs P6									***	*	**	**	*			
	CTR vs P7									***	*	**	**				
	CTR vs P8	*		**						***	*	**	*	**	*		
	CTR vs P9	**			*		***		**	**							
	CTR vs P10								*			*					
	CTR vs P11			*			**		**	**					**		
	CTR vs P12					*											
	CTR vs P13			**		*								***			
	CTR vs P14	**		***	*		*			***	*	**	**		*		
	CTR vs P15																
	CTR vs P16	**								***			*				
	CTR_H vs NCH644 exp		*					**			*						
	CTR_H vs P1			*				**					**				
	CTR_H vs P2		*		***			*			*		*				
	CTR_H vs P3																
	CTR_H vs P4												***				
	CTR_H vs P5																
	CTR_H vs P6		*														
	CTR_H vs P7				*												
	CTR_H vs P8		*														
	CTR_H vs P9							**		**							
	CTR_H vs P10							*									
	CTR_H vs P11				*			*			*		*				
	CTR_H vs P12							**									
	CTR_H vs P13							*						***			*
	CTR_H vs P14						*	*							*		
	CTR_H vs P15																
	CTR_H vs P16							*									
Passage 2	Conditions/Phenotypic states	P1	P2	P3	P4	P5	P6	P7	P8	P9	P10	P11	P12	P13	P14	P15	P16
	CTR vs NCH644 exp									***	*	*	*	*	**		
	CTR vs P1			**			***		*	***	*	*		**	**		
	CTR vs P2									***	*	*	**	**	**		
	CTR vs P3								*	***	*	*			**		
	CTR vs P4											*	*		*		
	CTR vs P5					*			*	***	*	**	*		**		
	CTR vs P6	*		**		*				***	*	**	**		**		
	CTR vs P7									***	*	*	**		**		
	CTR vs P8	**		***		*				***	*	**	**		**		
	CTR vs P9						**		**				**		*		
	CTR vs P10									**		*	*				
	CTR vs P11				*		**		**	**	*	*	*		**		
	CTR vs P12									**					*		
	CTR vs P13		*	***	*				*					**			
	CTR vs P14	***	**	***	*						*	*	**				
	CTR vs P15		**		*		***		**		*		**				
	CTR vs P16			*		**				***		**	**				
	CTR_H vs NCH644 exp												*				
	CTR_H vs P1		**	*				*									
	CTR_H vs P2							*									
	CTR_H vs P3																
	CTR_H vs P4		***		*												
	CTR_H vs P5																
	CTR_H vs P6																
	CTR_H vs P7																
	CTR_H vs P8																
	CTR_H vs P9							*									
	CTR_H vs P10							*									
	CTR_H vs P11							*									
	CTR_H vs P12																
	CTR_H vs P13													*			
	CTR_H vs P14							*									
	CTR_H vs P15																
	CTR_H vs P16																

Passage 3	Conditions/Phenotypic states	P1	P2	P3	P4	P5	P6	P7	P8	P9	P10	P11	P12	P13	P14	P15	P16
	CTR vs NCH644 exp									**	*	*	*		**		
	CTR vs P1	**		***			***		**	***		*			**		
	CTR vs P2			*						***	*	*		*	**		
	CTR vs P3						**		*	***	*	*			**		
	CTR vs P4					**				***	*	*	*		**		
	CTR vs P5		*			***				**	*	*	**				
	CTR vs P6	**	*	*		***				***	*	**	**				
	CTR vs P7		**		*		**			**	*	*	**		**		
	CTR vs P8	**	*	*		*				***	*	**	**				
	CTR vs P9						**		*								
	CTR vs P10									**					*		
	CTR vs P11			*			***		**	**	*				**		
	CTR vs P12									**							
	CTR vs P13		**	**	*									*			
	CTR vs P14	***	**	***							*	*	**				
	CTR vs P15				*		**		**	*			*				
	CTR vs P16																
	CTR_H vs NCH644 exp												*				
	CTR_H vs P1			**				**					*				
	CTR_H vs P2										**		**				
	CTR_H vs P3																
	CTR_H vs P4																
	CTR_H vs P5																
	CTR_H vs P6																
	CTR_H vs P7																
	CTR_H vs P8																
	CTR_H vs P9																
	CTR_H vs P10																
	CTR_H vs P11																
	CTR_H vs P12																
	CTR_H vs P13																
	CTR_H vs P14							*									
	CTR_H vs P15							*		**							
	CTR_H vs P16																
Passage 4	Conditions/Phenotypic states	P1	P2	P3	P4	P5	P6	P7	P8	P9	P10	P11	P12	P13	P14	P15	P16
	CTR vs NCH644 exp						**		*	**			*		*		
	CTR vs P1	*		*			***		*	**		*		*	*		
	CTR vs P2									***		*	*		*		
	CTR vs P3	*		**			***		*	***		*	*	*	*		
	CTR vs P4	**	*	**		***		***		***		*	*		*		
	CTR vs P5								*	***		*	*		*		
	CTR vs P6	*				**		*		***		*	*	*	*		
	CTR vs P7						*		*	***		*	*		*		
	CTR vs P8	*		**		***	*		**	***		*	*				
	CTR vs P9						**										
	CTR vs P10									**							
	CTR vs P11	**		*		*	**		*	***		*	*	*	*		
	CTR vs P12		*		*					**		*	*		*		
	CTR vs P13		*	**	*		**		*						*		
	CTR vs P14	*		**									*				
	CTR vs P15		*	**	*				*				*	***			
	CTR vs P16											*	*				
	CTR_H vs NCH644 exp																
	CTR_H vs P1				*			*									
	CTR_H vs P2																
	CTR_H vs P3			*													
	CTR_H vs P4																
	CTR_H vs P5																
	CTR_H vs P6																
	CTR_H vs P7																
	CTR_H vs P8						*										
	CTR_H vs P9																
	CTR_H vs P10																
	CTR_H vs P11																
	CTR_H vs P12																
	CTR_H vs P13																
	CTR_H vs P14																
	CTR_H vs P15													**			
	CTR_H vs P16																

Table S5. Independence analysis of 4 markers in state transitions in normoxia (A.) and in hypoxia (B.). Related to Fig. 2E and Fig. 3E respectively. Table presents transition probabilities considering only a single marker.

A. Marker dependency in normoxia

			Equilibrium calculated from sinlge marker state transitions	Equilibrium calculated from four markers state transitions
	CD133+	CD133-		
CD133+	97.48	2.52	77.18	79
CD133-	8.52	91.48	22.82	21
	CD44+	CD44-		
CD44+	95.96	4.04	46.17	41
CD44-	3.46	96.54	53.83	59
	A2B5+	A2B5-		
A2B5+	79.69	20.31	42.91	41.6
A2B5-	15.27	84.73	57.09	58.4
	CD15+	CD15-		
CD15+	93.11	6.89	36.43	39.5
CD15-	3.95	96.05	6.35	60.5

B. Marker dependency in hypoxia

			Equilibrium calculated from sinlge marker state transitions	Equilibrium calculated from four markers state transitions
	CD133+	CD133-		
CD133+	99.7	0.3	97.63	96.19
CD133-	12.4	87.6	2.37	3.81
	CD44+	CD44-		
CD44+	98.87	1.13	73.2	55.79
CD44-	3.09	96.91	26.79	44.21
	A2B5+	A2B5-		
A2B5+	94.05	5.95	40.68	33.92
A2B5-	4.08	95.92	59.32	66.08
	CD15+	CD15-		
CD15+	92.45	7.55	16.27	18.29
CD15-	1.47	98.53	83.73	81.71

Table S6. Statistical analysis of self-renewal potential of 16 FACS-sorted subpopulation in hypoxia. Related to Fig. 3B.

Matrix represents statistical changes by the Kruskal-Wallis test observed for sphere number in self-renewal test between subpopulations across 4 passages in hypoxia (*pvalue≤0.05). Note that statistical differences were present only upon two first passages.

		Passage 1																	
	Subpopulation	P1	P2	P3	P4	P5	P6	P7	P8	P9	P10	P11	P12	P13	P14	P15	P16	NCH644	
	P1									*	*		*	*	*	*	*		
	P2										*		*		*				
	P3	*	*								*		*		*				
	P4			*							*		*						
	P5										*		*		*				
	P6			*							*		*		*				
	P7			*							*		*		*				
	P8	*		*		*					*		*		*				
	P9			*					*		*		*		*			*	
	P10											*		*	*	*	*	*	
	P11	*	*		*			*	*				*		*				
	P12	*												*	*	*	*	*	
	P13								*						*			*	
	P14			*												*		*	
	P15	*	*		*			*	*									*	
	P16			*														*	
		Passage 2																	
		Passage 3																	
	Subpopulation	P1	P2	P3	P4	P5	P6	P7	P8	P9	P10	P11	P12	P13	P14	P15	P16	NCH644	
	P1																		
	P2																		
	P3																		
	P4																		
	P5																		
	P6																		
	P7																		
	P8																		
	P9																		
	P10																		
	P11																		
	P12																		
	P13																		
	P14																		
	P15																		
	P16																		
		Passage 4																	

Table S7. Antibodies used in the study.

Epitope	Conjugate	Clone	Supplier	Concentration
A2B5	APC/PE	105-HB29	Miltenyi	FC:10µl/test
A2B5	AF488	MAB312RX	Chemicon	ICC:1:20
CD15/SSEA-1	AF647	MC-480	Biolegend	FC:5µl/test
				ICC:1:50
CD15/SSEA-1	PE	MEM-158	Immunotools	FC:10µl/test
CD15/SSEA-1	PerCP-Cy5.5	W6D3	Biolegend	FC:5µl/test
CD24	PE	SN3	Immunotools	FC:10µl/test
CD29	APC	MEM-101A	Immunotools	FC:10µl/test
CD44	FITC	MEM-85	Immunotools	FC: 10µl/test
CD44	PE-Cy7	IM7	eBioscience	FC:1.2µl/test
				ICC:1:50
CD56	PE-Cy7	N-CAM	BD Bioscience	FC:5µl/test
CD90	PE-Cy7/APC	5E 10	BD Bioscience	FC:5µl/test
CD95	APC	Fas/APO1	BD Bioscience	FC:20µl/test
CD133-1	PE /APC	293C3/AC133	Miltenyi	FC:10µl/test
				ICC:1:50
CD195	PE	2D7/CCR5	BD Bioscience	FC:20µl/test
EGFR	PE	EGFR.1	BD Bioscience	FC:20µl/test
GFAP	AF647	1B4	BD Bioscience	FC:5µl/test
Isotype control IgG1	FITC	PPV-06	Immunotools	FC:5µl/test
Isotype control IgG1κ	PerCP-Cy5.5	MOPC-21	BD Bioscience	FC:5µl/test
Isotype control IgG2a	AF647	eBR2a	eBioscience	FC:5µl/test
Isotype control IgG2b	AF647	eB1491/10H5	eBioscience	FC:5µl/test
NG2	PE	LHM-2	R&D	FC:10µl/test
Nestin	PerCP-Cy5.5	25/NESTIN	BD Bioscience	FC:5µl/test
Nestin		10C2	Millipore	ICC: 1:200
Vimentin	FITC	V9	Thermo Fischer	FC:5µl/test
Vimentin		V10	Millipore	ICC: 1:200
B-III-tubulin	AF647	TUJ1	BD Bioscience	FC:5µl/test
B-III-tubulin		Tu-20	Millipore	ICC: 1:200
Goat anti-mouse IgG Alexa488	AF488	policlonal	Thermo Fischer	ICC: 1:500
Goat anti-rabbit IgG Alexa488	AF488	policlonal	Thermo Fischer	ICC: 1:500

FC = Flow cytometry (test 106 cells/100µl); ICC = Immunocytochemistry

PLOS | ONE

RESEARCH ARTICLE

Comprehensive Analysis of Glycolytic Enzymes as Therapeutic Targets in the Treatment of Glioblastoma

Morgane Sanzey[1], Siti Aminah Abdul Rahim[1], Anais Oudin[1], Anne Dirkse[1], Tony Kaoma[2], Laurent Vallar[2], Christel Herold-Mende[3], Rolf Bjerkvig[1,4,5], Anna Golebiewska[1], Simone P. Niclou[1,5]*

1 NorLux Neuro-Oncology Laboratory, Department of Oncology, Luxembourg Institute of Health (L.I.H.), Luxembourg, Luxembourg, **2** Genomics Research Unit, Luxembourg Institute of Health (L.I.H.), Luxembourg, Luxembourg, **3** Experimental Neurosurgery, Department of Neurosurgery, University of Heidelberg, Heidelberg, Germany, **4** NorLux Neuro-Oncology Laboratory, Department of Biomedicine, University of Bergen, Bergen, Norway, **5** KG Jebsen Brain Tumour Research Center, Department of Biomedicine, University of Bergen, Bergen, Norway

* simone.niclou@lih.lu

OPEN ACCESS

Citation: Sanzey M, Abdul Rahim SA, Oudin A, Dirkse A, Kaoma T, Vallar L, et al. (2015) Comprehensive Analysis of Glycolytic Enzymes as Therapeutic Targets in the Treatment of Glioblastoma. PLoS ONE 10(5): e0123544. doi:10.1371/journal.pone.0123544

Academic Editor: Maria G Castro, University of Michigan School of Medicine, UNITED STATES

Received: December 16, 2014

Accepted: March 5, 2015

Published: May 1, 2015

Data Availability Statement: All relevant data are within the paper and its Supporting Information files.

Funding: This work was supported by the Fonds National de la Recherche (FNR) of Luxembourg (ESCAPE 784322 BM to SPN and AFR grant to SAAR) and the Centre de Recherche Public de la Santé (CRP-Santé). The funders had no role in study design, data collection and analysis, decision to publish, or preparation of the manuscript.

Competing Interests: The authors have declared that no competing interests exist.

Abstract

Major efforts have been put in anti-angiogenic treatment for glioblastoma (GBM), an aggressive and highly vascularized brain tumor with dismal prognosis. However clinical outcome with anti-angiogenic agents has been disappointing and tumors quickly develop escape mechanisms. In preclinical GBM models we have recently shown that bevacizumab, a blocking antibody against vascular endothelial growth factor, induces hypoxia in treated tumors, which is accompanied by increased glycolytic activity and tumor invasiveness. Genome-wide transcriptomic analysis of patient derived GBM cells including stem cell lines revealed a strong up-regulation of glycolysis-related genes in response to severe hypoxia. We therefore investigated the importance of glycolytic enzymes in GBM adaptation and survival under hypoxia, both in vitro and in vivo. We found that shRNA-mediated attenuation of glycolytic enzyme expression interfered with GBM growth under normoxic and hypoxic conditions in all cellular models. Using intracranial GBM xenografts we identified seven glycolytic genes whose knockdown led to a dramatic survival benefit in mice. The most drastic effect was observed for *PFKP* (PFK1, +21.8%) and *PDK1* (+20.9%), followed by *PGAM1* and *ENO1* (+14.5% each), *HK2* (+11.8%), *ALDOA* (+10.9%) and *ENO2* (+7.2%). The increase in mouse survival after genetic interference was confirmed using chemical inhibition of PFK1 with clotrimazole. We thus provide a comprehensive analysis on the importance of the glycolytic pathway for GBM growth in vivo and propose PFK1 and PDK1 as the most promising therapeutic targets to address the metabolic escape mechanisms of GBM.

Introduction

With a prevalence of 2–3 cases per 100,000 people per year in Europe and North America, glioblastoma (GBM) is the most common primary brain tumor and also the deadliest one. The

5-year survival rate remains below 10% and median life expectancy does not exceed fifteen months [1]. Malignancy parameters, such as extensive angiogenesis, hypoxia and necrosis are hallmarks of GBMs that distinguish them from lower grade gliomas. Over the past decade, anti-angiogenic therapy has received considerable attention and a number of clinical trials have been conducted where the treatment was thought to prevent tumor development by inhibiting blood vessel formation and at the same time improve the delivery of chemotherapeutic agents via the functional normalization of existing blood vessels [2]. However, in the clinic, bevacizumab, an antibody targeting vascular endothelial growth factor (VEGF), failed to significantly improve overall patient survival [3, 4] suggesting that tumors quickly develop escape mechanisms [5]. In preclinical studies based on patient-derived GBM xenografts, we showed that bevacizumab reduced tumor blood flow and led to increased invasiveness and hypoxia [6]. Moreover, we observed a significant increase in lactate production within the tumors, and more recently we were able to confirm the induction of a glycolytic switch corresponding to uncoupling glycolysis from oxidative phosphorylation of the tricarboxylic acid (TCA) cycle in response to bevacizumab treatment [6, 7]. Thus the induction of hypoxia and the activation of the glycolytic pathway may mediate glioma resistance to anti-angiogenic treatment, suggesting that targeting the glycolytic pathway may represent a favorable therapeutic approach against GBM [8]. Moreover most solid tumors show increased glycolytic activity independent of oxygen supply (Warburg effect), which favors the production of biomass to sustain tumor cell proliferation through the generation of metabolic intermediates [9]. GBMs in particular display prominent areas of hypoxia surrounded by pseudopalissading cells suggesting that glycolysis is an interesting target for these tumors even at baseline. The glycolytic properties of cancer are demonstrated in the clinic by using positron emission tomography (PET) where the radiolabelled glucose analog, the 2-deoxy-2-(^{18}F)fluoro-D-glucose (^{18}F-FDG) is avidly taken up by tumor cells, including GBM [10].

Glycolysis represents a ten-step metabolic pathway that implicates more than 15 enzymes. The first glycolytic step generating glucose-6-phosphate is catalyzed by hexokinases (HK), where in particular the HK2 isoform is strongly expressed in cancer including GBM [11]. The phosphorylation of fructose-6-phosphate into fructose-1,6-biphosphate by phosphofructokinase 1 (PFK1), encoded by the *Phosphofructokinase, platelet (PFKP)* gene, is the rate limiting step of glycolysis. PFK1 modulation implicates several allosteric regulations including ATP, phosphoenolpyruvate (PEP) and fructose-2,6-biphosphate. From fructose-1,6-biphosphate, the sequential activities of aldolase A (ALDOA), glyceraldehyde 3-phosphate dehydrogenase (GAPDH) and phosphoglycerate kinase 1 (PGK1) lead to the generation of 3-phosphoglycerate, which is isomerized to 2-phosphoglycerate by phosphoglycerate mutase 1 (PGAM1). The latter was found to be over-expressed in glioma and to correlate with glioma grade [12]. Among the three enolase isoforms (ENO1-3) generating PEP, only ENO1 and ENO2 are expressed in the brain, and ENO1 is the major isoform in GBM (75–90% of total cellular enolase activity) [13]. A key glycolytic enzyme which is consistently altered in cancer cells is pyruvate kinase the enzyme catalyzing the conversion of PEP to pyruvate and ATP [14]. The fetal M2 isoform (PKM2) is more abundant in cancer cells and favors aerobic glycolysis to the benefit of anabolic processes in highly proliferating cells [15]. Finally, pyruvate dehydrogenase kinase 1 (PDK1), which is strongly expressed in GBM compared to normal brain [16], inhibits pyruvate dehydrogenase, thereby preventing the entry of pyruvate into the TCA cycle.

Here, we address in a comprehensive manner the role of glycolytic induction in hypoxic GBM cells and provide evidence through genetic and chemical interference that inhibition of the glycolytic pathway strongly affects GBM growth in patient-derived intracranial mouse models. Using transcriptomic and functional knockdown strategies in vitro and in vivo, we

identify PFK1, PDK1, PGAM1, ENO1, HK2, ALDOA and ENO2 as key glycolytic enzymes essential for GBM growth and propose them as potential therapeutic targets against GBM.

Materials and Methods

Ethics statement

Human glioblastoma biopsies were obtained from the Neurosurgery Department of the Centre Hospitalier in Luxembourg (CHL) (T16) or the Department of Neurosurgery, Haukeland University Hospital in Bergen (P3, P8), Norway. All patients had provided written informed consent, with procedures that were approved for the project (project number: REC-LRNO-20110708) by the National Research Ethics Committee for Luxembourg (CNER) or by the Regional Ethical Board at the Haukeland University Hospital in Bergen. The handling of the animals and the surgical procedures were performed in accordance with the European Directive on animal experimentation (2010/63/EU) and the national regulations of Luxembourg and the local ethical committee (the Animal Welfare Structure (AWS) LIH) approved the protocol.

Cell culture

Five patient-derived glioblastoma stem-like cell lines NCH421k, NCH660h, NCH465, NCH601 and NCH644 were generated in the laboratory of Dr Christel Herold-Mende (Department of Neurosurgery, University of Heidelberg) [17]. NCH421k, NCH660h, NCH465, NCH601 were cultured as non-adherent spheres in DMEM-F12 medium (Lonza) containing 1xBIT100 (Provitro), 2mM L-Glutamine, 30U/ml Pen-Strep, 1U/ml Heparin (Sigma), 20ng/ml bFGF (Miltenyi, 130-093-841) and 20ng/ml EGF (Provitro, 1325950500). NCH644 were grown in Neurobasal base medium (Life Technologies) supplemented with 1xB-27 (Life Technologies) 2mM L-Glutamine, 30U/ml Pen-Strep, 1U/ml Heparin (Sigma), 20ng/ml bFGF (Miltenyi, 130-093-841) and 20ng/ml EGF (Provitro, 1325950500). U251 cells were kindly provided by Dr. J. Carlsson, Uppsala University, Sweden [18]. U87 and T98G cells were obtained from the ATCC (Rockville, USA). U87 U251 and T98G cells were cultured as adherent monolayers in DMEM containing 10% FBS, 2mM L-Glutamine and 100U/ml Pen-Strep (all from Lonza). Normal human astrocytes (NHA), kindly provided by Dr Uros Rajcevic (National Institute of Biology, Ljubljana, Slovenia) were acquired from Lonza. NHA were grown in DMEM, 20% FBS, 2mM L-Glutamine and 100U/ml Pen-Strep (all from Lonza). Normoxic cultures were kept at 37°C under 5% CO_2 atmospheric oxygen. Hypoxic conditions at 0.1% O_2 were maintained in a hypoxic incubator chamber (Galaxy 48R incubator, New Brunswick, Canada).

Organotypic GBM biopsy derived spheroids

Organotypic GBM spheroids from patient samples were prepared as previously described [6, 19] and maintained in spheroid medium (DMEM medium, 10% FBS, 2mM L-Glutamine, 0.4mM NEAA and 100U/ml Pen-Strep; all from Lonza) in agar pre-coated flasks for 7–10 days. Primary adherent P3 cell line (P3A) was derived by plating P3 spheroids in uncoated flasks in spheroid medium until a confluent culture was obtained.

Genome-wide expression analysis

Total RNA was extracted using QIAGEN RNeasy Mini Kit (Qiagen), according to the manufacturer's protocol. GeneChip Human Gene 1.0ST Arrays (Affymetrix) were used to determine the genome-wide expression profiles. Total RNAs (250ng) were processed using the Affymetrix WT Expression kit before being hybridized on Affymetrix GeneChip Human Gene 1.0 ST arrays according to the manufacturer's instructions (protocol P/N 702808 Rev.6). Upon hybridization,

microarrays were washed, stained and scanned according to manufacturer's standard procedures. CEL files containing hybridization raw signal intensities were imported into the Partek GS software for further statistical analysis. First, probe intensities were summarized to gene expression signals using Partek default options (GC-content adjustment, RMA background correction, quantile normalization, log2 transformation and summarization by means. Gene expression profiles were established for cells cultured in normoxia and severe hypoxia (0.1% O_2) at two time points (12hours = 12h and 7 days = 7d). Lists of differentially expressed genes (DEGs) were obtained with ANOVA (False discovery rate (FDR) <0.001, any fold change (FC)). P-values were adjusted by Benjamin and Hochberg's False Discovery Rate (FDR) [20]. The Ingenuity Pathway Analysis (IPA, Ingenuity Systems) and the DAVID database (DAVID 6.7; http://david.abcc.ncifcrf.gov/) [21] were used for data mining. Right-tailed Fisher's exact test was used to calculate a p value for functional enrichment analysis in the IPA (threshold:-log (p-value)> 1,3). REVIGO server was used for summarization of the altered Gene Ontology (GO) terms [22]. Venn diagram analysis was performed with the SAB lab web tool (http://sablab.net/venn.php). Microarray data are available in the ArrayExpress database (www.ebi.ac.uk/arrayexpress) under accession number E-MTAB-3085.

Quantitative real-time PCR (QPCR)

1μg of total RNA was extracted using Qiagen RNeasy Mini Kit (Qiagen) and reverse transcribed to cDNA using the iScript cDNA Synthesis Kit (Bio-Rad), according to the manufacturer's protocol. QPCR was carried out using Fast SYBR Green Master Mix and the Viia 7 Real Time PCR System (Life Technologies; Ta = 60°C QPCR reaction was performed in 5μL volumeFold-change (FC) was calculated using the $\Delta\Delta C_t$ method and normalized to the expression of *EZRIN* (QBase software). See S1 Table for list of primers used.

Gene knockdown

Gene knockdown of glycolytic genes was performed in NCH644, NCH421k and U87 using lentiviral particles expressing specific shRNAs (shRNA sequences in S2 Table). Individual pGIPZ shRNAmir (Open Biosystems) constructs were obtained as *E. coli* cultures in LB-lenox (low salt) medium with 8% glycerol, 100 μg/ml carbenicillin and 25 μg/ml zeocin. Plasmids were amplified and purified using the Qiagen Plasmid Midi kit (Qiagen). Lentiviral particles were produced in HEK cells by co-transfection of the pGIPZ-shRNAmir-control (Scramble) or pGIPZ-shRNAmir-target gene vector with the viral core packaging construct pCMVdeltaR8.74 and the VSV-G envelope protein vector pMD.G.2 as previously described [23]. Supernatant containing viral particles was used to transduce 100,000 glioma cells and puromycine selection (0.5ug/mL for NCH421k, 1ug/mL for NCH644, 5ug/mL for U87) was applied to obtain stably transduced GFP-positive cells.

3D-sphere assay

96-well plates were pre-coated with 1.5% Noble Agar (BD Biosciences) to prevent cell attachment. 1,000 NCH644 or U87 cells were seeded in each well and the plates were incubated at 37°C, 5% CO_2 with gentle agitation to obtain uniform 3D spheres. Spheres were cultured for 7 days under severe hypoxia (0.1% O_2) in their respective media.

Cytotoxicity assay

Cytotoxicity test was carried out for clotrimazole (range 5–75μM), citrate (range 5-30mM), sodium dichloroacetate (DCA, range 0.5-50mM) and 3-bromopyruvate (BPA, range 50–700 μM)

(all from Sigma). Adherent cells were plated in semi-confluent concentration in 96 well plates. Increasing concentrations of compounds or DMSO were applied for 72h. Induction of cell death was measured with the Sulforhodamine (SRB) assay (In Vitro Toxicology Assay Kit, Sulforhodamine B based, Sigma) according to the manufacture's protocol. The optical density was measured at 540nm. The percentage inhibition of cell mass was determined as: % reduction of cell mass = (Mean $OD_{control}$—Mean OD_{sample}) X 100/ Mean $OD_{control}$. IC_{50} was determined with the GraphPad Prism 5 software.

To uniform the primary cultures for repeatable drug testing we created 3D spheroids form equal amount of tumor cells sorted directly from the xenografts samples. Using eGFP expressing mice for generation of spheroid-based xenografts [24] allowed us to create uniform spheroids composed of tumor cells only. 1000 tumor cells per well were plated in 96 well plates precoated with agar. Spheroids were used 3 days after sort and the size remained relatively similar within the first 7 days of culture in normoxia and hypoxia. As control NHA cells were also cultured under non-adherent conditions. Treatment was carried out for 72h in normoxic and hypoxic (0.1% O_2) conditions with 30μM clotrimazole (Sigma) and spheroid viability was tested with cell viability test. Experiments were carried out with at least 5 spheroids (n = 3).

Cell viability test

Cell viability in 3D cultures was assessed with the LIVE/DEAD Viability/Cytotoxicity assay kit (Molecular Probes). Spheres and spheroids were stained for 6 hours and measurements of viable (Calcein, 'green' florescence) and dead (Ethidium homodimer-1, 'red' fluorescence) cells were performed using fluorescence confocal microscopy (Zeiss LSM STO META) by obtaining 20–25 stacks of two-dimensional images from successive focal planes (5 μm). Quantification was performed using IMARIS software. The volume of viable and dead cells was calculated by multiplying the surface area of each component ('green' or 'red') per stack by the total height of the image stacks. The percentage of dead cell volume was calculated as: % dead cell in spheroids (volume) = Dead cell volume ('red') x 100/Total spheroid volume ('green' + 'red').

Lactate release assay

Cells were incubated for 48h in normoxia or 0.1% O_2 hypoxia. The culture medium was removed and filtered with the 10kD spin filter. The flow-through was diluted 20 times before the assay. Lactate concentration was established with the Lactate Assay Kit (BioVision) according to the manufacture's protocol and measured with the FLUORstar Optima (BMG Labtech). Results were normalized against the total number of cells in each sample.

In vivo shRNA screen

55 NCH421k cell lines harboring different shRNA knockdown and NCH421k cells with a control vector were premixed before implantation (55 x 2'500 = 137'500 cells). The total pool was implanted intracranially to immunodeficient NOD/SCID mice (n = 5). Mice were anesthetized with a mixture of ketamine (100mg/kg) and xylazine (10mg/kg) and fixed in a stereotactic frame (Narishige Group, Tokyo, Japan). Tumor cells (137'500 cells) were implanted into the right frontal cortex using a Hamilton syringe (Hamilton, Reno, NV, USA) and analgesic (Buprenorphine, 0.1 mg/kg) was administered subcutaneously to relieve post-operative pain. Mice were fed a standard pellet diet and were provided with water ad libitum. Animals were euthanized by cervical dislocation at the appearance of neurological symptoms and weight loss. Brains were removed and the presence of a tumor was assessed by *ex vivo* IVIS imaging (IVIS Lumina Fluorescence system; PerkinElmer Compagny). As a control 55 pooled cell lines was cultured for the same period of time (n = 3). Total DNA was extracted from pooled cells before

implantation ('Baseline level'), from developed tumor tissue and in vitro cultures. Barcodes were amplified by PCR with specific primers: Forward (5′ -CAAGGGGCTACTTTAGGAG CAATTATCTTG-3′), Reverse (5'-GGTTGATTGTTCCAGACGCGT-3') and 300ng of DNA template PCR reaction parameters: 94°C for 3min followed by 94°C for 35s, 62°C for 35s and 72°C for 1min (30 cycles). The quality of PCR amplification was assessed by the migration on 1.5% agarose gel (expected size: 250bp). The abundance of each shRNA was quantified by next generation sequencing (NGS Junior, Roche). Data were processed using Fuzznuc (http://emboss.sourceforge.net/apps/cvs/emboss/apps/fuzznuc.html). Depletion of the essential genes was calculated by comparing results from in vivo (n = 5) and in vitro control screen (n = 3) or DNA isolated directly after pooling ('Baseline level' for *PGAM1* and *PFKP*).

Survival study

NCH421k cell clones harboring a gene specific shRNA were stereotactically implanted in immunodeficient NOD/SCID mice (6–7 mice/clone, NOD.CB17-Prkdc scid/J, Charles River, Lyon). Control mice were implanted with cells carrying a scramble shRNA construct (21 mice). Mice were anesthetized with a mixture of ketamine (100mg/kg) and xylazine (10mg/kg) and fixed in a stereotactic frame (Narishige Group, Tokyo, Japan). Tumor cells (137'500 cells) were implanted into the right frontal cortex using a Hamilton syringe (Hamilton, Reno, NV, USA). Four parameters were monitored daily to evaluate brain tumor severity as described previously [19]: weight (loss superior to 10% of the starting weight), coat, lordosis and CNS symptoms, using a score between 0 (no symptoms) and 3 (severe symptoms). The animals were euthanized by cervical dislocation when one criterion reached 3 or when 3 criteria reached 2. After sacrifice, in situ fluorescent images of brain tumors were generated using the IVIS instrument. Half of each brain was embedded in paraffin for histology and half was frozen for knockdown efficiency evaluation by QPCR.

For clotrimazole treatment, GBM patient-derived P3 spheroids (6 spheroids/mice) were stereotactically implanted in the brain of nude mice (Crl:NU(Ico)-Foxn1nu, Charles River, Lyon). To facilitate tumor monitoring in vivo P3 cells were transduced with DsRed expressing lentiviral vector. At 3 weeks, the first fluorescent signal was visible (IVIS instrument) and mice were randomly divided in two groups (n = 7): (1) control group receiving saline solution and (2) treated group receiving 3 times weekly clotrimazole (150mg/kg) administered by oral gavage.

Results

Glycolysis is the major biological pathway induced by hypoxia

A drastic effect of hypoxia on gene expression has been widely demonstrated in several cancer types [25], however, the activated pathways in response to oxygen deprivation are largely cell type dependent [26]. To determine the response of GBM to hypoxia, we performed a genome-wide transcriptomic analysis on glioma stem-like cells (NCH644 and NCH421k) and on classical adherent glioma cells (U87 and U251) under short (12h) and long term (7d) severe hypoxia (0.1% O_2). The expression profiles were determined for each glioma cell line and the lists of differentially expressed genes (DEGs) were established by comparing hypoxia (12h or 7d) with normoxia (2-way ANOVA, FDR<0.001, any fold change). We further extracted genes commonly altered in all cells analysed (Fig 1A top). Interestingly, the number of common DEGs was similar after 12h and 7d (301 and 348 genes respectively). Using the DAVID functional annotation tool [27, 28], we found that glucose metabolism, and more specifically glycolysis, was highly enriched under hypoxia in both conditions (S1A Fig). This was confirmed by Ingenuity Pathway Analysis (IPA] where glycolysis was shown to be significantly altered in all hypoxic GBM cells (-log(p-value] = 7.28 and 7.75 upon 12h and 7d hypoxia respectively]. The comparison of DEGs

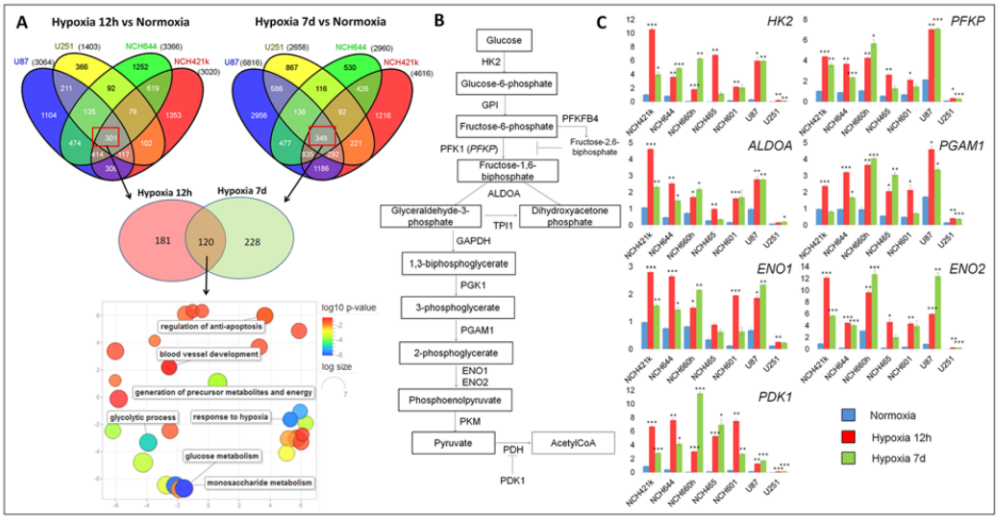

Fig 1. Glycolysis-related genes are up-regulated in glioblastoma cells under hypoxia. A. Stem-like (NCH644, NCH421k) and classical adherent (U87, U251) glioma cells were cultured in 0.1% O_2 for short term (12 hours = 12h) and long term (7 days = 7d). Differentially expressed genes (DEGs) were established between hypoxic and normoxic cells (n = 3–6). Venn diagrams (top) represent analysis of DEGs after 12h and 7d respectively (FDR<0.001; any fold change (FC)). Red squares highlight the genes commonly modulated in all four glioma cell lines. 120 genes were commonly deregulated upon 12h and 7d hypoxia (Venn diagram, middle) which were strongly associated with glycolysis (9 genes) and glucose metabolism (11 genes) (Revigo representation of significant GO terms, bottom). **B**. Schematic representation of the glycolytic pathway and associated enzymes. HK2 = hexokinase 2; PFK1 = phosphofructokinase 1 (encoded by *PFKP* = *Phosphofructokinase*, *platelet*); ALDOA = aldolase A; PGAM1 = phosphoglycerate mutase 1; ENO1 = enolase 1; ENO2 = enolase 2; PDH = pyruvate dehydrogenase; PDK1 = pyruvate dehydrogenase kinase 1. **C**. Quantitative PCR analysis of glycolytic gene expression in adherent glioma cells (U87 and U251) and glioma stem-like cells (NCH421k, NCH644, NCH660h, NCH465 and NCH601), under normoxia and hypoxia (12h and 7d). Data are presented as mean +/- SEM (n = 3). Data were normalized against *EZRIN* expression. NCH421k cells were used as an internal calibration (value = '1'); * p<0.05; p**<0.01; p***<0.001.

doi:10.1371/journal.pone.0123544.g001

after 12h and 7 days in hypoxia revealed that 120 genes were deregulated in both conditions (Fig 1A middle). Next to glycolysis and glucose metabolism the commonly deregulated genes were associated also to pathways regulating general hypoxia response, metabolism, apoptosis and angiogenesis (Fig 1A bottom).

To further select the genes most upregulated upon hypoxia we have imported the list of glycolysis-associated genes from Gene Onthology (GO:0006096) and KEGG databases (hsa00010, glycolysis/gluconeogenesis, [29]) and analysed gene expression changes occurring upon hypoxia (S3 Table). Importantly, the majority of core glycolytic genes (Fig 1B, S3 Table) were up-regulated whereas the pentose phosphate pathway (PPP)-related genes were down-regulated (S3 Table). This is in agreement with recent data showing that PPP enzymes are reduced in response to acute hypoxia, but their expression is up-regulated in vivo after prolonged hypoxia [7, 30].

We selected seven glycolytic genes (*HK2*, *PFKP*, *ALDOA*, *PGAM1*, *ENO1*, *ENO2* and *PDK1*; Fig 1B) and confirmed their strong up-regulation under hypoxia by QPCR in seven GBM cell lines (five patient derived glioma stem-like cells and two adherent GBM cell lines; Fig 1C). The increase of glycolytic genes was observed for all glioma cells already after 12h hypoxia and remained activated up to 7 days. Interestingly, in many cases the response was stronger in short term hypoxia, while expression levels had slightly decreased by 1 week. Also, the basal expression level of glycolytic genes and their induction by hypoxia was lower in U251 compared with other glioma cells.

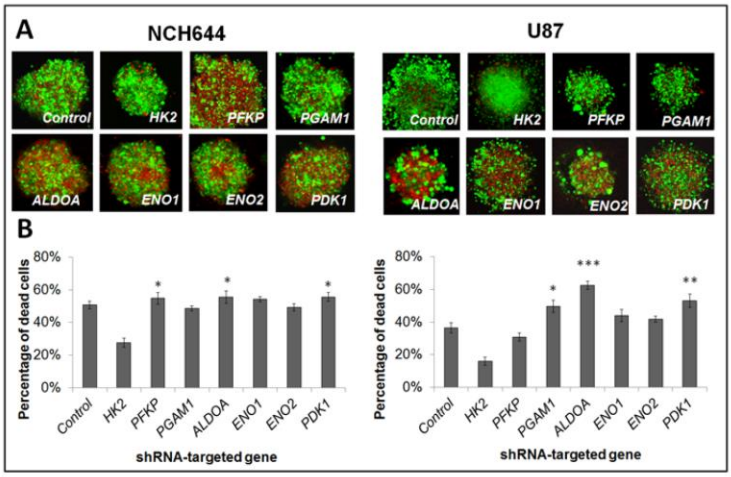

Fig 2. In vitro effect of glycolytic gene knockdown in glioblastoma cells. A. Cell viability test of 3D spheres carrying gene knockdowns under long-term (7d) hypoxia. Viable cells = 'green', dead cells = 'red'. Representative images are shown (n = 10). **B**. Quantification of the percentage of dead cells within 3D spheres in hypoxia (n = 10; mean ± SEM) (* p<0.05; ** p<0.01; *** p<0.001).

doi:10.1371/journal.pone.0123544.g002

To confirm the upregulation of glycolysis at the functional level we monitored the release of lactate in the extracellular medium. Under hypoxia, the lactate concentration in the medium was strongly augmented, indicating an increased pyruvate to lactate conversion in all cells, including astrocytes (S1B Fig).

In summary, we demonstrate, using several cellular GBM models, a strong induction of glycolysis under hypoxia, at the level of enzyme expression and functional activity. This metabolic activation highlights the importance of the glycolytic pathway for hypoxic glioma cells.

Knockdown of glycolytic enzymes affects GBM cell growth under hypoxia

To address the effect of gene knockdown of glycolytic enzymes on cell survival under hypoxia we used a cell viability assay. We have chosen seven genes that were strongly upregulated under hypoxia in all tumor cells analysed (S3 Table). Knock down efficiency for *HK2*, *PFKP*, *ALDOA*, *PGAM1*, *ENO1*, *ENO2* and *PDK1* in NCH644 and U87 cells is shown in S2 Fig. Since NCH644 cells grow as three dimensional spheres, we also generated spheres from U87 cells. After 7 days in severe hypoxia (0.1% O_2), spheres were generally smaller compared to those grown under normoxia (not shown), suggesting a lower proliferation rate under hypoxia. To determine the ratio of cell death, cells were stained with calcein (viable cells in green) and with ethidium bromide (dead cells in red) (Fig 2). We observed an increase in the number of dead cells for NCH644 when *PFKP*, *ALDOA* and *PDK1* genes were repressed. Similarly increased cell death was observed in U87 cells after silencing of *ALDOA*, *PDK1* and *PGAM1* (Fig 2A and 2B). Cell viability was not affected in 3D spheres grown in aerobic conditions upon respective gene knockdown (not shown). In summary, these observations indicate that the silencing of glycolytic genes affects cell survival under hypoxia in vitro, however the effect is to some extent enzyme and cell type dependent.

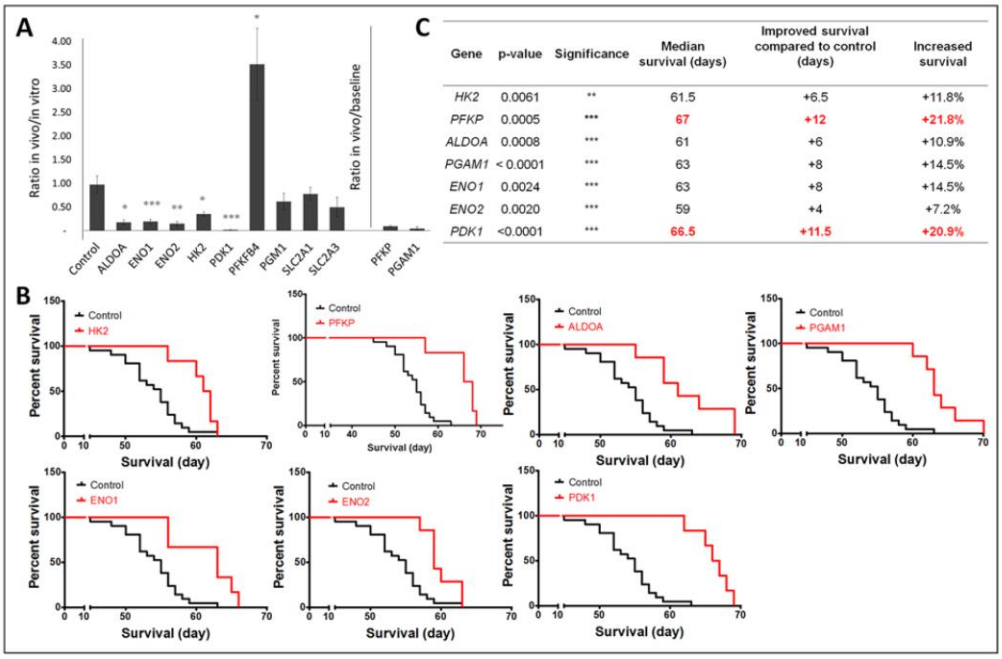

C

Gene	p-value	Significance	Median survival (days)	Improved survival compared to control (days)	Increased survival
HK2	0.0061	**	61.5	+6.5	+11.8%
PFKP	0.0005	***	67	+12	+21.8%
ALDOA	0.0008	***	61	+6	+10.9%
PGAM1	< 0.0001	***	63	+8	+14.5%
ENO1	0.0024	***	63	+8	+14.5%
ENO2	0.0020	***	59	+4	+7.2%
PDK1	<0.0001	***	66.5	+11.5	+20.9%

Fig 3. Mouse survival study revealed key glycolysis-related genes for in vivo tumor growth. A. Targeted in vivo shRNA screen in NCH421k cells. From 11 glycolytic target genes, five shRNA containing clones were depleted after in vivo growth compared to in vitro culture (*ALDOA*, *ENO1*, *ENO2*, *HK2*, *PDK1*) (* p<0.05; ** p<0.01; *** p<0.001; n = 3 for in vitro, n = 5 for in vivo). The number of shRNAs in each sample was quantified using NGS and is indicated as percentage of control. As *PGAM1* and *PFKP* knockdown clones were strongly depleted both in vivo and in vitro, these results were compared to baseline (original cell pool n = 1, p values not available). **B**. NCH421k cells with the indicated gene specific shRNAs were implanted intracranially into nude mice (n = 21 for control and n = 6–7 for glycolytic genes). Kaplan-Meier graphs show the effect of glycolytic gene knockdown on mouse survival. C. Table summarizing the effect of glycolytic gene knockdown on mouse survival (* p<0.05; ** p<0.01; *** p<0.001).

doi:10.1371/journal.pone.0123544.g003

Glycolytic enzymes are essential for in vivo tumor growth and their inhibition increases mouse survival

To determine the effect of glycolytic enzyme silencing on GBM growth in vivo, in the brain of NOD/SCID mice we implanted a pool of 55 shRNA-expressing glioma stem-like cells (NCH421k), targeting a number of different pathways, of which eleven were glycolytic genes found to be differentially expressed under hypoxia (S3 Table). These included the seven genes found to be essential for survival in vitro upon hypoxia *(HK2*, *PFKP*, *PGAM1*, *ALDOA*, *ENO1*, *ENO2* and *PDK1*) and four additional genes upregulated in hypoxia (*PGM1*, *PFKFB4*, *SLC2A1*, *SLC2A3*). A scramble shRNA vector was also included. We assumed that if the gene carried a survival advantage the knockdown cells would be depleted in the growing tumor. This allowed to determine in a single experiment which glycolytic enzymes were relevant for tumor growth in vivo. As a control pooled cells were cultured in vitro for the same period of time. Seven weeks after implantation, mice showed the first neurological symptoms and were sacrificed. Total DNA was extracted from GBM xenografts and in vitro cultures and the number of shRNA molecules was quantified. Interestingly, from the initial eleven shRNA-targeted glycolytic genes, seven (*HK2*, *PFKP*, *PGAM1*, *ALDOA*, *ENO1*, *ENO2* and *PDK1*) were significantly depleted in the xenografts, indicating that cells lacking these genes had a growth disadvantage in vivo (Fig 3A). Since

PGAM1 and *PFKP* were also depleted in the in vitro cultures, we compared their in vivo depletion to baseline (control cell pool before culture) (Fig 3A). *SLC2A3*, *SLC2A1* and *PGM1* were not depleted in vivo, while *PFKFB4* was depleted in vitro but not in vivo.

To determine the effect of knockdown on mouse survival, we separately implanted NCH421k cells expressing each a gene specific shRNA. In confirmation of the previous experiment, seven knockdowns led to a significant increase in mouse survival (Fig 3B and 3C). The most dramatic survival benefit was obtained with *PFKP* (+21.8%) and *PDK1* knockdown (+20.9%). A strong survival effect was also observed after silencing of *PGAM1* and *ENO1* (+14.5%), as well as after *HK2*, *ALDOA*, and *ENO2* knockdown (11.8%, 10.9% and 7.2% respectively) (Fig 3B and 3C). Gene knockdown in the xenografts was confirmed by QPCR on total RNA extracted from frozen tumor tissue, which reached more than 50% for all genes except *ENO1* (S3 Fig). In summary, we provide strong evidence that genetic interference with glycolysis slows GBM growth in vivo and we propose in particular PDK1 and PFK1 (*PFKP*) as promising targets for GBM treatment.

Increased mouse survival after chemical inhibition of PFK1

To determine whether chemical inhibition of glycolysis could be used to slow GBM growth, we tested several compounds previously reported to inhibit glycolytic enzymes. PFK1 can be targeted by clotrimazole and citrate [31, 32], dichloroacetate (DCA) is reported to inhibit PDK activity, whereas 3-bromopyruvate (BPA) is thought to affect HK2 and GAPDH activities [33]. We determined the IC50 of clotrimazole, citrate, DCA and BPA in patient-derived GBM cells (P3A) and normal astrocytes, under both normoxia and hypoxia (Fig 4A). The IC50 was also determined for classical adherent glioma cells U87, U251 and T98G (S4 Table). Except for citrate, GBM cells were more sensitive to drugs than astrocytes and for clotrimazole and DCA the sensitivity was increased under hypoxia. DCA and BPA were generally active only in the high micromolar range. Based on the best efficacy of clotrimazole and the strong impact of *PFKP* knockdown observed in vivo (Fig 3B), we focused on the chemical inhibition of PFK1 by clotrimazole. We evaluated the effect of clotrimazole in several patient-derived organotypic spheroids by performing viabilitytests in vitro. Primary spheroid cultures are more relevant tumor models for drug testing because they maintain the genetic features and some of the tissue complexity of patient tumor [34, 35]. Here we found that, under normoxia, clotrimazole induced cell death in P3, P8 and T16 GBM spheroids but had no effect on astrocyte spheres at the indicated concentration. Similar results were observed under hypoxic conditions (Fig 4B). Based on these data, we determined the effect of clotrimazole on the survival of mice implanted intracranially with a patient-derived GBM spheroids (P3). Clotrimazole (150mg/kg, 3-weekly) led to a small but significant improvement in mouse survival (+7 days; $p = 0.0272$, Fig 4C), indicating that glycolysis inhibition via chemical interference is effective in the treatment of patient derived GBMs and that PFK1 is a promising target for GBM therapy.

Discussion

In this study, we undertook a comprehensive analysis of transcriptomic data from patient-derived GBM stem-like cells and classical adherent GBM cell lines grown under short and long-term hypoxia. Using data mining tools, we identified glycolysis as a major pathway enabling the adaptation to oxygen deprivation in all cell lines. The activation of glycolysis was confirmed in all GBM cells studied at the protein level and at the functional level. These findings support the notion that GBM cells heavily rely on metabolic alterations to adapt to a changing microenvironment induced e.g. by anti-angiogenic treatment. By combining a targeted in vivo shRNA screen followed by survival studies in patient derived xenograft mouse models, we uncovered the importance of several key glycolytic enzymes including PFK1, PDK1, PGAM 1 and

A

Cell line	Inhibitory concentration (IC50)			
	GBM cells (P3A)		Astrocytes (NHA)	
Compound/Condition	N	H	N	H
Clotrimazole (mM)	39.8±11	37±9.4	88.6±10	65.5±5
Citrate (μM)	61±5	66±6	49±5	30±8
Dichloroacetate (mM)	132±11	109±5	159±8	304±12
Bromopyruvate (μM)	157±22	321±25	301±15	No effect

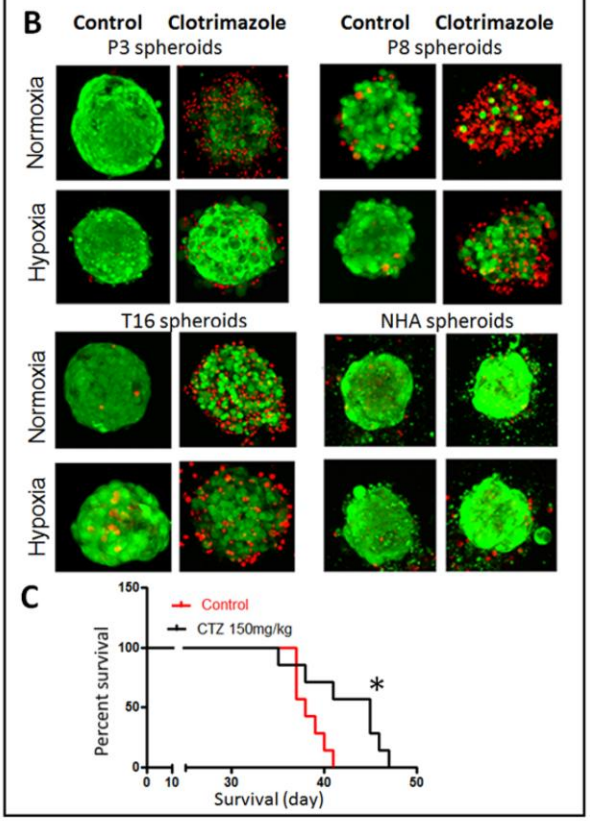

Fig 4. Glycolysis inhibition with clotrimazole affects glioma cell survival in vitro and delays tumor growth in vivo. A. The IC_{50} of different glycolysis inhibitors was determined for patient derived GBM cells (P3A) and normal human astrocytes (NHA). N: normoxia, H: hypoxia (0.1% O2). Cells were exposed to indicated compounds for 72h and IC_{50} was determined with the SRB assay (n = 3). **B**. The cytotoxic effect of clotrimazole (30μM) was assessed on organotypic spheroids of several patient-derived GBM (P3, P8, T16) and NHA, treated for 72h in normoxia and 0,1% O_2 (n = 5). Representative images showing viable cells in 'green', dead cells in 'red' fluorescence. **C**. P3 spheroids were implanted intracranially and clotrimazole (CTZ, 150mg/kg) treatment was started 3 weeks after implantation (n = 7). Kaplan-Meier curve shows significantly improved mouse survival (* $p<0.05$).

doi:10.1371/journal.pone.0123544.g004

ENO1 for intracranial growth of GBM. Although to a lesser extent also HK2, ALDOA and ENO2 were identified as important players for tumor progression in vivo. In view of the pronounced hypoxic areas in GBM and the general induction of hypoxia upon anti-angiogenic treatment, these data identify the key targets in the glycolytic pathway relevant for single agent or combination therapies.

The most prominent survival increase was seen after PFKP silencing (+21.8%), providing the first evidence that PFK1 constitutes an important target for GBM therapy. In agreement with this, a recent study identified 6-phosphofructo-2-kinase/fructose-2,6-biphosphatase 4 (PFKFB4) as essential for GBM cell survival in vitro [36]. PFKFB4 generates fructose-2,6-biphosphate which is responsible for the allosteric regulation of PFK1, suggesting that interference with PFK1 activity is detrimental for GBM growth. Nevertheless in our analysis we only identified PFK1, but not PFKFB4 as essential for tumor progression in vivo.

PDK1 knockdown increased mouse survival up to 20.9%. Via inhibition of pyruvate dehydrogenase, PDK1 is a gate-keeping mitochondrial enzyme preventing the entry of pyruvate into the TCA cycle thereby inhibiting the oxidative phosphorylation. Our data supports previous work implicating PDK1 in different cancers and indicating the beneficial effect of its inhibitor DCA in promoting tumor cell apoptosis and inhibiting cancer growth [37, 38]. Recently DCA has also been investigated in the treatment of GBM patients [39], although no large clinical studies are yet available. A recent pre-clinical study provided evidence for a synergistic effect of DCA with bevacizumab albeit this work was carried out in a subcutaneous U87 model [40].

PGAM1 has been reported to be overexpressed in high grade glioma [12]. Here we provide the first indication that PGAM1 plays an essential role in GBM and that PGAM1 silencing in intracranial tumors improves mouse survival. PGAM1 has been identified as a potential therapeutic target in hepatocellular carcinoma [41], however, its implication in cancer cell proliferation remains poorly understood and little is known on its regulation. Similarly, in our study the knockdown of the neuronal and non-neuronal form of enolase (ENO2 and ENO1 respectively) led to a significant survival benefit in mice. Knockdown of ENO2 was previously reported to affect GBM cell migration and sensitize them to hypoxia, radiotherapy and chemotherapy [42]. Of note in our hands ENO1 knockdown was more beneficial for mouse survival than ENO2 knockdown, despite the less efficient gene silencing obtained with ENO1 (S3 Fig).

Finally, we show the importance of HK2 and ALDOA in GBM growth in patient derived GBM xenografts. This is in agreement with previous work showing that HK2 depletion slowed U87 cell growth in vivo and restored oxidative phosphorylation in these cells [43]. Here we show that HK2 depletion in intracranial patient derived GBM xenografts led to a survival improvement of 11.8%. Similar to PDK1, interference with HK2 does not only affect cellular metabolism, but also induces apoptosis thereby conferring a growth advantage to cancer cells [44].

The last part of our study focused on testing chemical compounds known to inhibit glycolysis and shows that chemical interference with PFK1 activity through clotrimazole is effective for GBM treatment. Unfortunately however the effect was less pronounced than with the gene knockdown which is likely due to poor drug potency and limited availability in the tumor. Moreover like most available glycolysis related drugs, clotrimazole is rather unspecific and its mechanism of action is poorly understood. Known as an anti-fungal agent, it has been shown to affect PFK1 activity as well as HK2 binding to the mitochondrial outer membrane [32, 45]. Thus there is a need for more potent and more specific small molecule drugs to target the glycolytic pathway.

In conclusion, using a comprehensive analysis of the glycolytic metabolism in several in vitro and in vivo GBM models, we show that glycolysis is a promising target for GBM therapy, especially though the specific inhibition of the enzymes PFK1 and PDK1. To improve chemical inhibition of these targets, efforts should be concentrated on the synthesis of drugs with high potency and specificity for these two proteins.

Supporting Information

S1 Fig. Induction of glycolysis upon hypoxia. A.Differentially expressed genes (DEGs) between hypoxia (12h and 7d separately) and normoxia were determined with ANOVA (FDR<0,001, any fold change) and commonly altered genes were extracted from the Venn diagrams (Fig 1A). 301 and 348 genes were significantly modulated (up or down-regulated) after 12h and 7d respectively under hypoxia in all cell lines analysed. DEG lists were submitted to the DAVID database (DAVID 6.7; http://david.abcc.ncifcrf.gov/) for functional enrichment analysis. Significantly deregulated Gene Ontology (GO) terms after 12h (left) and 7d (right) are presented A strong increase in the concentration of lactate was observed in the extracellular medium of GBM cells subjected to 48h 0.1% O_2 (* $p<0.05$, n = 3).
(TIF)

S2 Fig. shRNA knockdown efficacy in U87 and NCH644 determined by QPCR. QPCR confirmed the silencing of glycolysis-related genes in shRNA-expressing NCH644 and U87 glioma cells. The residual expression of silenced genes was confirmed for each clone separately and compared to the control clone (n = 3; *** $p<0.001$; ** $p<0.01$; $p<0.05$).
(TIF)

S3 Fig. shRNA knockdown efficacy in mouse xenografts determined by QPCR. Total RNA was extracted from tumor mass developed in xenografts during the survival study. The residual expression of silenced genes was confirmed for each clone separately and compared to the control clone. QPCR confirmed the silencing of glycolysis-related genes (n = 5; *** $p<0.001$; ** $p<0.01$ * $p<0.05$).
(TIF)

S1 Table. Primers used in the study.
(DOCX)

S2 Table. Sequence of the 12 shRNAs used for in vitro and in vivo studies. Each shRNA was tagged with a barcode sequence. After tumor resection and DNA extraction, the barcode sequences were amplified and quantified by next generation sequencing (NGS).
(DOCX)

S3 Table. Gene expression changes for genes related to glucose metabolism. Genes associated with glycolysis were selected from the Kegg pathway and Gene ontology databases. The pentose phosphate pathway (PPP) genes were depicted from (30). *PDK1* and glucose transporters *SLC2A1* and *SLC2A3* were added manually as genes closely related to glycolysis. Expression of glycolysis-associated genes was analysed within DEG lists for short term hypoxia (12h) and long term hypoxia (7d) versus normoxia. Differentially expressed genes between hypoxic and normoxic cells were determined with ANOVA. Cut-off was set up for FDR<0.001 (Any fold change). Fold changes are presented only for the genes were significantly altered (FDR<0.001).
(DOCX)

S4 Table. IC50 on adherent glioma cells. Different glioma cell lines were exposed to the indicated compounds for 72 hours and the cytotoxic effects were assessed using the SRB assay. A concentration gradient of each compound was used for IC_{50} determination in the different cell types. The IC_{50} was determined by the SRB assay on three adherent cell lines U87, U251, T98G. Results are presented as a mean ± SEM of three independent experiments performed in triplicates. N: normoxia; H: hypoxia.
(DOCX)

Acknowledgments

We thank Virginie Baus, Jill Bohler and François Bernardin for excellent technical assistance, Dr. Peter Nazarov for help in statistical analysis and Arnaud Muller for support in microarray analysis. We are grateful to Dr. Uros Rajcevic (National Institute of Biology, Ljubljana, Slovenia), for human astrocytes.

Author Contributions

Conceived and designed the experiments: MS SAAR AG SPN. Performed the experiments: MS SAAR AO AD AG. Analyzed the data: MS SAAR AD TK AG. Contributed reagents/materials/analysis tools: CHM LV RB SPN. Wrote the paper: MS SAAR AO AD TK LV CHM RB AG SPN.

References

1. Weller M, Cloughesy T, Perry JR, Wick W. Standards of care for treatment of recurrent glioblastoma—are we there yet? Neuro-oncology. 2013; 15(1):4–27. doi: 10.1093/neuonc/nos273 PMID: 23136223
2. Carmeliet P, Jain RK. Principles and mechanisms of vessel normalization for cancer and other angiogenic diseases. Nature reviews Drug discovery. 2011; 10(6):417–27. doi: 10.1038/nrd3455 PMID: 21629292
3. Gilbert MR, Dignam JJ, Armstrong TS, Wefel JS, Blumenthal DT, Vogelbaum MA, et al. A randomized trial of bevacizumab for newly diagnosed glioblastoma. N Engl J Med. 2014; 370(8):699–708. doi: 10.1056/NEJMoa1308573 PMID: 24552317
4. Chinot OL, Wick W, Cloughesy T. Bevacizumab for newly diagnosed glioblastoma. N Engl J Med. 2014; 370(21):2049. doi: 10.1056/NEJMc1402987#SA1 PMID: 24860870
5. Plate KH, Scholz A, Dumont DJ. Tumor angiogenesis and anti-angiogenic therapy in malignant gliomas revisited. Acta neuropathologica. 2012; 124(6):763–75. doi: 10.1007/s00401-012-1066-5 PMID: 23143192
6. Keunen O, Johansson M, Oudin A, Sanzey M, Rahim SA, Fack F, et al. Anti-VEGF treatment reduces blood supply and increases tumor cell invasion in glioblastoma. Proceedings of the National Academy of Sciences of the United States of America. 2011; 108(9):3749–54. doi: 10.1073/pnas.1014480108 PMID: 21321221
7. Fack F, Espedal H, Keunen O, Golebiewska A, Obad N, Harter PN, et al. Bevacizumab treatment induces metabolic adaptation toward anaerobic metabolism in glioblastomas. Acta neuropathologica. 2014.
8. Stieber D, Abdul Rahim SA, Niclou SP. Novel ways to target brain tumour metabolism. Expert Opin Ther Targets. 2011; 15(10):1227–39. doi: 10.1517/14728222.2011.588211 PMID: 21635150
9. Vander Heiden MG, Cantley LC, Thompson CB. Understanding the Warburg effect: the metabolic requirements of cell proliferation. Science. 2009; 324(5930):1029–33. doi: 10.1126/science.1160809 PMID: 19460998
10. Chen W. Clinical applications of PET in brain tumors. J Nucl Med. 2007; 48(9):1468–81. PMID: 17704239
11. Wolf A, Agnihotri S, Munoz D, Guha A. Developmental profile and regulation of the glycolytic enzyme hexokinase 2 in normal brain and glioblastoma multiforme. Neurobiol Dis. 2011; 44(1):84–91. doi: 10.1016/j.nbd.2011.06.007 PMID: 21726646
12. Gao H, Yu B, Yan Y, Shen J, Zhao S, Zhu J, et al. Correlation of expression levels of ANXA2, PGAM1, and CALR with glioma grade and prognosis. J Neurosurg. 2013; 118(4):846–53. doi: 10.3171/2012.9.JNS112134 PMID: 23082878
13. Muller FL, Colla S, Aquilanti E, Manzo VE, Genovese G, Lee J, et al. Passenger deletions generate therapeutic vulnerabilities in cancer. Nature. 2012; 488(7411):337–42. doi: 10.1038/nature11331 PMID: 22895339
14. Mazurek S, Boschek CB, Hugo F, Eigenbrodt E. Pyruvate kinase type M2 and its role in tumor growth and spreading. Semin Cancer Biol. 2005; 15(4):300–8. PMID: 15908230
15. Christofk HR, Vander Heiden MG, Harris MH, Ramanathan A, Gerszten RE, Wei R, et al. The M2 splice isoform of pyruvate kinase is important for cancer metabolism and tumour growth. Nature. 2008; 452(7184):230–3. doi: 10.1038/nature06734 PMID: 18337823

16. Velpula KK, Bhasin A, Asuthkar S, Tsung AJ. Combined targeting of PDK1 and EGFR triggers regression of glioblastoma by reversing the Warburg effect. Cancer Res. 2013; 73(24):7277–89. doi: 10.1158/0008-5472.CAN-13-1868 PMID: 24148623

17. Campos B, Wan F, Farhadi M, Ernst A, Zeppernick F, Tagscherer KE, et al. Differentiation therapy exerts antitumor effects on stem-like glioma cells. Clin Cancer Res. 2010; 16(10):2715–28. doi: 10.1158/1078-0432.CCR-09-1800 PMID: 20442299

18. Torsvik A, Stieber D, Enger PO, Golebiewska A, Molven A, Svendsen A, et al. U-251 revisited: genetic drift and phenotypic consequences of long-term cultures of glioblastoma cells. Cancer medicine. 2014; 3(4):812–24. doi: 10.1002/cam4.219 PMID: 24810477

19. Golebiewska A, Bougnaud S, Stieber D, Brons NH, Vallar L, Hertel F, et al. Side population in human glioblastoma is non-tumorigenic and characterizes brain endothelial cells. Brain. 2013; 136(Pt 5):1462–75. doi: 10.1093/brain/awt025 PMID: 23460667

20. Benjamini Y, H Y. Controlling the False Discovery Rate: A Practical and Powerful Approach to Multiple Testing. Journal of the Royal Statistical Society. 1995; 57(1):289–300.

21. Dennis G Jr, Sherman BT, Hosack DA, Yang J, Gao W, Lane HC, et al. DAVID: Database for Annotation, Visualization, and Integrated Discovery. Genome Biol. 2003; 4(5):P3. PMID: 12734009

22. Supek F, Bosnjak M, Skunca N, Smuc T. REVIGO summarizes and visualizes long lists of gene ontology terms. PloS one. 2011; 6(7):e21800. doi: 10.1371/journal.pone.0021800 PMID: 21789182

23. Ahmed BY, Chakravarthy S, Eggers R, Hermens WT, Zhang JY, Niclou SP, et al. Efficient delivery of Cre-recombinase to neurons in vivo and stable transduction of neurons using adeno-associated and lentiviral vectors. BMC Neurosci. 2004; 5:4. PMID: 15005815

24. Niclou SP, Danzeisen C, Eikesdal HP, Wiig H, Brons NH, Poli AM, et al. A novel eGFP-expressing immunodeficient mouse model to study tumor-host interactions. Faseb J. 2008; 22(9):3120–8. doi: 10.1096/fj.08-109611 PMID: 18495755

25. Lal A, Peters H, St Croix B, Haroon ZA, Dewhirst MW, Strausberg RL, et al. Transcriptional response to hypoxia in human tumors. J Natl Cancer Inst. 2001; 93(17):1337–43. PMID: 11535709

26. Chi JT, Wang Z, Nuyten DS, Rodriguez EH, Schaner ME, Salim A, et al. Gene expression programs in response to hypoxia: cell type specificity and prognostic significance in human cancers. PLoS Med. 2006; 3(3):e47. PMID: 16417408

27. Huang da W, Sherman BT, Lempicki RA. Systematic and integrative analysis of large gene lists using DAVID bioinformatics resources. Nat Protoc. 2009; 4(1):44–57. doi: 10.1038/nprot.2008.211 PMID: 19131956

28. Huang da W, Sherman BT, Lempicki RA. Bioinformatics enrichment tools: paths toward the comprehensive functional analysis of large gene lists. Nucleic acids research. 2009; 37(1):1–13. doi: 10.1093/nar/gkn923 PMID: 19033363

29. Du J, Yuan Z, Ma Z, Song J, Xie X, Chen Y. KEGG-PATH: Kyoto encyclopedia of genes and genomes-based pathway analysis using a path analysis model. Molecular bioSystems. 2014; 10(9):2441–7. doi: 10.1039/c4mb00287c PMID: 24994036

30. Kathagen A, Schulte A, Balcke G, Phillips HS, Martens T, Matschke J, et al. Hypoxia and oxygenation induce a metabolic switch between pentose phosphate pathway and glycolysis in glioma stem-like cells. Acta neuropathologica. 2013; 126(5):763–80. doi: 10.1007/s00401-013-1173-y PMID: 24005892

31. Zhang X, Varin E, Allouche S, Lu Y, Poulain L, Icard P. Effect of citrate on malignant pleural mesothelioma cells: a synergistic effect with cisplatin. Anticancer Res. 2009; 29(4):1249–54. PMID: 19414371

32. Marcondes MC, Sola-Penna M, Zancan P. Clotrimazole potentiates the inhibitory effects of ATP on the key glycolytic enzyme 6-phosphofructo-1-kinase. Arch Biochem Biophys. 2010; 497(1–2):62–7. doi: 10.1016/j.abb.2010.03.013 PMID: 20346906

33. Ganapathy-Kanniappan S, Vali M, Kunjithapatham R, Buijs M, Syed LH, Rao PP, et al. 3-bromopyruvate: a new targeted antiglycolytic agent and a promise for cancer therapy. Curr Pharm Biotechnol. 2010; 11(5):510–7. PMID: 20420565

34. De Witt Hamer PC, Van Tilborg AA, Eijk PP, Sminia P, Troost D, Van Noorden CJ, et al. The genomic profile of human malignant glioma is altered early in primary cell culture and preserved in spheroids. Oncogene. 2008; 27(14):2091–6. PMID: 17934519

35. Hirschhaeuser F, Menne H, Dittfeld C, West J, Mueller-Klieser W, Kunz-Schughart LA. Multicellular tumor spheroids: an underestimated tool is catching up again. Journal of biotechnology. 2010; 148-(1):3–15. doi: 10.1016/j.jbiotec.2010.01.012 PMID: 20097238

36. Goidts V, Bageritz J, Puccio L, Nakata S, Zapatka M, Barbus S, et al. RNAi screening in glioma stem-like cells identifies PFKFB4 as a key molecule important for cancer cell survival. Oncogene. 2012; 31-(27):3235–43. doi: 10.1038/onc.2011.490 PMID: 22056879

37. Bonnet S, Archer SL, Allalunis-Turner J, Haromy A, Beaulieu C, Thompson R, et al. A mitochondria-K+ channel axis is suppressed in cancer and its normalization promotes apoptosis and inhibits cancer growth. Cancer cell. 2007; 11(1):37–51. PMID: 17222789

38. Sutendra G, Michelakis ED. Pyruvate dehydrogenase kinase as a novel therapeutic target in oncology. Frontiers in oncology. 2013; 3:38. doi: 10.3389/fonc.2013.00038 PMID: 23471124

39. Michelakis ED, Sutendra G, Dromparis P, Webster L, Haromy A, Niven E, et al. Metabolic modulation of glioblastoma with dichloroacetate. Science translational medicine. 2010; 2(31):31ra4.

40. Kumar K, Wigfield S, Gee HE, Devlin CM, Singleton D, Li JL, et al. Dichloroacetate reverses the hypoxic adaptation to bevacizumab and enhances its antitumor effects in mouse xenografts. Journal of molecular medicine. 2013; 91(6):749–58. doi: 10.1007/s00109-013-0996-2 PMID: 23361368

41. Ren F, Wu H, Lei Y, Zhang H, Liu R, Zhao Y, et al. Quantitative proteomics identification of phosphoglycerate mutase 1 as a novel therapeutic target in hepatocellular carcinoma. Mol Cancer. 2010; 9:81. doi: 10.1186/1476-4598-9-81 PMID: 20403181

42. Yan T, Skaftnesmo KO, Leiss L, Sleire L, Wang J, Li X, et al. Neuronal markers are expressed in human gliomas and NSE knockdown sensitizes glioblastoma cells to radiotherapy and temozolomide. BMC Cancer. 2011; 11:524. doi: 10.1186/1471-2407-11-524 PMID: 22185371

43. Wolf A, Agnihotri S, Micallef J, Mukherjee J, Sabha N, Cairns R, et al. Hexokinase 2 is a key mediator of aerobic glycolysis and promotes tumor growth in human glioblastoma multiforme. J Exp Med. 2011; 208(2):313–26. doi: 10.1084/jem.20101470 PMID: 21242296

44. Pastorino JG, Shulga N, Hoek JB. Mitochondrial binding of hexokinase II inhibits Bax-induced cytochrome c release and apoptosis. J Biol Chem. 2002; 277(9):7610–8. PMID: 11751859

45. Penso J, Beitner R. Clotrimazole and bifonazole detach hexokinase from mitochondria of melanoma cells. Eur J Pharmacol. 1998; 342(1):113–7. PMID: 9544799

Annex 11: Co-authored publication (not subject to thesis defence)

FULL PAPER

BJC

British Journal of Cancer (2017), 1–13 | doi: 10.1038/bjc.2017.263

Keywords: glioblastoma; autophagy; hypoxia; ATG9A; chloroquine; patient-derived xenografts

Regulation of hypoxia-induced autophagy in glioblastoma involves ATG9A

Siti Aminah Abdul Rahim[1], Anne Dirkse[1,2], Anais Oudin[1], Anne Schuster[1], Jill Bohler[1], Vanessa Barthelemy[1], Arnaud Muller[3], Laurent Vallar[3], Bassam Janji[4], Anna Golebiewska[1] and Simone P Niclou[*,1,5]

[1]NorLux Neuro-Oncology Laboratory, Department of Oncology, Luxembourg Institute of Health, L-1526 Luxembourg City, Luxembourg; [2]Faculty of Science, Technology and Communication, University of Luxembourg, Esch-sur-Alzette L-4365, Luxembourg; [3]Proteome and Genome Research Unit, Department of Oncology, Luxembourg Institute of Health, L-1526 Luxembourg City, Luxembourg; [4]Laboratory of Experimental Cancer Research, Department of Oncology, Luxembourg Institute of Health, L-1526 Luxembourg City, Luxembourg and [5]KG Jebsen Brain Tumour Research Center, Department of Biomedicine, University of Bergen, N-5019 Bergen, Norway

Background: Hypoxia is negatively associated with glioblastoma (GBM) patient survival and contributes to tumour resistance. Anti-angiogenic therapy in GBM further increases hypoxia and activates survival pathways. The aim of this study was to determine the role of hypoxia-induced autophagy in GBM.

Methods: Pharmacological inhibition of autophagy was applied in combination with bevacizumab in GBM patient-derived xenografts (PDXs). Sensitivity towards inhibitors was further tested *in vitro* under normoxia and hypoxia, followed by transcriptomic analysis. Genetic interference was done using ATG9A-depleted cells.

Results: We find that GBM cells activate autophagy as a survival mechanism to hypoxia, although basic autophagy appears active under normoxic conditions. Although single agent chloroquine treatment *in vivo* significantly increased survival of PDXs, the combination with bevacizumab resulted in a synergistic effect at low non-effective chloroquine dose. *ATG9A* was consistently induced by hypoxia, and silencing of *ATG9A* led to decreased proliferation *in vitro* and delayed tumour growth *in vivo*. Hypoxia-induced activation of autophagy was compromised upon *ATG9A* depletion.

Conclusions: This work shows that inhibition of autophagy is a promising strategy against GBM and identifies ATG9 as a novel target in hypoxia-induced autophagy. Combination with hypoxia-inducing agents may provide benefit by allowing to decrease the effective dose of autophagy inhibitors.

Despite considerable advancement in the molecular characterisation of glioblastoma (GBM), survival of patients under current treatment regimen remains disappointing. Treatment failure is partially due to the capacity of tumour cells to activate pro-survival pathways in an unfavourable microenvironment. The GBM vasculature is poorly functional, leading to insufficient oxygen supply and necrotic areas (Evans *et al*, 2004). Hypoxia and angiogenic factors are correlated with tumour grade and poor patient prognosis in brain tumours (Yang *et al*, 2012) and are linked to radiation- and chemotherapy resistance (Vaupel and Mayer, 2007). Although targeting angiogenesis has long been regarded as an attractive therapeutic approach, anti-angiogenic agents are incapable to halt tumour progression and improve patient survival (Gilbert, 2016). We have previously shown that administration of bevacizumab, an antibody against vascular endothelial growth factor (VEGF), resulted in an adaptive metabolic switch leading to an increased hypoxia and induction of glycolysis (Keunen *et al*, 2011; Fack *et al*, 2015). However, the

*Correspondence: Professor SP Niclou; E-mail: simone.niclou@lih.lu

Revised 7 June 2017; accepted 13 July 2017

exact mechanism of GBM cell survival and adaptation under hypoxia are still incompletely understood.

Solid tumours use autophagy as one of the survival mechanisms upon various stressors including metabolic stress and starvation (Yang *et al*, 2011), hypoxia (Rabinowitz and White, 2010; Rouschop *et al*, 2010), chemotherapy (Kanzawa *et al*, 2004; Ciechomska *et al*, 2013) and radiotherapy (Firat *et al*, 2012). In physiological situations, autophagy has an important role in organelle turnover, degradation of proteins, cellular differentiation and aging (Glick *et al*, 2010). During stress, autophagy protects cells by eliminating damaged organelles and proteins via autophagosomes. Autophagosomes fuse with lysosomes to form the autolysosome responsible for enzymatic self-digestion of cellular waste. Recycled cellular components may serve as an energy source during periods of starvation, hypoxia or high-energy demand. Under physiological hypoxia (0.1–3%O_2), the autophagic response is HIF1α-dependent (Mazure and Pouyssegur, 2010) and relies on the induction of the pro-autophagic genes *BNIP3 (BCL2/adenovirus E1B 19kDA interacting protein 3)* and *BNIP3L (BNIP3-like)* (Pouyssegur *et al*, 2006; Bellot *et al*, 2009). Furthermore, autophagy is strongly dependent on the synchronised action of autophagy-related (ATG) genes. Although many *ATG* genes are modulated upon induction of autophagy (Gasch *et al*, 2000), their specific roles are not always fully elucidated. ATG9A is the only transmembrane autophagy-related protein and has been associated with the regulation of autophagosome formation (Jin and Klionsky, 2014). ATG9A cycles between the Golgi network, endosomes and the so called 'ATG9A reservoir', and ATG9A-containing vesicles in cytoplasm, creating a ready source to support autophagosome formation (Reggiori and Tooze, 2012). Although the detailed mechanism is poorly understood, it is thought to support the growth and maturation of autophagic membranes by recruiting membrane structures to the LC3-positive autophagosomes (Orsi *et al*, 2012; Yamamoto *et al*, 2012; Corcelle-Termeau *et al*, 2016; Lamb *et al*, 2016).

Following up on our earlier studies (Fack *et al*, 2015; Sanzey *et al*, 2015), we addressed the role of autophagy in enabling cell survival in severe hypoxia and during anti-angiogenic treatment. We show that GBM cells activate autophagy in hypoxia and that ATG9A has an essential role in the autophagic response of GBM.

MATERIALS AND METHODS

GBM patient material. Human GBMs were obtained from the Neurosurgery Department of the Centre Hospitalier in Luxembourg (CHL) (T16) or the Department of Neurosurgery, Haukeland University Hospital in Bergen (P3, P8), Norway. All patients had provided informed consent, tumour collection was approved by the National Research Ethics Committee for Luxembourg (CNER) or by the Regional Ethical Board at the Haukeland University Hospital in Bergen. All biopsies were primary GBM based on neuropathological diagnosis and genomic analysis (Supplementary Table S1). The original organotypic GBM spheroids from patient samples were prepared as previously described (Keunen *et al*, 2011; Golebiewska *et al*, 2013; Bougnaud *et al*, 2016) and maintained in spheroid medium (DMEM medium, 10% FBS, 2 mM L-Glutamine, 0.4 mM NEAA and 100 U ml^{-1} Pen-Strep; Lonza, Basel , Switzerland) in agar pre-coated flasks for 7–10 days.

Orthotopic patient-derived GBM xenografts. Serial transplantation of PDXs in eGFP-expressing NOD/SCID mice were used to expand the tumour material and prepare spheroids for *in vitro* assays, as previously described (Niclou *et al*, 2008; Bougnaud *et al*, 2016). For treatment experiments, P3 and T16 GBM spheroids expressing RFP were orthotopically implanted into the right frontal lobe of Swiss nude mice (6 per mice). Tumour growth was monitored by *in vivo* fluorescence imaging (IVIS Lumina Fluorescence system; PerkinElmer, Waltham, MA, USA). Three weeks post implantation mice were randomly allocated into treatment groups (6–7 mice per group). Bevacizumab, chloroquine and normal saline were delivered by intraperitoneal injections. The treatment schedule is summarised in Supplementary Table S2. NCH421k and NCH644 harbouring *Scramble* or *ATG9A* shRNA were stereotactically implanted in NOD/SCID mice (13 7500 NCH421k cells or 50 000 NCH644 cells per animal; 6–7 per group). Animals were monitored daily and the following criteria were evaluated: (1) loss of >10% of body weight, (2) exhibition of strong neurological signs (3) increased lordosis or (4) swollen belly. The criteria were scored as: 0 = none, 1 = early, 2 = established, 3 = severe signs and animals were killed when three criteria with grade 2 or 1 criteria with grade 3 were reached. All procedures were approved by the national authorities responsible for animal experiments in Luxembourg.

Immunohistochemistry. For mouse-specific CD31 staining cryostat sections (10 μm) of flash-frozen brains were fixed in ice-cold acetone and acetone : chloroform (1 : 1) for 5 min each. Sections were blocked for 1 h in TBS/2% FCS, followed by a 1 h incubation in rat anti-mouse CD31 antibody (Merck Millipore, Nottingham, UK, 1 : 200). Alexa Fluor 488-conjugated secondary antibodies were applied for 1 h. Sections were analysed by fluorescence microscopy. Quantification of vessel staining was done using ImageJ (NHS, Bethesda, MA, USA) from 3–4 mice per group (9–34 images per mice).

Western blotting. GBM cells were cultured in normoxia or 0.1% O_2 hypoxia for 48 h. When indicated, 20 μM chloroquine was added 16 h before cell collection. Cultured cells or spheroids were lysed in RIPA buffer (Merck Millipore) with 0.1% SDS. Overall, 30 μg of proteins were loaded and separated in a NuPAGE Novex 4–12% Bis-Tris Gels (Life Technologies, Merelbeke, Belgium) followed by electroblot transfer to a PVDF membrane (Novex, Invitrolon PVDF, Life Technologies). Membranes were blocked with 2% non-fat milk in Tris-buffered saline containing 0.1% Triton-X before incubation with primary antibodies (LC3B: Cell Signaling Technology, Danvers, MA, USA, 1 : 2000; p62: BD Bioscience, Erembodegem, Belgium, 1 : 1000; Actin: Millipore, 1 : 10 000; Tubulin: Millipore, 1 : 5000). Secondary coupled to horseradish peroxidase were detected by enhanced chemiluminescence (ECL) (Lumigen TMA6, GE Healthcare) with luminescent image analyser (Image Quant LAS4000, GE Healthcare, Diegem, Belgium). Quantification was performed with the ImageQuant TL. Owing to the substantial normalisation problems linked to disturbed actin and tubulin signal in hypoxic cells upon induction of autophagy (Klionsky *et al*, 2016), WB signals were normalised to total protein content.

Cell viability in GBM spheroids. Cell viability after 72 h of treatment with inhibitors was assessed by double labelling with 2 μM Calcein AM and 4 μM Ethidium homodimer-1 (LIVE/DEAD Viability/Cytotoxicity assay kit, Molecular Probes, Eugene, OR, USA) for 6 h. Measurements of viable ('green') and dead ('red') cells were performed using fluorescence confocal microscopy (Zeiss LSM STO META, Zeiss, Zaventem, Belgium) by obtaining 20–25 stacks of two-dimensional images from successive focal planes (5 μm). Quantification was performed using IMARIS software (Bitplane, Belfast, UK). The volume of viable and dead cells within a spheroid was calculated by multiplying the surface area of each component per stack by the total height of the image stacks. The percentage of dead cell volume was calculated as: % dead cell in spheroids (volume) = Dead cell volume ('red')) × 100/ Total spheroid volume ('green' + 'red'). Experiments were carried out three times with at least five spheroids each.

Cell culture. The primary adherent P3 cells (P3A) was derived from patient xenograft-derived P3 3D spheroids grown in uncoated flasks until a confluent adherent culture was obtained.

P3A, U87, U251 and T98G cells were cultured as monolayers in DMEM containing 10% FBS, 2 mM L-glutamine and 100 U ml^{-1} Pen-Strep (Lonza). The normal human astrocytes (NHA) (kindly provided by Dr Uros Rajcevic, Ljubljana, Slovenia) grew in DMEM, 10% FBS, 2 mM L-glutamine and 100 100 U ml^{-1} Pen-Strep (Lonza). GBM stem-like cultures (NCH421k, NCH660h, NCH465, NCH601 and NCH644) were kindly provided by Christel Herold-Mende (University of Heidelberg, Germany) and were cultured as previously described (Sanzey *et al*, 2015). Normoxic cultures were performed at 37 °C under 5% CO_2 atmospheric oxygen. Hypoxic conditions at 0.1–0.5% O_2 were maintained in the hypoxic incubator chamber (Galaxy 48R incubator, New Brunswick, Eppendorf, Rotsellar, Belgium).

Cytotoxicity assay. Cells were plated at semi-confluency in 96 well plates. NCH644 were attached on ECM Cell-Tak (VWR, Leuven, Belgium) precoated plates. Increasing concentrations of tested compounds (chloroquine diphosphate (Sigma, Overijse, Belgium; C6628) and mefloquine hydrochloride (Sigma, M2319)) were applied for 72 h. Induction of cell death was measured after 72 h with the Sulforhodamine (SRB) assay (*In Vitro* Toxicology Assay Kit, Sigma). The optical density was measured at 540 nm. The percentage inhibition of cell mass was determined as: % cell mass reduction = (Mean $OD_{control}$ − mean OD_{sample}) × 100/Mean $OD_{control}$. IC_{50} was determined with the GraphPad Prism 5 (GraphPad Software, La Jolla, CA, USA).

Gene expression analysis. The gene expression profiles were analysed as described previously (Sanzey *et al*, 2015). Lists of differentially expressed genes (DEGs) were obtained with ANOVA (false discovery rate (FDR) < 0.01, any FC). The Ingenuity Pathway Analysis (IPA) (Ingenuity Systems) was used for data mining. Right-tailed Fisher's exact test was used to calculate a *P* value for functional enrichment analysis (threshold: $-\log(P \text{ value}) > 1.3$). Upstream regulator analysis was used to detect potential transcriptional regulators (an overlap of *P* value < 0.05 and activation *z*-score > 2). Venn diagram analysis was performed with the SUMO software (http://angiogenesis.dkfz.de/oncoexpress/software/). Microarray data are available in the ArrayExpress database (www.ebi.ac.uk/arrayexpress) under accession number E-MTAB-3085.

Real-time quantitative PCR. Overall, 1 μg of total RNA was reverse transcribed using iScript cDNA Synthesis Kit (BioRad, Temse, Belgium). Quantitative PCR (qPCR) was carried out using Fast SYBR Green Master Mix and the Viia 7 Real Time PCR System (Life Technologies) with *ATG9A* (F: GCCAGACG CCTTTTTGCCTGC; R: TAGGGATGCGCAGAGCGTGC) and *EZRIN* (F: TGCCCCACGTCTGAGAATC; R: CGGCGCATATA CAACTCATGG) primers. Fold-change (FC) was calculated using the $\Delta\Delta C_t$ method (QBase).

shRNA-mediated knockdown of *ATG9A*. A control shRNA (*shScramble*, Open Biosystems, RHS4346) or a shRNA targeting *ATG9A* (Open Biosystems, RHS4430-99150604) were introduced using lentiviral particles. Individual pGIPZ shRNAmir constructs were obtained as *E. coli* cultures in LB-lenox medium with 8% glycerol, 100 μg ml^{-1} carbenicillin and 25 μg ml^{-1} zeocin. Lentiviral particles were produced in HEK cells by co-transfection of the pGIPZ vector with the viral core packaging construct pCMVdeltaR8.74 and the VSV-G envelope protein vector pMD.G.2. Supernatant containing viral particles was used to transduce 100 000 cells and puromycine selection permitted to obtain 100% of stably transduced GFP-positive cells (0.5 μg ml^{-1} for NCH421k and U87, 1 μg ml^{-1} for NCH644 for at least 2 weeks). Cells were regularly verified for GFP expression via flow cytometry and puromycine selection was repeated, if required.

Transient transfection with LC3B. U87 and U251 were seeded in ibidi iTreat μ-Dish transfected using lipofectamine (Thermo Fisher, Illkirch, France) with 2 μg of LC3B-GFP or LC3-Tomato plasmid for 3 h. Transfected cells were incubated for 16 h in either normoxia or 0.1–0.5% O_2 hypoxia in the presence of 20 μM chloroquine. Nuclei were visualised with Hoechst33342. Images were taken using fluorescence confocal microscopy (Zeiss LSM STO META) by obtaining 20–25 stacks of two-dimensional images from successive focal planes (10–15 μm total). Quantification of autophagosomes was performed with ImageJ. Experiments were performed twice, 35 individual cells were acquired in total for analysis.

Cell proliferation assay. *shScramble* and *shATG9A* transfected NCH421k, NCH644 (10 000 cells) and U87 (5000 cells) were plated in 6 well plates. Cells were cultured for 4, 7 and 11 days. At each time point, total number of viable cells was measured with a Countess cell counter (Thermo Fisher). Experiments were performed three times with three replicates each.

Statistical analysis. The data was analysed with unpaired independent-samples *t*-test (Excel software, Microsoft, Redmond, Seattle, WA, USA). Kaplan–Meier survival curves, log-rank test for survival analysis and IC_{50} were calculated with the GraphPad Prism5. Data were considered statistically significant with a *P* value < 0.05.

RESULTS

Bevacizumab sensitises GBM cells to anti-autophagy treatment *in vivo* in orthotopic patient-derived xenografts. We showed previously that administration of bevacizumab (Bev), an anti-angiogenic agent, leads to a hypoxic signature in GBM patient-derived xenografts (PDXs) (Keunen *et al*, 2011; Demeure *et al*, 2015; Fack *et al*, 2015). As autophagy appears as an essential survival mechanism under hypoxia, we hypothesised that the combination of bevacizumab with an autophagy inhibitor would have an additional anti-tumour effect. We applied the well-known autophagy inhibitor chloroquine *in vivo* on two different PDXs. Organotypic P3 and T16 spheroids were orthotopically implanted into nude mice and treatment was started 3 weeks post implantation (Supplementary Table S2).

Chloroquine treatment (20 mg kg^{-1}) significantly prolonged survival of P3 mice (+18.4%; Figure 1A; Supplementary Table S2), whereas it had no effect in T16 xenografts; however, increasing the dose to 50 mg kg^{-1} (3 × -weekly) increased the survival (+9.6%; Figure 1B; Supplementary Table S2). As previously shown (Keunen *et al*, 2011; Golebiewska *et al*, 2013) treatment with bevacizumab did not significantly prolong survival of mice with these PDXs (Figure 1A and B), despite the fact that vessel morphology was normalised. At an effective chloroquine concentration, bevacizumab did not lead to a statistically significant additive benefit in both PDXs. However, the addition of bevacizumab led to a synergistic effect in the low chloroquine dose in T16 (11.5%; $P = 0.0095$), at a concentration where chloroquine was not effective as a single agent. The effect was equivalent to the high-dose chloroquine treatment (CQ 50 mg kg^{-1} *vs* CQ 20 mg kg^{-1} + Bev; $P = 0.85$) indicating that the addition of bevacizumab allows to lower the effective chloroquine treatment dose.

It has been shown that in melanoma chloroquine acts on the normalisation of tumour vessels independently of autophagy (Maes *et al*, 2014). We did not detect any direct effect of chloroquine on vessel normalisation: bevacizumab but not chloroquine significantly decreased vessel density, total vessel density reduced upon bevacizumab was not further affected by adding chloroquine (Figure 1C and D).

In conclusion, our data show that chloroquine has a therapeutic effect as a single agent in GBM PDXs, albeit the effective dose differing between GBM. Addition of bevacizumab allowed to lower the dose of chloroquine to reach the same survival benefit.

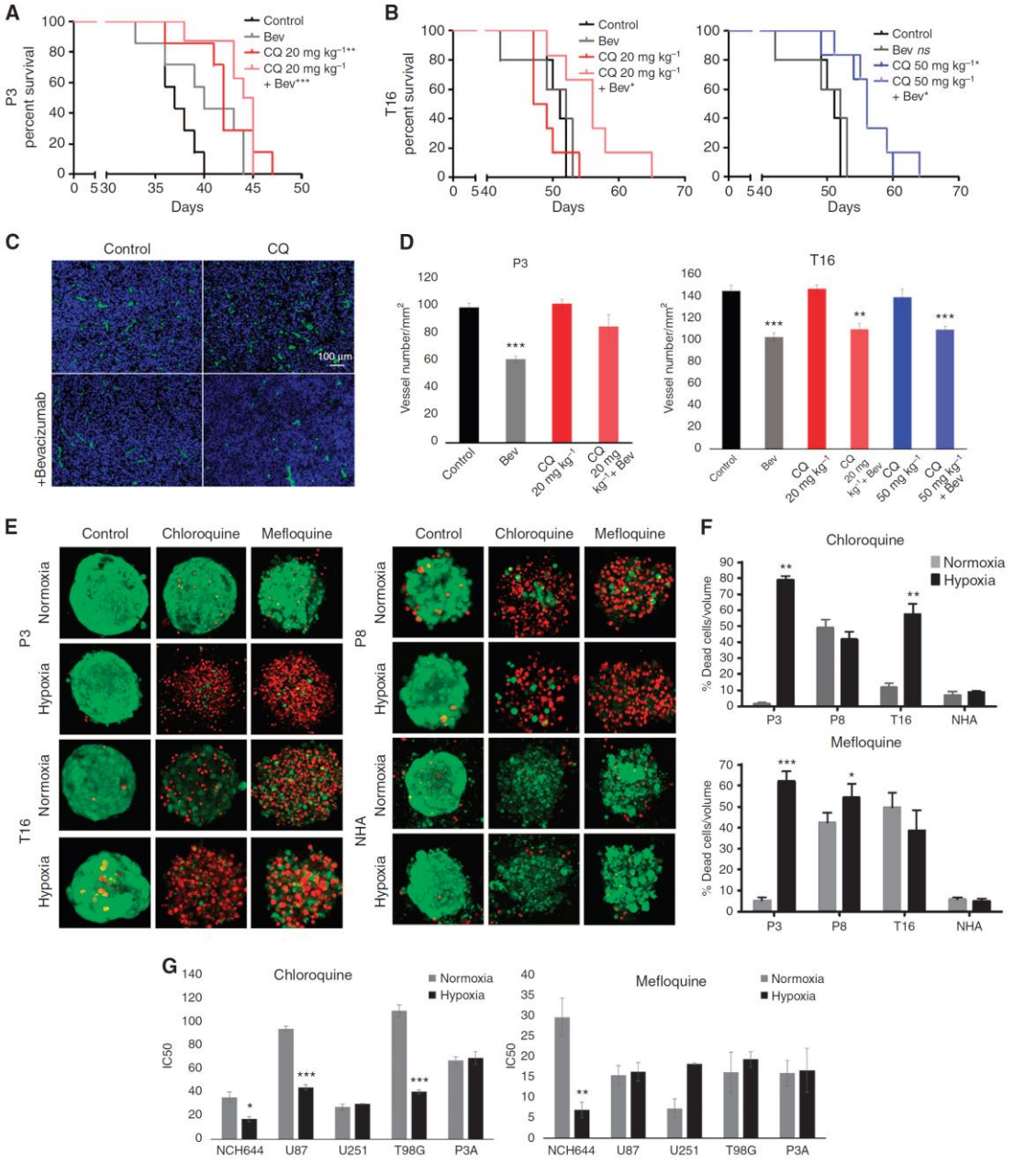

Figure 1. Hypoxia sensitises GBM cells to autophagy inhibitors. Chloroquine and bevacizumab were administered as single agents or simultaneously in P3 (**A**: 20 mg kg^{-1}) and T16 (**B**: 20 and 50 mg kg^{-1}) PDXs. Kaplan–Meier graphs show the survival of mice upon treatment. See Supplementary Table S1 for summary. Abbreviations: Bev = Bevacizumab; CQ = chloroquine; log-rank test, $*P<0.05$, $**P<0.01$, $***P<0.001$. (**C**) Blood vessels from control and treated P3 PDXs were visualised by mouse-specific anti-CD31 (scale bars 100 μm). (**D**) Quantification of vessel number per mm^2 upon treatment (mean ± s.e.m., $*P<0.05$, $**P<0.01$, $***P<0.001$). (**E**) The cytotoxic effect of inhibitors (chloroquine 20 μM, mefloquine 10 μM) was analysed for PDX-derived spheroids and NHA after 72 h treatment in normoxia and hypoxia. Representative images of treated spheroids are presented ('green' = viable, 'red' = dead). (**F**) Quantification of cell death upon treatment displayed as % of dead cells/volume ($n \geqslant 5$, $*P<0.05$, $**P<0.01$, $***P<0.001$). (**G**) Sensitivity of GBM cultures to chloroquine and mefloquine 72 h after treatment. Concentration gradients were used to determine the median inhibitory concentration (IC_{50}). IC_{50} are expressed as mean ± s.e.m. ($n \geqslant 3$, $*P<0.05$, $**P<0.01$, $***P<0.001$).

GBM cells exhibit increased sensitivity to chloroquine in hypoxia. To further confirm a role of hypoxia in the outcome of anti-autophagy treatment, we assessed the efficacy of two autophagy inhibitors, chloroquine and mefloquine, at different oxygen levels. We have first assessed the cytotoxic effects in primary PDX-derived 3D spheroids standardised for drug testing (Supplementary Figure S1), known to recapitulate well the genetic makeup of patient tumours (De Witt Hamer *et al*, 2008; Bougnaud *et al*, 2016) (Supplementary Table S1) and drug responses (Hirschhaeuser *et al*, 2010). Non-transformed human astrocytes (NHA) cultured under identical conditions were used as a control. Spheroids treated for 72 h with chloroquine (20 μM) or mefloquine (10 μM) in normoxia or severe hypoxia (0.1% O_2; Figure 1E and F) displayed a heterogeneous response to autophagy inhibitors. Little cell death was observed within P3 and T16 spheroids treated with chloroquine in normoxia, whereas cell death was markedly increased in hypoxia (Figure 1E and F). P8 spheroids were already sensitive to chloroquine in normoxia and exhibited no further increase in sensitivity under hypoxia. Mefloquine, a more potent lysosomotropic agent, was generally more toxic already in normoxia. In P3 spheroids, sensitivity, however strongly increased in hypoxia, which appeared relatively resistant to mefloquine in normoxia. At the indicated concentration, chloroquine and mefloquine did not induce cell death in astrocytes (Figure 1E and F), suggesting that astrocytes are less dependent on autophagy compared to GBM cells.

We further determined the half maximal inhibitory concentration (IC_{50}) for chloroquine and mefloquine in a panel of GBM cultures. Out of six cultures tested NCH644, U87 and T98G exhibited increased sensitivity to chloroquine in hypoxia (Figure 1G). U251 and P3A were already very sensitive under normoxia and no additive effect was observed in hypoxia (Figure 1G). Again, mefloquine was generally more potent in normoxia, and increased sensitivity in hypoxia was observed only for NCH644, which displayed highest IC_{50} at normal oxygen levels (Figure 1G).

Taken together, we show that hypoxia potentiates the cytotoxic effect of autophagy inhibitors in GBM spheroids and in GBM cultures. Similar to the *in vivo* situation, the GBM response is heterogeneous and the additive effect is observed in hypoxic cells only when the treatment reaches mild/moderate effect in normoxia.

Induction of autophagy at the transcript and protein level. We have recently shown that GBM cells can survive under long-term severe hypoxia, undergoing transcriptional changes and increasing dependency on glycolysis (Sanzey *et al*, 2015). Although autophagy is known to be regulated mainly at the post-transcriptional level, transcriptional regulation has an important role in the induction of the process (Moussay *et al*, 2011). We therefore investigated transcriptional regulation of autophagy-associated genes. Gene expression patterns were obtained from a panel of GBM cultures including glioma stem-like cells (NCH421k, NCH644) and classical GBM lines (U87, U251), cultured under short (12 h) and long-term (7 days) hypoxia. Differentially expressed genes (FDR $<$ 0.01; any FC) were further subjected for functional enrichment analysis by IPA. As genes associated with the autophagy pathway genes regulating autophagy are poorly annotated in ontology databases we applied an in-house gene list (244 genes referred as 'Autophagy pathway') (Moussay *et al*, 2011), revealing strong modulation of the autophagy pathway upon both short- and long-term hypoxia (Figure 2A). As expected, the upstream regulator analysis by IPA predicted the hypoxia inducible factor 1-alpha (HIF1A) transcription network to be strongly activated upon hypoxia (P value $<$ 0.05; z-score $>$ 2; Figure 2B), as was FOXO3A – one of the transcription factors responsible for induction of autophagy (Figure 2B).

Activation of autophagy was further visualised via increased conversion of LC3-I to LC3-II isoform under hypoxia (Figure 2C). To appropriately detect changes in the autophagic flux, experiments were performed in the absence and in the presence of the lysosomotropic agent chloroquine, which inhibits both the fusion of autophagosome with lysosome and lysosomal protein degradation. Contrary to the previous experiments where chloroquine was used as a treatment agent (Figure 1), the inhibition of the autophagic flux was detectable upon short chloroquine treatment (3–16 h) according to well-established protocols (Shintani and Klionsky, 2004; Klionsky *et al*, 2016). High levels of the LC3-II isoform were detected in all GBM cells treated with chloroquine upon hypoxia as reflected in the LC3-II/LC3-I ratios. Interestingly, NCH421k and U251 cells displayed high levels of LC3-II already in normoxia, suggesting their strong dependence on autophagy in normal conditions (Figure 2C). This is in accordance with the high sensitivity of U251 to chloroquine in both conditions (Figure1G). Induction of autophagy by hypoxia was further confirmed by a decrease in p62 (Figure 2D) and an increase in the number of autophagosomes visualised via transient LC3-GFP transfection (Figure 2E). In conclusion, these data indicate that autophagy is induced under severe hypoxia in GBM cells. The heterogeneous sensitivity to autophagy inhibition corroborates with the differential basal level of autophagy in normoxia and further activation of autophagy in hypoxic GBM cells.

ATG9A is involved in the hypoxia-dependent autophagic response. To further explore the GBM-specific response to hypoxia we focused on 98 specific regulators of autophagy (71-positive and 27-negative regulators, Supplementary Table S3). Although the number of deregulated genes and the extend of deregulation was variable, we found four commonly deregulated genes shared between short-term and long-term hypoxia (*ATG9A*, *BNIP3*, *BNIP3L* and *PIK3C3*; Figure 3A; Supplementary Table S3), showing increased levels upon hypoxia. BNIP3 and BNIP3L were previously associated with the autophagic response in hypoxic conditions (Mazure and Pouyssegur, 2010), whereas PIK3C3 is a well-known partner in the autophagy onset mechanism (Munson and Ganley, 2015). Of note, *MTOR*, a negative regulator of autophagy and of PIK3C3, was significantly downregulated in 3 out of 4 GBM cultures (Supplementary Table S3). Interestingly, within the ATG family, only *ATG9A* was upregulated in all GBM cells (Figure 3B; Supplementary Table S3), *ATG2A* was high only in 5 out of 8 conditions (Supplementary Table S3). The upregulation of *ATG9A* was confirmed by qPCR in GBM stem-like cells (NCH644, NCH421k, NCH660h, NCH601, NCH465) and adherent cultures (U87, U251) (Figure 3C).

Interestingly, analysis of the *ATG9A* gene promoter revealed the presence of five hypoxia response elements (HREs) in close proximity to the canonical transcription start site, confirmed to be functional according to the TRANSFAC database (Matys *et al*, 2006; Mole *et al*, 2009) (Supplementary Table S4). This was true also for *BNIP3*, *BNIP3L* and *PIK3C3* promoters, and is in line with the HIF-dependent regulation reported for the *BNIP3* and *BNIP3L* (Kothari *et al*, 2003; Mole *et al*, 2009; Slemc and Kunej, 2016). In summary, we show for the first time that *ATG9A* expression is strongly induced in hypoxic conditions, implicating ATG9A as a new player of hypoxia-dependent autophagic response in GBM.

Silencing of ATG9A affects GBM cell proliferation and tumour growth *in vivo*. To study the involvement of ATG9 in autophagy, we generated an efficient long-term *ATG9A* knockdown (75–98%, Figure 4A) in three GBM cultures, resulting in reduced proliferation both in normoxia and hypoxia (Figure 4B). Contrary to the control, *ATG9A*-depleted U87 cells did not increase the number of LC3-positive vesicles upon hypoxia (Figure 4C), suggesting inefficient activation of autophagy. To examine the effect of ATG9A silencing on tumour growth *in vivo*, we implanted *shATG9A* NCH421k and NCH644 cells into the brain of immunodeficient mice. *ATG9A* knockdown led to a significant increase in mouse survival (+12–18%; Figure 4D). Of note, two of the autopagy-associated genes, *ATG9A* and *BNIP3L*, were included

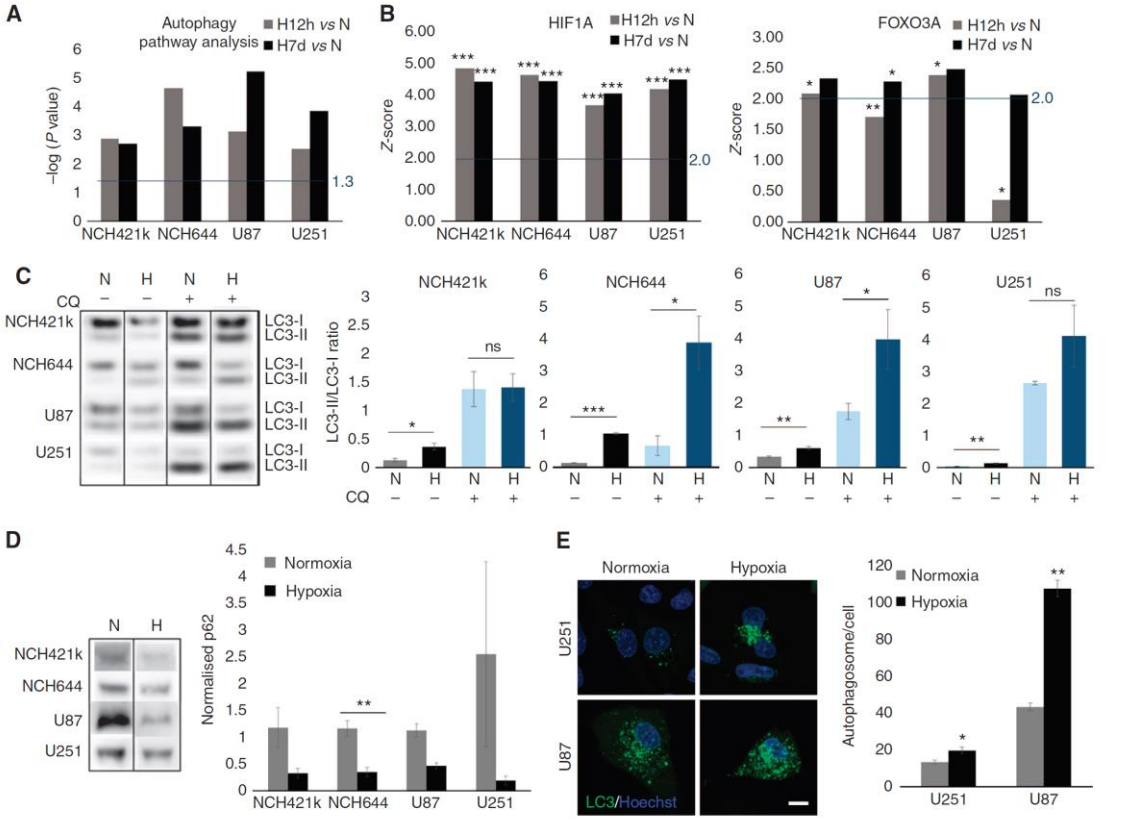

Figure 2. Hypoxia activates autophagy in GBM cells. (**A**) DEG lists between hypoxia 12 h *vs* normoxia and hypoxia 7 days *vs* normoxia (FDR < 0.01; any FC, $n = 3$–6) were subjected to IPA. Autophagy-associated genes (Moussay *et al*, 2011) were significantly altered (threshold: $-\log(P \text{ value}) > 1.3$). (**B**) Upstream Regulator analysis (IPA) predicted activation of HIF1α and FOXO3 network upon hypoxia (threshold: *z*-score > 2 and *P* value of overlap < 0.05; $^*P < 0.05$ $^{**}P < 0.01$, $^{***}P < 0.001$). (**C**) Western blot analysis showing LC3-I/II. Increase of autophagy in hypoxia is visualised by increased LC3-II (lower band)/LC3-I (upper band) ratio in the presence of chloroquine (mean ± s.e.m., $n = 3$; $^*P < 0.05$, $^{**}P < 0.01$, $^{***}P < 0.001$). Representative images were cropped from the same blot (CQ = chloroquine, N = normoxia, H: 0.1–0.5% O_2 48 h hypoxia). (**D**) Western blot analysis showing p62 degradation upon hypoxia (mean normalised to total protein content ± s.e.m., $n = 3$; $^{**}P < 0.01$). Representative images were cropped from the same blots. Control cells (normoxia, no chloroquine) were used as an internal calibration (value = '1'). (**E**) Representative images show an increase in autophagosome formation upon hypoxia. Cells were exposed to hypoxia for 16 h in the presence of chloroquine. Autophagosomes were counted as LC3B–GFP-positive vacuoles 24 h after transfection; (mean ± s.e.m.; $n = 34$; $^*P < 0.05$, $^{**}P < 0.01$).

in our previously reported targeted shRNA screen, where we examined the essentiality of 55 genes for survival of GBM cells *in vitro* and *in vivo* (Sanzey *et al*, 2015). Interestingly, *ATG9A* but not *BNIP3L* was also depleted both *in vitro* and *in vivo* (Figure 4E), indicating that ATG9A is essential for general GBM cell survival. Taken together, our data show that ATG9A is important for GBM growth both in normoxic and hypoxic conditions, and regulates activation of autophagy upon hypoxia. Interfering with ATG9A expression efficiently blocks tumour growth *in vivo*.

DISCUSSION

Hypoxia is a characteristic feature of malignant gliomas and drives tumour progression by adaptive cellular responses including angiogenesis, changes in tumour metabolism, motility and survival (Bertout *et al*, 2008). Increased hypoxia is also one of the escape mechanisms driving resistance to anti-angiogenic treatment in GBM. Here we find that the autophagy pathway is strongly induced in GBM under hypoxia, and we identify ATG9A as a novel regulator of autophagy induction. Inhibiting autophagy was shown to potentiate various anti-cancer therapies *in vitro*, including gliomas (Kanzawa *et al*, 2004; Shingu *et al*, 2009), where cells were subjected to external stress. Although, there are currently over 20 clinical studies involving the use of chloroquine and hydroxychloroquine in cancer treatment, in GBM both agents showed limited effect in non-toxic doses (Sotelo *et al*, 2006; Rosenfeld *et al*, 2014). Here we show a significant increase in survival of GBM PDXs when chloroquine was administered as a single agent, although with different effective dose. This is in accordance with the recent clinical trial showing dose-dependent inhibition of autophagy by hydroxychloroquine in GBM patients (Rosenfeld *et al*, 2014) and suggests that dosing needs to be adapted to the specific patient tumour. Of note, we show that certain tumour cells were sensitive to autophagy inhibitors also at normal oxygen, indicating a strong dependence on autophagy without additional environmental stress in a subgroup of GBM. This heterogeneous response suggests that the genetic background, for example, PTEN deletion, p53 mutation or EGFR amplification, may differentially

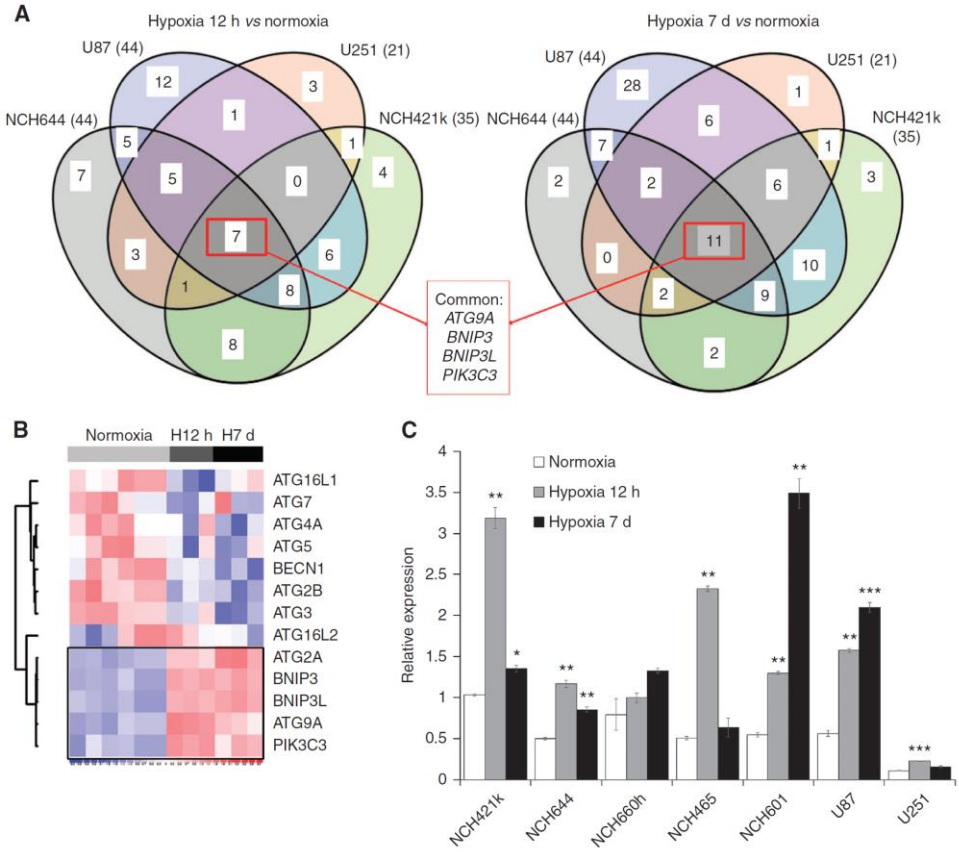

Figure 3. *ATG9A* is specifically activated upon autophagic response to hypoxia. (**A**) Genes directly related to autophagy (knowledge-driven selection) were extracted from DEG lists between hypoxia 12 h *vs* normoxia and hypoxia 7 days *vs* normoxia (FDR < 0.01; any FC) for each culture ($n = 3$–6). Venn diagrams reveal commonly deregulated genes. (**B**) Heatmap shows expression levels for selected genes in NCH421k in normoxia, 12 h and 7 days hypoxia. See Supplementary Table S3 for more autophagy-related genes. (**C**) QPCR confirmed increased *ATG9A* expression in hypoxia. *EZRIN* was used as a reference (mean ± s.e.m.; $n = 3$; $^*P < 0.05$, $^{**}P < 0.01$, $^{***}P < 0.001$). NCH421k cells were used as an internal calibration (value = '1').

affect the extent of basal level of autophagy and of treatment response in GBM and that appropriate biomarkers may be required to efficiently stratify patients. EGFR is known to negatively regulate autophagy (Chen *et al*, 2016) through multiple signalling pathways, thus EGFR overexpression may partly explain the lower sensitivity of T16 tumours to anti-autophagic treatment.

Importantly, we find that bevacizumab treatment sensitised GBM cells to autophagy inhibition allowing to reach survival benefit at lower dose. This was confirmed *in vitro*, where hypoxia increased sensitivity of GBM cells to autophagy inhibitors. The synergistic effect of bevacizumab was visible only when the anti-autophagy effect alone was mild or moderate at normal oxygen levels, but was masked if the autophagy inhibitor alone showed a strong effect. Interestingly, we have previously shown that bevacizumab leads to a lower number of mitochondria in tumour cells (Keunen *et al*, 2011), suggesting that mitophagy might be involved in the survival under hypoxia. A previous study has shown efficacy of chloroquine in combination with bevacizumab in subcutaneous U87 tumours, but failed to observe a tumour suppressive effect with chloroquine used as a single agent (Hu *et al*, 2012). This discrepancy may be due to the different tumour localisation and the heterogeneity in the GBM response to chloroquine described here. Although non-specific effects of chloroquine cannot be excluded (Maycotte *et al*, 2012; Maes *et al*, 2014), we did not observe vessel normalisation upon chloroquine treatment. In line with a previous study (Chen *et al*, 2008), normal astrocytes remained unaffected at the lowest chloroquine concentration affecting GBM cells, confirming more substantial dependence of tumour cells on autophagy. Although more potent inhibitors are warranted, our data suggest the existence of a 'therapeutic window' for autophagy inhibitors in GBM, and that co-treatment with anti-angiogenic agents allows to significantly lower effective doses.

We found that activation of autophagy in hypoxia was linked to transcriptional changes of numerous genes associated with autophagy, among which *BNIP3*, *BNIP3L*, *ATG9A* and *PIK3C3* were upregulated in all GBM cells. BNIP3 and BNIP3L, while activated by HIF1α, mediate autophagy by releasing Beclin1 from complexes with Bcl-2 and Bcl-X_L (Zhang *et al*, 2008; Bellot *et al*, 2009). Interestingly, within the ATG family, only *ATG9A* was transcriptionally activated in all GBM cells. Contrary to other ATG family members such as *ATG5* and *ATG7*, but similarly to *BNIP3* and *BNIP3L*, we identify *ATG9A* as potentially HIF1α responsive gene. These transcriptional changes were observed also in GBM cells that exhibit high basal autophagy at normal oxygen levels, suggesting that specific upstream molecules such as FOXO3A are involved in the regulation autophagy pathway at

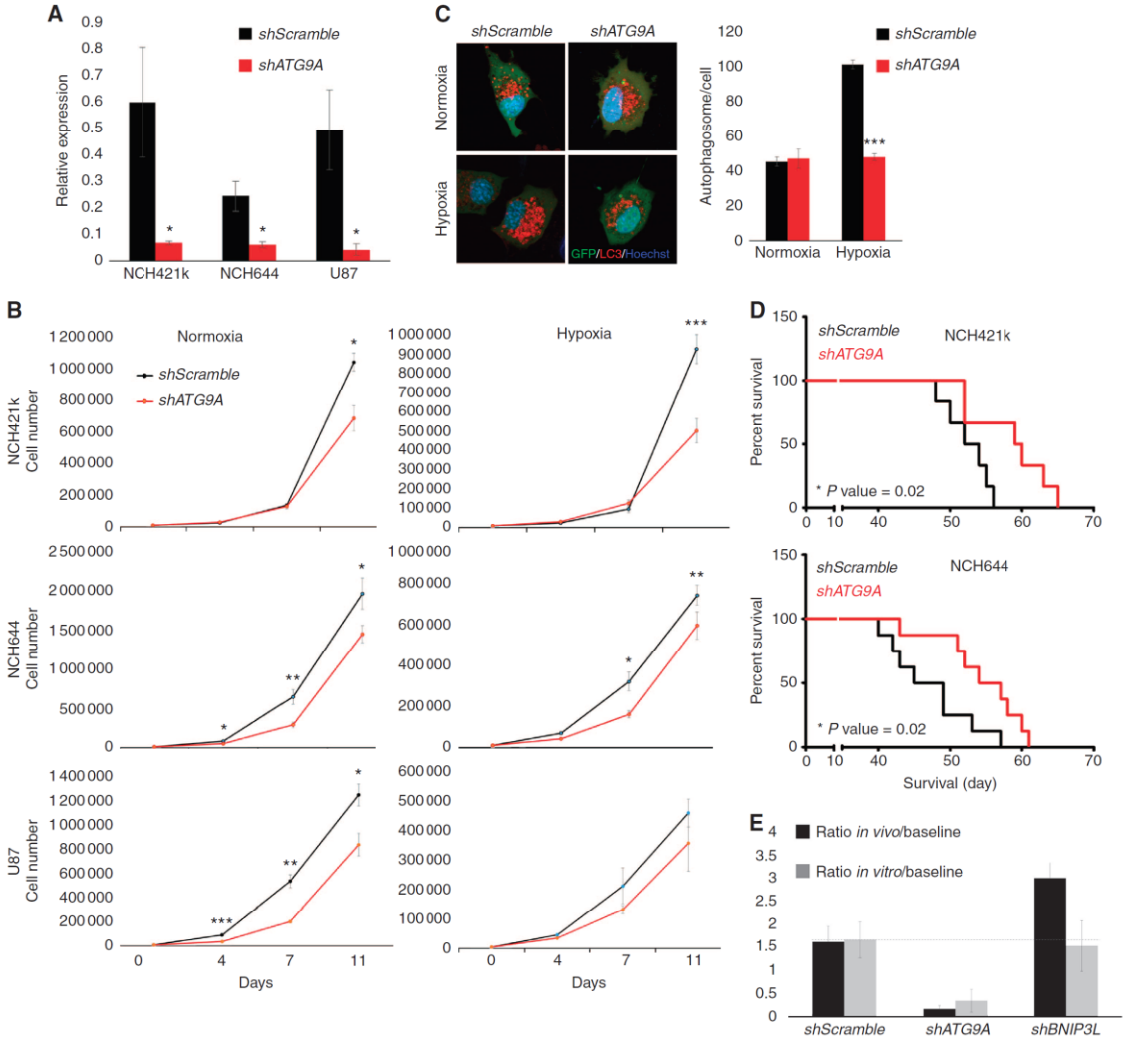

Figure 4. *ATG9A* knockdown decreases GBM cell proliferation and increases mouse survival. (**A**) QPCR confirmation of *shATG9A* knockdown (mean ± s.e.m.; $n=3$; $^{*}P<0.05$). (**B**) Proliferation of *shATG9A* cells was decreased significantly in normoxic and hypoxic conditions (mean ± s.e.m.; $n=3$; $^{*}P<0.05$, $^{**}P<0.01$, $^{***}P<0.001$). (**C**) Representative images show lack of increased autophagosome formation upon hypoxia in *shATG9* U87 cells. Cells were exposed to hypoxia for 16 h in the presence of chloroquine. Autophagosomes were counted as LC3B–Tomato-positive vacuoles 24 h after transfection; GFP positivity confirms shRNA expression (mean ± s.e.m.; $n=34$; $^{***}P$ value <0.001). (**D**) *ATG9A* depletion in NCH421k and NCH644 prolonged the survival of tumour-bearing mice ($n=6$–8). (**E**) Targeted *in vivo* shRNA screen in NCH421k cells. shRNA targeting *ATG9A* but not *BNIP3L* was depleted after *in vivo* ($n=5$) and *in vitro* (normoxia, $n=3$) growth. Relative representation of respective shRNAs after selection pressure is presented as ratios compared with the original shRNA pool before selection (baseline). For detailed experimental setup, see (Sanzey *et al*, 2015).

different oxygen levels. Pro-autophagic genes, such as Beclin1, ATG5, ATG7, BNIP3 and BNIP3L were previously found to be essential for autophagy in cancer cells (Zhang *et al*, 2008; Mazure and Pouyssegur, 2009). Here we show that ATG9A also represents an important pro-survival molecule, with ATG9A depletion leading to a strong reduction of tumour growth, thus confirming the relevance of autophagy as a promising target for GBM treatment. Of note, *ATG7* knockdown displayed a therapeutic outcome only during anti-angiogenic treatment (Hu *et al*, 2012).

ATG9A was shown to be essential for autophagosome biogenesis and membrane maturation; however, its mode of action remains enigmatic. Recent data suggest that the Pho–Rpd3 complex regulates expression of ATG9A and other ATG genes upon induction of autophagy (Jin and Klionsky, 2014) and that ATG9A-containing vesicles are generated *de novo* upon starvation (Yamamoto *et al*, 2012). Here we show that upon *ATG9A* depletion, GBM cells were not able to activate autophagy upon hypoxia. We propose that the lack of autophagic activation upon hypoxia may be due to inhibition of *de novo* autophagosome synthesis. This is in accordance with a recent report, where ATG9A was shown to have a key role in autophagosome formation during hypoxic stress (Weerasekara *et al*, 2014). Thus, ATG9A may become essential upon autophagy induction and an increased demand for new autophagosome membranes (Orsi *et al*, 2012).

In conclusion, our data support the notion that inhibiting autophagy represents an effective therapy in primary GBM, although it may be concentration and patient dependent. Anti-autophagy treatment using genetic and pharmacological intervention was effective as a single treatment. However, currently available drugs, including chloroquine and hydroxychloroquine are non-curative in non-toxic doses and novel more potent agents will be necessary for GBM patients. Drugs directly targeting essential proteins such as ATG9A may be of particular interest and a combination with anti-angiogenic therapy may be beneficial. Finally, the hypoxic microenvironment also contributes to immunoresistance and hypoxia-induced autophagy impairs cytotoxic T-lymphocyte-mediated cell lysis of tumour cells (Noman *et al*, 2011, 2012) and NK-mediated target cell apoptosis (Baginska *et al*, 2013; Viry *et al*, 2014). Therefore, targeting autophagy in tumour cells may not only lead to increased tumour cell death but also sensitise tumours to immunotherapies.

ACKNOWLEDGEMENTS

We thank Morgane Sanzey, Virginie Baus, and Amandine Bernard for technical assistance. We thank Dr Christel Herold-Mende (Department of Neurosurgery, University of Heidelberg, Germany) and Dr Uros Rajcevic (National Institute of Biology, Ljubljana, Slovenia) for providing cell lines. This work was supported by the Luxembourg Institute of Health (LIH), the Fonds National de la Recherche (FNR) of Luxembourg (ESCAPE 784322 BM, AFR grand to SAAR and AD) and the Fondation Cancer Luxembourg (INVGBM).

CONFLICT OF INTEREST

The authors declare no conflict of interest.

REFERENCES

Baginska J, Viry E, Berchem G, Poli A, Noman MZ, van Moer K, Medves S, Zimmer J, Oudin A, Niclou SP, Bleackley RC, Goping IS, Chouaib S, Janji B (2013) Granzyme B degradation by autophagy decreases tumor cell susceptibility to natural killer-mediated lysis under hypoxia. *Proc Natl Acad Sci USA* **110**: 17450–17455.

Bellot G, Garcia-Medina R, Gounon P, Chiche J, Roux D, Pouyssegur J, Mazure NM (2009) Hypoxia-induced autophagy is mediated through hypoxia-inducible factor induction of BNIP3 and BNIP3L via their BH3 domains. *Mol Cell Biol* **29**: 2570–2581.

Bertout JA, Patel SA, Simon MC (2008) The impact of O_2 availability on human cancer. *Nat Rev Cancer* **8**: 967–975.

Bougnaud S, Golebiewska A, Oudin A, Keunen O, Harter PN, Mader L, Azuaje F, Fritah S, Stieber D, Kaoma T, Vallar L, Brons NH, Daubon T, Miletic H, Sundstr½m T, Herold-Mende C, Mittelbronn M, Bjerkvig R, Niclou SP (2016) Molecular crosstalk between tumour and brain parenchyma instructs histopathological features in glioblastoma. *Oncotarget*.

Chen Y, Henson ES, Xiao W, Huang D, McMillan-Ward EM, Israels SJ, Gibson SB (2016) Tyrosine kinase receptor EGFR regulates the switch in cancer cells between cell survival and cell death induced by autophagy in hypoxia. *Autophagy* **12**: 1029–1046.

Chen Y, McMillan-Ward E, Kong J, Israels SJ, Gibson SB (2008) Oxidative stress induces autophagic cell death independent of apoptosis in transformed and cancer cells. *Cell Death Differ* **15**: 171–182.

Ciechomska IA, Gabrusiewicz K, Szczepankiewicz AA, Kaminska B (2013) Endoplasmic reticulum stress triggers autophagy in malignant glioma cells undergoing cyclosporine a-induced cell death. *Oncogene* **32**: 1518–1529.

Corcelle-Termeau E, Vindelov SD, Hamalisto S, Mograbi B, Keldsbo A, Brasen JH, Favaro E, Adam D, Szyniarowski P, Hofman P, Krautwald S, Farkas T, Petersen NH, Rohde M, Linkermann A, Jäättelä M (2016) Excess sphingomyelin disturbs ATG9A trafficking and autophagosome closure. *Autophagy* **12**: 833–849.

De Witt Hamer PC, Van Tilborg AA, Eijk PP, Sminia P, Troost D, Van Noorden CJ, Ylstra B, Leenstra S (2008) The genomic profile of human malignant glioma is altered early in primary cell culture and preserved in spheroids. *Oncogene* **27**: 2091–2096.

Demeure K, Fack F, Duriez E, Tiemann K, Bernard A, Golebiewska A, Bougnaud S, Bjerkvig R, Domon B, Niclou SP (2015) Targeted proteomics to assess the response to anti-angiogenic treatment in human glioblastoma. *Mol Cell Proteomics* **15**: 481–492.

Evans SM, Judy KD, Dunphy I, Jenkins WT, Nelson PT, Collins R, Wileyto EP, Jenkins K, Hahn SM, Stevens CW, Judkins AR, Phillips P, Geoerger B, Koch CJ (2004) Comparative measurements of hypoxia in human brain tumors using needle electrodes and EF5 binding. *Cancer Res* **64**: 1886–1892.

Fack F, Espedal H, Keunen O, Golebiewska A, Obad N, Harter PN, Mittelbronn M, Bahr O, Weyerbrock A, Stuhr L, Miletic H, Sakariassen PÄ, Stieber D, Rygh CB, Lund-Johansen M, Zheng L, Gottlieb E, Niclou SP, Bjerkvig R (2015) Bevacizumab treatment induces metabolic adaptation toward anaerobic metabolism in glioblastomas. *Acta Neuropathol* **129**: 115–131.

Firat E, Weyerbrock A, Gaedicke S, Grosu AL, Niedermann G (2012) Chloroquine or chloroquine-PI3K/Akt pathway inhibitor combinations strongly promote gamma-irradiation-induced cell death in primary stem-like glioma cells. *PloS ONE* **7**: e47357.

Gasch AP, Spellman PT, Kao CM, Carmel-Harel O, Eisen MB, Storz G, Botstein D, Brown PO (2000) Genomic expression programs in the response of yeast cells to environmental changes. *Mol Biol Cell* **11**: 4241–4257.

Gilbert MR (2016) Antiangiogenic therapy for glioblastoma: complex biology and complicated results. *J Clin Oncol* **34**: 1567–1569.

Glick D, Barth S, Macleod KF (2010) Autophagy: cellular and molecular mechanisms. *J Pathol* **221**: 3–12.

Golebiewska A, Bougnaud S, Stieber D, Brons NH, Vallar L, Hertel F, Klink B, Schrock E, Bjerkvig R, Niclou SP (2013) Side population in human glioblastoma is non-tumorigenic and characterizes brain endothelial cells. *Brain* **136**: 1462–1475.

Hirschhaeuser F, Menne H, Dittfeld C, West J, Mueller-Klieser W, Kunz-Schughart LA (2010) Multicellular tumor spheroids: an underestimated tool is catching up again. *J Biotechnol* **148**: 3–15.

Hu YL, DeLay M, Jahangiri A, Molinaro AM, Rose SD, Carbonell WS, Aghi MK (2012) Hypoxia-induced autophagy promotes tumor cell survival and adaptation to antiangiogenic treatment in glioblastoma. *Cancer Res* **72**: 1773–1783.

Jin M, Klionsky DJ (2014) Transcriptional regulation of ATG9 by the Pho23-Rpd3 complex modulates the frequency of autophagosome formation. *Autophagy* **10**: 1681–1682.

Kanzawa T, Germano IM, Komata T, Ito H, Kondo Y, Kondo S (2004) Role of autophagy in temozolomide-induced cytotoxicity for malignant glioma cells. *Cell Death Differ* **11**: 448–457.

Keunen O, Johansson M, Oudin A, Sanzey M, Abdul Rahim SA, Fack F, Thorsen F, Taxt T, Bartos M, Jirik R, Miletic H, Wang J, Stieber D, Stuhr L, Moen I, Rygh CB, Bjerkvig R, Niclou SP (2011) Anti-VEGF treatment reduces blood supply and increases tumor cell invasion in glioblastoma. *Proc Natl Acad Sci USA* **108**: 3749–3754.

Klionsky DJ, Abdelmohsen K, Abe A, Abedin MJ, Abeliovich H, Acevedo Arozena A, Adachi H, Adams CM, Adams PD, Adeli K, Adhihetty PJ, Adler SG, Agam G, Agarwal R, Aghi MK, Agnello M, Agostinis P, Aguilar PV, Aguirre-Ghiso J, Airoldi EM, Ait-Si-Ali S, Akematsu T, Akporiaye ET, Al-Rubeai M, Albaiceta GM, Albanese C, Albani D, Albert ML, Aldudo J, Algül H, Alirezaei M, Alloza I, Almasan A, Almonte-Beceril M, Alnemri ES, Alonso C, Altan-Bonnet N, Altieri DC, Alvarez S, Alvarez-Erviti L, Alves S, Amadoro G, Amano A, Amantini C, Ambrosio S, Amelio I, Amer AO, Amessou M, Amon A, An Z, Anania FA, Andersen SU, Andley UP, Andreadi CK, Andrieu-Abadie N, Anel A, Ann DK, Anoopkumar-Dukie S, Antonioli M, Aoki H, Apostolova N, Aquila S, Aquilano K, Araki K, Arama E, Aranda A, Araya J, Arcaro A, Arias E, Arimoto H, Ariosa AR, Armstrong JL, Arnould T, Arsov I, Asanuma K, Askanas V, Asselin E, Atarashi R, Atherton SS, Atkin JD, Attardi LD, Auberger P, Auburger G, Aurelian L, Autelli R, Avagliano L, Avantaggiati ML, Avrahami L, Awale S, Azad N, Bachetti T, Backer JM, Bae DH, Bae JS, Bae ON, Bae SH, Baehrecke EH, Baek SH, Baghdiguian S, Bagniewska-Zadworna A, Bai H, Bai J, Bai XY,

Bailly Y, Balaji KN, Balduini W, Ballabio A, Balzan R, Banerjee R, Bánhegyi G, Bao H, Barbeau B, Barrachina MD, Barreiro E, Bartel B, Bartolomé A, Bassham DC, Bassi MT, Bast Jr RC, Basu A, Batista MT, Batoko H, Battino M, Bauckman K, Baumgarner BL, Bayer KU, Beale R, Beaulieu JF, Beck Jr GR, Becker C, Beckham JD, Bédard PA, Bednarski PJ, Begley TJ, Behl C, Behrends C, Behrens GM, Behrns KE, Bejarano E, Belaid A, Belleudi F, Bénard G, Berchem G, Bergamaschi D, Bergami M, Berkhout B, Berliocchi L, Bernard A, Bernard M, Bernassola F, Bertolotti A, Bess AS, Besteiro S, Bettuzzi S, Bhalla S, Bhattacharyya S, Bhutia SK, Biagosch C, Bianchi MW, Biard-Piechaczyk M, Billes V, Bincoletto C, Bingol B, Bird SW, Bitoun M, Bjedov I, Blackstone C, Blanc L, Blanco GA, Blomhoff HK, Boada-Romero E, Böckler S, Boes M, Boesze-Battaglia K, Boise LH, Bolino A, Boman A, Bonaldo P, Bordi M, Bosch J, Botana LM, Botti J, Bou G, Bouché M, Bouchecareilh M, Boucher MJ, Boulton ME, Bouret SG, Boya P, Boyer-Guittaut M, Bozhkov PV, Brady N, Braga VM, Brancolini C, Braus GH, Bravo-San Pedro JM, Brennan LA, Bresnick EH, Brest P, Bridges D, Bringer MA, Brini M, Brito GC, Brodin B, Brookes PS, Brown EJ, Brown K, Broxmeyer HE, Bruhat A, Brum PC, Brumell JH, Brunetti-Pierri N, Bryson-Richardson RJ, Buch S, Buchan AM, Budak H, Bulavin DV, Bultman SJ, Bultynck G, Bumbasirevic V, Burelle Y, Burke RE, Burmeister M, Bütikofer P, Caberlotto L, Cadwell K, Cahova M, Cai D, Cai J, Cai Q, Calatayud S, Camougrand N, Campanella M, Campbell GR, Campbell M, Campello S, Candau R, Caniggia I, Cantoni L, Cao L, Caplan AB, Caraglia M, Cardinali C, Cardoso SM, Carew JS, Carleton LA, Carlin CR, Carloni S, Carlsson SR, Carmona-Gutierrez D, Carneiro LA, Carnevali O, Carra S, Carrier A, Carroll B, Casas C, Casas J, Cassinelli G, Castets P, Castro-Obregon S, Cavallini G, Ceccherini I, Cecconi F, Cederbaum AI, Ceña V, Cenci S, Cerella C, Cervia D, Cetrullo S, Chaachouay H, Chae HJ, Chagin AS, Chai CY, Chakrabarti G, Chamilos G, Chan EY, Chan MT, Chandra D, Chandra P, Chang CP, Chang RC, Chang TY, Chatham JC, Chatterjee S, Chauhan S, Che Y, Cheetham ME, Cheluvappa R, Chen CJ, Chen G, Chen GC, Chen H, Chen JW, Chen JK, Chen M, Chen M, Chen P, Chen Q, Chen SD, Chen S, Chen SS, Chen W, Chen WJ, Chen WQ, Chen W, Chen X, Chen YH, Chen YG, Chen Y, Chen YJ, Chen YQ, Chen Z, Cheng A, Cheng CH, Cheng H, Cheong H, Cherry S, Chesney J, Cheung CH, Chevet E, Chi HC, Chi SG, Chiacchiera F, Chiang HL, Chiarelli R, Chiariello M, Chieppa M, Chin LS, Chiong M, Chiu GN, Cho DH, Cho SG, Cho WC, Cho YY, Cho YS, Choi AM, Choi EJ, Choi EK, Choi J, Choi ME, Choi SI, Chou TF, Chouaib S, Choubey D, Choubey V, Chow KC, Chowdhury K, Chu CT, Chuang TH, Chun T, Chung H, Chung T, Chung YL, Chwae YJ, Cianfanelli V, Ciarcia R, Ciechomska IA, Ciriolo MR, Cirone M, Claerhout S, Clague MJ, Clària J, Clarke PG, Clarke R, Clementi E, Cleyrat C, Cnop M, Coccia EM, Cocco T, Codogno P, Coers J, Cohen EE, Colecchia D, Coletto L, Coll NS, Colucci-Guyon E, Comincini S, Condello M, Cook KL, Coombs GH, Cooper CD, Cooper JM, Coppens I, Corasaniti MT, Corazzari M, Corbalan R, Corcelle-Termeau E, Cordero MD, Corral-Ramos C, Corti O, Cossarizza A, Costelli P, Costes S, Cotman SL, Coto-Montes A, Cottet S, Couve E, Covey LR, Cowart LA, Cox JS, Coxon FP, Coyne CB, Cragg MS, Craven RJ, Crepaldi T, Crespo JL, Criollo A, Crippa V, Cruz MT, Cuervo AM, Cuezva JM, Cui T, Cutillas PR, Czaja MJ, Czyzyk-Krzeska MF, Dagda RK, Dahmen U, Dai C, Dai W, Dai Y, Dalby KN, Dalla Valle L, Dalmasso G, D'Amelio M, Damme M, Darfeuille-Michaud A, Dargemont C, Darley-Usmar VM, Dasarathy S, Dasgupta B, Dash S, Dass CR, Davey HM, Davids LM, Dávila D, Davis RJ, Dawson TM, Dawson VL, Daza P, de Belleroche J, de Figueiredo P, de Figueiredo RC, de la Fuente J, De Martino L, De Matteis A, De Meyer GR, De Milito A, De Santi M, de Souza W, De Tata V, De Zio D, Debnath J, Dechant R, Decuypere JP, Deegan S, Dehay B, Del Bello B, Del Re DP, Delage-Mourroux R, Delbridge LM, Deldicque L, Delorme-Axford E, Deng Y, Dengjel J, Denizot M, Dent P, Der CJ, Deretic V, Derrien B, Deutsch E, Devarenne TP, Devenish RJ, Di Bartolomeo S, Di Daniele N, Di Domenico F, Di Nardo A, Di Paola S, Di Pietro A, Di Renzo L, DiAntonio A, Díaz-Araya G, Díaz-Laviada I, Diaz-Meco MT, Diaz-Nido J, Dickey CA, Dickson RC, Diederich M, Digard P, Dikic I, Dinesh-Kumar SP, Ding C, Ding WX, Ding Z, Dini L, Distler JH, Diwan A, Djavaheri-Mergny M, Dmytruk K, Dobson RC, Doetsch V, Dokladny K, Dokudovskaya S, Donadelli M, Dong XC, Dong X, Dong Z, Donohue Jr TM, Doran KS, D'Orazi G, Dorn 2nd GW, Dosenko V, Dridi S, Drucker L, Du J, Du LL, Du L, du Toit A, Dua P, Duan L, Duann P, Dubey VK, Duchen MR, Duchosal MA, Duez H, Dugail I, Dumit VI, Duncan MC, Dunlop EA, Dunn Jr WA, Dupont N, Dupuis L, Durán RV, Durcan TM, Duvezin-Caubet S, Duvvuri U, Eapen V, Ebrahimi-Fakhari D, Echard A, Eckhart L, Edelstein CL, Edinger AL, Eichinger L, Eisenberg T, Eisenberg-Lerner A, Eissa NT, El-Deiry WS, El-Khoury V, Elazar Z, Eldar-Finkelman H, Elliott CJ, Emanuele E, Emmenegger U, Engedal N, Engelbrecht AM, Engelender S, Enserink JM, Erdmann R, Erenpreisa J, Eri R, Eriksen JL, Erman A, Escalante R, Eskelinen EL, Espert L, Esteban-Martínez L, Evans TJ, Fabri M, Fabrias G, Fabrizi C, Facchiano A, Færgeman NJ, Faggioni A, Fairlie WD, Fan C, Fan D, Fan J, Fang S, Fanto M, Fanzani A, Farkas T, Faure M, Favier FB, Fearnhead H, Federici M, Fei E, Felizardo TC, Feng H, Feng Y, Ferguson TA, Fernández ÁF, Fernandez-Barrena MG, Fernandez-Checa JC, Fernández-López A, Fernandez-Zapico ME, Feron O, Ferraro E, Ferreira-Halder CV, Fesus L, Feuer R, Fiesel FC, Filippi-Chiela EC, Filomeni G, Fimia GM, Fingert JH, Finkbeiner S, Finkel T, Fiorito F, Fisher PB, Flajolet M, Flamigni F, Florey O, Florio S, Floto RA, Folini M, Follo C, Fon EA, Fornai F, Fortunato F, Fraldi A, Franco R, Francois A, François A, Frankel LB, Fraser ID, Frey N, Freyssenet DG, Frezza C, Friedman SL, Frigo DE, Fu D, Fuentes JM, Fueyo J, Fujitani Y, Fujiwara Y, Fujiya M, Fukuda M, Fulda S, Fusco C, Gabryel B, Gaestel M, Gailly P, Gajewska M, Galadari S, Galili G, Galindo I, Galindo MF, Galliciotti G, Galluzzi L, Galy V, Gammoh N, Gandy S, Ganesan AK, Ganesan S, Ganley IG, Gannagé M, Gao FB, Gao F, Gao JX, García Nannig L, García Véscovi E, Garcia-Macía M, Garcia-Ruiz C, Garg AD, Garg PK, Gargini R, Gassen NC, Gatica D, Gatti E, Gavard J, Gavathiotis E, Ge L, Ge P, Ge S, Gean PW, Gelmetti V, Genazzani AA, Geng J, Genschik P, Gerner L, Gestwicki JE, Gewirtz DA, Ghavami S, Ghigo E, Ghosh D, Giammarioli AM, Giampieri F, Giampietri C, Giatromanolaki A, Gibbings DJ, Gibellini L, Gibson SB, Ginet V, Giordano A, Giorgini F, Giovannetti E, Girardin SE, Gispert S, Giuliano S, Gladson CL, Glavic A, Gleave M, Godefroy N, Gogal Jr RM, Gokulan K, Goldman GH, Goletti D, Goligorsky MS, Gomes AV, Gomes LC, Gomez H, Gomez-Manzano C, Gómez-Sánchez R, Gonçalves DA, Goncu E, Gong Q, Gongora C, Gonzalez CB, Gonzalez-Alegre P, Gonzalez-Cabo P, González-Polo RA, Goping IS, Gorbea C, Gorbunov NV, Goring DR, Gorman AM, Gorski SM, Goruppi S, Goto-Yamada S, Gotor C, Gottlieb RA, Gozes I, Gozuacik D, Graba Y, Graef M, Granato GE, Grant GD, Grant S, Gravina GL, Green DR, Greenhough A, Greenwood MT, Grimaldi B, Gros F, Grose C, Groulx JF, Gruber F, Grumati P, Grune T, Guan JL, Guan KL, Guerra B, Guillen C, Gulshan K, Gunst J, Guo C, Guo L, Guo M, Guo W, Guo XG, Gust AA, Gustafsson ÅB, Gutierrez E, Gutierrez MG, Gwak HS, Haas A, Haber JE, Hadano S, Hagedorn M, Hahn DR, Halayko AJ, Hamacher-Brady A, Hamada K, Hamai A, Hamann A, Hamasaki M, Hamer I, Hamid Q, Hammond EM, Han F, Han W, Handa JT, Hanover JA, Hansen M, Harada M, Harhaji-Trajkovic L, Harper JW, Harrath AH, Harris AL, Harris J, Hasler U, Hasselblatt P, Hasui K, Hawley RG, Hawley TS, He C, He CY, He F, He G, He RR, He XH, He YW, He YY, Heath JK, Hébert MJ, Heinzen RA, Helgason GV, Hensel M, Henske EP, Her C, Herman PK, Hernández A, Hernandez C, Hernández-Tiedra S, Hetz C, Hiesinger PR, Higaki K, Hilfiker S, Hill BG, Hill JA, Hill WD, Hino K, Hofius D, Hofman P, Höglinger GU, Höhfeld J, Holz MK, Hong Y, Hood DA, Hoozemans JJ, Hoppe T, Hsu C, Hsu CY, Hsu LC, Hu D, Hu G, Hu HM, Hu H, Hu MC, Hu YC, Hu ZW, Hua F, Hua Y, Huang C, Huang HL, Huang KH, Huang KY, Huang S, Huang S, Huang WP, Huang YR, Huang Y, Huber TB, Huebbe P, Huh WK, Hulmi JJ, Hur GM, Hurley JH, Husak Z, Hussain SN, Hussain S, Hwang JJ, Hwang S, Hwang TI, Ichihara A, Imai Y, Imbriano C, Inomata M, Into T, Iovane V, Iovanna JL, Iozzo RV, Ip NY, Irazoqui JE, Iribarren P, Isaka Y, Isakovic AJ, Ischiropoulos H, Isenberg JS, Ishaq M, Ishida H, Ishii I, Ishmael JE, Isidoro C, Isobe K, Isono E, Issazadeh-Navikas S, Itahana K, Itakura E, Ivanov AI, Iyer AK, Izquierdo JM, Izumi Y, Izzo V, Jäättelä M, Jaber N, Jackson DJ, Jackson WT, Jacob TG, Jacques TS, Jagannath C, Jain A, Jana NR, Jang BK, Jani A, Janji B, Jannig PR, Jansson PJ, Jean S, Jendrach M, Jeon JH, Jessen N, Jeung EB, Jia K, Jia L, Jiang H, Jiang L, Jiang T, Jiang X, Jiang Y, Jiménez A, Jin C, Jin H, Jin L, Jin M, Jin S, Jinwal UK, Jo EK, Johansen T, Johnson DE, Johnson GV, Johnson JD, Jonasch E, Jones C, Joosten LA, Jordan J, Joseph AM, Joseph B, Joubert AM, Ju D, Ju J, Juan HF, Juenemann K, Juhász G, Jung HS, Jung JU, Jung YK, Jungbluth H, Justice MJ, Jutten B, Kaakoush NO, Kaarniranta K, Kaasik A, Kabuta T, Kaeffer B, Kågedal K, Kahana A, Kajimura S, Kakhlon O, Kalia M, Kalvakolanu DV, Kamada Y, Kambas K, Kaminskyy VO, Kampinga HH, Kandouz M, Kang C, Kang R, Kang TC, Kanki T,

Kanneganti TD, Kanno H, Kanthasamy AG, Kantorow M, Kaparakis-Liaskos M, Kapuy O, Karantza V, Karim MR, Karmakar P, Kaser A, Kaushik S, Kawula T, Kaynar AM, Ke PY, Ke ZJ, Kehrl JH, Keller KE, Kemper JK, Kenworthy AK, Kepp O, Kern A, Kesari S, Kessel D, Ketteler R, Kettelhut Ido C, Khambu B, Khan MM, Khandelwal VK, Khare S, Kiang JG, Kiger AA, Kihara A, Kim AL, Kim CH, Kim DR, Kim DH, Kim EK, Kim HY, Kim HR, Kim JS, Kim JH, Kim JC, Kim JH, Kim KW, Kim MD, Kim MM, Kim PK, Kim SW, Kim SY, Kim YS, Kim Y, Kimchi A, Kimmelman AC, Kimura T, King JS, Kirkegaard K, Kirkin V, Kirshenbaum LA, Kishi S, Kitajima Y, Kitamoto K, Kitaoka Y, Kitazato K, Kley RA, Klimecki WT, Klinkenberg M, Klucken J, Knævelsrud H, Knecht E, Knuppertz L, Ko JL, Kobayashi S, Koch JC, Koechlin-Ramonatxo C, Koenig U, Koh YH, Köhler K, Kohlwein SD, Koike M, Komatsu M, Kominami E, Kong D, Kong HJ, Konstantakou EG, Kopp BT, Korcsmaros T, Korhonen L, Korolchuk VI, Koshkina NV, Kou Y, Koukourakis MI, Koumenis C, Kovács AL, Kovács T, Kovacs WJ, Koya D, Kraft C, Krainc D, Kramer H, Kravic-Stevovic T, Krek W, Kretz-Remy C, Krick R, Krishnamurthy M, Kriston-Vizi J, Kroemer G, Kruer MC, Kruger R, Ktistakis NT, Kuchitsu K, Kuhn C, Kumar AP, Kumar A, Kumar D, Kumar D, Kumar R, Kumar S, Kundu M, Kung HJ, Kuno A, Kuo SH, Kuret J, Kurz T, Kwok T, Kwon TK, Kwon YT, Kyrmizi I, La Spada AR, Lafont F, Lahm T, Lakkaraju A, Lam T, Lamark T, Lancel S, Landowski TH, Lane DJ, Lane JD, Lanzi C, Lapaquette P, Lapierre LR, Laporte J, Laukkarinen J, Laurie GW, Lavandero S, Lavie L, LaVoie MJ, Law BY, Law HK, Law KB, Layfield R, Lazo PA, Le Cam L, Le Roch KG, Le Stunff H, Leardkamolkarn V, Lecuit M, Lee BH, Lee CH, Lee EF, Lee GM, Lee HJ, Lee H, Lee JK, Lee J, Lee JH, Lee M, Lee MS, Lee PJ, Lee SW, Lee SJ, Lee SJ, Lee SY, Lee SH, Lee SS, Lee SJ, Lee S, Lee YR, Lee YJ, Lee YH, Leeuwenburgh C, Lefort S, Legouis R, Lei J, Lei QY, Leib DA, Leibowitz G, Lekli I, Lemaire SD, Lemasters JJ, Lemberg MK, Lemoine A, Leng S, Lenz G, Lenzi P, Lerman LO, Lettieri Barbato D, Leu JI, Leung HY, Levine B, Lewis PA, Lezoualc'h F, Li C, Li F, Li FJ, Li J, Li K, Li L, Li M, Li M, Li Q, Li R, Li S, Li W, Li X, Li Y, Lian J, Liang C, Liang Q, Liao Y, Liberal J, Liberski PP, Lie P, Lieberman AP, Lim HJ, Lim KL, Lim K, Lima RT, Lin CS, Lin CF, Lin F, Lin FC, Lin K, Lin KH, Lin PH, Lin T, Lin WW, Lin YS, Linden R, Lindholm D, Lindqvist LM, Lingor P, Linkermann A, Liotta LA, Lipinski MM, Lira VA, Lisanti MP, Liton PB, Liu B, Liu C, Liu CF, Liu F, Liu HJ, Liu J, Liu JJ, Liu JL, Liu K, Liu L, Liu Q, Liu RY, Liu S, Liu S, Liu W, Liu XD, Liu X, Liu XH, Liu Y, Liu Z, Liuzzi JP, Lizard G, Ljujic M, Lodhi IJ, Logue SE, Lokeshwar BL, Long YC, Lonial S, Loos B, López-Otín C, López-Vicario C, Lorente M, Lorenzi PL, Lõrincz P, Los M, Lotze MT, Lovat PE, Lu B, Lu J, Lu Q, Lu SM, Lu S, Lu Y, Luciano F, Luckhart S, Lucocq JM, Ludovico P, Lugea A, Lukacs NW, Lum JJ, Lund AH, Luo H, Luo J, Luo S, Luparello C, Lyons T, Ma J, Ma Y, Ma Y, Ma Z, Machado J, Machado-Santelli GM, Macian F, MacIntosh GC, MacKeigan JP, Macleod KF, MacMicking JD, MacMillan-Crow LA, Madeo F, Madesh M, Madrigal-Matute J, Maeda A, Maeda T, Maegawa G, Maellaro E, Maes H, Magariños M, Maiese K, Maiti TK, Maiuri L, Maiuri MC, Maki CG, Malli R, Malorni W, Maloyan A, Mami-Chouaib F, Man N, Mancias JD, Mandelkow EM, Mandell MA, Manfredi AA, Manié SN, Manzoni C, Mao K, Mao Z, Mao ZW, Marambaud P, Marconi AM, Marelja Z, Marfe G, Margeta M, Margittai E, Mari M, Mariani FV, Marin C, Marinelli S, Mariño G, Markovic I, Marquez R, Martelli AM, Martens S, Martin KR, Martin SJ, Martin S, Martin-Acebes MA, Martín-Sanz P, Martinand-Mari C, Martinet W, Martinez J, Martinez-Lopez N, Martinez-Outschoorn U, Martínez-Velázquez M, Martinez-Vicente M, Martins WK, Mashima H, Mastrianni JA, Matarese G, Matarrese P, Mateo R, Matoba S, Matsumoto N, Matsushita T, Matsuura A, Matsuzawa T, Mattson MP, Matus S, Maugeri N, Mauvezin C, Mayer A, Maysinger D, Mazzolini GD, McBrayer MK, McCall K, McCormick C, McInerney GM, McIver SC, McKenna S, McMahon JJ, McNeish IA, Mechta-Grigoriou F, Medema JP, Medina DL, Megyeri K, Mehrpour M, Mehta JL, Mei Y, Meier UC, Meijer AJ, Meléndez A, Melino G, Melino S, de Melo EJ, Mena MA, Meneghini MD, Menendez JA, Menezes R, Meng L, Meng LH, Meng S, Menghini R, Menko AS, Menna-Barreto RF, Menon MB, Meraz-Ríos MA, Merla G, Merlini L, Merlot AM, Meryk A, Meschini S, Meyer JN, Mi MT, Miao CY, Micale L, Michaeli S, Michiels C, Migliaccio AR, Mihailidou AS, Mijaljica D, Mikoshiba K, Milan E, Miller-Fleming L, Mills GB, Mills IG, Minakaki G, Minassian BA, Ming XF, Minibayeva F, Minina EA, Mintern JD, Minucci S, Miranda-Vizuete A, Mitchell CH, Miyamoto S, Miyazawa K, Mizushima N, Mnich K, Mograbi B, Mohseni S, Moita LF, Molinari M, Molinari M, Møller AB, Mollereau B, Mollinedo F, Mongillo M, Monick MM, Montagnaro S, Montell C, Moore DJ, Moore MN, Mora-Rodriguez R, Moreira PI, Morel E, Morelli MB, Moreno S, Morgan MJ, Moris A, Moriyasu Y, Morrison JL, Morrison LA, Morselli E, Moscat J, Moseley PL, Mostowy S, Motori E, Mottet D, Mottram JC, Moussa CE, Mpakou VE, Mukhtar H, Mulcahy Levy JM, Muller S, Muñoz-Moreno R, Muñoz-Pinedo C, Münz C, Murphy ME, Murray JT, Murthy A, Mysorekar IU, Nabi IR, Nabissi M, Nader GA, Nagahara Y, Nagai Y, Nagata K, Nagelkerke A, Nagy P, Naidu SR, Nair S, Nakano H, Nakatogawa H, Nanjundan M, Napolitano G, Naqvi NI, Nardacci R, Narendra DP, Narita M, Nascimbeni AC, Natarajan R, Navegantes LC, Nawrocki ST, Nazarko TY, Nazarko VY, Neill T, Neri LM, Netea MG, Netea-Maier RT, Neves BM, Ney PA, Nezis IP, Nguyen HT, Nguyen HP, Nicot AS, Nilsen H, Nilsson P, Nishimura M, Nishino I, Niso-Santano M, Niu H, Nixon RA, Njar VC, Noda T, Noegel AA, Nolte EM, Norberg E, Norga KK, Noureini SK, Notomi S, Notterpek L, Nowikovsky K, Nukina N, Nürnberger T, O'Donnell VB, O'Donovan T, O'Dwyer PJ, Oehme I, Oeste CL, Ogawa M, Ogretmen B, Ogura Y, Oh YJ, Ohmuraya M, Ohshima T, Ojha R, Okamoto K, Okazaki T, Oliver FJ, Ollinger K, Olsson S, Orban DP, Ordonez P, Orhon I, Orosz L, O'Rourke EJ, Orozco H, Ortega AL, Ortona E, Osellame LD, Oshima J, Oshima S, Osiewacz HD, Otomo T, Otsu K, Ou JH, Outeiro TF, Ouyang DY, Ouyang H, Overholtzer M, Ozbun MA, Ozdinler PH, Ozpolat B, Pacelli C, Paganetti P, Page G, Pages G, Pagnini U, Pajak B, Pak SC, Pakos-Zebrucka K, Pakpour N, Palková Z, Palladino F, Pallauf K, Pallet N, Palmieri M, Paludan SR, Palumbo C, Palumbo S, Pampliega O, Pan H, Pan W, Panaretakis T, Pandey A, Pantazopoulou A, Papackova Z, Papademetrio DL, Papassideri I, Papini A, Parajuli N, Pardo J, Parekh VV, Parenti G, Park JI, Park J, Park OK, Parker R, Parlato R, Parys JB, Parzych KR, Pasquet JM, Pasquier B, Pasumarthi KB, Patschan D, Patterson C, Pattingre S, Pattison S, Pause A, Pavenstädt H, Pavone F, Pedrozo Z, Peña FJ, Peñalva MA, Pende M, Peng J, Penna F, Penninger JM, Pensalfini A, Pepe S, Pereira GJ, Pereira PC, Pérez-de la Cruz V, Pérez-Pérez ME, Pérez-Rodríguez D, Pérez-Sala D, Perier C, Perl A, Perlmutter DH, Perrotta I, Pervaiz S, Pesonen M, Pessin JE, Peters GJ, Petersen M, Petrache I, Petrof BJ, Petrovski G, Phang JM, Piacentini M, Pierdominici M, Pierre P, Pierrefite-Carlevarle V, Pietrocola F, Pimentel-Muiños FX, Pinar M, Pineda B, Pinkas-Kramarski R, Pinti M, Pinton P, Piperdi B, Piret JM, Platanias LC, Platta HW, Plowey ED, Pöggeler S, Poirot M, Polčic P, Poletti A, Poon AH, Popelka H, Popova B, Poprawa I, Poulose SM, Poulton J, Powers SK, Powers T, Pozuelo-Rubio M, Prak K, Prange R, Prescott M, Priault M, Prince S, Proia RL, Proikas-Cezanne T, Prokisch H, Promponas VJ, Przyklenk K, Puertollano R, Pugazhenthi S, Puglielli L, Pujol A, Puyal J, Pyeon D, Qi X, Qian WB, Qin ZH, Qiu Y, Qu Z, Quadrilatero J, Quinn F, Raben N, Rabinowich H, Radogna F, Ragusa MJ, Rahmani M, Raina K, Ramanadham S, Ramesh R, Rami A, Randall-Demllo S, Randow F, Rao H, Rao VA, Rasmussen BB, Rasse TM, Ratovitski EA, Rautou PE, Ray SK, Razani B, Reed BH, Reggiori F, Rehm M, Reichert AS, Rein T, Reiner DJ, Reits E, Ren J, Ren X, Renna M, Reusch JE, Revuelta JL, Reyes L, Rezaie AR, Richards RI, Richardson DR, Richetta C, Riehle MA, Rihn BH, Rikihisa Y, Riley BE, Rimbach G, Rippo MR, Ritis K, Rizzi F, Rizzo E, Roach PJ, Robbins J, Roberge M, Roca G, Roccheri MC, Rocha S, Rodríguez CI, de Cordoba SR, Rodriguez-Muela N, Roelofs J, Rogov VV, Rohn TT, Rohrer B, Romanelli D, Romani L, Romano PS, Roncero MI, Rosa JL, Rosello A, Rosen KV, Rosenstiel P, Rost-Roszkowska M, Roth K, Rodrigues CMA, Roué G, Rouis M, Rouschop KM, Ruan DT, Ruano D, Rubinsztein DC, Rucker 3rd EB, Rudich A, Rudolf E, Rudolf R, Ruegg MA, Ruiz-Roldan C, Ruparelia AA, Rusmini P, Russ DW, Russo GL, Russo G, Russo R, Rusten TE, Ryabovol V, Ryan KM, Ryter SW, Sabatini DM, Sacher M, Sachse C, Sack MN, Sadoshima J, Saftig P, Sagi-Eisenberg R, Sahni S, Saikumar P, Saito T, Saitoh T, Sakakura K, Sakoh-Nakatogawa M, Sakuraba Y, Salazar-Roa M, Salomoni P, Saluja AK, Salvaterra PM, Salvioli R, Samali A, Sanchez AM, Sánchez-Alcázar JA, Sanchez-Prieto R, Sandri M, Sanjuan MA, Santaguida S, Santambrogio L, Santoni G, Dos Santos CN, Saran S, Sardiello M, Sargent G, Sarkar P, Sarkar S, Sarrias MR, Sarwal MM, Sasakawa C, Sasaki M, Sass M, Sato K, Sato M, Satriano J, Savaraj N, Saveljeva S, Schaefer L, Schaible UE, Scharl M, Schatzl HM, Schekman R, Scheper W, Schiavi A, Schipper HM, Schmeisser H, Schmidt J, Schmitz I, Schneider BE, Schneider EM, Schneider JL, Schon EA, Schönenberger MJ, Schönthal AH, Schorderet DF, Schröder B, Schuck S, Schulze RJ, Schwarten M, Schwarz TL, Sciarretta S, Scotto K,

Scovassi AI, Screaton RA, Screen M, Seca H, Sedej S, Segatori L, Segev N, Seglen PO, Seguí-Simarro JM, Segura-Aguilar J, Seki E, Sell C, Seiliez I, Semenkovich CF, Semenza GL, Sen U, Serra AL, Serrano-Puebla A, Sesaki H, Setoguchi T, Settembre C, Shacka JJ, Shajahan-Haq AN, Shapiro IM, Sharma S, She H, Shen CK, Shen CC, Shen HM, Shen S, Shen W, Sheng R, Sheng X, Sheng ZH, Shepherd TG, Shi J, Shi Q, Shi Q, Shi Y, Shibutani S, Shibuya K, Shidoji Y, Shieh JJ, Shih CM, Shimada Y, Shimizu S, Shin DW, Shinohara ML, Shintani M, Shintani T, Shioi T, Shirabe K, Shiri-Sverdlov R, Shirihai O, Shore GC, Shu CW, Shukla D, Sibirny AA, Sica V, Sigurdson CJ, Sigurdsson EM, Sijwali PS, Sikorska B, Silveira WA, Silvente-Poirot S, Silverman GA, Simak J, Simmet T, Simon AK, Simon HU, Simone C, Simons M, Simonsen A, Singh R, Singh SV, Singh SK, Sinha D, Sinha S, Sinicrope FA, Sirko A, Sirohi K, Sishi BJ, Sittler A, Siu PM, Sivridis E, Skwarska A, Slack R, Slaninová I, Slavov N, Smaili SS, Smalley KS, Smith DR, Soenen SJ, Soleimanpour SA, Solhaug A, Somasundaram K, Son JH, Sonawane A, Song C, Song F, Song HK, Song JX, Song W, Soo KY, Sood AK, Soong TW, Soontornniyomkij V, Sorice M, Sotgia F, Soto-Pantoja DR, Sotthibundhu A, Sousa MJ, Spaink HP, Span PN, Spang A, Sparks JD, Speck PG, Spector SA, Spies CD, Springer W, Clair DS, Stacchiotti A, Staels B, Stang MT, Starczynowski DT, Starokadomskyy P, Steegborn C, Steele JW, Stefanis L, Steffan J, Stellrecht CM, Stenmark H, Stepkowski TM, Stern ST, Stevens C, Stockwell BR, Stoka V, Storchova Z, Stork B, Stratoulias V, Stravopodis DJ, Strnad P, Strohecker AM, Ström AL, Stromhaug P, Stulik J, Su YX, Su Z, Subauste CS, Subramaniam S, Sue CM, Suh SW, Sui X, Sukseree S, Sulzer D, Sun FL, Sun J, Sun SY, Sun Y, Sundaramoorthy V, Sung J, Suzuki H, Suzuki K, Suzuki N, Suzuki T, Suzuki YJ, Swanson MS, Swanton C, Swärd K, Swarup G, Sweeney ST, Sylvester PW, Szatmari Z, Szegezdi E, Szlosarek PW, Taegtmeyer H, Tafani M, Taillebourg E, Tait SW, Takacs-Vellai K, Takahashi Y, Takáts S, Takemura G, Takigawa N, Talbot NJ, Tamagno E, Tamburini J, Tan CP, Tan L, Tan ML, Tan M, Tan YJ, Tanaka K, Tanaka M, Tang D, Tang G, Tanida I, Tanji K, Tannous BA, Tapia JA, Tasset-Cuevas I, Tatar M, Tavassoly I, Tavernarakis N, Taylor A, Taylor GS, Taylor GA, Taylor JP, Taylor MJ, Tchetina EV, Tee AR, Teixeira-Clerc F, Telang S, Tencomnao T, Teng BB, Teng RJ, Terro F, Tettamanti G, Theiss AL, Theron AE, Thomas KJ, Thomé MP, Thomes PG, Thorburn A, Thorner J, Thum T, Thumm M, Thurston TL, Tian L, Till A, Ting JP, Titorenko VI, Toker L, Toldo S, Tooze SA, Topisirovic I, Torgersen ML, Torosantucci L, Torriglia A, Torrisi MR, Tournier C, Towns R, Trajkovic V, Travassos LH, Triola G, Tripathi DN, Trisciuoglio D, Troncoso R, Trougakos IP, Truttmann AC, Tsai KJ, Tschan MP, Tseng YH, Tsukuba T, Tsung A, Tsvetkov AS, Tu S, Tuan HY, Tucci M, Tumbarello DA, Turk B, Turk V, Turner RF, Tveita AA, Tyagi SC, Ubukata M, Uchiyama Y, Udelnow A, Ueno T, Umekawa M, Umemiya-Shirafuji R, Underwood BR, Ungermann C, Ureshino RP, Ushioda R, Uversky VN, Uzcátegui NL, Vaccari T, Vaccaro MI, Váchová L, Vakifahmetoglu-Norberg H, Valdor R, Valente EM, Vallette F, Valverde AM, Van den Berghe G, Van Den Bosch L, van den Brink GR, van der Goot FG, van der Klei IJ, van der Laan LJ, van Doorn WG, van Egmond M, van Golen KL, Van Kaer L, van Lookeren Campagne M, Vandenabeele P, Vandenberghe W, Vanhorebeek I, Varela-Nieto I, Vasconcelos MH, Vasko R, Vavvas DG, Vega-Naredo I, Velasco G, Velentzas AD, Velentzas PD, Vellai T, Vellenga E, Vendelbo MH, Venkatachalam K, Ventura N, Ventura S, Veras PS, Verdier M, Vertessy BG, Viale A, Vidal M, Vieira HL, Vierstra RD, Vigneswaran N, Vij N, Vila M, Villar M, Villar VH, Villarroya J, Vindis C, Viola G, Viscomi MT, Vitale G, Vogl DT, Voitsekhovskaja OV, von Haefen C, von Schwarzenberg K, Voth DE, Vouret-Craviari V, Vuori K, Vyas JM, Waeber C, Walker CL, Walker MJ, Walter J, Wan L, Wan X, Wang B, Wang C, Wang CY, Wang D, Wang F, Wang G, Wang HJ, Wang H, Wang HG, Wang HD, Wang J, Wang M, Wang MQ, Wang PY, Wang P, Wang RC, Wang S, Wang TF, Wang X, Wang XJ, Wang XW, Wang Y, Wang YJ, Wang YT, Wang ZN, Wappner P, Ward C, Ward DM, Warnes G, Watada H, Watanabe Y, Watase K, Weaver TE, Weekes CD, Wei J, Weide T, Weihl CC, Weindl G, Weis SN, Wen L, Wen X, Wen Y, Westermann B, Weyand CM, White AR, White E, Whitton JL, Whitworth AJ, Wiels J, Wild F, Wildenberg ME, Wileman T, Wilkinson DS, Wilkinson S, Willbold D, Williams C, Williams K, Williamson PR, Winklhofer KF, Witkin SS, Wohlgemuth SE, Wollert T, Wolvetang EJ, Wong E, Wong GW, Wong RW, Wong VK, Woodcock EA, Wright KL, Wu C, Wu D, Wu GS, Wu J, Wu J, Wu M, Wu M, Wu S, Wu WK, Wu Y, Wu Z, Xavier CP, Xavier RJ, Xia GX, Xia T, Xia W, Xia Y, Xiao H, Xiao J, Xiao S, Xiao W, Xie CM, Xie Z, Xilouri M, Xiong Y, Xu C, Xu F, Xu H, Xu J, Xu L, Xu X, Xu Y, Xu ZX, Xu Z, Xue Y, Yamada T, Yamamoto A, Yamanaka K, Yamashina S, Yamashiro S, Yan B, Yan X, Yan Z, Yanagi Y, Yang DS, Yang JM, Yang L, Yang M, Yang PM, Yang P, Yang Q, Yang W, Yang WY, Yang X, Yang Y, Yang Z, Yao MC, Yao PJ, Yao X, Yao Z, Yasui LS, Ye M, Yedvobnick B, Yeganeh B, Yeh ES, Yeyati PL, Yi F, Yi L, Yin XM, Yip CK, Yoo YM, Yoo YH, Yoon SY, Yoshida K, Yoshimori T, Young KH, Yu H, Yu JJ, Yu JT, Yu J, Yu L, Yu WH, Yu XF, Yu Z, Yuan J, Yuan ZM, Yue BY, Yue J, Yue Z, Zacks DN, Zacksenhaus E, Zaffaroni N, Zaglia T, Zakeri Z, Zecchini V, Zeng J, Zeng M, Zeng Q, Zervos AS, Zhang DD, Zhang F, Zhang G, Zhang GC, Zhang H, Zhang J, Zhang JP, Zhang L, Zhang MY, Zhang X, Zhang XD, Zhang Y, Zhao M, Zhao WL, Zhao X, Zhao YG, Zhao Y, Zhao YX, Zhao Z, Zhao ZJ, Zheng D, Zheng XL, Zheng X, Zhivotovsky B, Zhong Q, Zhou GZ, Zhou G, Zhou H, Zhou SF, Zhou XJ, Zhu H, Zhu WG, Zhu W, Zhu XF, Zhu Y, Zhuang SM, Zhuang X, Ziparo E, Zois CE, Zoladek T, Zong WX, Zorzano A, Zughaier SM (2016) Guidelines for the use and interpretation of assays for monitoring autophagy (3rd edition). *Autophagy* **12**: 1–222.

Kothari S, Cizeau J, McMillan-Ward E, Israels SJ, Bailes M, Ens K, Kirshenbaum LA, Gibson SB (2003) BNIP3 plays a role in hypoxic cell death in human epithelial cells that is inhibited by growth factors EGF and IGF. *Oncogene* **22**: 4734–4744.

Lamb CA, Nuhlen S, Judith D, Frith D, Snijders AP, Behrends C, Tooze SA (2016) TBC1D14 regulates autophagy via the TRAPP complex and ATG9 traffic. *EMBO J* **35**: 281–301.

Maes H, Kuchnio A, Peric A, Moens S, Nys K, De Bock K, Quaegebeur A, Schoors S, Georgiadou M, Wouters J, Vinckier S, Vankelecom H, Garmyn M, Vion AC, Radtke F, Boulanger C, Gerhardt H, Dejana E, Dewerchin M, GhesquiÒre B, Annaert W, Agostinis P, Carmeliet P (2014) Tumor vessel normalization by chloroquine independent of autophagy. *Cancer Cell* **26**: 190–206.

Matys V, Kel-Margoulis OV, Fricke E, Liebich I, Land S, Barre-Dirrie A, Reuter I, Chekmenev D, Krull M, Hornischer K, Voss N, Stegmaier P, Lewicki-Potapov B, Saxel H, Kel AE, Wingender E (2006) TRANSFAC and its module TRANSCompel: transcriptional gene regulation in eukaryotes. *Nucleic Acids Res* **34**: D108–D110.

Maycotte P, Aryal S, Cummings CT, Thorburn J, Morgan MJ, Thorburn A (2012) Chloroquine sensitizes breast cancer cells to chemotherapy independent of autophagy. *Autophagy* **8**: 200–212.

Mazure NM, Pouyssegur J (2009) Atypical BH3-domains of BNIP3 and BNIP3L lead to autophagy in hypoxia. *Autophagy* **5**: 868–869.

Mazure NM, Pouyssegur J (2010) Hypoxia-induced autophagy: cell death or cell survival? *Curr Opin Cell Biol* **22**: 177–180.

Mole DR, Blancher C, Copley RR, Pollard PJ, Gleadle JM, Ragoussis J, Ratcliffe PJ (2009) Genome-wide association of hypoxia-inducible factor (HIF)-1alpha and HIF-2alpha DNA binding with expression profiling of hypoxia-inducible transcripts. *J Biol Chem* **284**: 16767–16775.

Moussay E, Kaoma T, Baginska J, Muller A, Van Moer K, Nicot N, Nazarov PV, Vallar L, Chouaib S, Berchem G, Janji B (2011) The acquisition of resistance to TNFalpha in breast cancer cells is associated with constitutive activation of autophagy as revealed by a transcriptome analysis using a custom microarray. *Autophagy* **7**: 760–770.

Munson MJ, Ganley IG (2015) MTOR, PIK3C3, and autophagy: signaling the beginning from the end. *Autophagy* **11**: 2375–2376.

Niclou SP, Danzeisen C, Eikesdal HP, Wiig H, Brons NH, Poli AM, Svendsen A, Torsvik A, Enger PO, Terzis JA, Bjerkvig R (2008) A novel eGFP-expressing immunodeficient mouse model to study tumor-host interactions. *FASEB J* **22**: 3120–3128.

Noman MZ, Janji B, Berchem G, Mami-Chouaib F, Chouaib S (2012) Hypoxia-induced autophagy: a new player in cancer immunotherapy? *Autophagy* **8**: 704–706.

Noman MZ, Janji B, Kaminska B, Van Moer K, Pierson S, Przanowski P, Buart S, Berchem G, Romero P, Mami-Chouaib F, Chouaib S (2011) Blocking hypoxia-induced autophagy in tumors restores cytotoxic T-cell activity and promotes regression. *Cancer Res* **71**: 5976–5986.

Orsi A, Razi M, Dooley HC, Robinson D, Weston AE, Collinson LM, Tooze SA (2012) Dynamic and transient interactions of Atg9 with autophagosomes, but not membrane integration, are required for autophagy. *Mol Biol Cell* **23**: 1860–1873.

Pouyssegur J, Dayan F, Mazure NM (2006) Hypoxia signalling in cancer and approaches to enforce tumour regression. *Nature* **441**: 437–443.

Rabinowitz JD, White E (2010) Autophagy and metabolism. *Science* **330**: 1344–1348.
Reggiori F, Tooze SA (2012) Autophagy regulation through Atg9 traffic. *J Cell Biol* **198**: 151–153.
Rosenfeld MR, Ye X, Supko JG, Desideri S, Grossman SA, Brem S, Mikkelson T, Wang D, Chang YC, Hu J, McAfee Q, Fisher J, Troxel AB, Piao S, Heitjan DF, Tan KS, Pontiggia L, O?Dwyer PJ, Davis LE, Amaravadi RK (2014) A phase I/II trial of hydroxychloroquine in conjunction with radiation therapy and concurrent and adjuvant temozolomide in patients with newly diagnosed glioblastoma multiforme. *Autophagy* **10**: 1359–1368.
Rouschop KM, van den Beucken T, Dubois L, Niessen H, Bussink J, Savelkouls K, Keulers T, Mujcic H, Landuyt W, Voncken JW, Lambin P, van der Kogel AJ, Koritzinsky M, Wouters BG (2010) The unfolded protein response protects human tumor cells during hypoxia through regulation of the autophagy genes MAP1LC3B and ATG5. *J Clin Invest* **120**: 127–141.
Sanzey M, Abdul Rahim SA, Oudin A, Dirkse A, Kaoma T, Vallar L, Herold-Mende C, Bjerkvig R, Golebiewska A, Niclou SP (2015) Comprehensive analysis of glycolytic enzymes as therapeutic targets in the treatment of glioblastoma. *PLoS One* **10**: e0123544.
Shingu T, Fujiwara K, Bogler O, Akiyama Y, Moritake K, Shinojima N, Tamada Y, Yokoyama T, Kondo S (2009) Inhibition of autophagy at a late stage enhances imatinib-induced cytotoxicity in human malignant glioma cells. *Int J Cancer* **124**: 1060–1071.
Shintani T, Klionsky DJ (2004) Autophagy in health and disease: a double-edged sword. *Science* **306**: 990–995.
Slemc L, Kunej T (2016) Transcription factor HIF1A: downstream targets, associated pathways, polymorphic hypoxia response element (HRE) sites, and initiative for standardization of reporting in scientific literature. *Tumour Biol* **37**: 14851–14861.
Sotelo J, Briceno E, Lopez-Gonzalez MA (2006) Adding chloroquine to conventional treatment for glioblastoma multiforme: a randomized, double-blind, placebo-controlled trial. *Ann Intern Med* **144**: 337–343.
Vaupel P, Mayer A (2007) Hypoxia in cancer: significance and impact on clinical outcome. *Cancer Metastasis Rev* **26**: 225–239.
Viry E, Baginska J, Berchem G, Noman MZ, Medves S, Chouaib S, Janji B (2014) Autophagic degradation of GZMB/granzyme B: a new mechanism of hypoxic tumor cell escape from natural killer cell-mediated lysis. *Autophagy* **10**: 173–175.
Weerasekara VK, Panek DJ, Broadbent DG, Mortenson JB, Mathis AD, Logan GN, Prince JT, Thomson DM, Thompson JW, Andersen JL (2014) Metabolic-stress-induced rearrangement of the 14-3-3zeta interactome promotes autophagy via a ULK1- and AMPK-regulated 14-3-3zeta interaction with phosphorylated Atg9. *Mol Cell Biol* **34**: 4379–4388.
Yamamoto H, Kakuta S, Watanabe TM, Kitamura A, Sekito T, Kondo-Kakuta C, Ichikawa R, Kinjo M, Ohsumi Y (2012) Atg9 vesicles are an important membrane source during early steps of autophagosome formation. *J Cell Biol* **198**: 219–233.
Yang L, Lin C, Wang L, Guo H, Wang X (2012) Hypoxia and hypoxia-inducible factors in glioblastoma multiforme progression and therapeutic implications. *Exp Cell Res* **318**: 2417–2426.
Yang ZJ, Chee CE, Huang S, Sinicrope FA (2011) The role of autophagy in cancer: therapeutic implications. *Mol Cancer Ther* **10**: 1533–1541.
Zhang H, Bosch-Marce M, Shimoda LA, Tan YS, Baek JH, Wesley JB, Gonzalez FJ, Semenza GL (2008) Mitochondrial autophagy is an HIF-1-dependent adaptive metabolic response to hypoxia. *J Biol Chem* **283**: 10892–10903.

Supplementary Information accompanies this paper on British Journal of Cancer website (http://www.nature.com/bjc)

References

8. References

ABDUL RAHIM, S. A., DIRKSE, A., OUDIN, A., SCHUSTER, A., BOHLER, J., BARTHELEMY, V., MULLER, A., VALLAR, L., JANJI, B., GOLEBIEWSKA, A. & NICLOU, S. P. 2017. Regulation of hypoxia-induced autophagy in glioblastoma involves ATG9A. *Br J Cancer,* 117**,** 813-825.

ABERNATHY, K. & BURKE, J. 2016. Modeling the Treatment of Glioblastoma Multiforme and Cancer Stem Cells with Ordinary Differential Equations. *Comput Math Methods Med,* 2016**,** 1239861.

ABNEY, E. R., WILLIAMS, B. P. & RAFF, M. C. 1983. Tracing the development of oligodendrocytes from precursor cells using monoclonal antibodies, fluorescence-activated cell sorting, and cell culture. *Dev Biol,* 100**,** 166-71.

AGAMANOLIS, D. P. 2017. *Neuropathology - An illustrated interactive course for medical students and residents* [Online]. Available: http://neuropathology-web.org/chapter7/chapter7bGliomas.html.

AGNIHOTRI, S., BURRELL, K. E., WOLF, A., JALALI, S., HAWKINS, C., RUTKA, J. T. & ZADEH, G. 2013. Glioblastoma, a brief review of history, molecular genetics, animal models and novel therapeutic strategies. *Arch Immunol Ther Exp (Warsz),* 61**,** 25-41.

AL-HAJJ, M., WICHA, M. S., BENITO-HERNANDEZ, A., MORRISON, S. J. & CLARKE, M. F. 2003. Prospective identification of tumorigenic breast cancer cells. *Proc Natl Acad Sci U S A,* 100**,** 3983-8.

AL-MAYHANI, M. T., GRENFELL, R., NARITA, M., PICCIRILLO, S., KENNEY-HERBERT, E., FAWCETT, J. W., COLLINS, V. P., ICHIMURA, K. & WATTS, C. 2011. NG2 expression in glioblastoma identifies an actively proliferating population with an aggressive molecular signature. *Neuro Oncol,* 13**,** 830-45.

ANDOLFO, I., LIGUORI, L., DE ANTONELLIS, P., CUSANELLI, E., MARINARO, F., PISTOLLATO, F., GARZIA, L., DE VITA, G., PETROSINO, G., ACCORDI, B., MIGLIORATI, R., BASSO, G., IOLASCON, A., CINALLI, G. & ZOLLO, M. 2012. The micro-RNA 199b-5p regulatory circuit involves Hes1, CD15, and epigenetic modifications in medulloblastoma. *Neuro Oncol,* 14**,** 596-612.

ANIDO, J., SAEZ-BORDERIAS, A., GONZALEZ-JUNCA, A., RODON, L., FOLCH, G., CARMONA, M. A., PRIETO-SANCHEZ, R. M., BARBA, I., MARTINEZ-SAEZ, E., PRUDKIN, L., CUARTAS, I., RAVENTOS, C., MARTINEZ-RICARTE, F., POCA, M. A., GARCIA-DORADO, D., LAHN, M. M., YINGLING, J. M., RODON, J., SAHUQUILLO, J., BASELGA, J. & SEOANE, J. 2010. TGF-beta Receptor Inhibitors Target the CD44(high)/Id1(high) Glioma-Initiating Cell Population in Human Glioblastoma. *Cancer Cell,* 18**,** 655-68.

AUFFINGER, B., TOBIAS, A. L., HAN, Y., LEE, G., GUO, D., DEY, M., LESNIAK, M. S. & AHMED, A. U. 2014. Conversion of differentiated cancer cells into cancer stem-like cells in a glioblastoma model after primary chemotherapy. *Cell Death Differ,* 21**,** 1119-31.

AUVERGNE, R., WU, C., CONNELL, A., AU, S., CORNWELL, A., OSIPOVITCH, M., BENRAISS, A., DANGELMAJER, S., GUERRERO-CAZARES, H., QUINONES-HINOJOSA, A. & GOLDMAN, S. A. 2016. PAR1 inhibition suppresses the self-renewal and growth of A2B5-defined glioma progenitor cells and their derived gliomas in vivo. *Oncogene,* 35**,** 3817-28.

AUVERGNE, R. M., SIM, F. J., WANG, S., CHANDLER-MILITELLO, D., BURCH, J., AL FANEK, Y., DAVIS, D., BENRAISS, A., WALTER, K., ACHANTA, P., JOHNSON, M., QUINONES-HINOJOSA, A., NATESAN, S., FORD, H. L. & GOLDMAN, S. A. 2013. Transcriptional differences between normal and glioma-derived glial progenitor cells identify a core set of dysregulated genes. *Cell Rep,* 3**,** 2127-41.

BALL, E. D., SCHWARZ, L. M. & BLOOMFIELD, C. D. 1991. Expression of the CD15 antigen on normal and leukemic myeloid cells: effects of neuraminidase and variable detection with a panel of monoclonal antibodies. *Mol Immunol,* 28**,** 951-8.

BAO, S., WU, Q., MCLENDON, R. E., HAO, Y., SHI, Q., HJELMELAND, A. B., DEWHIRST, M. W., BIGNER, D. D. & RICH, J. N. 2006a. Glioma stem cells promote radioresistance by preferential activation of the DNA damage response. *Nature,* 444**,** 756-60.

BAO, S., WU, Q., SATHORNSUMETEE, S., HAO, Y., LI, Z., HJELMELAND, A. B., SHI, Q., MCLENDON, R. E., BIGNER, D. D. & RICH, J. N. 2006b. Stem cell-like glioma cells promote tumor angiogenesis through vascular endothelial growth factor. *Cancer Res,* 66**,** 7843-8.

BAR, E. E., LIN, A., MAHAIRAKI, V., MATSUI, W. & EBERHART, C. G. 2010. Hypoxia increases the expression of stem-cell markers and promotes clonogenicity in glioblastoma neurospheres. *Am J Pathol,* 177**,** 1491-502.

BARRANTES-FREER, A., RENOVANZ, M., EICH, M., BRAUKMANN, A., SPRANG, B., SPIRIN, P., PARDO, L. A., GIESE, A. & KIM, E. L. 2015. CD133 Expression Is Not Synonymous to Immunoreactivity for AC133 and Fluctuates throughout the Cell Cycle in Glioma Stem-Like Cells. *PLoS One,* 10**,** e0130519.

BARRAUD, P., STOTT, S., MOLLGARD, K., PARMAR, M. & BJORKLUND, A. 2007. In vitro characterization of a human neural progenitor cell coexpressing SSEA4 and CD133. *J Neurosci Res,* 85**,** 250-9.

BARRETT, L. E., GRANOT, Z., COKER, C., IAVARONE, A., HAMBARDZUMYAN, D., HOLLAND, E. C., NAM, H. S. & BENEZRA, R. 2012. Self-renewal does not predict tumor growth potential in mouse models of high-grade glioma. *Cancer Cell,* 21**,** 11-24.

BASAKRAN, N. S. 2015. CD44 as a potential diagnostic tumor marker. *Saudi Med J,* 36**,** 273-9.

BAUER, N., FONSECA, A. V., FLOREK, M., FREUND, D., JASZAI, J., BORNHAUSER, M., FARGEAS, C. A. & CORBEIL, D. 2008. New insights into the cell biology of hematopoietic progenitors by studying prominin-1 (CD133). *Cells Tissues Organs,* 188**,** 127-38.

BAUER, N., WILSCH-BRAUNINGER, M., KARBANOVA, J., FONSECA, A. V., STRAUSS, D., FREUND, D., THIELE, C., HUTTNER, W. B., BORNHAUSER, M. & CORBEIL, D. 2011. Haematopoietic stem cell differentiation promotes the release of prominin-1/CD133-containing membrane vesicles--a role of the endocytic-exocytic pathway. *EMBO Mol Med,* 3**,** 398-409.

BEIER, D., HAU, P., PROESCHOLDT, M., LOHMEIER, A., WISCHHUSEN, J., OEFNER, P. J., AIGNER, L., BRAWANSKI, A., BOGDAHN, U. & BEIER, C. P. 2007. CD133(+) and CD133(-) glioblastoma-derived cancer stem cells show differential growth characteristics and molecular profiles. *Cancer Res,* 67**,** 4010-5.

BEIER, D., ROHRL, S., PILLAI, D. R., SCHWARZ, S., KUNZ-SCHUGHART, L. A., LEUKEL, P., PROESCHOLDT, M., BRAWANSKI, A., BOGDAHN, U., TRAMPE-KIESLICH, A., GIEBEL, B., WISCHHUSEN, J., REIFENBERGER, G., HAU, P. & BEIER, C. P. 2008. Temozolomide preferentially depletes cancer stem cells in glioblastoma. *Cancer Res,* 68**,** 5706-15.

BEROUKHIM, R., GETZ, G., NGHIEMPHU, L., BARRETINA, J., HSUEH, T., LINHART, D., VIVANCO, I., LEE, J. C., HUANG, J. H., ALEXANDER, S., DU, J., KAU, T., THOMAS, R. K., SHAH, K., SOTO, H., PERNER, S., PRENSNER, J., DEBIASI, R. M., DEMICHELIS, F., HATTON, C., RUBIN, M. A., GARRAWAY, L. A., NELSON, S. F., LIAU, L., MISCHEL, P. S., CLOUGHESY, T. F., MEYERSON, M., GOLUB, T. A., LANDER, E. S., MELLINGHOFF, I. K. & SELLERS, W. R. 2007. Assessing the significance of chromosomal aberrations in cancer: methodology and application to glioma. *Proc Natl Acad Sci U S A,* 104**,** 20007-12.

BERTOUT, J. A., PATEL, S. A. & SIMON, M. C. 2008. The impact of O2 availability on human cancer. *Nat Rev Cancer,* 8**,** 967-75.

BHAT, K. P. L., BALASUBRAMANIYAN, V., VAILLANT, B., EZHILARASAN, R., HUMMELINK, K., HOLLINGSWORTH, F., WANI, K., HEATHCOCK, L., JAMES, J. D., GOODMAN, L. D., CONROY, S., LONG, L., LELIC, N., WANG, S., GUMIN, J., RAJ, D., KODAMA, Y., RAGHUNATHAN, A., OLAR, A., JOSHI, K., PELLOSKI, C. E., HEIMBERGER, A., KIM, S. H., CAHILL, D. P., RAO, G., DEN DUNNEN, W. F. A., BODDEKE, H., PHILLIPS, H. S., NAKANO, I., LANG, F. F., COLMAN, H., SULMAN, E. P. & ALDAPE, K. 2013. Mesenchymal differentiation mediated by NF-kappaB promotes radiation resistance in glioblastoma. *Cancer Cell,* 24**,** 331-46.

BITON, A., BERNARD-PIERROT, I., LOU, Y., KRUCKER, C., CHAPEAUBLANC, E., RUBIO-PEREZ, C., LOPEZ-BIGAS, N., KAMOUN, A., NEUZILLET, Y., GESTRAUD, P., GRIECO, L., REBOUISSOU, S., DE REYNIES, A., BENHAMOU, S., LEBRET, T., SOUTHGATE, J., BARILLOT, E., ALLORY, Y., ZINOVYEV, A. & RADVANYI, F. 2014. Independent component analysis uncovers the landscape of the bladder tumor transcriptome and reveals insights into luminal and basal subtypes. *Cell Rep,* 9**,** 1235-45.

BONAGUIDI, M. A., MCGUIRE, T., HU, M., KAN, L., SAMANTA, J. & KESSLER, J. A. 2005. LIF and BMP signaling generate separate and discrete types of GFAP-expressing cells. *Development,* 132**,** 5503-14.

BONNER, W. H., HR.; SWEET, RG.; HERZENBERG, LA. 1972. Fluorescence activated cell sorting. *The review of scientific instruments,* 43**,** 5.

BOSE, B., KATIKIREDDY, K. R. & SHENOY, P. S. 2014. Regenerative medicine for diabetes: differentiation of human pluripotent stem cells into functional beta-cells in vitro and their proposed journey to clinical translation. *Vitam Horm,* 95**,** 223-48.

BOUGNAUD, S., GOLEBIEWSKA, A., OUDIN, A., KEUNEN, O., HARTER, P. N., MADER, L., AZUAJE, F., FRITAH, S., STIEBER, D., KAOMA, T., VALLAR, L., BRONS, N. H., DAUBON, T., MILETIC, H., SUNDSTROM, T., HEROLD-MENDE, C., MITTELBRONN, M., BJERKVIG, R. & NICLOU, S. P. 2016. Molecular crosstalk between tumour and brain parenchyma instructs histopathological features in glioblastoma. *Oncotarget,* 7**,** 31955-71.

BOZIC, I., GEROLD, J. M. & NOWAK, M. A. 2016. Quantifying Clonal and Subclonal Passenger Mutations in Cancer Evolution. *PLoS Comput Biol,* 12**,** e1004731.

BRENNAN, C. W., VERHAAK, R. G., MCKENNA, A., CAMPOS, B., NOUSHMEHR, H., SALAMA, S. R., ZHENG, S., CHAKRAVARTY, D., SANBORN, J. Z., BERMAN, S. H., BEROUKHIM, R., BERNARD, B., WU, C. J., GENOVESE, G., SHMULEVICH, I., BARNHOLTZ-SLOAN, J., ZOU, L., VEGESNA, R., SHUKLA, S. A., CIRIELLO, G., YUNG, W. K., ZHANG, W., SOUGNEZ, C., MIKKELSEN, T., ALDAPE, K., BIGNER, D. D., VAN MEIR, E. G., PRADOS, M., SLOAN, A., BLACK, K. L., ESCHBACHER, J., FINOCCHIARO, G., FRIEDMAN, W., ANDREWS, D. W., GUHA, A., IACOCCA, M., O'NEILL, B. P., FOLTZ, G., MYERS, J., WEISENBERGER, D. J., PENNY, R., KUCHERLAPATI, R., PEROU, C. M., HAYES, D. N., GIBBS, R., MARRA, M., MILLS, G. B., LANDER, E., SPELLMAN, P., WILSON, R., SANDER, C., WEINSTEIN, J., MEYERSON, M., GABRIEL, S., LAIRD, P. W., HAUSSLER, D., GETZ, G., CHIN, L. & NETWORK, T. R. 2013. The somatic genomic landscape of glioblastoma. *Cell,* 155**,** 462-77.

BRESCIA, P., ORTENSI, B., FORNASARI, L., LEVI, D., BROGGI, G. & PELICCI, G. 2013a. CD133 Is Essential for Glioblastoma Stem Cell Maintenance. *STEM CELLS,* 31**,** 857-869.

BROOKS, S. A. & LEATHEM, A. J. 1995. Expression of the CD15 antigen (Lewis x) in breast cancer. *Histochem J,* 27**,** 689-93.

BROWN, D. V., DANIEL, P. M., D'ABACO, G. M., GOGOS, A., NG, W., MOROKOFF, A. P. & MANTAMADIOTIS, T. 2015. Coexpression analysis of CD133 and CD44 identifies proneural and mesenchymal subtypes of glioblastoma multiforme. *Oncotarget,* 6**,** 6267-80.

BROWN, D. V., FILIZ, G., DANIEL, P. M., HOLLANDE, F., DWORKIN, S., AMIRIDIS, S., KOUNTOURI, N., NG, W., MOROKOFF, A. P. & MANTAMADIOTIS, T. 2017. Expression of CD133 and CD44 in glioblastoma stem cells correlates with cell proliferation, phenotype stability and intra-tumor heterogeneity. *PLoS One,* 12**,** e0172791.

BU, P., CHEN, K. Y., LIPKIN, S. M. & SHEN, X. 2013. Asymmetric division: a marker for cancer stem cells in early stage tumors? *Oncotarget,* 4**,** 950-1.

BUDER, T., DEUTSCH, A., SEIFERT, M. & VOSS-BOHME, A. 2017. CellTrans: An R Package to Quantify Stochastic Cell State Transitions. *Bioinform Biol Insights,* 11**,** 1177932217712241.

BURRELL, K., SINGH, S., JALALI, S., HILL, R. P. & ZADEH, G. 2014. VEGF regulates region-specific localization of perivascular bone marrow-derived cells in glioblastoma. *Cancer Res,* 74**,** 3727-39.

BURRELL, R. A., MCGRANAHAN, N., BARTEK, J. & SWANTON, C. 2013. The causes and consequences of genetic heterogeneity in cancer evolution. *Nature,* 501**,** 338-45.

CABRERA, M. C., HOLLINGSWORTH, R. E. & HURT, E. M. 2015. Cancer stem cell plasticity and tumor hierarchy. *World J Stem Cells,* 7**,** 27-36.

CAIRNS, J. 1975. Mutation selection and the natural history of cancer. *Nature,* 255**,** 197-200.

CALABRESE, C., POPPLETON, H., KOCAK, M., HOGG, T. L., FULLER, C., HAMNER, B., OH, E. Y., GABER, M. W., FINKLESTEIN, D., ALLEN, M., FRANK, A., BAYAZITOV, I. T., ZAKHARENKO, S. S., GAJJAR, A., DAVIDOFF, A. & GILBERTSON, R. J. 2007. A perivascular niche for brain tumor stem cells. *Cancer Cell,* 11**,** 69-82.

CAMPOS, B., CENTNER, F. S., BERMEJO, J. L., ALI, R., DORSCH, K., WAN, F., FELSBERG, J., AHMADI, R., GRABE, N., REIFENBERGER, G., UNTERBERG, A., BURHENNE, J. & HEROLD-MENDE, C. 2011a. Aberrant expression of retinoic acid signaling molecules influences patient survival in astrocytic gliomas. *Am J Pathol,* 178**,** 1953-64.

CAMPOS, B., WAN, F., FARHADI, M., ERNST, A., ZEPPERNICK, F., TAGSCHERER, K. E., AHMADI, R., LOHR, J., DICTUS, C., GDYNIA, G., COMBS, S. E., GOIDTS, V., HELMKE, B. M., ECKSTEIN, V., ROTH, W., BECKHOVE, P., LICHTER, P., UNTERBERG, A., RADLWIMMER, B. & HEROLD-MENDE, C. 2010. Differentiation therapy exerts antitumor effects on stem-like glioma cells. *Clin Cancer Res,* 16**,** 2715-28.

CAMPOS, B., WEISANG, S., OSSWALD, F., ALI, R., SEDLMEIER, G., BAGERITZ, J., MALLM, J. P., HARTMANN, C., VON DEIMLING, A., POPANDA, O., GOIDTS, V., PLASS, C., UNTERBERG, A., SCHMEZER, P., BURHENNE, J. & HEROLD-MENDE, C. 2015. Retinoid resistance and multifaceted impairment of retinoic acid synthesis in glioblastoma. *Glia,* 63**,** 1850-9.

CAMPOS, B., ZENG, L., DAOTRONG, P. H., ECKSTEIN, V., UNTERBERG, A., MAIRBAURL, H. & HEROLD-MENDE, C. 2011b. Expression and regulation of AC133 and CD133 in glioblastoma. *Glia,* 59**,** 1974-86.

CANCER GENOME ATLAS RESEARCH, N. 2008. Comprehensive genomic characterization defines human glioblastoma genes and core pathways. *Nature,* 455**,** 1061-8.

CANCER GENOME ATLAS RESEARCH, N., WEINSTEIN, J. N., COLLISSON, E. A., MILLS, G. B., SHAW, K. R., OZENBERGER, B. A., ELLROTT, K., SHMULEVICH, I., SANDER, C. & STUART, J. M. 2013. The Cancer Genome Atlas Pan-Cancer analysis project. *Nat Genet,* 45**,** 1113-20.

CAPELA, A. & TEMPLE, S. 2002. LeX/ssea-1 is expressed by adult mouse CNS stem cells, identifying them as nonependymal. *Neuron,* 35**,** 865-75.

CAPELA, A. & TEMPLE, S. 2006. LeX is expressed by principle progenitor cells in the embryonic nervous system, is secreted into their environment and binds Wnt-1. *Dev Biol,* 291**,** 300-13.

CARMELIET, P., DOR, Y., HERBERT, J. M., FUKUMURA, D., BRUSSELMANS, K., DEWERCHIN, M., NEEMAN, M., BONO, F., ABRAMOVITCH, R., MAXWELL, P., KOCH, C. J., RATCLIFFE, P., MOONS, L., JAIN, R. K., COLLEN, D. & KESHERT, E. 1998. Role of HIF-1alpha in hypoxia-mediated apoptosis, cell proliferation and tumour angiogenesis. *Nature,* 394**,** 485-90.

CARUBIA, J. M., YU, R. K., MACALA, L. J., KIRKWOOD, J. M. & VARGA, J. M. 1984. Gangliosides of normal and neoplastic human melanocytes. *Biochem Biophys Res Commun,* 120**,** 500-4.

CECCARELLI, M., BARTHEL, F. P., MALTA, T. M., SABEDOT, T. S., SALAMA, S. R., MURRAY, B. A., MOROZOVA, O., NEWTON, Y., RADENBAUGH, A., PAGNOTTA, S. M., ANJUM, S., WANG, J., MANYAM, G., ZOPPOLI, P., LING, S., RAO, A. A., GRIFFORD, M., CHERNIACK, A. D., ZHANG, H., POISSON, L., CARLOTTI, C. G., JR., TIRAPELLI, D. P., RAO, A., MIKKELSEN, T., LAU, C. C., YUNG, W. K., RABADAN, R., HUSE, J., BRAT, D. J., LEHMAN, N. L., BARNHOLTZ-SLOAN, J. S., ZHENG, S., HESS, K., RAO, G., MEYERSON, M., BEROUKHIM, R., COOPER, L., AKBANI, R., WRENSCH, M., HAUSSLER, D., ALDAPE, K. D., LAIRD, P. W., GUTMANN, D. H., NETWORK, T. R., NOUSHMEHR, H., IAVARONE, A. & VERHAAK, R. G. 2016. Molecular Profiling Reveals Biologically Discrete Subsets and Pathways of Progression in Diffuse Glioma. *Cell,* 164**,** 550-63.

CHAFFER, C. L., MARJANOVIC, N. D., LEE, T., BELL, G., KLEER, C. G., REINHARDT, F., D'ALESSIO, A. C., YOUNG, R. A. & WEINBERG, R. A. 2013. Poised chromatin at the ZEB1 promoter enables breast cancer cell plasticity and enhances tumorigenicity. *Cell,* 154**,** 61-74.

CHAICHANA, K., ZAMORA-BERRIDI, G., CAMARA-QUINTANA, J. & QUINONES-HINOJOSA, A. 2006. Neurosphere assays: growth factors and hormone differences in tumor and nontumor studies. *Stem Cells,* 24**,** 2851-7.

CHAN, K. S., ESPINOSA, I., CHAO, M., WONG, D., AILLES, L., DIEHN, M., GILL, H., PRESTI, J., JR., CHANG, H. Y., VAN DE RIJN, M., SHORTLIFFE, L. & WEISSMAN, I. L. 2009. Identification, molecular characterization, clinical prognosis, and therapeutic targeting of human bladder tumor-initiating cells. *Proc Natl Acad Sci U S A,* 106**,** 14016-21.

CHARAFE-JAUFFRET, E., GINESTIER, C., IOVINO, F., WICINSKI, J., CERVERA, N., FINETTI, P., HUR, M. H., DIEBEL, M. E., MONVILLE, F., DUTCHER, J., BROWN, M., VIENS, P., XERRI, L., BERTUCCI, F., STASSI, G., DONTU, G., BIRNBAUM, D. & WICHA, M. S. 2009. Breast cancer cell lines contain functional cancer stem cells with metastatic capacity and a distinct molecular signature. *Cancer Res,* 69**,** 1302-13.

CHARLES, N., OZAWA, T., SQUATRITO, M., BLEAU, A. M., BRENNAN, C. W., HAMBARDZUMYAN, D. & HOLLAND, E. C. 2010. Perivascular nitric oxide activates notch signaling and promotes stem-like character in PDGF-induced glioma cells. *Cell Stem Cell,* 6**,** 141-52.

CHEN, R., NISHIMURA, M. C., BUMBACA, S. M., KHARBANDA, S., FORREST, W. F., KASMAN, I. M., GREVE, J. M., SORIANO, R. H., GILMOUR, L. L., RIVERS, C. S., MODRUSAN, Z., NACU, S., GUERRERO, S., EDGAR, K. A., WALLIN, J. J., LAMSZUS, K., WESTPHAL, M., HEIM, S., JAMES, C. D., VANDENBERG, S. R., COSTELLO, J. F., MOOREFIELD, S., COWDREY, C. J., PRADOS, M. & PHILLIPS, H. S. 2010. A hierarchy of self-renewing tumor-initiating cell types in glioblastoma. *Cancer Cell,* 17**,** 362-75.

CHINOT, O. L., WICK, W., MASON, W., HENRIKSSON, R., SARAN, F., NISHIKAWA, R., CARPENTIER, A. F., HOANG-XUAN, K., KAVAN, P., CERNEA, D., BRANDES, A. A., HILTON, M., ABREY, L. & CLOUGHESY, T. 2014. Bevacizumab plus radiotherapy-temozolomide for newly diagnosed glioblastoma. *N Engl J Med,* 370**,** 709-22.

CLARKE, M. F., DICK, J. E., DIRKS, P. B., EAVES, C. J., JAMIESON, C. H., JONES, D. L., VISVADER, J., WEISSMAN, I. L. & WAHL, G. M. 2006. Cancer stem cells--perspectives on current status and future directions: AACR Workshop on cancer stem cells. *Cancer Res,* 66**,** 9339-44.

CLEMENT, V., SANCHEZ, P., DE TRIBOLET, N., RADOVANOVIC, I. & RUIZ I ALTABA, A. 2007. HEDGEHOG-GLI1 signaling regulates human glioma growth, cancer stem cell self-renewal, and tumorigenicity. *Curr Biol,* 17**,** 165-72.

CLEVERS, H. 2011. The cancer stem cell: premises, promises and challenges. *Nat Med,* 17**,** 313-9.

COLLINGRIDGE, D. R., PIEPMEIER, J. M., ROCKWELL, S. & KNISELY, J. P. 1999. Polarographic measurements of oxygen tension in human glioma and surrounding peritumoural brain tissue. *Radiother Oncol,* 53**,** 127-31.

COLLINS, A. T., BERRY, P. A., HYDE, C., STOWER, M. J. & MAITLAND, N. J. 2005. Prospective identification of tumorigenic prostate cancer stem cells. *Cancer Res,* 65**,** 10946-51.

COLLINS, V. P. 2004. Brain tumours: classification and genes. *J Neurol Neurosurg Psychiatry,* 75 Suppl 2**,** ii2-11.

CONTI, L., POLLARD, S. M., GORBA, T., REITANO, E., TOSELLI, M., BIELLA, G., SUN, Y., SANZONE, S., YING, Q. L., CATTANEO, E. & SMITH, A. 2005. Niche-independent symmetrical self-renewal of a mammalian tissue stem cell. *PLoS Biol,* 3**,** e283.

CORBEIL, D., MARZESCO, A. M., WILSCH-BRAUNINGER, M. & HUTTNER, W. B. 2010. The intriguing links between prominin-1 (CD133), cholesterol-based membrane microdomains, remodeling of apical plasma membrane protrusions, extracellular membrane particles, and (neuro)epithelial cell differentiation. *FEBS Lett,* 584**,** 1659-64.

CORBEIL, D., ROPER, K., WEIGMANN, A. & HUTTNER, W. B. 1998. AC133 hematopoietic stem cell antigen: human homologue of mouse kidney prominin or distinct member of a novel protein family? *Blood,* 91**,** 2625-6.

CURLEY, M. D., THERRIEN, V. A., CUMMINGS, C. L., SERGENT, P. A., KOULOURIS, C. R., FRIEL, A. M., ROBERTS, D. J., SEIDEN, M. V., SCADDEN, D. T., RUEDA, B. R. & FOSTER, R. 2009. CD133 expression defines a tumor initiating cell population in primary human ovarian cancer. *Stem Cells,* 27**,** 2875-83.

DALERBA, P., DYLLA, S. J., PARK, I. K., LIU, R., WANG, X., CHO, R. W., HOEY, T., GURNEY, A., HUANG, E. H., SIMEONE, D. M., SHELTON, A. A., PARMIANI, G., CASTELLI, C. & CLARKE, M. F. 2007. Phenotypic characterization of human colorectal cancer stem cells. *Proc Natl Acad Sci U S A,* 104**,** 10158-63.

DE WITT HAMER, P. C., VAN TILBORG, A. A., EIJK, P. P., SMINIA, P., TROOST, D., VAN NOORDEN, C. J., YLSTRA, B. & LEENSTRA, S. 2008. The genomic profile of human malignant glioma is altered early in primary cell culture and preserved in spheroids. *Oncogene,* 27**,** 2091-6.

DELEYROLLE, L. P., HARDING, A., CATO, K., SIEBZEHNRUBL, F. A., RAHMAN, M., AZARI, H., OLSON, S., GABRIELLI, B., OSBORNE, G., VESCOVI, A. & REYNOLDS, B. A. 2011. Evidence for label-retaining tumour-initiating cells in human glioblastoma. *Brain,* 134**,** 1331-43.

DEMEURE, K., FACK, F., DURIEZ, E., TIEMANN, K., BERNARD, A., GOLEBIEWSKA, A., BOUGNAUD, S., BJERKVIG, R., DOMON, B. & NICLOU, S. P. 2016. Targeted Proteomics to Assess the Response to Anti-Angiogenic Treatment in Human Glioblastoma (GBM). *Mol Cell Proteomics,* 15**,** 481-92.

DENICOLAI, E., TABOURET, E., COLIN, C., METELLUS, P., NANNI, I., BOUCARD, C., TCHOGHANDJIAN, A., MEYRONET, D., BAEZA-KALLEE, N., CHINOT, O. & FIGARELLA-BRANGER, D. 2016. Molecular heterogeneity of glioblastomas: does location matter? *Oncotarget,* 7**,** 902-13.

DURANTE, F. 1874. Nesso fisio-pathologico tra la struttura dei nei materni e la genesi di alcuni tumori maligni. *Arch Memori ed Osservazioni di Chirugia Practica,* 11**,** 9.

DZWONEK, J. & WILCZYNSKI, G. M. 2015. CD44: molecular interactions, signaling and functions in the nervous system. *Front Cell Neurosci,* 9**,** 175.

EALES, K. L., HOLLINSHEAD, K. E. & TENNANT, D. A. 2016. Hypoxia and metabolic adaptation of cancer cells. *Oncogenesis,* 5**,** e190.

EASWARAN, H., TSAI, H. C. & BAYLIN, S. B. 2014. Cancer epigenetics: tumor heterogeneity, plasticity of stem-like states, and drug resistance. *Mol Cell,* 54**,** 716-27.

EGEBLAD, M., NAKASONE, E. S. & WERB, Z. 2010. Tumors as organs: complex tissues that interface with the entire organism. *Dev Cell,* 18**,** 884-901.

EGGENS, I., FENDERSON, B., TOYOKUNI, T., DEAN, B., STROUD, M. & HAKOMORI, S. 1989. Specific interaction between Lex and Lex determinants. A possible basis for cell recognition in preimplantation embryos and in embryonal carcinoma cells. *J Biol Chem,* 264**,** 9476-84.

EISENBARTH, G. S., WALSH, F. S. & NIRENBERG, M. 1979. Monoclonal antibody to a plasma membrane antigen of neurons. *Proc Natl Acad Sci U S A,* 76**,** 4913-7.

ENDERLING, H., ANDERSON, A. R., CHAPLAIN, M. A., BEHESHTI, A., HLATKY, L. & HAHNFELDT, P. 2009. Paradoxical dependencies of tumor dormancy and progression on basic cell kinetics. *Cancer Res,* 69**,** 8814-21.

ERAMO, A., RICCI-VITIANI, L., ZEUNER, A., PALLINI, R., LOTTI, F., SETTE, G., PILOZZI, E., LAROCCA, L. M., PESCHLE, C. & DE MARIA, R. 2006. Chemotherapy resistance of glioblastoma stem cells. *Cell Death Differ,* 13**,** 1238-41.

ERNST, M. & JENKINS, B. J. 2004. Acquiring signalling specificity from the cytokine receptor gp130. *Trends Genet,* 20**,** 23-32.

ESTELLER, M., GARCIA-FONCILLAS, J., ANDION, E., GOODMAN, S. N., HIDALGO, O. F., VANACLOCHA, V., BAYLIN, S. B. & HERMAN, J. G. 2000. Inactivation of the DNA-repair gene MGMT and the clinical response of gliomas to alkylating agents. *N Engl J Med,* 343**,** 1350-4.

EVANS, S. M., JENKINS, K. W., JENKINS, W. T., DILLING, T., JUDY, K. D., SCHRLAU, A., JUDKINS, A., HAHN, S. M. & KOCH, C. J. 2008. Imaging and analytical methods as applied to the evaluation of vasculature and hypoxia in human brain tumors. *Radiat Res,* 170**,** 677-90.

EVANS, S. M., JUDY, K. D., DUNPHY, I., JENKINS, W. T., NELSON, P. T., COLLINS, R., WILEYTO, E. P., JENKINS, K., HAHN, S. M., STEVENS, C. W., JUDKINS, A. R., PHILLIPS, P., GEOERGER, B. & KOCH, C. J. 2004. Comparative measurements of hypoxia in human brain tumors using needle electrodes and EF5 binding. *Cancer Res,* 64**,** 1886-92.

FARGEAS, C. A., HUTTNER, W. B. & CORBEIL, D. 2007. Nomenclature of prominin-1 (CD133) splice variants - an update. *Tissue Antigens,* 69**,** 602-6.

FEARON, E. R. & VOGELSTEIN, B. 1990. A genetic model for colorectal tumorigenesis. *Cell,* 61**,** 759-67.

FENDERSON, B. A., ZEHAVI, U. & HAKOMORI, S. 1984. A multivalent lacto-N-fucopentaose III-lysyllysine conjugate decompacts preimplantation mouse embryos, while the free oligosaccharide is ineffective. *J Exp Med,* 160**,** 1591-6.

FERLAY J, S. I., ERVIK M, DIKSHIT R, ESER S, MATHERS C, REBELO M, PARKIN DM, FORMAN D, BRAY, F 2012. Cancer Incidence and Mortality Worldwide: IARC CancerBase No. 11. *http://globocan.iarc.fr; Lyon, France: International Agency for Research on Cancer*.

FERLAY, J., STELIAROVA-FOUCHER, E., LORTET-TIEULENT, J., ROSSO, S., COEBERGH, J. W., COMBER, H., FORMAN, D. & BRAY, F. 2013. Cancer incidence and mortality patterns in Europe: estimates for 40 countries in 2012. *Eur J Cancer,* 49**,** 1374-403.

FINE, H. A. 2014. Bevacizumab in glioblastoma--still much to learn. *N Engl J Med,* 370**,** 764-5.

FORTE, S., PAGLIUCA, A., MANISCALCHI, E. T., GULINO, R., CALABRESE, G., RICCI-VITIANI, L., PALLINI, R., SIGNORE, M., PARENTI, R., DE MARIA, R. & GULISANO, M. 2013. Gene expression analysis of PTEN positive glioblastoma stem cells identifies DUB3 and Wee1 modulation in a cell differentiation model. *PLoS One,* 8**,** e81432.

FOX, N., DAMJANOV, I., MARTINEZ-HERNANDEZ, A., KNOWLES, B. B. & SOLTER, D. 1981. Immunohistochemical localization of the early embryonic antigen (SSEA-1) in postimplantation mouse embryos and fetal and adult tissues. *Dev Biol,* 83**,** 391-8.

FURNARI, F. B., FENTON, T., BACHOO, R. M., MUKASA, A., STOMMEL, J. M., STEGH, A., HAHN, W. C., LIGON, K. L., LOUIS, D. N., BRENNAN, C., CHIN, L., DEPINHO, R. A. & CAVENEE, W. K. 2007. Malignant astrocytic glioma: genetics, biology, and paths to treatment. *Genes Dev,* 21**,** 2683-710.

FURTH, J. K., M. 1937. The transmission of leukemia of mice with a single cell. *Am J Cancer,* 31**,** 6.

GALLI, R., BINDA, E., ORFANELLI, U., CIPELLETTI, B., GRITTI, A., DE VITIS, S., FIOCCO, R., FORONI, C., DIMECO, F. & VESCOVI, A. 2004. Isolation and characterization of tumorigenic, stem-like neural precursors from human glioblastoma. *Cancer Res,* 64**,** 7011-21.

GERSTNER, E. R. & BATCHELOR, T. T. 2012. Antiangiogenic therapy for glioblastoma. *Cancer J,* 18**,** 45-50.

GHODS, A. J., IRVIN, D., LIU, G., YUAN, X., ABDULKADIR, I. R., TUNICI, P., KONDA, B., WACHSMANN-HOGIU, S., BLACK, K. L. & YU, J. S. 2007. Spheres isolated from 9L gliosarcoma rat cell line possess chemoresistant and aggressive cancer stem-like cells. *Stem Cells,* 25**,** 1645-53.

GINESTIER, C., HUR, M. H., CHARAFE-JAUFFRET, E., MONVILLE, F., DUTCHER, J., BROWN, M., JACQUEMIER, J., VIENS, P., KLEER, C. G., LIU, S., SCHOTT, A., HAYES, D., BIRNBAUM, D., WICHA, M. S. & DONTU, G. 2007. ALDH1 is a marker of normal and malignant human mammary stem cells and a predictor of poor clinical outcome. *Cell Stem Cell,* 1**,** 555-67.

GOLEBIEWSKA, A., BOUGNAUD, S., STIEBER, D., BRONS, N. H., VALLAR, L., HERTEL, F., KLINK, B., SCHROCK, E., BJERKVIG, R. & NICLOU, S. P. 2013. Side population in human glioblastoma is non-tumorigenic and characterizes brain endothelial cells. *Brain,* 136**,** 1462-75.

GOMPERTS, M., GARCIA-CASTRO, M., WYLIE, C. & HEASMAN, J. 1994. Interactions between primordial germ cells play a role in their migration in mouse embryos. *Development,* 120**,** 135-41.

GRAEBER, T. G., OSMANIAN, C., JACKS, T., HOUSMAN, D. E., KOCH, C. J., LOWE, S. W. & GIACCIA, A. J. 1996. Hypoxia-mediated selection of cells with diminished apoptotic potential in solid tumours. *Nature,* 379**,** 88-91.

GREAVES, M. & MALEY, C. C. 2012. Clonal evolution in cancer. *Nature,* 481**,** 306-13.

GREEN, C. L., LOKEN, M., BUCK, D. & DEEG, H. J. 2000. Discordant expression of AC133 and AC141 in patients with myelodysplastic syndrome (MDS) and acute myelogeneous leukemia (AML). *Leukemia,* 14**,** 770-2.

GRIGUER, C. E., OLIVA, C. R., GOBIN, E., MARCORELLES, P., BENOS, D. J., LANCASTER, J. R., JR. & GILLESPIE, G. Y. 2008. CD133 is a marker of bioenergetic stress in human glioma. *PLoS One,* 3**,** e3655.

GUADAGNO, E., BORRELLI, G., CALIFANO, M., CALI, G., SOLARI, D. & DEL BASSO DE CARO, M. 2016. Immunohistochemical expression of stem cell markers CD44 and nestin in glioblastomas: Evaluation of their prognostic significance. *Pathol Res Pract,* 212**,** 825-32.

GUNTHER, H. S., SCHMIDT, N. O., PHILLIPS, H. S., KEMMING, D., KHARBANDA, S., SORIANO, R., MODRUSAN, Z., MEISSNER, H., WESTPHAL, M. & LAMSZUS, K. 2008. Glioblastoma-derived stem cell-enriched cultures form distinct subgroups according to molecular and phenotypic criteria. *Oncogene,* 27**,** 2897-909.

GUPTA, P. B., FILLMORE, C. M., JIANG, G., SHAPIRA, S. D., TAO, K., KUPERWASSER, C. & LANDER, E. S. 2011. Stochastic state transitions give rise to phenotypic equilibrium in populations of cancer cells. *Cell,* 146**,** 633-44.

GUPTA, R. G. & SOMER, R. A. 2017. Intratumor Heterogeneity: Novel Approaches for Resolving Genomic Architecture and Clonal Evolution. *Mol Cancer Res,* 15**,** 1127-1137.

HALEY, E. M. & KIM, Y. 2014. The role of basic fibroblast growth factor in glioblastoma multiforme and glioblastoma stem cells and in their in vitro culture. *Cancer Lett,* 346**,** 1-5.

HALL, P. A. & D'ARDENNE, A. J. 1987. Value of CD15 immunostaining in diagnosing Hodgkin's disease: a review of published literature. *J Clin Pathol,* 40**,** 1298-304.

HAMBARDZUMYAN, D. & BERGERS, G. 2015. Glioblastoma: Defining Tumor Niches. *Trends Cancer,* 1**,** 252-265.

HAN, Y., WANG, H., HUANG, Y., CHENG, Z., SUN, T., CHEN, G., XIE, X., ZHOU, Y. & DU, Z. 2015. Isolation and characteristics of CD133/A2B5+ and CD133/A2B5 cells from the SHG139s cell line. *Mol Med Rep,* 12**,** 7949-56.

HANAHAN, D. & WEINBERG, R. A. 2000. The hallmarks of cancer. *Cell,* 100**,** 57-70.

HANAHAN, D. & WEINBERG, R. A. 2011. Hallmarks of cancer: the next generation. *Cell,* 144**,** 646-74.

HE, J., LIU, Y., ZHU, T., ZHU, J., DIMECO, F., VESCOVI, A. L., HETH, J. A., MURASZKO, K. M., FAN, X. & LUBMAN, D. M. 2012. CD90 is identified as a candidate marker for cancer stem cells in primary high-grade gliomas using tissue microarrays. *Mol Cell Proteomics,* 11**,** M111 010744.

HE, S., NAKADA, D. & MORRISON, S. J. 2009. Mechanisms of stem cell self-renewal. *Annu Rev Cell Dev Biol,* 25**,** 377-406.

HEBERT, T. L., WU, X., YU, G., GOH, B. C., HALVORSEN, Y. D., WANG, Z., MORO, C. & GIMBLE, J. M. 2009. Culture effects of epidermal growth factor (EGF) and basic fibroblast growth factor (bFGF) on cryopreserved human adipose-derived stromal/stem cell proliferation and adipogenesis. *J Tissue Eng Regen Med,* 3**,** 553-61.

HEDDLESTON, J. M., HITOMI, M., VENERE, M., FLAVAHAN, W. A., YANG, K., KIM, Y., MINHAS, S., RICH, J. N. & HJELMELAND, A. B. 2011. Glioma stem cell maintenance: the role of the microenvironment. *Curr Pharm Des,* 17**,** 2386-401.

HEDDLESTON, J. M., LI, Z., MCLENDON, R. E., HJELMELAND, A. B. & RICH, J. N. 2009. The hypoxic microenvironment maintains glioblastoma stem cells and promotes reprogramming towards a cancer stem cell phenotype. *Cell Cycle,* 8**,** 3274-84.

HEGI, M. E., DISERENS, A. C., GORLIA, T., HAMOU, M. F., DE TRIBOLET, N., WELLER, M., KROS, J. M., HAINFELLNER, J. A., MASON, W., MARIANI, L., BROMBERG, J. E., HAU, P., MIRIMANOFF, R. O., CAIRNCROSS, J. G., JANZER, R. C. & STUPP, R. 2005. MGMT gene silencing and benefit from temozolomide in glioblastoma. *N Engl J Med,* 352**,** 997-1003.

HJELMELAND, A. B., LATHIA, J. D., SATHORNSUMETEE, S. & RICH, J. N. 2011a. Twisted tango: brain tumor neurovascular interactions. *Nat Neurosci,* 14**,** 1375-81.

HJELMELAND, A. B., WU, Q., HEDDLESTON, J. M., CHOUDHARY, G. S., MACSWORDS, J., LATHIA, J. D., MCLENDON, R., LINDNER, D., SLOAN, A. & RICH, J. N. 2011b. Acidic stress promotes a glioma stem cell phenotype. *Cell Death Differ,* 18**,** 829-40.

HOLMQUIST-MENGELBIER, L., FREDLUND, E., LOFSTEDT, T., NOGUERA, R., NAVARRO, S., NILSSON, H., PIETRAS, A., VALLON-CHRISTERSSON, J., BORG, A., GRADIN, K., POELLINGER, L. & PAHLMAN, S. 2006. Recruitment of HIF-1alpha and HIF-2alpha to common target genes is differentially regulated in neuroblastoma: HIF-2alpha promotes an aggressive phenotype. *Cancer Cell,* 10**,** 413-23.

HOLMQUIST, L., JOGI, A. & PAHLMAN, S. 2005. Phenotypic persistence after reoxygenation of hypoxic neuroblastoma cells. *Int J Cancer,* 116**,** 218-25.

HSIEH, A., ELLSWORTH, R. & HSIEH, D. 2011. Hedgehog/GLI1 regulates IGF dependent malignant behaviors in glioma stem cells. *J Cell Physiol,* 226**,** 1118-27.

HU, Y. & SMYTH, G. K. 2009. ELDA: extreme limiting dilution analysis for comparing depleted and enriched populations in stem cell and other assays. *J Immunol Methods,* 347**,** 70-8.

HU, Y. L., DELAY, M., JAHANGIRI, A., MOLINARO, A. M., ROSE, S. D., CARBONELL, W. S. & AGHI, M. K. 2012. Hypoxia-induced autophagy promotes tumor cell survival and adaptation to antiangiogenic treatment in glioblastoma. *Cancer Res,* 72**,** 1773-83.

HUBBI, M. E. & SEMENZA, G. L. 2015. Regulation of cell proliferation by hypoxia-inducible factors. *Am J Physiol Cell Physiol,* 309**,** C775-82.

IGNATOVA, T. N., KUKEKOV, V. G., LAYWELL, E. D., SUSLOV, O. N., VRIONIS, F. D. & STEINDLER, D. A. 2002. Human cortical glial tumors contain neural stem-like cells expressing astroglial and neuronal markers in vitro. *Glia,* 39**,** 193-206.

INOUE, A., TANAKA, J., TAKAHASHI, H., KOHNO, S., OHUE, S., UMAKOSHI, A., GOTOH, K. & OHNISHI, T. 2016. Blood vessels expressing CD90 in human and rat brain tumors. *Neuropathology,* 36**,** 168-80.

ISHIGURO, T., OHATA, H., SATO, A., YAMAWAKI, K., ENOMOTO, T. & OKAMOTO, K. 2017. Tumor-derived spheroids: Relevance to cancer stem cells and clinical applications. *Cancer Sci,* 108**,** 283-289.

ISHII, S., FORD, R., THOMAS, P., NACHMAN, A., STEELE, G., JR. & JESSUP, J. M. 1993. CD44 participates in the adhesion of human colorectal carcinoma cells to laminin and type IV collagen. *Surg Oncol,* 2**,** 255-64.

JAGGUPILLI, A. & ELKORD, E. 2012. Significance of CD44 and CD24 as cancer stem cell markers: an enduring ambiguity. *Clin Dev Immunol,* 2012**,** 708036.

JAKSCH, M., MUNERA, J., BAJPAI, R., TERSKIKH, A. & OSHIMA, R. G. 2008. Cell cycle-dependent variation of a CD133 epitope in human embryonic stem cell, colon cancer, and melanoma cell lines. *Cancer Res,* 68**,** 7882-6.

JIJIWA, M., DEMIR, H., GUPTA, S., LEUNG, C., JOSHI, K., OROZCO, N., HUANG, T., YILDIZ, V. O., SHIBAHARA, I., DE JESUS, J. A., YONG, W. H., MISCHEL, P. S., FERNANDEZ, S., KORNBLUM, H. I. & NAKANO, I. 2011. CD44v6 regulates growth of brain tumor stem cells partially through the AKT-mediated pathway. *PLoS One,* 6**,** e24217.

JORDAN, C. T. 2009. Cancer stem cells: controversial or just misunderstood? *Cell Stem Cell,* 4**,** 203-5.

JOSEPH, J. V., CONROY, S., PAVLOV, K., SONTAKKE, P., TOMAR, T., EGGENS-MEIJER, E., BALASUBRAMANIYAN, V., WAGEMAKERS, M., DEN DUNNEN, W. F. & KRUYT, F. A. 2015.

Hypoxia enhances migration and invasion in glioblastoma by promoting a mesenchymal shift mediated by the HIF1alpha-ZEB1 axis. *Cancer Lett,* 359**,** 107-16.

JURAFSKY, D. M., JH. 2008. *Speech and Language Processing*, Prentice Hall.

KATAGIRI, Y. U., SLEEMAN, J., FUJII, H., HERRLICH, P., HOTTA, H., TANAKA, K., CHIKUMA, S., YAGITA, H., OKUMURA, K., MURAKAMI, M., SAIKI, I., CHAMBERS, A. F. & UEDE, T. 1999. CD44 variants but not CD44s cooperate with beta1-containing integrins to permit cells to bind to osteopontin independently of arginine-glycine-aspartic acid, thereby stimulating cell motility and chemotaxis. *Cancer Res,* 59**,** 219-26.

KELLY, P. N., DAKIC, A., ADAMS, J. M., NUTT, S. L. & STRASSER, A. 2007. Tumor growth need not be driven by rare cancer stem cells. *Science,* 317**,** 337.

KEMPER, K., SPRICK, M. R., DE BREE, M., SCOPELLITI, A., VERMEULEN, L., HOEK, M., ZEILSTRA, J., PALS, S. T., MEHMET, H., STASSI, G. & MEDEMA, J. P. 2010. The AC133 epitope, but not the CD133 protein, is lost upon cancer stem cell differentiation. *Cancer Res,* 70**,** 719-29.

KENNEY-HERBERT, E., AL-MAYHANI, T., PICCIRILLO, S. G., FOWLER, J., SPITERI, I., JONES, P. & WATTS, C. 2015. CD15 Expression Does Not Identify a Phenotypically or Genetically Distinct Glioblastoma Population. *Stem Cells Transl Med,* 4**,** 822-31.

KEUNEN, O., JOHANSSON, M., OUDIN, A., SANZEY, M., ABDUL RAHIM, S. A., FACK, F., THORSEN, F., TAXT, T., BARTOS, M., JIRIK, R., MILETIC, H., WANG, J., STIEBER, D., STUHR, L., MOEN, I., RYGH, C. B., BJERKVIG, R. & NICLOU, S. P. 2011. Anti-VEGF treatment reduces blood supply and increases tumor cell invasion in glioblastoma. *Proc Natl Acad Sci U S A*.

KIM, H., ZHENG, S., AMINI, S. S., VIRK, S. M., MIKKELSEN, T., BRAT, D. J., GRIMSBY, J., SOUGNEZ, C., MULLER, F., HU, J., SLOAN, A. E., COHEN, M. L., VAN MEIR, E. G., SCARPACE, L., LAIRD, P. W., WEINSTEIN, J. N., LANDER, E. S., GABRIEL, S., GETZ, G., MEYERSON, M., CHIN, L., BARNHOLTZ-SLOAN, J. S. & VERHAAK, R. G. 2015. Whole-genome and multisector exome sequencing of primary and post-treatment glioblastoma reveals patterns of tumor evolution. *Genome Res,* 25**,** 316-27.

KINDT, N., JOURNE, F., LAURENT, G. & SAUSSEZ, S. 2016. Involvement of macrophage migration inhibitory factor in cancer and novel therapeutic targets. *Oncol Lett,* 12**,** 2247-2253.

KLEBER, S., SANCHO-MARTINEZ, I., WIESTLER, B., BEISEL, A., GIEFFERS, C., HILL, O., THIEMANN, M., MUELLER, W., SYKORA, J., KUHN, A., SCHREGLMANN, N., LETELLIER, E., ZULIANI, C., KLUSSMANN, S., TEODORCZYK, M., GRONE, H. J., GANTEN, T. M., SULTMANN, H., TUTTENBERG, J., VON DEIMLING, A., REGNIER-VIGOUROUX, A., HEROLD-MENDE, C. & MARTIN-VILLALBA, A. 2008. Yes and PI3K bind CD95 to signal invasion of glioblastoma. *Cancer Cell,* 13**,** 235-48.

KLEIHUES, P., BURGER, P. C. & SCHEITHAUER, B. W. E. 1993. *Histological Typing of Tumours of the Central Nervous System. World Health Organization International Histological Classification of Tumours.,* Berlin Heidelberg, Springer Verlag.

KOOCHEKPOUR, S., MERZAK, A. & PILKINGTON, G. J. 1996. Vascular endothelial growth factor production is stimulated by gangliosides and TGF-beta isoforms in human glioma cells in vitro. *Cancer Lett,* 102**,** 209-15.

KRACKHARDT, D. 1994. Graph theoretical dimensions of informal organizations. *Computational organization theory,* 89**,** 123-140.

KRESO, A., O'BRIEN, C. A., VAN GALEN, P., GAN, O. I., NOTTA, F., BROWN, A. M., NG, K., MA, J., WIENHOLDS, E., DUNANT, C., POLLETT, A., GALLINGER, S., MCPHERSON, J., MULLIGHAN, C. G., SHIBATA, D. & DICK, J. E. 2013. Variable clonal repopulation dynamics influence chemotherapy response in colorectal cancer. *Science,* 339**,** 543-8.

KROGH PETERSEN, J., JENSEN, P., DAHL SORENSEN, M. & WINTHER KRISTENSEN, B. 2016. Expression and Prognostic Value of Oct-4 in Astrocytic Brain Tumors. *PLoS One,* 11**,** e0169129.

KUMAR, A., BOYLE, E. A., TOKITA, M., MIKHEEV, A. M., SANGER, M. C., GIRARD, E., SILBER, J. R., GONZALEZ-CUYAR, L. F., HIATT, J. B., ADEY, A., LEE, C., KITZMAN, J. O., BORN, D. E.,

SILBERGELD, D. L., OLSON, J. M., ROSTOMILY, R. C. & SHENDURE, J. 2014. Deep sequencing of multiple regions of glial tumors reveals spatial heterogeneity for mutations in clinically relevant genes. *Genome Biol,* 15**,** 530.

KUMAR, H. & CHOI, D. K. 2015. Hypoxia Inducible Factor Pathway and Physiological Adaptation: A Cell Survival Pathway? *Mediators Inflamm,* 2015**,** 584758.

LATHIA, J. D., GALLAGHER, J., HEDDLESTON, J. M., WANG, J., EYLER, C. E., MACSWORDS, J., WU, Q., VASANJI, A., MCLENDON, R. E., HJELMELAND, A. B. & RICH, J. N. 2010. Integrin alpha 6 regulates glioblastoma stem cells. *Cell Stem Cell,* 6**,** 421-32.

LATHIA, J. D., HEDDLESTON, J. M., VENERE, M. & RICH, J. N. 2011a. Deadly teamwork: neural cancer stem cells and the tumor microenvironment. *Cell Stem Cell,* 8**,** 482-5.

LATHIA, J. D., HITOMI, M., GALLAGHER, J., GADANI, S. P., ADKINS, J., VASANJI, A., LIU, L., EYLER, C. E., HEDDLESTON, J. M., WU, Q., MINHAS, S., SOEDA, A., HOEPPNER, D. J., RAVIN, R., MCKAY, R. D., MCLENDON, R. E., CORBEIL, D., CHENN, A., HJELMELAND, A. B., PARK, D. M. & RICH, J. N. 2011b. Distribution of CD133 reveals glioma stem cells self-renew through symmetric and asymmetric cell divisions. *Cell Death Dis,* 2**,** e200.

LEE, J., KOTLIAROVA, S., KOTLIAROV, Y., LI, A., SU, Q., DONIN, N. M., PASTORINO, S., PUROW, B. W., CHRISTOPHER, N., ZHANG, W., PARK, J. K. & FINE, H. A. 2006. Tumor stem cells derived from glioblastomas cultured in bFGF and EGF more closely mirror the phenotype and genotype of primary tumors than do serum-cultured cell lines. *Cancer Cell,* 9**,** 391-403.

LEE, J., SON, M. J., WOOLARD, K., DONIN, N. M., LI, A., CHENG, C. H., KOTLIAROVA, S., KOTLIAROV, Y., WALLING, J., AHN, S., KIM, M., TOTONCHY, M., CUSACK, T., ENE, C., MA, H., SU, Q., ZENKLUSEN, J. C., ZHANG, W., MARIC, D. & FINE, H. A. 2008. Epigenetic-mediated dysfunction of the bone morphogenetic protein pathway inhibits differentiation of glioblastoma-initiating cells. *Cancer Cell,* 13**,** 69-80.

LEE, J. K., WANG, J., SA, J. K., LADEWIG, E., LEE, H. O., LEE, I. H., KANG, H. J., ROSENBLOOM, D. S., CAMARA, P. G., LIU, Z., VAN NIEUWENHUIZEN, P., JUNG, S. W., CHOI, S. W., KIM, J., CHEN, A., KIM, K. T., SHIN, S., SEO, Y. J., OH, J. M., SHIN, Y. J., PARK, C. K., KONG, D. S., SEOL, H. J., BLUMBERG, A., LEE, J. I., IAVARONE, A., PARK, W. Y., RABADAN, R. & NAM, D. H. 2017. Spatiotemporal genomic architecture informs precision oncology in glioblastoma. *Nat Genet,* 49**,** 594-599.

LEHMANN, C., JOBS, G., THOMAS, M., BURTSCHER, H. & KUBBIES, M. 2012. Established breast cancer stem cell markers do not correlate with in vivo tumorigenicity of tumor-initiating cells. *Int J Oncol,* 41**,** 1932-42.

LEMKE, D., WEILER, M., BLAES, J., WIESTLER, B., JESTAEDT, L., KLEIN, A. C., LOW, S., EISELE, G., RADLWIMMER, B., CAPPER, D., SCHMIEDER, K., MITTELBRONN, M., COMBS, S. E., BENDSZUS, M., WELLER, M., PLATTEN, M. & WICK, W. 2014. Primary glioblastoma cultures: can profiling of stem cell markers predict radiotherapy sensitivity? *J Neurochem,* 131**,** 251-64.

LEUNG, E. L., FISCUS, R. R., TUNG, J. W., TIN, V. P., CHENG, L. C., SIHOE, A. D., FINK, L. M., MA, Y. & WONG, M. P. 2010. Non-small cell lung cancer cells expressing CD44 are enriched for stem cell-like properties. *PLoS One,* 5**,** e14062.

LI, C., HEIDT, D. G., DALERBA, P., BURANT, C. F., ZHANG, L., ADSAY, V., WICHA, M., CLARKE, M. F. & SIMEONE, D. M. 2007. Identification of pancreatic cancer stem cells. *Cancer Res,* 67**,** 1030-7.

LI, H., TONG, S., LIU, J., HAN, L., YANG, X., HOU, H., YAN, Q. & WANG, X. Q. 2012. Differential fucosyltransferase IV expression in squamous carcinoma cells is regulated by promoter methylation. *Cell Mol Biol Lett,* 17**,** 206-16.

LI, Z., BAO, S., WU, Q., WANG, H., EYLER, C., SATHORNSUMETEE, S., SHI, Q., CAO, Y., LATHIA, J., MCLENDON, R. E., HJELMELAND, A. B. & RICH, J. N. 2009. Hypoxia-inducible factors regulate tumorigenic capacity of glioma stem cells. *Cancer Cell,* 15**,** 501-13.

LIGON, K. L., ALBERTA, J. A., KHO, A. T., WEISS, J., KWAAN, M. R., NUTT, C. L., LOUIS, D. N., STILES, C. D. & ROWITCH, D. H. 2004. The oligodendroglial lineage marker OLIG2 is universally expressed in diffuse gliomas. *J Neuropathol Exp Neurol,* 63**,** 499-509.

LIN, Q. & YUN, Z. 2010. Impact of the hypoxic tumor microenvironment on the regulation of cancer stem cell characteristics. *Cancer Biol Ther,* 9**,** 949-56.

LIU, A., YU, Q., PENG, Z., HUANG, Y., DIAO, S., CHENG, J., WANG, W. & HONG, M. 2017. miR-200b inhibits CD133+ glioma cells by targeting the AKT pathway. *Oncol Lett,* 13**,** 4701-4707.

LIU, D., MARTIN, V., FUEYO, J., LEE, O. H., XU, J., CORTES-SANTIAGO, N., ALONSO, M. M., ALDAPE, K., COLMAN, H. & GOMEZ-MANZANO, C. 2010. Tie2/TEK modulates the interaction of glioma and brain tumor stem cells with endothelial cells and promotes an invasive phenotype. *Oncotarget,* 1**,** 700-9.

LIU, G., YUAN, X., ZENG, Z., TUNICI, P., NG, H., ABDULKADIR, I. R., LU, L., IRVIN, D., BLACK, K. L. & YU, J. S. 2006. Analysis of gene expression and chemoresistance of CD133+ cancer stem cells in glioblastoma. *Mol Cancer,* 5**,** 67.

LIU, P., BROWN, S., GOKTUG, T., CHANNATHODIYIL, P., KANNAPPAN, V., HUGNOT, J. P., GUICHET, P. O., BIAN, X., ARMESILLA, A. L., DARLING, J. L. & WANG, W. 2012. Cytotoxic effect of disulfiram/copper on human glioblastoma cell lines and ALDH-positive cancer-stem-like cells. *Br J Cancer,* 107**,** 1488-97.

LONG, H., XIE, R., XIANG, T., ZHAO, Z., LIN, S., LIANG, Z., CHEN, Z. & ZHU, B. 2012. Autocrine CCL5 signaling promotes invasion and migration of CD133+ ovarian cancer stem-like cells via NF-kappaB-mediated MMP-9 upregulation. *Stem Cells,* 30**,** 2309-19.

LOTTAZ, C., BEIER, D., MEYER, K., KUMAR, P., HERMANN, A., SCHWARZ, J., JUNKER, M., OEFNER, P. J., BOGDAHN, U., WISCHHUSEN, J., SPANG, R., STORCH, A. & BEIER, C. P. 2010. Transcriptional profiles of CD133+ and CD133- glioblastoma-derived cancer stem cell lines suggest different cells of origin. *Cancer Res,* 70**,** 2030-40.

LOUIS, D. N., OHGAKI, H., WIESTLER, O. D., CAVENEE, W. K., BURGER, P. C., JOUVET, A., SCHEITHAUER, B. W. & KLEIHUES, P. 2007. The 2007 WHO classification of tumours of the central nervous system. *Acta Neuropathol,* 114**,** 97-109.

LOUIS, D. N., PERRY, A., REIFENBERGER, G., VON DEIMLING, A., FIGARELLA-BRANGER, D., CAVENEE, W. K., OHGAKI, H., WIESTLER, O. D., KLEIHUES, P. & ELLISON, D. W. 2016. The 2016 World Health Organization Classification of Tumors of the Central Nervous System: a summary. *Acta Neuropathol,* 131**,** 803-20.

LOVE, M. I., HUBER, W. & ANDERS, S. 2014. Moderated estimation of fold change and dispersion for RNA-seq data with DESeq2. *Genome Biol,* 15**,** 550.

MA, S., CHAN, K. W., HU, L., LEE, T. K., WO, J. Y., NG, I. O., ZHENG, B. J. & GUAN, X. Y. 2007. Identification and characterization of tumorigenic liver cancer stem/progenitor cells. *Gastroenterology,* 132**,** 2542-56.

MACOSKO, E. Z., BASU, A., SATIJA, R., NEMESH, J., SHEKHAR, K., GOLDMAN, M., TIROSH, I., BIALAS, A. R., KAMITAKI, N., MARTERSTECK, E. M., TROMBETTA, J. J., WEITZ, D. A., SANES, J. R., SHALEK, A. K., REGEV, A. & MCCARROLL, S. A. 2015. Highly Parallel Genome-wide Expression Profiling of Individual Cells Using Nanoliter Droplets. *Cell,* 161**,** 1202-1214.

MANGRAVITI, A., TZENG, S. Y., GULLOTTI, D., KOZIELSKI, K. L., KIM, J. E., SENG, M., ABBADI, S., SCHIAPPARELLI, P., SARABIA-ESTRADA, R., VESCOVI, A., BREM, H., OLIVI, A., TYLER, B., GREEN, J. J. & QUINONES-HINOJOSA, A. 2016. Non-virally engineered human adipose mesenchymal stem cells produce BMP4, target brain tumors, and extend survival. *Biomaterials,* 100**,** 53-66.

MAO, X. G., ZHANG, X., XUE, X. Y., GUO, G., WANG, P., ZHANG, W., FEI, Z., ZHEN, H. N., YOU, S. W. & YANG, H. 2009. Brain Tumor Stem-Like Cells Identified by Neural Stem Cell Marker CD15. *Transl Oncol,* 2**,** 247-57.

MARANI, E., VAN OERS, J. W., TETTEROO, P. A., POELMANN, R. E., VAN DER VEEKEN, J. & DEENEN, M. G. 1986. Stage specific embryonic carbohydrate surface antigens of primordial germ

cells in mouse embryos: FAL (S.S.E.A.-1) and globoside (S.S.E.A.-3). *Acta Morphol Neerl Scand,* 24**,** 103-10.

MARCUCCI, F., RUMIO, C. & LEFOULON, F. 2016. Anti-Cancer Stem-like Cell Compounds in Clinical Development - An Overview and Critical Appraisal. *Front Oncol,* 6**,** 115.

MARUSYK, A. & POLYAK, K. 2010. Tumor heterogeneity: causes and consequences. *Biochim Biophys Acta,* 1805**,** 105-17.

MAZURE, N. M. & POUYSSEGUR, J. 2010. Hypoxia-induced autophagy: cell death or cell survival? *Curr Opin Cell Biol,* 22**,** 177-80.

MAZUTIS, L., GILBERT, J., UNG, W. L., WEITZ, D. A., GRIFFITHS, A. D. & HEYMAN, J. A. 2013. Single-cell analysis and sorting using droplet-based microfluidics. *Nat Protoc,* 8**,** 870-91.

MCCORD, A. M., JAMAL, M., SHANKAVARAM, U. T., LANG, F. F., CAMPHAUSEN, K. & TOFILON, P. J. 2009. Physiologic oxygen concentration enhances the stem-like properties of CD133+ human glioblastoma cells in vitro. *Mol Cancer Res,* 7**,** 489-97.

MEACHAM, C. E. & MORRISON, S. J. 2013. Tumour heterogeneity and cancer cell plasticity. *Nature,* 501**,** 328-37.

MEGOVA, M., DRABEK, J., KOUDELAKOVA, V., TROJANEC, R., KALITA, O. & HAJDUCH, M. 2014. Isocitrate dehydrogenase 1 and 2 mutations in gliomas. *J Neurosci Res,* 92**,** 1611-20.

MELLAI, M., MONZEGLIO, O., PIAZZI, A., CALDERA, V., ANNOVAZZI, L., CASSONI, P., VALENTE, G., CORDERA, S., MOCELLINI, C. & SCHIFFER, D. 2012. MGMT promoter hypermethylation and its associations with genetic alterations in a series of 350 brain tumors. *J Neurooncol,* 107**,** 617-31.

MEYER, M., REIMAND, J., LAN, X., HEAD, R., ZHU, X., KUSHIDA, M., BAYANI, J., PRESSEY, J. C., LIONEL, A. C., CLARKE, I. D., CUSIMANO, M., SQUIRE, J. A., SCHERER, S. W., BERNSTEIN, M., WOODIN, M. A., BADER, G. D. & DIRKS, P. B. 2015. Single cell-derived clonal analysis of human glioblastoma links functional and genomic heterogeneity. *Proc Natl Acad Sci U S A,* 112**,** 851-6.

MILLER, C. R. & PERRY, A. 2007. Glioblastoma. *Arch Pathol Lab Med,* 131**,** 397-406.

MILOTTI, E., STELLA, S. & CHIGNOLA, R. 2017. Pulsation-limited oxygen diffusion in the tumour microenvironment. *Sci Rep,* 7**,** 39762.

MIRAGLIA, S., GODFREY, W., YIN, A. H., ATKINS, K., WARNKE, R., HOLDEN, J. T., BRAY, R. A., WALLER, E. K. & BUCK, D. W. 1997. A novel five-transmembrane hematopoietic stem cell antigen: isolation, characterization, and molecular cloning. *Blood,* 90**,** 5013-21.

MITTELBRONN, M., PLATTEN, M., ZEINER, P., DOMBROWSKI, Y., FRANK, B., ZACHSKORN, C., HARTER, P. N., WELLER, M. & WISCHHUSEN, J. 2011. Macrophage migration inhibitory factor (MIF) expression in human malignant gliomas contributes to immune escape and tumour progression. *Acta Neuropathol,* 122**,** 353-65.

MOHYELDIN, A., GARZON-MUVDI, T. & QUINONES-HINOJOSA, A. 2010. Oxygen in stem cell biology: a critical component of the stem cell niche. *Cell Stem Cell,* 7**,** 150-61.

MONTI, A. F., FRIGERIO, M. & FRIGERIO, G. 2003. Visual verification of linac light and radiation fields coincidence. *Med Dosim,* 28**,** 91-3.

MONZANI, E., FACCHETTI, F., GALMOZZI, E., CORSINI, E., BENETTI, A., CAVAZZIN, C., GRITTI, A., PICCININI, A., PORRO, D., SANTINAMI, M., INVERNICI, G., PARATI, E., ALESSANDRI, G. & LA PORTA, C. A. 2007. Melanoma contains CD133 and ABCG2 positive cells with enhanced tumourigenic potential. *Eur J Cancer,* 43**,** 935-46.

MORATH, I., HARTMANN, T. N. & ORIAN-ROUSSEAU, V. 2016. CD44: More than a mere stem cell marker. *Int J Biochem Cell Biol,* 81**,** 166-173.

MORI, H., NINOMIYA, K., KINO-OKA, M., SHOFUDA, T., ISLAM, M. O., YAMASAKI, M., OKANO, H., TAYA, M. & KANEMURA, Y. 2006. Effect of neurosphere size on the growth rate of human neural stem/progenitor cells. *J Neurosci Res,* 84**,** 1682-91.

MOSOYAN, G., NAGI, C., MARUKIAN, S., TEIXEIRA, A., SIMONIAN, A., RESNICK-SILVERMAN, L., DIFEO, A., JOHNSTON, D., REYNOLDS, S. R., ROSES, D. F. & MOSOIAN, A. 2013. Multiple

breast cancer cell-lines derived from a single tumor differ in their molecular characteristics and tumorigenic potential. *PLoS One,* 8**,** e55145.

NAVIN, N., KENDALL, J., TROGE, J., ANDREWS, P., RODGERS, L., MCINDOO, J., COOK, K., STEPANSKY, A., LEVY, D., ESPOSITO, D., MUTHUSWAMY, L., KRASNITZ, A., MCCOMBIE, W. R., HICKS, J. & WIGLER, M. 2011. Tumour evolution inferred by single-cell sequencing. *Nature,* 472**,** 90-4.

NICLOU, S. P., DANZEISEN, C., EIKESDAL, H. P., WIIG, H., BRONS, N. H., POLI, A. M., SVENDSEN, A., TORSVIK, A., ENGER, P. O., TERZIS, J. A. & BJERKVIG, R. 2008. A novel eGFP-expressing immunodeficient mouse model to study tumor-host interactions. *Faseb J,* 22**,** 3120-8.

NOWELL, P. C. 1976. The clonal evolution of tumor cell populations. *Science,* 194**,** 23-8.

O'BRIEN, C. A., POLLETT, A., GALLINGER, S. & DICK, J. E. 2007. A human colon cancer cell capable of initiating tumour growth in immunodeficient mice. *Nature,* 445**,** 106-10.

OGDEN, A. T., WAZIRI, A. E., LOCHHEAD, R. A., FUSCO, D., LOPEZ, K., ELLIS, J. A., KANG, J., ASSANAH, M., MCKHANN, G. M., SISTI, M. B., MCCORMICK, P. C., CANOLL, P. & BRUCE, J. N. 2008. Identification of A2B5+CD133- tumor-initiating cells in adult human gliomas. *Neurosurgery,* 62**,** 505-14; discussion 514-5.

OHGAKI, H. & KLEIHUES, P. 2013. The definition of primary and secondary glioblastoma. *Clin Cancer Res,* 19**,** 764-72.

OLSSON, R., MAXHUNI, A. & CARLSSON, P. O. 2006. Revascularization of transplanted pancreatic islets following culture with stimulators of angiogenesis. *Transplantation,* 82**,** 340-7.

PALLINI, R., RICCI-VITIANI, L., BANNA, G. L., SIGNORE, M., LOMBARDI, D., TODARO, M., STASSI, G., MARTINI, M., MAIRA, G., LAROCCA, L. M. & DE MARIA, R. 2008. Cancer stem cell analysis and clinical outcome in patients with glioblastoma multiforme. *Clin Cancer Res,* 14**,** 8205-12.

PARANJPE, A., ZHANG, R., ALI-OSMAN, F., BOBUSTUC, G. C. & SRIVENUGOPAL, K. S. 2014. Disulfiram is a direct and potent inhibitor of human O6-methylguanine-DNA methyltransferase (MGMT) in brain tumor cells and mouse brain and markedly increases the alkylating DNA damage. *Carcinogenesis,* 35**,** 692-702.

PARK, N. I., GUILHAMON, P., DESAI, K., MCADAM, R. F., LANGILLE, E., O'CONNOR, M., LAN, X., WHETSTONE, H., COUTINHO, F. J., VANNER, R. J., LING, E., PRINOS, P., LEE, L., SELVADURAI, H., ATWAL, G., KUSHIDA, M., CLARKE, I. D., VOISIN, V., CUSIMANO, M. D., BERNSTEIN, M., DAS, S., BADER, G., ARROWSMITH, C. H., ANGERS, S., HUANG, X., LUPIEN, M. & DIRKS, P. B. 2017. ASCL1 Reorganizes Chromatin to Direct Neuronal Fate and Suppress Tumorigenicity of Glioblastoma Stem Cells. *Cell Stem Cell,* 21**,** 411.

PARSONS, D. W., JONES, S., ZHANG, X., LIN, J. C., LEARY, R. J., ANGENENDT, P., MANKOO, P., CARTER, H., SIU, I. M., GALLIA, G. L., OLIVI, A., MCLENDON, R., RASHEED, B. A., KEIR, S., NIKOLSKAYA, T., NIKOLSKY, Y., BUSAM, D. A., TEKLEAB, H., DIAZ, L. A., JR., HARTIGAN, J., SMITH, D. R., STRAUSBERG, R. L., MARIE, S. K., SHINJO, S. M., YAN, H., RIGGINS, G. J., BIGNER, D. D., KARCHIN, R., PAPADOPOULOS, N., PARMIGIANI, G., VOGELSTEIN, B., VELCULESCU, V. E. & KINZLER, K. W. 2008. An integrated genomic analysis of human glioblastoma multiforme. *Science,* 321**,** 1807-12.

PASTRANA, E., SILVA-VARGAS, V. & DOETSCH, F. 2011. Eyes wide open: a critical review of sphere-formation as an assay for stem cells. *Cell Stem Cell,* 8**,** 486-98.

PATEL, A. P., TIROSH, I., TROMBETTA, J. J., SHALEK, A. K., GILLESPIE, S. M., WAKIMOTO, H., CAHILL, D. P., NAHED, B. V., CURRY, W. T., MARTUZA, R. L., LOUIS, D. N., ROZENBLATT-ROSEN, O., SUVA, M. L., REGEV, A. & BERNSTEIN, B. E. 2014. Single-cell RNA-seq highlights intratumoral heterogeneity in primary glioblastoma. *Science,* 344**,** 1396-401.

PAUL, Y., MONDAL, B., PATIL, V. & SOMASUNDARAM, K. 2017. DNA methylation signatures for 2016 WHO classification subtypes of diffuse gliomas. *Clin Epigenetics,* 9**,** 32.

PEACH, R. J., HOLLENBAUGH, D., STAMENKOVIC, I. & ARUFFO, A. 1993. Identification of hyaluronic acid binding sites in the extracellular domain of CD44. *J Cell Biol,* 122**,** 257-64.

PENUELAS, S., ANIDO, J., PRIETO-SANCHEZ, R. M., FOLCH, G., BARBA, I., CUARTAS, I., GARCIA-DORADO, D., POCA, M. A., SAHUQUILLO, J., BASELGA, J. & SEOANE, J. 2009. TGF-beta increases glioma-initiating cell self-renewal through the induction of LIF in human glioblastoma. *Cancer Cell,* 15**,** 315-27.

PERROT, G., LANGLOIS, B., DEVY, J., JEANNE, A., VERZEAUX, L., ALMAGRO, S., SARTELET, H., HACHET, C., SCHNEIDER, C., SICK, E., DAVID, M., KHRESTCHATISKY, M., EMONARD, H., MARTINY, L. & DEDIEU, S. 2012. LRP-1--CD44, a new cell surface complex regulating tumor cell adhesion. *Mol Cell Biol,* 32**,** 3293-307.

PHILLIPS, H. S., KHARBANDA, S., CHEN, R., FORREST, W. F., SORIANO, R. H., WU, T. D., MISRA, A., NIGRO, J. M., COLMAN, H., SOROCEANU, L., WILLIAMS, P. M., MODRUSAN, Z., FEUERSTEIN, B. G. & ALDAPE, K. 2006. Molecular subclasses of high-grade glioma predict prognosis, delineate a pattern of disease progression, and resemble stages in neurogenesis. *Cancer Cell,* 9**,** 157-73.

PHUPHANICH, S., WHEELER, C. J., RUDNICK, J. D., MAZER, M., WANG, H., NUNO, M. A., RICHARDSON, J. E., FAN, X., JI, J., CHU, R. M., BENDER, J. G., HAWKINS, E. S., PATIL, C. G., BLACK, K. L. & YU, J. S. 2013. Phase I trial of a multi-epitope-pulsed dendritic cell vaccine for patients with newly diagnosed glioblastoma. *Cancer Immunol Immunother,* 62**,** 125-35.

PICCIRILLO, S. G., COLMAN, S., POTTER, N. E., VAN DELFT, F. W., LILLIS, S., CARNICER, M. J., KEARNEY, L., WATTS, C. & GREAVES, M. 2015. Genetic and functional diversity of propagating cells in glioblastoma. *Stem Cell Reports,* 4**,** 7-15.

PICCIRILLO, S. G., COMBI, R., CAJOLA, L., PATRIZI, A., REDAELLI, S., BENTIVEGNA, A., BARONCHELLI, S., MAIRA, G., POLLO, B., MANGIOLA, A., DIMECO, F., DALPRA, L. & VESCOVI, A. L. 2009. Distinct pools of cancer stem-like cells coexist within human glioblastomas and display different tumorigenicity and independent genomic evolution. *Oncogene,* 28**,** 1807-11.

PICCIRILLO, S. G., REYNOLDS, B. A., ZANETTI, N., LAMORTE, G., BINDA, E., BROGGI, G., BREM, H., OLIVI, A., DIMECO, F. & VESCOVI, A. L. 2006. Bone morphogenetic proteins inhibit the tumorigenic potential of human brain tumour-initiating cells. *Nature,* 444**,** 761-5.

PIERCE, G. S., WC. 1988. Tumors as caricatures of the process of tissue renewal: prospects for therapy by directing diferentiation. *Cancer research,* 48**,** 8.

PODERGAJS, N., MOTALN, H., RAJCEVIC, U., VERBOVSEK, U., KORSIC, M., OBAD, N., ESPEDAL, H., VITTORI, M., HEROLD-MENDE, C., MILETIC, H., BJERKVIG, R. & TURNSEK, T. L. 2016. Transmembrane protein CD9 is glioblastoma biomarker, relevant for maintenance of glioblastoma stem cells. *Oncotarget,* 7**,** 593-609.

POLLARD, S. M., YOSHIKAWA, K., CLARKE, I. D., DANOVI, D., STRICKER, S., RUSSELL, R., BAYANI, J., HEAD, R., LEE, M., BERNSTEIN, M., SQUIRE, J. A., SMITH, A. & DIRKS, P. 2009. Glioma stem cell lines expanded in adherent culture have tumor-specific phenotypes and are suitable for chemical and genetic screens. *Cell Stem Cell,* 4**,** 568-80.

PUBCAN 2014. WHO Classification of Tumours.

QUINN T. OSTROM, H. G., JORDAN XU, COURTNEY KROMER, YINGLI WOLINSKY, CAROL KRUCHKO, JILL S. BARNHOLTZ-SLOAN 2016. CBTRUS Statistical Report: Primary Brain and Central Nervous System Tumors Diagnosed in the United States in 2009–2013. *Neuro Oncol,* 18 (suppl 5)**,** v1-v75

QUINTANA, E., SHACKLETON, M., FOSTER, H. R., FULLEN, D. R., SABEL, M. S., JOHNSON, T. M. & MORRISON, S. J. 2010. Phenotypic heterogeneity among tumorigenic melanoma cells from patients that is reversible and not hierarchically organized. *Cancer Cell,* 18**,** 510-23.

QUINTANA, E., SHACKLETON, M., SABEL, M. S., FULLEN, D. R., JOHNSON, T. M. & MORRISON, S. J. 2008. Efficient tumour formation by single human melanoma cells. *Nature,* 456**,** 593-8.

R, B. M. A. E. 2016. alluvial: R Package for Creating Alluvial Diagrams.

RAHMAN, M., AZARI, H., DELEYROLLE, L., MILLETTE, S., ZENG, H. & REYNOLDS, B. A. 2013. Controlling tumor invasion: bevacizumab and BMP4 for glioblastoma. *Future Oncol,* 9**,** 1389-96.

RANSOHOFF, R. M. & ENGELHARDT, B. 2012. The anatomical and cellular basis of immune surveillance in the central nervous system. *Nat Rev Immunol,* 12**,** 623-35.
RAUVALA, H. 1976. Gangliosides of human kidney. *J Biol Chem,* 251**,** 7517-20.
RAVINDRANATH, M. H., TSUCHIDA, T., MORTON, D. L. & IRIE, R. F. 1991. Ganglioside GM3:GD3 ratio as an index for the management of melanoma. *Cancer,* 67**,** 3029-35.
READ, T. A., FOGARTY, M. P., MARKANT, S. L., MCLENDON, R. E., WEI, Z., ELLISON, D. W., FEBBO, P. G. & WECHSLER-REYA, R. J. 2009. Identification of CD15 as a marker for tumor-propagating cells in a mouse model of medulloblastoma. *Cancer Cell,* 15**,** 135-47.
REIFENBERGER, G., BILZER, T., SEITZ, R. J. & WECHSLER, W. 1989. Expression of vimentin and glial fibrillary acidic protein in ethylnitrosourea-induced rat gliomas and glioma cell lines. *Acta Neuropathol,* 78**,** 270-82.
REYA, T., MORRISON, S. J., CLARKE, M. F. & WEISSMAN, I. L. 2001. Stem cells, cancer, and cancer stem cells. *Nature,* 414**,** 105-11.
REYNOLDS, B. A. & VESCOVI, A. L. 2009. Brain cancer stem cells: Think twice before going flat. *Cell Stem Cell,* 5**,** 466-7; author reply 468-9.
REYNOLDS, B. A. & WEISS, S. 1992. Generation of neurons and astrocytes from isolated cells of the adult mammalian central nervous system. *Science,* 255**,** 1707-10.
RICCI-VITIANI, L., LOMBARDI, D. G., PILOZZI, E., BIFFONI, M., TODARO, M., PESCHLE, C. & DE MARIA, R. 2007. Identification and expansion of human colon-cancer-initiating cells. *Nature,* 445**,** 111-5.
RICHARDSON, G. D., ROBSON, C. N., LANG, S. H., NEAL, D. E., MAITLAND, N. J. & COLLINS, A. T. 2004. CD133, a novel marker for human prostatic epithelial stem cells. *J Cell Sci,* 117**,** 3539-45.
RIPPERT, V. 1904. Ueber ein myosarcoma striocellulare des nierenbeckens und des ureters. *Bonn: Geschwulstlehre,* Bonn: Das carcinom des menschen: 1911.
ROESCH, A., FUKUNAGA-KALABIS, M., SCHMIDT, E. C., ZABIEROWSKI, S. E., BRAFFORD, P. A., VULTUR, A., BASU, D., GIMOTTY, P., VOGT, T. & HERLYN, M. 2010. A temporarily distinct subpopulation of slow-cycling melanoma cells is required for continuous tumor growth. *Cell,* 141**,** 583-94.
RUBBEN, A. & ARAUJO, A. 2017. Cancer heterogeneity: converting a limitation into a source of biologic information. *J Transl Med,* 15**,** 190.
SAITO, M., KITAMURA, H. & SUGIYAMA, K. 2001. The specificity of monoclonal antibody A2B5 to c-series gangliosides. *J Neurochem,* 78**,** 64-74.
SANTÉ, M. D. L. 2014. Statistiques des causes de décès pour l'année 2014. *Le Gouvernement du Grand-Ducé de Luxembourg*.
SANZEY, M., ABDUL RAHIM, S. A., OUDIN, A., DIRKSE, A., KAOMA, T., VALLAR, L., HEROLD-MENDE, C., BJERKVIG, R., GOLEBIEWSKA, A. & NICLOU, S. P. 2015. Comprehensive analysis of glycolytic enzymes as therapeutic targets in the treatment of glioblastoma. *PLoS One,* 10**,** e0123544.
SCREATON, G. R., BELL, M. V., JACKSON, D. G., CORNELIS, F. B., GERTH, U. & BELL, J. I. 1992. Genomic structure of DNA encoding the lymphocyte homing receptor CD44 reveals at least 12 alternatively spliced exons. *Proc Natl Acad Sci U S A,* 89**,** 12160-4.
SEIDEL, S., GARVALOV, B. K., WIRTA, V., VON STECHOW, L., SCHANZER, A., MELETIS, K., WOLTER, M., SOMMERLAD, D., HENZE, A. T., NISTER, M., REIFENBERGER, G., LUNDEBERG, J., FRISEN, J. & ACKER, T. 2010. A hypoxic niche regulates glioblastoma stem cells through hypoxia inducible factor 2 alpha. *Brain,* 133**,** 983-95.
SELLERIO, A. L., CIUSANI, E., BEN-MOSHE, N. B., COCO, S., PICCININI, A., MYERS, C. R., SETHNA, J. P., GIAMPIETRO, C., ZAPPERI, S. & LA PORTA, C. A. 2015. Overshoot during phenotypic switching of cancer cell populations. *Sci Rep,* 5**,** 15464.
SHACKLETON, M., QUINTANA, E., FEARON, E. R. & MORRISON, S. J. 2009. Heterogeneity in cancer: cancer stem cells versus clonal evolution. *Cell,* 138**,** 822-9.

SHAPIRO, J. R., YUNG, W. K. & SHAPIRO, W. R. 1981. Isolation, karyotype, and clonal growth of heterogeneous subpopulations of human malignant gliomas. *Cancer Res,* 41**,** 2349-59.

SHEN, Q., GODERIE, S. K., JIN, L., KARANTH, N., SUN, Y., ABRAMOVA, N., VINCENT, P., PUMIGLIA, K. & TEMPLE, S. 2004. Endothelial cells stimulate self-renewal and expand neurogenesis of neural stem cells. *Science,* 304**,** 1338-40.

SHI, X., LENG, L., WANG, T., WANG, W., DU, X., LI, J., MCDONALD, C., CHEN, Z., MURPHY, J. W., LOLIS, E., NOBLE, P., KNUDSON, W. & BUCALA, R. 2006. CD44 is the signaling component of the macrophage migration inhibitory factor-CD74 receptor complex. *Immunity,* 25**,** 595-606.

SHIMOJIMA, M., NISHIMURA, Y., MIYAZAWA, T., KATO, K., TOHYA, Y. & AKASHI, H. 2003. CD56 expression in feline lymphoid cells. *J Vet Med Sci,* 65**,** 769-73.

SILVER, D. J., SINYUK, M., VOGELBAUM, M. A., AHLUWALIA, M. S. & LATHIA, J. D. 2016. The intersection of cancer, cancer stem cells, and the immune system: therapeutic opportunities. *Neuro Oncol,* 18**,** 153-9.

SIMONS, K. & IKONEN, E. 1997. Functional rafts in cell membranes. *Nature,* 387**,** 569-72.

SINGH, S. K., CLARKE, I. D., HIDE, T. & DIRKS, P. B. 2004a. Cancer stem cells in nervous system tumors. *Oncogene,* 23**,** 7267-73.

SINGH, S. K., CLARKE, I. D., TERASAKI, M., BONN, V. E., HAWKINS, C., SQUIRE, J. & DIRKS, P. B. 2003. Identification of a cancer stem cell in human brain tumors. *Cancer Res,* 63**,** 5821-8.

SINGH, S. K., HAWKINS, C., CLARKE, I. D., SQUIRE, J. A., BAYANI, J., HIDE, T., HENKELMAN, R. M., CUSIMANO, M. D. & DIRKS, P. B. 2004b. Identification of human brain tumour initiating cells. *Nature,* 432**,** 396-401.

SKOG, J., WURDINGER, T., VAN RIJN, S., MEIJER, D. H., GAINCHE, L., SENA-ESTEVES, M., CURRY, W. T., JR., CARTER, B. S., KRICHEVSKY, A. M. & BREAKEFIELD, X. O. 2008. Glioblastoma microvesicles transport RNA and proteins that promote tumour growth and provide diagnostic biomarkers. *Nat Cell Biol,* 10**,** 1470-6.

SMITH, S. J., WILSON, M., WARD, J. H., RAHMAN, C. V., PEET, A. C., MACARTHUR, D. C., ROSE, F. R., GRUNDY, R. G. & RAHMAN, R. 2012. Recapitulation of tumor heterogeneity and molecular signatures in a 3D brain cancer model with decreased sensitivity to histone deacetylase inhibition. *PLoS One,* 7**,** e52335.

SOEDA, A., PARK, M., LEE, D., MINTZ, A., ANDROUTSELLIS-THEOTOKIS, A., MCKAY, R. D., ENGH, J., IWAMA, T., KUNISADA, T., KASSAM, A. B., POLLACK, I. F. & PARK, D. M. 2009. Hypoxia promotes expansion of the CD133-positive glioma stem cells through activation of HIF-1alpha. *Oncogene,* 28**,** 3949-59.

SON, M. J., WOOLARD, K., NAM, D. H., LEE, J. & FINE, H. A. 2009. SSEA-1 is an enrichment marker for tumor-initiating cells in human glioblastoma. *Cell Stem Cell,* 4**,** 440-52.

SONG, W., LI, H., TAO, K., LI, R., SONG, Z., ZHAO, Q., ZHANG, F. & DOU, K. 2008. Expression and clinical significance of the stem cell marker CD133 in hepatocellular carcinoma. *Int J Clin Pract,* 62**,** 1212-8.

SOTTORIVA, A., SPITERI, I., PICCIRILLO, S. G., TOULOUMIS, A., COLLINS, V. P., MARIONI, J. C., CURTIS, C., WATTS, C. & TAVARE, S. 2013. Intratumor heterogeneity in human glioblastoma reflects cancer evolutionary dynamics. *Proc Natl Acad Sci U S A,* 110**,** 4009-14.

STEWART, J. M., SHAW, P. A., GEDYE, C., BERNARDINI, M. Q., NEEL, B. G. & AILLES, L. E. 2011. Phenotypic heterogeneity and instability of human ovarian tumor-initiating cells. *Proc Natl Acad Sci U S A,* 108**,** 6468-73.

STIEBER, D., GOLEBIEWSKA, A., EVERS, L., LENKIEWICZ, E., BRONS, N. H., NICOT, N., OUDIN, A., BOUGNAUD, S., HERTEL, F., BJERKVIG, R., VALLAR, L., BARRETT, M. T. & NICLOU, S. P. 2014. Glioblastomas are composed of genetically divergent clones with distinct tumourigenic potential and variable stem cell-associated phenotypes. *Acta Neuropathol,* 127**,** 203-19.

STOLTZ, K., SINYUK, M., HALE, J. S., WU, Q., OTVOS, B., WALKER, K., VASANJI, A., RICH, J. N., HJELMELAND, A. B. & LATHIA, J. D. 2015. Development of a Sox2 reporter system modeling cellular heterogeneity in glioma. *Neuro Oncol,* 17**,** 361-71.

STUPP, R., MASON, W. P., VAN DEN BENT, M. J., WELLER, M., FISHER, B., TAPHOORN, M. J., BELANGER, K., BRANDES, A. A., MAROSI, C., BOGDAHN, U., CURSCHMANN, J., JANZER, R. C., LUDWIN, S. K., GORLIA, T., ALLGEIER, A., LACOMBE, D., CAIRNCROSS, J. G., EISENHAUER, E., MIRIMANOFF, R. O., EUROPEAN ORGANISATION FOR, R., TREATMENT OF CANCER BRAIN, T., RADIOTHERAPY, G. & NATIONAL CANCER INSTITUTE OF CANADA CLINICAL TRIALS, G. 2005. Radiotherapy plus concomitant and adjuvant temozolomide for glioblastoma. *N Engl J Med,* 352**,** 987-96.

SU, W., SIN, M., DARROW, A. & SHERMAN, L. S. 2003. Malignant peripheral nerve sheath tumor cell invasion is facilitated by Src and aberrant CD44 expression. *Glia,* 42**,** 350-8.

SUN, T., CHEN, G., LI, Y., XIE, X., ZHOU, Y. & DU, Z. 2015. Aggressive invasion is observed in CD133-/A2B5+ glioma-initiating cells. *Oncol Lett,* 10**,** 3399-3406.

SUVA, M. L., RIGGI, N., JANISZEWSKA, M., RADOVANOVIC, I., PROVERO, P., STEHLE, J. C., BAUMER, K., LE BITOUX, M. A., MARINO, D., CIRONI, L., MARQUEZ, V. E., CLEMENT, V. & STAMENKOVIC, I. 2009. EZH2 is essential for glioblastoma cancer stem cell maintenance. *Cancer Res,* 69**,** 9211-8.

SVENDSEN, A., VERHOEFF, J. J., IMMERVOLL, H., BROGGER, J. C., KMIECIK, J., POLI, A., NETLAND, I. A., PRESTEGARDEN, L., PLANAGUMA, J., TORSVIK, A., KJERSEM, A. B., SAKARIASSEN, P. O., HEGGDAL, J. I., VAN FURTH, W. R., BJERKVIG, R., LUND-JOHANSEN, M., ENGER, P. O., FELSBERG, J., BRONS, N. H., TRONSTAD, K. J., WAHA, A. & CHEKENYA, M. 2011. Expression of the progenitor marker NG2/CSPG4 predicts poor survival and resistance to ionising radiation in glioblastoma. *Acta Neuropathol,* 122**,** 495-510.

SVENNERHOLM, L. 1963. Chromatographic Separation of Human Brain Gangliosides. *J Neurochem,* 10**,** 613-23.

TAMAKI, S., ECKERT, K., HE, D., SUTTON, R., DOSHE, M., JAIN, G., TUSHINSKI, R., REITSMA, M., HARRIS, B., TSUKAMOTO, A., GAGE, F., WEISSMAN, I. & UCHIDA, N. 2002. Engraftment of sorted/expanded human central nervous system stem cells from fetal brain. *J Neurosci Res,* 69**,** 976-86.

TCHOGHANDJIAN, A., BAEZA, N., COLIN, C., CAYRE, M., METELLUS, P., BECLIN, C., OUAFIK, L. & FIGARELLA-BRANGER, D. 2010. A2B5 cells from human glioblastoma have cancer stem cell properties. *Brain Pathol,* 20**,** 211-21.

TEAM, R. C. 2013. R: A language and environment for statistical computing. R Foundation for Statistical Computing, Vienna, Austria.

TILGHMAN, J., SCHIAPPARELLI, P., LAL, B., YING, M., QUINONES-HINOJOSA, A., XIA, S. & LATERRA, J. 2016. Regulation of Glioblastoma Tumor-Propagating Cells by the Integrin Partner Tetraspanin CD151. *Neoplasia,* 18**,** 185-98.

TIROSH, I., IZAR, B., PRAKADAN, S. M., WADSWORTH, M. H., 2ND, TREACY, D., TROMBETTA, J. J., ROTEM, A., RODMAN, C., LIAN, C., MURPHY, G., FALLAHI-SICHANI, M., DUTTON-REGESTER, K., LIN, J. R., COHEN, O., SHAH, P., LU, D., GENSHAFT, A. S., HUGHES, T. K., ZIEGLER, C. G., KAZER, S. W., GAILLARD, A., KOLB, K. E., VILLANI, A. C., JOHANNESSEN, C. M., ANDREEV, A. Y., VAN ALLEN, E. M., BERTAGNOLLI, M., SORGER, P. K., SULLIVAN, R. J., FLAHERTY, K. T., FREDERICK, D. T., JANE-VALBUENA, J., YOON, C. H., ROZENBLATT-ROSEN, O., SHALEK, A. K., REGEV, A. & GARRAWAY, L. A. 2016a. Dissecting the multicellular ecosystem of metastatic melanoma by single-cell RNA-seq. *Science,* 352**,** 189-96.

TIROSH, I., VENTEICHER, A. S., HEBERT, C., ESCALANTE, L. E., PATEL, A. P., YIZHAK, K., FISHER, J. M., RODMAN, C., MOUNT, C., FILBIN, M. G., NEFTEL, C., DESAI, N., NYMAN, J., IZAR, B., LUO, C. C., FRANCIS, J. M., PATEL, A. A., ONOZATO, M. L., RIGGI, N., LIVAK, K. J., GENNERT, D., SATIJA, R., NAHED, B. V., CURRY, W. T., MARTUZA, R. L., MYLVAGANAM, R., IAFRATE, A. J., FROSCH, M. P., GOLUB, T. R., RIVERA, M. N., GETZ, G., ROZENBLATT-ROSEN, O., CAHILL, D.

P., MONJE, M., BERNSTEIN, B. E., LOUIS, D. N., REGEV, A. & SUVA, M. L. 2016b. Single-cell RNA-seq supports a developmental hierarchy in human oligodendroglioma. *Nature,* 539**,** 309-313.

TODARO, M., ALEA, M. P., DI STEFANO, A. B., CAMMARERI, P., VERMEULEN, L., IOVINO, F., TRIPODO, C., RUSSO, A., GULOTTA, G., MEDEMA, J. P. & STASSI, G. 2007. Colon cancer stem cells dictate tumor growth and resist cell death by production of interleukin-4. *Cell Stem Cell,* 1**,** 389-402.

TOWNSEND, N., WILSON, L., BHATNAGAR, P., WICKRAMASINGHE, K., RAYNER, M. & NICHOLS, M. 2016. Cardiovascular disease in Europe: epidemiological update 2016. *Eur Heart J,* 37**,** 3232-3245.

TREPS, L., PERRET, R., EDMOND, S., RICARD, D. & GAVARD, J. 2017. Glioblastoma stem-like cells secrete the pro-angiogenic VEGF-A factor in extracellular vesicles. *J Extracell Vesicles,* 6**,** 1359479.

UCHIDA, N., BUCK, D. W., HE, D., REITSMA, M. J., MASEK, M., PHAN, T. V., TSUKAMOTO, A. S., GAGE, F. H. & WEISSMAN, I. L. 2000. Direct isolation of human central nervous system stem cells. *Proc Natl Acad Sci U S A,* 97**,** 14720-5.

VARKI, A. 1997. Sialic acids as ligands in recognition phenomena. *FASEB J,* 11**,** 248-55.

VASSILOPOULOS, A., WANG, R. H., PETROVAS, C., AMBROZAK, D., KOUP, R. & DENG, C. X. 2008. Identification and characterization of cancer initiating cells from BRCA1 related mammary tumors using markers for normal mammary stem cells. *Int J Biol Sci,* 4**,** 133-42.

VENTEICHER, A. S., TIROSH, I., HEBERT, C., YIZHAK, K., NEFTEL, C., FILBIN, M. G., HOVESTADT, V., ESCALANTE, L. E., SHAW, M. L., RODMAN, C., GILLESPIE, S. M., DIONNE, D., LUO, C. C., RAVICHANDRAN, H., MYLVAGANAM, R., MOUNT, C., ONOZATO, M. L., NAHED, B. V., WAKIMOTO, H., CURRY, W. T., IAFRATE, A. J., RIVERA, M. N., FROSCH, M. P., GOLUB, T. R., BRASTIANOS, P. K., GETZ, G., PATEL, A. P., MONJE, M., CAHILL, D. P., ROZENBLATT-ROSEN, O., LOUIS, D. N., BERNSTEIN, B. E., REGEV, A. & SUVA, M. L. 2017. Decoupling genetics, lineages, and microenvironment in IDH-mutant gliomas by single-cell RNA-seq. *Science,* 355.

VERHAAK, R. G., HOADLEY, K. A., PURDOM, E., WANG, V., QI, Y., WILKERSON, M. D., MILLER, C. R., DING, L., GOLUB, T., MESIROV, J. P., ALEXE, G., LAWRENCE, M., O'KELLY, M., TAMAYO, P., WEIR, B. A., GABRIEL, S., WINCKLER, W., GUPTA, S., JAKKULA, L., FEILER, H. S., HODGSON, J. G., JAMES, C. D., SARKARIA, J. N., BRENNAN, C., KAHN, A., SPELLMAN, P. T., WILSON, R. K., SPEED, T. P., GRAY, J. W., MEYERSON, M., GETZ, G., PEROU, C. M., HAYES, D. N. & CANCER GENOME ATLAS RESEARCH, N. 2010. Integrated genomic analysis identifies clinically relevant subtypes of glioblastoma characterized by abnormalities in PDGFRA, IDH1, EGFR, and NF1. *Cancer Cell,* 17**,** 98-110.

VERMEULEN, L., DE SOUSA E MELO, F., RICHEL, D. J. & MEDEMA, J. P. 2012. The developing cancer stem-cell model: clinical challenges and opportunities. *Lancet Oncol,* 13**,** e83-9.

VERMEULEN, L., TODARO, M., DE SOUSA MELLO, F., SPRICK, M. R., KEMPER, K., PEREZ ALEA, M., RICHEL, D. J., STASSI, G. & MEDEMA, J. P. 2008. Single-cell cloning of colon cancer stem cells reveals a multi-lineage differentiation capacity. *Proc Natl Acad Sci U S A,* 105**,** 13427-32.

VERMEULEN, P. J., ANTEN, N. P., STUEFER, J. F. & DURING, H. J. 2013. Whole-canopy carbon gain as a result of selection on individual performance of ten genotypes of a clonal plant. *Oecologia,* 172**,** 327-37.

VIRCHOW, R. 1855. Editorial Archiv fuer pathologische Anatomie und Physiologie und fuer klinische Medizin. 8.

VIRCHOW, R. 1863. Die Krankhafte Geschwulste. *Bd I. Berlin: Hirschwald*.

VISVADER, J. E. & LINDEMAN, G. J. 2012. Cancer stem cells: current status and evolving complexities. *Cell Stem Cell,* 10**,** 717-28.

WAINWRIGHT, E. N. & SCAFFIDI, P. 2017. Epigenetics and Cancer Stem Cells: Unleashing, Hijacking, and Restricting Cellular Plasticity. *Trends Cancer,* 3**,** 372-386.

WALSH, J. C., LEBEDEV, A., ATEN, E., MADSEN, K., MARCIANO, L. & KOLB, H. C. 2014. The clinical importance of assessing tumor hypoxia: relationship of tumor hypoxia to prognosis and therapeutic opportunities. *Antioxid Redox Signal,* 21**,** 1516-54.

WANG, J., SAKARIASSEN, P. O., TSINKALOVSKY, O., IMMERVOLL, H., BOE, S. O., SVENDSEN, A., PRESTEGARDEN, L., ROSLAND, G., THORSEN, F., STUHR, L., MOLVEN, A., BJERKVIG, R. & ENGER, P. O. 2008. CD133 negative glioma cells form tumors in nude rats and give rise to CD133 positive cells. *Int J Cancer,* 122**,** 761-8.

WANG, Q., HU, B., HU, X., KIM, H., SQUATRITO, M., SCARPACE, L., DECARVALHO, A. C., LYU, S., LI, P., LI, Y., BARTHEL, F., CHO, H. J., LIN, Y. H., SATANI, N., MARTINEZ-LEDESMA, E., ZHENG, S., CHANG, E., SAUVE, C. G., OLAR, A., LAN, Z. D., FINOCCHIARO, G., PHILLIPS, J. J., BERGER, M. S., GABRUSIEWICZ, K. R., WANG, G., ESKILSSON, E., HU, J., MIKKELSEN, T., DEPINHO, R. A., MULLER, F., HEIMBERGER, A. B., SULMAN, E. P., NAM, D. H. & VERHAAK, R. G. W. 2017. Tumor Evolution of Glioma-Intrinsic Gene Expression Subtypes Associates with Immunological Changes in the Microenvironment. *Cancer Cell,* 32**,** 42-56 e6.

WANG, X., CHEN, L., XIAO, Z., WANG, Y., LIU, T., ZHANG, T. & ZHANG, Y. 2016. Screening glioma stem cells in U251 cells based on the P1 promoter of the CD133 gene. *Oncol Lett,* 12**,** 2457-2462.

WANG, Y., WATERS, J., LEUNG, M. L., UNRUH, A., ROH, W., SHI, X., CHEN, K., SCHEET, P., VATTATHIL, S., LIANG, H., MULTANI, A., ZHANG, H., ZHAO, R., MICHOR, F., MERIC-BERNSTAM, F. & NAVIN, N. E. 2014. Clonal evolution in breast cancer revealed by single nucleus genome sequencing. *Nature,* 512**,** 155-60.

WARD, R. J., LEE, L., GRAHAM, K., SATKUNENDRAN, T., YOSHIKAWA, K., LING, E., HARPER, L., AUSTIN, R., NIEUWENHUIS, E., CLARKE, I. D., HUI, C. C. & DIRKS, P. B. 2009. Multipotent CD15+ cancer stem cells in patched-1-deficient mouse medulloblastoma. *Cancer Res,* 69**,** 4682-90.

WEBER, G. F., ASHKAR, S., GLIMCHER, M. J. & CANTOR, H. 1996. Receptor-ligand interaction between CD44 and osteopontin (Eta-1). *Science,* 271**,** 509-12.

WEI, Y., JIANG, Y., ZOU, F., LIU, Y., WANG, S., XU, N., XU, W., CUI, C., XING, Y., LIU, Y., CAO, B., LIU, C., WU, G., AO, H., ZHANG, X. & JIANG, J. 2013. Activation of PI3K/Akt pathway by CD133-p85 interaction promotes tumorigenic capacity of glioma stem cells. *Proc Natl Acad Sci U S A,* 110**,** 6829-34.

WEIGMANN, A., CORBEIL, D., HELLWIG, A. & HUTTNER, W. B. 1997. Prominin, a novel microvilli-specific polytopic membrane protein of the apical surface of epithelial cells, is targeted to plasmalemmal protrusions of non-epithelial cells. *Proc Natl Acad Sci U S A,* 94**,** 12425-30.

WEIL, R. J. 2006. Glioblastoma multiforme--treating a deadly tumor with both strands of RNA. *PLoS Med,* 3**,** e31.

WEN, J., REN, C., HUANG, N., LIU, Y. & ZENG, R. 2015. Draft genome of bagasse-degrading bacteria Bacillus aryabhattai GZ03 from deep sea water. *Mar Genomics,* 19**,** 13-4.

WHITFIELD, M. L., SHERLOCK, G., SALDANHA, A. J., MURRAY, J. I., BALL, C. A., ALEXANDER, K. E., MATESE, J. C., PEROU, C. M., HURT, M. M., BROWN, P. O. & BOTSTEIN, D. 2002. Identification of genes periodically expressed in the human cell cycle and their expression in tumors. *Mol Biol Cell,* 13**,** 1977-2000.

WOLANCZYK, M., HULAS-BIGOSZEWSKA, K., WITUSIK-PERKOWSKA, M., PAPIERZ, W., JASKOLSKI, D., LIBERSKI, P. P. & RIESKE, P. 2010. Imperfect oligodendrocytic and neuronal differentiation of glioblastoma cells. *Folia Neuropathol,* 48**,** 27-34.

WU, B., SUN, C., FENG, F., GE, M. & XIA, L. 2015. Do relevant markers of cancer stem cells CD133 and Nestin indicate a poor prognosis in glioma patients? A systematic review and meta-analysis. *J Exp Clin Cancer Res,* 34**,** 44.

WU, Z., HAN, Y., LI, Y., LI, X., SUN, T., CHEN, G., HUANG, Y., ZHOU, Y. & DU, Z. 2016. MiR-218-5p inhibits the stem cell properties and invasive ability of the A2B5(+)CD133(-) subgroup of human glioma stem cells. *Oncol Rep,* 35**,** 869-77.

YAN, H., PARSONS, D. W., JIN, G., MCLENDON, R., RASHEED, B. A., YUAN, W., KOS, I., BATINIC-HABERLE, I., JONES, S., RIGGINS, G. J., FRIEDMAN, H., FRIEDMAN, A., REARDON, D., HERNDON, J., KINZLER, K. W., VELCULESCU, V. E., VOGELSTEIN, B. & BIGNER, D. D. 2009. IDH1 and IDH2 mutations in gliomas. *N Engl J Med,* 360**,** 765-73.

YANAGISAWA, M. 2011. Stem cell glycolipids. *Neurochem Res,* 36**,** 1623-35.

YANG, Z. F., HO, D. W., NG, M. N., LAU, C. K., YU, W. C., NGAI, P., CHU, P. W., LAM, C. T., POON, R. T. & FAN, S. T. 2008. Significance of CD90+ cancer stem cells in human liver cancer. *Cancer Cell,* 13**,** 153-66.

YASAKA, N., FURUE, M. & TAMAKI, K. 1995. CD44 expression in normal human skin and skin tumors. *J Dermatol,* 22**,** 88-94.

YEH, S. C., WANG, P. Y., LOU, Y. W., KHOO, K. H., HSIAO, M., HSU, T. L. & WONG, C. H. 2016. Glycolipid GD3 and GD3 synthase are key drivers for glioblastoma stem cells and tumorigenicity. *Proc Natl Acad Sci U S A,* 113**,** 5592-7.

YIN, A. H., MIRAGLIA, S., ZANJANI, E. D., ALMEIDA-PORADA, G., OGAWA, M., LEARY, A. G., OLWEUS, J., KEARNEY, J. & BUCK, D. W. 1997. AC133, a novel marker for human hematopoietic stem and progenitor cells. *Blood,* 90**,** 5002-12.

YIN, D., OGAWA, S., KAWAMATA, N., TUNICI, P., FINOCCHIARO, G., EOLI, M., RUCKERT, C., HUYNH, T., LIU, G., KATO, M., SANADA, M., JAUCH, A., DUGAS, M., BLACK, K. L. & KOEFFLER, H. P. 2009. High-resolution genomic copy number profiling of glioblastoma multiforme by single nucleotide polymorphism DNA microarray. *Mol Cancer Res,* 7**,** 665-77.

YU, H., ALFSEN, A., TUDOR, D. & BOMSEL, M. 2008. The binding of HIV-1 gp41 membrane proximal domain to its mucosal receptor, galactosyl ceramide, is structure-dependent. *Cell Calcium,* 43**,** 73-82.

YU, Y., FLINT, A., DVORIN, E. L. & BISCHOFF, J. 2002. AC133-2, a novel isoform of human AC133 stem cell antigen. *J Biol Chem,* 277**,** 20711-6.

YUAN, G. L., ZOU, P., CHENG, F. J., LIU, L. B., WU, X. F. & WANG, H. X. 2004. [Expansion of marrow hematopoietic progenitor cells ex vivo supported by culture system from mouse marrow embryonic fibroblasts and leukemia inhibitory factor]. *Zhongguo Shi Yan Xue Ye Xue Za Zhi,* 12**,** 807-11.

ZAGZAG, D., AMIRNOVIN, R., GRECO, M. A., YEE, H., HOLASH, J., WIEGAND, S. J., ZABSKI, S., YANCOPOULOS, G. D. & GRUMET, M. 2000. Vascular apoptosis and involution in gliomas precede neovascularization: a novel concept for glioma growth and angiogenesis. *Lab Invest,* 80**,** 837-49.

ZAPPERI, S. & LA PORTA, C. A. 2012. Do cancer cells undergo phenotypic switching? The case for imperfect cancer stem cell markers. *Sci Rep,* 2**,** 441.

ZHANG, S., BALCH, C., CHAN, M. W., LAI, H. C., MATEI, D., SCHILDER, J. M., YAN, P. S., HUANG, T. H. & NEPHEW, K. P. 2008. Identification and characterization of ovarian cancer-initiating cells from primary human tumors. *Cancer Res,* 68**,** 4311-20.

ZHANG, W., CHEN, H., LV, S. & YANG, H. 2016. High CD133 Expression Is Associated with Worse Prognosis in Patients with Glioblastoma. *Mol Neurobiol,* 53**,** 2354-60.

ZHOU, B. B., ZHANG, H., DAMELIN, M., GELES, K. G., GRINDLEY, J. C. & DIRKS, P. B. 2009. Tumour-initiating cells: challenges and opportunities for anticancer drug discovery. *Nat Rev Drug Discov,* 8**,** 806-23.

ZHU, T. S., COSTELLO, M. A., TALSMA, C. E., FLACK, C. G., CROWLEY, J. G., HAMM, L. L., HE, X., HERVEY-JUMPER, S. L., HETH, J. A., MURASZKO, K. M., DIMECO, F., VESCOVI, A. L. & FAN, X. 2011. Endothelial cells create a stem cell niche in glioblastoma by providing NOTCH ligands that nurture self-renewal of cancer stem-like cells. *Cancer Res,* 71**,** 6061-72.

ZHU, Y., YU, J., WANG, S., LU, R., WU, J. & JIANG, B. 2014. Overexpression of CD133 enhances chemoresistance to 5-fluorouracil by activating the PI3K/Akt/p70S6K pathway in gastric cancer cells. *Oncol Rep,* 32**,** 2437-44.

ZOLLER, M. 2011. CD44: can a cancer-initiating cell profit from an abundantly expressed molecule? *Nat Rev Cancer,* 11**,** 254-67.

ZOZULYA, A. L., REINKE, E., BAIU, D. C., KARMAN, J., SANDOR, M. & FABRY, Z. 2007. Dendritic cell transmigration through brain microvessel endothelium is regulated by MIP-1alpha chemokine and matrix metalloproteinases. *J Immunol,* 178**,** 520-9.